Process Development for the Manufacture of an Integrated Dispenser Cathode Assembly Using Laser Chemical Vapor Deposition

A Thesis
Presented to
The Academic Faculty

by

Ryan William Johnson

In Partial Fulfillment
of the Requirements for the Degree
Doctor of Philosophy

School of Mechanical Engineering
Georgia Institute of Technology
May 2005

Process Development for the Manufacture of an Integrated Dispenser Cathode Assembly Using Laser Chemical Vapor Deposition

Approved by:

Dr. W. Jack Lackey, Advisor
School of Mechanical Engineering
Georgia Institute of Technology

Dr. David Rosen
School of Mechanical Engineering
Georgia Institute of Technology

Dr. Pradeep K. Agrawal
School of Chemical Engineering
Georgia Institute of Technology

Dr. Suresh Sitaraman
School of Mechanical Engineering
Georgia Institute of Technology

Dr. Andrei Fedorov
School of Mechanical Engineering
Georgia Institute of Technology

Dr. Thomas Starr
School of Chemical Engineering
University of Louisville

Date Approved: 7 December 2004

This body of work is dedicated to my wife Alisha. She has worked many long, stressful hours while I pursued this dream, and throughout, she always remained by biggest supporter. Her love and support has been unwavering and unconditional. Her positive attitude and willingness to listen is infinite. She is my best friend, and I will cherish her love and support forever.

ACKNOWLEDGEMENTS

The process of pursuing a Ph.D. requires the contributions of many people. My advisor, Dr. Jack Lackey has served as a mentor and guide throughout this process. He has patiently answered many questions (some of the same ones multiple times) and taught me numerous lessons about academics, research, and life. My decision to do my Ph.D. under his guidance was undoubtedly one of the best decisions I will ever make. He has been an inspiration and a role model that I will never forget.

In addition to Dr. Lackey, I thank my Ph.D. Reading Committee members for their input and suggestions during this process. The members were Dr. Pradeep Agrawal, Dr. Andrei Fedorov, Dr. David Rosen, Dr. Suresh Sitaraman, and Dr. Thomas Starr.

I must thank all the current and former members of Georgia Tech's CVD/LCVD lab, especially Dr. Chad Duty and Dr. Dan Jean. Chad and Dan welcomed me into the lab and spent many hours transferring their knowledge and understanding of the LCVD process to me. They provided guidance about the graduate school process and they fostered an environment in our lab that made learning and research truly enjoyable. Dr. MingXuan Jiang also spent significant time helping me learn the procedures of materials analysis and characterization. Mr. Tarek Elkhatib, Mr. Joshua Gillespie, and Ms. Jian Mi all worked closely with me to use and maintain the LCVD equipment. Their efforts are greatly appreciated.

I must say a special thanks to Dr. Scott Bondi. Sharing an office with him for 4+ years made for many experiences and conversations that I will always cherish. We spent many long, frustrating hours in the lab fixing equipment and discussing the world's problems. His friendship made this process infinitely more enjoyable and fulfilling. For that, I am grateful.

Many people helped me learn the processes of materials characterization by making

their time and equipment available. Dr. Lisa Detter–Hoskin of GTRI gave me both training and access to her SEM and other characterization equipment. Mr. Michael Haluska prepared and performed X–ray diffraction studies of LCVD samples.

Some experimental procedures required the skills and equipment of others. Dr. Paul Kohl gave me access to his nitrogen glove box for transferring $MoCl_5$ powder into the sublimation chamber. Due to various equipment malfunctions and operator errors, his student, Dr. Ketack Kim, had to help me with this 5 times. I am grateful for his patience and assistance with that process.

A special thanks to the National Science Foundation who through its IGERT Fellowship Program and Georgia Tech's TI:GER Program provided an expansive education in innovation and technology commercialization along with financial support for two years. I am also thankful for the Manufacturing Education Program Fellowship of Georgia Tech's Manufacturing Research Center and the Sam Nunn International Security Fellowship of Georgia Tech's School of International Affairs, both of which provided rewarding educational opportunities and financial support during my graduate studies.

Family and friends outside of the immediate academic environment also contributed greatly to this process. My wife's family has provided support and encouragement throughout. I must especially recognize Dr. David Steadman who gave much needed guidance and wisdom about the Ph.D. process.

My immediate family has patiently supported my efforts through all 22 years of my formal education. I must thank my parents Jim and Jean Johnson who, with the help of God, made this whole thing possible. Their love and support throughout my life has given me the confidence to pursue ambitious goals. I do not believe there are any better parents in the world.

TABLE OF CONTENTS

LIST OF TABLES

LIST OF FIGURES

SUMMARY

Laser chemical vapor deposition, or LCVD, is an advanced fabrication process that offers many unique advantages. The process is a derivative of traditional chemical vapor deposition (CVD). It works by using a laser to locally heat a substrate in the presence of a reagent gas mixture. The heat enables a localized surface deposition reaction. By manipulating the relationship between the laser and the substrate, a variety of different structures can be grown. The two most basic structures are vertical fibers and horizontal lines.

One promising application of LCVD is in the fabrication of an integrated dispenser cathode assembly. This is a cathode device used primarily as the emission source in a class of vacuum tubes termed microwave power tubes. These tubes are used as amplifiers in high powered RF circuits such as those found in radar, satellite communications, and UHF television broadcasting systems. The current fabrication methods for these devices are tedious and expensive. The performance of the devices, and ultimately, the systems they support, is limited by the current fabrication process. LCVD offers the ability to decrease the cost and increase the performance of dispenser cathodes by enabling the fabrication of smaller, more complex assemblies in one continuous, automated manufacturing process.

This investigation focuses on advancing the capability of the LCVD process towards building a dispenser cathode device. The study incorporates experiments, analysis, and computational modeling to better understand the complexities of the LCVD process and simultaneously increase its capability. Three materials are studied: carbon, boron nitride, and molybdenum.

Carbon deposition is used to characterize the LCVD process through a series of designed experiments. The data is fit to both phenomenological and theoretical models for

use in the development of process planning algorithms. The knowledge gained is used in conjunction with an advanced temperature control system to enable deposition of the first uniform, multi–layered, carbon wall structures via LCVD. LCVD carbon fibers are analyzed using X-ray diffraction and found to be crystalline with a hexagonal microstructure very similar to pyrolytic graphite.

Furthermore, the carbon deposition experiments provide the foundation for advanced computational modeling simulations. Models are developed using the computational fluid dynamics (CFD) code, FLUENT, that incorporate heat transfer, fluid flow, and species transport in a single integrated modeling environment. The models are used to study the carbon deposition process. Insight is gained into the relationships among the process parameters and the deposition rates and deposition rate profiles. Phenomena such as thermal diffusion and the relative importance of mass convection and mass diffusion are explored. A designed set of model cases is executed and the results used to develop a simple polynomial expression for relating experiment conditions to deposit attributes.

Structural models are created in the finite element code ANSYS. The models are motivated by the finding that many carbon LCVD structures exhibit significant internal cracking. The cause of the cracks is believed to be thermal stress induced during the deposition process. In order to better understand the implications of the extreme temperature gradients that exist during LCVD, a thermal simulation of a carbon fiber during growth is created. The temperature levels and profiles within the deposit are shown to be strongly influenced by the properties of the deposit material. The results of the thermal analyses are used as loads in a structural analysis. Results show that the magnitude of thermally–induced stress within LCVD structures can greatly exceed the strength of the deposited materials. Both the carbon deposition rate models and carbon fiber thermal–structural models serve to improve the understanding and control of the LCVD process.

The second phase of the current study focuses on the deposition and analysis of the two materials required in the dispenser cathode assembly: boron nitride (BN) and molybdenum

(Mo). Experimental development of both materials proceeds along a general development path whereby LCVD fiber growth is used to learn, analyze, control, and characterize each new material system. After successful fiber growth, line growth is investigated. Finally, composite line growth is studied whereby alternating sections of BN and Mo are deposited per the requirements of the dispenser cathode application.

Boron nitride growth from borazine is found to have a dynamic transition period as growth begins on the surface. At the surface, the reaction is very unstable and sporadic, but as significant deposit forms, it becomes more stable. Throughout the process, the BN deposition temperature remains very sensitive to input laser power. Some of the dynamic behavior at the substrate surface is attributed to differences in substrate and deposit material properties, while some is found inherent in the process itself.

Successful BN fiber growth is accomplished by manually controlling the laser power to maintain a fixed deposition temperature. Formal designed experiments show BN deposition to be a transport–limited process. A theoretical upper limit of deposition rate is computed from species transport equations using an identical CFD model as was used to study carbon deposition. The upper limits computed in the model show good agreement with experimentally measured values. The shape of deposition rate profiles for this transport–limited process are found to be significantly different from those of a kinetically–limited process. Factors such as thermal diffusion and reagent flow rate are shown to have a large effect on deposition rates.

BN line growth is studied using successful conditions from BN fiber growth. The sporadic and unstable growth at the substrate surface makes control and repeatability of the process difficult. The utility of the optimized fiber growth conditions is minimized by the importance of these surface effects. Some success is found by using a constant laser power during each layer of growth, but the deposition temperature remains very sensitive to the power level. BN wall growth is further complicated by the sporadic nature of the growth process and tends to produce arrays of fibers rather than smooth, layered walls.

Molybdenum LCVD from $MoCl_5$ is shown to be a sensitive, but stable process. The growth rate for Mo is much slower than for either carbon or boron nitride. Efforts to increase growth rate focus on both transport and kinetic parameters. Increases in transport variables such as flow rate are plagued by the formation of extraneous powder and debris on the substrate surface around the deposition zone. Efforts to increase temperature are limited on the low end by the machine instrumentation, and on the high end by substrate surface damage.

Molybdenum line deposition is explored using the best conditions found from Mo fiber experiments. Due to the slow growth rate, the lines are very thin, but the growth process remains stable and sensitive. The lines are shown to be electrically conductive. The same limiting factors pertinent to increasing Mo fiber growth rates applies to lines.

The deposition of a ceramic–metal laminate is demonstrated by producing a BN-Mo composite. The composite experiments use conditions derived from the most successful line conditions for each individual material. BN line growth is shown to be the most difficult part of the composite fabrication due to its sporadic nature. The very slow rate of Mo growth limits the practicality of the process. Limitations and potential improvements to Georgia Tech's LCVD system for producing composites of this type are identified.

Experimentally, this work represents the most advanced study reported of LCVD fabrication of layered structures. This is an important growth mode of LCVD that has practical application in producing integrated dispenser cathode assemblies. For the first time, LCVD of boron nitride is well characterized, while controlled molybdenum deposition is achieved. The materials are combined into one of the first examples of ceramic–metal composites produced using LCVD.

CHAPTER I

INTRODUCTION

1.1 The Laser Chemical Vapor Deposition Process

Laser Chemical Vapor Deposition, or LCVD, is a fabrication process capable of producing small, complex devices from a variety of materials. As the name implies, LCVD is a derivative of the traditional Chemical Vapor Deposition (CVD) process. CVD is a thermally driven coating process normally used to produce thin film metallic or ceramic materials. The process works by heating an object known as a substrate in the presence of specific reagent gases to the temperature necessary for surface reactions. In CVD, the substrate surface temperature is nearly uniform which results in a thin film coating over the entire substrate.

LCVD employs a localized CVD reaction to generate patterns or structures by using the energy of a laser beam to induce a chemical reaction on the substrate surface. By using a laser with a sufficiently small beam diameter and manipulating the laser or substrate appropriately, one can draw patterns on the substrate surface or grow vertical structures away from the surface. Figure 1.1 illustrates the different methods of growth LCVD enables.[1]

LCVD processes are divided into two categories based on how the photons in the laser beam interact with the gas and substrate during the process. The first category is photolytic LCVD where the reagent gas molecule–photon interaction causes the molecule to dissociate and the resulting solid particulate is deposited onto a nearby substrate. This process is essentially a homogenous reaction with some degree of spatial control enabled by the locality of the reaction in and around the laser beam.[2]

The second category of LCVD is pyrolytic. Here, a laser is used to locally heat the substrate to the necessary temperature to cause the surface reaction. Ideally, in pyrolytic

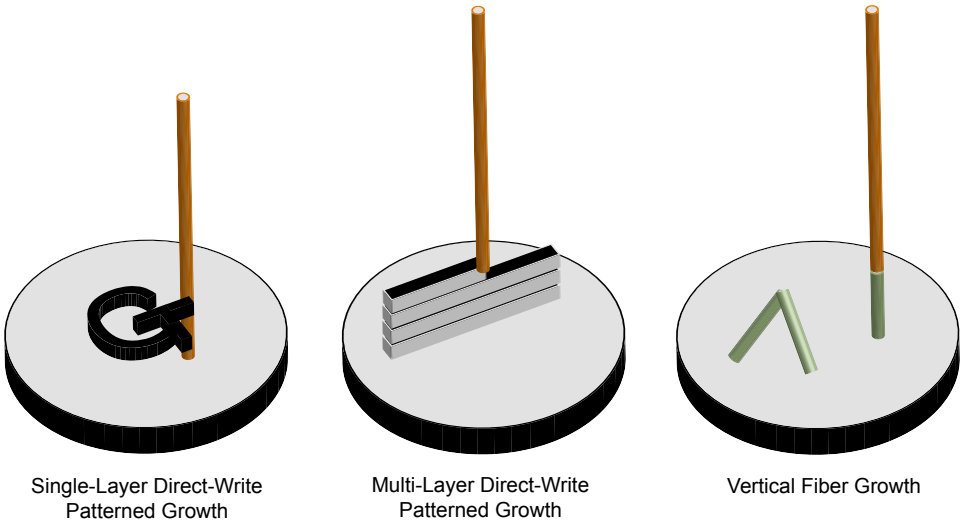

Figure 1.1: Different growth modes enabled by LCVD

LCVD there are no interactions between the laser beam and the reagent gas molecules (i.e., the absorbtion of the laser beam radiation by the reagent gas is minimized). The temperature rise induced by the photon interaction with the substrate surface is designed to initiate a surface reaction.

As with CVD, LCVD can be used to deposit a wide variety of engineering materials. Table 1.1 provides a list of these materials taken from the review article by Duty et al.[3] The material flexibility of the process makes LCVD an attractive technology for a vari-

Table 1.1: Different types of materials deposited using the LCVD process

Metals	Ceramics
Aluminum (Al)	Aluminum Oxides (Al_xO_y)
Boron (B)	Boron Nitride (BN)
Copper (Cu)	Boron Nitrogen Carbides ($B_xN_yC_z$)
Iron (Fe)	Carbon (C)
Molybdenum (Mo)	Silicon Carbide (SiC)
Nickel (Ni)	Silicon Nitrides (Si_xN_y)
Silicon (Si)	Titanium Carbide (TiC)
Titanium (Ti)	Titanium Nitride (TiN)
Tungsten (W)	Tungsten Carbide (WC)

ety of applications. One limitation that precludes certain materials from being deposited is the high temperature involved with the deposition reaction. Both the substrate and the deposited material must be capable of tolerating the reaction temperature without degradation. The materials used in the LCVD process are therefore particularly well suited to high temperature applications.

1.2 Applications of LCVD

The first LCVD deposits were reported by Nelson and Richardson in 1972 and consisted of carbon fibers or rods.[4] The direct write nature of the process provides tremendous flexibility and many applications were soon envisioned. Researchers became interested in the use of LCVD for the fabrication or repair of electronic circuits or photolithography masks.[5] However, the flexibility of any vector–driven direct write process comes at a cost of speed. The need to trace every feature using one dimensional strokes is time consuming which makes the process impractical for large scale manufacturing operations. LCVD did find some limited application in repairing damaged electrical circuits;[6–8] however, the scales of electronic circuitry eventually exceeded the minimum resolution achievable with the process.

The recent interest in LCVD is driven by ongoing research thrusts towards miniaturization and mass customization. There are micro and nano-scale research initiatives both in the United States and worldwide. The impetus for this scaling down varies depending on the device, but can include among others, increased energy efficiency (enabling battery/-portable usage), increased speed, increased reliability, decreased manufacturing costs, and "systems on a chip" ideas. Because LCVD offers the attractive ability to deposit both metal and ceramic materials in complex three dimensional patterns on scales approaching 10 μm, it is an ideal candidate for the fabrication of some of these miniature devices. Mass customization is the ability to use computer–aided manufacturing systems to produce custom output on a low–cost high–volume basis.

The primary limitation to the use of LCVD has been related to the difficulty in producing consistent, geometrically uniform parts. Much proof of concept work has been done for the deposition of different materials in many different shapes and structures. However, most of the success reported has relied on operator experience and or educated guesswork rather than robust process planning and control algorithms. It can be said that LCVD is not yet understood well enough for widespread commercial applications. However, there are currently at least four areas of potential application highlighted in the literature: photonic band gap structures, solar cells, microelectromechanical systems (MEMS), and electron emission devices.

Photonic band gap structures are devices that are used to filter, amplify, or otherwise control high frequency electromagnetic waves such as light. The devices consist of arrays of three dimensional structures whose size, spacing, and feature type are chosen based on the frequency of radiation the device will manipulate. Wanke[9] and Dean[10] have both shown success in using LCVD to deposit photonic band gap structures. Hixson[11] et al. have explored the deposition of solar cell arrays using LCVD. The flexibility of the LCVD process would enable the placement of small patterns of solar cells on sensors and other small devices, relieving the need for other on-board energy sources. Different types of MEMS devices have been made using LCVD as shown by both Maxwell[12] and Williams.[13] They both have fabricated micro-scale solenoids, motors, and springs using LCVD, thus illustrating the potential use of LCVD in the MEMS world. Finally, several research groups have focused on building various types of electron emission devices using the LCVD process. Bjorklund[14] has reported the fabrication of arrays of single crystal tungsten fibers to be used for field emission applications. Fuhrman[15] and Duty[2] have both worked towards the production of a thermionic emission device using LCVD.

1.2.0.1 Dispenser Cathodes

The present work focuses on developing the LCVD process to fabricate a complex metal-ceramic device termed an integrated dispenser cathode assembly. Cathode devices are used as the electron sources in electron guns. Dispenser cathodes find a wide range of applications in electron gun devices, but are particularly prevalent in the area of microwave power tubes. Microwave power tubes are a broad class of vacuum tubes used to amplify radio frequency (RF) signals to extremely high power levels. Such tubes find use in UHF-TV transmission, shipboard and ground-based radar, weapons guidance systems, electronic countermeasure systems, satellite communications, tropospheric scatter communications, and fusion research. Figure 1.2 is a schematic of a microwave power tube that uses a dispenser cathode.

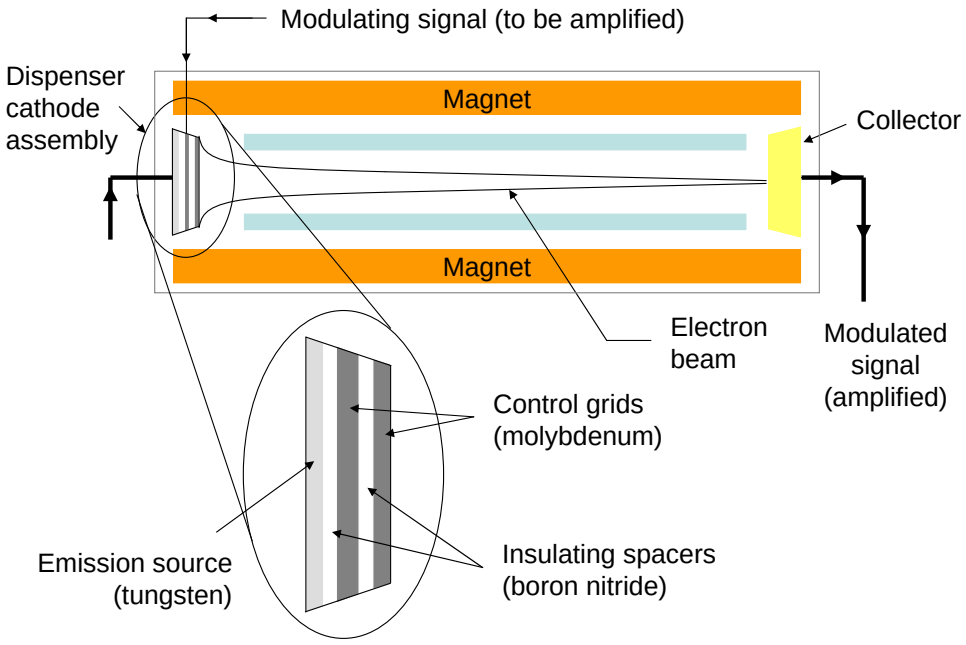

Figure 1.2: Schematic of microwave power tube with dispenser cathode assembly

The dispenser cathode assembly within the microwave tube is composed of an electron emission material, ceramic insulators, and refractory metal conductors. Most dispenser cathodes use a bulk emission material of a porous refractory metal, usually tungsten (approximately 80% density), impregnated with barium calcium aluminate in one of several

ratios.[16] Sometimes, the impregnated tungsten is also sputter coated with an osmium–ruthenium alloy or iridium to improve performance. A second configuration sometimes used is to put a reservoir of barium calcium aluminate behind a plug of the porous emitting material. In either case, the concept is that at the elevated temperatures of operation (1000–1200°C), the barium calcium aluminate will react with the tungsten releasing barium which migrates to the emitting surface helping to reduce the work function of the emitter. In essence, the emission efficiency of the refractory metal is significantly increased by the presence of barium.

The cathode assembly contains one or two "control grids" used to modulate the current output of the device. These grids are placed very close to the cathode surface for enhanced electrical performance, and due to the elevated temperatures of operation, are required to be made of a refractory metal, often molybdenum. The grids have a pattern of holes or voids which are designed to help shape the emerging electron beam.

In order to maintain electrical isolation between the tungsten emission material and the control grids, insulating spacers are inserted between the surfaces. These electrical insulators must be thermally conductive to assist in the cooling of the metal control grids. The material must also be dimensionally stable under extreme temperature cycling so as to maintain the proper separation between the control grids and the emission material without distortion. One of the few materials offering high electrical resistance and low thermal resistance is boron nitride.

An integrated cathode-grid assembly has been conceived as a promising application of LCVD technology. Figure 1.3 illustrates the specifications of a potential device. In concept, this structure serves as an ideal example of the type of device LCVD is suited to produce. It exhibits complex geometry on a small scale and requires the precise deposition of both ceramic and metal materials. The surface of a dispenser cathode is often concave as shown in Figure 1.3 (b). This shape is chosen to help in the formation of a compact beam yielding desirable current profiles, and is characteristic of all Pierce type electron guns. While

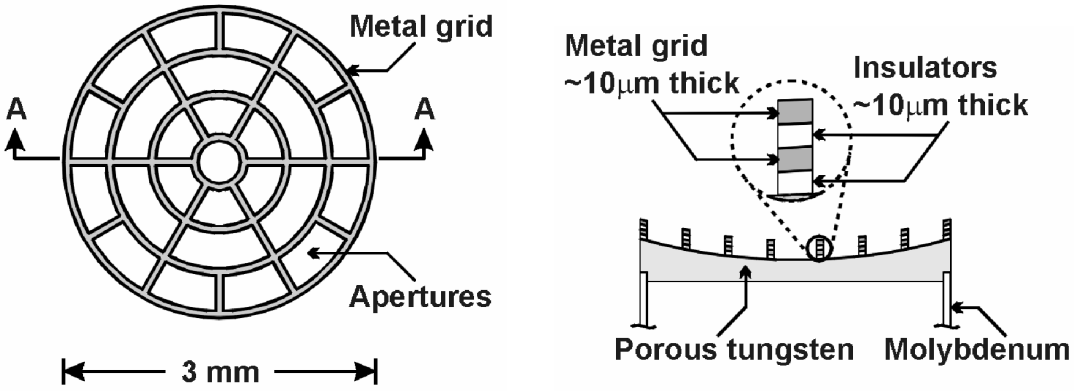

(a) Top View **(b) Side View**

Figure 1.3: Dispenser cathode assembly to be fabricated using LCVD

some layer–based fabrication processes or techniques might struggle to accommodate this feature, the flexibility of LCVD enabled by use of vapor phase reagents easily supports the geometry.

The current method of fabricating a dispenser cathode assembly of the type shown in Figure 1.3 involves several complex steps. First, the metal control grids are made using some type of machining process such as EDM. Next, the cathode unit is assembled manually by stacking the insulating spacers on the tungsten and then the control grid on the spacers. If a second control grid is desired, an additional layer of spacers and grid is added. After the unit is assembled, it is clamped together, and an external cage assembly is welded in place to hold the unit intact. Due to the scale of these assembly operations, they are often done underneath a microscope. Assembly and welding operations on this scale are difficult and expensive. Moreover, the complexity and performance of potential dispenser cathode designs is limited by the current fabrication process. More intricate geometries with more closely spaced components could theoretically offer superior performance. In sum, there is both an economic and performance incentive to develop a new process capable of making dispenser cathode assemblies. Others have done some preliminary "proof of concept" work that inspired the current investigation.[2,15]

1.3 Fundamental Concepts

At its core, LCVD is a complex process. A review of its most fundamental aspects can provide valuable insight into its dynamics. The equations governing deposition processes include the mass continuity equation, the momentum transport equation, the energy transport equation, and the species transport equation(s). In conjunction with these fundamental equations, additional concepts apply. Near the substrate surface, the analysis focuses on the balance between diffusion of reagents to the surface and the overall kinetics of the reaction.

The LCVD process starts with the introduction of a mixture of reagent and carrier gases into the system. As these gases heat up and begin to interact amongst themselves, both homogenous and heterogenous chemical reactions begin to occur. Most chemical reactions proceed through complicated mechanisms whereby tens or hundreds of simultaneous gas phase reactions involving tens or hundreds of species can occur simultaneously. While the details of these reaction mechanisms are often unknown, the overall process can be approximated by simple stoichiometric reactions. The reactions proceed toward thermodynamic equilibrium at some finite rate given by the chemical kinetics.

On the molecular level, the surface deposition reaction involves several important steps. First, one or more of the species molecules containing the desired elements in the deposit must diffuse through the boundary layer above the substrate towards the surface. The species that ultimately diffuses to the substrate surface might be either one of the original reagent species or a different species that resulted from a homogenous reaction. Next, the species molecule must adsorb onto the substrate surface. After a finite amount of time, having remained in the necessary energy state, a portion of the adsorbed molecules will dissociate into the desired product while yielding byproducts. The byproducts must then desorb from the surface and diffuse away from the deposition zone yielding a site for another adsorbed molecule. Figure 1.4 illustrates these different steps. Any one of these steps can be the “rate–limiting” step in the process.

The common framework for CVD analysis, which is also applicable to LCVD, involves

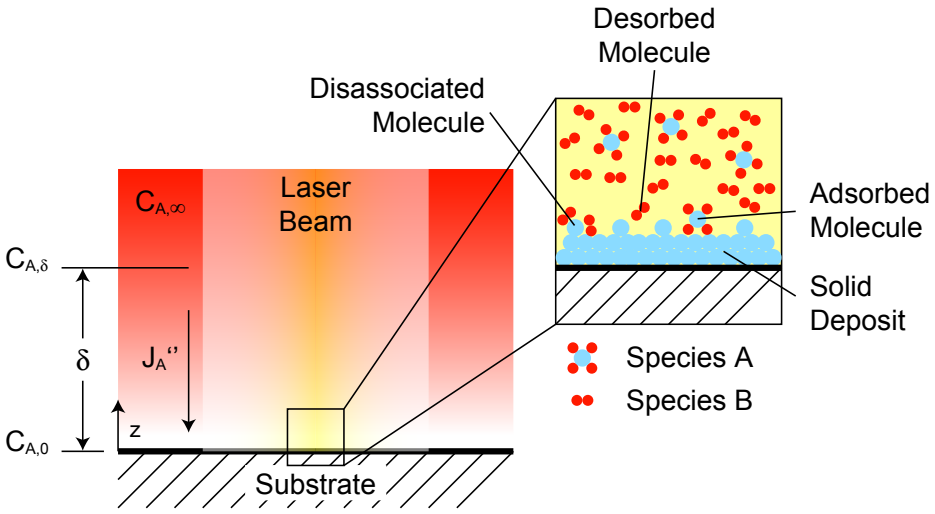

Figure 1.4: Diffusion and molecular dynamics of LCVD

the consideration of two different rate–limiting regimes. The first regime is transport–limited wherein the reaction rate is limited by the transport of the primary reagent species to the surface. The second regime is kinetically–limited which implies that the chemical kinetics are slower than the transport processes, and the reaction rate is limited by energy or temperature. These two rate–limiting regimes become very distinct when plotting experimental data with the natural log of reaction rate plotted against the inverse temperature. Such a plot is termed an Arrhenius plot, an example of which is shown in Figure 1.5.

The two rate–limiting regimes are distinguished by the slopes of the lines within them. At high temperatures, the reaction rate is moderately sensitive to temperature as indicated by the slope on the left side of the plot. This is the transport–limited regime. A variety of transport mechanisms can be involved in moving the reagent species to the substrate surface (or the gaseous reaction products away from the surface) depending upon the reactor configuration and the process conditions. The two most prevalent transport modes are convection and diffusion. Convective transport is that due to the bulk motion of the fluid while diffusive transport is the molecular transport mode that arises due to concentration gradients within a fluid. The zero slip boundary condition of a fluid at a surface dictates that as molecules near the surface, convective transport becomes less important and diffusion

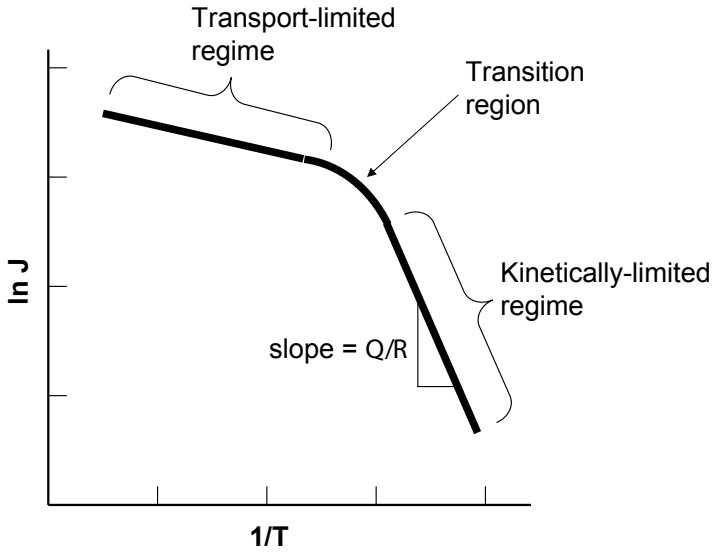

Figure 1.5: Arrhenius plot showing the rate–limiting regimes

due to concentration gradients becomes the primary driving force. As such, it is important to understand conceptually the diffusion process.

In the simplified one-dimensional situation depicted in Figure 1.4, with only two species present in the gas mixture, the diffusion of reagent gases through the boundary layer is given conceptually in one dimension by Fick's Law.

$$\vec{J}_A = -D_{AB}\frac{dC_A}{dz} \tag{1.1}$$

Fick's Law states that the molar rate of diffusion in the z direction of a species (A) through a domain is proportional to the concentration gradient dC_A/dz. The degree of proportionality is given by the diffusivity, D_{AB}. For a binary system involving two species, A and B, in which species A is considered dilute, a first order relation of D_{AB} to total pressure P and temperature T is given by:[17]

$$D_{AB} \sim P^{-1}\,T^{3/2} \tag{1.2}$$

The moderate relation to temperature shown in the transport–limited regime of Figure 1.5 is an implication of the relationship between mass diffusivity and temperature.

We can envision a simple case of diffusion through a boundary layer of thickness δ where δ is defined as the distance from the substrate surface to a point in the bulk fluid

where $C_A = 0.99 C_{A,\infty}$ where $C_{A,\infty}$ is the concentration of species A in the bulk fluid. If we define $C_{A,0}$ to be the concentration of species A at the substrate surface, the concentration gradient through this boundary layer is thus approximated:

$$\frac{dC_A}{dz} \approx \frac{C_{A,\infty} - C_{A,0}}{\delta} \tag{1.3}$$

and Equation 1.1 becomes:

$$\vec{J}_A = \frac{-D_{AB}}{\delta}(C_{A,\infty} - C_{A,0}) \tag{1.4}$$

The quantity $-D_{AB}/\delta$ is sometimes referred to as the mass transfer coefficient, k_t, thus,

$$\vec{J}_A = k_t(C_{A,\infty} - C_{A,0}) \tag{1.5}$$

As temperature (or energy) decreases from left to right on the Arrhenius plot, the rate–limiting mechanism transitions from transport to kinetic.

At low temperatures, the reaction rate will be highly sensitive to temperature as indicated by the steep slope on the right side of the plot in Figure 1.5. This is the kinetically–limited regime. Within this region, the reaction rate is limited not by a lack of reagent species, but by the amount of energy in the system. Increasing the energy in the system directly and exponentially effects the reaction rate. The common equation for expressing a surface reaction is the expression:

$$J''_A = k_r C^n_{A,0} \tag{1.6}$$

which states that the reaction rate, J''_A, is proportional to the concentration of the reactant species at the surface, $C_{A,0}$, to some power, n, where n is the order of the reaction. J''_A can be thought of as the net rate of creation or destruction of species A, and if the stoichiometric ratio of reagent A to solid deposit is 1:1, the J''_A is equivalent to the molar rate of deposition. The rate constant, k_r is given by the Arrhenius expression:

$$k_r = k_0 e^{\frac{-Q}{RT}} \tag{1.7}$$

where k_0 represents the pre–exponential factor, Q is the activation energy, R is the universal gas constant, and T is the absolute reaction temperature.

Assuming a first order reaction (n = 1), Equation 1.6 can be rearranged and solved for $C_{A,0}$ and the result plugged into Equation 1.5 yielding:

$$\vec{J_A} = k_t(C_{A,\infty} - \frac{J''_A}{k_r}) \tag{1.8}$$

During deposition, a balance must exist between the rate of molar flux to the substrate surface due to transport and the surface molar reaction rate ($\vec{J_A} = J''_A$); Equation 1.8 can thus be rewritten:

$$\vec{J_A} = \frac{C_{A,\infty}}{\left(\frac{1}{k_t} + \frac{1}{k_r}\right)} \tag{1.9}$$

A useful interpretation of Equation 1.9 is to consider both the transport process and the kinetic process to each have a resistance expressed by $1/k_t$ and $1/k_r$, respectively. If the mass transfer coefficient k_t is small compared to k_r, the transport resistance term dominates the reaction rate equation. Whereas if k_t is large compared to k_r, the kinetic resistance dominates. Thus, a comparison of k_t to k_r for a given process gives insight into identification of the rate–limiting regime.

The existence of a transport–limited and a kinetically–limited regime has many practical implications for deposition processes.[18] The primary goal of industrial CVD processes it to produce uniform coatings of material at a reasonable rate. The simplest strategy for maximizing deposition rate might be to increase temperature as much as possible and move to the far left of the Arrhenius plot. This strategy would seem to have the additional benefit of making the process somewhat less sensitive to temperature variations throughout the CVD chamber. However, operating in the transport–limited regime causes the geometry of the CVD reactor to strongly influence the uniformity of the deposited coatings through its effect on the transport boundary layer characteristics. The limitations on the geometric arrangement within the reactor prohibit the parallel processing of large batches of substrates. In order to reduce the sensitivity of coating uniformity to geometry, the reactor pressure can be reduced significantly to enhance diffusive transport and force the kinetics to become

rate–limiting. It is normally possible to design a chamber and a controller that yields a uniform reaction chamber temperature which allows for uniform deposition rates throughout the system and high packing factors for substrates.

These two rate–limiting regimes also have a profound impact on the LCVD process. The energy source in LCVD is a laser. The energy from the laser must be directed and focused in order to achieve the desired laser spot size and position on the substrate. The laser spot size dictates the minimum in–plane feature size achievable with the process. The optics involved present the typical trade–off between laser spot size and Rayleigh range. The Rayleigh range is important because it represents the axial distance over which the minimum laser beam diameter remains relatively constant. This Rayleigh range must be larger in magnitude than the resolution of the substrate positioning system so that the substrate surface can remain within the Rayleigh range during deposition.

Laser beams typically emerge from their source with some type of non-uniform energy profile. Gaussian shaped beams are common. These are beams whose energy flux is represented by Equation 1.10.[19]

$$P(r) = \frac{2P_0}{\pi R_0^2} e^{\frac{-2r^2}{R_0^2}} \tag{1.10}$$

where P_0 is the nominal laser power, R_0 is the $1/e^2$ radius of the laser beam, and r is the radial distance from the center of the laser spot. The nonuniform energy flux induces a nonuniform temperature field on the surface of the substrate. This complex temperature field is one of the primary differences between LCVD and CVD and has many implications.

Due to the extremely nonisothermal conditions in and around the laser spot, both transport–limited and kinetically–limited regimes could co–exist at different positions in the same deposit area. Nonetheless, on an aggregate scale it is likely that certain LCVD processes will be governed by transport limitations while others are governed by kinetic limitations. In addition to influencing the overall deposition rate, the rate–limiting regime can strongly effect the shape of the deposit. For example the cross–sectional profile of a line deposit could be significantly different depending upon the operating regime. With a thorough

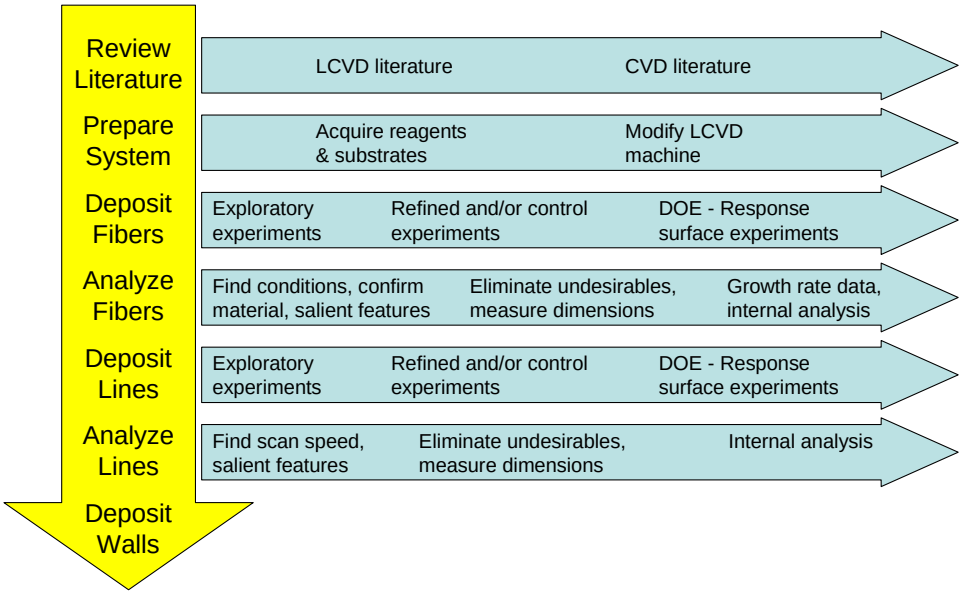

Figure 1.6: Experimental development path of a typical LCVD material

understanding of the relationship between the processing parameters and the rate–limiting regime, one might manipulate the process so as to force operation in a particular regime depending upon the desired deposition rate and deposit characteristics. Such characteristics are often dictated by the application of interest. The link between the rate–limiting regime and LCVD deposit shape is a central theme of this research.

1.4 Proposed Research

The research to be done will focus on utilization and understanding of the LCVD process and Georgia Tech's LCVD equipment in the fabrication of the integrated dispenser cathode assembly described in Section 1.2.0.1. Toward that end, a combination of experimental, analytical, and computational modeling work will be executed. Details of the proposed work are presented below.

1.4.1 Experimental Development Path

Figure 1.6 illustrates how the experimental development of a typical LCVD material proceeds. On the left, the large downward arrow indicates the major phases of experimental

development. Out to the right beside each major phase are some of the tasks associated with that phase. Naturally, the first phase in the experimental development process is the literature review. The literature review focuses on previous work in the LCVD of the material of interest and if prior work does not exist, the CVD literature can be used for reference. The literature review yields which precursors have successfully been used to deposit the material and the conditions at which the deposition occurred.

Next, the LCVD system is prepared for deposition of the new material. The preparation involves the acquisition of new reagent chemicals, and if the reagents are not in the vapor phase at room temperature, the acquisition or fabrication of the equipment needed to vaporize the chemical. Depending upon the application, the substrate material must be chosen and acquired. Substrate preparation involves cutting and polishing to a uniform and repeatable surface condition. Also, depending upon specific requirements of a material and its reagents, the LCVD system may have to be modified. Modifications can include adding of heaters or changing the gas delivery system to accommodate additional equipment.

The substantial portion of the experimental development path begins with the fiber deposit experiments. Vertical growth in the form of straight fibers is the least complicated deposition process because the dynamics of a transient substrate surface are not involved. The experiments begin with exploratory experiments designed to confirm the feasibility of the process and find suitable conditions for deposition. Typically, these experiments are analyzed using optical and scanning electron microscopy (SEM) to identify any unique features of the deposited structures and confirm the presence of the desired elements.

Once a preliminary understanding of the process develops, more refined experiments are executed. Refined experiments are those that involve the systematic variation of different parameters within the apparent experimental operating boxes. The goal of refined experiments is to reduce the occurrence of undesirable deposit features. These experiments are also used to explore the use of Georgia Tech's automatic temperature control subsystem with the particular reagent–material system. The refined experiment deposits are analyzed

similar to the exploratory experiments, but additional quantitative measurements (e.g. fiber height, fiber diameter, etc.) are also performed.

Finally, as the deposition of fibers matures, formal designed experiments are used to identify the optimum growth conditions and study the growth rates of the deposits. The analysis of the formal experiments typically includes the dissection of some of the deposits to investigate the internal microstructure. When possible, more advanced analysis techniques such as X-ray diffraction (XRD) and TEM are used to study the crystalline structure of deposits.

The second fundamental growth mode of LCVD is line or patterned growth. This phase of experimental development often begins after the conditions for depositing fibers are well understood. Line deposition proceeds along a very similar path to fibers with some differences due to the new parameters inherent in line growth. Wall deposition follows the successful growth of single–layer lines and normally requires some degree of automatic temperature control to counter the positive feedback nature of multi–layered processes.

1.4.2 Experiments

While not directly necessary for the fabrication of an integrated dispenser cathode assembly, some carbon deposition and analysis will be done. In terms of the experimental development path, carbon is a mature material. The knowledge surrounding carbon deposition provides an excellent framework for gaining deeper insight into the mechanisms of LCVD. This existing knowledge base combined with experimental capability and more sophisticated monitoring and control systems provide an incentive to use carbon deposition as a vehicle for learning more about the LCVD process in general. The goal is to transfer the capabilities and understanding of the carbon LCVD process to the other material systems as they mature.

Experimental work involving carbon has two goals. First, line deposition and particularly multi–line or wall deposition process will be thoroughly investigated. Only recently

have control strategies emerged that suggest multilayered LCVD structures might be practical. The work will focus on building geometrically uniform carbon walls. Second, a series of carbon fiber experiments will be performed as part of a kinetics study. More refined kinetic data are needed for the development of fully integrated deposition rate models. Some of the carbon line and fiber deposition work will provide an experimental database for use in formulating process–property relationships for carbon LCVD structures.

Several major experimental steps are necessary in the pursuit of LCVD dispenser cathode fabrication. The first step is to expand upon Duty's deposition of boron nitride (BN) from the borazine reagent by designing and executing a comprehensive set of experiments. As described previously, dispenser cathodes normally employ a porous refractory metal as the bulk emission material, thus tungsten substrates will be used for the deposition. The dynamics of depositing a ceramic material, BN, on a metal substrate, W, will be a central theme of these studies. The requirements of the boron nitride material to be used in the dispenser cathode are multifaceted.

The shape of the deposits is critical. The shape suggested by Figure 1.3 is a boron nitride line (or wall) of rectangular cross–section with width on the order of 100 μm and a height on the order of 10 μm. Perfectly rectangular cross–sectioned lines are nearly prohibited by the physics of the LCVD process, but it is desirable to find process conditions that permit approaching this shape. In addition to the cross sectional shape, the cross section must remain uniform throughout the length of the line. Uniform lines have historically been difficult to accomplish in LCVD without sophisticated real–time process control. Other properties of the boron nitride are of significant importance to the dispenser cathode application: adhesion of boron nitride to the tungsten substrate, mechanical strength, electrical resistivity, and thermal conductivity. The investigative process for boron nitride deposition will follow the experimental road map presented in Section 1.4.1, beginning with fiber deposition and proceeding to line and/or wall deposition.

Subsequently, the same experimental process will be used for the deposition of molybdenum from molybdenum pentachloride ($MoCl_5$) and hydrogen (H_2). Duty also showed some success depositing molybdenum on different substrates, and his work is the starting point for the proposed investigation. The dispenser cathode requires that molybdenum be deposited on boron nitride substrates. The implications of depositing a metal material on a ceramic substrate will be an important aspect of this process. The required shape of the molybdenum deposits is very similar to that of the boron nitride deposits: lines with 100 μm wide by 10 μm tall cross sections remaining uniform along the line length. Other properties of importance include the adhesion to the BN substrate, mechanical integrity, and electrical conductivity.

After successful deposition of the boron nitride and molybdenum separately, experiments will be performed to determine the feasibility of directly depositing a $BN-Mo$ composite on a tungsten substrate as is specified for the integrated dispenser cathode assembly. Limited work has been done in the LCVD of multi-material laminates, particularly metal-ceramic laminates. Important questions arise when considering the deposition of a metal–ceramic composite using this process. One issue that is immediately obvious is how materials with different coefficients of thermal expansion (CTE), like metals and ceramics, might react when heated to high temperatures by the laser. Will it be possible to deposit a ceramic onto a metal substrate (or metal on ceramic) and obtain acceptable adherence? Will the resulting deposits have structural integrity? These questions are crucial measures of the ability of LCVD to achieve its stated advantages as a manufacturing process.

In sum, the ultimate goal of the boron nitride and molybdenum experimental work will be to produce lines of the appropriate size and shape required by the dispenser cathode application. Toward this end, a series of experiments will be performed, beginning with fiber deposition, moving on to line and perhaps wall deposition, and finally to the deposition of a metal–ceramic laminate.

1.4.3 Modeling

While LCVD process research has been ongoing for years, there are still aspects of this process that are not understood and have not been thoroughly studied. The published models of the LCVD process have historically focused on certain aspects of the process while ignoring or greatly minimizing the significance of other aspects. In terms of deposition rates and profiles, more comprehensive computational models of the LCVD process will be developed that will incorporate fluid flow, heat transport, mass transport, thermodynamics, and chemical kinetics.

The comprehensive models, to be developed in the CFD package FLUENT, will provide valuable information about the critical parameters of the LCVD process. Specifically, the models will be used to predict the shapes of deposited structures. The surface profile of LCVD deposits is governed by the reaction limiting mechanism. The reaction rate limiting mechanism can be either transport or kinetic in nature. Combining convective flow, thermal effects, species diffusion, and chemical kinetics into the same modeling environment provides a comprehensive means of studying the overall effects of the different process parameters on deposition rates and deposit shapes. The models will be verified by comparing experimentally observed temperature profiles with model results and by comparing deposit measurements to those predicted by the models. The information gained through the models will supplement that gained through experimentation, thus complementing the research process.

The extreme temperature gradients known to exist in LCVD due to the laser heating process bring concerns about the structural integrity of the underlying substrate or deposit material. In fact, evidence has shown that in some material systems, significant cracks develop within deposited structures.[20] No work has been done to study the thermal and thermally induced stress and strain fields within an LCVD deposit during growth. A computational model using the finite element method (FEM) will be developed using the ANSYS software package to study the temperatures within an LCVD fiber during growth.

These temperatures will be used as the loading function in a thermal stress analysis to determine the magnitude and orientation of stresses within the fiber during growth. The predicted stress state will be compared with the experimentally observed crack patterns within LCVD deposits.

In sum, the proposed modeling research has two major goals. First, an advanced integrated deposition rate and deposition rate profile modeling environment will be created in FLUENT and used to study the LCVD process of different material systems. Second, the ANSYS FEM code will be used to build a structural model of an LCVD fiber to study the interaction of the temperature and stress fields within the deposit during growth.

CHAPTER II

LITERATURE REVIEW AND PRIOR WORK

In an effort to gain the understanding necessary to propel LCVD into commercial adoption, several research groups are actively investigating different aspects of the technology. Several comprehensive reviews have been presented in the literature regarding the progression and status of LCVD research. Mazumder and Kar have provided a text that covers many of the fundamental aspects of laser–based deposition processes.[21] Baum and Comita summarized the deposition of metals using LCVD, with an emphasis on electronic applications.[5] Duty et al. provided a more recent review of the status of LCVD research with an emphasis on process control techniques.[3] The goal here is to review those topics most pertinent to the use of LCVD for fabrication of an integrated dispenser cathode device.

2.1 Materials

Many different materials have been deposited using LCVD.[3] Generally, any traditional CVD reaction can be replicated in an LCVD environment after making some adjustments. The materials studied by LCVD researchers have evolved as the technology and envisioned applications of LCVD have changed. Three materials were deposited during the execution of this work: carbon, boron nitride, and molybdenum.

2.1.1 Carbon

Carbon was the first,[4] and is one of the most common, materials deposited with LCVD. The wide range of conditions under which carbon deposition occurs combined with the availability of the hydrocarbon reagents as well as their limited toxicity make carbon deposition an ideal process for research. Carbon can be deposited in many different forms

under a wide range of conditions.

Some have investigated the use of a laser–based CVD process for on–line coating of optical fibers.[22,23] The fiber is made to pass through an atmosphere of methane, butane, propane, or some other hydrocarbon wherein a laser irradiates the fiber causing a carbon deposition reaction. The carbon produced is typically partially disordered with a preference for depositing with the $\langle 001 \rangle$ direction perpendicular to the surface of the substrate.

Others have grown complex carbon shapes by manipulating the laser–substrate relationship.[24] Pegna used an Ar^+ laser with ethylene reagent over a pressure range of 100–500 Torr to grow angled carbon fibers. Maxwell grew both straight carbon fibers and coiled carbon springs from ethylene at pressures of 1–11 bar.[12] This high pressure LCVD process enabled carbon linear growth rates of over 12 cm/s.[10]

A variety of reagent systems have been used to deposit carbon in LCVD. One such system uses methane and hydrogen reagent gases to deliver the carbon atoms into the chamber. The overall reaction for the methane process is given by Equation 2.1.

$$CH_4(g) + \text{xs } H_2(g) \rightarrow C(s) + 2H_2(g) + \text{xs } H_2(g) \tag{2.1}$$

Extensive carbon LCVD work has also been done in Georgia Tech's LCVD apparatus. Jean used both propylene and methane reagent systems in conjunction with a novel temperature control system to fabricate carbon fibers and lines.[1,25] He studied the kinetics of carbon LCVD and developed a variety of process–property relationships. A thermodynamic analysis was done that yielded insight into the cause of the volcano effect for carbon deposition. Finally, he utilized the feedback temperature control system to produce carbon fiber truss structures which helped demonstrate the geometric flexibility of the LCVD process.

Johnson et al. has also done extensive work in Georgia Tech's LCVD system on carbon line and wall deposition.[26] He has used the advanced temperature control system to produce the most uniform multi–layered carbon walls seen in the literature. Johnson and

Park have done work supporting the development of process planning parameters for carbon deposition.[27,28] Studies were done for both carbon fibers and carbon lines that related the deposit size and shape to the processing conditions. More details of this work are given in Chapter 4, because some of the work was done in support of the current investigation.

2.1.2 Boron Nitride

Boron nitride is a ceramic material that offers a variety of unique properties.[29,30] The material has high chemical inertness and a high melting point. It is often used for its good dielectric properties in conjunction with its high thermal conductivity. Compared to other materials with similar properties such as diamond, boron nitride adheres very well to some metals. Heated crucibles, microwave guide tubes, and high temperature electrical insulators are common applications of BN. Its properties make boron nitride the ideal material for the integrated dispenser cathode control grid insulator application.

Boron nitride can have different microstructures much like carbon. Boron nitride has an amorphous phase, a hexagonal crystal (h-BN) phase analogous to graphite, a turbostratic microstructure (t-BN) analogous to turbostratic carbon, and a cubic crystal structure (c-BN) analogous to diamond. In fact, comparisons between boron nitride and carbon, particularly c-BN and diamond are common in the literature.

2.1.2.1 CVD of Boron Nitride

CVD is often used to deposit pyrolytic boron nitride coatings. These coatings are usually a combination of mostly h-BN, with some t-BN and amorphous BN.[30] Pyrolytic BN exhibits few pores, high purity, extreme chemical inertness, high thermal conductivity, extremely high dielectric strength, reasonable resistance to oxidation, and negligible outgassing. The CVD of boron nitride is done under a variety of conditions using a variety of reagent gas systems. Variations on the traditional CVD methods have also been employed in efforts to encourage the deposition of BN with particular properties or crystal structures.

The two reagent species commonly used in boron nitride deposition are boron trichloride (BCl_3) plus ammonia (NH_3) and borazine ($B_3N_3H_6$). The BCl_3 is perhaps the most common reagent system, but researchers have had little success using this system in LCVD.[15] The reaction of interest in the current work is the borazine decomposition reaction.

Borazine ($B_3N_3H_6$) is a ring shaped molecule closely resembling benzene. It is a liquid at room temperature but quickly decomposes. Storing the liquid at or below 0°C reduces the rate of the decomposition significantly. Boron nitride deposition from borazine occurs via the following overall reaction:

$$B_3N_3H_6(g) + \text{xs } N_2(g) \rightarrow 3BN(s) + 3H_2(g) + \text{xs } N_2(g) \tag{2.2}$$

Researchers have been intrigued by the possibility of depositing BN from borazine for several reasons.[31] First, borazine has the correct 1:1 stoichiometric ratio of boron to nitrogen for BN deposition and thus offers a single reagent source for the process. Second, borazine thermally decomposes at relatively low temperatures which gives the potential for pyrolysis to open the ring structure and form a linear molecule on the substrate surface.[32] Third, borazine has a relatively high vapor pressure allowing it to be easily transported into a CVD furnace. The primary disadvantage of using borazine for BN deposition is its instability, high cost, and limited availability.

Adams deposited BN films on silicon substrates in a hot wall, low pressure CVD reactor from borazine.[33] No additional carrier or diluent gases were used. Borazine was stored and used at 0°C and delivered to the substrate via a needle valve. Pressures were varied from 0.1 to 0.8 Torr and temperatures from 300-650°C. Deposition rates were seen to increase from about 3 Å/min to 25 Å/min as temperature increased from 300 to 550°C. Deposition rates then quickly declined as reagent depletion due to deposition on furnace walls became important. Apparent activation energy for the low temperature range was given to be 9.6 kcal/mol and the deposition rate was observed to increase with the square root of borazine partial pressure. The BN films deposited from borazine between 300 and 450°C were shown to be unstable over time as they readily reacted with atmospheric moisture.

Gomez-Aleixandre deposited BN from a mixture of diborane (B_2H_6) and ammonia (NH_3).[29,34] In the work, a discussion of the reaction mechanisms for BN deposition in different temperature ranges is presented. Borazine is shown to be an intermediate species if the initial B_2H_6:NH_3 ratio is 1:2 and deposition temperature is $> 775^{\circ}$C. It is not known for sure that borazine is the molecular precursor for deposition but based on its stoichiometric ratio and the near stoichiometric ratio of the resulting film, it seems plausible. Gomez-Aleixandre states that through heating of the borazine molecule a progressive loss of hydrogen leads to boron nitride. The activation energy of BN deposition from the borazine precursor at temperatures between 775 and 850°C is reported to be 35 kcal/mol. The BN films deposited in this temperature range are said to be dense and stable.

Rye has used an interesting hot filament activated CVD process with borazine reagent to deposit a combination of transparent amorphous BN and opague polycrystalline h-BN.[35] The process involves heating a tungsten filament in close proximity to the substrate to a high temperature (1400°C) and using the radiative heat from the filament to heat a local area on the substrate surface to between 100 and 400°C. He varies the substrate temperature by varying the distance between the substrate and the filament. Amorphous BN grows on the lower temperature substrate, while h-BN deposition occurs on the high temperature filament. Rye notes that at the 0.1 Torr of borazine dynamic pressure used, the BN deposition rate is extremely sensitive to the filament to substrate distance.

Demin has reported depositing BN films in a cold wall reactor from the $B_3N_3H_6$ plus N_2 system at temperatures from $1300 - 1750^{\circ}$C.[30] Total pressure was made to vary from $1 - 10$ Torr. Throughout the temperature range studied, a strong relationship between gas flow rate and deposition rate existed. Also, the deposition rate increased approximately linearly with increasing partial pressure of borazine. Both of these observations indicated the reaction was transport–limited. The composition of the BN films was shown to be about 80% h-BN at 1300°C and increased with increasing temperature and/or increasing borazine partial pressure.

Kouvetakis reported on a study of BN deposition from borazine using hot walled, cold walled, and plasma enhanced reactor configurations.[36] He varied the substrate temperature between 475 and 550°C. The borazine was kept at -45°C and the bubbler helium flow was 5 sccm yielding a borazine partial pressure of 0.2 Torr. Total flow rates were about 30 sccm and the total pressure was BN 2 Torr. Growth rates were about 25 Å/min at 500°C. The resulting amorphous films were consistently boron rich with a B:N ratio of about 60:40. Using the in situ gas sampling mass spectrometer he identifies an empirical relationship corresponding to the chemical equation below.

$$B_3N_3H_6(g) \rightarrow B_3N_2(s) + \frac{1}{2}N_2(g) + 3H_2(g) \tag{2.3}$$

Researchers have also investigated various plasma enhanced CVD (PECVD) processes as a means of depositing BN films. Plasma enhanced processes are often seen as a way to achieve CVD quality films without requiring the high temperatures typical of many CVD processes. Plasmas are also thought to provide an effective means of breaking the borazine molecule enabling efficient BN deposition.

In a derivative of his traditional CVD work, Kouvetakis used a plasma enhanced process that yielded stoichiometric, hexagonal polycrystalline BN films with higher growth rates (50-75 Å/min vs 25 Å/min) than the strictly thermal process.[36]

Kane presented results of BN film deposition on silicon using a PECVD process.[37] His flow rates were 25 sccm of $B_3N_3H_6$ and 500 sccm total flow. The pressure was 2 Torr and the substrate temperature was 400°C. Growth rates were on the order of 300 Å/min. The result was a stoichiometric film with an index of refraction of 1.73, a dielectric constant of 4.1, breakdown potential of 7–8 MV/cm and a residual stress of 4.2×10^8 Pa.

Nguyen also used a PECVD system to deposit BN films on Si wafers from borazine. His flow rates were 100 sccm for borazine and 200 sccm for N_2. The process pressure was 3 Torr and the substrate temperature was 300°C. The process yielded a stoichiometric film that grew at 300 nm/min. The index of refraction was 1.746, the density was 1.89 g/cm^3, the dielectric constant was 3.8-5.7, and the breakdown potential was 6 to 7 MV/cm. The

structure of the film was largely amorphous, however traces of hexagonal and cubic BN appeared. Film stresses were determined to be between -2x10^8 and -4x10^8 Pa.

Kosinova has used remote plasma enhanced CVD (RPECVD) with an additional d.c. electric bias to deposit BN from borazine.[38] The deposition temperatures ranged from 373 - 823 K and the partial pressure of borazine ranged between 3x10^{-3} and 5x10^{-5} Torr. The RF (40.68 MHz) power was held constant at 0.2 W/cm^3 and the d.c. bias voltage ranged from 0 to 220 V. The resulting films were predominantly polycrystalline h-BN.

Smirnova has also used RPECVD in a borazine charged system.[39] His temperature values were 473 and 873 K and his borazine pressures ranged from 4 to 8 Pa. He reported the formation of a thin (2 nm) layer of amorphous BN between the surface of the Si substrate and the outer polycrystalline layer. The outer layer was formed of a mostly h-BN film with about 15% c-BN at rates from 0.4 to 4 nm/min.

Other more elaborate experiments have also been used to deposit BN from borazine reagent. Kim has presented work based on helicon wave plasma assisted CVD of boron nitride films from borazine.[40,41] His work represents one of the few cases where films of predominantly c-BN were successfully deposited from borazine. Paisley reported on use of microwave electron cyclotron resonance plasma CVD to deposit BN on Si from borazine.[42] His conditions yielded films consisting of mixed composition of amorphous, hexagonal, and cubic phases of BN. A Ni sputtered substrate surface showed no difference than bare Si, while an Al sputtered surface showed enhanced deposition of h-BN. Molian used a combination of laser ablation and photolytic LCVD to deposit BN films from borazine.[32] Shanfield and Wolfson used an ion beam setup to deposit BN from ionized borazine.[43]

2.1.2.2 LCVD of Boron Nitride

Some researchers have attempted Laser CVD of boron nitride using one of the reagent systems described above. Notably, Furhman[15] investigated BN deposition in Georgia Tech's

LCVD system using the boron trichloride plus ammonia reaction:

$$BCl_3(g) + NH_3(g) \rightarrow BN(s) + 3HCl(g) \tag{2.4}$$

His experiments resulted in no BN formation but an abundance of white powder deposited throughout the inside of the LCVD chamber. A thermodynamic analysis showed the white powder to likely be an ammonium chloride salt (NH_4Cl) that forms at temperatures below 600 K when mixing BCl_3 and NH_3. He concluded that due to this undesirable reaction, deposition of BN from the boron trichloride and ammonia system was not feasible in Georgia Tech's LCVD system.

Duty used boron trichloride and nitrogen in Georgia Tech's LCVD system.[2,44]

$$2BCl_3(g) + N_2(g) + \text{xs } H_2(g) \rightarrow 2BN(s) + 6HCl(g) \tag{2.5}$$

He executed experiments under a variety of conditions with several different substrates. He determined that high leak rates (> 0.10 Torr/min) led to the formation of salts similar to those observed by Fuhrman. After reducing the leak rate, most of his experiments yielded no significant deposit. However, a subset of trials with no nitrogen reagent did result in pure boron fibers rather than BN .

Some research into the LCVD of BN from borazine as in Equation 2.2 has been reported and has shown great potential. Ugarov used an excimer laser to induce deposition of BN films on silicon substrates.[31] His setup utilized a substrate heater to provide the majority of energy input while a KrF excimer laser with 20 ns pulses of 248 nm radiation at frequencies up to 50 Hz provided the marginal energy input required for deposition. For a near optimal laser fluence of 15 J/cm^2, his results indicated that deposition occurred at substrate temperatures less than 25°C and the deposition rate did not depend significantly upon substrate temperature until the temperature exceeded 100°C. Deposition rate then increased with increasing temperature up to a maximum value around 230°C after which it decreased with increasing temperature. At temperatures above 350°C he observed spontaneous pyrolytic BN deposition regardless of laser beam activity. He reported a positive

linear dependence of deposition rate with borazine vapor pressure (0.1–5 Torr) for a fixed substrate temperature. The total deposition pressure was not reported. Note that the 20 ns period over which deposition occurs when using the laser is too short to allow for direct measurement of the process variables of interest such as temperature. His analysis of the resulting films show that the deposits were mostly h-BN. He does not provide a study on the long term stability of the deposited films. Others have concluded that BN films deposited from borazine at temperatures below 500°C are not stable.[33]

Ugarov also addressed some theoretical considerations associated with the LCVD of BN from borazine.[31] He suggests that deposition when using an excimer laser involves two major steps. Between laser pulses, net borazine adsorption onto the substrate surface occurs forming the adlayer. This layer consists of primarily two phases, a multi-layer physisorbed layer and a weakly chemisorbed layer. Gates has studied the atomic composition of the Si substrate surface during BN deposition from borazine over a range of temperatures.[45] During the laser pulse, the strong physisorbed $B_3N_3H_6$ layer is thermally decomposed yielding the BN deposit. In order to quantify the adsorption reaction process, Ugarov includes a kinetics study involving adsorption and desorption rates. This analysis yields activation energies of 4500 and 10000 K for the physisorbtion and chemisorbtion processes, respectively. He also presents an analysis of the thermal decomposition rate with the caveat that a solution is not possible without knowing the temperature–time relationship during the laser pulse. No consideration is given to the fact that spontaneous homogenous BN formation was observed at temperatures exceeding 350°C.

Most recently, Duty reported BN deposition from borazine reagent.[2,44] His work reveals the first reported deposition of BN films from borazine using a continuous wave CO_2 laser. The substrates chosen by Duty included graphite, aluminum oxide (alumina), and tungsten. His experiments were run at a total pressure of 101 kPa with a N_2 vaporizer flow of 50 sccm (yielding a calculated $B_3N_3H_6$ flow rate at 0°C of 6.3 sccm) and diluent N_2 flow of 450 sccm. He focused on growing BN fibers and observed an extremely sharp upward

step change in deposition temperature after initial growth would begin.

On graphite, Duty classified his fibers into those grown below 1100°C and those grown above 2500°C. It was difficult to maintain constant temperatures at any value in between these numbers. The fibers were very short with smooth center areas and raised bumpy edges. On alumina, fibers deposited at less than 2000°C appeared to grow in controlled uniform ways whereas those whose temperature exceeded this value grew extremely fast (approximately 5 g/m^2-s) and almost uncontrollably. The surface of these high growth rate fibers was very coarse and nonuniform. Tungsten, being a reflective metal, requires significantly more laser power to achieve deposition temperatures. The fiber deposition process on W typically involved a dwell period after the laser was engaged before any deposition began. Upon the initiation of deposition, rapid growth (approximately 6 g/m^2-s) quickly ensued leading to tall fibers with a morphology similar to those grown on alumina. The goal of the boron nitride deposition in the current work is to build upon Duty's efforts in order to achieve geometrically well-defined, structurally sound BN deposits.

2.1.3 Molybdenum

Molybdenum is widely used for its refractory nature and its chemical inertness. The integrity of molybdenum at temperatures of 1000-1200°C along with its electrical conductivity make it an ideal material for use in the dispenser cathode control grid application. Industrial processes that deposit molybdenum from the vapor phase go back until at least 1950.[46]

There are two primary reagents used to deposit molybdenum from the vapor phase. The first, molybdenum hexacarbonyl, $Mo(CO)_6$, is used in the decomposition reaction:

$$Mo(CO)_6(g) \rightarrow Mo(s) + 6CO(g) \tag{2.6}$$

One advantage of this system is that $Mo(CO)_6$ is a vapor at room temperature and the decomposition reaction does not require an additional input gas stream. Experimentally, these advantages simplify the setup. Additionally, the reaction in Equation 2.6 has been shown to

occur at temperatures as low as 400°C at atmospheric pressure. The primary disadvantage of the $Mo(CO)_6$ system is that the molybdenum deposits are often contaminated with both carbon and oxygen. This contamination hinders the electrical conductivity of the material.

Higher purity molybdenum deposits can be made using the molybdenum pentachloride reagent system:

$$MoCl_5(g) + \frac{5}{2}H_2(g) \rightarrow Mo(s) + 5HCl(g) \tag{2.7}$$

The disadvantage to using this system is that molybdenum pentachloride is a solid at room temperature and must be sublimated in order to deliver its vapor into a CVD or LCVD system. Additionally, $MoCl_5$ is very sensitive to moisture and other impurities which requires it be handled in an inert environment and housed in a leak tight reagent delivery system. The carrier gases used to flow the $MoCl_5$ must be clean and dry. Due to the need for high purity Mo in the dispenser cathode application, the molybdenum pentachloride reagent system was chosen for this study.

2.1.3.1 CVD of Molybdenum from $MoCl_5$

Because there have been limited reported instances of successful LCVD of Mo from $MoCl_5$,[2,44] the CVD literature was reviewed. Childs deposited Mo on metal substrates from the $MoCl_5$ reduction reaction with H_2.[46] He studied the deposition reaction at 20 and 760 Torr. At the lower pressure, the partial pressure of $MoCl_5$ was kept at about 0.1 the partial pressure of H_2, and molybdenum deposition occurred at temperatures ranging from 800 to 1000°C with no homogenous powder formation. Deposition at the higher pressure, 760 Torr, was complicated by the excessive formation of powder in the gas phase. Only by keeping the partial pressure of $MoCl_5$ below about 1.5 Torr could the powder formation problem be mitigated and at these conditions growth was rather slow. Deposit conditions were also shown to influence grain size, coating strength, and bonding strength. Larger grain size material typically exhibited better mechanical properties. Adhesion of the molybdenum coating to the substrate was enhanced by interdiffusion between the coating and the substrate.

Sugano et al. have deposited molybdenum from $MoCl_5$ on silicon wafer substrates.[47] A chamber was used to sublimate the $MoCl_5$ at temperatures between 70 and 120°C. The vaporizer H_2 flow was kept at 50 sccm while the diluent H_2 flow ranged between 500 and 2000 sccm. The lines for the hydrogen flow were heated to a temperature 20°C higher than the respective sublimation chamber temperature. Substrate temperatures were varied between 400 and 1200°C. The order of the reaction with respect to $MoCl_5$ concentration is shown to be approximately 1. The best Mo deposition occurred at substrate temperatures between 500 and 800°C. The maximum deposition rate for a $MoCl_5$ concentration of 0.0043 mole percent was observed at 600°C to be approximately 20 Å/min.

A thermodynamic analysis revealed the mechanism of hydrogen reduction of $MoCl_5$ to be $MoCl_5$ to $MoCl_4$ to $MoCl_3$ to $MoCl_2$ to Mo. In equilibrium, the rate limiting step appears to be the production of solid $MoCl_3$. The lowest temperature shown to deposit Mo in these calculations is 720 K.

Yasuda has reported the successful CVD of molybdenum from $MoCl_5$ in a low pressure reactor.[48] He sublimated $MoCl_5$ at 170°C and varied the reactor temperature between 500 and 800°C. He concludes that at low pressures, the deposition rate is dictated by the surface reaction up to a higher temperature (approximately 700°C) than for the atmospheric pressure (600°C) case. During the surface reaction limiting regime, the deposition rate is proportional to the $\frac{3}{2}$ power of the partial pressure of H_2.

Yoshikawa has reported the deposition of Mo films from $MoCl_5$ in a heated fused silica tube reactor.[49] Conditions included a pressure of 101.3 kPa, substrate temperatures between 773 and 1223 K, total gas flow rates ranging from 3.8 to 11.5 sccm with partial pressures of $MoCl_5$ between 0.51 and 1.17 kPa and those of H_2 between 8.3 and 62.9 kPa. The carrier gas was argon. Films deposited at temperatures below 900 K contained some impurities while those deposited above 1223 K consisted of particles from gas phase reactions. He observed a significant relationship among the partial pressure of $MoCl_5$, H_2, position along the tube reactor, and growth rate. For a total gas flow rate of 7.7 sccm with

a partial pressure of $MoCl_5$ of 0.83 kPa and H_2 of 27 kPa the apparent activation energy of the reaction was shown to be 68.5 kJ/mol.

Yoshikawa presented some theoretical discussion of the thermodynamics and kinetics involved in Mo deposition from the $MoCl_5$ and H_2 system. Thermodynamic calculations revealed that at a temperature of 433 K, virtually all of the $MoCl_5$ vapor will be converted to $MoCl_4$ through the reaction:

$$MoCl_5(g) + H_2(g) \rightarrow MoCl_4(g) + HCl(g) \tag{2.8}$$

Furthermore, $MoCl_4$ is believed to reduce through an intermediate chemical reaction to $MoCl_3(s)$ and $MoCl_3(s)$ is reduced to $MoCl_2$ and $MoCl_4$ at a temperature of 926 K through the reaction:

$$MoCl_3(s) \rightarrow MoCl_2(s) + MoCl_4(g) \tag{2.9}$$

In modeling the deposition of molybdenum from $MoCl_5$, Yoshikawa explicitly considers three chemical reactions. The first is the gas phase reaction

$$MoCl_4(g) + \frac{(4-x)}{2}H_2(g) = MoCl_x(g) + (4-x)HCl(g) \tag{2.10}$$

The other two reactions are surface reactions that yield the Mo deposit.

$$MoCl_4(g) + H_2(g) = Mo(s) + 4HCl(g) \tag{2.11}$$

$$2MoCl_x(g) + xH_2(g) = 2Mo(s) + 2xHCl(g) \tag{2.12}$$

The reaction rate of Equation 2.12 was assumed to be much higher than Equation 2.11 so the concentration of $MoCl_x$ at the substrate could be assumed zero.

2.1.3.2 LCVD of Molybdenum

Several researchers have used laser–based CVD processes to deposit molybdenum. Using the H_2 reduction of MoF_6, Bjorklund et al. have grown molybdenum rods on tungsten wire substrates.[50] The partial pressure of MoF_6 was varied between 14 and 50 mbar while

that of the H_2 ranged from 75 to 850 mbar. The fiber tip temperatures were kept between 705 and 840 K. In a cold wall reactor configuration, the molybdenum structures had severe volcanos attributed to the etching of both the substrate and the deposit by the MoF_6. After changing to a hot wall configuration, tall molybdenum rods were grown that exhibited a crystalline morphology with molar ratios of $MoF_6 : H_2$ ranging from 1:3 to 1:9. The rods were over 100 μm tall and 50 μm in diameter. When using a MoF_6/H_2 ratio of 1:13 and 1:17, the rods had a more dendrite–like appearance.

Houle and Singmaster give an exhaustive study of the mechanisms of molybdenum deposition from $Mo(CO)_6$ on Si $< 100 >$.[51] Two experimental setups were used: low–vacuum LV (10^{-4} Torr) and high–vacuum HV (10^{-8} Torr). The vapor pressure of $Mo(CO)_6$ under the conditions used was 85 mTorr. The Ar^+ laser was focused to 10 μm and delivered incident power from 1.5 to 4 MW/cm^2 for exposure times between 200 ms and 120 s. The LV films were smoother than the HV films. The resulting deposits had a distinct raised outer ring surrounding an inner dome shape. Growth rates were estimated to be between 2000 and 6000 Å/s.

Duty has investigated molybdenum fiber deposition from the $MoCl_5$ reagent system.[2,44] Substrates included graphite, alumina, and tungsten. He sublimated the $MoCl_5$ powder at 150°C and delivered it to the reaction chamber using H_2 carrier gas. Additional diluent H_2 gas was added prior to delivery through the gas nozzle. Typical flow rates were 1–2 sccm of $MoCl_5$, 50–100 sccm H_2 carrier, and 400–450 sccm H_2 diluent. Chamber pressure ranged from 50 to 200 kPa and substrate temperatures were kept between 1000 and 1500°C. The resulting structures were best described as thin coatings or spots with different morphologies depending upon the deposition conditions. High temperatures (> 1150°C) yielded porous and fibrous deposits while low temperatures resulted in flat, flaky coatings. Low pressure experiments (50 kPa) produced molybdenum coatings with a nodular appearance.

Others have used the common $Mo(CO)_6$ reagent system to draw molybdenum lines. Radloff and Below studied the relationship between molybdenum line growth rates and

incident laser power.[52] While there appeared to be good adherence of the deposits to the underlying substrates, the material had a specific resistivity of more than two orders of magnitude above that of bulk molybdenum.

Reisse et al. deposited Mo lines on $SiO_2/c-Si$ substrates.[53] The partial pressure of $Mo(CO)_6$ ranged between 100 and 260 Pa with a H_2 partial pressure of 13 kPa. A laser power of 2.2–2.7 W over a 30 μm spot diameter was used with a scan speed of 0.2 mm/s. The resulting lines were 125 nm thick and 12 μm wide with maximum vertical deposition rates of about 1.1 μm/s. The lines were shown to have a high content (50 at%) of carbon and oxygen impurities. The resistivity of the lines was between $1.2-3\times10^{-}5$ Ω-m which is significantly higher than bulk molybdenum ($5.34\times10^{-}8$ Ω-m) and was attributed to the presence of impurities.

2.2 Process Modeling

Models of the LCVD process offer the ability to study, on a very detailed level, the physics and chemistry that control the dynamics of the reactions. Accurate models also allow the establishment of relationships between process parameters and deposit attributes which reduces the need for excessive experimentation. These process–property models are the basis for the development of process planning algorithms that translate three dimensional geometry and material information, representing a physical object, into the necessary machine parameters and commands needed to produce the desired object. The complexities of LCVD have historically dictated modeling approaches that focus only on certain fundamental principles: energy transport, thermodynamics, mass transport, or chemical kinetics. These focused modeling efforts serve as a foundation for developing more complex models that seek to integrate these different fundamental principles into a single modeling environment.

2.2.1 Energy Transport and Temperature Models

The laser heating process used in LCVD must be well understood before other fundamental aspects can be analyzed. Under certain specific conditions, the temperature field induced by a laser beam impinging on a surface can be computed analytically. Kokorowski[54] and Lax[55] are credited with formulating some of the first analytical models of steady state temperature profiles induced by a laser beam.

Of specific interest to the direct–write LCVD growth mode is the substrate surface temperature field induced by a scanning laser beam. Advanced analytical techniques have been used to study the thermal conditions surrounding a scanning energy beam. Cline and Anthony presented an energy analysis of a scanning Gaussian beam used for heat treating, melting, or welding.[56] Moody and Hendel developed a model of continuous wave Gaussian beam heating that incorporated temperature dependent material properties.[57] Kar and Mazumder provided a three–dimensional transient analysis of the laser heating process incorporating three modes of heat transfer: conduction, convection, and radiation.[58]

Numerical models have also been used to investigate the thermal effects associated with laser heating. The advantages of numerical models include the ability to consider nonlinear effects, and the ability to couple the conditions of the surrounding fluids to the substrate temperature fields. Several authors have used finite difference formulations to solve the temperature fields in a laser heating process.[59,60] Kodas et al. focused on analyzing a complex multi–layered substrate which has application in devices requiring multiple layers (e.g. integrated dispenser cathode assembly). Steen developed a finite element model of a forced flow laser heating process with an inert gas nozzle oriented coaxially with the laser beam.[61] Yu and Duncan employed a similar model using a fiber on a substrate, but instead of studying forced convection, they studied natural convection.[62] Zhang combined both a scanning laser beam and natural convection in his model development.[63] Bondi also studied a scanning laser beam with natural convection in a CFD model developed in FLUENT.[64]

The unique angled gas jet configuration of Georgia Tech's LCVD system has been studied by Duty et al.[2,65–67] He developed both two and three–dimensional thermal models using the commercial CFD package FLUENT. The two–dimensional models did not incorporate the fluid zone above the substrate surface and thus were used to study the "no flow" nozzle condition in which axisymmetric conditions existed. The two–dimensional models were used to determine the appropriate domain and boundary conditions to use in the three dimensional model. Relationships among laser power, substrate material, and temperature profiles were studied with these two-dimensional models. The three dimensional model included forced flow through the gas nozzle and its impact on the temperature field within the fluid domain and the substrate. He used the models to study the relationships among laser power, gas nozzle flow rate, and substrate material. Ultimately, the model results were verified using the high–resolution thermal image camera described in Section 3.4.

2.2.2 Thermodynamic Models

Thermodynamic calculations are often used in studying CVD processes to determine the feasibility of certain deposition processes and to establish a theoretical equilibrium deposition efficiency. LCVD researchers use thermodynamic calculations for a similar purpose. These models are inherently oriented towards a particular material system, thus for the current investigation, three material systems were of interest: methane–carbon deposition, borazine–boron nitride deposition, and molybdenum pentachloride–molybdenum deposition.

Jean has published a thermodynamic analysis of carbon deposition.[1,25] He computed the equilibrium molar quantities of different species at temperature values between 1000 and 3000 K. The deposition efficiency for carbon dropped from nearly 100% at temperatures up to and including 2000 K to nearly 0% at a temperature of 2500 K. At temperatures above 2500 K, the formation of other hydrocarbon gaseous species is shown to be thermodynamically favored over the formation of solid carbon. In light of his conclusion that

carbon deposition from methane is a kinetically–limited process, the formation of the volcano effect seen at high deposition temperatures is thus attributable to thermodynamics rather than transport effects for this material system.

Kuznetsov has provided a thermodynamic analysis of BN deposition from the borazine reagent system.[68] His investigation involved both the $B_3N_3H_6$:N_2 and $B_3N_3H_6$:NH_3 systems at total pressures of 1 Torr and 10^{-2} Torr for a variety of temperatures between 800 and 2300 K and for different initial gas mixtures. Results indicate that wurtzite BN is not stable at any of the modeled conditions, c-BN is formed at temperatures below 1804 K and h-BN exists above 1804 K. Increasing pressure of the system shifts the boundaries on the phase diagrams significantly, largely by increasing the region of stability for h-BN. The N_2 system is shown to be more favorable for h-BN deposition than the NH_3 system.

Thermodynamic calculations of molybdenum deposition from molybdenum pentachloride have been executed by Yoshikawa as discussed in Section 2.1.3 above.[49]

2.2.3 Mass Transport and Chemical Kinetics Modeling

A first order approach to modeling the kinetics of LCVD involves use of the concepts presented in Section 1.3. For kinetically–limited processes this approach is appropriate because the concentration at the substrate surface can confidently be assumed to be minimally different than the bulk concentration and the temperature across the laser spot can be computed using thermal models of laser heating. After the kinetic parameters are extracted from experimental data, the Arrhenius expression allows prediction of reaction rates and deposit profiles. Some authors have presented simple kinetic models of the LCVD of different material systems.

Park and Lee developed an analytical kinetic expression for the axial and the diametral growth rate of silicon rods which agreed well with experiments.[69] Jean presented a study of carbon fiber growth kinetics in which he fit experimental data to the Arrhenius expression and derived the necessary parameters for predicting LCVD growth rates.[1,25] His analysis

showed reasonable agreement between the theoretical predictions and the observed values. Johnson and Park did similar kinetic experiments and extended the analysis by developing carbon fiber, line, and wall shape prediction equations.[27] Maxwell[12] and Williams[13] developed an analytical expression for the thickness of a growing film as a function of time at the center of a scanning laser spot by integrating the Arrhenius growth rate equation and combining it with an analytical expression for the substrate temperature field such as that given by Lax.[55]

Han and Jensen present a thorough thermal–kinetic analysis of LCVD of copper lines on silicon substrates.[70] Their model involved the solution of the energy equation for both the copper deposit and the silicon substrate. A scanning laser beam was simulated and considerations were made for the changes in the substrate properties per the evolution of the deposit. The deposition reaction mechanisms were derived experimentally from surface chemistry and spectroscopy studies. The deposition kinetics are modeled via the Langmuir–Hinshelwood rate equation. The model was able to predict line shapes that exhibited good agreement with experiments. In particular, the volcano shape that appeared at high temperatures was attributed to the desorbtion of the reagent species at these higher temperatures. The Han and Jensen model is one of the most thorough investigations of the relationship between LCVD kinetics and line shape; however, it is limited by the lack of explicit consideration of the fluid zones surrounding the deposition region. The energy losses to the fluid zones and the species interactions between the surface concentration and the bulk fluid concentration are not considered, disallowing the application of this model to a transport–limited process.

Nassar et al. have recently published a mathematical model of three–dimensional kinetically–limited LCVD that is utilized in a process planning capacity to determine the necessary parameters for producing a prespecified geometry.[71] The application of interest was a parabolic microlens made of nickel. The model involved the heat conduction equations for both the substrate and the deposited material and the Arrhenius expression

for reaction rate. The laser dwell time required to yield growth of a specified height is computed for each point in a two–dimensional grid by integrating the fundamental equations over time. The model was successfully used to specify process parameters for nickel deposition.

In reality, the interaction among mass transport and chemical kinetics ultimately determines both the surface deposition rate and deposit shapes. In order to capture these interactions, more complete models that consider the fluid zone above the substrate, the substrate, and perhaps the evolving deposit must be employed. The extreme temperature gradients within the LCVD deposition zone complicate the study of the transport and kinetic phenomena. Thus, only after the thermal models mentioned in Section 2.2.1 were developed has significant progress been made in understanding these effects. A few authors have developed comprehensive models of the thermal, mass and momentum transport, and chemical kinetic aspects of laser chemical vapor deposition.

Fischer et al. used the finite–difference method to consider both the energy and the diffusion mass transport governing equations simultaneously.[72] His temperature model only allowed heat transfer via conduction and radiation while his transport model only allowed transport due to ordinary diffusion.

Bauerle et al. have developed an elegant mathematical formulation of the governing equations within both the fluid and the solid substrate zones.[73] Several important assumptions are necessary for these analytical formulations. The models are used to investigate the importance of temperature and concentration dependent thermal conductivity and diffusivity. Considering diffusivity as a function of temperature greatly impacted the overall deposition rate while thermal conductivities that varied with temperature had minimal effect on deposition rate. Concentration dependencies of these properties was also deemed minimally important. Furthermore, the importance of thermal diffusion in both kinetically-limited and transport–limited LCVD processes was highlighted through its effect on the overall deposition rates. In light of the simplifying assumptions employed, the complexity

of the mathematical formulations developed by Bauerle et al. elucidate the complexity of the LCVD process.

Arnold et al. have presented an analytical treatment of LCVD fiber growth utilizing both thermal and mass transport equations.[74] The analysis is aimed at understanding fiber deposit shape responses to changes in different parameters: laser power, laser spot size, activation energy, diffusion limitations, and temperature dependence of thermal conductivity. Discussion is presented regarding the relationship between rate–limiting regime and fiber size and shape.

Duty expanded upon his FLUENT modeling work by developing a finite difference model of the mass transport near the LCVD deposition zone.[2, 66, 67] This approach utilized fluid velocity and temperature data from the three–dimensional forced flow CFD model and solved the species transport equation within a two dimensional domain. One concern with the approach related to the formulation of the boundary condition on the reacting surface. A mesh dependence was introduced by modeling the reaction as a homogenous volumetric reaction as opposed to a surface reaction boundary condition. Nonetheless, the model provided useful qualitative insight into the effectiveness of Georgia Tech's LCVD system's gas nozzle. Overall, Duty's implementation of the mass transport model required a cumbersome interface between two software programs.

Perhaps the most comprehensive model of LCVD to date was recently presented by Koutlas et al.[75] A CFD package was used to solve the continuity and momentum transport equations, energy transport equation, and species transport equation in a forced flow LCVD reactor. The simulator was used to study the deposition of titanium carbide upon AISI 1060 carbon steel.

2.3 Shapes and Structures

The dynamic relationship between the laser beam and the substrate enables LCVD to create sophisticated geometries. As shown in Figure 1.1, there are two fundamental growth modes

of LCVD, fiber growth and line growth. Researchers manipulate the laser-substrate position so as to achieve the proper growth mode or combination of growth modes for their desired geometry or application. A review of the different shapes and structures built using LCVD highlights the flexibility of the process.

2.3.1 Vertical Growth

The most basic LCVD growth mode is when the substrate remains fixed relative to the laser beam and growth is initiated in one particular spot. In the literature, depending upon the thickness of the deposit, h, shapes created using this growth mode are referred to as "spots" for thin films with $h \ll d$ where d is deposit diameter or "fibers" or "rods" when $h \geq d$. Because of its simplicity, vertical growth is often used when commencing an LCVD investigation of a different material. For this reason, vertically grown LCVD structures are common in the literature. The relative ease of vertical growth makes it the foundation for the other more advanced deposition modes and deposit shapes.

2.3.1.1 Shape and Morphology

Spots are often characterized by their surface morphology. Depending upon the deposited material, a number of unique features have been identified for LCVD spots. A ubiquitous feature of many LCVD deposits is a depression in the center of the deposit which usually correlates to the center of the laser spot.[51,76,77] This phenomenon is referred to as the "volcano effect." An abundance of different theories exist as to the reason for this observed effect for different materials and processing conditions. Another notable feature of spot deposits includes periodic variations in deposit height as one moves radially outward from the center of the deposit.

The shape of fibers grown in LCVD depends on the crystallinity of the deposit. Single crystal deposits such as tungsten have a distinctly faceted appearance with a sharp point at the fiber tip.[7] Polycrystalline or amorphous materials usually acquire a cylindrical shape with a smooth, rounded fiber tip. As with spots, the volcano effect is common in LCVD

fiber deposits.

Due to its significance in LCVD, the volcano effect deserves special mention. A number of different theories have been proposed to explain the effect. For a given material system, and for different processing conditions, the effect could arise for different reasons. The theories relate to different aspects of the physical and chemical reactions inherent in LCVD: thermodynamics, mass transport, and surface reaction kinetics.

Thermodynamics dictates which chemical reactions will occur for a given set of conditions. The concept of thermodynamic deposition efficiency refers to the fraction of solid deposited species to reagent gas species for given conditions. A decrease in thermodynamic efficiency with an increase beyond a certain temperature is seen in some material systems. Jean presents a thermodynamic model that predicts for carbon deposition the volcano effect will emerge when deposition temperatures exceed 2000 K. If temperatures exceed 2500 K, a negative reaction will occur wherein the solid carbon deposit will react with excess hydrogen in the system to produce hydrocarbon gases (e.g. C_2H_2). The fact that carbon LCVD has been shown to be kinetically limited for the conditions that yield the volcano effect further supports the thermodynamic explanation of its occurrence.

Other volcano effect theories focus on mass transport limitations. Near the center of the laser spot, the diffusion pathways available to deliver reagents are effectively one–dimensional, whereas, on the outer edges of the deposit, the deposit "sees" more pathways. Along similar lines, depending upon the relative molecular mass of the various gas species present, thermal diffusion could reduce the concentration of the reagent species in the maximum temperature zone at the center of the laser spot. Whatever the cause, a limitation in the effectiveness of the mass transport processes will increase the likelihood of operating in a combined transport–limited and kinetically–limited regime thus having significant implications on deposit shape.

For cases when neither thermodynamics nor transport limitations can explain the volcano shape, surface physics and kinetics must be investigated. It has been explained

that there are several steps involved in establishing a sustained transformation of gaseous reagent molecules near the substrate surface into solid surface atoms of a desired material. First the gaseous molecules adsorb onto the surface, next the molecules migrate around on the surface to a preferred site, some of the molecules acquire the energy state necessary for dissociation, and the reaction byproduct gas species molecules desorb from the substrate surface. Each of these steps requires a finite amount of time. Under certain conditions, some material systems have been shown to prefer desorbtion of the undissociated reagent molecules over disassociation. This change could emerge due to the change in substrate properties as a deposit evolves or it could simply be a function of temperature. Either way, if a system exhibits this desorbtion tendency, a volcano shape could develop during growth. Han and Jensen showed in their analysis of copper deposition on silicon substrates that desorbtion was the explanation for the volcano effect.[70]

Carbon fibers normally exhibit a fairly uniform cylindrical shape with a smooth, rounded tip. This shape is consistent with the fact that carbon LCVD typically occurs in a kinetically–limited regime.[1,12,78] At high temperatures, carbon fibers acquire a bulging profile with a distinct volcano–like depression in the center.

Duty provides the only attempt to deposit BN fibers in LCVD. His deposits were large structures, over 500 μm in diameter and height, that exhibited a very rough, cauliflower–like surface morphology. The growths were white translucent colored and were surrounded by bright white powder. These BN fibers had severe volcano effects and discoloration in their center.

Houle reported on the change in the shape of molybdenum spots as they evolved from flat disks to round spots having a raised ring around the outer edge with a center domed structure exhibiting a faceted appearance.[51] Bjorklund grew high aspect ratio Mo fibers with an octagonal cross section and a very faceted morphology.[50] Duty's efforts to deposit Mo fibers resulted in thin coatings of material with a slight bowl shape. No significant vertical growth was observed.

2.3.1.2 Complex Fiber-Based Deposits

As evidence of the flexibility of the LCVD process, several authors have reported the fabrication of complex structures. By slowly translating the substrate underneath the laser as the fiber grew vertically, Pegna[24] and Jean[1] both deposited angled carbon fibers that were ultimately joined to form truss structures. Parallel banks of aluminum oxide rods were deposited with different orientations for use as photonic band–gap structures by Wanke et al.[9]

The fully three–dimensional nature of the LCVD process has been demonstrated through the fabrication of coiled structures resembling springs. Johansson et al. have deposited boron fibers and springs by simultaneously rotating and translating the substrate during deposition[79] Maxwell et al. have achieved similar results with carbon deposition.[12] Dean et al. illustrated the utility of these spring–like devices by fabricating arrays of carbon coils to be used as THz antennas.[10]

2.3.2 Horizontal Patterned Growth

The second fundamental growth mode of LCVD is the "direct–write" or patterned mode. Much like vertical growth, there are different terms for these deposits depending upon the height to width aspect ratio. For the case of thin deposits with $h \ll w$, the deposit is usually termed a line; whereas, for the case of $h \geq w$, the deposit is called a wall.

2.3.2.1 Line Shape and Morphology

The shape of LCVD line cross sections varies for different materials and processing conditions. In the transport–limited regime, the cross sections often have a rectangular shape with a relatively flat top, whereas lines grown in a kinetically–limited process exhibit a rounded Gaussian shaped cross section. Boughaba discusses the relation between the rate–limiting regime and LCVD line shape in his study of nickel lines.[80] Westberg also gives some results of the shape of titanium carbide lines under kinetically controlled conditions.[81]

Analogous to the vertical growth mode, horizontal LCVD structures commonly exhibit the volcano effect. Han and Jensen used both models and experiments to determine the underlying reason for the volcano shape in copper line deposition was desorbtion of reagent molecules under certain conditions, namely high surface temperatures.[70] Milne et al. report the occurrence of the volcano effect in silicon line deposits.[82]

Spatially periodic growth is also witnessed during the deposition of certain materials. For example, Grossman and Karnezos report that under certain conditions, the deposition of a tungsten line on a boron nitride coated silicon substrate results in a very periodic bumpy surface. They reason that this effect is due to the "self–limiting" nature of the metal deposition on a ceramic substrate. Du et al. identify a similar mechanism as the cause of the periodic nature of silicon lines deposited on a glass substrate.[83] Han and Jensen attribute the spatially periodic nature of copper line deposits to a nonlinear coupling between heat conduction and chemical kinetics.[70] A very complex spatially periodic superstructure was shown by Milne et al. in silicon line depositions. The periodicity extended both along the length of the line as bumps and across the line width as "tracks."

In order to accommodate some stated applications of the LCVD process, intersecting lines must be deposited. For certain applications, the line intersections must maintain minimal electrical resistance. Depending on the materials involved, maintaining line height and width uniformity during the deposition of line intersections can be very difficult. The challenge lies in the step change in substrate properties that accompanies the laser scan path's intersection with an existing line deposit. Grossman and Karnezos present a good discussion of the complexities of depositing intersecting lines in their study of tungsten deposition on BN coated silicon wafers.[7] They were able to create connected lines by doubling the laser power when passing over previously deposited lines. Morishige and Kishida highlighted the successful deposition of gold lines and their intersection with existing gold interconnects on polyimide substrates. The contact resistance of these intersections was measured to be about 0.5 Ω.[6]

The deposition of 7 μm wide carbon lines has been reported by Leyendecker.[78] No LCVD of boron nitride lines has been reported. Reisse's molybdenum lines were described as smooth and were 125 nm thick and 12 μm wide. No detailed discussion of the profile was given.

2.3.2.2 Multi-layer Lines or Walls

In order to achieve the higher aspect ratio of a wall ($h > w$), it is usually necessary to deposit multiple lines on top of each other. Without a robust process control system to combat the positive feedback tendency of multi-layer deposition, it is very difficult to produce uniform structures of this type. Jean has reported on the integration of an advanced temperature control system in Georgia Tech's LCVD system that allows production of uniform multi–layered walls.[1] Johnson et al. have exploited this system to produce carbon walls with promising uniformity and structural integrity.[26] Gillespie has shown the ability to use LCVD to fabricate multi–layered laminated materials.[84] He deposited a wall consisting of alternating sections of two each of carbon and silicon carbide. Each section of each material consisted of 10 layers.

2.3.3 Properties of LCVD Deposits

Each application of LCVD demands certain properties of the deposited materials and structures. These properties include obvious attributes such as size and shape as well as physical properties such as strength and resistivity. These macro–scale properties can be linked to the internal microstructure of the deposits. Investigations of the relationships among processing conditions and deposit properties are critical in the development of new LCVD materials and applications. A sample of typical microstructure and physical property values for LCVD materials with a focus on carbon, boron nitride, and molybdenum is provided below.

2.3.3.1 Internal Microstructure of LCVD Deposits

Researchers have investigated the elemental composition, phase composition, crystallinity, and integrity of LCVD deposits. Carbon deposition has been the subject of LCVD investigations for over 30 years. LCVD carbon has been described as both amorphous[12] and polycrystalline.[78]

Interestingly, the first reported LCVD of carbon contained micrographs that illustrated internal periodic cracks throughout the length of a carbon fiber that were oriented parallel to the curved fiber tip surface.[4] Leyendecker also showed evidence of internal cracks in carbon fiber deposits.[85]

Only recently has there been a concerted effort to study the cracks observed in carbon LCVD deposits.[20] Kang et al. have observed that the cracks occur parallel to the plate–like structures seen (presumably the basal planes) within the deposited carbon. These platelets are oriented parallel to the fiber surface which changes from horizonal in the center of the fiber to nearly vertical near the fiber edge. Thus, the observed cracks acquire this same curved shape. Cracks along the direction of the basal planes are enabled by the fact that the Van der Waals bonds between the basal planes are weak. The cracks were wider at the center of the fiber than at the edges, and the vertical spacing between the cracks was shown to decrease with increasing temperature. Kang suggests that the cracks are related to the thermal stresses that arise during the growth process.

Limited discussion of the microstructure of boron nitride and molybdenum deposits is available in the literature, because of the relative immaturity of these deposition processes. Ugarov found that his BN LCVD deposits were largely hexagonal boron nitride, h-BN.[31] Duty only provided elemental composition information indicating the presence of boron nitride.[2,44]

Houle studied the radial variation in the composition of molybdenum LCVD spots produced from $Mo(CO)_6$.[51] The center of the spots was shown to be mostly pure Mo with upper limits of carbon and oxygen contamination of 2% and 1%, respectively. This pure

metal composition extended beyond the diameter of the 10 μm laser spot. The outer edge of the deposit with the annular ring showed a more significant presence of C and O. Analysis also revealed that the "layers" of deposit nearest the Si surface were nearly stoichiometric MoCO, but upon further growth the purer metal with the radially varying composition described above was found. Reaction mechanisms and surface kinetics were found to explain the complex stoichiometry of the deposited molybdenum structures.

The underlying microstructure of a deposit gives rise to its macro–scale mechanical and physical properties. Few attempts have been made to examine these properties of LCVD deposits, but again, in order to realize its application, this aspect of the LCVD process must be understood and characterized.

2.3.3.2 Mechanical and Physical Properties

In terms of mechanical properties, Boman has reported the average fracture stress of a LCVD produced silicon rod to be about 3 GPa which corresponded to a fracture strain of approximately 2.5%.[86] Johansson measured the elastic modulus of amorphous boron fibers to be between 420 and 450 GPa with a fracture stress of 12–17 GPa corresponding to fracture strains of 2.7–3.7%. Wallenberger has reported the tensile strength of boron LCVD fibers to be 5.2–7.6 GPa.[87] He has also reported tensile strength of carbon fibers to be 3.0 GPa.[88] No such data is reported for boron nitride or molybdenum deposits.

A mechanical property that is important for many applications of line deposition is the adherence of the deposit to the substrate. A variety of tests can be used to measure adherence, but one of the easiest and most effective to to use the tape test. Using the tape test, Houle et al. reported that copper LCVD lines adhered well to silicon.[89] Radloff and Below reported good adherence of their molybdenum lines to the substrate surface.[52]

For certain applications, the electrical properties of deposits are also important. Boman reported tungsten coils to have a resistivity of 0.08 Ω-mm^2/m which is about 40% higher than bulk tungsten.[86] Boughaba states that his nickel lines had a resistivity ranging from 1.5

to 10 times that of bulk nickel.[80] Interestingly, he reported a trend of decreasing resistivity with increasing reagent partial pressure which implies a relation between the transport–limiting regime and the electrical properties of the deposited lines. Houle et al. report the resistivity of LCVD copper lines to be 3.6 $\pm 1 \times 10^{-6}\Omega$ cm which is about twice the resistivity of bulk copper.[89] Jubber et al. found the resistivity of gold lines to be about 4.2 $\mu\Omega$-cm which is comparable to bulk gold.[90] The molybdenum lines grown by both Radloff[52] and Reisse[53] had resistivity values more than two to three orders of magnitude larger than that of bulk molybdenum ($1.2 - 3 \times 10^{-}5\Omega$-m vs $5.34 \times 10^{-}8\Omega$-m).

Overall, there is a lack of comprehensive knowledge regarding the mechanical and physical properties of LCVD deposits. However, for the properties that have been measured, such as electrical resistivity, LCVD deposits tend to differ by a factor of between 2 and 1000 from the bulk material values. The differences are normally attributed to contamination in the deposits rather than to any inherent flaw in the LCVD process. The strengths reported for silicon and boron fibers are very impressive. The anecdotal evidence in the literature suggests that with proper experimental procedures and equipment, the LCVD process can produce very pure materials with properties approaching those of the bulk materials.

CHAPTER III

GEORGIA TECH'S LCVD SYSTEM

Georgia Tech's LCVD system was designed and assembled by Duty, Jean, Fuhrman, and Lackey and incorporates several novel features.[1,2,15,91–93] It has been in operation for about six years. During that time, the system has undergone some major changes as the applications and materials of interest have evolved. Several different materials have been produced in the system: bulk carbon, carbon nanotubes, silicon carbide, boron, boron nitride, and molybdenum.

3.1 LCVD Chamber and Reagent Delivery Subsystem

The system itself is a unique design consisting of two chambers, a lower chamber for housing the mechanical stages, and an upper chamber where the deposition reaction occurs. Figure 3.1 illustrates the system setup.

The chambers are separated by a flexible rubber bellows which prevent the reagent gases in the upper chamber from entering the lower chamber. A vertical shaft connecting the substrate holder to the mechanical stages protrudes through the bellows. During operation, the lower chamber remains filled with an inert gas, typically argon, at a pressure equal to the upper chamber. The upper chamber has a variety of gas ports to allow for entry and exit of gases and several optical ports to provide line of sight access to the deposition zone. The upper chamber also incorporates a gas nozzle that is used to locally deliver reagent gases to the reaction zone. Figure 3.2 depicts the setup of the upper deposition chamber.

Outside of the chambers lie all the necessary equipment for delivering the reagent gases into the chamber. Depending upon the desired reaction, reagent gases may be sublimated from a solid powder in a sublimation chamber, vaporized from a liquid in a vaporizer,

or delivered as a gas from a tank. Other equipment necessary for delivering gases to the chambers include mass flow controllers, throttle valves, and solenoid valves.

3.2 Substrate Motion Control Subsystem

Georgia Tech's LCVD system uses a combination of linear and rotational motion stages housed in the lower chamber to manipulate the substrate. The original design incorporated two linear motion stages and one rotational stage. The linear motion stages were Aerotech ATS03005 stages while the rotational stage consisted of an Aerotech BM75 motor coupled to a reduction gearbox (12:1) whose output shaft connects directly to the substrate holder shaft. Table 3.1 gives some of the important specifications of the stages. One linear motion stage was oriented horizontally (x–axis) to enable line growth while the second was oriented vertically (y–axis) to enable fiber growth. The rotational stage rotates about the center of the substrate holder (z–axis). Proper manipulation of these three axes allows access to any point in the three dimensional space defined by the limits of the stages. The rotational z–axis system was chosen over a third linear stage to simplify the fabrication of

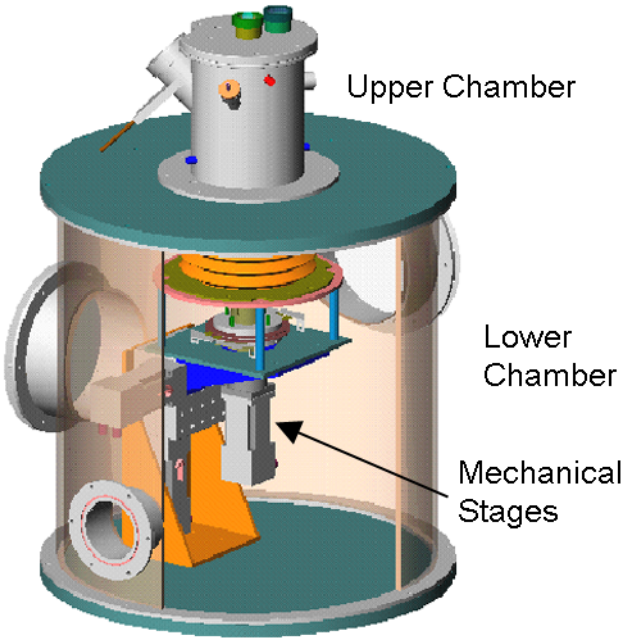

Figure 3.1: The two chamber design of Georgia Tech's LCVD system

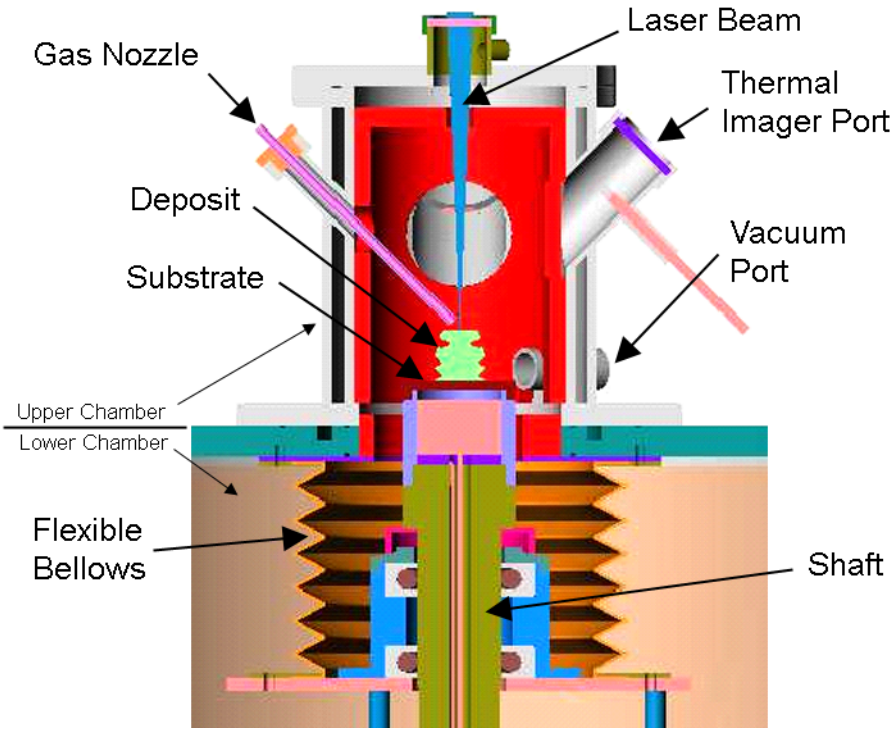

Figure 3.2: Important features of the upper reaction chamber

axisymmetric geometries.

All of the Aerotech stages are controlled through an I/O card mounted in the main Windows 2000 based control PC. Aerotech provides a driver for the stages that allows configuration of the stage parameters and defines an array of commands that can be used to control the stages. Aerotech also provides some VIs that allow the LabVIEW environment discussed in detail in section 3.5 to interface with the stage control software.

3.2.1 Addition of Fourth Axis

It became apparent during deposition experiments involving simple geometries, particularly intersecting lines, that using the three axis with z rotational stage system was cumbersome. Thus, a fourth stage was purchased to allow more flexibility in deposit geometries. The fourth stage was installed horizontally, perpendicular to the existing x–stage and is referred to as the u–axis.

Table 3.1: Specifications of motion stages

	Linear Stages	Rotational Stage
Stage	ATS03005-M-5-NC	Unknown
Motor	BM75-MS-E1000H /ES13675 or BMS60-A-E1000H-VAC3/ES13459-1	BM75-MS-E1000H /ES13675
Machine Resolution	0.0001 mm	0.00001 uu
Programming Resolution	0.0001 mm	0.0001 mm
Maximum Speed	240 mm / min	1560 uu / /min

The addition of a fourth stage was a design challenge due to the space constraints imposed by the size of the lower chamber. Also, the maximum allowable loads for each stage required extensive modification to the existing system of counterweights such that the new configuration would not exceed the maximum allowable load for any individual stage. Finally, it was desirable that with the addition of the new stage, the existing stage configuration would be re-centered such that when the substrate was in the center of the upper chamber (i.e. in the center of the allowable deposition space) all three stages, x, y, and u, would be in the center of their travel ranges.

The new stage was installed virtually using the SolidWorks solid modeling package. After it was confirmed that there was sufficient clearance to mount a fourth stage in the lower chamber, the mounting system was designed. Figure 3.3 illustrates the original 3–axis stage system while Figure 3.4 shows the additions made to accommodate the new u–axis linear stage. Three new mounting brackets were designed and fabricated to accommodate the u–axis: an offset plate, an x–u coupling bracket, and a base relocation plate. These parts are shown in Figures 3.5 (a), (b), and (c), respectively.

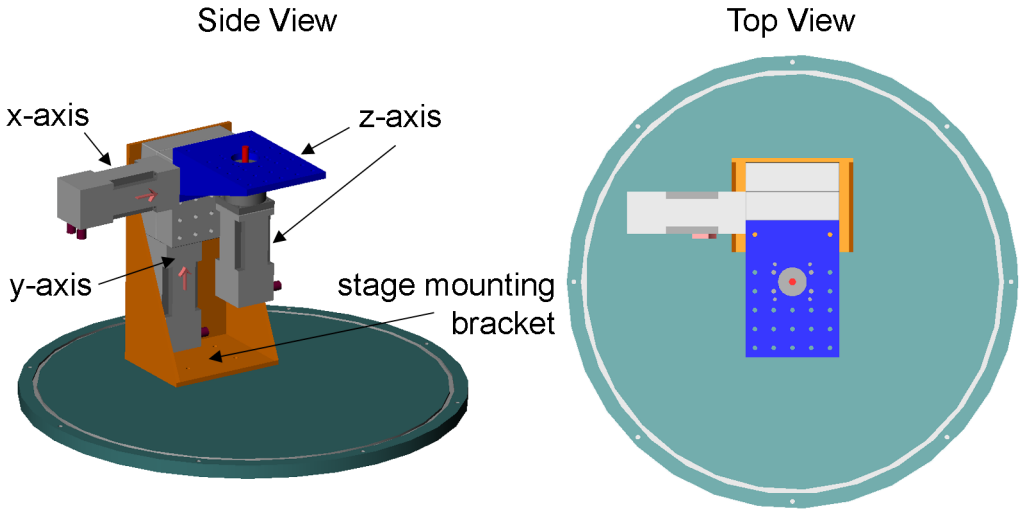

Figure 3.3: Original 3–axis stage configuration

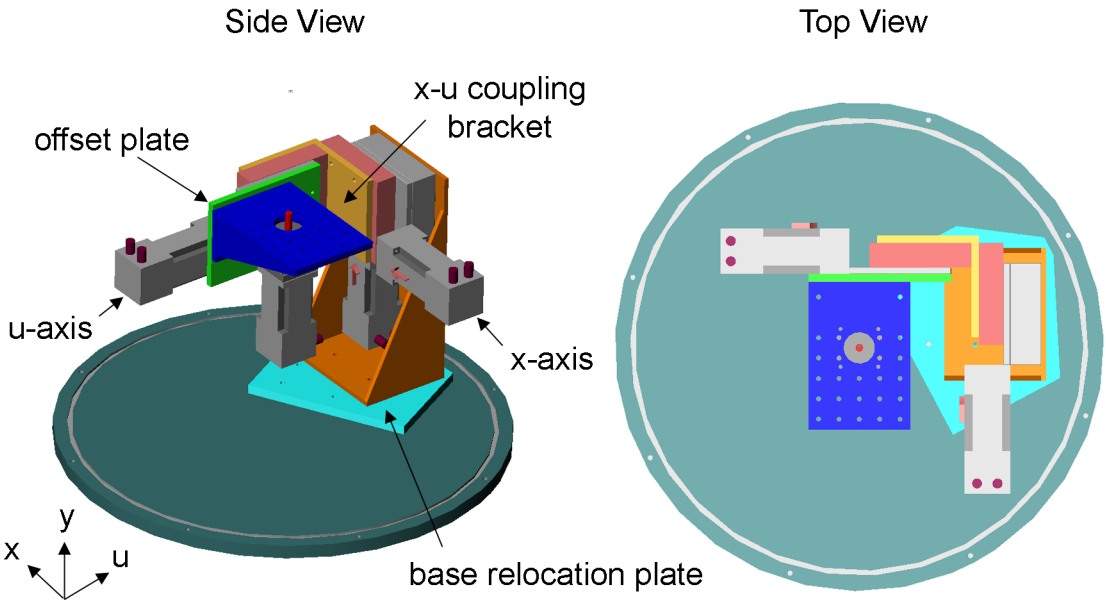

Figure 3.4: Modified 4–axis stage configuration

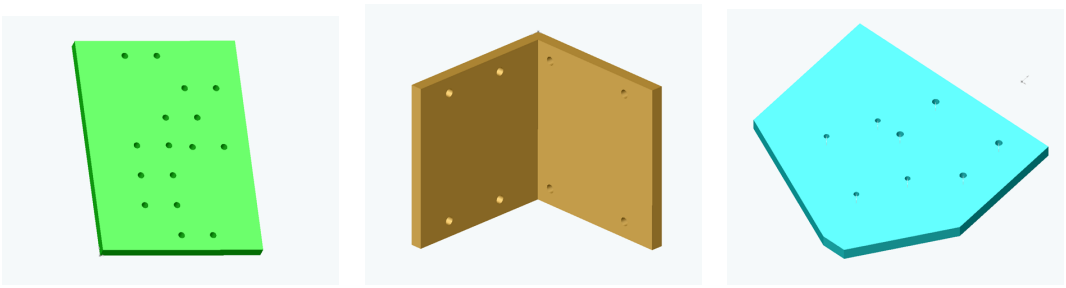

(a) Offset plate **(b) x–u coupling bracket** **(c) Base relocation plate**

Figure 3.5: New hardware required for mounting fourth stage

3.3 Laser Subsystem

The laser used is a Synrad Evolution 100 CO_2 laser with a maximum power output of 100 W. The specifications, as given by the manufacturer, are reported in Table 3.2.

The laser beam is delivered to the substrate through a series of mirrors and lenses. Originally, the optical train for the CO_2 laser beam was specified by the supplier of the optical components with the goal being to focus the beam to a diameter of about 200 μm at the substrate surface. In addition to the mirrors used to steer the beam, a beam collimator and a focusing lens are used to resize the beam. The beam collimator uses an expansion lens to diverge the beam and then uses a converging lens to reduce or eliminate the divergence angle. The distance between the two lenses is adjustable and this distance controls the

Table 3.2: Synrad Evolution 100 laser specifications

Output Power	100 W
Mode Quality	TEM_{00}, 90% purity, $M^2 < 1.2$
Ellipticity	< 1.2
Rise Time	< 150 μsec
Beam Diameter	4 μm
Beam Divergence (Full Angle)	3.5 mR
Wavelength	10.59 μm
Power Stability, from cold start	$\pm$5%
Polarization	Linear (Vertical)

exit diameter and divergence angle of the beam. The focusing lens receives the collimated beam and converges it to a small diameter. The distance between the focusing lens and the substrate is controlled by the position of the vertical mechanical stage (y–axis). In order to accomplish deposition with a beam of minimum diameter, the distance between the focusing lens and the substrate must be made equal to the theoretical distance from the lens to the focal plane. Figure 3.6 is a sketch of the final part of the optical train for Georgia Tech's LCVD system illustrating the different components.

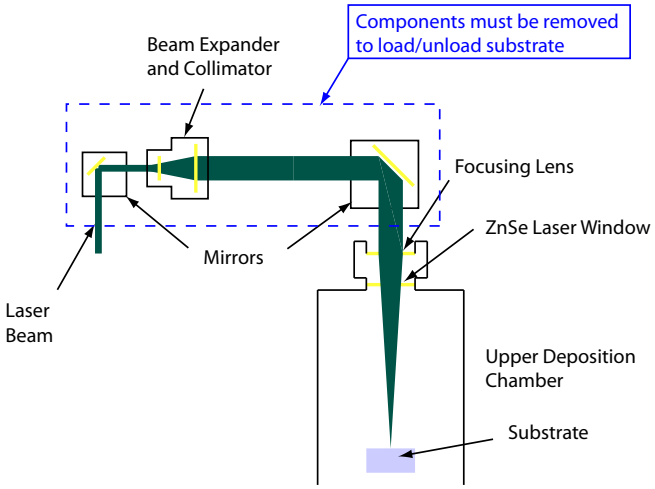

Figure 3.6: Important components of LCVD system optical train

Unfortunately, the existing LCVD system design requires that several of the components in the optical train be removed each time a new substrate is loaded or removed from the chamber. Originally, the assembly containing the focusing lens and laser window also had to be removed each time a substrate was removed or loaded. The seal between the laser window and the top of the upper chamber was a simple clamped pressure seal. Due to persistent leaks around the laser window, a new lens and window holder was designed and installed. The details of this design change are given elsewhere.[64]

The constant movement of the laser optics creates an opportunity for the optics to become misaligned or damaged making it difficult to maintain a consistent beam shape. The size and energy distribution of the laser beam was investigated using a Spiricon Pyrocam

III laser beam profiler. As seen in Figure 3.7, the beam was shown to have significant asymmetries. These features are likely related to the observed damage on the ZnSe coated beam optical components due to dirt and debris contamination.

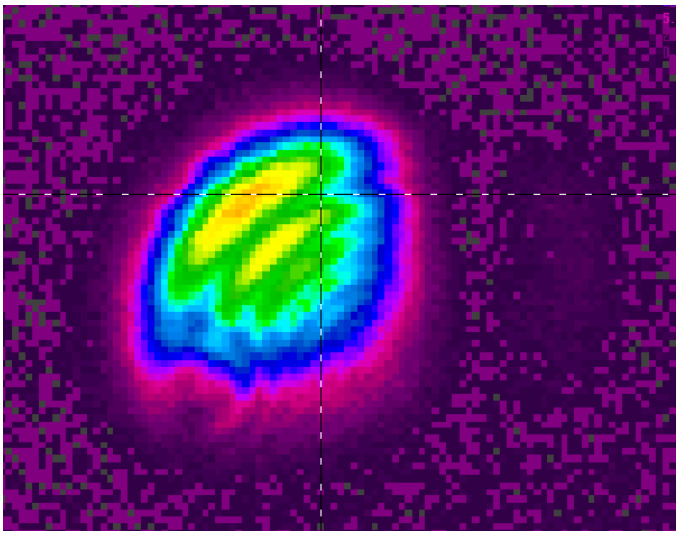

Figure 3.7: Spiricon beam analyzer image of CO_2 laser beam shape

Slight anomalies in the precise distribution of the laser beam are likely mitigated by the heat transfer in the substrate. However, if the distribution is significantly different than expected, it could influence the substrate surface temperature distribution, and ultimately, the shape of a growing deposit. While far from optimal, the CO_2 beam shape measured for the system was still believed to be a sufficient heat source for investigating the LCVD of new materials.

The CO_2 laser is controlled by sending a 0-10 V analog signal to the laser controller. The laser controller converts the input voltage to a pulse width modulated signal that drives the laser. The relationship between input voltage (entered by the operator) and the laser power output was measured by Duty and is given in Equation 3.1 with P representing laser power and x representing the input control voltage.[2] Figure 3.8 illustrates the nonlinearity of the relationship.

$$P = 0.0067x^3 - 0.8261x^2 + 17.575x - 0.8492 \tag{3.1}$$

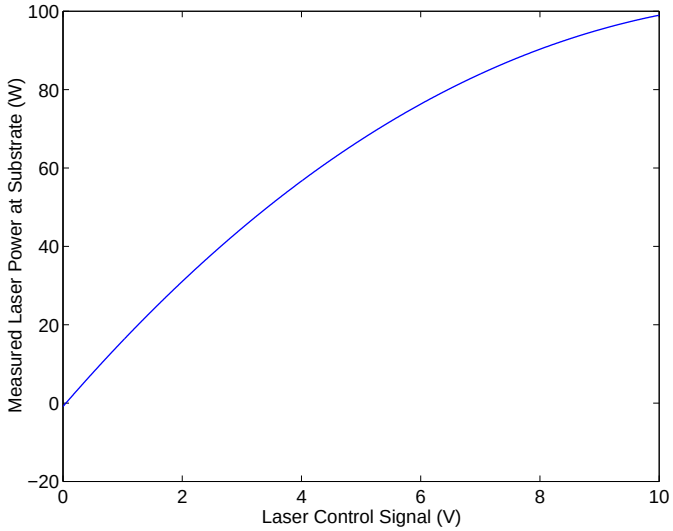

Figure 3.8: Laser power at substrate versus control voltage

Georgia Tech's system also has a Stabilite 2017 continuous wave Ar^+ ion laser installed. This laser has a wavelength of 457.9–514.5 nm and is capable of operating in several modes. In TEM_{00} mode, the laser produces the typical Gaussian shaped beam which can theoretically be focused to a diameter of less than 10 μm. The upper chamber has been modified to allow for dual entry of the argon laser beam. However, only limited work has been done in determining the necessary processing steps for using the argon laser during deposition. The Ar^+ ion laser was not used as a part of this work.

3.4 Thermal Imaging Subsystem

Perhaps the most important feature of the system is a Mikron M9104 Pyrovision ultra–high resolution thermal imager that allows detailed observation of the substrate temperature during deposition. The thermal imaging camera is oriented at an angle of 45° relative to the normally horizontal substrate surface and has a standoff distance from the substrate of about 150 mm. The viewing port for the imager is a quartz window with minimum attenuation in the near infrared (800–900 nm) spectrum used by the sensor. The use of the near infrared spectrum also minimizes the dependence of the measured temperature values on surface emissivity. Figure 3.9 illustrates the relationship among the thermal imager, the

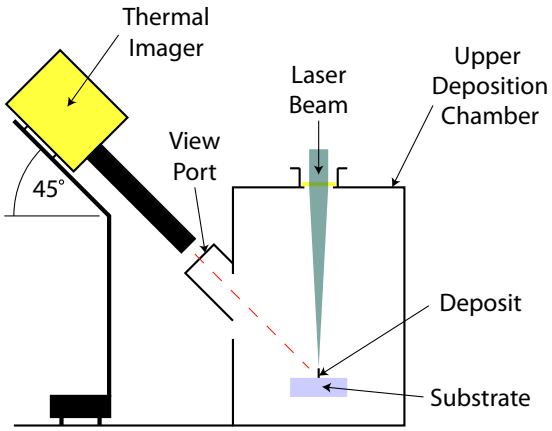

Figure 3.9: Thermal imager setup

viewing port, and the substrate.

The thermal imager is equipped with a microscopic lens assembly with two zoom settings, 1.5X and 4.5X, the highest of which yields a maximum spatial resolution of 3.5 μm per pixel when focused on a substrate positioned at the proper height. The sensor has a spatial resolution of 640 x 480 pixels and a temperature resolution of 1°C. The accuracy of the system is specified to be $\pm$1% of reading, however, the accuracy is also effected by the value of emissivity provided to the software by the user. The system provides a new temperature measurement for all pixels at a rate of 30 Hz. The system has a total temperature range of 850 to 2525°C which is broken into seven subranges depending upon the zoom setting. Table 3.3 indicates the temperature range of each subrange.

Table 3.3: Subrange temperature values for thermal imager

Range	Zoom	T_{min} (°C)	T_{max} (°C)
1	1.5	850	1090
2	1.5	1040	1380
3	1.5	1300	1800
4	1.5	1680	2525
1	4.5	955	1255
2	4.5	1190	1600
3	4.5	1495	2170

The display of the thermal imager is fed into a Windows based PC which provides a real–time display of the 640 x 480 pixel temperature field. The 8 bit resolution of the sensor allows 256 possible temperature values (and display colors) within each temperature range. The software interface allows the creation of multiple “Regions of Interest” or ROIs which are areas in which the processor will report the minimum, maximum, or mean temperature value. These ROIs interface to an 8–channel isolated current output module that allows the temperature data to be used as a feedback signal in automated control applications. Figure 3.10 presents a typical screenshot from the thermal imaging camera software during deposition.

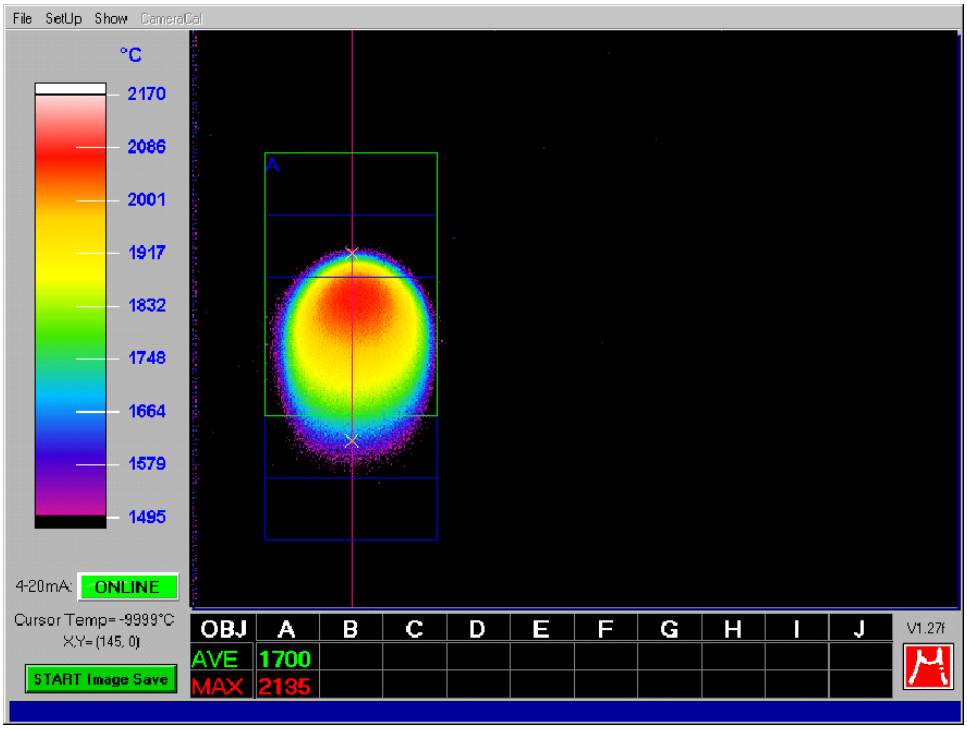

Figure 3.10: Typical screenshot of thermal imager software during deposition

3.4.1 Growth Rate Measurement Using the Thermal Images

The deposit growth rate in LCVD is important for many reasons. The growth rate places practical limits on the size of parts and features that can be produced using the process. The growth rate also gives insight into the rate–limiting regime of the process which becomes

important for deposit shape and other properties. In situ growth rate measurement provides opportunities for enhanced process control and analysis.

The thermal imaging camera on Georgia Tech's system is oriented at an angle of 45° with respect to the substrate surface as shown in Figure 3.9. This configuration enables the detection of height changes through a vertical shift that appears on the thermal imager screen. If the spatial resolution of the imager screen is known, a change in deposit height can be quantified with reasonable accuracy.

A calibration experiment was done to confirm the spatial resolution of the thermal imager. First, a piece of white paper was placed on the substrate holder. Next, pieces of pencil lead of different diameters were measured and placed on the white paper. The diode laser used to align the CO_2 laser beam was then used to illuminate the pencil lead on the substrate surface. The thermal imaging camera was placed in "visible" mode, and the setup was viewed. The different reflectivity of the graphite pencil lead compared to the white paper underneath it made the two objects distinct in the imaging window. Figure 3.11 shows a typical image.

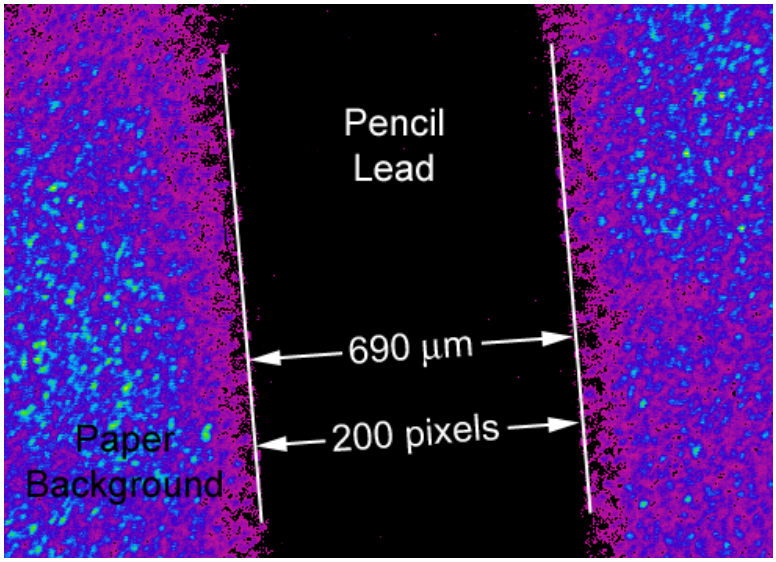

Figure 3.11: Calibration method used to determine spatial resolution of thermal imager

The size of each pixel on the thermal imaging screen could easily be determined from

Figure 3.11 by dividing the measured diameter of the pencil lead by the observed number of dark pixels on the screen across the diameter. After using three different size pieces of pencil lead and multiple images and computations, it was established that the spatial resolution of the imaging camera was approximately 3.5 μm per pixel.

The process of using the thermal imager to measure growth rate first requires the capture of a series of thermal images; the imaging system software enables the capture of thermal images at a specified frequency. These images are saved as 8 bit (256 color) bitmap files and are named according to the value (in ms) of an internal timer. In order to analyze the temperature data contained within the images, the images must be converted from a color matrix to a temperature matrix. The MATLAB code written to execute this conversion is provided in Appendix B.1.

Next, these images must be compared to determine the height change that has occurred between their capture. In order to make a valid comparison, the thermal imager needs to have remained fixed relative to the substrate during the capture of the image series. Because the thermal imager only provides a color or temperature map, an important assumption must be made relating the temperature field to its position on a growing deposit.

The typical fiber exhibits a rounded profile along its top surface with the tip of the fiber being the tallest point as illustrated in Figure 3.12. During growth, it is reasonable to assume the very tip of the fiber remains at the highest temperature. This assumption is justified by a) the fact that the laser energy flux is maximum at this point and b) the protrusion of this tip inhibits conduction of heat away from itself. The assumption is further validated by the analysis presented in Chapter 6. In the event that a fiber or deposit does not exhibit the rounded profile shown in Figure 3.12, such as when the “volcano effect” has occurred, this assumption does not hold and the measurement technique can not be used. It is also assumed that the point of maximum temperature moves strictly vertically during growth and does not migrate around on the fiber tip.

The assumption that the point of maximum temperature corresponds to the tip of a

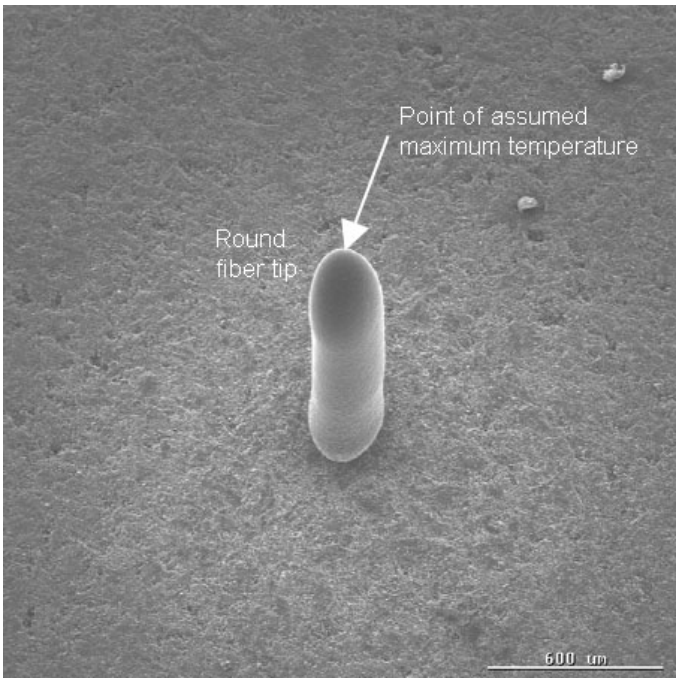

Figure 3.12: Typical profile of LCVD fiber

growing deposit allows the development of an algorithm that can find the position of the fiber tip via the value of the maximum temperature within a thermal image. This procedure is executed for each thermal image in a series, and the change in the vertical position of the maximum temperature is measured in pixels. The pixels are converted to spatial units using the 3.5 μm per pixel value derived above and the result is divided by $\sin(45^\circ)$ to account for the orientation of the thermal imager. This height change at the point of maximum temperature is divided by the time elapsed between the thermal images being analyzed. This time value is computed by finding the difference between the names of the files. The growth rate is thus given in units of length/time. Figure 3.13 illustrates how this process works. The MATLAB code used to execute the calculations is presented in Appendix B.2.

When measuring growth rates in LCVD, it is usually desirable to maintain a constant temperature profile; however, this is not always possible. There is always a transient period during the initiation of an LCVD deposit when the laser interaction with the substrate coupled with the evolution of the first molecular layers of a deposit causes instabilities. The instabilities in this transient period make it very difficult to maintain a constant temperature

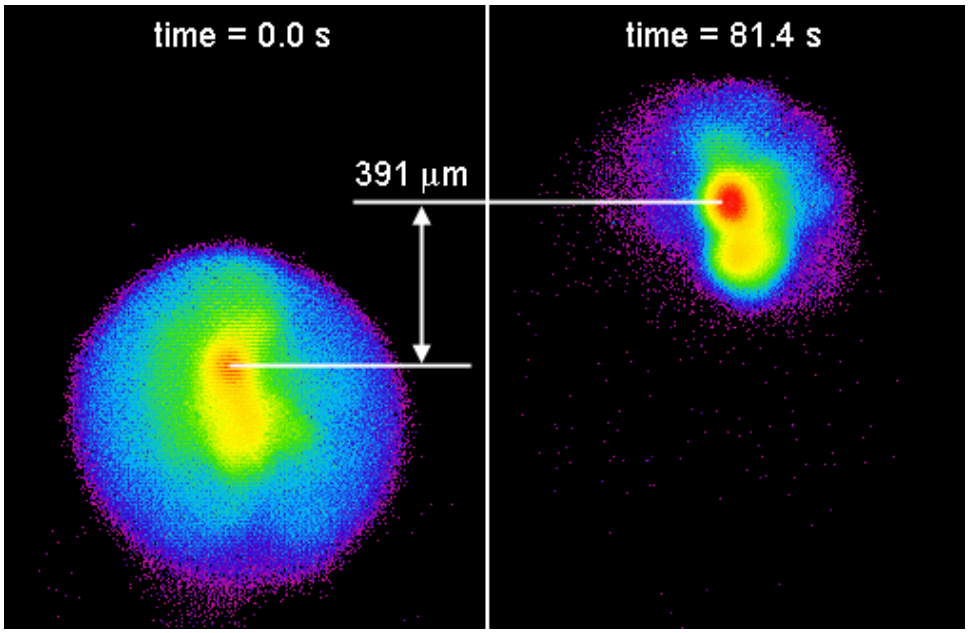

Figure 3.13: Illustration of how fiber growth rate can be computed from a series of thermal images

profile. Some deposition processes also exhibit such extreme temperature sensitivity to laser power that sustained temperature control is difficult. However, during the growth of these materials it is often possible to have periods, sometimes lasting 20–30 s or more, when a relatively constant temperature profile emerges.

The complexities in maintaining constant temperature sometimes during LCVD growth invalidate the obvious growth rate computation method of dividing the overall measured height of the deposit by the overall elapsed time of the experiment. The use of the thermal imaging measurement technique circumvents this problem by allowing the selection of a subset of thermal images captured during an experiment over a period of relatively constant temperature. In fact, different growth rate values can be generated within the same experiment if multiple regions of constant but distinct temperatures existed.

3.5 Control and Data Acquisition Subsystem

Hardware and software from National Instruments (NI) is used to control the LCVD system. All input and output is handled by a NI PCI–MIO–16E–4 board mounted in a Windows 2000 based PC. This DAQ card operates in multiplexed mode and interfaces with an SCXI chasis that houses four additional I/O cards: an SCXI–1102B analog input card, an SCXI–1160 digital I/O card, and two SCXI–1124 analog output cards. The external hardware such as pressure transducers, mass flow controllers, valves, the thermal imager, and the laser connect to the appropriate I/O card(s). National Instruments' NIDAQ package provides the necessary drivers for controlling the I/O hardware. NIDAQ offers the software developer a variety of programming language options for providing operator interface to the hardware. Georgia Tech's LCVD system uses an operator interface that was developed with National Instruments' LabVIEW package. Fuhrman did the majority of the original software development for the LCVD system.[15] LabVIEW is a software development environment built around the graphical programming language G which utilizes the dataflow programming paradigm.

LabVIEW integrates well with the National Instruments DAQ hardware used in the current LCVD setup. Each material system(s) use a different LabVIEW interface with the appropriate mass flow controllers and ranges for the desired reagent flow. Figure 3.14 is a screenshot of the typical LabView interface used for carbon deposition. The interface is fairly intuitive with stage control in the upper left, laser control on the middle left, pressure gages in lower left, reagent flow control on the right, and temperature in the center.

3.5.1 Feedback Temperature Control

Substrate surface temperature is one of the primary variables in determining the LCVD reaction rate. By monitoring the temperature and adjusting the laser power, one can keep the temperature constant. The thermal imaging camera on Georgia Tech's system provides a unique capability to measure, with high spatial resolution, the substrate surface temperature

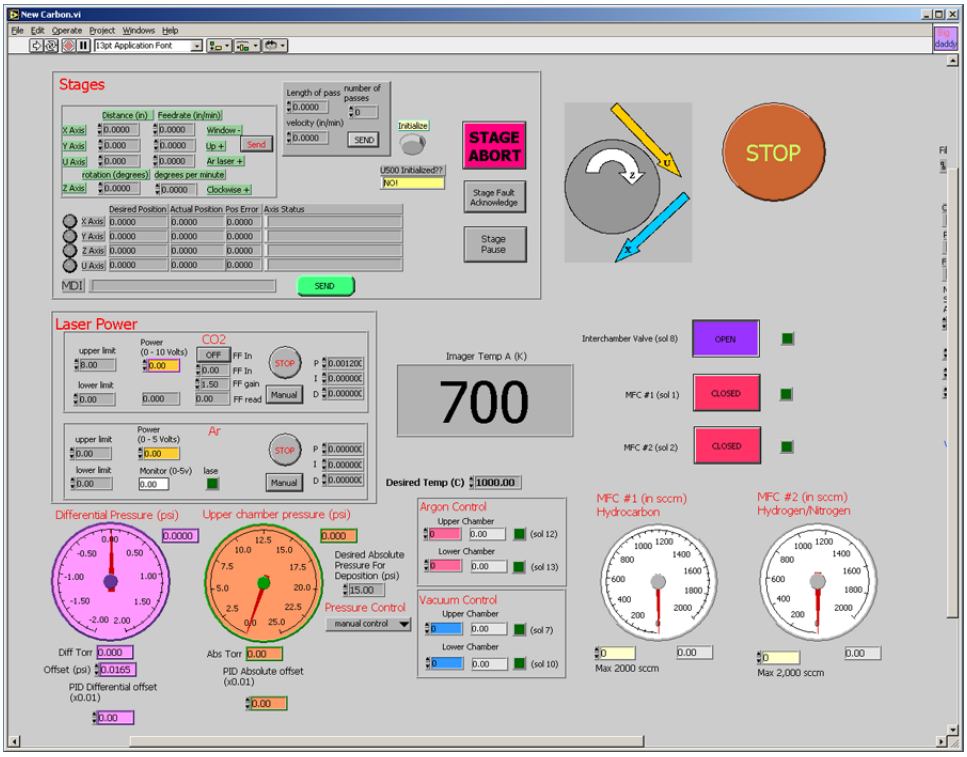

Figure 3.14: Typical screenshot of the LabVIEW operator interface

during deposition. The software interface of the camera allows the definition of Regions of Interest which can be used to output minimum, maximum, or mean temperature values. These ROIs are geometric shapes such as lines, rectangles, or circles.

The ROI output value is fed into the LabVIEW control computer as an analog current signal. The LabVIEW control program uses the input temperature as the feedback in a PID control loop to modulate the laser power in an effort to maintain constant temperature. Figure 3.15 is a diagram of the basic feedback temperature control system.

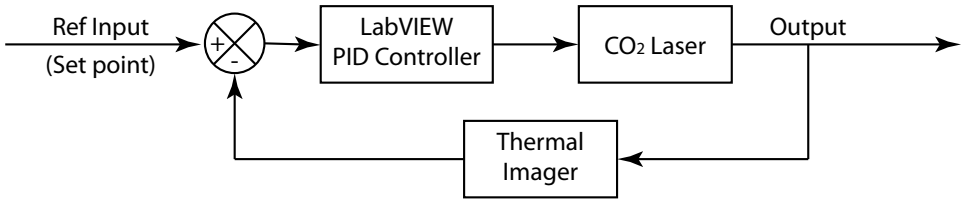

Figure 3.15: Block diagram of basic automatic temperature control system

The transfer function for a PID controller is given by

$$G_c(s) = K_p + \frac{K_i}{s} + K_d s \tag{3.2}$$

where K_p, K_i, and K_d are the proportional gain, integral gain, and derivative gain for the controller, and s is a complex variable in the frequency domain that results from the Laplace transform. If the controller input is the error signal, $e(t)$, then the output from the PID controller in the time domain, $m(t)$ is given by

$$m(t) = K_p\, e(t) + K_i \int_{-\infty}^{t} e(t)\, dt + K_d \frac{de(t)}{dt} \tag{3.3}$$

Proper tuning of the PID control loop requires finding values for K_p, K_i, and K_d that enable satisfactory behavior of the controller. Finding these values for the LCVD process has been challenging. The diagram of Figure 3.15 depicts a simplified interpretation of LCVD process control. The changing optical and thermal properties of the substrate as LCVD growth occurs as well as the heat of the deposition reaction are just a few examples of additional factors that complicate real–time temperature control of LCVD. The influence of these additional factors is shown in Figure 3.16.

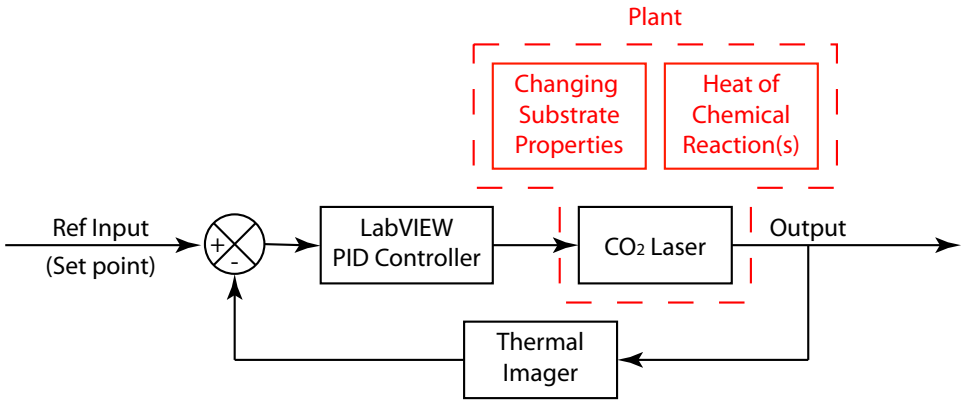

Figure 3.16: Block diagram showing the influence of LCVD process dynamics on the automatic temperature control system

The current implementation utilizes a combination of a LabVIEW PID controller and an additional integral–type controller. Normally, the ROI used is either a circle or a rectangle,

and the mean temperature value within the ROI is fed into the LabVIEW controller. Mean values are used due to their inherent resistance to noise effects.

One limitation of the current system is the speed of the control loop. While the thermal imager provides updated temperature data at a rate of 30 Hz, the cycle time for each loop of the LabVIEW controller for the entire LCVD system (and the temperature control subloop) is about 333 ms (3 Hz). Thus, only about 10% of the information acquired by the thermal imager is ultimately used by the control algorithm.

Overall, the temperature control system works well for processes that exhibit only moderate temperature sensitivity to laser input power within the operational domain established by the limitations of the DAQ hardware, LabVIEW software, CO_2 laser, and thermal imaging camera. The deposition of carbon from methane is one such process. Improvements in the sophistication of the control methods are necessary to enable practical temperature control of more sensitive processes.

CHAPTER IV

CARBON EXPERIMENTS

Carbon deposition has been widely explored in Georgia Tech's LCVD system. There are several reasons including the expanse of literature regarding the CVD of carbon, the availability and stability of hydrocarbon reagents, the robust nature of carbon deposition, and previous experience with the CVD of carbon coatings. Much of this carbon deposition experience utilized a reagent system consisting of a mixture of methane and hydrogen.

Carbon was used as a prototype material in the development of process planning algorithms for the LCVD process.[28] Some of the experiments presented here were done in support of the process planning work. More refined geometries included both advanced line pattern experiments and multi-layered carbon walls. Finally, more detailed characterization of carbon deposits was done through an X-ray diffraction technique.

4.1 Experimental Setup for Carbon Deposition

All carbon deposition done for this investigation utilized the methane–hydrogen reagent system. The overall chemical reaction was given by Equation 2.1:

$$\mathrm{CH_4}(g) + \text{xs } \mathrm{H_2}(g) \rightarrow \mathrm{C}(s) + 2\mathrm{H_2}(g) + \text{xs } \mathrm{H_2}(g) \tag{2.1}$$

The $\mathrm{CH_4}$ and $\mathrm{H_2}$ were both supplied from commercially available gas cylinders. The cylinders were connected to the upper deposition chamber through two separate mass flow controllers. Prior to entering the chamber, the species were mixed and made to flow through either the upper chamber side port or the reagent gas nozzle. During operation, gas flows into the chamber and is removed from the chamber at the same rate so as to maintain constant pressure. Figure 4.1 illustrates this reagent delivery system for carbon deposition.

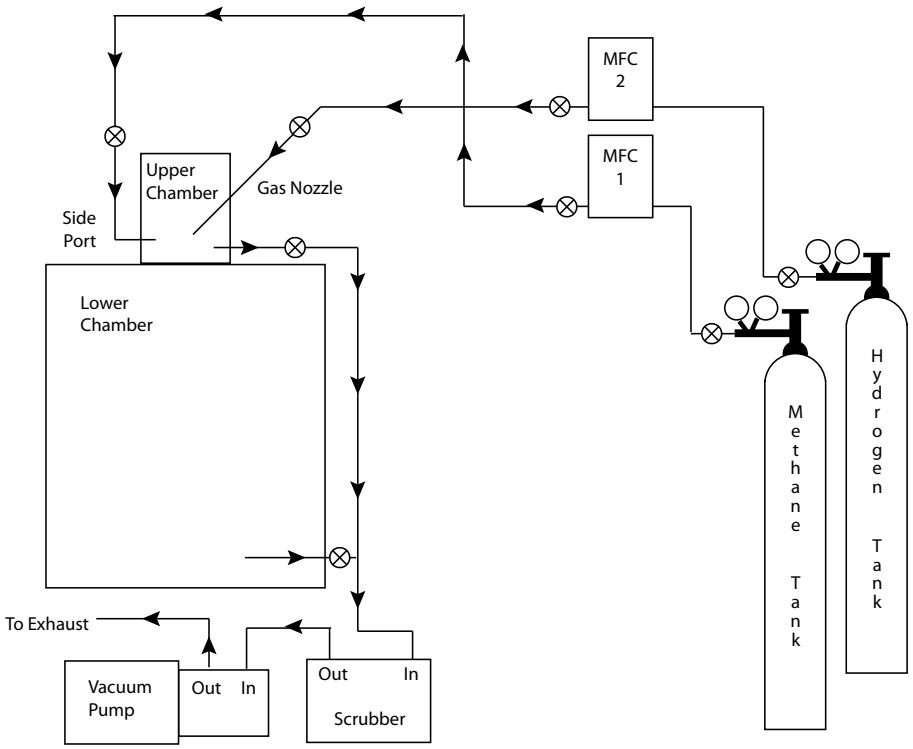

Figure 4.1: Setup for methane and hydrogen reagent delivery into chamber

The substrates used in carbon deposition were normally graphite. Graphite is an ideal substrate material because it can tolerate the high energy flux and high temperatures associated with the laser heating process without damage. Graphite is also widely available and is robust during handling. An additional benefit of using graphite is that if LCVD carbon deposits exhibit the hexagonal crystal structure of graphite as was shown in Section 4.7, the bonding between the substrate and the deposit may be enhanced. The similar coefficients of thermal expansion will also enhance adherence.

The substrates used in carbon deposition were typically one of two types of graphite: Industrial Sales Associates SK-85 or POCO AXF-5Q. The properties of these materials are given in Table A.1. All substrates were disks that were cut from a 19.05 mm diameter rod to a nominal thickness of 2.54 mm. The surface was sanded using 400 – 600 grit SiC grinding paper and then cleaned using compressed air. The substrates were stored in an air oven at 60°C for at least 24 hours prior to use.

4.2 Process Planning and Kinetic Studies for Carbon Fibers

One of the ultimate goals of LCVD research is to enable a system whereby a digitally defined part or pattern could be produced in the LCVD system in an automated fashion. The digital part definition as it exists in the software would be the only input required of the designer. Computer software would be used to decompose the defined part model into the appropriate machine settings for production of the deposit geometry. The process of translating geometric models into machine settings is termed *process planning*.

In support of Park's work developing the computer software for LCVD process planning, a number of carbon deposition experiments were executed.[28] The purpose of these experiments was to establish numerical relationships between the LCVD machine parameters and the resulting carbon deposit shapes. Ideally, these relationships are expressed as mathematical equations such as Equation 4.1

$$Y = \beta_0 + \beta_1 X_1 + \beta_2 X_2 + \beta_3 X_3 + \ldots \tag{4.1}$$

where Y is a particular deposit attribute (e.g. fiber diameter) that is given as a function of operating parameters, X_i (e.g. laser power, operating pressure, etc.). β_i are the regression coefficients that are determined by fitting experimental data to the equation.

Various techniques can be used in fitting experimental LCVD data to an expression. One method does not consider any theoretical relationship among the process variables and the deposit attributes, but simply seeks a statistical relationship. This type of approach provides a sufficient basis for process planning algorithms, but is strictly limited to predicting conditions within the range defined by the experimental data. A second method for approaching the regression process is to use equations with theoretical origins and regress the experimental data against these equations. These two methods for studying process–property relationships were compared.

A large set of carbon fiber experiments were performed and the data were used to derive both statistical and kinetic relationships between process parameters and deposit attributes.

The purely statistical regressions were termed *geometric regressions* and the kinetic studies were termed *kinetic regressions*.

After loading the graphite substrate and filling the chamber with the desired CH_4:H_2 mixture, the standard procedure for deposition of fibers in Georgia Tech's LCVD system is to initiate growth by engaging the laser at a constant high power (usually about 90 W) until the average temperature read by the thermal imager in the region of interest (ROI) approaches the desired average temperature for deposition. The time required for the temperature to reach this value differs somewhat with process conditions, but ranges from 20 to 90 s. Upon reaching the desired average temperature, the control mode for laser power is switched from manual to automatic and feedback control is used for the duration of the experiment in an effort to maintain a constant average temperature. Table 4.1 summarizes the conditions for all fiber experiments that were done in this investigation.

Table 4.1: Experimental conditions for carbon fiber deposition

Parameter	Value(s)
Substrate	AXF-5Q Graphite
Pressure (Torr)	600, 700, 800
CH_4 Flow (sccm)	325
H_2 Flow (sccm)	125
Avg ROI Temp (°C)	1600, 1625, 1650, 1675, 1700, 1725
ROI size (pixels)	143 x 220 AutoDetect
TI Zoom	R3Z4.5
Time (min)	2, 4, 6, 8

As seen in the table, the independent variables studied were chamber pressure, average temperature, and deposition time. The values for the variables were chosen based on prior experience and knowledge gained through the successful deposition of carbon fibers in Georgia Tech's LCVD system by others.[1]

All fibers were measured using a Southern Micro Instruments microscope with Nikon 20x/0.40 (WD 11.0) lens that has a coordinate display. For diameter measurements, the

top view of a fiber was used and both the maximum and minimum diameter values were recorded. Fiber heights were measured from the side view. Deposition rates were computed from the height measurements and the growth time.

4.2.1 Geometric Regression

Geometric models were generated for three fiber attributes: maximum diameter, minimum diameter, and height. Independent variables were deposition time, average ROI temperature, and total pressure. While not intentionally varied, substrate thickness was also measured and considered as a variable in the geometric regression models. The procedure was to generate different transformations of independent variables consistent with physical reasoning and then use the stepwise regression method to identify a useful subset of predictors. The regression models with the largest R^2 value were chosen as "best" since a higher R^2 indicates that the variability in the data is better explained by the model. Residual plots were also used to check for a normal distribution when determining the appropriateness of a model. Table 4.2 shows the best geometric regression models for each fiber deposit attribute,[28] where t_{dep} is the deposition time (min), T_{ROI} is the average ROI deposition

Table 4.2: Geometric regression models for carbon fiber attributes

Response Var	Regression Equation	R^2
Max dia (μm)	$-1411 + 7.83\,t_{dep} + 1.01\,T_{ROI} + 1146\,S_t$	85.4%
Min dia (μm)	$-401 + 0.000317\,T_{ROI}^2 - 0.213\,P_{sys}$	82.3%
Height (μm)	$-2.25E4 + 1.56E2\,t_{dep} - 1.47E7\,\frac{1}{T_{ROI}}$ $+5.02E3\ln P_{sys} - 4\times10^{-6}\,P_{sys}^3$	90.7%

temperature (°C), S_t is the substrate thickness (in), and P_{sys} is deposition pressure (Torr). It is unclear how the substrate thickness affects the deposit parameters under a temperature controlled process. As indicated by the values of R^2, all regression models were found to account for the variability in the data reasonably well.

4.2.2 Kinetic Regression

The experiments done in this study were not specifically designed to study the kinetics of the reaction; however, enough data were generated during the process to fit data to a kinetic expression. Under the conditions normally used in LCVD, it has been shown that carbon deposition from methane is a kinetically limited reaction.[1] The kinetic expression that gives the deposition rate as a function of concentration and temperature was given in Equation 1.6, and is rewritten here specifically for this reaction:

$$J''_{\mathrm{C}} = k_r C^n_{\mathrm{CH_4}} \tag{4.2}$$

which states that the reaction rate, J''_{C} (kmol/m^2-s), is proportional to the surface concentration of the reactant species, $C_{\mathrm{CH_4}}$ (kmol/m^3), to some power, n, where n is the order of the reaction. The rate constant, k_r was given by:

$$k_r = k_0 e^{\frac{-Q}{RT}} \tag{4.3}$$

where k_0 represented the pre–exponential factor (m/s), Q was the activation energy (kJ/k-mol), R was the universal gas constant (8.314 kJ/kmol K), and T was the temperature of deposition (K). The kinetic regression procedure involves fitting experimental data to the above equations to determine the parameters n, k_0, and Q. While different unit systems can be used for kinetic studies, due to the empirical relationship derived through the regression process, it is important to use consistent units for predictive purposes as were used for regression purposes.

As described in Section 3.4.1, during growth, a normal fiber can be assumed to have a maximum temperature at its tip. For these carbon experiments, fiber height was determined by measuring from the substrate surface to the fiber tip. Thus, for each fiber, the kinetic analysis was applied at the center of the fiber where the maximum temperature coincided with the fiber tip.

The maximum temperature was obtained for each fiber by using a MATLAB program to convert a thermal image captured during deposition into a temperature map and then

searching the temperature map for the maximum value. The maximum temperature during deposition was known to remain relatively constant because active temperature control was used throughout the growth process. The program written for this purpose is listed in Appendix B.1. Because valid thermal images were obtained for only eleven of the fibers, the kinetic regression analysis was limited to these fibers.

The methane concentration value, C_{CH_4} (kmol/m^3), for each experiment was computed using Equation 4.4

$$C_{CH_4} = \frac{F_{CH_4}}{F_{tot}} \frac{P_{tot}}{RT} \tag{4.4}$$

where F_{CH_4} is the flow rate of methane (sccm), F_{tot} is the total gas flow rate into the chamber (sccm), P_{tot} is the deposition chamber pressure (kPa), R is the universal gas constant (8.314 kPa-m^3/kmol-K), and T is temperature (K).

The correct value to use for temperature in Equation 4.4 is not obvious. One choice would be the temperature of the methane gas at the source, which would normally be close to room temperature (20–25°C). However, due to the high temperatures in the deposition zone, the absolute molar concentration changes significantly as the gas moves from the source toward the deposition surface. This fact leads to another choice of temperature in computing concentration, which is to use the value of the maximum temperature in the laser spot as found using the MATLAB program described above. This approach makes the reasonable assumption that the gas temperature directly above the substrate is equal to the maximum substrate temperature. The concern with adjusting the reagent concentration by the temperature in the deposition zone is that it correlates the two variables of temperature and concentration; however, it was deemed the more appropriate approach to use in fitting LCVD experimental data to the kinetic expression. Thus, for clarity, we rewrite Equation 4.4 replacing T with T_{max}:

$$C_{CH_4} = \frac{F_{CH_4}}{F_{tot}} \frac{P_{tot}}{RT_{max}} \tag{4.5}$$

The measurements of fiber height and growth times were used to compute the deposition rate J''_C (kmol/m^2-s) for the fibers.

$$J''_C = \frac{h}{t}\frac{\rho_C}{M_{w,C}} \tag{4.6}$$

where h is the fiber height (m), t is the total fiber growth time (s), ρ_C is the density of the deposited carbon (kg/m^3), and $M_{w,C}$ is the molecular weight of carbon (kg/kmol). The values used for ρ_C and $M_{w,C}$ were assumed to be close to those of bulk carbon, 1760 kg/m^3 and 12.0107 kg/kmol, respectively. Values of h and t along with the T_{max} and C_{CH_4} for all fibers used in the kinetic regression are given in Table 4.3.

Table 4.3: Data used in kinetic regression analysis for carbon fibers

Experiment	Sample	Height, h (m)	Time, t (s)	Dep Rate, J (kmol/m^2-s)	Conc, C_{CH_4} (kmol/m^3)	Temp, T_{max} (K)
L228	3	1.17E-03	360	4.76E-04	3.98E-03	2330
L229	1	1.62E-03	480	4.94E-04	3.98E-03	2330
L229	12	1.60E-03	300	7.83E-04	3.91E-03	2372
L229	13	2.37E-03	480	7.24E-04	3.91E-03	2372
L230	9	1.53E-03	480	4.68E-04	2.96E-03	2351
L231	2	8.11E-04	480	2.48E-04	3.06E-03	2274
L231	11	1.07E-03	360	4.34E-04	2.95E-03	2359
L232	3	1.61E-03	480	4.93E-04	3.49E-03	2322
L232	13	1.06E-03	480	3.23E-04	3.53E-03	2295
L233	1	1.24E-03	240	7.58E-04	3.42E-03	2372
L233	12	1.44E-03	360	5.86E-04	3.42E-03	2372

In order to use multivariate linear regression techniques, the kinetic expressions given in Equation 4.2 and Equation 4.3 were combined and transformed:

$$\begin{aligned} J''_C &= k_0 C_{CH_4}^n e^{\frac{-Q}{RT_{max}}} \\ \ln J''_C &= \ln k_0 + n \ln C_{CH_4} - \frac{Q}{R}\frac{1}{T_{max}} \end{aligned} \tag{4.7}$$

Equation 4.7 is easily related to the general linear regression expression

$$Y = \beta_0 + \beta_1 X_1 + \beta_2 X_2 \tag{4.8}$$

with

$$Y = \ln J''_{\mathrm{C}} \tag{4.9}$$

$$\beta_0 = \ln k_0 \tag{4.10}$$

$$\beta_1 = n \tag{4.11}$$

$$X_1 = \ln C_{\mathrm{CH_4}} \tag{4.12}$$

$$\beta_2 = \frac{-Q}{R} \tag{4.13}$$

$$X_2 = \frac{1}{T_{max}} \tag{4.14}$$

The results of the multiple regression analysis are shown in Table 4.4, and the regression equation generated by the analysis was:

$$\ln J''_{\mathrm{C}} = 18.6724 + 1.01853 \ln C_{\mathrm{CH_4}} - 48003.1 \frac{1}{T_{max}} \tag{4.15}$$

By using Equation 4.10, Equation 4.11, and Equation 4.13 in conjunction with the coefficients shown in Equation 4.15, the kinetic parameters for carbon fiber LCVD could be determined. These parameters are summarized in Table 4.5, and the final Arrhenius expression is given in Equation 4.16:

$$J''_{\mathrm{C}} = 1.2856 \times 10^8 C_{\mathrm{CH_4}}^{1.0185} e^{\frac{-3.9911 \times 10^8}{RT_{max}}} \tag{4.16}$$

where $C_{\mathrm{CH_4}}$ is measured in kmol/m^3 and T_{max} is measured in K. R is 8314 J/kmol-K.

The results from the kinetic regression model were encouraging. First, note the value of n, the order of the reaction, is 1.019. While Jean's value of n was significantly different from 1 at 3.46,[1] others' carbon CVD kinetic data supports the idea that n should be approximately equal to 1.[94] Next, the value of Q from the regression is shown to be 399 kJ/mol. Again, while this value differs from Jean's reported value of 176 kJ/mol, the value of 399 kJ/mol is more aligned with the reported values ranging from 430 to 450 kJ/mol of CVD of carbon from methane.[94] In sum, the regression fit the data reasonably well with

Table 4.4: Carbon fiber multiple regression analysis

Dependent variable: $\ln J''_C$

Parameter	Estimate	Standard Error	T Statistic	P-Value
CONSTANT	18.6724	2.6326	7.09279	0.0001
$\ln C_{C\,H_4}$	1.01853	0.294407	3.45959	0.0086
$1/T_{max}$	-48003.1	5465.62	-8.78275	0.0000

Analysis of Variance

Source	Sum of Squares	Df	Mean Square	F-Ratio	P-Value
Model	1.15669	2	0.578343	51.06	0.0000
Residual	0.0906187	8	0.0113273		
Total (Corr.)	1.24731	10			

R-squared = 92.7 percent
R-squared (adjusted for d.f.) = 90.9 percent
Standard Error of Est. = 0.10643
Mean absolute error = 0.0759425
Durbin-Watson statistic = 2.94589 (P=0.0218)
Lag 1 residual autocorrelation = -0.562263

Table 4.5: Kinetic parameters for carbon fiber LCVD

Parameter	Symbol	Value
Pre–exponential factor (m/s)	k_0	1.2856×10^8
Reaction order	n	1.0185
Activation Energy (J/kmol)	Q	3.9911×10^8

an R squared value of 92.7 and an adjusted R squared value of 90.9; therefore, it seems the kinetic expression given in Equation 4.15 is a suitable model for the LCVD of carbon from a methane precursor within the space defined by operating conditions used in this investigation.

4.2.3 Model Comparison

It was useful to determine whether the geometric regression models or the kinetic regression models were more capable of predicting fiber deposit height. The only fibers for which valid temperature data were available were the same eleven used in the kinetic analysis; therefore, these fibers were used in a simple point–wise comparison between the geometric and kinetic regression models. Figure 4.2 is a bar chart comparing the predicted height using the two regression equations to the measured fiber height. Overall, both models predict the height reasonably well. Figure 4.3 depicts the error value at each fiber for the two regression methods. In general, the geometric regression model under–predicted the fiber height while the kinetic model error was balanced between over and under–predicting. In conclusion, when possible, it is desirable to use kinetic regression models; because of their theoretical origins, they can be used with some confidence outside of the envelope of experimental data used in their derivation. The results of a geometric regression model must **only** be applied within the experimental envelope used in their generation.

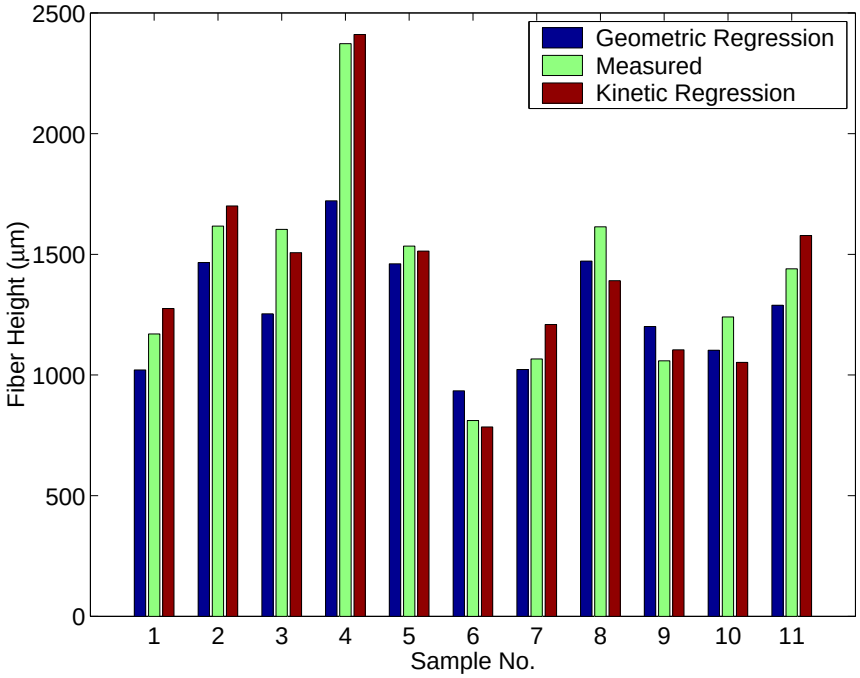

Figure 4.2: Comparison of regression model predictions to measured fiber heights

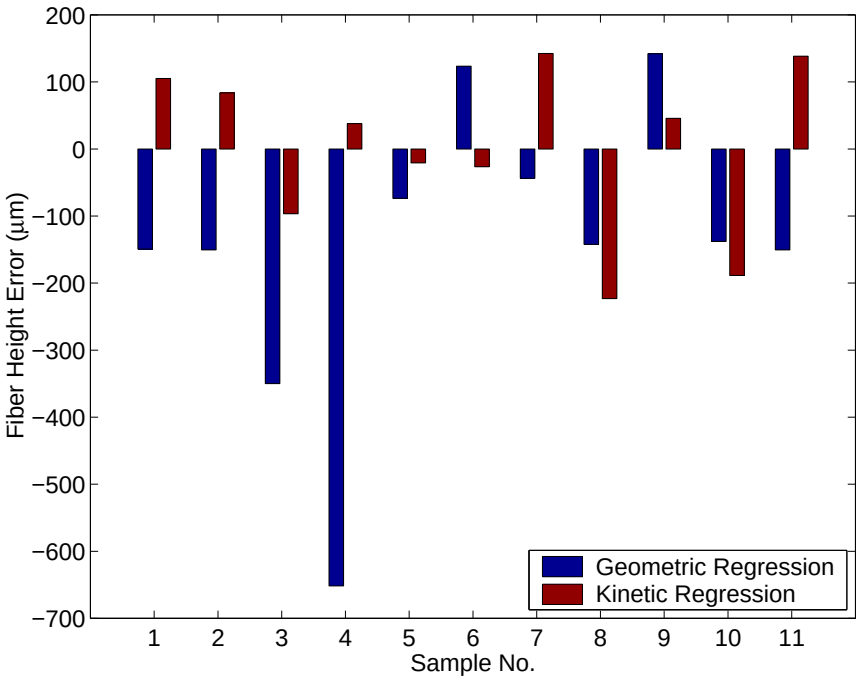

Figure 4.3: Fiber height error comparison between the two regression model predictions

4.3 Carbon Line Experiments

The second fundamental LCVD growth mode is horizontal or patterned growth. The primitive shape representative of this growth mode is the single layer line. An array of carbon line experiments were executed in an attempt to better understand and characterize the relation between the process conditions and line geometry.

4.3.1 Exploratory and Refined Experiments

The first task was to establish some basic understanding of the relationships among the different variables in carbon line deposition. This was accomplished by executing various experiments in which all but one variable were held constant. Some selected experiments are discussed below.

Experiment C-181L was used to explore the relationship between laser scan speed and line morphology. A series single layer of lines was run on SK-85 graphite substrates. The total chamber pressure was 760 Torr with a CH_4:H_2 partial pressure ratio of 3:1. Flow was maintained through the upper chamber side port (no nozzle flow) at 500 sccm using the same 3:1 partial pressure ratio. Laser power was kept constant at 90.3 W and laser scan speeds ranged from 0.229 to 127 mm/min. The micrographs in Figure 4.4 illustrate how the lines changed at these different scan speeds.

The carbon growth rate imposes a lower limit on the line scan speed. If the scan speed is too slow, the growth will extend from the substrate as an angled fiber. In fact, this is the technique used to grow truss structures.[1] The slowest scan speed of 0.229 mm/min produced just such a structure. Once the minimum line scan speed was exceeded, scan speeds up to 2.54 mm/min produced very distinct lines with a well–defined region of bulk growth in their center. Scan speeds of 6.35 to 25.4 mm/min produced less distinct lines with a continuously varying node size across their width. These growth nodes are small and flaky far from the line center and become progressively larger and more spherical near the line center. The average node size is shown to decrease with increasing scan speed. The

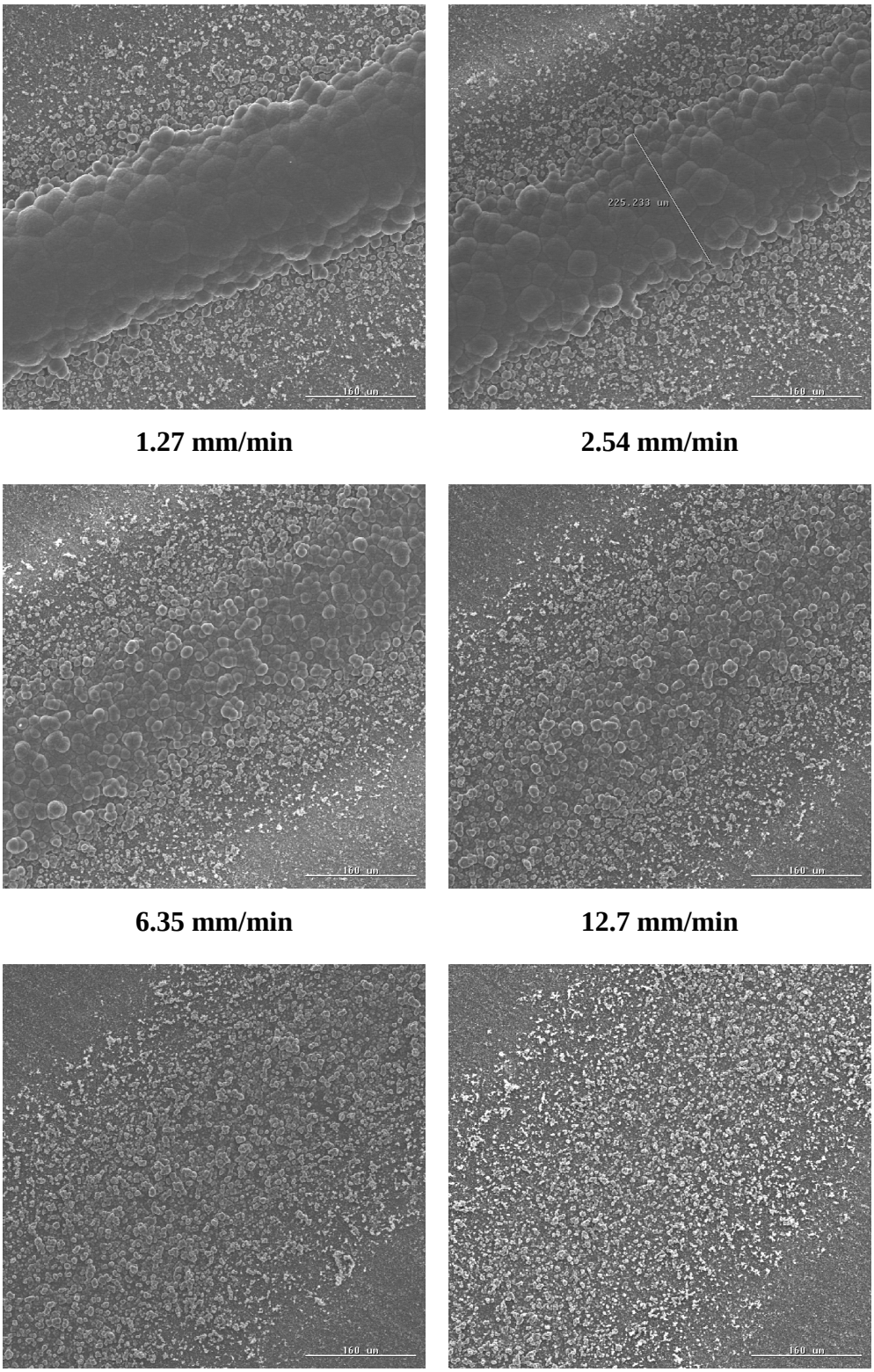

1.27 mm/min **2.54 mm/min**

6.35 mm/min **12.7 mm/min**

25.4 mm/min **63.5 mm/min**

Figure 4.4: Morphology of carbon lines at different laser scan speeds

63.5 mm/min scan speed produced a wide area of very small growth flakes or nodes. The coverage area of these nodes was not more than 75%, even in the center of the line. These results indicated that speeds of 2.54 mm/min or less should be used if the goal is to create a well–defined line of bulk carbon. Such a line is an important first step in the growth of uniform carbon walls as will be discussed in Section 4.6

Experience has shown that in its current state, the automatic temperature control system does not always improve the temperature stability of single layer carbon line growth. For a constant power, the temperature is observed to be relatively stable. The relationship between laser power and average surface temperature was investigated using the thermal imaging camera.

In C-189L, a series of 10 lines was run using different power levels on SK-85 graphite substrates. The total chamber pressure was 760 Torr with a CH_4:H_2 partial pressure ratio of 3:1. Flow was maintained through the upper chamber side port (no nozzle flow) at 500 sccm using the same 3:1 partial pressure ratio. The thermal imager Region of Interest (ROI) was a 150 pixel diameter circle. Laser scan speed was kept at 2.54 mm/min.

The laser control voltage, power, average ROI temperature and its standard deviation are given in Table 4.6 with a plot of the data shown in Figure 4.5.

The average ROI temperature is shown to be linearly related to the incident laser power. The temperature is shown to have a standard deviation of between 20 and 30 K for most of the lines. SEM micrographs of the resulting lines revealed that the carbon growth nodes were larger for scans using a higher laser power. These results were consistent with those of Experiment C-181L.

4.3.2 Designed Experiments

Similar to the case of carbon fibers, several designed experiments were run with single layer carbon lines. These experiments were used to establish the numerical relationships between line shapes and process conditions. For most of the lines, the height and width

Table 4.6: Experimental conditions for C-189L laser power vs temperature study

Laser Control (V)	Laser Power (W)	Average ROI Temp (K)	Temp Std. Deviation (K)
5.0	67.2	1954	18.2
5.5	71.9	1977	21.4
6.0	76.3	1996	16.2
6.5	80.3	2007	23.4
7.0	84.0	2023	28.2
7.5	87.3	2050	24.1
8.0	90.3	2071	22.7
8.5	93.0	2092	23.4
9.0	95.3	2126	22.0
9.5	97.3	2139	29.4

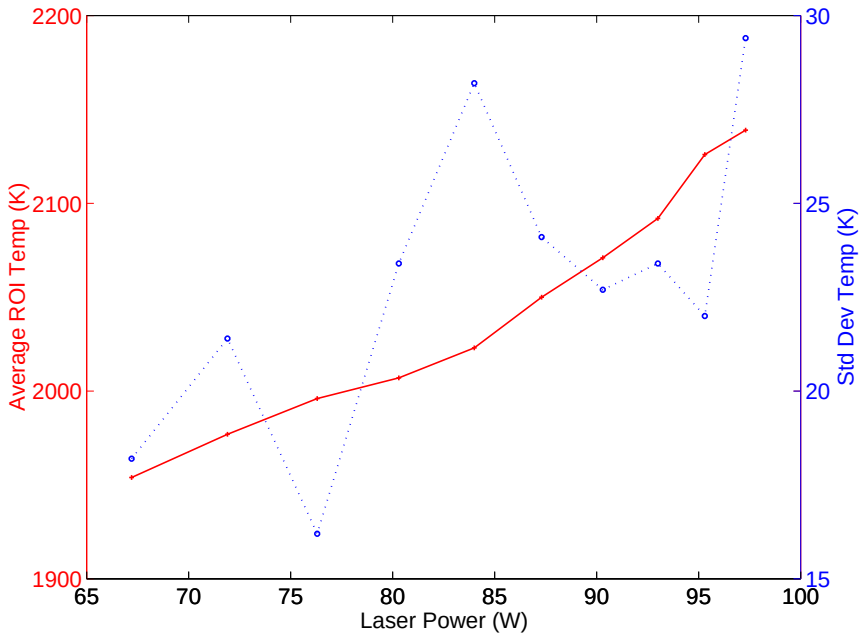

Figure 4.5: Average laser spot temperature during laser scan for different incident power

was measured using a CyberScan LV profilometer made by CyberOptics. Three profiles were taken of each line and the height and width from all three were averaged. The data were fit to regression equations for use in process planning algorithms.[28] The procedure for finding suitable regression expressions used the same stepwise regression technique as the geometric regressions for fibers in Section 4.2.1.

The first experiment set, C-DOE-L1, utilized SK–85 graphite substrates. The experiment conditions can be found in Table 4.7. The best equations for predicting line height and

Table 4.7: Conditions for C-DOE-L1 carbon line experiments on SK–85 graphite

Experiment Nos.	C-221L–C-225L
Substrate	SK–85 graphite
Scan Speed (mm/min)	1.27, 2.54, 3.81, 5.08, 6.35
Pressure (Torr)	800
CH_4 Flow (sccm)	375
H_2 Flow (sccm)	125
Nozzle Status	OFF
Laser Control (V)	4, 5, 6, 7, 8
Laser Power (W)	57, 67, 76, 84, 90
ROI (pixels)	200 ∅ circle
TI Zoom	R3Z4.3

width from process parameters are given in Table 4.8,[28] where L_p is the laser power (W), S_t is the substrate thickness (in), and V_s is the laser scan velocity (in/min). As indicated

Table 4.8: Geometric regression models for lines on SK–85

Response Variable	Regression Equation	R^2
Height (μm)	$-92.7+47.6\ln L_p+1.44\frac{1}{S_t}+1.28\frac{1}{V_s}$	74.6%
Width (μm)	$-519+10.7\frac{1}{S_t}+333\ln L_p$	89.4%

by the values of R^2, all regression models were found to account for the variability in the data reasonably well.

Two additional experiment sets were performed on AXF–5Q graphite substrates. The

significant difference between the SK–85 graphite and the AXF–5Q graphite was the grain size, 200 μm and 5 μm, respectively. The smaller grain size provided a more uniform surface for line deposition. It was also observed to require more laser power to achieve the same surface temperature. Conditions for the AXF–5Q line experiments are provided in Table 4.9.

Table 4.9: Conditions for carbon line experiments on AXF–5Q graphite

	C-DOE-L2	C-DOE-L3
Experiments	C-234L–C-244L	C-245L–C248L
Substrate	AXF–5Q graphite	AXF–5Q graphite
Scan Speed (mm/min)	1.27, 2.54, 3.81, 5.08, 6.35	1.02, 1.52, 2.03, 2.54
Pressure (Torr)	600, 700, 800	800
CH4 Flow (sccm)	325	325
H2 Flow (sccm)	125	125
Nozzle	OFF	OFF
Laser Control (V)	4, 5, 6, 7, 8	7, 7.5, 8, 8.5, 9
Laser Power (W)	57, 67, 76, 84, 90	84, 87, 90, 93, 95
ROI (pixels)	200 ∅ circle	200 ∅ circle
Zoom	R3Z4.4	R3Z4.5

Much like C-DOE-L1, the data from C-DOE-L2 and C-DOE-L3 were used in a regression analysis to derive equations relating the height and width as a function of process parameters. The resulting equations are given in Table 4.10[28] where the only new variable is the total chamber pressure, P_{sys}.

Table 4.10: Geometric regression models for lines on AXF–5Q

Response Variable	Regression Equation	R^2
Height (μm)	$6.3 + 0.0631\frac{1}{V_s^2} + 99.5\ln L - 50720\frac{1}{P_{sys}} + 58.2\ln S_t$	86.3%
Width (μm)	$12206 - 827V_s + 375\ln L - 12.7\frac{1}{S_t} - 1648\ln P_{sys}$ $-1259877\frac{1}{P_{sys}}$	77.3%

4.4 Kinetic Analysis of Line Deposition

In order to do a kinetic analysis like the one in Section 4.2, a period of constant temperature growth must be maintained. The dynamic nature of LCVD line growth does not provide such a period. However, because the carbon fibers and lines were grown under very similar conditions, it was determined that the fiber kinetic parameters could be used to estimate line attributes, specifically line height.

The first step in the analysis was to acquire a thermal image taken during line growth. Just like the fiber kinetic studies, this image was converted to a temperature map. From the temperature map, temperature profiles across the laser spot could be generated as shown in Figure 4.6. If we assume that the timescale of conduction is significantly smaller than that of the laser scanning, the temperature profile can be assumed to be symmetrical with respect to the laser scan direction. The horizontal axis on a temperature profile like that shown in Figure 4.6 can be converted to a time axis by dividing the position by the scan speed. The resulting temperature time curve can then be divided into a series of discrete time interval as shown in Figure 4.7. For each discrete time interval, the average temperature was computed, and this temperature was used to compute the deposition rate from Equation 4.16. The deposition rate was multiplied by the size of the time interval Δt to yield a finite volume or height of deposit. Finally, the deposit quantities from all time intervals were summed to give a total deposit quantity or deposit height. Much like the fiber kinetic analysis, the line kinetic analysis is limited in application to the point of maximum temperature, which is assumed to occur in the center of a carbon line. Therefore, the predicted height value is for the center of the line.

The described analysis was executed using Sample 6 from carbon line experiment C-243L. This experiment was part of the C-DOE-L2 set described in Section 4.3.2. Specific conditions are given in Table 4.11 along with the measured line height and the predicted line height using both the geometric and kinetic regression equations. The kinetic model is shown to be more appropriate for this particular line sample for predicting line heights.

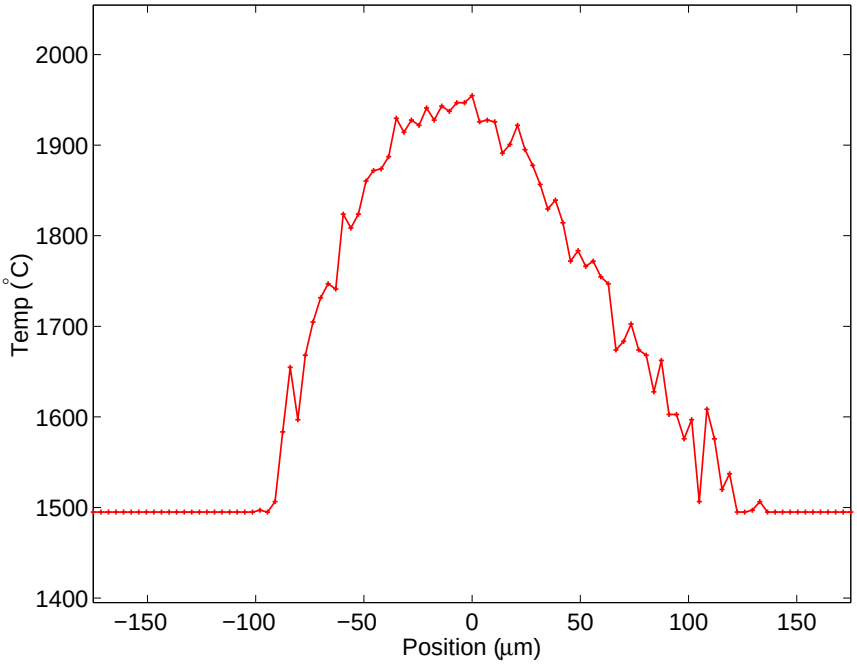

Figure 4.6: Example temperature profile across laser spot extracted from thermal image for C-243-L Sample 6

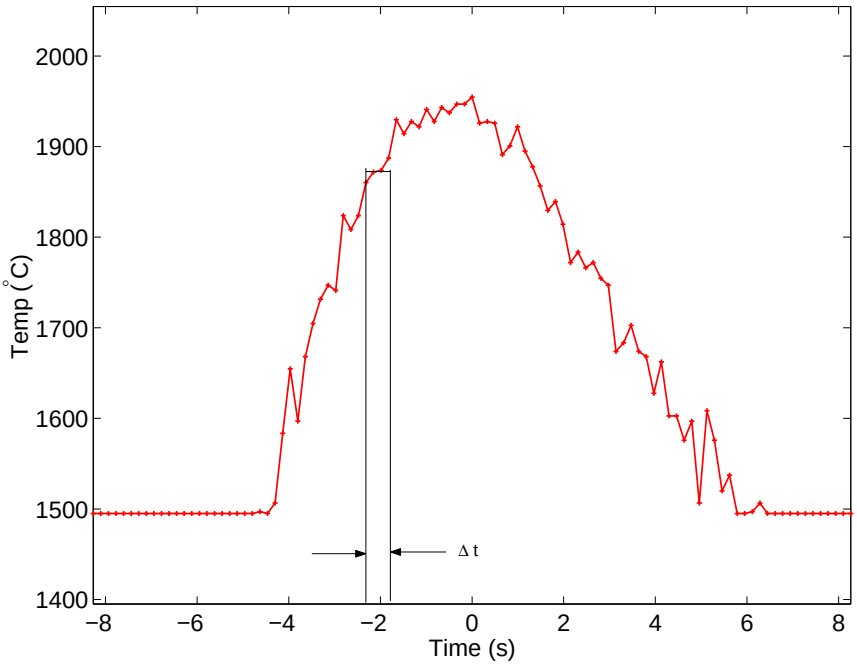

Figure 4.7: Transformed temperature–position profile into temperature–time profile for C-243-L Sample 6

Table 4.11: Comparison of geometric and kinetic regression models of carbon line height

Pressure (Torr)	Laser Power (W)	Scan Speed (mm/min)	Measured Height (μm)	Geometric (μm)	Kinetic (μm)
800	84.0	1.27	6.7	13.3	4.71

This should be considered when developing process planning algorithms for carbon LCVD.

4.5 Advanced Carbon Line Patterns

In order to realize the deposition of the dispenser cathode assembly, the necessary materials must be deposited in a specific circular pattern. Carbon lines were deposited in a circular pattern resembling that required by the cathode specification to illustrate the capability of Georgia Tech's LCVD system to produce this geometry. The experiment used a pressure of 760 Torr, 500 sccm of CH_4:H_2 mixture in a 3:1 ratio, and a constant laser power of 90.3 W. The substrate was SK–85 graphite and the target laser scan speed was 2.54 mm/min. Figure 4.8 illustrates the result of this experiment.

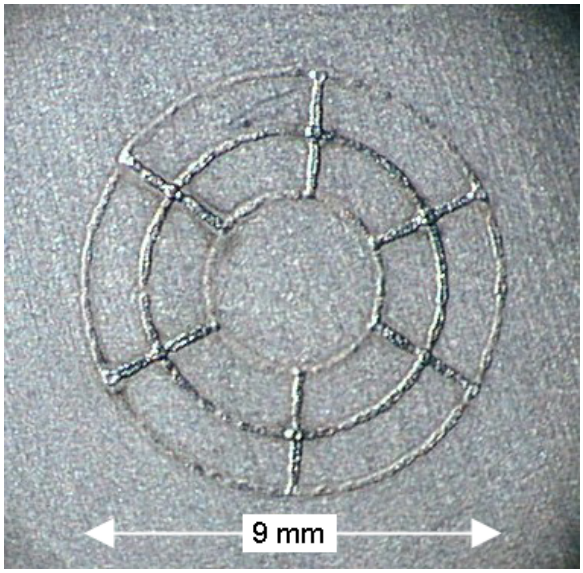

Figure 4.8: Circular pattern of carbon line deposition illustrating machine capability

Note that the circular lines were more sparse and nonuniform than were the straight lines of previous experiments. The primary reason for the nonuniform deposition is that

when depositing circles using the existing LCVD stage control system, the operator can not directly enter the line scan speed. The scan speed must be entered in units of degrees/min for the rotational z-axis. The circumference of the desired circle and the desired line scan speed can be used to calculate the necessary rotational speed in degrees/minute. However, this calculation requires accurate knowledge of the radius of the circle which depends on the accurate alignment of the laser beam to the center of the rotational z-stage. While reasonable efforts were made to keep the beam aligned to the center of the z-stage, this was not always possible due to the need to remove the laser optics during substrate loading and unloading. It was particularly difficult to align the beam to the stage prior to installation of the fourth mechanical stage. The uncertainty in the line scan speed for the circles derives from the uncertainty in a priori knowledge of the circle diameter.

This circular carbon line pattern contains many instances of intersecting lines. The deposition of intersection lines is difficult because of the positive feedback tendency of the process. Only through very robust temperature control can the deposition of intersecting lines be made possible. This particular structure involved the deposition of single layer carbon lines and did not utilize the automatic temperature control system. The intersections show a tendency to be much taller than the adjoining lines which confirms the need for robust temperature control in these types of patterns.

4.6 Carbon Wall Deposition

An extension of the carbon line deposition growth mode is the deposition of multi-layered structures known as walls. Walls are grown by scanning the substrate back and forth beneath the laser to build a structure via the deposition of layers. Layered processes are common in rapid prototyping due to their inherent ability to build three dimensional objects from a series of two dimensional data known as slices. In support of some of the envisioned applications of LCVD, it was pertinent to demonstrate the successful deposition of multi-layered structures.

As mentioned above, single–layer carbon lines can be deposited without using feedback temperature control. In the fabrication of a multi–layered wall, it becomes important to know when, during the deposition process, is the ideal time to engage the feedback temperature control system. Experiment C-182L involved the deposition of a series of 4–layer carbon walls on SK-85 graphite. These walls were run under a constant laser power of 90.3 W with each using a different scan speed ranging from 1.27 to 228.6 mm/min. Other conditions included a total pressure of 760 Torr, partial pressure CH_4:H_2 ratio of 3:1, and a total gas flow of 500 sccm.

The resulting carbon walls closely resembled the single layer lines run at different scan speeds in Experiment C-181L. The difference was that because these walls were four layers thick as opposed to one layer, the mass of deposit was significantly higher in all cases.

During the C-182L experiments, the thermal imager was used to record the average laser spot temperature. These plots revealed several interesting trends as shown in Figure 4.9. For the 2.54 mm/min scan speed, the temperature was shown to increase during the initial portion of the first layer. This could be the reflection of transient heating of the substrate which has been studied by others.[64] After about 0.2 mm, the first layer showed a jump from about 1625 to about 1725°C. This could reflect the beginning of the deposition process. The average temperature increased with each successive layer, likely the result of increased thermal resistance. The temperature variation increased significantly after the second layer suggesting the need for feedback control. All layers showed an asymmetrical temperature profile along the length. The end where deposition initiated showed a consistently lower temperature than the mean. The opposite end shows a consistently higher temperature than the mean. This temperature asymmetry is reflected in the shape of almost all multi–layered LCVD structures and is one of the prime motivations for using feedback temperature control.

For the higher scan speeds of 6.35, 12.7 mm/min, and others (not shown), the temperature profiles showed a linear relationship to position. The initial end is always the lowest

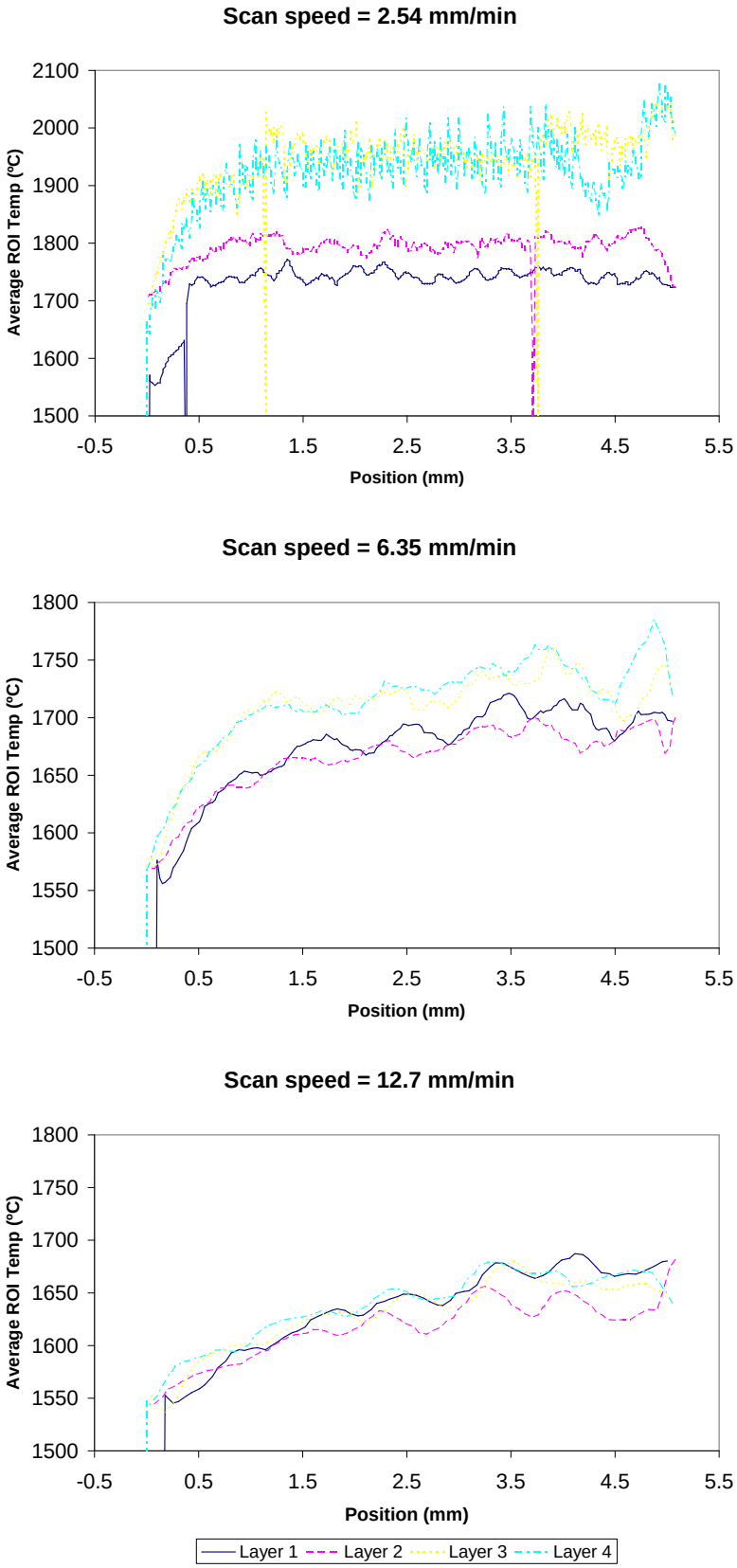

Figure 4.9: Average ROI temperature vs position for 4–layer carbon walls

temperature point, and the opposite end is the highest temperature point. The 6.35 mm/min scan speed showed an increase in mean temperature after the second layer of deposit, but higher scan speeds revealed no such shift. The increase in mean temperature is related to the change in substrate material properties and shape resulting from the newly formed deposit. In addition to transient heating effects, the longitudinal asymmetry of the walls could be related to the position of the line on the graphite disk substrate (i.e., distance from the substrate edge); however, thus far no strong evidence has emerged to support this theory.

The results of C-182L suggest that if the goal is to build a base layer of carbon lines for the subsequent use of the feedback temperature control system, a single layer line with a scan speed of 2.54 mm/min is optimal. As shown in Figure 4.9, the first layer under these conditions yielded a uniform temperature along the wall length and produced significant bulk growth. The second layer demonstrated an upward shift in mean temperature, but still produced a very uniform temperature along the line length. The third layer showed a substantial increase in both mean temperature and temperature variation. The feedback control system should be engaged after the first layer. At this point, there is a substantial amount of bulk growth that can serve as the foundation for a wall. The temperature stability within the second layer will help keep the system stable during the transition from constant laser power to feedback control. Also, engagement of the feedback control earlier in the process helps prevent the formation of local disparities that tend to exacerbate temperature fluctuations within layers.

A series of experiments, identified as C-204L, was performed to better understand the evolution of carbon walls with the addition of successive layers. The setup was the normal 760 Torr total pressure with a 3:1 ratio of CH_4:H_2. Flow was 500 sccm of the 3:1 mixture through the side port. The procedure was to deposit a series of walls with different numbers of layers ranging from 1 to 16. All walls used the exact same processing conditions on a per layer basis. The first two layers (where applicable) were deposited using a constant laser power of 90.3 W and a scan speed of 5.08 mm/min. All additional layers used a

scan speed of 5.08 mm/min with feedback temperature control. The thermal imager ROI was a 150 pixel diameter circle with an average ROI temperature setpoint of 1700°C. The micrographs in Figure 4.10 show how the carbon wall surface changed with the addition of successive layers.

The single layer line shows a similar structure to the lines grown under similar conditions in Experiments C-181L and C-189L. The line consists of a bulk region of distinct growth nodes that appear to have evolved from the original growth sites on the substrate surface. As layers are added these growth nodes become larger and less pronounced. The largest changes in surface morphology appeared in the first 4–6 layers. The 10 layer wall shows the surface has become relatively smooth and the width of the taller part of the wall appears to be only about 2/3 the width of the wall base. The 16 layer wall has a similar appearance as the 10 layer one albeit is narrower at the top and shows an ever smoother surface.

The culmination of the carbon line and wall experiments involved the fabrication of a 20 layer structure utilizing optimal scanning conditions for each layer. The substrate was an SK–85 graphite disk. The conditions included a total pressure of 760 Torr with the typical 3:1 ratio of CH_4:H_2. The flow was 500 sccm through the gas nozzle of the same mixture. The first layer was run using a constant 8 V laser control signal (90.3 W) at a scan speed of 2.54 mm/min. Subsequent layers were run using the feedback temperature control system at a constant scan speed of 2.54 mm/min. The thermal imager ROI was a 150 pixel diameter circle and the average temperature within the circle was controlled to 1650°C. Figure 4.11 shows the thermal imager interface during the later stages of wall growth. Notice the very distinct elongated shape of the laser spot due to the presence of the wall.

The overall length of the wall was 5.08 mm. An optical microscope image of the resulting deposit is shown in Figure 4.12.

This wall was mounted and polished for SEM observation of the cross section along its length. As can be seen in Figure 4.13, the micrographs revealed some interesting details

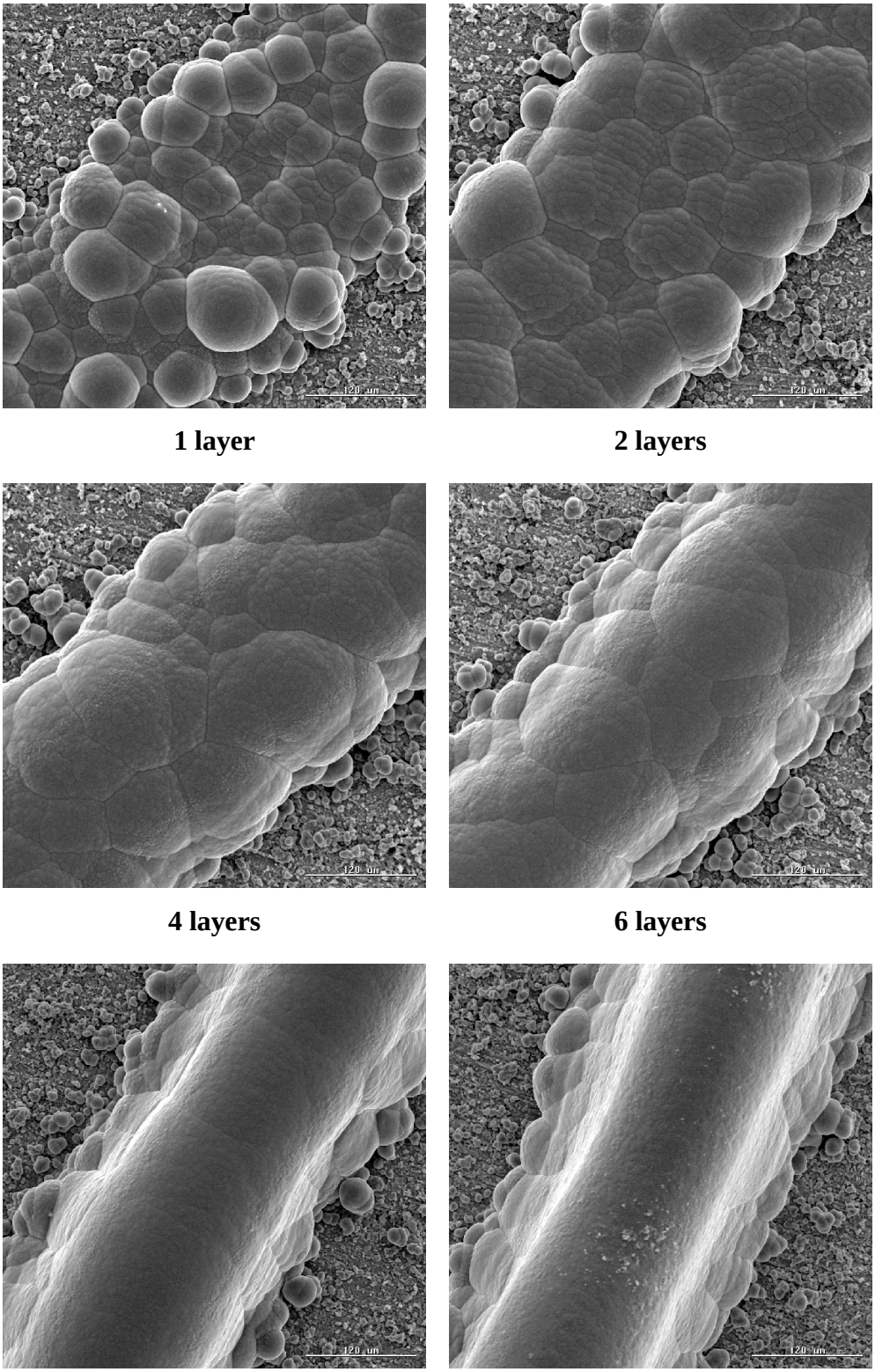

Figure 4.10: Evolution of the surface morphology of a carbon wall

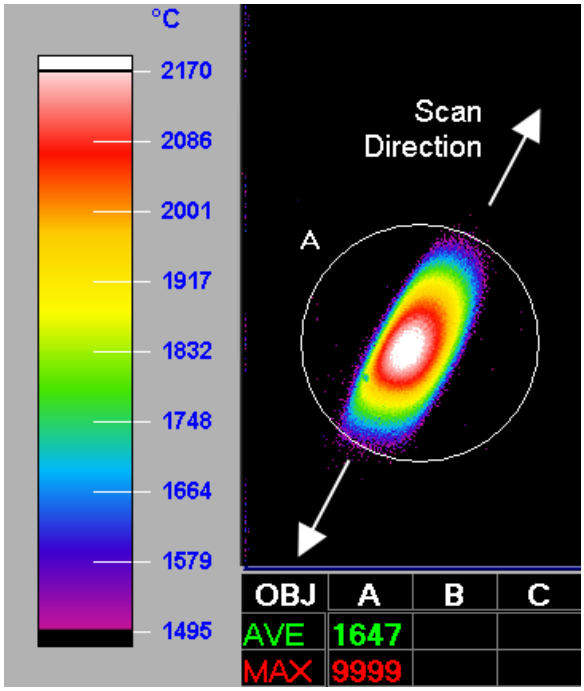

Figure 4.11: Thermal imager screen during wall deposition

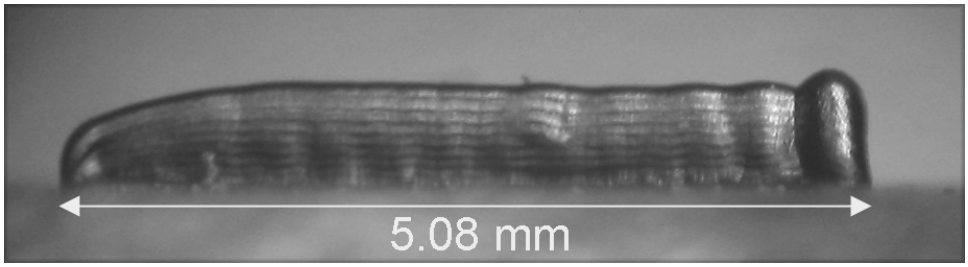

Figure 4.12: Optical microscope image of 20 layer carbon wall

within the multi–layered structure. Figures (a) and (b) show the left and right end of the wall, respectively, while Figures (c) and (d) highlight the substrate–wall interface at these same ends. The layers in the wall are apparent due to the dark lines at the layer interfaces. These dark lines represent a change in some material property in this region which could be related to a change in microstructure or a change in density. In general, the carbon layers are consistently between 30 and 40 μm thick. Cracks are apparent in some of the layer interfaces such as shown in Figure (e) and within individual layers as seen in Figure (f). Figure (f) shows the deposit–substrate interface to look very similar to the interface between the deposit layers.

The cracks observed in C-262L-1 could have been created or exacerbated by the mounting and polishing process. A second carbon wall, C-262L-2, was grown using identical conditions as C-262L-1 except that it was 15 layers instead of 20 layers thick. In order to determine if an as–grown wall exhibited similar structural defects, C-262L-2 was analyzed using a computed X-ray tomography technique. This process works by scanning circles around a sample so as to create cross–sectional views of the interior density. This procedure was done at several points along the length of the carbon wall. An example of a cross–section from the computed tomography investigation is shown in Figure 4.14.

The light and dark areas in the X-ray image represent regions of different densities. The dark areas along the interface of many of the carbon layers could indicate cracks. The presence of cracks in this ”as–deposited” sample confirms that these cracks were created during the deposition process and are not caused by the metallographic preparation.

The internal cracks of the carbon LCVD deposits are consistent with those observed by others.[20] It is believed they are an implication of thermal stresses induced within the structure during the deposition process.

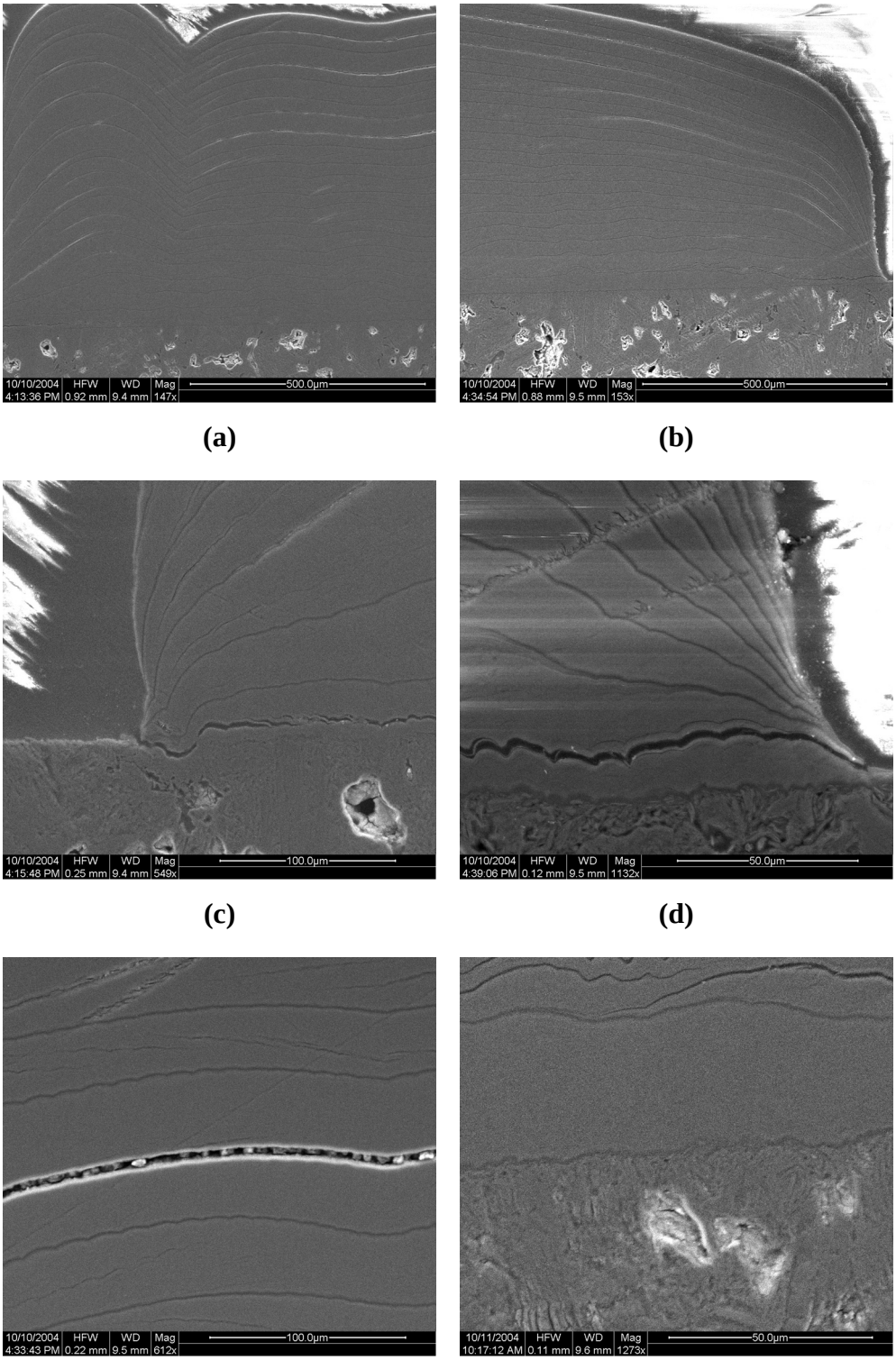

Figure 4.13: SEM micrographs from 20 layer carbon wall (C-262L-1)

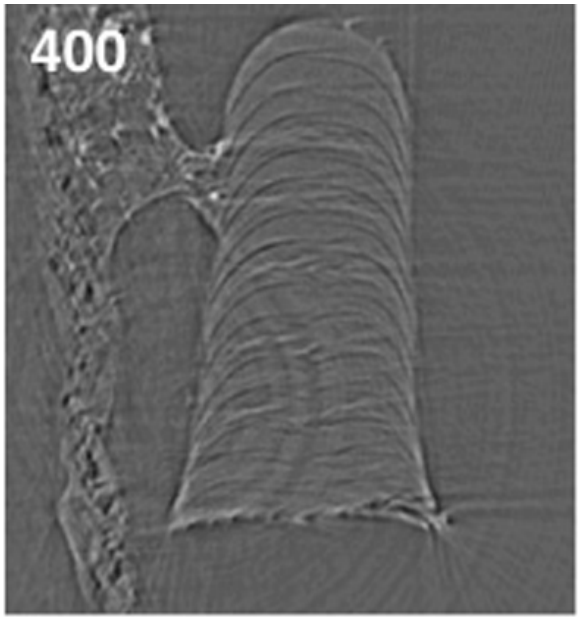

Figure 4.14: Computed X-ray tomography slice of 15 layer carbon wall

4.7 Crystal Structure of LCVD Carbon Fibers

Historically, the material composition of Georgia Tech's LCVD deposits has been analyzed using Energy Dispersive X–ray analysis (EDX or EDS). This technique provides quantitative elemental composition information but provides no insight into the microstructural arrangement of the material. The microstructure of the material has significant implications for the bulk material properties.

X-ray diffraction (XRD) analysis is a common technique that is used to study the crystallinity of solid materials. XRD was used to analyze a selection of carbon fibers grown during the process planning and fiber kinetics experiments discussed above. The fibers were loaded vertically into a glass tube to a height of approximately 1 cm. The tube containing the fibers was then inserted into the XRD machine. This procedure differed somewhat from the traditional powder XRD process whereby the analysis of a powder inherently provides a randomized crystal orientation. The randomization of the orientation yields an unbiased spectrum of crystallographic data. The analysis of the LCVD fibers oriented vertically in a tube inherently exhibits a bias consistent with the natural tendency for a particular crystal

orientation during growth.

A plot of the results of the XRD analysis for the carbon fibers is shown in Figure 4.15. The best match to the measured spectrum contained in the powder diffraction database was PDF#26-1080 which is pyrolytic carbon with a hexagonal structure; this confirmed that the LCVD carbon fibers were largely crystalline with the structure of graphite.

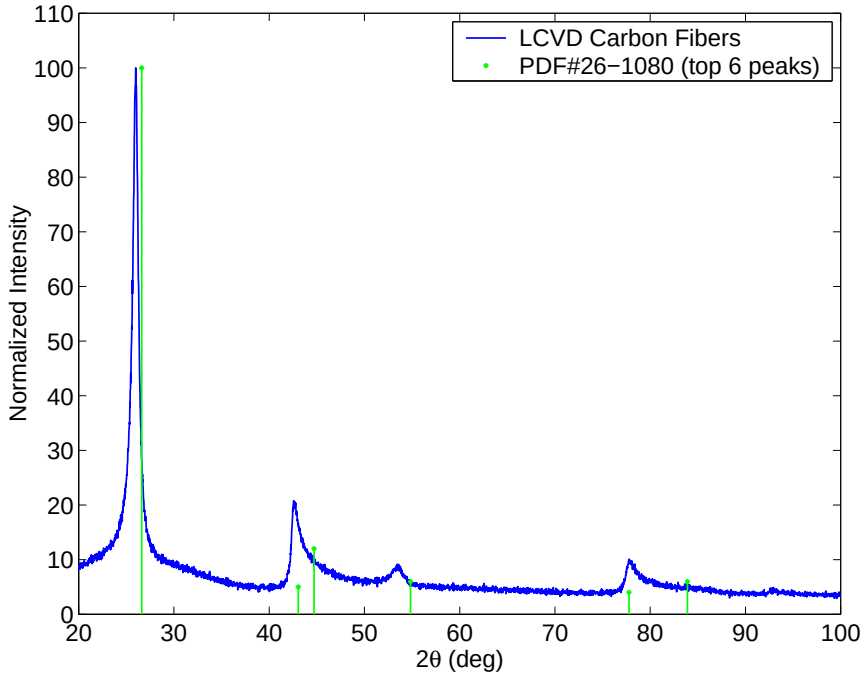

Figure 4.15: Comparison of XRD analysis of LCVD carbon fibers with closest match in database, PDF#26-1080

Some discrepancy between the measured data and the PDF card in the database could be related to the difference between analyzing a solid fiber sample which likely contains some preferred crystallographic orientation and a powder sample which, due to its random nature, contains no preferred orientation. The existence of a preferred orientation could explain the smaller number of peaks seen in the measured data as well as the discrepancy in peak intensity.

From the results, the d spacing of the $\langle 002 \rangle$ plane can be computed using Bragg's Law:

$$d = \frac{\lambda}{2sin(\theta_B)} \tag{4.17}$$

where d is the plane spacing in Å, λ is the wavelength of CuKα radiation, 1.541 Å, and θ_B is the diffraction angle of the $\langle 002 \rangle$ peak, 12.997°. After executing these calculations for the carbon fibers, the value of d is found to be 3.426 Å. This value compares reasonably well with the d spacing of the $\langle 002 \rangle$ plane given by PDF#26-1080 to be 3.348 Å. Some have reported the d spacing of pyrolytic carbon to range from 3.35 to 3.41 Å, where the lower values correspond to higher deposition temperatures.[95]

The widths of the peaks seen in an XRD spectrum are related to the particle or grain size within the material. XRD allows estimation of the grain size or particle size of a material sample through Equation 4.18 known as the Scherrer formula.

$$t = \frac{0.9\lambda}{B cos(\theta_B)}; \tag{4.18}$$

where d is the spacing in Å, λ is the wavelength of CuKα radiation 1.541 Å, θ_B is the diffraction angle of the $\langle 002 \rangle$ peak, 12.997°, and B is the width of the intensity peak in radians at the diffraction angle measured at one half the maximum intensity height. For the carbon fibers, the value of t is found to be 123 Å.

XRD patterns can also provide information regarding the residual stress condition within a specimen. A uniform stress throughout the specimen will cause the peak position to shift along the 2θ axis. A nonuniform stress composed of both tensile and compressive components will cause the diffraction peaks to increase in breadth. Residual stresses in LCVD deposits are of particular interest due to the large temperature gradients present during the deposition process. The shift in the $\langle 002 \rangle$ peak position between the LCVD carbon fibers and the PDF#26-1080 standard could thus be interpreted as a uniform residual stress present in the samples. Such residual stress would not be surprising given the internal cracks seen in carbon fibers.[20] A specimen known to be residual stress–free was not available to infer information regarding the uniformity of the residual stress state.

In sum, the XRD analysis of a subset of carbon fibers made by LCVD shows the material to be highly crystalline graphite. The grain or particle size was estimated at 123 Å.

CHAPTER V

DEPOSITION RATE MODELING

The primary goals of modeling the LCVD process are to further the understanding of the relationship between the LCVD machine parameters and the resulting deposit characteristics and to provide insight into the deposition mechanisms. The foundation of this understanding lies in the transport and chemical reaction phenomena that occur in and around the deposition zone. Of primary importance in the LCVD process are the physical parameters of temperature, fluid velocity, and species concentration. Ultimately, all of these parameters need to be studied in a single integrated simulation environment to properly capture the complex interactions among them.

As shown in Section 2.2, a significant amount of effort has been reported in the literature related to modeling the LCVD process. Of primary relevance to the current work is that reported by Duty.[2,67] FLUENT is a commercially available computational fluid dynamics (CFD) code that is well suited to modeling complex thermal and mass transport phenomena. Duty has developed geometric models of Georgia Tech's LCVD system in the software and used them to study the relationship among substrate material, gas nozzle flow, laser power, and temperature profiles. Duty's models did not incorporate species transport and chemical reaction calculations within the CFD environment. The work done here focused on modifying and enhancing Duty's thermal and flow models using FLUENT's capability to model species transport. Overall, the goal was to create a single integrated simulation environment for studying Georgia Tech's LCVD process.

5.1 Model Geometry and Meshing

The overall geometry used for the model was identical to that employed elsewhere[2] and is depicted in Figure 5.1. The three–dimensional domain contains a semi-circular volume that is divided into two parts. The vertical plane across the diameter of the semi-circle represents a plane of symmetry and is omitted in Figure 5.1 for clarity. The lower part of the domain represents the solid substrate material, while the upper part represents the fluid region adjacent to the substrate surface. Protruding into the fluid region is the gas nozzle with its axis aligned such that if extended, it would intersect the center of the laser spot on the substrate surface. The substrate diameter of 75 mm and height of 25 mm is representative of the dimensions of Georgia Tech's LCVD system substrate holder. The fluid volume of 75 mm diameter and 25 mm height is believed sufficiently large to capture all important phenomena occurring near the deposition zone.

Figure 5.2 is a view of the three dimensional mesh on the symmetry plane in the vicinity of the laser spot. The figure illustrates the dimensions of the gas nozzle and its position relative to the substrate surface. An expanded view of the area immediately surrounding the laser spot highlights the mesh density in the most critical region. The mesh convergence study presented in Section 5.3.4 was used to determine the appropriate mesh size. Along the 200 μm laser-heated zone across the substrate surface, there were 40 nodes spaced 5 μm apart. The symmetry plane shown in Figure 5.2 is a particularly important aspect of the model for visualizing the computation results.

5.2 Boundary Conditions

The equations and many of the boundary conditions used in the model are universally applicable to all LCVD simulations regardless of the material system. The FLUENT package solves a variety of fundamental conservation equations depending upon the situation of

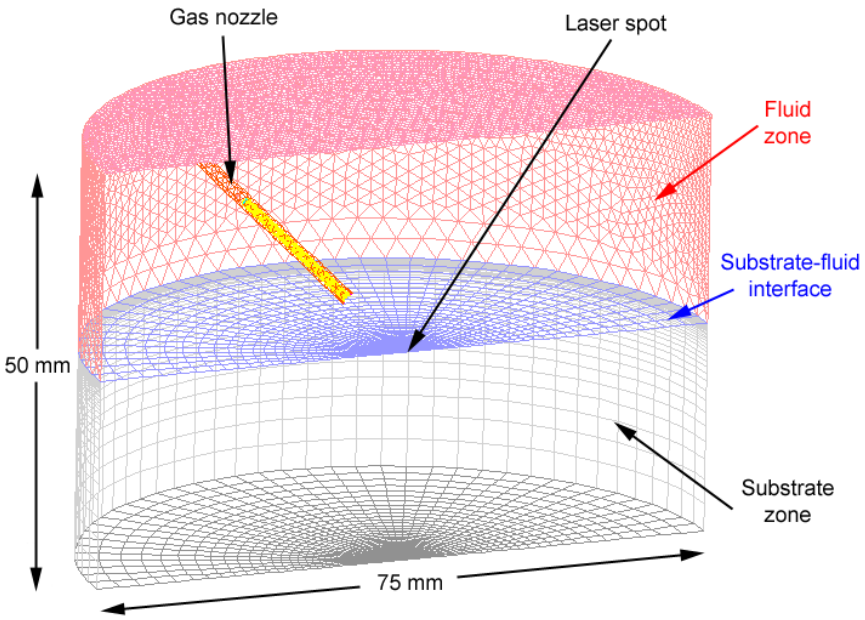

Figure 5.1: Overview of 3-D model domain

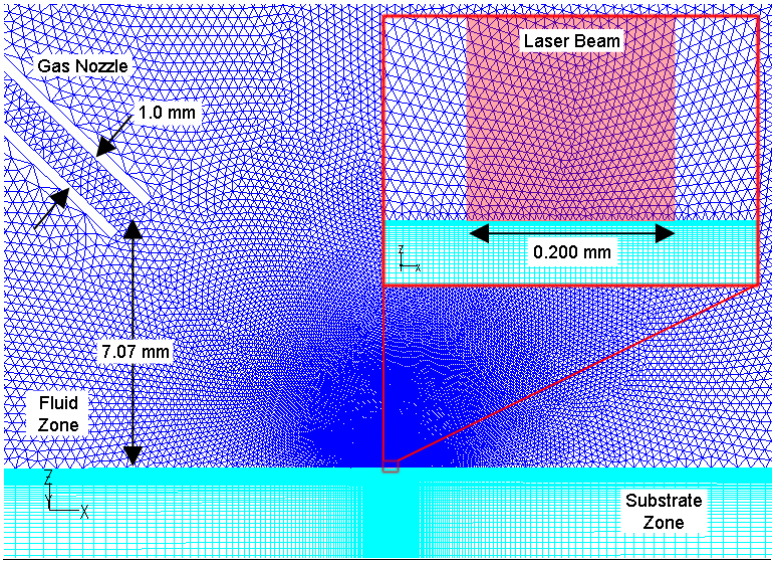

Figure 5.2: Mesh density on symmetry plane

interest. In modeling LCVD, four primary equations apply: mass conservation (or continuity), momentum conservation, energy conservation, and species conservation. Formulations of each of these equations are available in any text on the subjects, and each is discussed below for completeness.[96] Each one of these equations has boundary conditions that must be defined in the code.

5.2.1 Mass and Momentum Conservation Equations

Equation 5.1 is the general form of the mass conservation or continuity equation used by the solver in the fluid zone:

$$\frac{\partial \rho}{\partial t} + \nabla \cdot (\rho \vec{v}) = S_m \tag{5.1}$$

where ρ is the fluid density, t is time, $\vec{v}$ is the local velocity vector, and S_m is a mass source (or sink) term arising from phase transformations or other defined sources.

The simulations done in this analysis are steady state, therefore the first term on the left side of the equation is not considered. The second term on the left accounts for mass transport due to convective forces. The mass sink term is used to account for mass depleted from the gas phase of the model due to chemical reactions.

The formulation of the momentum conservation equation for laminar flow is also solved within the fluid zone of the model:

$$\frac{\partial}{\partial t}(\rho \vec{v}) + \nabla \cdot (\rho \vec{v}\vec{v}) = -\nabla p + \nabla \cdot (\bar{\bar{\tau}}) + \rho \vec{g} + \vec{F} \tag{5.2}$$

where p is the pressure, $\bar{\bar{\tau}}$ is the shear stress tensor, $\vec{g}$ is gravity, and $\vec{F}$ represents additional body forces.

The left side of Equation 5.2 represents the acceleration terms and the right side represents the forces acting on the fluid. The acceleration terms include both the temporal and spatial considerations, while the force terms include those due to pressure, viscosity, gravity, and other external body forces. For the LCVD simulation, the time dependent term on the far left is not applicable and the third term on the right representing gravitational

forces was neglected due to computational expense and the minimal significance of natural convection in a forced flow environment.[2]

Within the fluid domain, flow is specified as a velocity magnitude normal to the gas nozzle inlet. Both the top and side faces of the fluid zone are defined as pressure outlets with gauge pressure specified to be zero. In sum, the gases enter the fluid domain through the nozzle inlet and exit through the top and side pressure outlets.

5.2.2 Energy Conservation Equation

The energy equation is the primary transport equation that couples the substrate zone to the fluid zone and is therefore solved throughout the entire domain of the model. The solver uses

$$\frac{\partial}{\partial t}(\rho h) + \nabla \cdot (\vec{v}\rho h) = \nabla \cdot (k\nabla T) + S_h \tag{5.3}$$

for the solid zone heat transfer calculations, where ρ represents the density of the solid, h is the specific enthalpy, $\vec{v}$ is the velocity vector of the solid if moving, k is the thermal conductivity, T is temperature, and S_h is volumetric heat generation rate. The analysis done for the LCVD process is steady state with no solid zone motion resulting in the left side of Equation 5.3 equaling zero. The first term on the right-hand side represents conductivity of heat through the solid and the S_h term represents the volumetric heat generation within the solid.

The laser energy is simulated in the model as volumetric heat generation in the surface layer of substrate cells. A volumetric approach was chosen because specification of a heat flux through the substrate surface disables the computation of convective and radiative heat transfer from the surface. It was considered important that these values be computed in the model.

The CO_2 laser employed in Georgia Tech's LCVD system emits a 90% TEM_{00} beam which can be modeled as a Gaussian energy flux. Equation 1.10 gave the Gaussian laser

beam energy profile:

$$P(r) = \frac{2P_0}{\pi R_0^2} e^{\frac{-2r^2}{R_0^2}} \tag{1.10}$$

where P_0 is the nominal laser power, R_0 is the $1/e^2$ radius of the laser beam, and r is the radial distance from the center of the laser spot. Equation 1.10 can be modified to express a volumetric heat generation rate by dividing by the depth of the cell d in which the energy is applied as shown in Equation 5.4. The value of d for the mesh used was X m. This equation also includes the term $\rho_{10.59}$ to account for substrate reflectivity at the laser wavelength of 10.59 μm.

$$P(r) = \frac{2P_0(1-\rho_{10.59})}{\pi R_0^2 d} e^{\frac{-2r^2}{R_0^2}} \tag{5.4}$$

A user defined function (UDF) was used to implement this volumetric energy generation in the LCVD model. The UDF computed the appropriate amount of energy to be generated by each cell depending upon the nominal laser power, cell size, and cell position relative to the center of the laser spot. The UDF limited volumetric energy generation to those cells in the top layer of the substrate and within the 200 μm diameter of the laser spot as indicated by Figure 5.3.

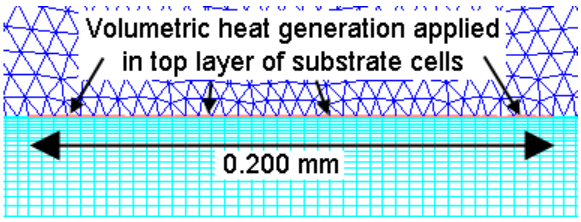

Figure 5.3: Cells used in generating laser heating function

The UDF also implemented a crude approximation of heat loss from the substrate surface due to radiation. Previous work had shown that boundary conditions for FLUENT's internal radiation models were difficult to implement with the given geometry, and even when implemented, significant computation expense was incurred without adding significantly to the results. A suitable approximation was found by using the simple equation for

radiation heat transfer:[2]

$$q_r'' = \varepsilon\sigma(T_s^4 - T_{ref}^4) \tag{5.5}$$

where q_r'' is heat flux, ε is average hemispherical emissivity over the entire spectral range, σ is the Stefan–Boltzmann constant (5.670×10^{-8} W/m^2-K^4), T_s is the radiating surface temperature, and T_{ref} is the temperature of the remote surface being irradiated. T_{ref} was set at 300 K for all models in order to simulate the inner surface of the cold wall reaction chamber.

The radiative heat flux had to be adjusted to account for the volumetric implementation by dividing q_r'' by the depth of the top layer of cells d. The result was subtracted from the laser power $P(r)$ computed in Equation 5.4 to account for the radiative heat loss. This calculation provided the volumetric heat generation rate used in the energy equation:

$$S_h = P(r) - \frac{q_r''}{d}$$

It was assumed that the laser spot is the only area where temperatures are sufficiently high for radiative effects to become important. Thus, this calculation was limited to those surface cells within the region of $r < 10R_0$. The C code for the UDF incorporating both the laser power input and the radiation approximation was linked to the solver at runtime. A listing of the source code can be found in Appendix B.3.

In addition to the volumetric heat generation function, other boundary conditions for the energy equation in the solid zone consisted of convective heat transfer from the side and bottom of the substrate. For the side, the temperature of the adjacent fluid (this fluid was not explicitly modeled) was defined to be 300 K and the convective heat transfer coefficient, h was specified to be 5 W/m^2-K. The bottom of the substrate was insulated. These thermal boundary conditions were taken from Duty's work.[2] Note that the spatial position of the laser generation function was kept fixed within the substrate representing the LCVD vertical–growth mode.

A slightly different version of the energy conservation equation was applied in the fluid

domain:

$$\frac{\partial}{\partial t}(\rho E) + \nabla \cdot (\vec{v}(\rho E + p)) = \nabla \cdot \left(k_{\text{eff}} \nabla T - \sum_j h_j \vec{J}_j + (\overline{\overline{\tau}}_{\text{eff}} \cdot \vec{v}) \right) + S_h \tag{5.6}$$

where ρ is the density of the fluid, $\vec{v}$ is the fluid velocity vector, p is the pressure, k_{eff} is the effective conductivity of the fluid, T is the temperature, h_j is the enthalpy of species j, $\vec{J}_j$ is the diffusion flux of species j, $\overline{\overline{\tau}}_{\text{eff}}$ is the shear stress tensor, and S_h includes any additional volumetric heat sources in the fluid. E is given by:

$$E = h - \frac{p}{\rho} + \frac{v^2}{2} \tag{5.7}$$

where h is the enthalpy of the fluid, and all other variables are as defined above. The second and third term in this expression represent pressure work and kinetic energy and are excluded from the current computations due to their minimal influence on the results.

Only some of the terms in the general equation, Equation 5.6, are pertinent to the LCVD model. Specifically, the simulation is steady state, eliminating the first term on the left-hand side. The second term on the left-hand side accounts for energy entering and leaving the system via mass flow across the boundaries and is applicable. The first two terms on the right-hand side of the equation respectively represent conduction through the fluid and enthalpy transport through the fluid due to diffusion. Both are considered. The viscous dissipation term, third on the right, is not considered in the current model because its contribution is believed relatively insignificant in the LCVD process. Finally, the S_h term is used to account for the heat of chemical reactions taking place within the fluid domain.

The boundary conditions on the energy equation in the fluid zone involve specification of the temperature at the nozzle inlet and the backflow temperature along the fluid zone top and side faces. The value used for both inflow and outflow boundaries was 300 K. At the fluid–solid interface, the energy equations for each zone are coupled through the temperature.

5.2.3 Species Conservation Equation

The distinguishing aspect of the current model is the explicit modeling of the species transport processes in the gas phase surrounding the LCVD reaction zone. The species conservation equations are solved for each individual species defined in the mixture comprising the fluid zone. The general form of the species conservation equation is

$$\frac{\partial}{\partial t}(\rho Y_i) + \nabla \cdot (\rho \vec{v} Y_i) = -\nabla \cdot \vec{J_i} + R_i + S_i \tag{5.8}$$

where ρ is the density of the mixture, Y_i is the mass fraction of species i, $\vec{v}$ is the local velocity vector, $\vec{J_i}$ is the diffusion flux of species i, R_i is the net volumetric rate of species production due to chemical reactions, and S_i is the rate of creation or destruction of dispersed phases or other processes.

The simulation of the LCVD process is steady state; therefore, the first term on the left-hand side representing time dependency is not applicable. The last term on the right-hand side representing species concentration changes due to particulate–forming homogenous reactions is also not applicable in the current setup. The R_i term in Equation 5.8 is used to compute the homogenous creation or consumption of species i. No volumetric reactions were included in the current study, thus, this term did not apply.

The second term on the left represents the convective transport of species i due to bulk fluid flow. This term is important in simulations involving gas flow through the nozzle and/or natural convection. The first term on the right side of the equation represents the transport of species i due to diffusion. Different types of diffusion can be considered, but the primary types are concentration (or ordinary or Fickian) diffusion and thermal diffusion.

Concentration diffusion refers to the tendency of a molecule to move from a region of high concentration to that of lower concentration within a system. In traditional CVD, species transport to the substrate surface via concentration diffusion is the primary delivery method. Even in the forced flow LCVD system, the presence of a boundary layer and the no-slip condition along the substrate cause concentration diffusion to remain the primary

mechanism for final delivery of the reagent to the surface.

Thermal diffusion or the Soret effect is the transport of molecules due the presence of a temperature gradient.[96] For binary mixtures of dilute gases, the species with a larger molecular weight tends to move from regions of high temperature to those of lower temperature. For mixtures of similar molecular weight species, the molecule with a larger diameter tends to diffuse from high temperature to low temperature.

The flux of species i due to these two types of diffusion in laminar flows is given by Fick's law:

$$\vec{J_i} = -\rho D_{i,m} \nabla Y_i - D_{T,i} \frac{\nabla T}{T} \tag{5.9}$$

where $\vec{J_i}$ is the mass flux of species i, ρ is the density of the mixture, $D_{i,m}$ is the diffusion coefficient of species i in the mixture, Y_i is the local mass fraction of species i, $D_{T,i}$ is the thermal diffusion coefficient of species i, and T is the local temperature of the mixture. Equation 5.9 is only valid when the dilute approximation holds (i.e. $Y_i \ll 1$ for all i except the carrier gas).

When the dilute approximation does not hold, a different formulation derived from the Maxwell–Stefan equations can be used for the diffusive mass flux:

$$\vec{J_i} = -\sum_{j=1}^{N-1} \rho D_{ij} \nabla Y_i - D_{T,i} \frac{\nabla T}{T} \tag{5.10}$$

where N is the number of chemical species in the mixture, $D_{i,j}$ is a matrix of generalized Fick's law diffusion coefficients, and Y_i is the mass fraction of species i. This full multicomponent diffusion model was preferred in most LCVD simulations because the dilute approximation does not always hold. The consideration of thermal diffusion is optional in the FLUENT solution procedure, and depending upon the deposition process under consideration, it may be evaluated. Note that in order to use either Equation 5.9 or 5.10, values for the both the concentration diffusion coefficients and the thermal diffusion coefficients must be available.

As was highlighted in Section 1.3, the transport of the reagent species to the substrate

surface during LCVD must be balanced by the substrate reaction rate. The deposition reaction was considered as a boundary condition on the species transport equation. FLUENT incorporates several different models for simulating chemical reactions. The most general model, and that used in all LCVD simulations, is the laminar finite–rate model.

Ignoring surface site specific considerations, the general equation for an overall surface reaction can be expressed as:

$$\sum_{i=1}^{N_g} g'_{i,r} G_i + \sum_{i=1}^{N_b} b'_{i,r} B_i \overset{K_r}{\rightleftharpoons} \sum_{i=1}^{N_g} g''_{i,r} G_i + \sum_{i=1}^{N_b} b''_{i,r} B_i \tag{5.11}$$

where G_i and B_i represent gas phase species and the bulk (solid) species, respectively. N_g and N_b are the total numbers of each of these species types, $g'_{i,r}$ and $b'_{i,r}$ are the stoichiometric coefficients for each reactant species, $g''_{i,r}$ and $b''_{i,r}$ are the stoichiometric coefficients for each product species, and K_r is the rate constant for the overall reaction. The net molar rate of creation or destruction of species i is given by:

$$\hat{R}_{i,\text{gas}} = \sum_{r=1}^{N_{\text{rxn}}} (g''_{i,r} - g'_{i,r}) \mathscr{R}_r \quad i = 1,2,3,\ldots,N_g \tag{5.12}$$

$$\hat{R}_{i,\text{bulk}} = \sum_{r=1}^{N_{\text{rxn}}} (b''_{i,r} - b'_{i,r}) \mathscr{R}_r \quad i = 1,2,3,\ldots,N_b \tag{5.13}$$

The rate of reaction $\mathscr{R}_r$ is given by:

$$\mathscr{R}_r = k_{f,r} \prod_{i=1}^{N_g} [G_i]_{\text{wall}}^{g'_{i,r}} \tag{5.14}$$

where $k_{f,r}$ is the forward reaction rate and $[G_i]_{\text{wall}}$ represents the molar concentration of the i^{th} gas species at the wall. The forward reaction rate $k_{f,r}$ is computed from the common Arrhenius expression for reaction rate:

$$k_{f,r} = k_{0,r} e^{\frac{-Q}{RT}} \tag{5.15}$$

where $k_{0,r}$ is the pre-exponential factor, Q is the activation energy, R is the universal gas constant, and T is temperature.

The formulation of the boundary condition at the wall surface is given by:

$$\left(\vec{J}_i \cdot \vec{n}\right)_{\text{wall}} - \dot{m}_{\text{dep}} Y_{i,\text{wall}} = M_{w,i} \hat{R}_{i,\text{gas}} \quad i = 1,2,3,\ldots,N_g \tag{5.16}$$

where $(\vec{J}_i \cdot \vec{n})_{wall}$ is the diffusive flux of species i given in Equation 5.10 computed at the wall in the direction normal to the wall, $Y_{i,\text{wall}}$ is the mass fraction of species i at the wall, $M_{w,i}$ is the molecular weight of species i, and $\hat{R}_{i,\text{gas}}$ is as given in Equation 5.12. The net rate of deposition (or etching) of the surface reaction is given by:

$$\dot{m}_{\text{dep}} = \sum_{i=1}^{N_b} M_{w,i} \hat{R}_{i,\text{bulk}} \tag{5.17}$$

Finally, $Y_{i,wall}$ is related to the concentration of the i^{th} gas species $[G_i]_{\text{wall}}$ through:

$$[G_i]_{\text{wall}} = \frac{\rho_{\text{wall}} Y_{i,\text{wall}}}{M_{w,i}} \tag{5.18}$$

where ρ_{wall} is the density of the fluid at the wall. Equation 5.16 ensures, for each gas species, a balance between transport to or from the surface and the rate of destruction or creation on the surface.

All chemical reactions to be allowed in the model are explicitly defined within the fluid. This definition occurs when setting up the fluid mixture properties. The reactions are defined by their reactants, products, stoichiometric coefficients, rate exponents, pre-exponential factors, and activation energies. The reaction is also defined as either a volumetric (homogenous) or surface (heterogenous) reaction.

Other boundary conditions for the species conservation equation included specification of the species mass fractions at the domain inlets and exits. These values changed depending upon the configuration being simulated.

5.3 Carbon Deposition Simulations

As previously described, carbon deposition is a relatively mature process. Due to its controllability, carbon deposition is a suitable material for kinetic studies such as the one presented in Section 4.2. The FLUENT deposition rate model was used to investigate the carbon deposition process.

5.3.1 Material Properties

Accurate models and simulations require accurate knowledge of all pertinent material properties. For LCVD, these properties include those of the reagent gases, the substrate material, and the deposited material. The extreme temperature gradients that emerge as a result of laser heating imply that material properties should be modeled as functions of temperature wherever possible.

5.3.1.1 Methane and Hydrogen Species Properties

The carbon deposition reaction studied here used the methane and hydrogen precursors as was indicated by Equation 2.1.

$$\mathrm{CH_4}(g) + \text{xs } \mathrm{H_2}(g) \rightarrow \mathrm{C}(s) + 2\mathrm{H_2}(g) + \text{xs } \mathrm{H_2}(g) \tag{2.1}$$

The fluid zone in the model was represented by a mixture of all these species. First, the properties of each species were defined and then the mixture was defined by specifying the constituent species and the appropriate mixing rules.

The properties required of the fluid species included

- Molecular weight, M_w (kg/kmol)
- Standard state enthalpy, H° (J/kmol)
- Standard state entropy, S° (J/kmol-K)
- Reference temperature for enthalpy and entropy, T_{ref} (K)
- Leonard-Jones characteristic length, σ (Å)
- Leonard-Jones energy parameter, (ε/k_B) (K)
- Specific heat capacity at constant pressure, C_p (J/kg-K)
- Viscosity, μ (kg/m-s)

- Thermal conductivity, k(W/m-K)

Some of these properties specified for the reagent gases did not allow or require specification as a function of temperature. These properties are identified and their values given in Table 5.1.

Table 5.1: Constant properties of reagent gases used in carbon deposition simulation

Property	Methane, CH_4	Hydrogen, H_2
Molecular weight, M_w (kg/kmol)	16.04	2.02
Standard state enthalpy, H° (J/kmol)	-7.490×10^7	0
Standard state entropy, S° (J/kmol-K)	1.860×10^5	1.306×10^5
Reference temperature, T_{ref} (K)	298.15	298.15
Leonard–Jones characteristic length, σ (Å)	3.75	2.92
Leonard–Jones energy parameter, (ε/k_B) (K)	141	38

The additional properties required for the model were defined as a function of temperature. Heat capacity as a function of temperature over the range of 300 – 3000 K at a pressure of 1 atm was given for methane by Gurvich[97] and was obtained via NIST.[98] For inputting the data into the FLUENT code, a subset of points was chosen and the points were connected by a piecewise-linear interpolation.

The C_p of hydrogen as a function of temperature was calculated using the Shomate equation:[98]

$$C_p = A + B*t + C*t^2 + D*t^3 + \frac{E}{t^2} \tag{5.19}$$

where C_p is in J/mol-K and $t = T/1000$ where T is temperature in K. The coefficients in Equation 5.19 were provided by Chase[99] through NIST[98] as shown in Table 5.2. The hydrogen C_p curve was put into FLUENT using a series of data points over the temperature range 300 – 4000 K that were connected by a piecewise-linear interpolation. Figure 5.4 illustrates how C_p varies with temperature for both methane and hydrogen.

Measured viscosity values for methane and hydrogen were only available up to a temperature of 1000 and 2000 K, respectively. The temperatures used in the LCVD of carbon

Table 5.2: Constants for Shomate equation, Equation

Temp Range [K]	298 – 1000	1000 – 2500	2500 – 6000
A	33.066178	18.563083	43.413560
B	-11.363417	12.257357	-4.293079
C	11.432816	-2.859786	1.272428
D	-2.772874	0.268238	-0.096876
E	-0.158558	1.977990	-20.533862

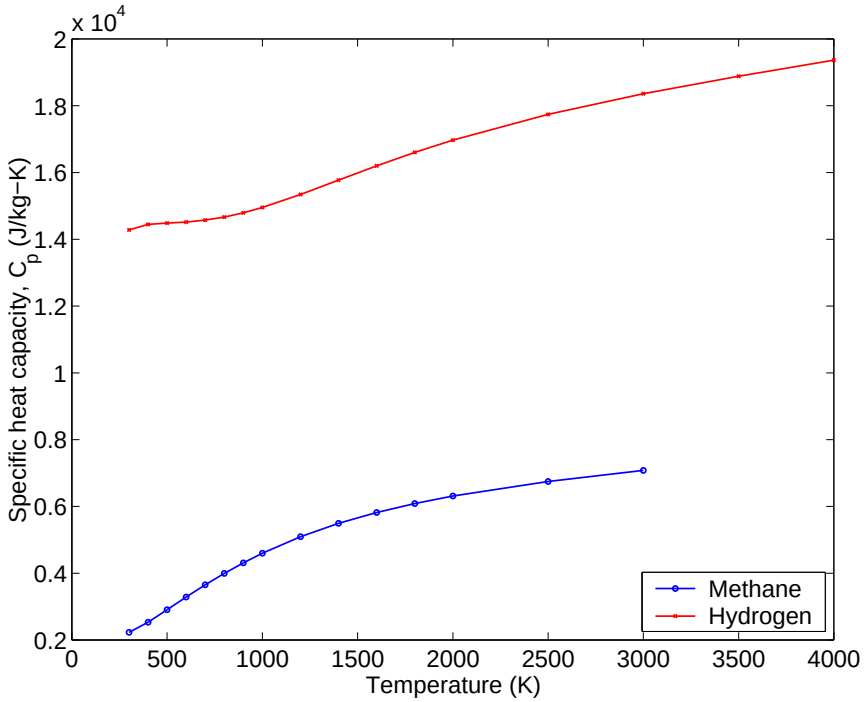

Figure 5.4: Heat capacity of carbon reagent gases

often exceed 2000 K in the deposition zone; therefore it was deemed more appropriate to use kinetic theory to compute the values of viscosity. The equation from kinetic theory is:[100]

$$\mu = 2.67 \times 10^{-6} \frac{\sqrt{M_w T}}{\sigma^2 \Omega_\mu} \tag{5.20}$$

where μ is viscosity (kg/m-s), M_w is the molecular weight of the gas (kg/kmol), T is the temperature of the gas (K), σ is the Leonard-Jones characteristic length (Å), and Ω_μ is the collision integral. The collision integral of a perfectly rigid molecule would be exactly 1; this integral accounts for the fact that no perfectly rigid molecules exist. Equations for

approximating collision integrals are provided by:[96]

$$\Omega_\mu = \frac{A}{T^{*B}} + \frac{C}{e^{DT^*}} + \frac{E}{e^{FT^*}} \tag{5.21}$$

where T^* is given by:

$$T^* = \frac{T}{(\varepsilon/k_B)} \tag{5.22}$$

where T is the temperature of the gas (K) and (ε/k_B) is the Leonard-Jones energy parameter for the gas (K). A through F in Equation 5.21 are constants given in Table 5.3. Figure 5.5 illustrates how the gas viscosity varies with temperature according to Equation 5.20.

Table 5.3: Constants for viscosity collision integral formula

A	1.16145	B	0.14874	C	0.52487
D	0.77320	E	2.16178	F	2.43787

Reported thermal conductivity values for methane and hydrogen were also limited in availability to the maximum temperature of 1000 and 2000 K, respectively. Again, by using kinetic theory, changes in thermal conductivity at temperatures in excess of these values could be considered. The equation from kinetic theory for computing gas thermal conductivity is:[100]

$$k = \frac{15}{4}\frac{R}{M_w}\mu\left(\frac{4}{15}\frac{C_p M_w}{R} + \frac{1}{3}\right) \tag{5.23}$$

where k is the thermal conductivity of the gas (W/m-K), R is the universal gas constant (8314 J/kmol-K), M_w is the molecular weight of the gas (kg/kmol), and C_p is the specific heat capacity of the gas (J/kg-K). Figure 5.6 illustrates how k varies with temperature.

5.3.1.2 Methane and Hydrogen Mixture Properties

After defining the properties for the species, the mixture of methane and hydrogen was created. The definition of a mixture includes a list of the species in the mixture, a description of all possible chemical reactions involving the mixture, the appropriate mixing laws for computing mixture properties, and specification of the diffusivity calculation method to be used within the mixture.

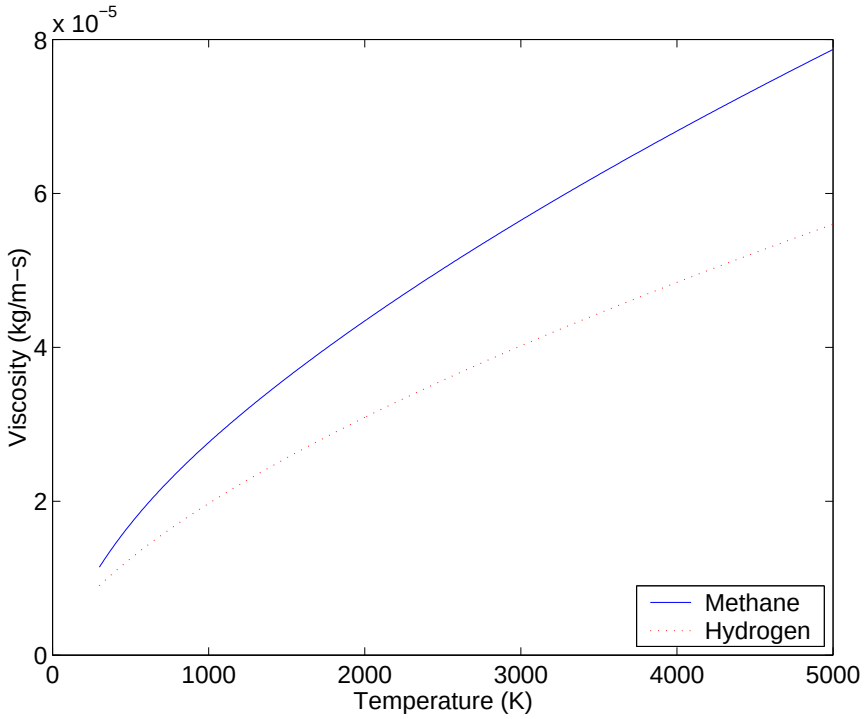

Figure 5.5: Viscosity of carbon reagent gases

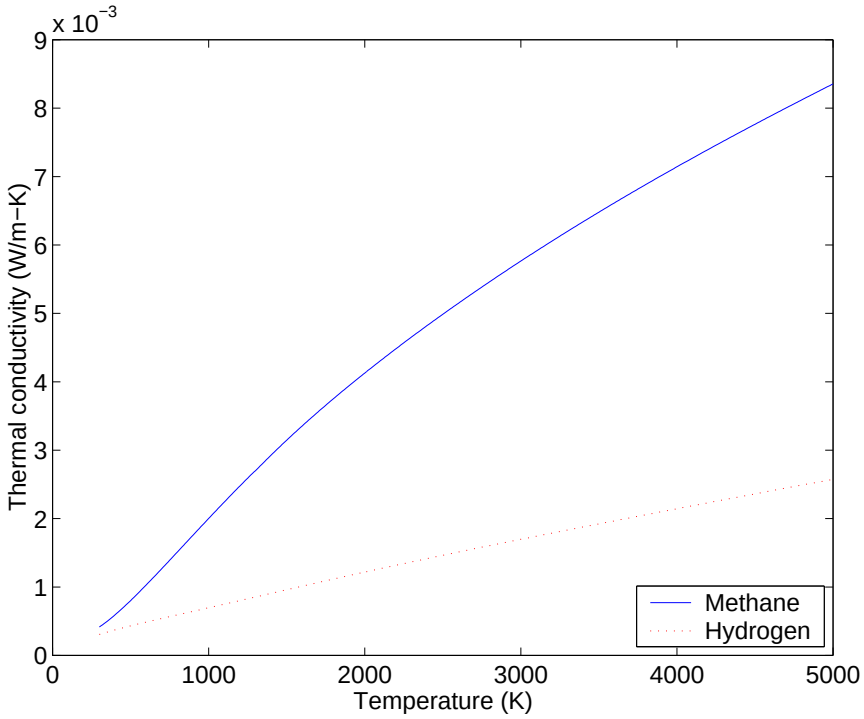

Figure 5.6: Thermal conductivity of carbon reagent gases

The species in the mixture included methane, hydrogen, and solid carbon. The solid carbon was defined as a gas species, but was explicitly identified in the mixture as a solid species. This species was important in accounting for the mass of elemental carbon that was removed from the fluid zone as deposition proceeded. The material properties of this bulk gas species did not impact the model results beyond the mass conservation implications.

While the FLUENT code has the ability to model a set of homogenous and heterogenous surface reactions simultaneously, the simplified overall surface reaction of Equation 2.1 was the only one modeled. The kinetic parameters for the global reaction have been reported in the literature.[1,25] Similar kinetic experiments were repeated as a part of this work as summarized in Section 4.2. For convenience, the results of these experiments are shown again in Table 5.4. These kinetic parameters for the methane decomposition were entered into the reaction definition and the reaction was defined exclusively as a wall surface reaction.

Table 5.4: Kinetic parameters for carbon fiber LCVD

Parameter	Symbol	Value
Pre–exponential factor (m/s)	k_0	1.2856×10^8
Reaction order	n	1.0185
Activation Energy (J/kmol)	Q	3.9911×10^8

The properties of the gas mixture that are derived from the properties of the individual species were computed using mixing laws. The specific mixing laws used are reported in Table 5.5.

Table 5.5: Mixing laws used in CH_4–H_2 mixture definition

Density, ρ (kg/m^3)	ideal-gas
Specific heat capacity, C_p (J/kg-K)	mixing-law
Thermal conductivity, k (W/m-K)	ideal-gas-mixing-law
Viscosity, μ (kg/m-s)	ideal-gas-mixing-law

FLUENT incorporates several methods for computing the ordinary diffusion of species

within a defined mixture. The full multicomponent diffusion model was used to calculate ordinary diffusion, because the mass fraction of the methane reagent species was too large for it to be considered dilute. The modified Chapman–Enskog formula, Equation 5.24, was used to compute the necessary diffusion coefficients between each pair of species.[96]

$$D_{ij} = 0.0188 \frac{\left[T^3 \left(\frac{1}{M_{w,i}} + \frac{1}{M_{w,j}}\right)\right]^{1/2}}{P_{abs}\sigma_{ij}^2 \Omega_D} \tag{5.24}$$

where T is the temperature of the mixture in (K), $M_{w,i}$ and $M_{w,j}$ are the molecular weights of species i and j respectively (kg/kmol), P_{abs} is the absolute pressure (Pa), σ_{ij} is the arithmetic average of the individual species characteristic lengths, $\sigma_{ij} = (1/2) \times (\sigma_i + \sigma_j)$, and Ω_D is the diffusion collision integral which is a measure of the interaction of the molecules in the system. Ω_D is given by Equation 5.25.[96]

$$\Omega_D = \frac{A}{T_D^{*B}} + \frac{C}{e^{DT_D^*}} + \frac{E}{e^{FT_D^*}} + \frac{G}{e^{HT_D^*}} \tag{5.25}$$

A through H in Equation 5.25 are constants given in Table 5.6. T_D^* in Equation 5.25 is given

Table 5.6: Constants for diffusion collision integral formula

A	1.06036	B	0.15610	C	0.19300	D	0.47635
E	1.03587	F	1.52996	G	1.76474	H	3.89411

by:

$$T_D^* = \frac{T}{(\varepsilon/k_B)_{ij}} \tag{5.26}$$

and $(\varepsilon/k_B)_{ij}$ is the Leonard-Jones energy parameter for the mixture (K) given by:

$$(\varepsilon/k_B)_{ij} = \sqrt{(\varepsilon/k_B)_i (\varepsilon/k_B)_j} \tag{5.27}$$

The thermal diffusion coefficients were computed empirically by FLUENT for each species:

$$D_{T,i} = -2.59 \times 10^{-7} T^{0.659} \left[\frac{M_{w,i}^{0.511} X_i}{\sum_{i=1}^{N} M_{w,i}^{0.511} X_i} - Y_i \right] \cdot \left[\frac{\sum_{i=1}^{N} M_{w,i}^{0.511} X_i}{\sum_{i=1}^{N} M_{w,i}^{0.489} X_i} \right] \tag{5.28}$$

where T is the local temperature (K), $M_{w,i}$ is the molecular weight of species i (kg/kmol), X_i is the mole fraction of species i, Y_i is the mass fraction of species i, and N is the number of species present in the mixture.

5.3.1.3 Graphite Substrate Properties

Most of the carbon deposition done in Georgia Tech's LCVD system has utilized graphite as the substrate material. A wide variety of graphite materials are available commercially with a wide variety of material properties. The properties are closely linked to the manufacturing process used to produce the graphite. As discussed in Section 4.1, the substrates used were normally either SK-85 or AXF-5Q graphite disks. Temperature dependent material properties were not available for these graphite materials, but data were available in the literature for ATJ graphite. Given the similarities in the manufacturing processes, ATJ graphite should be representative of the graphite used for the LCVD carbon substrates.

Several properties of the substrate material are important in simulating the deposition process:

- Density, ρ (kg/m^3)
- Specific heat capacity at constant pressure, C_p (J/kg-K)
- Thermal conductivity, k (W/m-K)
- Reflectivity, ρ
- Emissivity, ε

The density of graphite is given to be 1760 kg/m^3 and is held constant during the simulations. Specific heat capacity, C_p varies similarly with temperature for all types of graphite. Using the data in the literature,[101] a series of data points was input into the FLUENT code with a piecewise-linear interpolation used between the points. Figure 5.7 illustrates the temperature dependence of heat capacity.

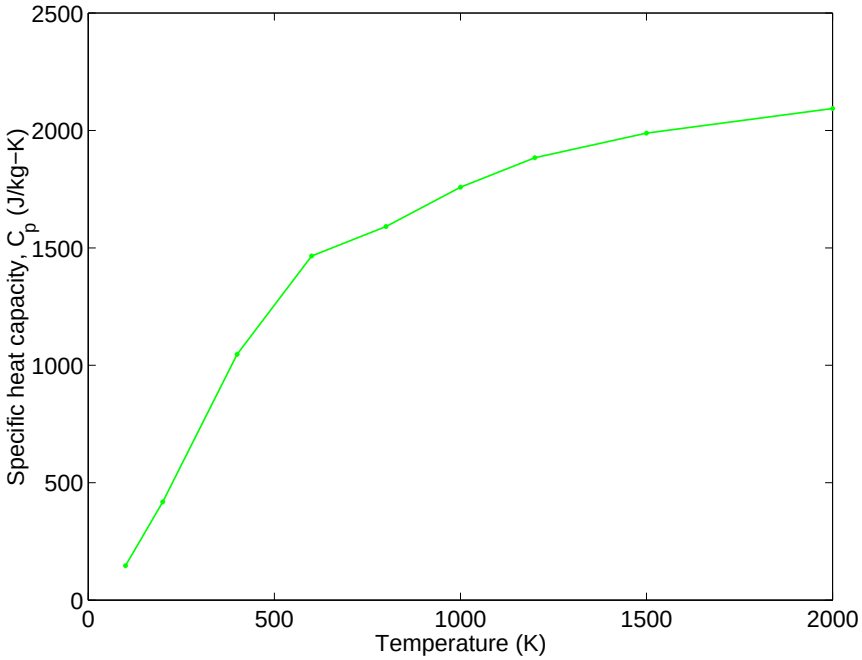

Figure 5.7: Dependence of ATJ graphite C_p on temperature

The thermal conductivity of graphite is complex. Conductivity values as well as the degree of anisotropy in the graphite vary drastically depending on how the material was produced. The conductivity of ATJ graphite is slightly anisotropic relative to the direction of applied molding pressure during manufacturing. This anisotropy is ignored in the model, and the values for thermal conductivity perpendicular to the direction of molding pressure were used as isotropic values.[102] A series of data points was used to define the temperature dependence of the conductivity. Again, a piecewise-linear interpolation function was used between the data points. A plot of the relationship between thermal conductivity and temperature is presented in Figure 5.8.

The reflectivity nor emissivity of graphite were explicitly defined in the material properties database of the FLUENT code. However, the user defined function described in Section 5.2.2 incorporated reflectivity at the 10.59 μm wavelength of the laser. The reflectivity of the graphite substrate depends upon the surface conditions. Substrates are normally prepared by cutting with a diamond saw followed by sanding with 400 – 600 grit SiC grinding paper to produce a smooth, uniform finish. The value of $\rho_{10.59}$ was set at 0.4 which was

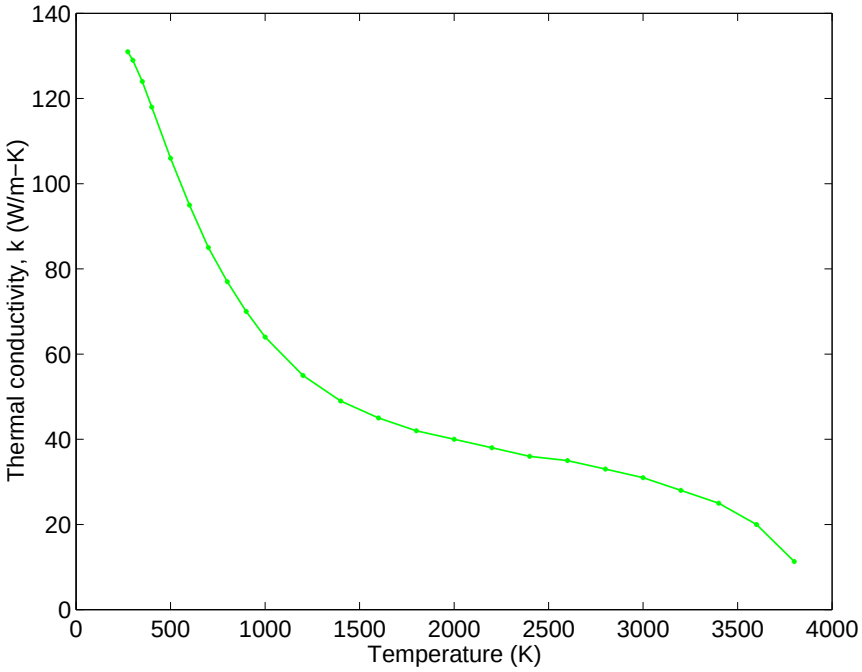

Figure 5.8: Dependence of ATJ graphite *k* on temperature

determined by Duty through a combination of theoretical and experimental studies.[2] The value of ε was determined by Duty to be approximately 0.9.

5.3.2 Solution Parameters

After defining all material properties and boundary conditions in the code, the solution was initialized. Values of the pressure, the *x*, *y*, and *z* components of velocity, the CH_4 mass fraction, and the temperature were specified based on the simulated conditions. FLUENT allows the user to patch values into the solver by defining specific regions of interest. For the LCVD simulations, two unique regions were defined. First, a cylinder extending from the entrance of the gas nozzle to the substrate surface was defined and the *x* and *z* components of the velocity for the given case were patched into this region. Next, a region of cells very near the substrate surface where the laser spot impinged was patched with a temperature value of 2000 K for all cases. This setup accelerated convergence in the solver. Typically, models were run for 1000 iterations, where the residual plots and plots of solution variables confirmed convergence.

5.3.3 Flow Regime Calculation

Prior to the execution of extensive studies, it was necessary to ensure the laminar flow models described in Section 5.2 were appropriate. The flow regime is dictated by the value of the dimensionless Reynolds number. For internal pipe flow:

$$Re = \frac{\rho V D}{\mu} \tag{5.29}$$

where ρ is the density of the fluid (kg/m^3), V is the average fluid velocity (m/s), D is the internal pipe diameter (0.001 m), and μ is the viscosity of the fluid (kg/m-s).

For the current case, the density was computed using the ideal gas law, $\rho = P/RT$ at a pressure of 101.3 kPa and a temperature of 300 K. Velocity was computed from the maximum total volumetric flow rate Q (500 sccm) and the cross sectional area of the pipe A, $V = Q/A$. The viscosity used was a weighted average of that of methane and hydrogen in a 3:1 ratio at a pressure of 760 Torr and a temperature of 300 K.

The Reynolds number for such a case is 529, well below the 2100 that is typically considered the upper limit of the laminar flow regime. This value represents an upper limit for the Reynolds number over the range of model cases studied because the velocity was at a maximum under these conditions. The result justifies the use of the laminar flow models for the transport equations.

5.3.4 Mesh Convergence Study

With any numerical or computational model, it is important to investigate the relationship between the mesh size and the solution results. The mesh size used in the current study is best quantified by considering the maximum dimension of the elements across the substrate surface within the diameter of the laser spot. The initial mesh was the same as that used by Duty[2] which used 20 elements across the 200 μm diameter laser giving a mesh size of 10 μm. A second mesh was created by doubling the number of elements in the vicinity of the laser spot to 40, giving a mesh size of 5 μm. A comparison of these two meshes is shown in Figure 5.9.

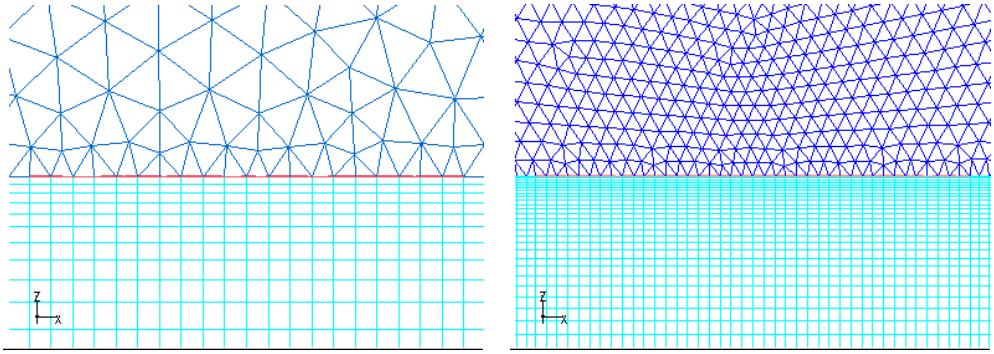

10 μm spacing **5 μm spacing**

Figure 5.9: Comparison of two mesh sizes used in convergence study

The models were run using the conditions in Table 5.7 for carbon deposition from methane. The variables of interest were plotted along the substrate surface in the region near the laser spot as shown in Figure 5.10.

Table 5.7: Conditions used in the mesh convergence study

Pressure (Torr)	Total Flow (sccm)	CH_4:H_2 Ratio	Laser Power (W)
760	500	3:1	44

The temperature and CH_4 molar concentration profiles showed little difference at the different mesh sizes; however, the carbon deposition rate profile was significantly higher for the 5 μm mesh than the 10 μm mesh.

Calculations were done at the center of the laser spot for all three variables to quantify the change in the results with the change in mesh size. Table 5.8 summarizes the findings.

Table 5.8: Change in solution values at center of laser spot for different mesh sizes

Mesh Size (μm)	Temperature (K)	CH_4 Concentration (kmol/m^3)	Deposition Rate (kg/m^2-s)
10	2157	0.00346	0.000982
5	2190	0.00341	0.001392
change	1.53%	-1.45%	41.8%

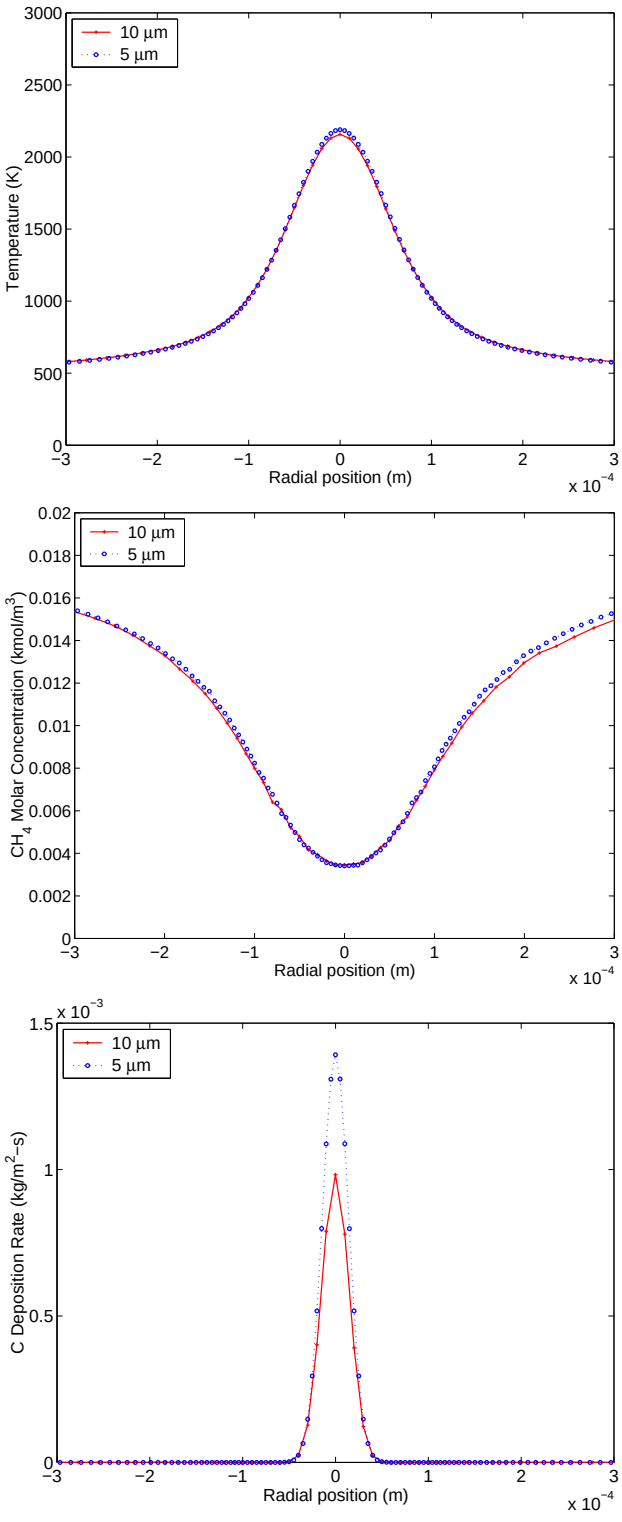

Figure 5.10: Profiles of the variables of interest across the laser spot diameter for mesh sizes of 10 and 5 μm

The temperature and methane concentration values exhibit small enough changes to consider the solution converged with regard to the mesh size. The large discrepancy in the deposition rate is attributable to the changes in the temperature and concentration values. Under the simulated conditions, carbon deposition from methane is a kinetically–limited process whose deposition rate was given by the Arrhenius expression:

$$J''_{\mathrm{C}} = 1.2856 \times 10^{8} \cdot [\mathrm{CH_4}]^{1.0185} \cdot e^{\frac{-48004}{T}} \tag{4.16}$$

where J''_{C} is the molar deposition rate (kmol/m^2-s), $[\mathrm{CH_4}]$ is the molar concentration of methane (kmol/m^3), and T is the local temperature (K). The mass deposition rate is computed by multiplying Equation 4.16 by the molecular weight of solid carbon (12 kg/kmol).

As shown in Equation 4.16, the deposition rate is exponentially dependent on temperature while almost linearly dependent on concentration. This explains why only a 1.53% change in local temperature caused a change of 41.8% in the computed deposition rate. Further calculations revealed that in order to achieve a change in computed deposition rate that falls below the standard 5% mesh convergence criteria at the given levels, the temperature value could only change by 5 K between the models, which for a temperature of 2157, represents a change of less than 0.24%.

Reducing the mesh resolution further was precluded by the size of the model. The 5 μm mesh grid was over 150 MB in size and required in excess of 1.5 GB of RAM to solve. One thousand iterations using this grid required about 18 hours of processing time. A 2.5 μm mesh was successfully created using the grid generation and adaption software Gambit, but the computers available were not suited to execute the calculations. Given these limitations, and recognition of the fact that the deposition rate variable is so sensitive to the temperature values, it was deemed sufficient to use the 5 μm mesh for all calculations. The model results should be interpreted loosely with regard to the nominal values of deposition rate, but all other values of interest including temperature, concentration, and velocity are considered relatively accurate.

5.3.5 Two Factor, Three Level, Carbon Deposition Study

In order to illustrate the utility of the fully integrated FLUENT model of LCVD, a series of typical carbon LCVD conditions were simulated. The models studied two factors at three levels: laser power and reagent nozzle flow rate. The levels are given in Table 5.9 along with other parameter values.

Table 5.9: Simulated conditions in carbon deposition rate model

Pressure (Torr(	Fill Ratio (P_{CH_4}:P_{H_2})	Total Flow (sccm)	Flow Ratio (Q_{CH_4}:Q_{H_2})	Laser Power (W)
760	3:1	0, 250, 500	3:1	39, 44, 49

One of the advantages of using a CFD package to study the LCVD process is that with sufficient mesh resolution, the code allows for the study of extremely localized phenomena. Ultimately it is these local conditions in the deposition zone that dictate the resulting deposit shape. Localized phenomena are critical in LCVD due to the coupling of the extreme temperature gradients that emerge from laser heating to the nonlinear relationship of growth rate with temperature.

The results of the numerical computations provided by FLUENT yield a tremendous amount of information regarding the details of the LCVD process. This information can be presented in a variety of ways depending upon the intent of the analysis. Contour plots provide an effective means of quickly verifying the overall patterns within the solution domain. Figures 5.12 are example contour plots in the joint fluid symmetry–substrate symmetry plane for the case with laser power of 44 W and a flow rate of 250 sccm.

More detailed insight into the dynamics of LCVD is presented through a series of *xy* plots in specific areas of interest. Figure 5.11 illustrates the regions used for generation of such plots. This detailed analysis can be used to examine the boundary layer and deposition rate profiles in different directions under different conditions. Finally, the model results can be aggregated and used as a basis to develop simple polynomial expressions that relate

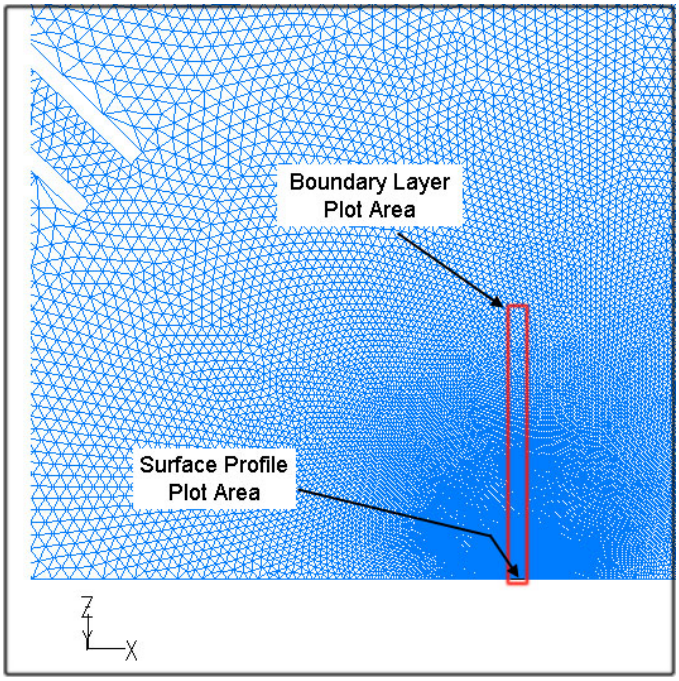

Figure 5.11: Illustration of regions used in generating surface profile and boundary layer plots

process variables to deposit attributes. Such expressions are a useful way to predict deposit properties for given experimental conditions.

5.3.5.1 Comparison of Different Laser Power Levels

The primary implication of a change in laser power is its obvious impact on deposition zone temperature. It is important to understand how this change in temperature effects the concentration of reagent species and the overall deposition rate for the reaction. For the case of 250 sccm total reagent flow, plots of these variables are shown in Figure 5.13. As expected, the temperature is shown to increase significantly with increasing laser power. The molar concentration is shown to decrease with increased laser power, and the deposition rate profiles are shown to increase in both height and width with increased power. Note that the deposition rate axis is logarithmic due to the extremely large changes in deposition rates over the range of laser powers considered here.

In order to understand which rate–limiting regime is applicable in the simulated model,

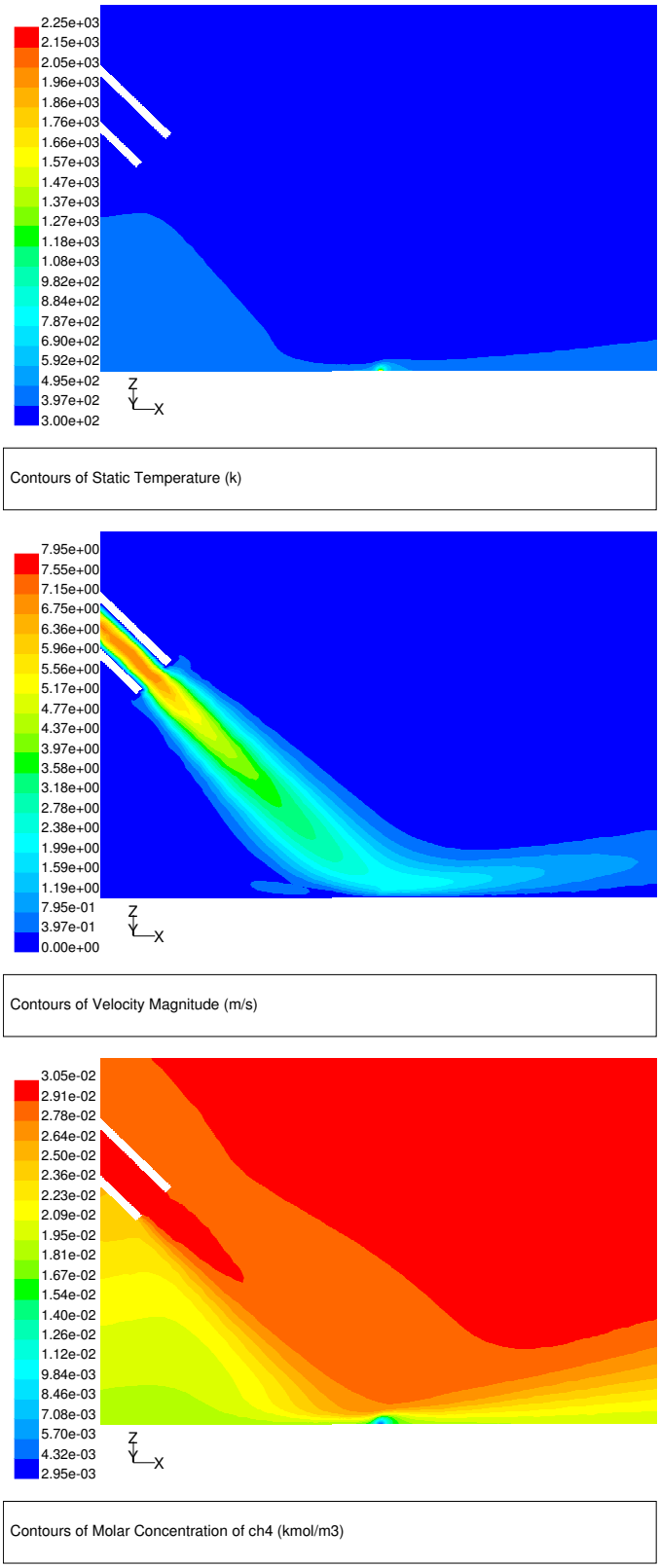

Figure 5.12: Examples of solution contours in the fluid symmetry plane for temperature, velocity magnitude, and CH_4 molar concentration

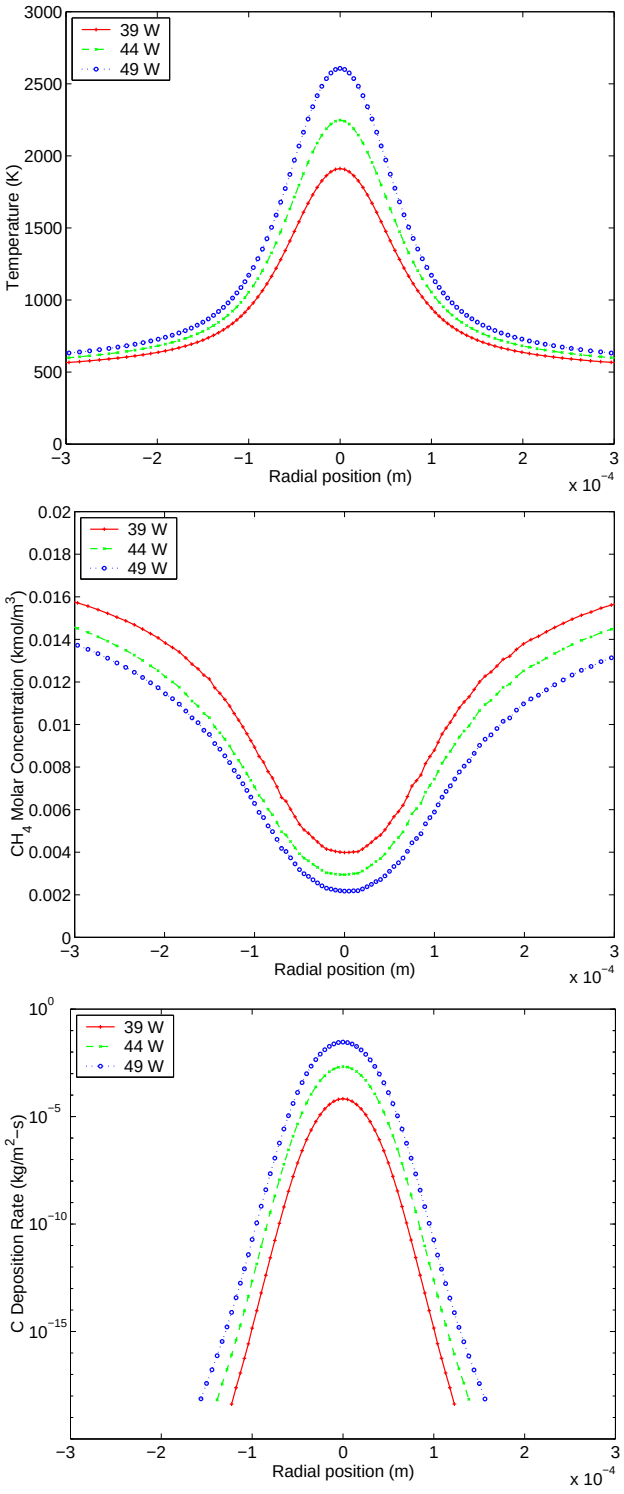

Figure 5.13: Profiles of the variables of interest across the laser spot diameter in the fluid symmetry plane for different laser powers with flow of 250 sccm

it is important to understand the concentration profiles across the laser spot. The change in molar concentration can be attributed to either a change in density, due to a change in temperature, or a change in the relative concentration of CH_4:H_2.

It was possible to quantify the percentage of CH_4 concentration change due exclusively to the density change. The molar density of the fluid mixture at the center of the laser spot was determined using the ideal gas law $\rho_{min} = P/RT_{max}$ with T_{max} equal to the maximum substrate surface temperature. For the case with a pressure of 760 Torr and a laser power of 44 W, the maximum substrate surface temperature was 2248 K which resulted in a minimum density ρ_{min} of 0.00542 kmol/m^3. The maximum density was computed at a point far from the laser spot at a reference temperature of 397 K. The resulting ρ_{max} value was 0.0307 kmol/m^3. The ratio of ρ_{min}/ρ_{max} was therefore equal to 0.177. The ratio of minimum to maximum molar concentration of CH_4 was computed using the values supplied by FLUENT with temperature equal to 2248 and 397 K respectively. The values were $C_{min} = 0.00295$ and $C_{max} = 0.0264$ kmol/m^3, yielding a C_{min}/C_{max} ratio of 0.112. Thus the density of the fluid was reduced by a factor of $1/0.177$ or 5.65 while the CH_4 concentration was reduced by a factor of 8.93. The value of the CH_4 concentration at 397 K due only to the temperature change was estimated by multiplying C_{max} by the density reduction factor 0.177. This results in a temperate adjusted minimum concentration $C_{min,\text{temp}}$ of 0.00466 kmol/m^3. Finally, the fraction of the change in CH_4 concentration attributed to the fluid density change is computed from:

$$\frac{C_{max} - C_{min,\text{temp}}}{C_{max} - C_{min}} = 0.927$$

Thus, almost 93% of the CH_4 concentration change is due to the temperature change of the fluid while the remainder of the concentration change can be attributed to a change in relative concentration of CH_4:H_2 due to diffusion or kinetic effects.

Figure 5.14 is a plot of fluid density, CH_4 mass fraction, and CH_4 molar concentration across the laser spot for the case with laser power of 49 W. The fact that the minimum mass fraction of CH_4 remained above 0.80 at the highest laser power indicated that under these

conditions, this reaction is dominated by kinetic effects.

In addition to investigating the solution variables at the substrate surface across the laser spot diameter, it is interesting to investigate the solution variables in the fluid above the substrate. Figure 5.15 plots vertical position or height above the substrate on the *y* axis and *x* velocity, *y* velocity, and *z* velocity, on the *x* axis, respectively. Note that the vertical axis extends 1 mm above the substrate. For reference, the center of the gas nozzle exit was located at a position of *x* = -7.07 mm and *z* = 7.07 mm, well above and left of the depicted region.

In Figure 5.15, the velocity profiles are very similar for all power levels. This is expected given the fact that all three cases have the same flow conditions. One notable discrepancy is with the 49 W case in the *y* and *z* velocity components. Very near the substrate, there appears a sharp increase in the *y* and *z* components in their respective negative directions. The *x* scale on the *y* velocity plot is an order of magnitude shorter than that of the *x* and *z* component plots, therefore the *y* component discrepancy is relatively insignificant compared to that of the *z* component. The increase in the *z* velocity component in the negative direction is likely due to the reduction in fluid density accompanying the increased temperature near the substrate surface for this high power case (assuming a fixed molar flux).

Other variables of interest in the fluid zone above the substrate include the temperature, overall velocity magnitude, and molar concentration. Plots of these values are given in Figure 5.16. As expected, a comparison of the thermal boundary layer profiles reveals higher temperatures with increased laser power. At all power levels, the thermal boundary layer thickness δ_t is about 0.5 mm. The momentum boundary layer is dominated by the shape of the *x* velocity component with some influence from the *z* component. It's thickness, δ_m, is approximately 0.6 mm. The species boundary layer shows a reduction in CH_4 molar concentration with increased laser power due to the increased deposition rates with increased temperature. The species boundary layer δ_c is approximately 0.5 mm thick.

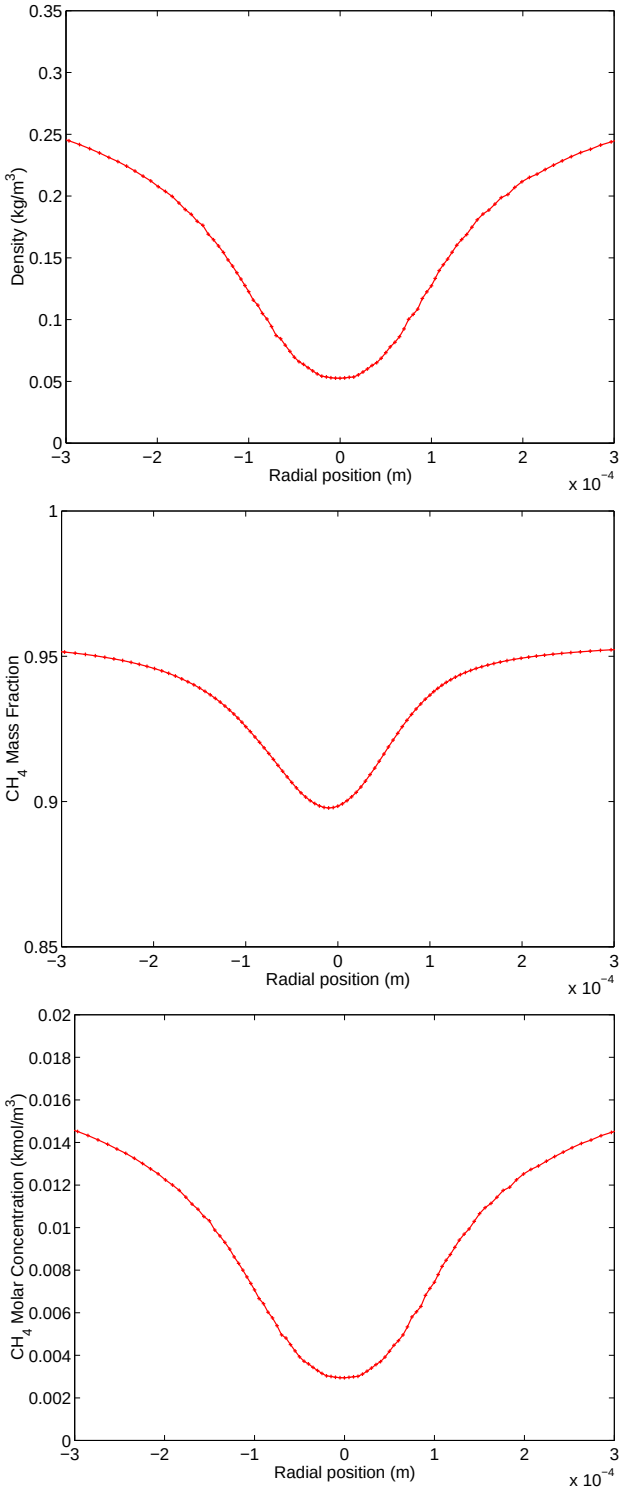

Figure 5.14: Profiles of different concentration measures across the laser spot diameter in the fluid symmetry plane

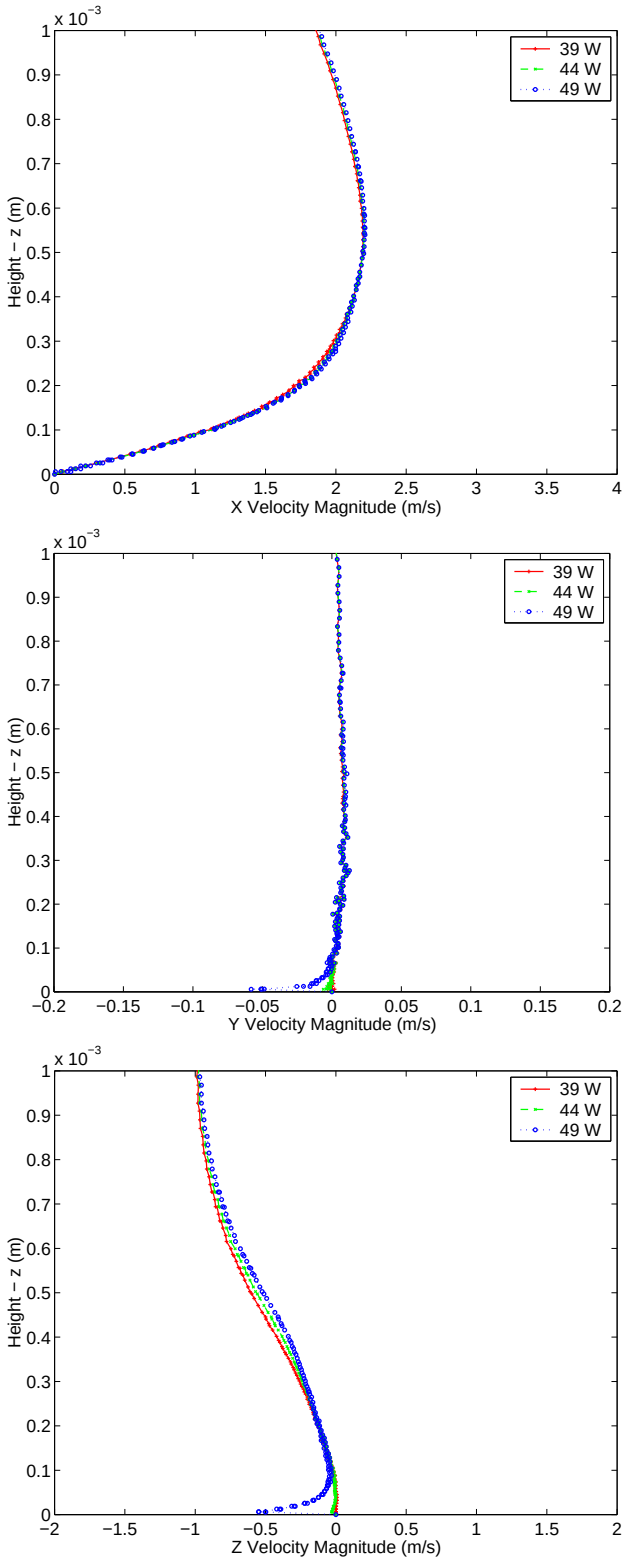

Figure 5.15: Profiles of velocity component magnitudes above the laser spot in the fluid symmetry plane for different laser powers

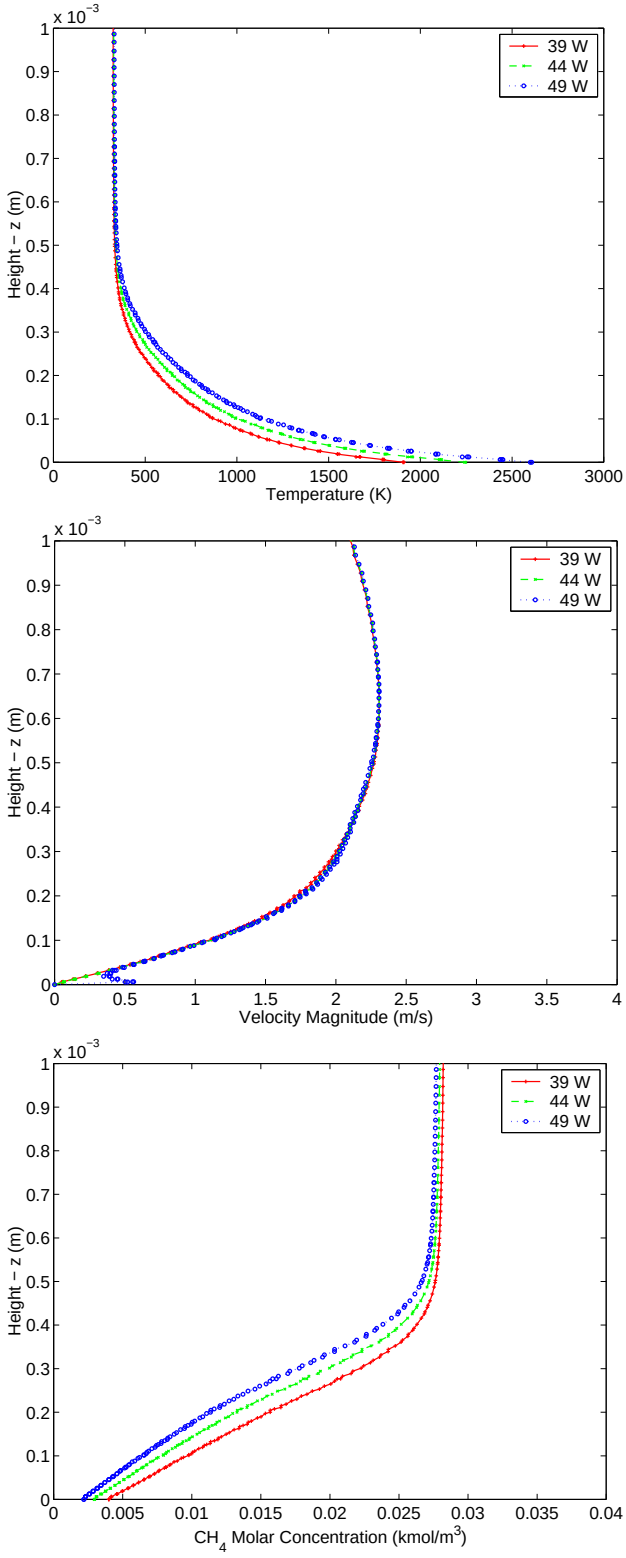

Figure 5.16: Profiles of boundary layers above the center of the laser spot in the fluid symmetry plane for different laser powers

5.3.5.2 Comparison of Different Flow rates

Similar to the investigation into the effect of laser power level on deposition variables, a study of different flow rates (0, 250, and 500 sccm) at a constant laser power of 44 W was conducted. The plots in Figure 5.17 indicate how the temperature, CH_4 molar concentration, and carbon deposition rate vary across the laser diameter on the substrate surface. The temperature plot shows there to be a convective cooling effect with increased gas flow rate through the nozzle. This result was also show by Duty.[2] The concentration profiles indicate that at the center of the laser spot, the concentration values are very similar. The slight discrepancy is likely due to the temperature effect on concentration. As one moves away from the center of the substrate, the differences in concentration increase somewhat due to the shorter residence time created by increasing the flow rate. The deposition rate profiles show that increased flow rate actually causes a decrease in deposition rate. Given the fact that under these conditions, carbon deposition is very much kinetically–limited, and that there is a convective cooling effect from the gas nozzle, this result is not surprising. The exponential relationship between temperature and deposition rate causes a large change in deposition rate for a seemingly small change in temperature.

The boundary layer plots in the fluid directly above the laser spot are given in Figure 5.18. Note again that the height extends 1 mm above the substrate. For reference, the center of the gas nozzle exit was located at a position of x = -7.07 mm and z = 7.07 mm, well above and left of the depicted region.

The thermal boundary layer thickness δ_t is shown to decrease from about 0.5 to 0.3 mm with the increase from 250 to 500 sccm in flow rate. As expected, the profiles of velocity magnitude are significantly different for the different flow conditions. The species boundary layer decreases from 0.5 to 0.3 mm with the increased flow rate. The significant impact of the nozzle flow rate on the boundary layer thickness confirms the utility of it as a design feature in the LCVD system. However, as discussed above, for kinetically–limited processes such as carbon deposition from methane, it does not enhance the deposition

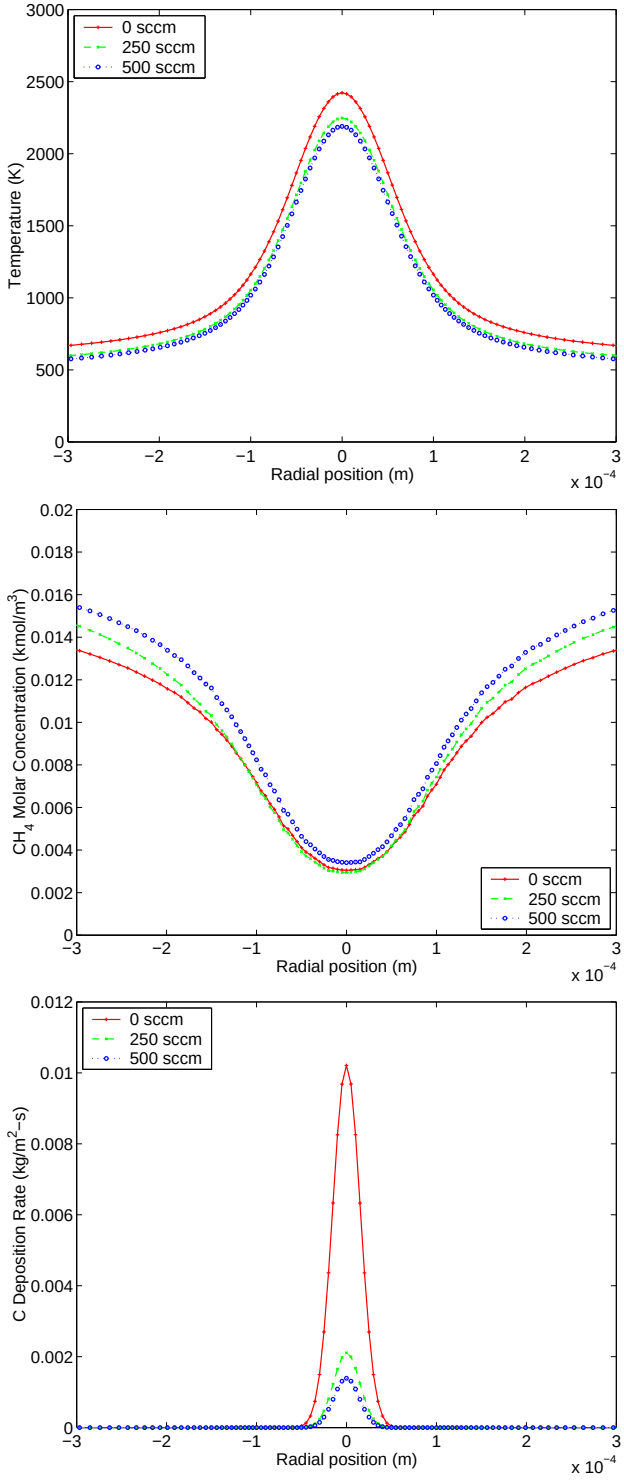

Figure 5.17: Profiles across the laser spot diameter on the substrate surface for different flow rates with a laser power of 44 W

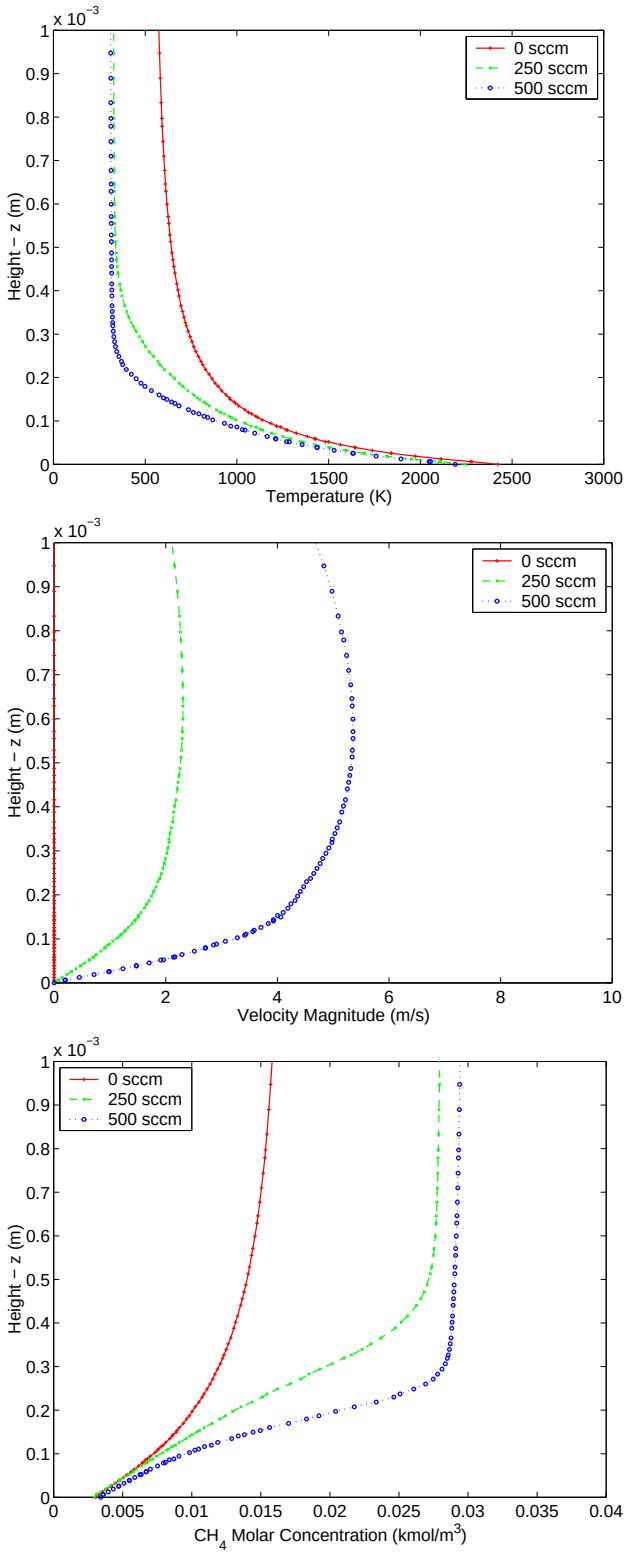

Figure 5.18: Profiles of boundary layers above the center of the laser spot in the fluid symmetry plane for different flow rates with a laser power of 44 W

process.

5.3.5.3 Deposition Rate Profile Studies

Different applications of LCVD may require different deposit shape profiles, thus, an understanding of how the profile is affected by the process parameters is desirable. FLUENT provides calculations of mass deposition rates along surfaces that participate in chemical reactions. Contour plots as shown in Figure 5.19 of the temperature, concentration, and deposition rates on the substrate surface illustrate the large gradients in the region near the laser spot.

A comparison among the deposition rate profiles in different radial directions from the center of the substrate was done to investigate whether the directional setup of the gas nozzle caused any asymmetrical effects. The angular directions were defined as shown in Figure 5.20. The worst case scenario was the case of laser power 49 W and flow rate of 500 sccm. Figure 5.21 shows that the rate profile in the different angular directions is practically identical.

Notice that the rate profiles in Figure 5.21 take on a Gaussian shape. In fact, a comparison was made between the Gaussian laser beam energy flux and the surface temperature profile and another between the computed deposition rate profile and the surface temperature profile. Figures 5.22 and 5.23 provide these comparisons.

The strong connection between the shape of the temperature curve and the shape of the deposition rate curve is a result of the kinetically–limited nature of the carbon deposition reaction. This process is so strongly influenced by kinetics that a comparison between the deposit profile predicted through the sophisticated CFD model to that of a crude manual calculation was prudent.

The manual calculation of deposition rate extends from Equation 4.16. The two unknowns in the equation are methane concentration $[CH_4]$ and temperature T. In reality it is difficult to know either of these values with a high degree of accuracy. For comparison, the

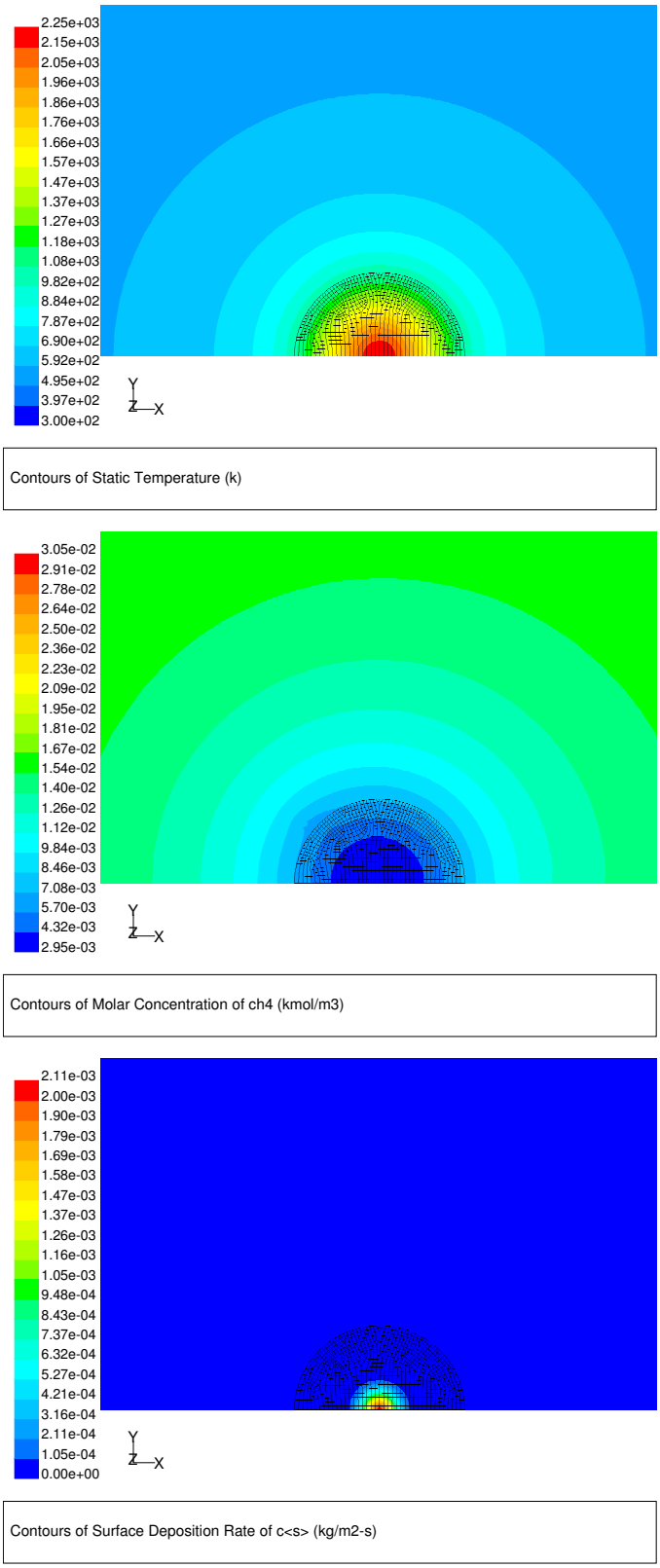

Figure 5.19: Example of temperature, CH_4 molar concentration, and deposition rate contours on the substrate surface in the vicinity of the laser spot

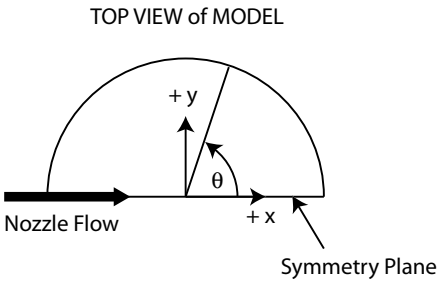

Figure 5.20: Definition of angular directions for profile studies

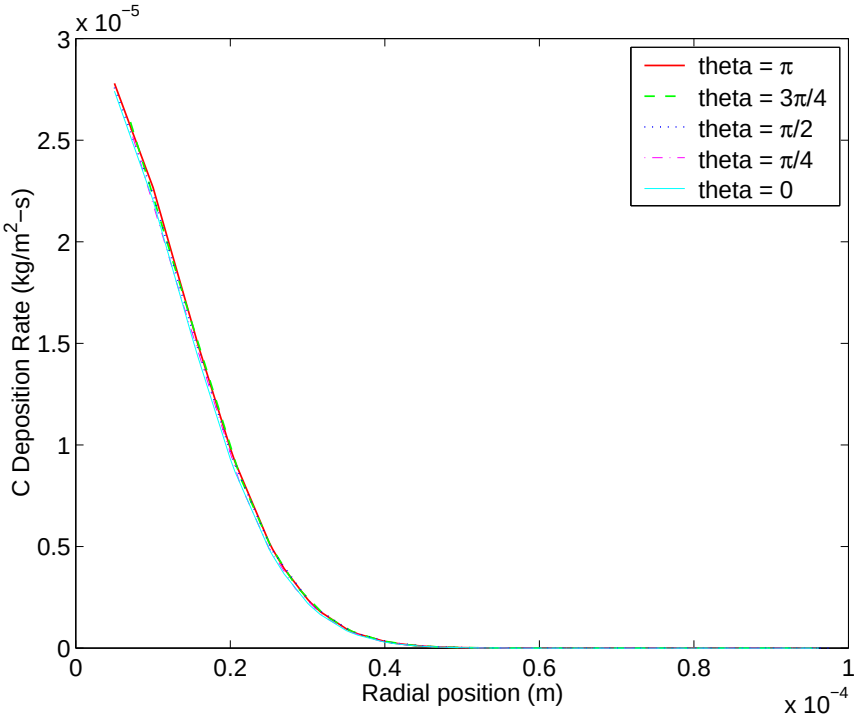

Figure 5.21: Comparison of deposition rate profiles in five different angular directions

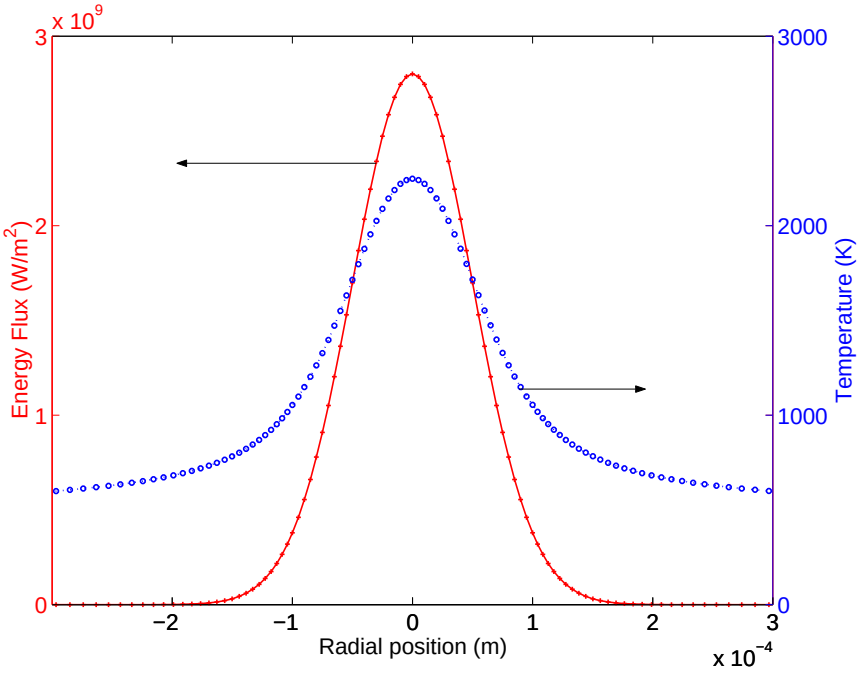

Figure 5.22: Comparison of Gaussian energy distribution to substrate surface temperature profile

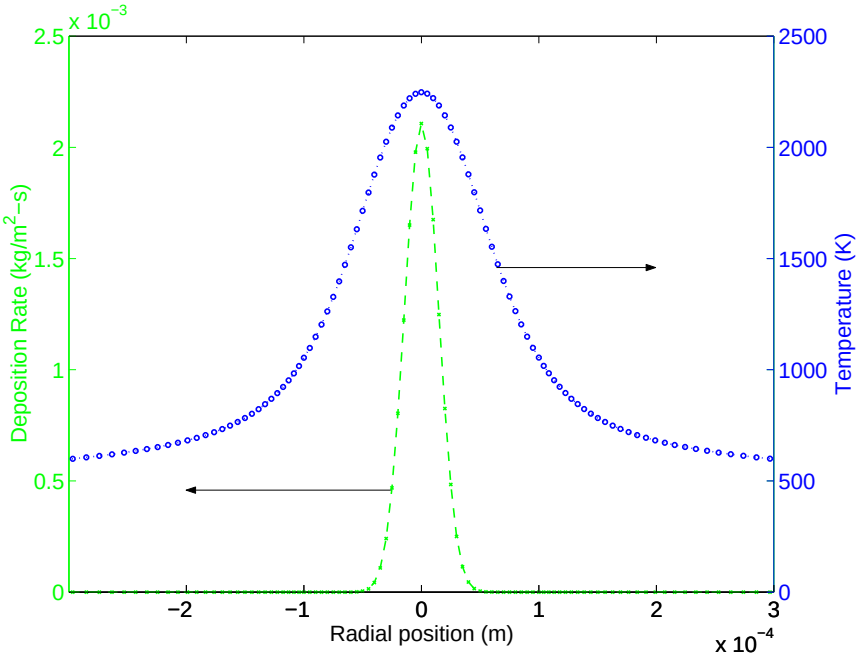

Figure 5.23: Comparison of substrate surface temperature profile to deposition rate profile

temperatures used were the same as those predicted by the CFD model.

Due to the interaction of the transport and kinetic phenomena, it is very difficult to know the actual methane concentration $[CH_4]$ at the substrate surface during an experiment. The most appropriate estimate of concentration can be computed by adjusting the known global concentration (which is dictated by experimental conditions) from its value when delivered into the LCVD system to its value at operating conditions. It is reasonable to assume that at the substrate surface, the reagent mixture is at the same temperature as the surface. In the manual calculation, for each node in the CFD model, the bulk CH_4 concentration was adjusted to the local surface temperature. This approach accounts for the temperature influence on concentration, but ignores the depletion due to other factors such as diffusion or the surface reaction itself. For a strongly kinetically–limited process, this temperature–adjusted concentration approach will account for the majority of the concentration change as discussed in Section 5.3.5.1.

At each node, the deposition rate was computed using Equation 4.16 with the temperature and concentration values as described above. Figure 5.24 is a comparison of the two deposition rate profiles for the case of laser power 44 W and flow rate 250 sccm.

Given the sensitivity of the predicted deposition rate profile to the computed temperature values as discussed in the mesh convergence study of Section 5.3.4, for a process known to be strongly kinetically–limited, a simple kinetic model is perhaps sufficient to provide a first order estimate of deposition rates.

There is some limitation to the applicability of the FLUENT model results to a typical carbon deposition experiment. Due to transient thermal effects that have been investigated by Bondi,[64] the current steady state case implies that the laser has been heating the substrate for 5 minutes or more. Therefore, the exact situation being simulated in the model was that of pre–heating the graphite substrate with the laser for at least five minutes in an inert gas environment, and then providing an instant change of the gaseous environment to the reagent mixture of interest. Experimentally, this is not the normal procedure used

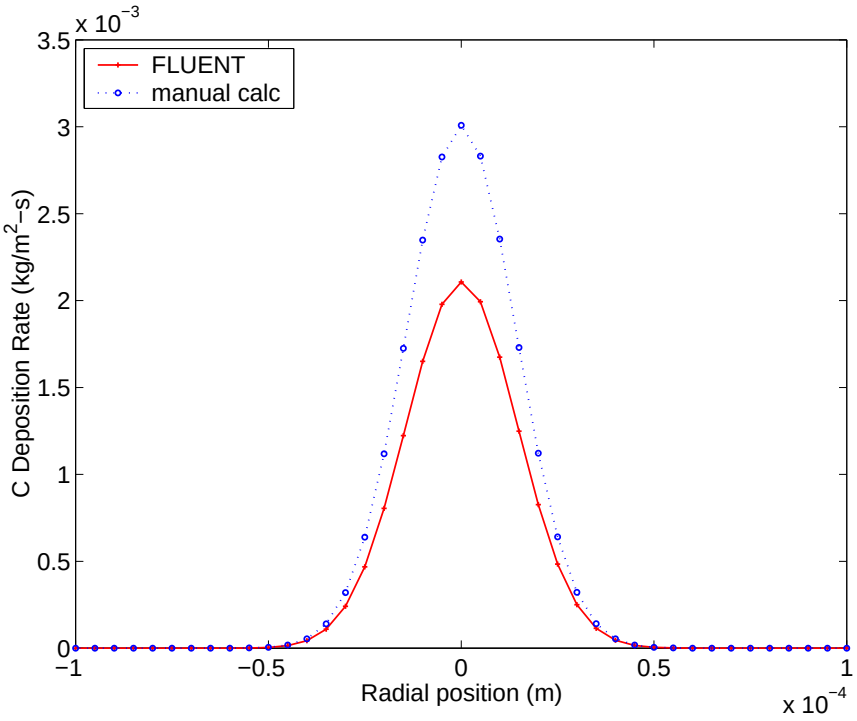

Figure 5.24: Comparison of FLUENT deposition rate with simple kinetic calculation at each node

for carbon deposition. However, a transient analysis of the current situation was deemed impractical due to computational expense.

5.3.5.4 Relation Between Deposition Rate Profiles and Deposit Shape

The mass deposition rate profiles such as that shown in Figure 5.24 are directly linked to the shape of an LCVD deposit. The units of mass deposition rate on a surface, J, are kg/m^2-s. If the density of the deposit material ρ (kg/m^3) is assumed constant throughout the growth process, a growth velocity, j_v in m/s can be computed:

$$j_v = \frac{J}{\rho}$$

The growth velocity can be thought of as the rate of increase in deposit thickness in the direction normal to the substrate surface. If the substrate surface is isothermal with equal concentration everywhere, the growth velocity of the deposited coating will be equal everywhere and will thus remain normal to the original substrate surface. This is normally

the situation in traditional CVD.

The temperature, velocity, and concentration gradients of LCVD complicate the growth rate and deposit shape analysis considerably. During the initial growth period, it is assumed that most growth occurs in a direction normal to the substrate surface. Hence, the deposition rate profiles shown in Section 5.3.5.3 represent the deposit shape. At the center of the laser spot, the growth velocity direction can be considered to remain normal to the underlying substrate surface, similar to CVD. In fact, the kinetic analysis of Chapter 4 was conducted at the center of the laser spot for this reason.

After growth begins, the properties and shape of the growth surface change from those of the underlying substrate material to those of the deposited material. Changed properties include the reflectivity, absorptivity, density, specific heat, thermal conductivity, and emissivity.

The change in deposit surface shape will effect the local fluid variables such as temperature, velocity, and concentration through its impact on the overall flow patterns and the boundary layer profiles. The change in deposit surface shape will also effect the deposit surface temperature through a change in conductive, convective, and radiative heat transfer both within the deposited material and at the surface.

The evolving deposit shape is directly related to the underlying deposit surface shape through the fact that locally, deposition occurs in the direction normal to the underlying surface. If the deposit growth direction remains normal to the deposition surface, after the initial growth period represented by the profiles typified in figures such as 5.21 and 5.24, the deposit growth direction will change considerably. A new growth *rate* will arise due to changes in the surface temperature or concentration and a new growth *direction* will arise due to the change in the shape of the underlying deposit surface.

Figure 5.25 is a conceptual drawing of how deposit shape might evolve with time. The bottom plot represents a normalized growth rate profile, Profile 1, computed from the FLUENT case with a laser power of 44 W and a nozzle flow rate of 250 sccm. The

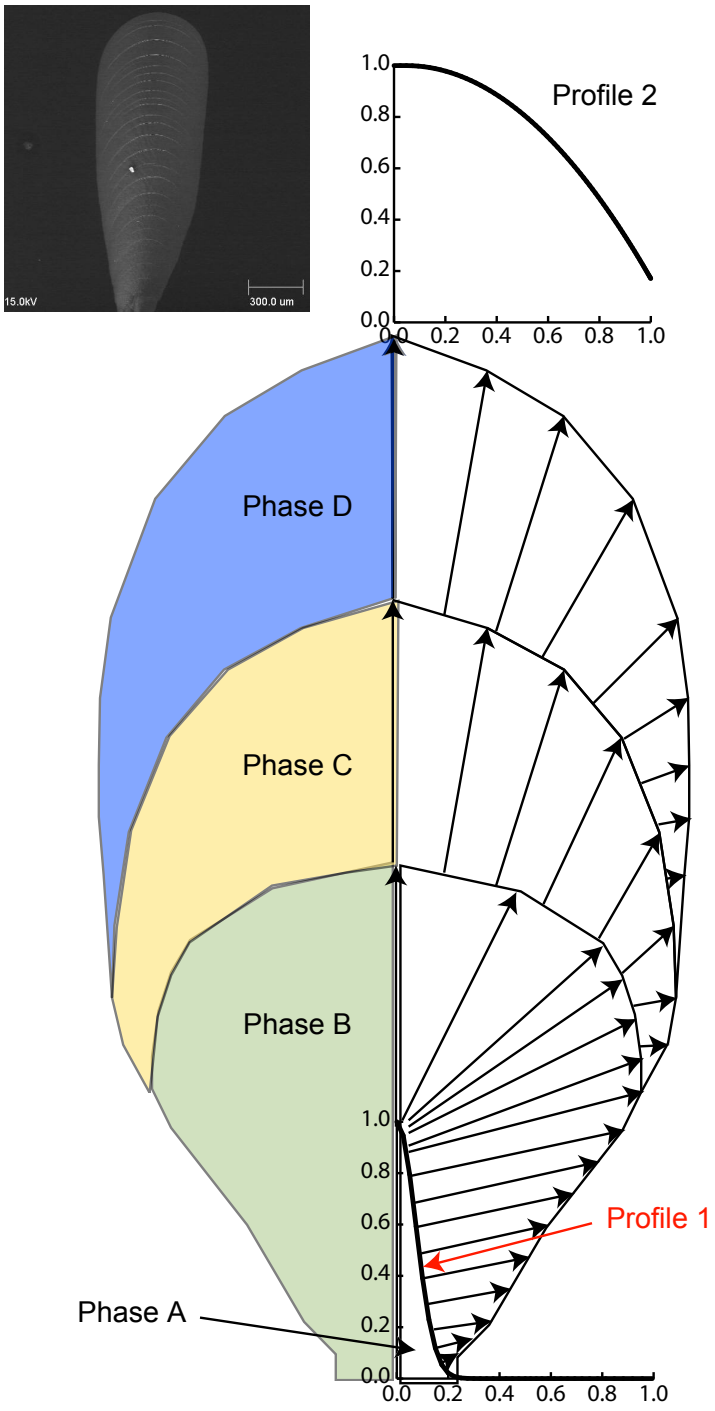

Figure 5.25: Conceptual evolution of carbon fiber deposit shape

horizontal position axis is normalized to 2× the laser beam spot radius. This profile was computed for a flat substrate surface. We assume that the first phase of growth, Phase A, acquires the shape of this initial growth rate profile.

On top of Profile 1 is a depiction of the shape the second phase of growth may yield. This shape was derived by superimposing Profile 1 on top of itself. The procedure was to draw vectors with their origin located on the Profile 1 curve at different radial positions along the profile. The magnitude of each vector was determined by the height of Profile 1 at the radial position corresponding to the vector's origin. The direction of each vector was outward normal to the Profile 1 curve. The series of vectors was joined at their tips to create the deposit shape after growth Phase B. Notice that the both the height and the diameter of the growth increased significantly during Phase B.

As mentioned previously, the deposition surface properties change considerably after a deposit emerges from the flat substrate surface. Most importantly for a kinetically–limited process such as carbon LCVD, the temperature profiles on the deposition surface change. In order to capture these changes in the shape evolution analysis, a new normalized deposition rate profile shape was computed using experimentally measured temperature data from a growing carbon fiber and the kinetic expression of Equation 4.16. Profile 2 represents the shape of this new rate profile.

The shape analysis continues by superimposing deposition rate Profile 2 on the deposit shape resulting from Phase B growth. Using the same procedure to get the position, magnitude, and direction of the vectors, the shape of Phase C growth becomes apparent. During Phase C, the deposit diameter increased slightly, while the height increased significantly. The procedure was repeated by again superimposing Profile 2 on the shape following Phase C to arrive at the shape of Phase D. It becomes obvious during Phase D that the deposit has reached a steady–state diameter while it continues to increase in height with time.

The shape predicted by the analysis in Figure 5.25 can be compared to the carbon fiber deposit depicted in the upper left corner of the figure. The shape of the actual deposit is

representative of that proposed by the conceptual analysis which suggests that the relation between deposition rate profiles and deposit shape is partially explained by this analysis.

The current CFD deposition rate model does not explicitly account for the dynamics of the growth process through the creation of new solid material; therefore, the deposition rate profiles only serve as indicators of the deposit shape during the initial growth periods. The overall magnitude of the growth rate at the center of the laser point does serve as a viable reference point for comparing the model to experimental results. Some insight into the changing thermal conditions within a growing LCVD carbon fiber is gained through the analysis in Chapter 6.

5.3.5.5 Maximum Growth Rate Response Surface Studies

One of the most practical contributions of a fully integrated model of the LCVD process is the ability to reduce the complex interactions and relationships among the different process parameters to a single response surface. The surface can be represented by a multivariate polynomial expression and provides a useful prediction tool for developing process planning algorithms.

As described in Section 5.3.5.4, the FLUENT model of carbon LCVD is most applicable at the center of the laser spot. Table 5.10 lists the computed value of temperature, molar concentration, and deposition rate at this position for each of the nine cases in the current study.

Two response surfaces were generated using the data in Table 5.10. The first was the deposition velocity response to the explicitly defined levels of laser power and nozzle flow rate. Figure 5.26 shows the nine maximum deposition rate data points taken from the nine model cases along with the response surface generated by fitting the data using a multiple linear regression technique. The details of the regression output are provided in Table 5.11.

Table 5.10: Temperature, concentration, and deposition rates computed at center of laser spot for nine model cases

Laser Power (W)	Flow Rate (sccm)	Temp (K)	CH_4 Conc (kmol/m^3)	C Dep Rate (kg/m^2-s)	C Dep Vel (μm/s)
39	0	2066	2.39E-03	2.61E-04	0.148
39	250	1912	3.98E-03	6.72E-05	0.038
39	500	1859	3.60E-03	2.96E-05	0.017
44	0	2423	3.05E-03	1.02E-02	5.801
44	250	2248	2.95E-03	2.11E-03	1.197
44	500	2190	3.41E-03	1.39E-03	0.791
49	0	2792	1.59E-03	7.16E-02	40.707
49	250	2608	2.17E-03	2.94E-02	16.677
49	500	2546	2.85E-03	2.49E-02	14.140

The final regression equation is given by Equation 5.30.

$$\begin{aligned} DepositionVelocity &= 571.246 - 29.2416 * LaserPower + 0.177125 * FlowRate \\ &\quad + 0.374327 * LaserPower^2 \\ &\quad - 0.0052872 * LaserPower * FlowRate \\ &\quad + 0.0000687467 * FlowRate^2 \end{aligned} \tag{5.30}$$

where $DepositionVelocity$ is in μm/s, $LaserPower$ in in W, and $FlowRate$ is in sccm.

Equations that reduce the complex interactions among the process variables to simple expressions are powerful tools for the development of process planning algorithms. They provide a practical way to determine a priori the proper machine parameters to produce an LCVD deposit of a certain size and shape.

The second response surface stemming from the data in Table 5.10 is shown in Figure 5.27 and was created by regressing the computed deposition velocity against the computed temperature and molar concentration values. Because carbon deposition is kinetically–limited, this surface can be thought of as an approximation to the Arrhenius expression over a range of temperatures and concentrations. The surface is compared to the experimental

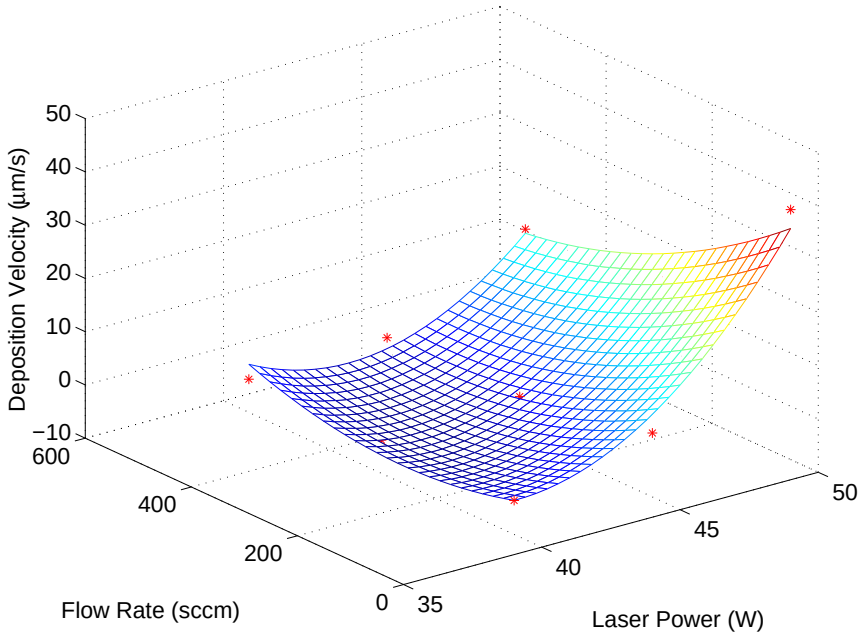

Figure 5.26: Response surface for deposition velocity as a function of laser power and nozzle flow rate compared with maximum deposition rate data points from 9 model cases

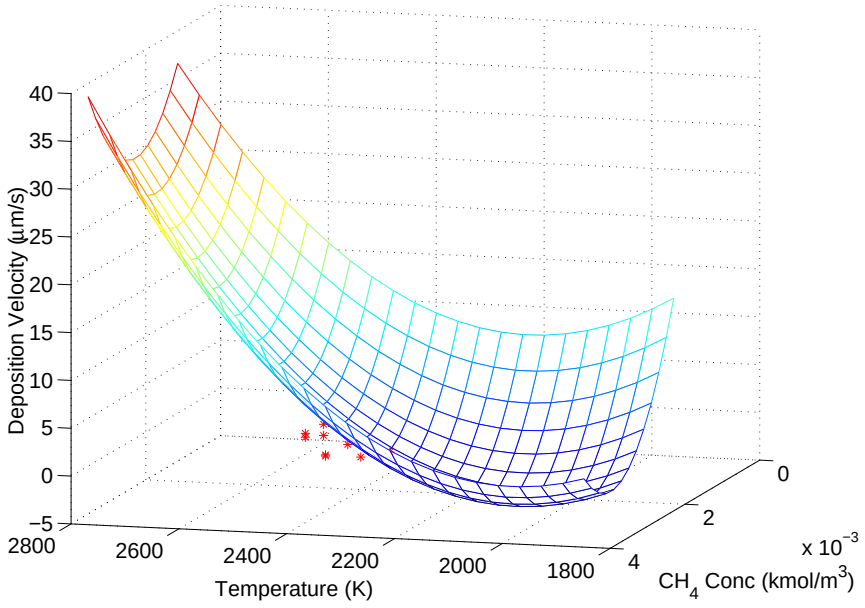

Figure 5.27: Response surface for deposition velocity as a function of temperature and molar concentration compared with experimental data points used in kinetic regression

data used to generate the kinetic parameters (see Section 4.2) for carbon deposition in Figure 5.27.

5.3.6 Relative Importance of Convection and Diffusion

Carbon deposition from methane is strongly kinetically–limited at the conditions studied. Using the model, an interesting study was performed to determine if deposition could still occur under conditions when the convective effects of the gas nozzle flow inhibited reagent delivery to the substrate surface. The setup simulated a statically filled reaction chamber with the typical 3:1 partial pressure ratio of methane to hydrogen by setting the CH_4 mass fraction to 0.96 on the pressure outlets along the top and sides of the fluid zone. The nozzle flow was set to 500 sccm of H_2 only. In order for deposition to occur in this scenario, the CH_4 species had to diffuse into and through the H_2 convective flow region to the substrate surface. The relative importance of diffusion to convection could thus be inferred by comparing the concentration profiles and deposition rate profiles of this case to the case of 0.96 CH_4 mass fraction in both the static fill and the nozzle flow. The laser power was 44 W in both cases which yielded almost identical temperature profiles.

Figures 5.28 and 5.29 show the differences in CH_4 mass fraction contours near the laser surface between the two cases. The case of flowing the 3:1 mixture shows a change in mass fraction of about 0.04 as it goes from 0.96 to 0.92. As expected, the concentration of CH_4 is significantly reduced in the case of 100% H_2 flow. The change in methane mass fraction in this case is shown to be about 0.5 going from 0.96 to about 0.46. However, sufficient methane remains in the deposition zone to enable the surface reaction to proceed, albeit at a slower rate.

Figure 5.30 compares the predicted deposition rate profiles for the two cases. The pure H_2 flow through the nozzle reduces the maximum deposition rate by almost a factor of 3. Therefore, the convective effect of the gas nozzle does impede the diffusion of reagent species to the surface, but it does not prevent deposition entirely. Another conclusion that

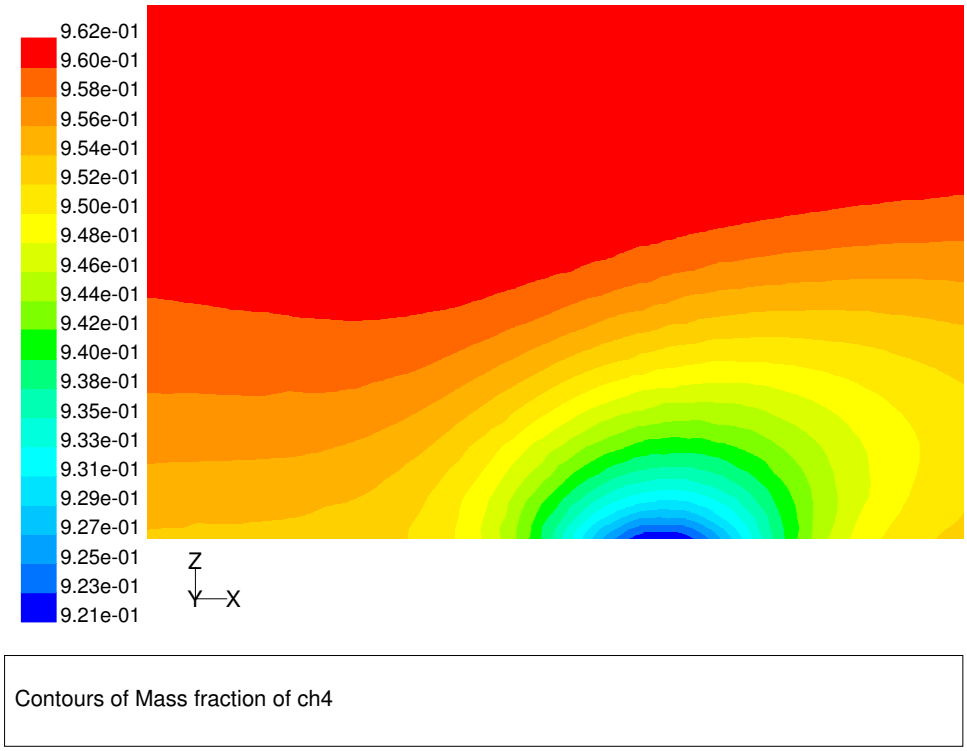

Figure 5.28: CH_4 mass fraction contours in fluid symmetry plane for case of 75% CH_4 25% H_2 nozzle flow

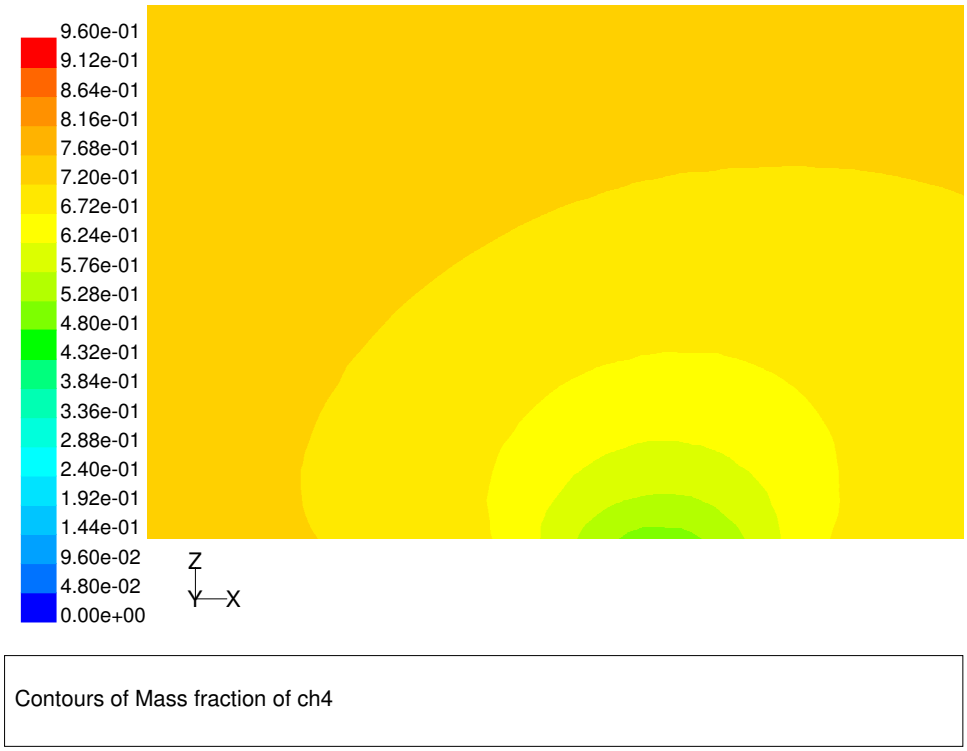

Figure 5.29: CH_4 mass fraction contours in fluid symmetry plane for case of 100% H_2 nozzle flow

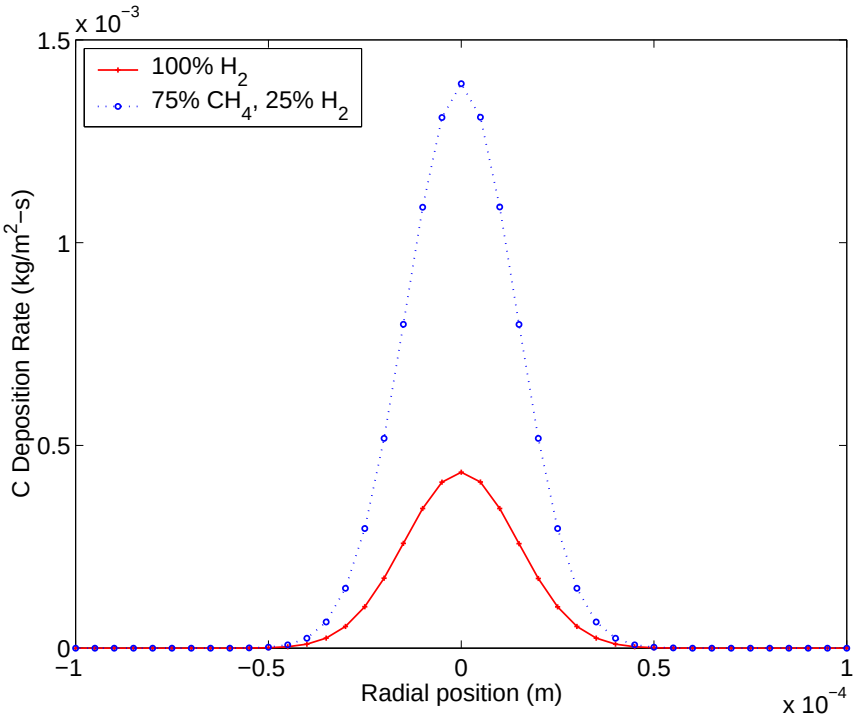

Figure 5.30: Comparison of C deposition rate profiles for case of 100% H_2 vs 75% CH_4:25% H_2 nozzle flow

can be drawn from the results is that the ambient gas in the chamber has some influence on the gas composition at the laser spot even when the gas jet is used.

5.3.7 Analysis of the Significance of Thermal Diffusion

It is generally thought that thermal diffusion is an important mass transport mechanism in LCVD due to the large temperature gradients that exist in and around the laser spot. FLUENT uses Equation 5.10 to compute the total diffusion of species *i* in the fluid domain due to both ordinary diffusion and thermal diffusion.

$$\vec{J}_i = -\sum_{j=1}^{N-1} \rho D_{ij} \nabla Y_i - D_{T,i} \frac{\nabla T}{T} \tag{5.10}$$

The overall impact of thermal diffusion on the CH_4 concentration profile along the substrate over the laser spot can be seen by comparing two cases: one with thermal diffusion calculations enabled and a second with them disabled. The results for this study with a laser power of 44 W and a flow of 250 sccm are plotted in Figure 5.31. It can be seen that the

overall effect of thermal diffusion was to reduce the concentration of CH_4 in the deposition zone. Figure 5.32 illustrates how the thermal diffusion factors affects the deposition rate profiles. A 33% reduction in maximum deposition rate is observed for these cases.

The fact that thermal diffusion influences the strongly kinetically–limited process of carbon LCVD so significantly illustrates its significance in LCVD. For processes that are transport–limited, understanding the relationship between ordinary diffusion and thermal diffusion could be paramount to understanding deposit shapes.

5.4 Summary

A comprehensive computational model has been developed to represent Georgia Tech's forced flow LCVD system. The model has been prototyped using the well–known carbon deposition process from the CH_4:H_2 reagent system. A number of studies were used to validate the model and gain insight into the detailed dynamics of the carbon LCVD process.

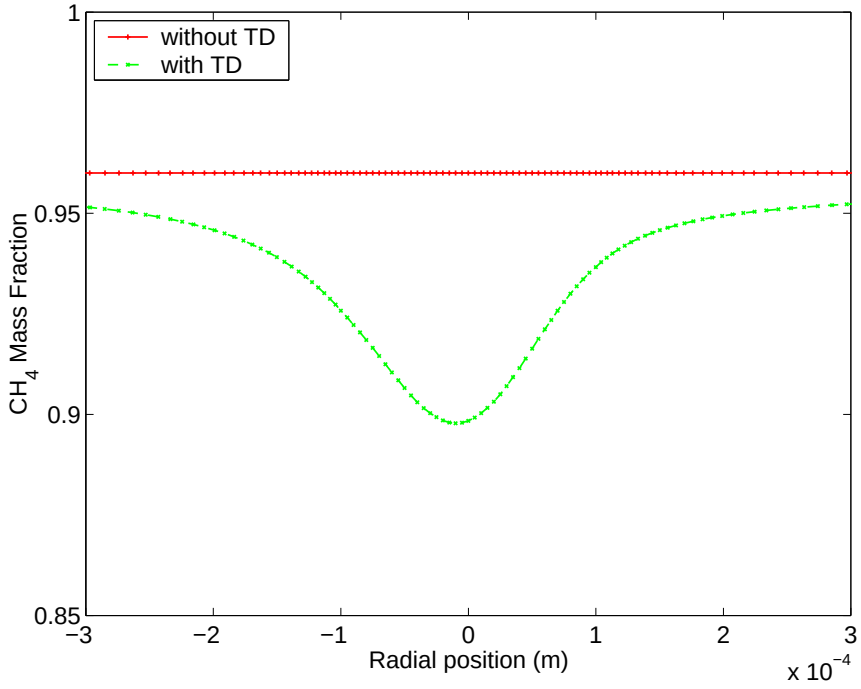

Figure 5.31: Comparison of CH_4 mass fraction profiles for cases of thermal diffusion enabled and disabled

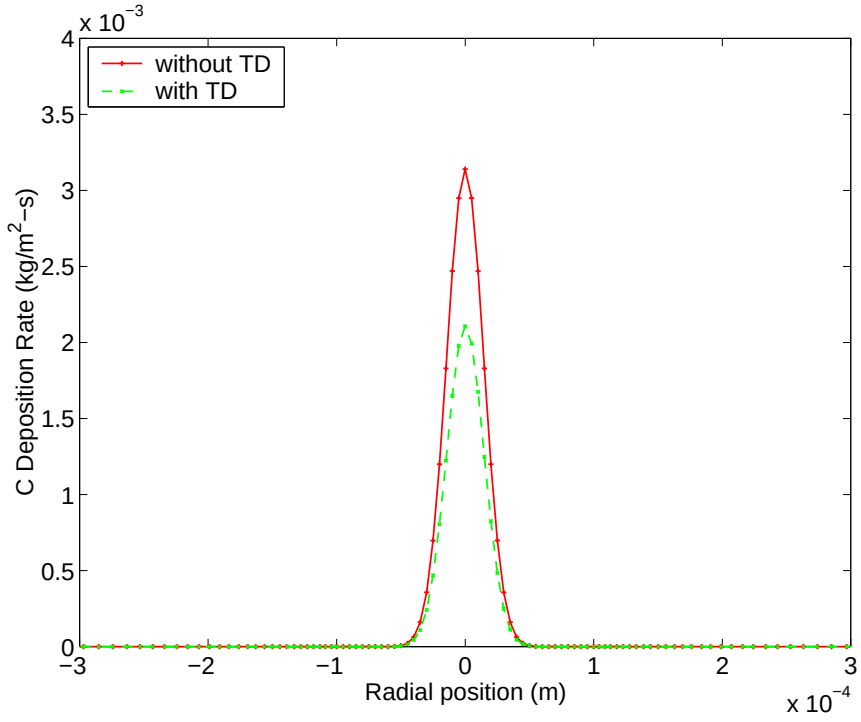

Figure 5.32: Comparison of C deposition rate profiles for cases of thermal diffusion enabled and disabled

Table 5.11: Carbon Fiber Multiple Regression Analysis

Regression coeffs. for Deposition Velocity

constant	571.246
A:Laser Power	-29.2416
B:Flow Rate	0.177125
AA	0.374327
AB	-0.0052872
BB	0.0000687467

Analysis of Variance

Source	Sum of Squares	Df	Mean Square	F-Ratio	P-Value
A:Laser Power	847.781	1	847.781	38.43	0.0085
B:Flow Rate	167.566	1	167.566	7.60	0.0704
AA	175.151	1	175.151	7.94	0.0669
AB	174.716	1	174.716	7.92	0.0671
BB	36.9227	1	36.9227	1.67	0.2864
Total error	66.187	3	22.0623		
Total (corr.)	1468.32	8			

R-squared = 95.5 percent
R-squared (adjusted for d.f.) = 88.0 percent
Standard Error of Est. = 4.69706
Mean absolute error = 2.36598
Durbin-Watson statistic = 2.34074 (P=0.0905)
Lag 1 residual autocorrelation = -0.174742

CHAPTER VI

THERMALLY–INDUCED CONDITIONS DURING FIBER GROWTH

The existence of large thermal gradients within a material always brings concerns about thermal stress and strain. During the LCVD process, the presence of large, transient temperature gradients could cause damage to the underlying deposit or substrate, compromising the mechanical integrity of the materials. In fact, some have shown that carbon structures grown with LCVD exhibit signs of large, periodic cracks.[20] Chapter 4 presented a multi–layered carbon wall that showed evidence of internal cracks. Little work has been done to better understand the thermal stress fields that exist within an LCVD structure during deposition. Ultimately, these stress fields and their implications on material properties must be better understood if LCVD is to become a viable manufacturing process.

In order to study the implications of these large temperature gradients, a structural model of a carbon fiber was developed using the finite element code ANSYS. The modeling was done in two phases. The first phase involved a thermal analysis of an LCVD fiber during growth. After the thermal model was developed, the temperature field within the fiber at two different time points (and growth heights) was obtained. The second phase of model development used the temperature fields as loads in a structural model to examine the thermal stresses induced by these loads.

6.1 Model Geometry and Meshing

The first step in the fiber thermal and structural modeling process was to formulate an appropriate geometry for studying an LCVD fiber during growth. The axisymmetric nature of the physical system was exploited to allow model development in two dimensions. A

fiber with a radius of 0.2 mm and a height of 1.0 mm was positioned coaxially on a substrate with a thickness of 2.54 mm and a radius of 9.525 mm. Consistent with observed carbon fiber profiles, the fiber tip was round with a radius of 0.2 mm as shown in Figure 6.1. These dimensions represented typical carbon fibers such as Sample 3 of experiment C-228F used in Section 4.2. The height of 1.0 mm was chosen to represent a fiber that would have reached a steady state growth condition.

Several factors complicated the creation of the fiber geometry. First, there was the need to define material properties as a function of position at different locations along the fiber radius. An explanation of this requirement is given in Section 6.2. The fiber body and the fiber tip were modeled as 10 separate areas as shown in Figure 6.2.

A second complexity in modeling the fiber geometry related to the laser energy input boundary condition. As with the deposition rate models described in Chapter 5, the laser energy was modeled as volumetric heat generation within the top layer of surface elements. A volumetric heat generation method is preferred over a specified heat flux, because a heat flux boundary condition prohibits the calculation of convective and radiative heat transfer. Unfortunately, the volumetric heat generation method couples the laser power generation to the element size within the model. In order to accurately compute the volumetric heat generation values in the region effected by the laser, the size of each mesh element must be known. Thus, a structured mesh was created using a concentric semi–circular arc within the fiber tip. This area can be seen in the close–up view of the fiber geometry shown in Figure 6.3.

In order to capture the changes that occur with time (and fiber growth), two model geometries representing two “snapshots” in time were created. The first geometry was that illustrated in Figure 6.1 and was termed the “short fiber” case. The underlying geometry of the second case was identical to the short fiber case, with the addition of extra material on the fiber tip. This extra material represented new material grown between the two time points. The second case was referred to as the “tall fiber” case. Figure 6.3 shows the fiber

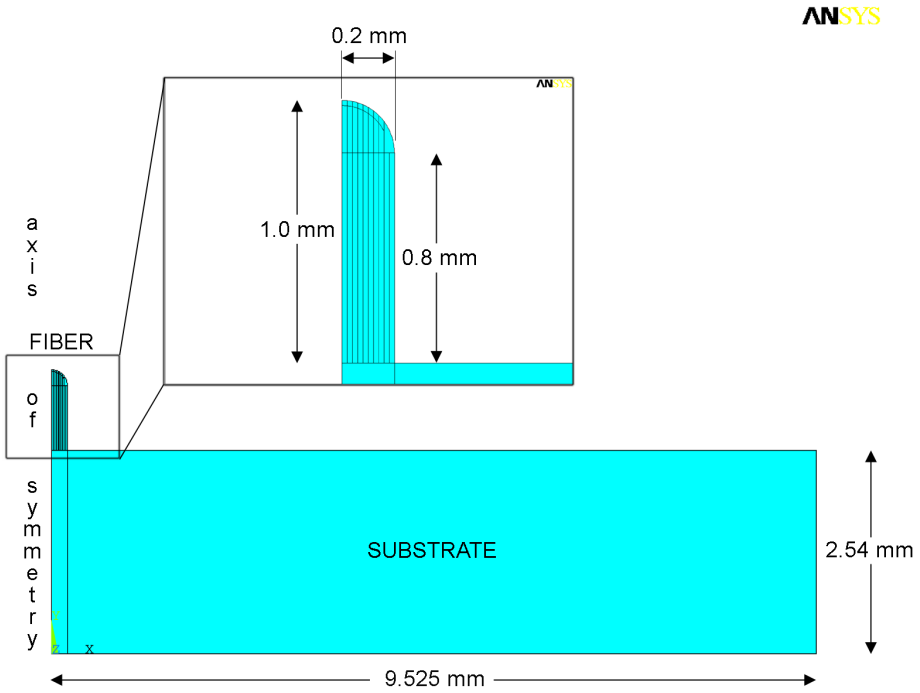

Figure 6.1: Geometry used in fiber thermal stress model

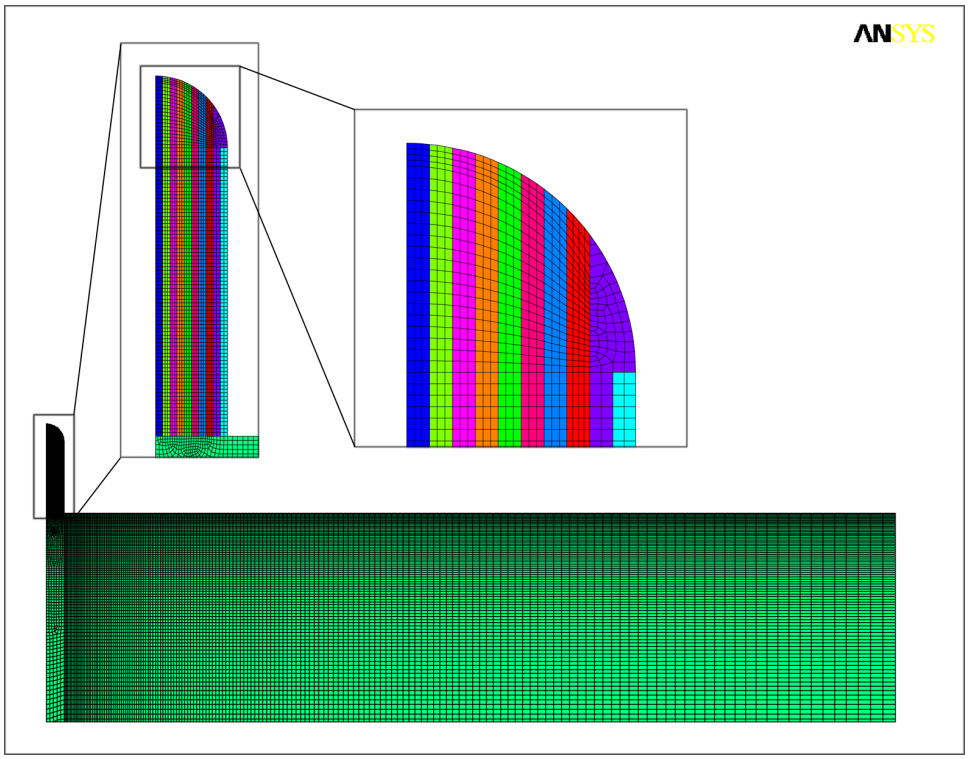

Figure 6.2: Separate areas used in fiber body and fiber tip to allow material property definitions

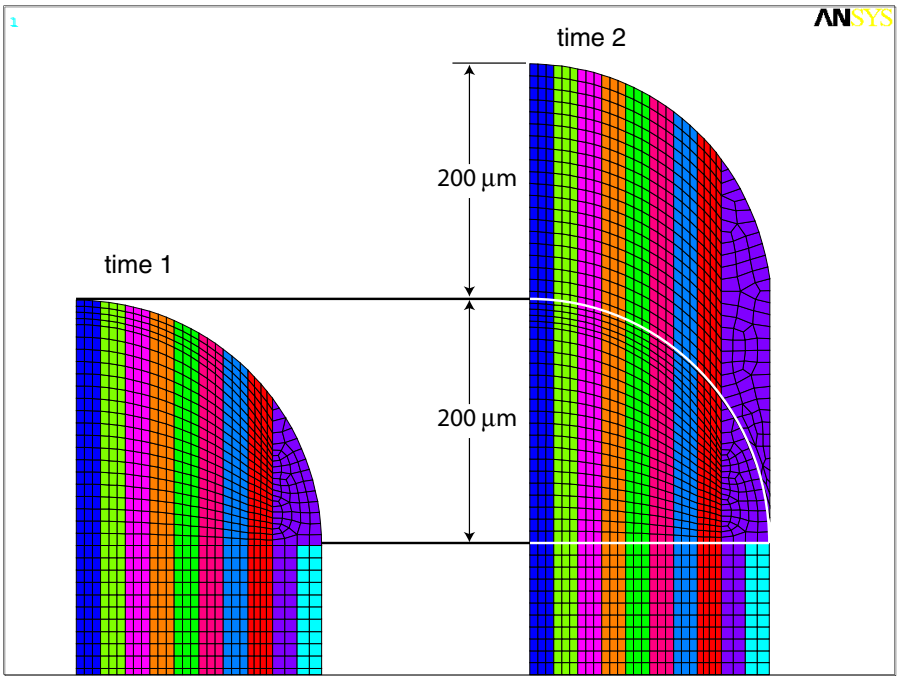

Figure 6.3: Illustration of fiber tip mesh showing different materials in both short and tall fiber cases

tip region for both the short and tall fiber cases.

The amount of material added in the tall fiber case was chosen based on the spacing between cracks observed by Kang.[20] The goal was to ensure that enough material was added to "capture" the conditions that lead to the observed cracks. The spacing reported by Kang varied from 100 to 150 μm, therefore, 200 μm of height was added to the short fiber to create the tall fiber.

In order to directly compare the model results at the two time points, it was necessary to maintain node numbering consistency between the short and tall models. This was achieved by initially creating the tall fiber geometry in all models and then subtracting the additional material region on the fiber tip to get the short fiber geometry.

Once the underlying geometry was created, the areas were meshed. The thermal model used PLANE77 elements. PLANE77 is an 8–node thermal element that has one degree of freedom, temperature, at each node. The 8–node elements have compatible temperature

shapes and are well suited to modeling curved boundaries. The emphasis on curved boundaries was important, because the primary area of interest in the thermal model was the fiber tip. PLANE77 also supports the axisymmetric geometry used in the model.

The structural model used PLANE82 elements which are the structural counterpart to the PLANE77 thermal elements. Again, the 8–node elements facilitated model accuracy near curved boundaries. PLANE82 is an 8–node element that has two displacement degrees of freedom at each node.

Because of the steep temperature gradients known to exist within an LCVD fiber, a meshing scheme was devised that provided a fine mesh within the fiber and transitioned to a coarser mesh as it moved into the substrate. The average element size within the fiber tip and the fiber body was 7 μm which gave an average node spacing of 3.5 μm. The element size and node spacing at the outer edges of the substrate furthest from the fiber were about 200 and 100 μm, respectively.

In order to ensure mesh independence of the solution, a mesh convergence study was performed. Due to an ANSYS software limitation of the maximum number of nodes, the mesh resolution could not be increased significantly from the initial design. However, several different mesh sizes were created that were larger than the 7μm case and the results at each size were compared. Table 6.1 lists two different cases that were run along with the results. The results were computed by taking the average of all nodal temperature values in the top 90 μm of the fiber measured vertically. For the given conditions, a change in computed temperature of 2.95% occurred between the mesh sizes which is below the typical 5% criteria used to indicate satisfactory mesh independence. Due to the large temperature gradients (and presumed stress gradients) within the model and because little computational expense was incurred in doing so, the highest resolution mesh possible was used.

Table 6.1: Thermal model mesh convergence cases

Min Element Dim (μm)	Avg Temp ($^\circ$C)	Change from low resolution
14	888.3	
7	914.5	2.95%

6.2 Material Properties

The material properties needed for the LCVD fiber thermal analysis included the density ρ, specific heat capacity C_p, thermal conductivity k, emissivity ε, and reflectivity $\rho_{10.59}$ of the fiber and substrate materials. Of these, C_p and k were defined as a function of temperature.

The substrate material was the same ATJ graphite used in the deposition rate models in Section 5.3.1.3 of Chapter 5. The material properties for ATJ graphite were provided there and are not repeated here. As discussed in Section 4.7, the crystal structure of LCVD carbon fibers closely resembles the hexagonal structure in graphite. Material properties of pyrolytic graphite made using traditional CVD can be extremely anisotropic relative to the orientation of the hexagonal microstructure. For example, the thermal conductivity in the $\langle 001 \rangle$ direction is over 100 times that in the $\langle 100 \rangle$ or $\langle 010 \rangle$ directions.

The density of pyrolytic graphite is assumed to be 1.76 g/cm^3. The specific heat capacity was specified as a function of temperature by defining a lookup table in the ANSYS code. The heat capacity of all forms of graphite including ATJ and pyrolytic, is approximately the same; therefore, the values used were the same as those used in the deposition rate model. A plot of the C_p of graphite was shown in Figure 5.7. The average spectral emissivity of all forms of graphite was taken to be 0.9.

It has been observed that pyrolytic graphite has a strong tendency to deposit with its hexagonal planes parallel to the deposition surface (i.e., normal to the (001) plane). The same has been reported for LCVD carbon fibers.[20] Therefore, for an LCVD structure such as a fiber, the orientation of the (001) plane changes as one moves from the fiber center radially outward. The two SEM micrographs in 6.4 show the orientation of graphite platelets

in carbon LCVD fibers.[20] It is believed that the graphite basal planes are coincident with the major dimensions of these platelets. Figure 6.5a is a schematic of this situation.

With this change in crystallographic orientation comes a change in material properties. In order to accommodate these varying material properties, the carbon fiber was divided into ten separate regions as was shown in Figure 6.3. Each region was defined as a separate anisotropic material. An anisotropic material was defined by specifying property values for the *x*, *y*, and *z* directions. The *x*, *y*, and *z* directions were defined relative to the global cartesian coordinate system used in creating the geometry. The assumption was made that all carbon growth occurred normal to the semi–circular fiber tip. Thus, property values specified for the *x* direction at the center of the fiber needed to be the same values specified for the *y* direction at the edge of the fiber. Likewise, the specified *y* direction properties at the fiber center needed to be the *x* direction properties on the edge. A function was written to transform the anisotropic material properties into the appropriate *x* and *y* components as the fiber radius increased. Equations 6.1 and 6.2 give this transformation:

$$S_{x,i} = \sqrt{\left(S_{\parallel} sin\theta_i\right)^2 + \left(S_{\perp} cos\theta_i\right)^2} \tag{6.1}$$

$$S_{y,i} = \sqrt{\left(S_{\parallel} cos\theta_i\right)^2 + \left(S_{\perp} sin\theta_i\right)^2} \tag{6.2}$$

where $S_{x,i}$ and $S_{y,i}$ represent generic anisotropic material properties of material i in the global cartesian coordinate system of the model. $S_{\parallel}$ and $S_{\perp}$ are the graphite material properties in the directions parallel and perpendicular to the basal planes, respectively. θ_i is the angle shown in Figure 6.5b and was computed from:

$$\theta_i = arccos\left(\frac{x_{c,i}}{R_f}\right) \tag{6.3}$$

where $x_{c,i}$ is the radial distance to the center of material i and R_f is the radius of the fiber tip.

For the thermal model, the conductivity of graphite was transformed using Equations 6.1 and 6.2. For reference, values of $k_{\parallel}$ and $k_{\perp}$ at different temperatures are given in Table 6.2.[102]

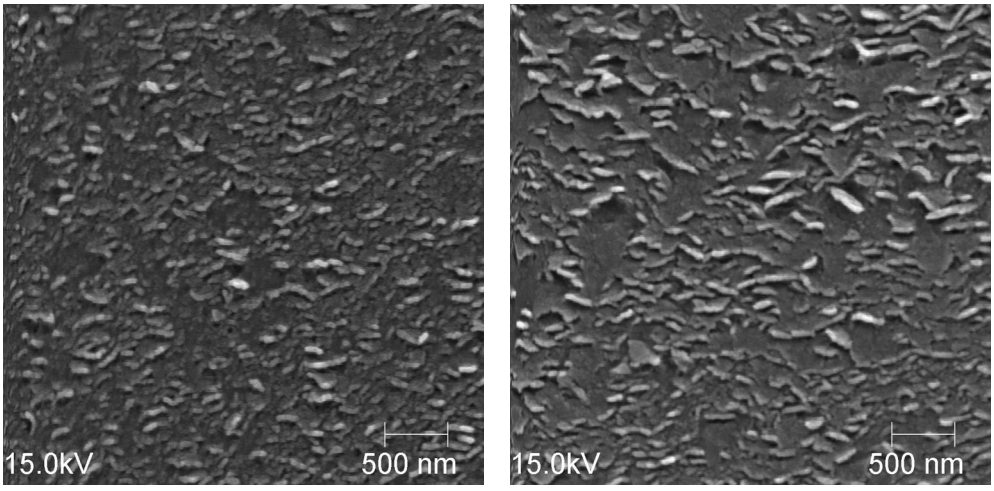

Left side **Center region**

Figure 6.4: SEM micrographs of graphite platelet orientation in LCVD carbon fibers[20]

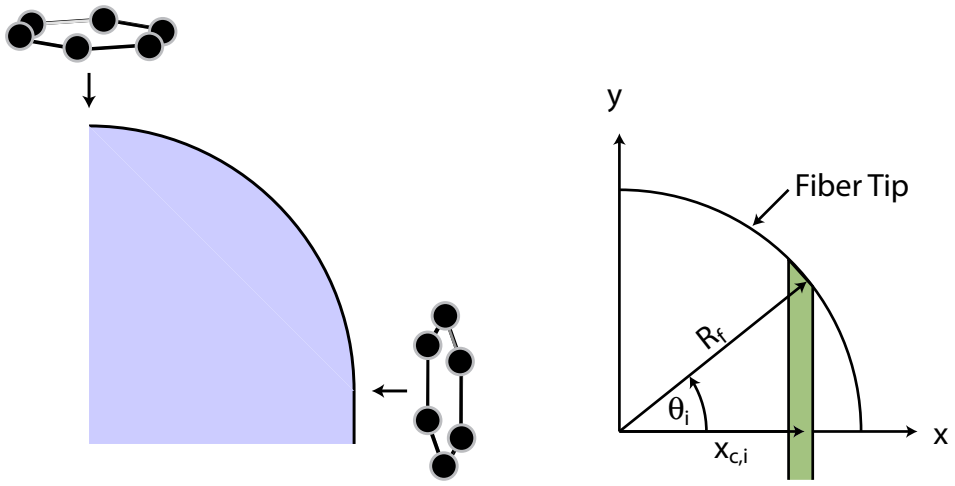

(a) **(b)**

Figure 6.5: Orientation of pyrolytic graphite basal planes and resulting material properties

Table 6.2: Thermal conductivity of pyrolytic graphite

Temperature (K)	$k_{\parallel}$ (W/m-K)	$k_{\perp}$ (W/m-K)
300	2000	9.5
350	1690	8
400	1460	7
500	1130	5.4
600	930	4.4
700	790	3.8
800	680	3.2
900	600	2.8
1000	530	2.5
1100	480	2.3
1200	440	2.1
1300	400	1.9
1400	370	1.7
1500	340	1.6
1600	320	1.5
1700	300	1.4
1800	280	1.3
1900	260	1.25
2000	250	1.2

Another complexity with LCVD carbon material properties related to the definition of the coefficient of thermal expansion (CTE). Much like thermal conductivity, the CTE of pyrolytic graphite is extremely anisotropic relative to the direction of the (001) plane. Thus, Equations 6.1 and 6.2 were used to transform the CTE for the different materials in the carbon fiber. Values of $\alpha_{\parallel}$ and $\alpha_{\perp}$ are given in Table 6.3 for different temperatures.[103]

Table 6.3: Coefficient of thermal expansion of pyrolytic graphite

Temperature (K)	$\alpha_{\parallel}$ ($\times 10^{-6}\mathrm{K}^{-1}$)	$\alpha_{\perp}$ ($\times 10^{-6}\mathrm{K}^{-1}$)
293	-0.60	23.1
400	-0.30	23.8
600	0.30	24.9
800	0.80	25.9
1000	1.40	26.8
1200	1.90	27.6
1400	2.30	28.3
1600	2.70	28.9
1800	3.10	29.4
2000	3.40	29.8
2200	3.70	30.0
2400	4.00	30.2
2600	4.20	30.3
2800	4.40	30.3
3000	4.60	30.3
3200	4.70	30.3
3300	4.70	30.4

In addition to defining the CTE as a function of temperature and position, a reference temperature must be specified at which the thermal strain in the material is zero. Generally, in a deposition process, the deposited material can be assumed to be stress–free at the temperature of deposition. This is especially true for high temperature processes, because the mobility of the atoms is enhanced. Higher atom mobility supports establishment of a

crystal structure with equilibrium lattice spacing. It has been shown in CVD that this equilibrium lattice spacing decreases significantly with increasing deposition temperature.[95] In LCVD, the large temperature gradients within the diameter of the laser spot mean that the strain–free temperature for deposited material is different at different positions within the deposition zone. Specifically, because of the shape of the temperature profile, the strain–free temperature is a function of the radial distance from the center of the laser spot.

ANSYS did not allow the specification of multiple strain–free temperatures within a material. Therefore, the use of the ten different materials within the fiber enabled an approximation of the physical situation by allowing the specification of a different strain–free temperature in each material. For each material, the strain–free temperature was computed by averaging the short fiber thermal model result temperatures along the fiber tip surface nodes. An implied assumption of this approach was that all of the underlying carbon fiber material at a given radial distance would have the same strain–free temperature as the fiber tip. This assumption is very reasonable and is likely related to the existence of the observed cracks within LCVD deposits.

Other material properties needed for the structural model included Young's modulus and Poisson's ratio. Very little data are available for LCVD carbon regarding these values. Data is available in the literature for pyrolytic graphite made by CVD. The Young's modulus is given to be 28 – 31 GPa,[104] and values of Poisson's ratio are reported between 0.09 and 0.3.[105] Values used in the current study were 30 GPa for Young's modulus, and 0.14 for Poisson's ratio.

6.3 Thermal Model

6.3.1 Boundary Conditions

The governing equation for the thermal model was the general form of the heat conduction equation given in Chapter 5:

$$\frac{\partial}{\partial t}(\rho h) + \nabla \cdot (\vec{v}\rho h) = \nabla \cdot (k\nabla T) + S_h \tag{5.3}$$

where t is time, ρ is density, h is specific enthalpy, $\vec{v}$ is the velocity vector of the solid if moving, k is thermal conductivity, T is temperature, and S_h is volumetric heat generation rate.

The fiber model was evaluated at two discrete time points. At each point, the system was assumed to be in steady state, thus, the time dependent term on the left side of Equation 5.3 did not apply. The model geometry was stationary which eliminated the second term on the left. The remaining terms were the conductivity term, represented by the first term on the right, and the volumetric heat generation represented by S_h.

The laser energy was simulated in the fiber thermal model using a similar technique as was used in the deposition rate model. A volumetric heat generation was specified in the first layer of cells within the radius of the laser beam. The equation used to compute the necessary heat generation value within each element was:

$$P(r) = \frac{2P_0(1-\rho_{10.59})}{\pi R_0^2 d} e^{\frac{-2r^2}{R_0^2}} \tag{5.4}$$

where P_0 is the nominal laser power, $\rho_{10.59}$ is the reflectivity of the carbon fiber at the laser wavelength of 10.59 μm, R_0 is the radius of the laser beam, d is the thickness of the mesh element, and r is the radial distance from the center of the laser spot.

The method for entering this volumetric heat generation into the ANSYS code was to define a look-up table that listed pre–computed values of volumetric heat generation (W/m^3) as a function of radial position (m). For each case of interest, this tabular data was computed using a MATLAB script. The volumetric heat generation function was applied to the line that defined the top edge of the fiber as indicated by Figure 6.6. Each node along this line was assigned a value from the laser power lookup table depending on its x position. The procedure used by the solver to apply nodal values of volumetric heat generation along a line required that an adjustment be made to the values computed from Equation 5.4. The adjustment was to multiply all values by a factor of 2. A post–processing check of the total energy input to the model under specified conditions confirmed the viability of this approach. Figure 6.6 illustrates the nature of the heat generation function on the fiber tip.

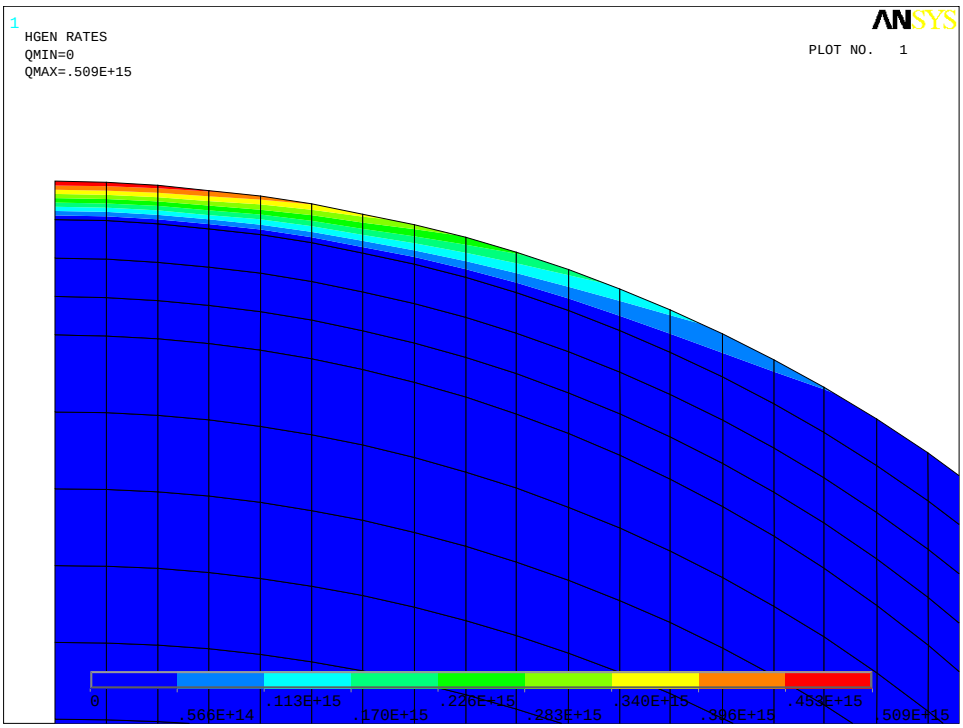

Figure 6.6: Heat generation function along fiber tip

The boundary condition used in conjunction with Equation 5.3 for the thermal model was convective heat transfer from each of the boundary surfaces. With the exception of one case, radiation was not considered. The model did not involve fluid motion; therefore, only natural convection along the boundary surfaces was pertinent. With the exception of the bottom of the substrate, these boundary conditions accurately represent the physical situation. The convective heat transfer boundary condition is given by Newton's law of cooling:[17]

$$q'' = h(T_s - T_\infty) \tag{6.4}$$

where q'' is the local heat flux, h is the local convection coefficient, T_s is the temperature of the boundary surface, and T_∞ is the free stream temperature of the fluid. The total heat transfer rate through the surface is obtained by integrating 6.4 over the entire surface. Assuming isothermal conditions, the equation for total heat transfer rate can be written:

$$q = \bar{h} A_s (T_s - T_\infty) \tag{6.5}$$

where $\bar{h}$ is an average convection coefficient over the surface, and A_s is the area of the surface. T_∞ was specified to be 300 K in the current model.

Values of $\bar{h}$ for the boundary surfaces were computed using empirical correlations for external free convection flow. For the vertical edge of the substrate and the fiber, the specific equation used for the Nusselt number was:[17]

$$\overline{Nu_L} = 0.68 + \frac{0.670 Ra_L^{1/4}}{[1+(0.492/Pr)^{9/16}]^{4/9}}$$

where $\overline{Nu_L}$ is the average Nusselt number, Ra_L is the Rayleigh number, and Pr is the Prandtl number. The average convection coefficient, $\bar{h}_{edge}$ was related to the Nusselt number by:

$$\overline{Nu_L} = \frac{\bar{h}_{edge} L}{k}$$

where L was the length of the edge and k was the conductivity of the fluid.

Similarly, for the horizontal top surface of the substrate and the rounded surface of the fiber tip, a horizontal flat plate empirical correlation was used:[17]

$$\overline{Nu_L} = 0.54 Ra_L^{1/4}$$

where the average Nusselt number was related to the average convection coefficient:

$$\overline{Nu_L} = \frac{\bar{h}_{top} L}{k}$$

For simplicity, calculations of $\bar{h}_{edge}$ and $\bar{h}_{top}$ were made using the properties of air evaluated at the average temperature T. These calculations were repeated for a number of different T_s values and stored in tabular form. The ANSYS solver used the lookup tables of average h values when computing the convective heat transfer from the model boundary surfaces.

The bottom of the substrate normally rests on the substrate holder. In Georgia Tech's LCVD system, this substrate holder is a large piece of graphite 75 mm in diameter and 25 mm thick. For simplicity, the substrate holder was not modeled here. It was possible to simulate heat transfer from the bottom of the substrate by specifying a convection

boundary condition. The value of h_b was chosen such that a bottom surface temperature of approximately 500 K was maintained. The value of 500 K was determined experimentally by placing a thermocouple between the graphite disk substrate and the substrate holder and heating the substrate with the laser to a steady state temperature. Figure 6.7 indicates which calculation and corresponding lookup table were used on each boundary.

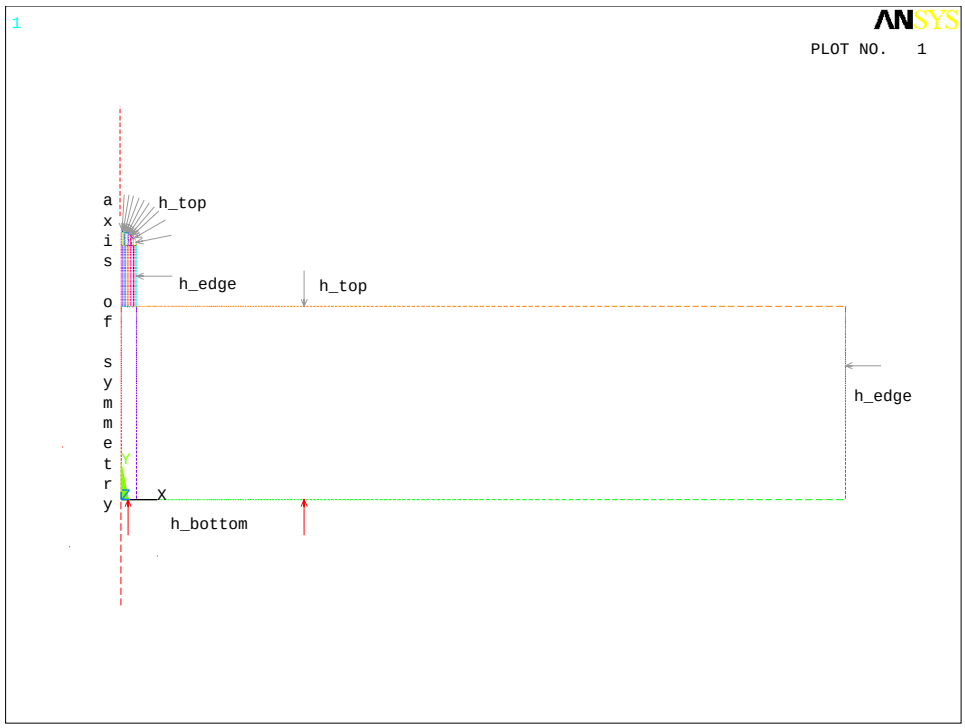

Figure 6.7: Convective boundary conditions on surfaces

Due to computational time and complexity, the nonlinear radiation calculations were only considered in one model case. The radiation boundary condition was implemented using the radiosity solver in the ANSYS code. The solver was configured to compute radiation between the boundary surfaces and free space using the equation:

$$q_r'' = \varepsilon\sigma(T_s^4 - T_{ref}^4) \tag{5.5}$$

where q_r'' is heat flux, ε is average hemispherical emissivity over the entire spectral range, σ is the Stefan–Boltzmann constant (5.670×10^{-8} W/m^2-K^4), T_s is the radiating surface temperature, and T_{ref} is the temperature of the remote surface being irradiated. T_{ref} was

set at 300 K for all models in order to simulate the inner surface of the cold wall reaction chamber.

6.3.2 Solution Procedure and Results

The ANSYS model was implemented using the software's internal scripting language, APDL. A single text file accomplished geometry creation, meshing, material property definition, load application, boundary condition specification, and execution of the calculations. For the most part, the code was parametric and it enabled the solution of either the short fiber or the tall fiber case simply by changing an indicator variable near the beginning of the code. The APDL code for the thermal model is listed in Appendix B.4 for reference.

The thermal model was run using a range of conditions similar to those that experimentally produced a fiber of similar size and shape. For example, Sample 3 of Experiment L-228 used in the kinetic analysis of Section 4.2 was produced under a power of about 20 W with a presumed laser spot size of about 200 μm diameter. An initial model was run using a laser power of 20 W with a reflectivity of zero and a convective heat transfer coefficient along the bottom of the substrate, h_b of 125 W/m^2-K. The fiber thermal properties varied with radial position as described above. Figure 6.8 is a contour plot of the resulting temperatures.

Overall, the results are reasonable with a maximum temperature at the fiber tip and a steep negative temperature gradient in both the radial and axial direction moving down the fiber. The substrate temperature is similar everywhere with a high temperature region directly under the fiber.

Because this model was designed to simulate the conditions within a growing carbon fiber, the power level and the h value along the substrate bottom were adjusted until the maximum temperature at the fiber tip and the temperature along the substrate bottom were approximately equal to experimentally observed values. The target range for T_{max} was 2300 – 2400 K and the target substrate bottom temperature, T_{min}, was 450 – 525 K. The case

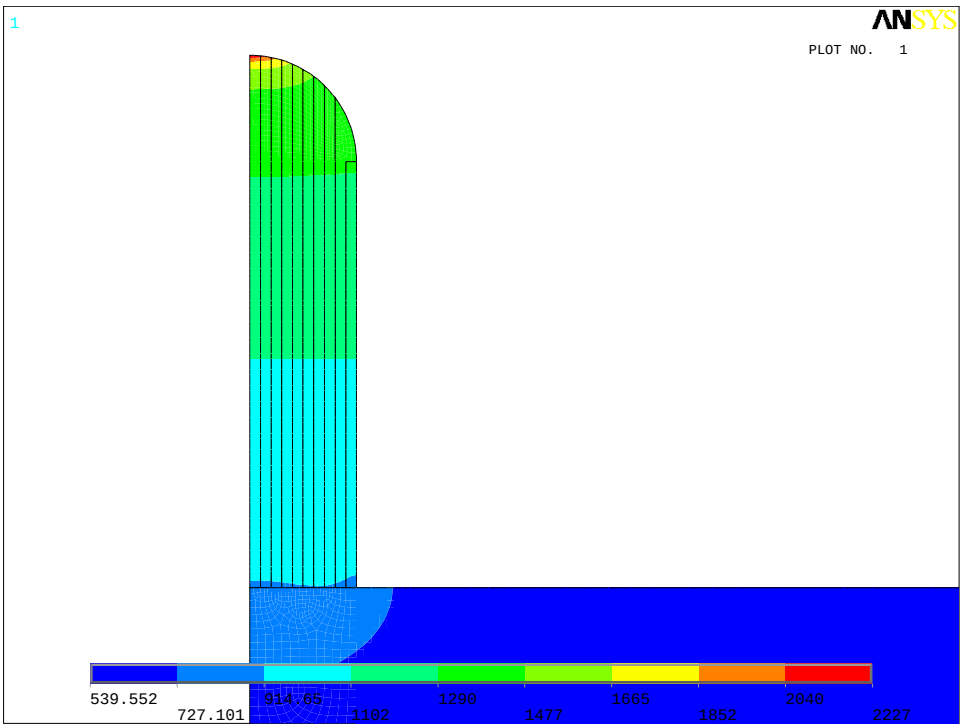

Figure 6.8: Temperature contours for short fiber case

depicted in Figure 6.8 shows the fiber tip temperature to be too low and the substrate bottom temperature to be too high. Thus, the laser power was increased, and the convective transfer coefficient was increased until values were obtained that yielded the desired temperatures.

A laser power of 21 W with zero reflectivity and an h_b along the substrate bottom of 135 W/m^2-K yielded a T_{max} and T_{min} within the acceptable ranges. A laser power of 21 W is slightly higher than the values used experimentally to achieve a similar temperature at the fiber tip. It has been observed that carbon LCVD fibers have a shiny metallic appearance which would seem to indicate high reflectivity. However, the shiny metallic appearance is observed in the visible spectrum, whereas the CO_2 laser operates at a wavelength of 10.59 μm. No reflectivity measurements at this wavelength for pyrolytic LCVD carbon were available. Overall, the model parameters that yielded experimentally similar temperature profiles were in good agreement with the levels of experimental parameters at these two discrete points.

It was possible to experimentally measure temperature profiles on a fiber surface during

deposition using the thermal imaging camera. The orientation of the thermal imager and the spherical shape of typical LCVD carbon fibers as described and exploited in Section 3.4.1 for measuring fiber growth rates introduced a complexity when trying to measure a simple radial temperature profile. Figure 6.9 illustrates the relationship among the thermal imaging camera's 2–D plane of view, the fiber tip, and the *x* spatial coordinate of the actual radial distance from the fiber center.

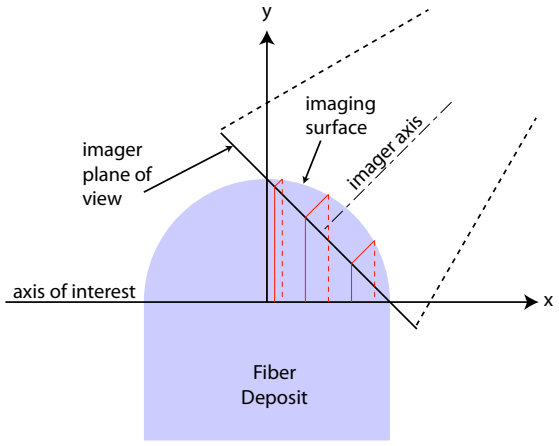

Figure 6.9: Relationship between thermal imager and fiber tip dimensions

In order to convert the pixel position in the image to spatial coordinates, a transformation function was developed. This transformation function accounted for both the 45° angle of the imager and the fiber tip curvature. The function was implemented using a MATLAB script that is listed in Appendix B.5.

Figure 6.10 is a comparison of the temperature profile computed by ANSYS to a measured fiber tip temperature profile. Notice that the absolute maximum temperature of both cases was very similar. As described above, the model parameters were intentionally adjusted until this condition was satisfied. The shape of the temperature profiles is quite different.

The orientation of the anisotropic material properties of the carbon fiber could have a big impact on the predicted temperature profile shapes. In order to study this impact, several material property setups were analyzed in addition to the radially varying property

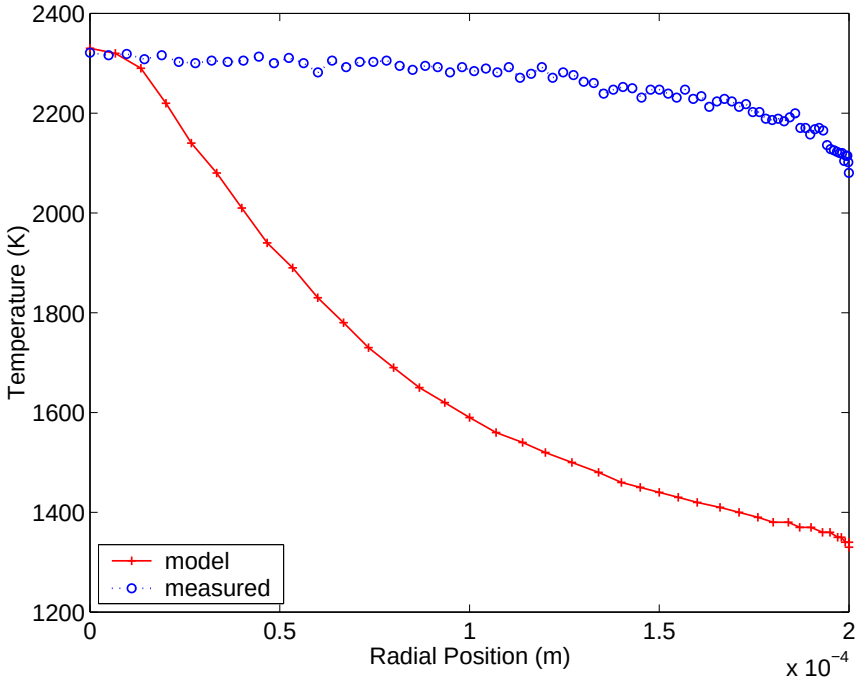

Figure 6.10: Comparison of predicted fiber tip temperature profile to experimental data

case described previously. Three cases of pyrolytic carbon properties were applied to the fiber. First, all ten materials within the fiber body were oriented with their [001] direction in the global x direction. Next, all ten materials were oriented with their [001] direction oriented to $\theta = 45^{\circ}$. Finally, a case was studied with the carbon basal planes assumed to lie in parallel to the global x direction ($\theta = 90^{\circ}$). In addition to these variations of pyrolytic graphite, a case was run using ATJ graphite properties for the carbon fiber as well as the graphite substrate.

The model settings along with the minimum and maximum temperature from each case are summarized in Table 6.4. The shapes of the radial and axial temperature profiles were compared. Figures 6.11 and 6.12 illustrate the different radial and axial temperature profiles for the cases listed in Table 6.4. Figure 6.11 also includes the experimental data curve for comparison. All of the temperature profiles were normalized by dividing the temperatures by the maximum temperature for each respective case.

A study was conducted to determine the sensitivity of the resulting temperature profiles

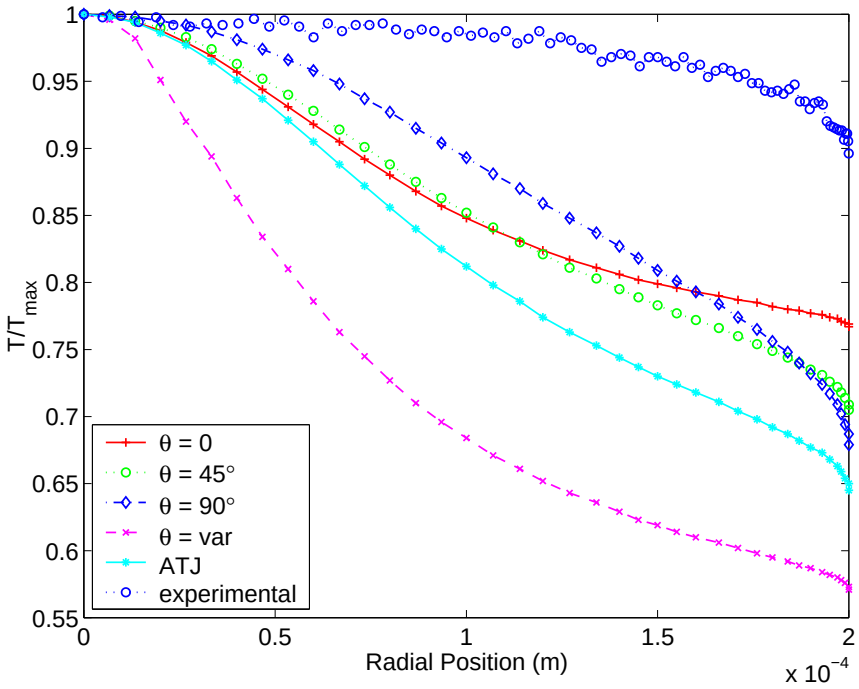

Figure 6.11: Radial temperature profiles on fiber tip surface

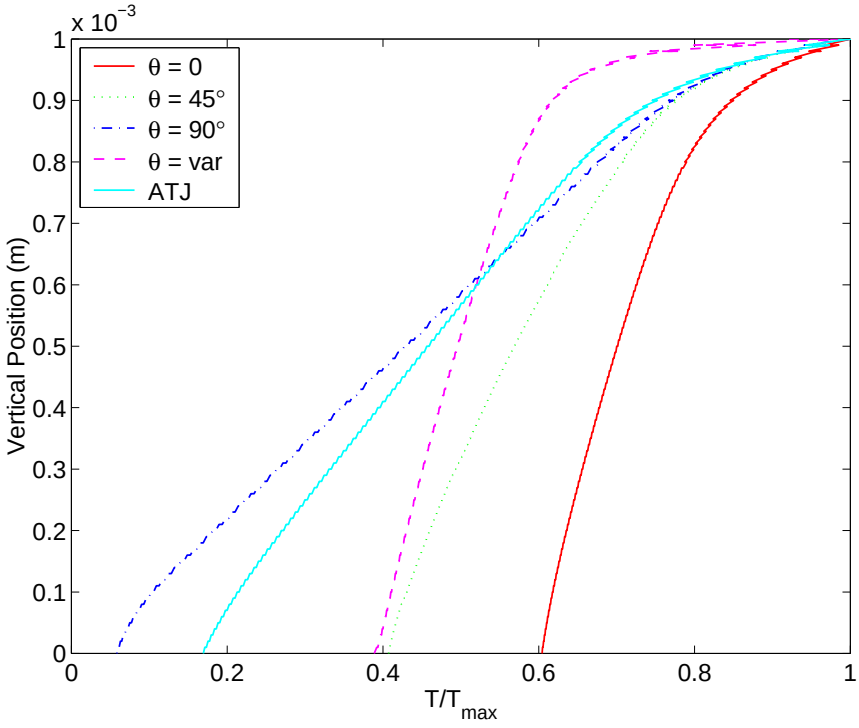

Figure 6.12: Axial temperature profiles along fiber center

Table 6.4: Absolute temperature values for different material properties

Graphite Type	[001] Direction θ	T_{min} (K)	T_{max} (K)
pyrolytic	0°	526	1540
pyrolytic	45°	525	2280
pyrolytic	90°	516	15900
pyrolytic	variable	526	2330
ATJ	isotropic	523	5740

to laser power input, P_0, and the heat transfer coefficient on the substrate bottom, h_b. It was expected that changing both of these parameters would effect the absolute temperatures in the model, because they inherently affect the amount of thermal energy in the system. Figure 6.13 shows the radial temperature profiles along the fiber tip for three different P_0 levels while holding h_b constant at 135 W/m^2-s, while Figure 6.14 shows profiles for three different levels of h_b with P_0 held constant at 21 W.

It was important to determine if changing either of these parameters significantly changed the shape of the temperature profiles along the fiber tip. Ideally, the change in parameters would shift the absolute temperature curve up or down, depending on the nature of the change, but would minimally impact the shape of the temperature profile. Figures 6.13 and 6.14 show that this is indeed the case.

An additional explanation of the observed disagreement between the computed and the measured fiber tip temperature profiles could be related to radiative heat transfer from the surfaces of the fiber and substrate. One model was run that considered radiation. The model parameters were a laser power of 21 W and an h_b value of 135 W/m^2-s. The absolute fiber tip radial temperature profiles for the case with and without radiation are compared in Figures 6.15 and 6.16.

As expected, the inclusion of radiation calculations led to an overall decrease of temperatures through the model domain. For the given conditions, the peak temperature was shown to decrease by almost 200 K from 2330 to 2142 K. The substrate bottom temperature

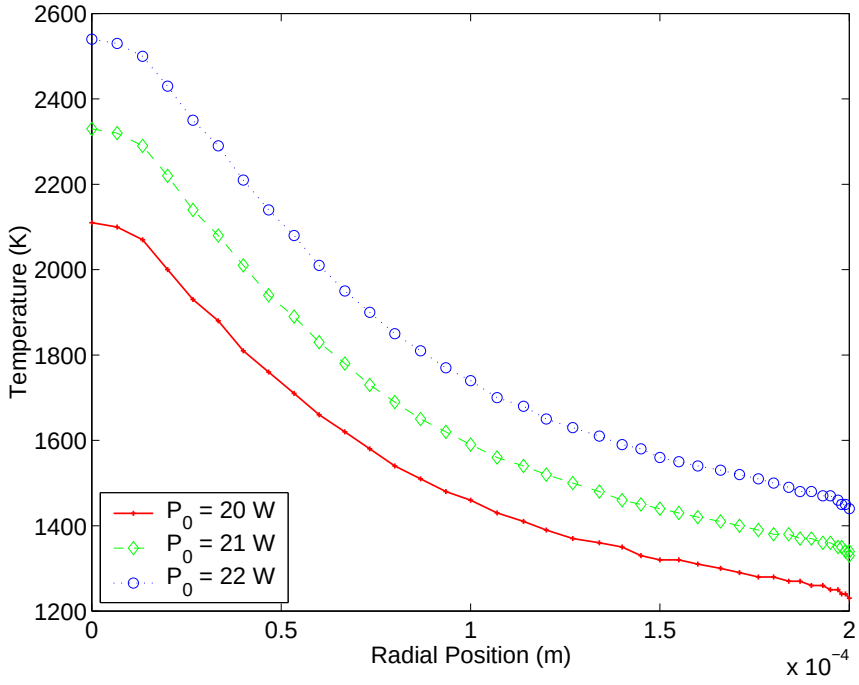

Figure 6.13: Fiber temperature profiles for different laser power levels

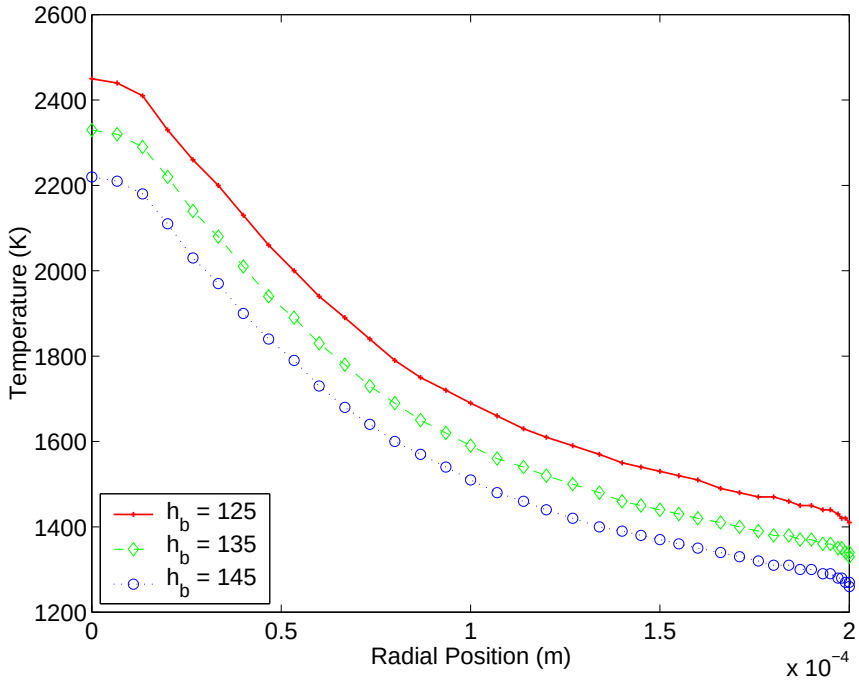

Figure 6.14: Fiber temperature profiles for different h_b levels

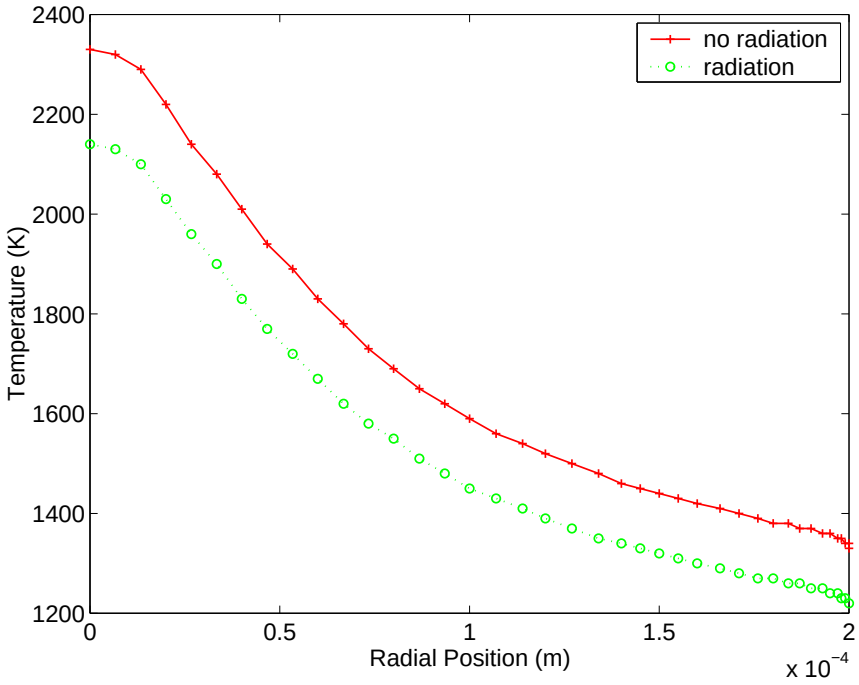

Figure 6.15: Effect of radiation on absolute temperature values on fiber tip surface

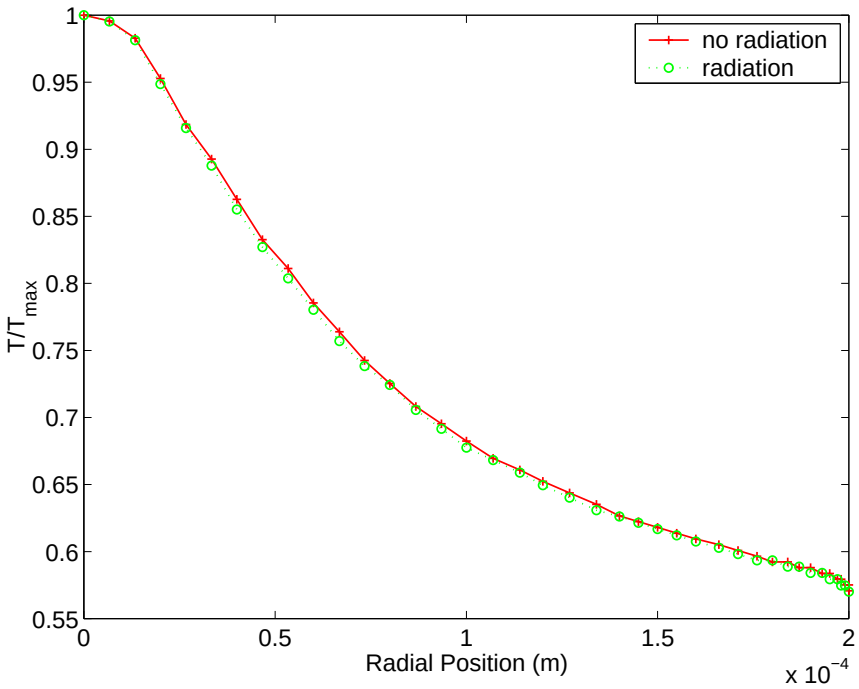

Figure 6.16: Effect of radiation on normalized temperature profile shape on fiber tip surface

fell by about 50 K from 526 K to 471 K. More importantly, the shape of the temperature profile did not change significantly as shown by the normalized temperature plots in Figure 6.16. Thus, neglecting radiation in the model shifts the relationship between incident laser power and absolute temperature values, but it does not explain the temperature profile shape differences seen in the comparison of the model results to the experimental data.

Neither the convective nor the radiation boundary conditions significantly impacted the shapes of the temperature profiles. The profiles appeared to be dominated by the conductivity and conduction pathways. Two observed anomalies of LCVD carbon fibers could contribute to the disagreement between the measured and computed temperature profiles.

The motivation for a thermal stress analysis of an LCVD carbon fiber was the finding that these structures have persistent internal cracking. The cracks tend to be oriented parallel to the fiber tip surface and occur periodically throughout the fiber height. It is believed these cracks form during the growth process as the thermal stress accumulates to the point of fracturing the graphite deposit. It is presumed that the samples used to capture the thermal images during fiber growth already contained a significant amount of thermal cracking. Therefore, the observed temperature profiles could have been distorted by the presence of cracks. If cracks were present, the nature of distortion in the profile is consistent with physical reasoning. Their presence would severely limit conduction through the center of the fiber body forcing the heat flow around the cracks and near the fiber surface. This would undoubtably increase the observed fiber surface temperatures.

A second area that could affect heat conduction through the carbon fiber and into the substrate was the interface between the fiber and the substrate. It has been shown that the fiber diameter at the substrate interface is often much less than the observed bulk fiber diameter. See Section 5.3.5.4 for a discussion of LCVD carbon fiber shapes. The body of the fiber was modeled as a perfect cylinder which would provide a better conduction path from the fiber into the substrate than the tapered shape observed experimentally. This “necking down” at the interface would cause the fiber to be hotter throughout and would reduce the

temperature gradient on the fiber surface because of the orientation of the graphite [001] direction in this region. Also, depending on the nature of the bond between the fiber and the substrate, there could be significant thermal contact resistance at the interface. This contact resistance would increase the temperature of the fiber for a given laser power, and could impact the shape of the temperature profiles. No such resistance was considered in the model.

The tall fiber case was also analyzed using the thermal model. Using the same conditions (power of 21 W, reflectivity of 0, and h_b of 135), the peak temperature value was higher than the short fiber case. This result is expected due to the increased resistance to thermal conduction that accompanies the increased fiber length. Experimentally, as a fiber grows, laser power is slowly decreased in order to maintain a constant fiber tip temperature. The model values of laser power and h_b were adjusted until the peak temperature and substrate bottom temperature values were similar to those of the short fiber case. This scenario simulated growth under constant temperature conditions.

The model parameters that yielded a tall fiber case with similar temperature values as the short fiber case were laser power of 21.9 W and h_b of 134 W/m^2-s. Figure 6.17 compares the temperature contours within the short fiber tip for the two cases. Notice the change in temperature values near the original short fiber tip within the body of the tall fiber. These changes are further highlighted in the comparison of the radial and axial temperature profiles of Figures 6.18 and 6.19.

The nodal temperature data from both the short fiber and the tall fiber thermal models depicted in Figure 6.17 was exported for use later as the loads in the structural model.

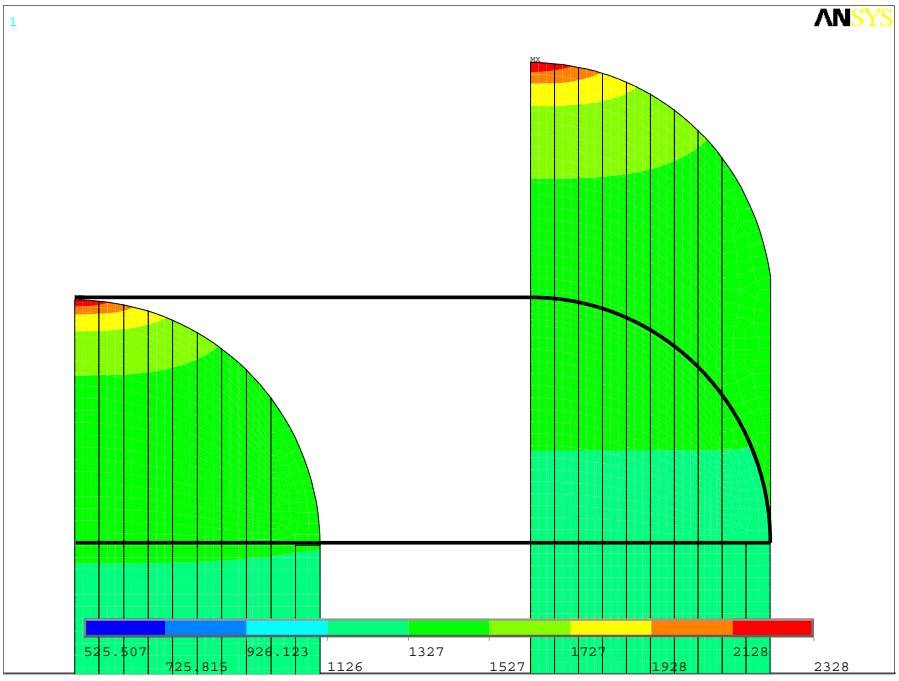

Figure 6.17: Comparison of temperature contours for short and tall fiber

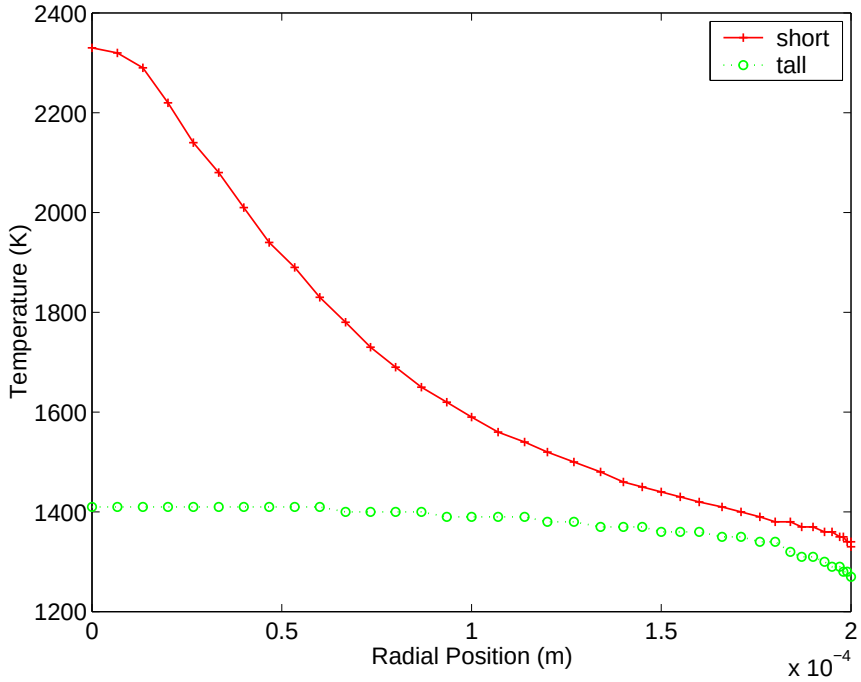

Figure 6.18: Comparison of radial temperature profiles along original short fiber tip surface between short and tall fiber case

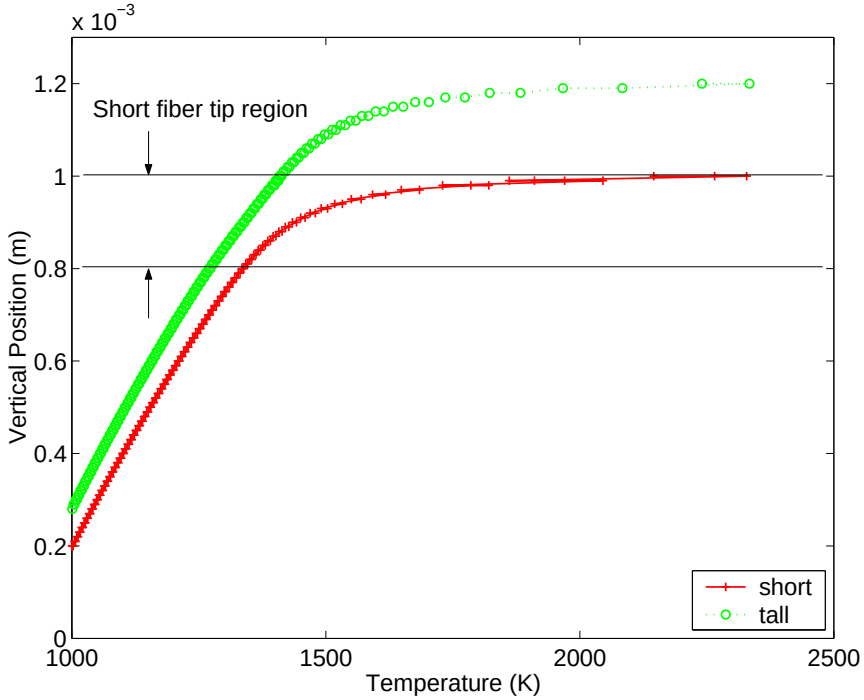

Figure 6.19: Comparison of axial temperature profiles along original short fiber tip surface between short and tall fiber case

6.4 Structural Model

The structural model consisted strictly of the short fiber geometry. The goal was to see how the change in temperatures between the discrete time points captured by the short and tall thermal models would impact the stress within the original short fiber structure. The thermal models used to generate the temperature data were those with the radially varying orientation of pyrolytic graphite. The CTEs used in the structural model were implemented using the same radially varying property transformations.

6.4.1 Boundary Conditions

The governing equation for the stress–strain relationship throughout the model domain was:

$$\vec{\varepsilon} = \vec{\varepsilon_{th}} + D^{-1}\vec{\sigma} \tag{6.6}$$

where $\vec{\varepsilon}$ is the total strain vector, $\vec{\varepsilon_{th}}$ is the thermal strain vector, D^{-1} is the compliance matrix, and $\vec{\sigma}$ is the stress vector. The thermal strain vector, $\vec{\varepsilon_{th}}$, is defined as:

$$\vec{\varepsilon_{th}} = \Delta T[\alpha_x\ \alpha_y\ \alpha_z\ 0\ 0\ 0]^T \tag{6.7}$$

where ΔT is the change in temperature from the strain–free reference temperature, and the α's are the CTE's in the *x*, *y*, and *z* directions.

Zero displacement boundary conditions were imposed to properly constrain the system. These conditions were applied along all substrate boundaries and the base of the fiber. The *x* displacement was also set to zero along the fiber axis of symmetry. Other boundaries of the fiber were allowed to deform.

The only imposed loads in the stress model were the temperatures computed in the thermal models of Section 6.3 above. Two load steps were used to represent the two different time points. The first load step was the application of the temperatures from the short fiber thermal model. The zero strain reference temperatures for the CTE were determined by averaging the surface node temperature values within each material along the short fiber tip

surface. The second load step was the application of the subset of temperatures from the tall fiber model that applied to the original short fiber geometry.

6.4.2 Solution Procedure and Results

Again, APDL code was used to formulate the structural model in the ANSYS environment. A listing of the code can be found in Appendix B.6. The solver provided access to solution data from both time points.

Figure 6.20 is a contour plot of the *y* component of the stress, σ_y, which is the component in the direction normal to the observed crack directions as seen in Figure 6.21. The deformed boundaries of the fibers are an exaggerated depiction of the nodal displacement within the structure.

The discrete nature of the contours relative to the different materials is a direct result of the need to specify a single zero strain reference value for the entire material. The high stresses at the interface of the fiber to the substrate are a reflection of the imposed zero displacement boundary conditions, and the different CTEs of the fiber material and substrate materials interacting in this region.

Of particular interest are the stress contours within the body of the fiber. The nature of the contours is consistent with the observed cracks in LCVD carbon fibers. There is a large tensile stress along the axis of the fiber with a maximum value occurring near the bottom. The overall deformation of the fiber structure is consistent with the observed round crack profiles. This complex shape is a result of the complex material properties and temperature fields within the structure.

A closer analysis of the region within the fiber body seen to have the largest stress is shown in Figure 6.22 as contours of the maximum tensile principal stress, σ_1, in the center area of the fiber body. The location of this local maximum stress is about 100 μm above the substrate surface. This value correlates well to the 100 – 150 μm spacing between carbon LCVD fiber cracks observed by Kang.[20] Using the maximum normal stress fracture

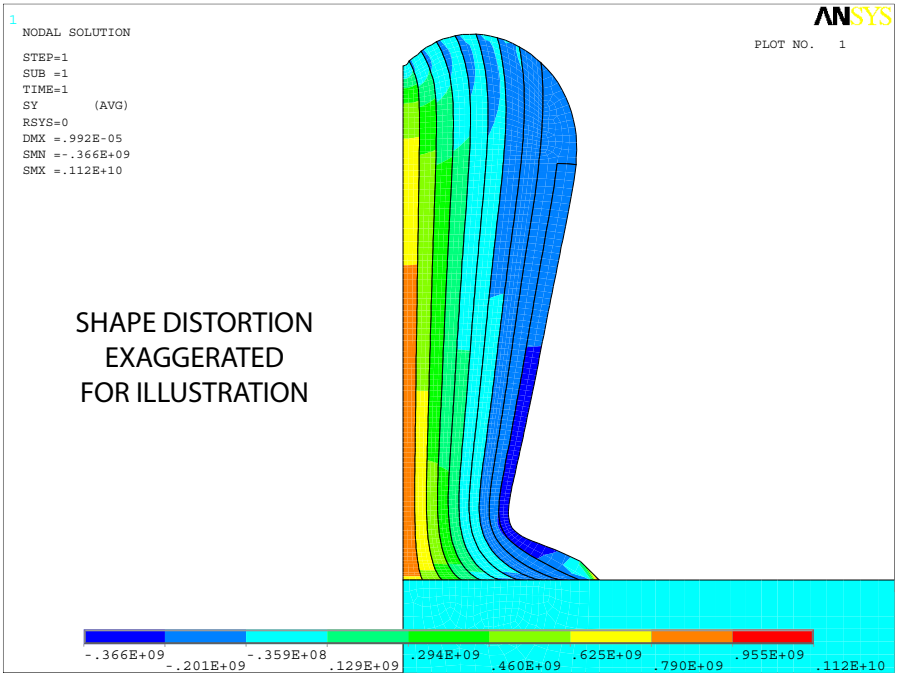

Figure 6.20: *y* component of stress (Pa) in fiber at time point 1

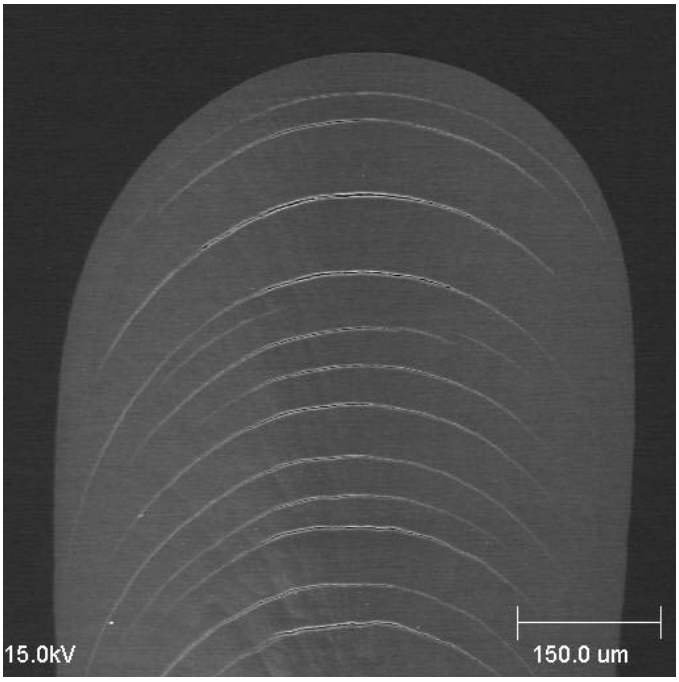

Figure 6.21: Typical cracks seen in LCVD carbon fibers

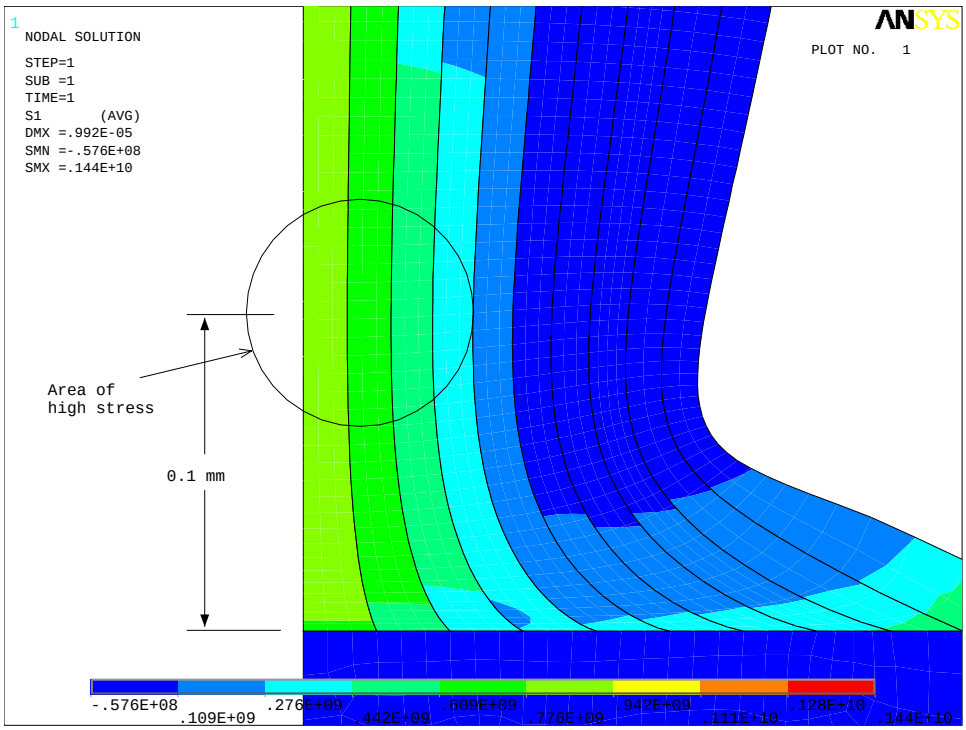

Figure 6.22: σ_1 in high stress region at time point 1

criterion, these values can be compared to the fracture strength of graphite.

Very limited data on the strength of LCVD carbon is available in the literature. Wallenberger reported a tensile strength of 3.0 GPa for a very small diameter carbon fiber grown in a high pressure LCVD reaction chamber from methane reagents.[88] This value is significantly higher than that of typical graphite whose tensile strength is reported to vary between 1.4 and 110 MPa.[105] Pyrolytic graphite has been reported to have a flexural strength of 80 – 170 MPa in the *c* direction and a tensile strength of 110 MPa in the *ab* directions.[104]

The values of σ_1 shown in Figure 6.22 greatly exceed even the highest of the reported strength values for pyrolytic graphite (170 MPa). This confirmed that cracks would likely have developed in the carbon fiber long before the fiber height reached that of the modeled geometry. The result is consistent with the periodic cracks shown in many LCVD carbon fibers. As the fiber grows, thermal stresses accumulate until they exceed the fracture strength of the material. Upon reaching this critical point, a crack initiates and propagates

in the direction perpendicular to the induced thermal stresses. The thermal stresses decrease with increasing radial position, and the cracks ultimately terminate before reaching the surface. The fact that cracks are widest at their center and narrow as they approach the surface further suggests a decrease in thermal stress with increasing radial position.

A comparison between the two time points provided information as to the change in thermal stress values with a given change in time and fiber height. The tall fiber thermal model added 0.2 mm of height to the original 1.0 mm fiber. The spacing between the cracks within LCVD fibers is reported to be between 100 and 150 μm; thus, the addition of 200 μm should provide adequate time for at least one crack to develop. A typical growth rate for carbon fibers is near 5 μm/s. Therefore, the addition of this material represented a time increment of about 40 s.

The comparison of the stress state at the two time points was done by observing the the contour levels of the principal stresses near the fiber tip as shown in Figures 6.23 and 6.24. The interface between the 4th and 5th contour level at time 1 was 609 MPa while the same transition showed a stress of 650 MPa for time 2. Overall, this represents a stress change of about 40 MPa. In both cases, this transition occurred approximately 80 – 100 μm below the fiber tip. While 40 MPa is well below some of the reported strength values of graphite, it is within the 1.4 – 110 MPa range highlighted earlier. Without reliable data on the material properties of LCVD carbon or fracture strength of the same, these quantitative results should be interpreted loosely. Nonetheless, the combined thermal and structural models of LCVD carbon fibers have shown that the combination of complex material properties combined with steep temperature gradients leads to internal stresses well above the reported strength of graphite materials. These results support experimental results and further elucidate the need for a deeper investigation into the material properties of LCVD materials.

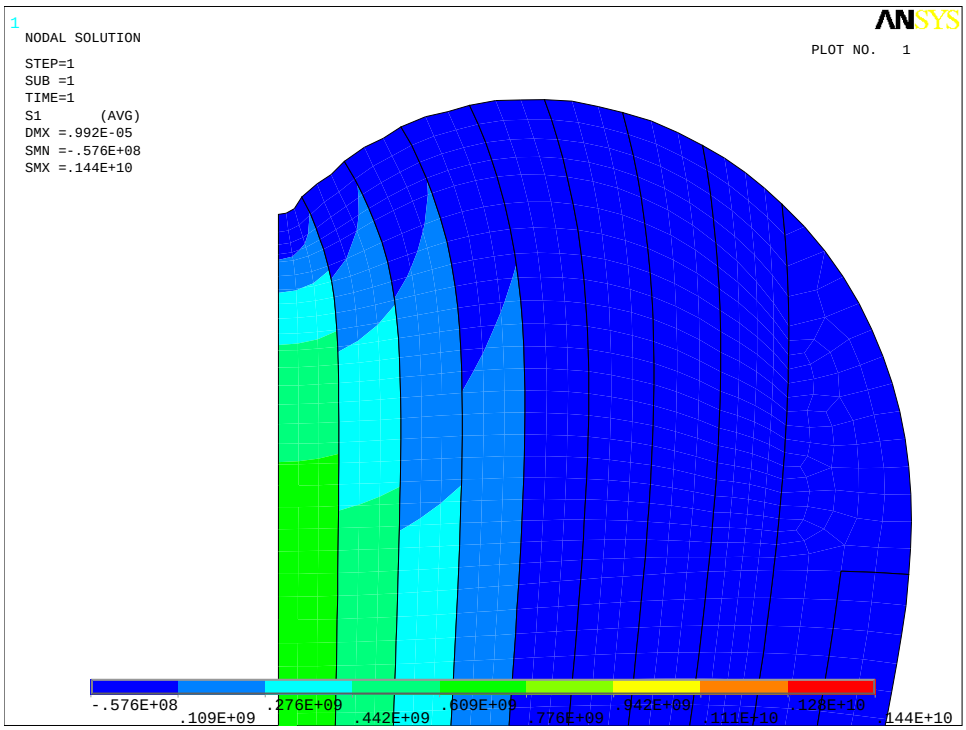

Figure 6.23: σ_1 principal stress near fiber tip at time point 1

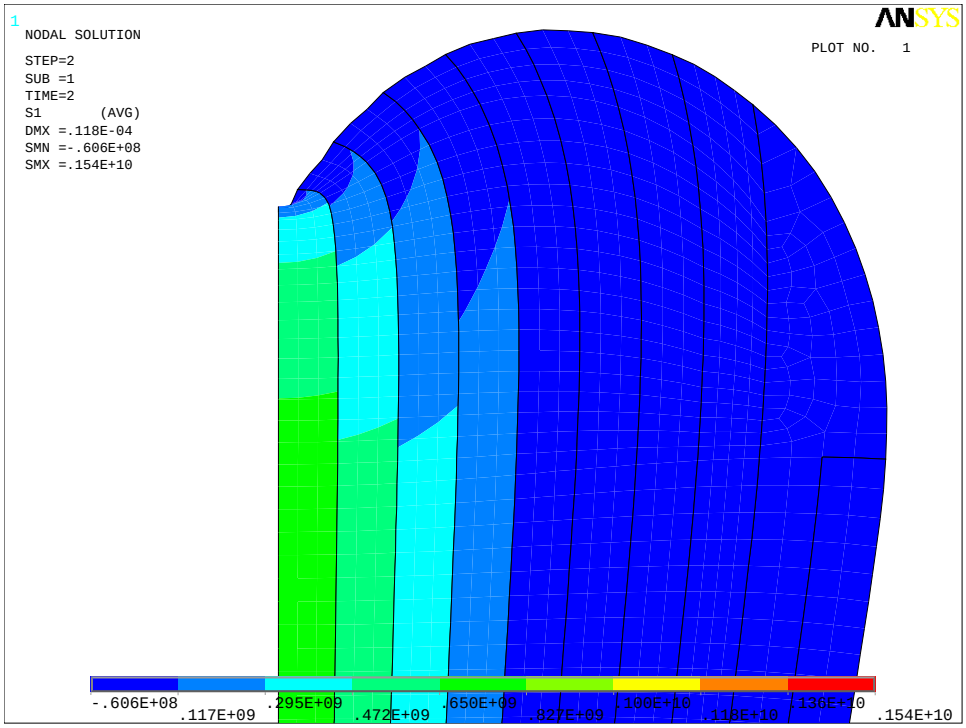

Figure 6.24: σ_1 principal stress near fiber tip at time point 2

CHAPTER VII

BORON NITRIDE EXPERIMENTS

The deposition of boron nitride (BN) in Georgia Tech's LCVD system is an important prerequisite to producing a dispenser cathode assembly. Duty's prior work in this area served as a starting point for the current study.[2,44] He successfully deposited boron nitride using a mixture of borazine and nitrogen as a precursor. Substrates used included graphite, aluminum oxide, and tungsten. Duty's work proved the feasibility of depositing boron nitride in the LCVD system, but as shown in Figure 7.1, the shape and morphology of the deposits was significantly different from that required by the cathode application.

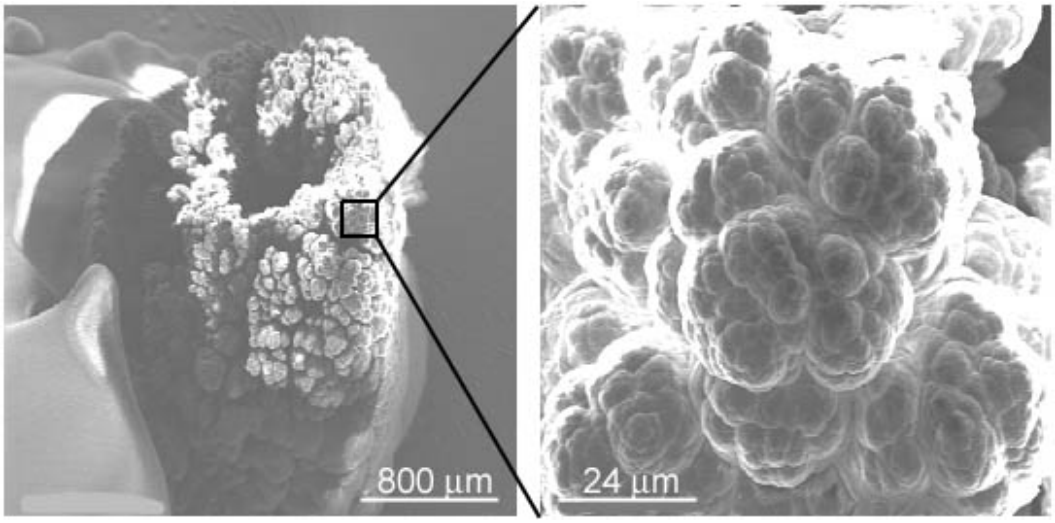

Figure 7.1: Example of Duty's boron nitride deposit on tungsten substrate[2]

The ultimate goal of the boron nitride experiments done herein was to produce smooth, uniform lines of boron nitride on a tungsten substrate. The experimental development path presented in Section 1.4.1 was used to guide the process.

7.1 Experimental Setup for BN Deposition

The overall reaction for the deposition of BN from borazine was given in Equation 2.2:

$$B_3N_3H_6(g) + \text{xs } N_2(g) \rightarrow 3BN(s) + 3H_2(g) + \text{xs } N_2(g) \tag{2.2}$$

The experimental setup involved configuring the LCVD system for reagent delivery and acquiring and preparing the substrates.

7.1.1 Borazine Setup and Delivery

The borazine reagent requires some special handling considerations. Borazine is best preserved by keeping it at or below 0°C. When not being used, the borazine was stored in a freezer at approximately -30°C. At these temperatures, borazine is a liquid. When using a liquid reagent for CVD or LCVD, a vaporizer can be used to vaporize the liquid prior to delivering it to the reaction vessel. The reagent supply setup used to deposit boron nitride from borazine is illustrated in Figure 7.2.

Nitrogen gas was delivered to the borazine vaporizer through a mass flow controller, MFC 5. The flow exiting the vaporizer consisted of both borazine and nitrogen gas. The amount of each was estimated using the partial pressure ratio between the gases. The partial pressure of borazine, P_{bor}, was given by the vapor pressure which has been reported by various authors in the literature as shown in Table 7.1. Due to its flexibility, the equation

Table 7.1: Vapor pressure values of borazine reported in literature

Author	Vapor Pressure (Torr)	Temperature (K)
Adams[33]	$\log P = 7.714 - 1609/T$	variable
Paisley[42]	67.5	293 °C
Kane[37]	76	273 °C
Gates[45]	80	273 °C
Boron Technologies[106]	84.8, 170	273, 290 °C

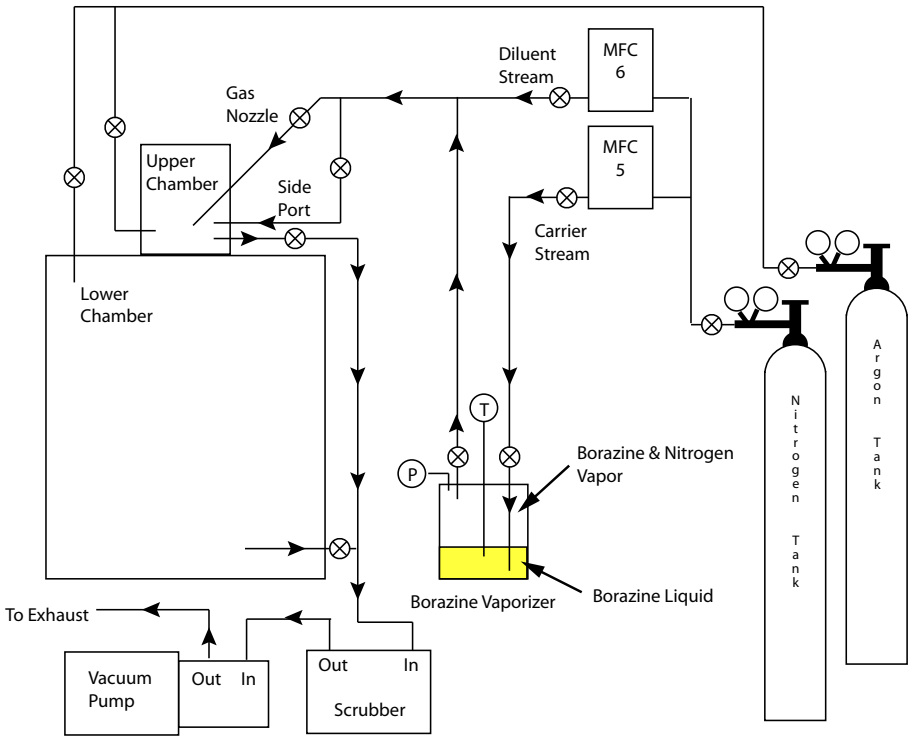

Figure 7.2: Piping configuration used to deliver borazine to deposition zone

given by Adams was used here:

$$\log P_{bor} = 7.714 - \frac{1609}{T} \tag{7.1}$$

where P_{bor} is the vapor pressure (Torr) and T is the temperature of the borazine liquid (K). The partial pressure of the nitrogen carrier (Torr), P_{car}, was given by equation 7.2.

$$P_{car} = P_{tot} - P_{bor} \tag{7.2}$$

where P_{tot} is the total pressure in the vaporizer which was assumed to be equal to the pressure in the deposition chamber. The flow rate of borazine exiting the vaporizer (sccm) was given by equation 7.3.

$$Q_{bor} = Q_{car}\frac{P_{bor}}{P_{car}} \tag{7.3}$$

where Q_{car} was the flow rate of nitrogen (sccm) into the vaporizer through MFC 5.

After the vaporizer, additional nitrogen could be added through MFC 6 to the $B_3N_3H_6$:N_2 mixture flow exiting the vaporizer. This additional flow stream was termed the diluent.

Ultimately, the reagent stream entered the upper deposition chamber through the gas nozzle or the side port.

The concentration of borazine delivered through the nozzle was computed from the reagent flow rate and chamber pressure assuming that all gas species behave as ideal gases. First, the mole fraction of $B_3N_3H_6$ reagent was computed using equation 7.4:

$$X_{bor} = \frac{Q_{bor}}{Q_{bor} + Q_{car} + Q_{dil}} \tag{7.4}$$

The molar concentration was then computed from equation 7.5:

$$C_{bor} = X_{bor} \frac{P_{tot}}{RT} \tag{7.5}$$

where C_{bor} is the concentration of borazine (mol/m^3), P_{tot} is the total pressure in the deposition chamber or vaporizer (Torr), R is the universal gas constant (0.062363891 (Torr-m^3/mol-K)), and T is the local temperature of borazine (K).

7.1.2 Substrate Preparation

Tungsten was used as the primary substrate material for the boron nitride experiments because of its role in the dispenser cathode application. The substrates were typically 0.254 mm thick tungsten sheets. Two sizes were used: 25.4 x 25.4 x 0.254 mm and 25.4 x 12.7 x 0.254 mm. The substrates were prepared by sanding them with 400 grit sandpaper and the dust was removed with compressed air to provide a clean uniform surface for deposition. When not in use, the substrates were stored in an oven at 70°C to minimize moisture content.

A limited number of more specialized tungsten substrates were also available for use in BN deposition. These substrates were 6.35 mm diameter by 6.35 mm tall 80% dense porous tungsten cylinders acquired from one of the primary manufacturers of dispenser cathodes, Semicon Associates. No surface preparation was done when using these tungsten cylinder substrates. It is believed that once BN LCVD is developed on solid tungsten sheets, the transition to porous substrates will be straightforward.

7.1.3 General Procedure

The general procedure for deposition began by loading the tungsten substrates into the upper deposition chamber. The chamber was then sealed and evacuated. A leak check was performed. The upper chamber was filled with nitrogen through the window port to the desired deposition pressure. The window port nitrogen flow rate was then set to 1500 sccm and the machine was put in "Keep Constant" mode so as to maintain the desired pressure. Meanwhile, the borazine vaporizer was removed from the freezer and placed in a cooler packed with ice. The vaporizer was attached to the appropriate gas lines. The carrier and diluent flow lines were evacuated and filled with nitrogen. This purge cycle was repeated three times to remove all air and other residual gases from the lines prior to opening the vaporizer. When ready to begin deposition, MFC 5 was set to the desired carrier flow rate, the inlet valve on the vaporizer was opened, the exit valve on the vaporizer was opened, and MFC 6 was set to the desired diluent flow rate. After waiting for about two minutes for the flow to stabilize, the laser could be engaged.

In preliminary experiments, the zinc selenide window for the CO_2 laser beam was observed to quickly cloud up with a white powder after the laser was engaged. This behavior was due to some nicks and scratches on the window causing it to absorb CO_2 laser energy and heat up. In order to combat this problem, a steady nitrogen flow was made to pass through the gas port adjacent to the laser window. Due to the distance between this window gas port and the gas nozzle exit, it was assumed the window port gas flow did not effect the local reagent concentration in the deposition zone. The laser window gas flow prevented the formation of the white powder on the laser window.

7.2 Boron Nitride Fiber Experiments

The methodology used in the development of BN fiber deposition followed a natural progression from exploratory experiments designed to confirm the feasibility of the process to refined experiments where parameters were systematically varied and deposit attributes

were quantified and finally to formal designed experiments wherein optimized BN fiber deposition was sought. The objective of the fiber experiments was to produce tall fibers of uniform diameter and smooth surface morphology. Fibers with these attributes would be used to quantify the process–property relations and measure boron nitride growth rates.

7.2.1 BN Fiber Exploratory Experiments

The first set of experiments, BN-1F-A, involved the deposition of three fibers and illustrated the reproducibility of Duty's experiments. Samples 1 and 2 used the standard tungsten sheet substrate while sample 3 was deposited on one of the porous tungsten cylinders. For simplicity, these experiments were run at a constant laser power. The chamber pressure was held constant at 760 Torr. Other specific conditions of the experiments are given in Table 7.2.

Table 7.2: BN-1F-A experiment conditions

No.	Borazine Temp (°C)	Carrier Flow (sccm)	Diluent Flow (sccm)	Borazine Flow (sccm)	Total Flow (sccm)	Borazine Conc (mol/m^3)	Laser Power (W)	Time (min)
1	0.0	50.0	0.0	4.80	54.80	3.91	67.21	2.00
2	0.0	50.0	0.0	4.80	54.80	3.91	67.21	4.00
3	0.0	50.0	0.0	4.80	54.80	3.91	44.62	2.00

The results of the experiments were large bowl-shaped growths with drastically different characteristics as one moved from the center of the bowl out radially. Figure 7.3 illustrates the nature of all three of these deposits.

All deposits exhibited an asymmetry that appeared related to the gas nozzle. The growth was tallest on the side furthest from the reagent nozzle and a long white powder trail extended away from the growth in the same direction as the gas flow. In the center was a deep depression extending almost to the tungsten substrate with a dark black metallic looking surface. As one moved up the walls of the depression from the center, the color changed to a translucent white color. This translucent white material was very similar to that shown by

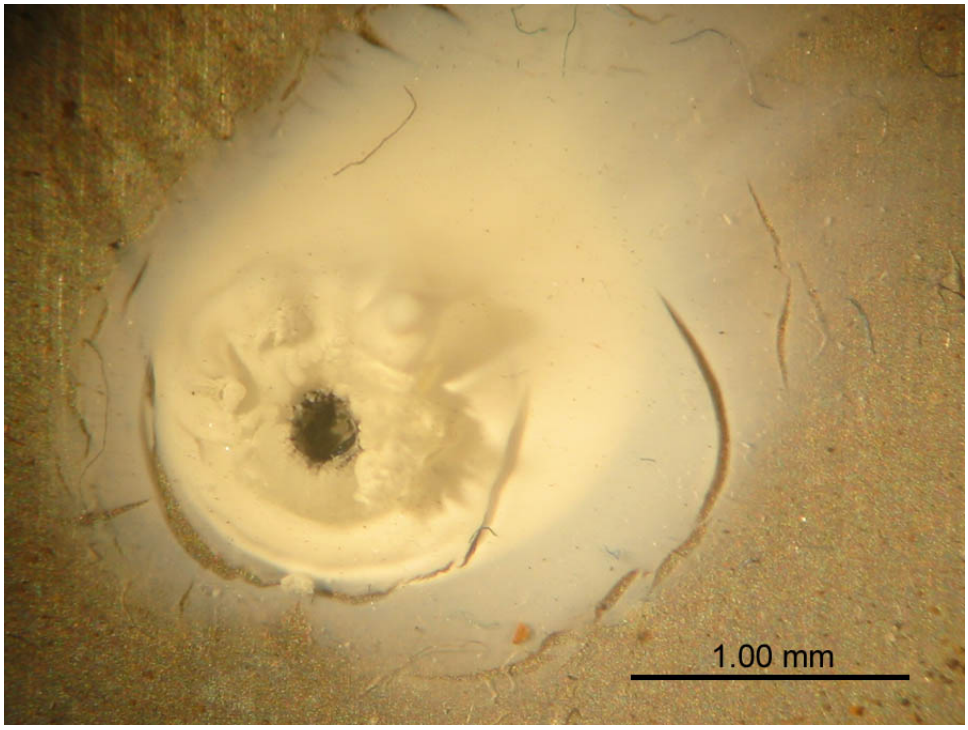

Figure 7.3: Optical microscope image of BN-1A Sample 1

Duty to be boron nitride. The translucent white material was partially covered by tall powdery growth, particularly on the side opposite the gas nozzle. The deposit was surrounded by a large quantity of white powder that does not appear to be well adhered to the substrate surface. The size and shape of the deposits indicated that the processing conditions used exceeded the optimum values for deposition.

Experiment BN-1F-B was done to explore suitable conditions for producing fibers of smaller, more uniform diameter without the severe volcano effect. Both the vaporizer carrier N_2 flow rate and the laser power were varied during this experiment. Substrates were tungsten sheets and the chamber pressure was maintained at 760 Torr for all samples. The specific conditions for the samples in experiment BN-1F-B are given in Table 7.3.

BN-1F-B could be described as a study of the effect of two factors on BN fiber deposit shape: total flow rate through the gas nozzle and laser power. Note that in these early exploratory experiments where constant laser power was used rather than constant temperature, there was a coupling between laser power and total flow rate due to convective heat

Table 7.3: BN-1F-B experiment conditions

No.	Borazine Temp (°C)	Carrier Flow (sccm)	Diluent Flow (sccm)	Borazine Flow (sccm)	Total Flow (sccm)	Borazine Conc (mol/m^3)	Laser Power (W)	Time (min)
1	0.0	50.0	0.0	4.80	54.80	3.91	15.91	2.00
2	0.0	50.0	0.0	4.80	54.80	3.91	7.73	2.00
3	0.0	50.0	0.0	4.80	54.80	3.91	23.68	2.00
4	0.0	50.0	0.0	4.80	54.80	3.91	15.91	1.00
5	0.0	50.0	0.0	4.80	54.80	3.91	11.87	2.00
6	0.0	50.0	0.0	4.80	54.80	3.91	19.84	2.00
7	0.0	25.0	0.0	2.40	27.40	3.91	19.84	2.00
8	0.0	75.0	0.0	7.20	82.20	3.91	19.84	2.00
9	0.0	25.0	0.0	2.40	27.40	3.91	19.84	2.00
10	0.0	25.0	0.0	2.40	27.40	3.91	31.05	2.00
11	0.0	75.0	0.0	7.20	82.20	3.91	31.05	2.00
12	0.0	50.0	0.0	4.80	54.80	3.91	34.59	2.00
13	0.0	25.0	0.0	2.40	27.40	3.91	38.03	2.00
14	0.0	25.0	0.0	2.40	27.40	3.91	11.87	2.00
15	0.0	25.0	0.0	2.40	27.40	3.91	7.73	2.00
16	0.0	10.0	0.0	0.96	10.96	3.91	7.73	2.00

transfer from the substrate surface.

The total flow rate through the nozzle is thought to be important because of its influence on the height of the concentration boundary layer above the substrate surface. For a fixed concentration, higher flow rates should lead to a reduced concentration boundary layer thickness which increases the concentration gradient through the boundary layer. For a transport limited process, the increased concentration gradient leads to higher diffusion rates and higher deposition rates. The laser power directly affects the substrate temperature which influences the deposition rate and deposition rate profiles. The deposition rate profiles are ultimately responsible for the shape of an LCVD deposit.

The results of BN-1F-B were analyzed by observation in an optical microscope. The fibers of BN-1F-B were smaller than those of BN-1F-A. Samples 2, 5, 7, and 16 did not yield any significant deposit. As for the remainder of the samples, all but one fiber (Sample 15) still exhibited a significant volcano effect with black coloration in the center of the deposit. Figure 7.4 (a) illustrates a typical example of the deposits in experiment BN-1F-B.

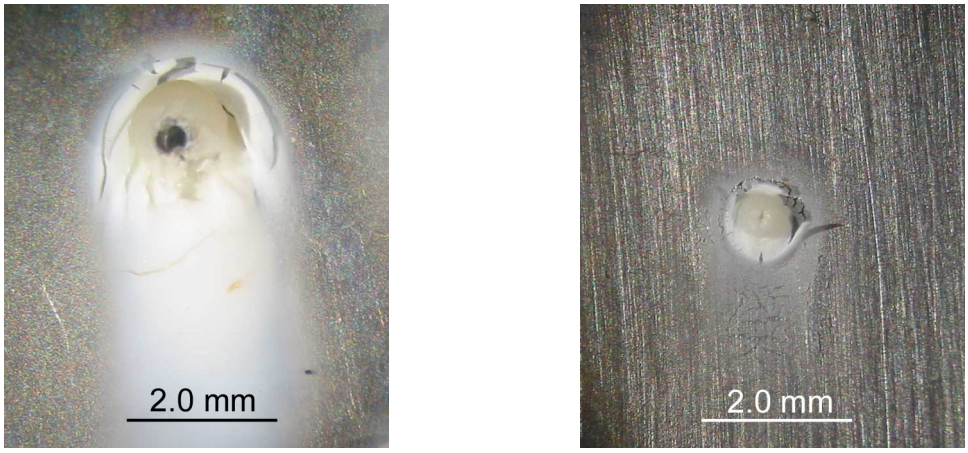

(a) Sample 12 **(b) Sample 15**

Figure 7.4: Optical microscope images of BN-1F-B experiment results

The overall shape of Sample 12 in Figure 7.4 (a) was much more uniform than BN-1F-A Sample 1. Sample 15 in Figure 7.4 (b) was the best looking fiber deposit. It consisted of vertical growth of translucent material with only a small volcano in the center and no

indication of black coloration. The fiber was generally symmetrical and was surrounded by a faint coating of white powder. While the samples at the lowest laser power levels, 7.73 and 11.87 W, did not always yield significant deposit, when they did, the deposit shape was favorable. Thus, BN-1F-B provided good information regarding the proper laser power levels for BN fiber deposition.

Experiment set BN-2F was a designed response surface experiment centered around the best sample, Sample 15, in BN-1F-B. The design was a rotatable central composite design with four factors: pressure, carrier flow rate (or total flow rate because no diluent flow was used), laser power, and growth time, and it incorporated four center point experiments making the total number of runs 28. All experiments were done on the standard tungsten sheet substrates. Table 7.4 shows specific conditions used in these experiments in the order they were run. The order was not completely randomized due to the complexity of the operational procedure required to change the system pressure.

Notice the change in borazine temperature during the course of the experiments. This effect stemmed from the difficulty of keeping the borazine at a fixed temperature and unfortunately directly impacted the borazine concentration delivered through the nozzle. The borazine concentration was also affected by changing the pressure of the chamber (which changes the pressure in the vaporizer). The laser power used in BN-2F was based on the optimum responses observed in BN-1F-B. Again, because the total reagent flow rate changes with changes in the carrier flow rate, there is a coupling between the carrier flow variable and the laser power variable.

Both optical and scanning electron microscopy were used to study the fibers grown in BN-2F. In order to systematically analyze the results using the optical microscope, some quantitative metrics were created. Two features that are most apparent in the boron nitride fiber deposits are a depression in the center of the deposit (termed the volcano effect) and dark black coloration on parts of the deposit surface. A scale of 1 to 7 with 1 representing no presence and 7 representing significant presence was used to record the degree to which

Table 7.4: BN-2F experiment conditions

No.	Total Press (Torr)	Borazine Temp (°C)	Carrier Flow (sccm)	Borazine Flow (sccm)	Total Flow (sccm)	Borazine Conc (mol/m^3)	Laser Power (W)	Time (min)
1	625	-19.0	17.5	0.70	18.20	1.52	14.80	1.50
2	625	-18.0	42.5	1.81	44.31	1.61	14.80	1.50
3	625	-18.0	42.5	1.81	44.31	1.61	14.80	2.50
4	625	-16.8	17.5	0.80	18.30	1.71	5.81	2.50
5	625	-16.1	17.5	0.84	18.34	1.78	14.80	2.50
6	625	-16.1	17.5	0.84	18.34	1.78	5.81	1.50
7	625	-14.8	42.5	2.19	44.69	1.90	5.81	2.50
8	625	-14.4	42.5	2.24	44.74	1.94	5.81	1.50
9	275	-12.8	42.5	6.03	48.53	2.11	14.80	1.50
10	275	-12.2	42.5	6.26	48.76	2.17	5.81	2.50
11	275	-11.6	17.5	2.68	20.18	2.24	5.81	1.50
12	275	-11.2	17.5	2.75	20.25	2.28	14.80	2.50
13	275	-10.4	17.5	2.89	20.39	2.38	14.80	1.50
14	275	-9.8	17.5	3.00	20.50	2.45	5.81	2.50
15	275	-7.9	42.5	8.20	50.70	2.69	14.80	2.50
16	275	-7.3	42.5	8.51	51.01	2.77	5.81	1.50
17	100	-5.7	30.0	29.86	59.86	2.99	10.43	2.00
18	450	-2.4	30.0	4.53	34.53	3.50	10.43	2.00
19	450	-1.8	30.0	4.69	34.69	3.60	10.43	1.00
20	450	-0.9	30.0	4.94	34.94	3.75	0.85	2.00
21	450	-0.4	30.0	5.09	35.09	3.84	10.43	2.00
22	450	-0.1	30.0	5.18	35.18	3.89	10.43	2.00
23	450	0.1	5.0	0.87	5.87	3.93	10.43	2.00
24	450	0.2	30.0	5.27	35.27	3.95	10.43	3.00
25	450	0.2	30.0	5.27	35.27	3.95	10.43	2.00
26	450	0.3	30.0	5.30	35.30	3.96	18.97	2.00
27	450	0.4	55.0	9.78	64.78	3.98	10.43	2.00
28	800	0.7	30.0	2.83	32.83	4.04	10.43	2.00

Table 7.5: BN-2F experiment results

No.	Volcano (1–7)	Black (1–7)	Diameter (μm)
2			446 *
3	5.8	3.4	908
5			220 *
15	3.4	4.6	750
17	3.4	3.4	1040
21	4.6	1	800
22	4.6	1	985
24	4.6	1	1157
25	5.8	3.4	968
26	5.8	3.4	1039
27	5.8	1	985

* deposits had no significant height

each sample exhibited each of these traits.

Table 7.5 shows the values of the response variables for the 11 samples that yielded some deposit. The sparse nature of the response data in BN-2F did not allow a robust analysis of the experimental results for either the volcano effect nor the black coloration. A simple multiple regression analysis was done for these features, and neither analysis detected a statistically significant relation between the factors and the response at the 90% confidence level.

The SEM allowed accurate measurement of fiber size, and an analysis of the fiber diameter response was performed. A standardized pareto chart of the factors and the interactions is shown in Figure 7.5. The vertical line on the chart represents $\alpha = 0.10$. Thus, there are three factors that were statistically significant at the 90% level: laser power, carrier flow, and time. Furthermore, these three factors exhibit a positive effect on the response with an increase in any one of the factors leading to an increase in fiber diameter. These results are expected, but the sparse data again prohibited more detailed analysis of the experimental results.

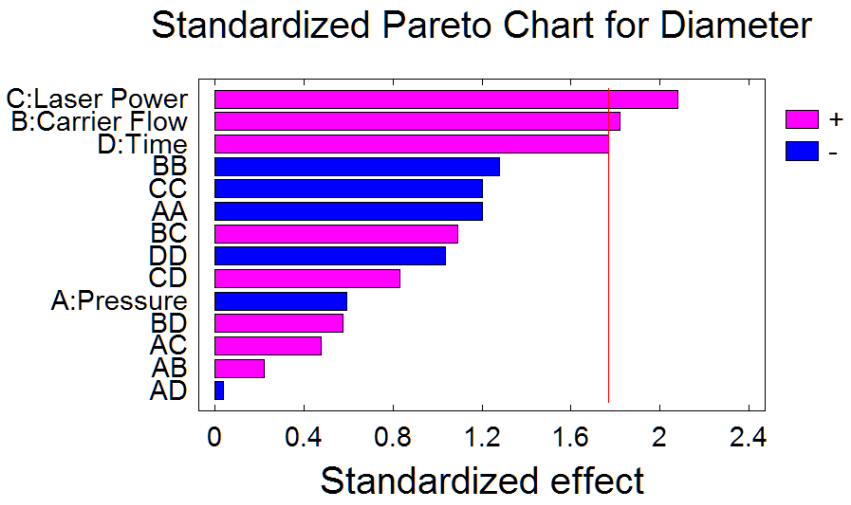

Figure 7.5: Main factor and interaction effects on BN fiber diameter

The "binary" results of BN-2F with regard to the presence of a deposit was not expected. For example, the four center point experiments with conditions: Pressure = 450 Torr, Carrier Flow = 30 sccm, Laser Power = 10.43 W, and Time = 2.0 min, resulted in three instances of fiber growth of approximately the same size and shape and one instance of no growth. This type of binary behavior was interpreted as a sign that the BN deposition process was extremely sensitive to one or more process parameters. Observations made during the experiments indicated an extreme sensitivity of the temperatures viewed on the thermal imager to the laser power level. By comparison, the sensitivity was much greater than that observed for carbon deposition.

An EDX analysis of the BN fibers was used to determine the elemental composition of the deposits. A low magnification SEM micrograph of Sample 27 is shown in Figure 7.6. The EDX analysis was done by zooming in on the area indicated to a magnification of 2000x. First an EDX analysis was done on the tungsten sheet substrate at a point that had no deposited material. Figure 7.7 was the output of the analysis that is dominated by the tungsten element. Figure 7.8 was the output of the analysis performed on Sample 27 of the experiment. The EDX plot shows a presence of both boron and nitrogen although the

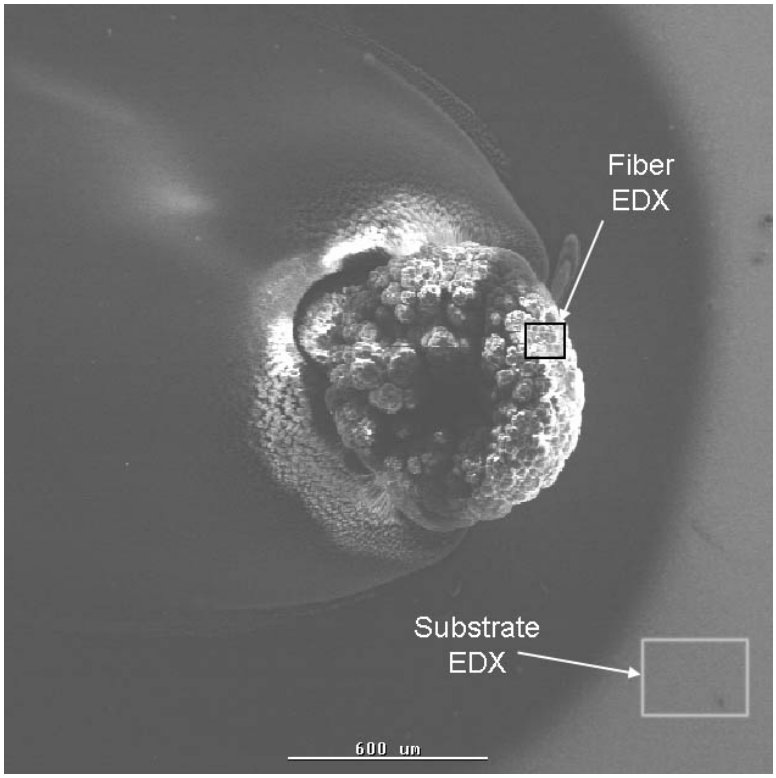

Figure 7.6: SEM micrograph of Sample 27 of BN-2F showing area used in EDX analysis

count ratio does not represent the desired stoichiometry of 1:1. The composition appears to be more closely 1:2 of B:N.

Experiment set BN-3F was designed to further explore the observed sensitivity of reaction temperature to laser power. The substrates used were tungsten sheets and the pressure was held constant at 760 Torr. No diluent flow was used and the laser window nitrogen flow was set at the normal 1500 sccm. The only variable used in this set was the laser power and the power was held constant throughout the growth of each sample at the specified value. Some minor variation in borazine concentration occurred due to changes in the vaporizer temperature. Specific conditions for the experiment are given in Table 7.6.

The results of BN-3F fell into three distinct categories. Samples 4 and 8, both run at 4.35 W, defined the first category which was no significant deposition. The second category consisted of samples that showed a significant volcano effect with some degree of black coloration in the center as shown in Figure 7.9 (a). The presence of the black coloration

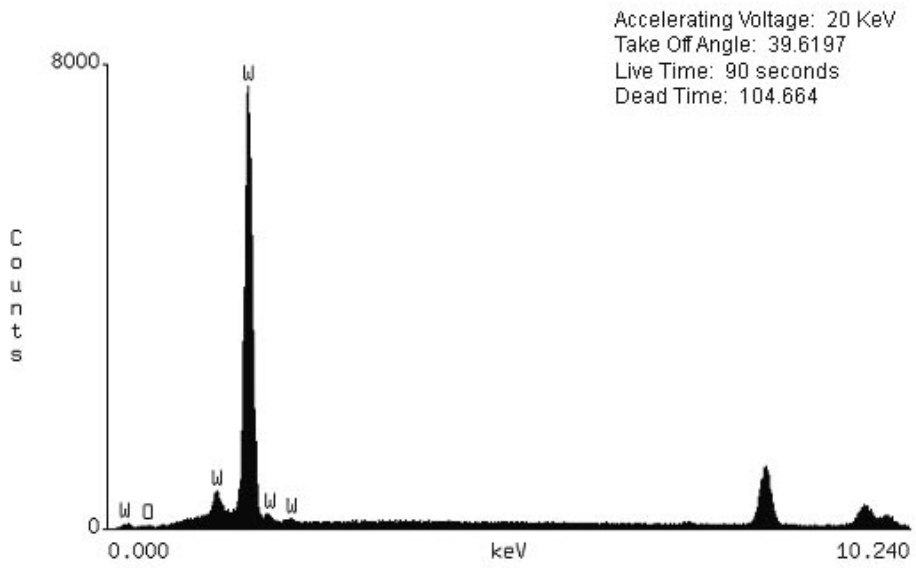

Figure 7.7: EDX output from analysis done on tungsten substrate

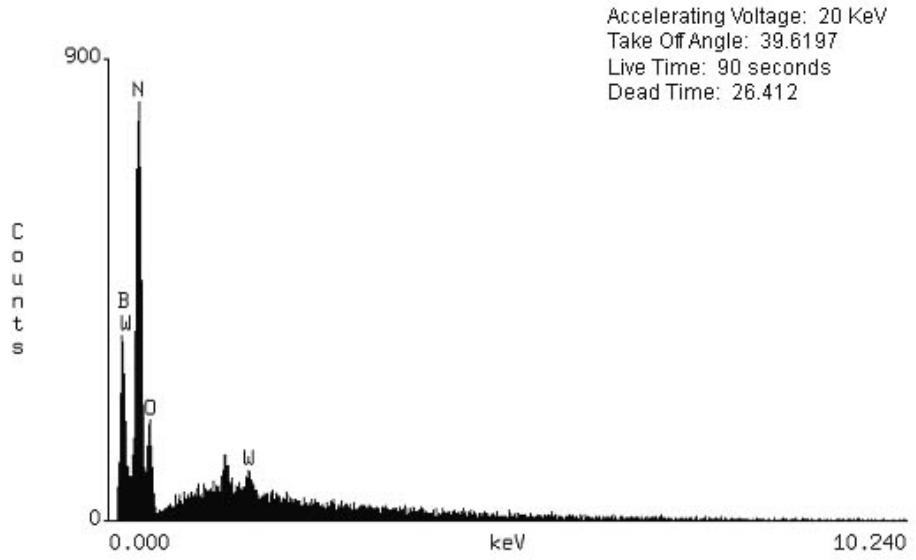

Figure 7.8: EDX output from analysis done on fiber Sample 27

Table 7.6: BN-3 experiment conditions

No.	Borazine Temp (°C)	Carrier Flow (sccm)	Diluent Flow (sccm)	Borazine Flow (sccm)	Total Flow (sccm)	Borazine Conc (mol/m^3)	Laser Power (W)	Time (min)
1	-4.5	25.0	0.0	1.88	26.88	3.17	7.73	1.50
2	-5.0	25.0	0.0	1.83	26.83	3.09	7.73	1.50
3	-5.5	25.0	0.0	1.78	26.78	3.02	6.05	1.50
4	-6.0	25.0	0.0	1.73	26.73	2.95	4.35	5.00
5	-6.5	25.0	0.0	1.68	26.68	2.88	6.89	1.50
6	-7.0	25.0	0.0	1.63	26.63	2.81	5.20	1.50
7	-7.5	25.0	0.0	1.59	26.59	2.74	5.20	1.50
8	-7.0	25.0	0.0	1.63	26.63	2.81	4.35	8.00
9	-6.5	25.0	0.0	1.68	26.68	2.88	7.73	5.00

appears to indicate excessive temperatures in that portion of the deposit area. Samples 1, 2, 5, and 9 made up this category.

Samples 3, 6, and 7 made up the best results of BN-3F. They exhibited asymmetrical growth of the translucent white material with a minimal volcano effect as shown in Figure 7.9 (b). The asymmetry of the growth seemed to be related to the directional nature of the nozzle reagent flow with the side of the fiber nearest the nozzle exhibiting more growth.

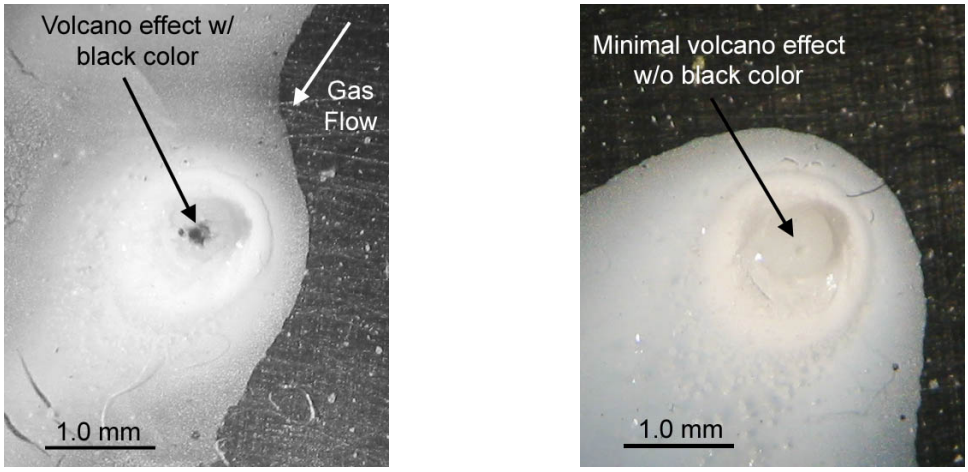

(a) Sample 2 **(b) Sample 6**

Figure 7.9: Sample fibers from BN-3F

The results of BN-3F show that for the given conditions, laser powers above 5.20 and less than 6.05 W yield the best fiber deposits. The samples run at 4.35 W yielded no significant deposits. The samples run at powers of 6.89 W or greater exhibited the black coloration in the center of the volcano effect. These results further suggest that the size and shape of the boron nitride fiber deposits was extremely sensitive to the incident laser power.

In light of this sensitivity, the stability of the CO_2 laser became important. The stability of the laser was influenced by several factors. First, the laser documentation specified the power stability to be $\pm 5\%$ of full scale. Thus, because the laser was a 100 W laser, the power output could vary by as much as 5 W in either direction for a constant control signal. This specification appeared to be much more conservative than observed instabilities.

In addition to the laser power variation, potential variation existed in the 0-10 V analog control signal sent from the LabVIEW control computer to the laser signal generator. This control signal corresponded to 100 mV/W meaning that a 100 mV increase in control signal caused a change of 1 W in laser power output. The control signal was generated by a LabVIEW SCXI 1124 analog output card with a resolution of 12 bits, a relative accuracy of $\pm$LSB, and an absolute accuracy of 0.05% of full scale. When configured for an output between 0 and 10 V, the relative accuracy translated to ± 1.22 mV and the absolute accuracy translated to 5 mV. In the absence of other effects, variation in the analog output from LabVIEW could cause a variation in laser power of ± 0.05 W.

Another potential source of variation in the delivered laser power was noise in the 0-10 V analog control signal from LabVIEW. The signal is delivered from the SCXI 1124 card to the laser signal generator via a military grade shielded BNC cable. The noise in this line was observed on an oscilloscope to have peak to peak values exceeding 25 mV. The noise in this control signal could lead to ± 0.25 W fluctuations in the output laser power.

The laser power signal generator used the 0-10 V analog input signal provided by LabVIEW to produce a pulse width modulated signal that was delivered to the laser power

supply. A source of laser power variation could also be noise in the wire that carriers the PWM signal from the signal generator to the laser power supply. The magnitude of this noise is unknown, but it is likely it could cause output laser power fluctuations of ± 0.25 W or more.

In sum, the potential variation in the laser power delivered to the substrate is significant relative to the sensitivity of boron nitride fiber growth to laser power delivered. This sensitivity made it difficult to utilize the LCVD system's feedback temperature control system during boron nitride deposition.

Experiment set BN-4F was designed to further investigate the successful conditions used in BN-3F to deposit boron nitride fibers. All conditions in BN-4F were the same as those in BN-3F except as indicated by Table 7.7. The results of BN-4F further confirmed

Table 7.7: BN-4F experiment conditions

No.	Borazine Temp (°C)	Carrier Flow (sccm)	Diluent Flow (sccm)	Borazine Flow (sccm)	Total Flow (sccm)	Borazine Conc (mol/m^3)	Laser Power (W)	Time (min)
1	-9.0	25.0	0.0	1.46	26.46	2.55	4.86	10.00
2	-10.5	25.0	0.0	1.34	26.34	2.36	5.20	10.00
3	-12.5	25.0	0.0	1.20	26.20	2.14	5.54	10.00
4	-12.5	25.0	0.0	1.20	26.20	2.14	5.88	2.00
5	-12.4	25.0	0.0	1.20	26.20	2.15	5.71	2.50
6	-11.7	25.0	0.0	1.25	26.25	2.23	5.71*	10.00

**Laser power was varied after growth initiated at 5.71 W*

the extreme sensitivity of BN fiber deposition to laser power delivered. Samples 1, 2, and 3 did not produce any significant deposit, while samples 4 and 5 produced samples very similar to samples 3, 6, and 7 of BN-3F. Note that the laser power used in sample 3 was 5.54 W and after 10 minutes this power produced no boron nitride deposit. Sample 5 used laser power of 5.71 W and after 2.5 minutes produced a fiber deposit of significant height and width. Thus, a change of 0.17 W in laser power made the difference between producing nothing and producing a significant deposit. This small change in laser power

only represents 0.17% of the full scale output values and is less than the potential variation in power due to noise and other uncontrollable effects.

Sample 6 of BN-4F was initiated at the same conditions used in sample 5; however, after growth began, the laser power was varied intentionally in an effort to maintain the maximum temperature in the deposition zone around 1000°C. Manual laser power control was used because some preliminary trials involving the feedback temperature control system proved unsuccessful, likely because of the process sensitivity.

The result of Sample 6 was a fiber of significant height made of the translucent white material that appears to be boron nitride. This fiber is shown in Figure 7.10. It exhibited a varying diameter which is likely due to the crude effort at temperature control. Of great importance was the fact that this fiber exhibited no volcano effect. Apparently, the maximum temperature during growth did not exceed the critical value that leads to the volcano shape or the black coloration.

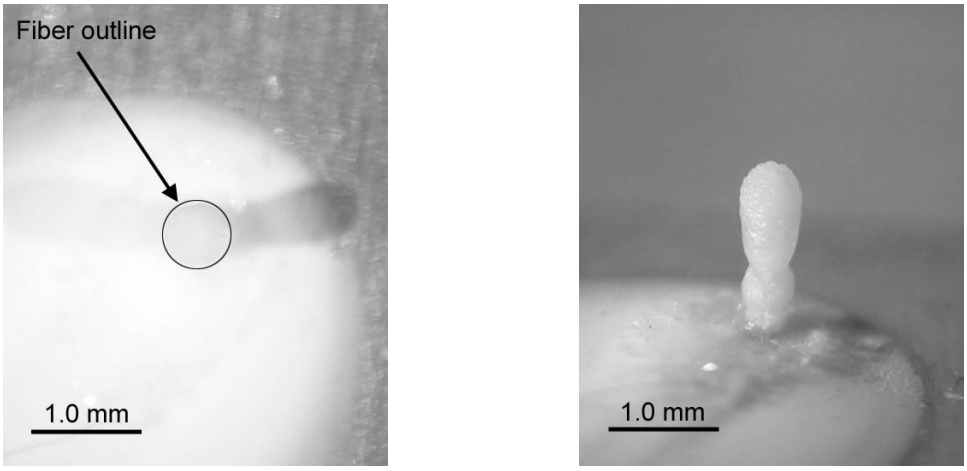

(a) Top View **(b) Side View**

Figure 7.10: BN-4F Sample 6 experiment results

The different process used to grow Sample 6 and the successful results of the experiment indicated that in order to achieve tall, volcano–less fibers, a varying laser power approach should be used. Regardless of specific material considerations, the emergence of vertical growth on the substrate surface during LCVD reduces the conduction pathways

from the point of laser incidence into bulk substrate material. The loss of conduction paths means that in order to achieve the same temperature on the growth tip as previously existed on the flat substrate surface, less incident power is needed. In addition to these geometric considerations, the differences in material properties of metals and ceramics exacerbates the severity of the initial transition period in boron nitride growth on tungsten.

Both the optical and the thermal properties of ceramics are significantly different from those of metals. In boron nitride deposition, as the process began, the properties of the substrate quickly changed from those of tungsten to those of boron nitride. In order to understand the significance of these substrate changes on the deposition parameters, some analytical calculations were performed.

In terms of optical properties, ceramics often have low reflectance, moderate absorbance and moderate to high transmittance. Metals are characterized by high reflectance, high absorbance, and low transmittance. The high reflectivity of a metal substrate material requires the delivery of significantly more laser power than a ceramic substrate material to achieve the same net energy delivery into the substrate. Once the infrared CO_2 laser energy penetrates the surface, it is either absorbed by the substrate atoms or transmitted through the substrate. For pyrolytic LCVD, it is desirable that the energy be absorbed near the substrate surface, because the absorbed energy is converted into heat which drives the surface reactions.

The amount of laser energy absorbed by the substrate can be computed from the absorption index which is the imaginary component of the full complex refractive index. The absorption coefficient can be computed from the absorption index using Equation 7.6:[107]

$$\beta = 4\pi k/\lambda \tag{7.6}$$

where λ is the wavelength of interest. Using Equation 7.7, the fraction of energy absorbed (I/I_0) as a function of depth, z, into the substrate can be computed:

$$I/I_0 = e^{-\beta z} \tag{7.7}$$

For tungsten, others have reported that the absorption coefficient is about 55.01 μm^{-1} which was used in conjunction with Equation 7.7 to show that 99% of the energy would be absorbed in the first 0.018 μm of the substrate surface.[2] This absorbed energy is converted into heat.

Similar calculations can be done treating the growing boron nitride as the substrate material. If we assume that the BN produced in LCVD is similar to pyrolytic BN produced in traditional CVD, we can use material property data from commercial producers. Figure 7.11 is a plot of the absorption coefficient for infrared energy for General Electric's pyrolytic boron nitride.[108]

From the plot, the absorbtion coefficient at 10.59 μm is between 700 and 900 cm^{-1}. Taking the average, 800 cm^{-1}, and plugging into Equation 7.7, the fraction of incident energy remaining can be plotted as a function of depth, *z*, into the substrate. Figure 7.12 contains such a plot. Notice that only about 50% of the non–reflected energy is absorbed in the first 10μm of material and it takes about 60 μm of growth before all of this energy is absorbed. These dimensions are significant relative to the size of some BN deposits, especially lines.

In order to maintain a constant surface temperature, the lower reflectivity of BN relative to W would require a drop in laser power, while the reduced absorptivity of the BN deposit material would require an increase in laser power. These changes in optical properties are coupled to the thermal properties of the substrate and deposit materials.

The absorbed laser energy is converted into heat. The analysis in Chapter 6 showed the temperature profiles on an LCVD fiber surface to be dominated by the conductivity of the underlying material. For comparison, a plot of thermal conductivity as a function of temperature for both tungsten[109] and pyrolytic boron nitride[108] is presented in Figure 7.13.

As shown in the figure, pyrolytic boron nitride, much like pyrolytic graphite, is extremely anisotropic in its thermal conductivity. The origin of this anisotropy lies in the

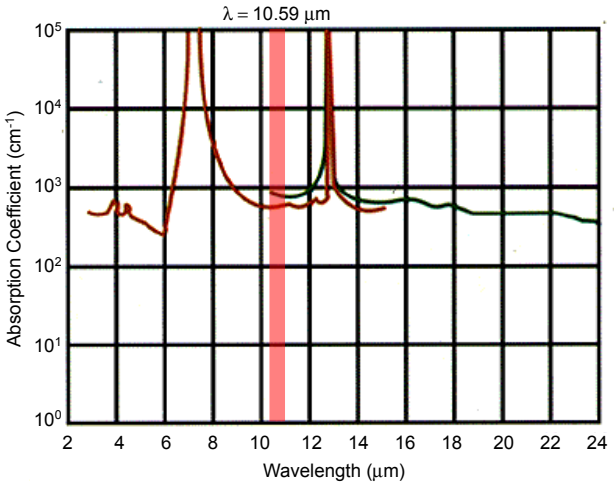

Figure 7.11: Absorption coefficient of GE's pyrolytic BN in infrared band[108]

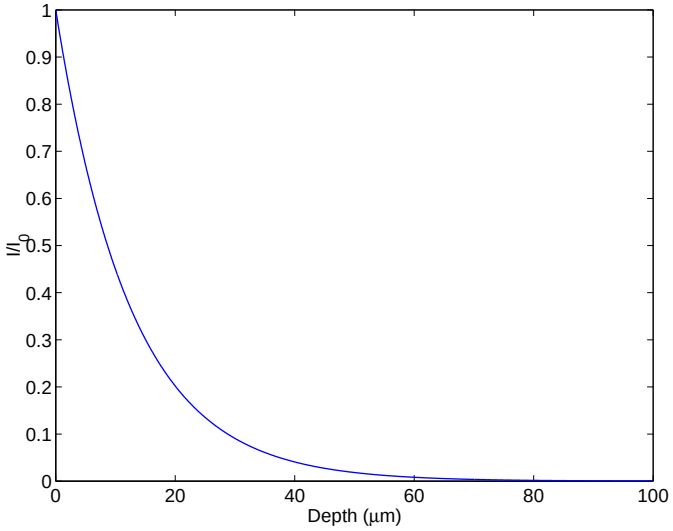

Figure 7.12: Fraction of incident laser energy remaining with increasing depth into pyrolytic BN substrate

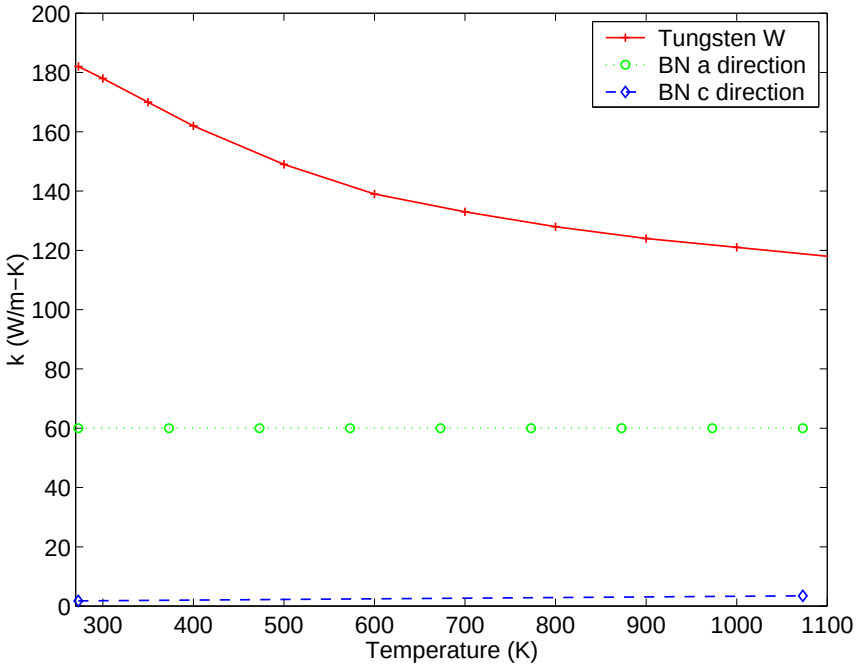

Figure 7.13: Comparison of thermal conductivity of tungsten and pyrolytic BN

hexagonal crystal structure of the material. At 500°C, W has a thermal conductivity 2.5 times that of the *a* direction of pyrolytic BN and over 54 times that of the *c* direction!

The effect of thermal conductivity on maximum temperature rise, T_{max}, at the beam center on the substrate surface within the laser spot can be approximated using Lax's[55] expression:

$$T_{max} = \frac{P}{2\pi k}\left\langle \frac{1}{r} \right\rangle \tag{7.8}$$

where P is the incident laser power, k is thermal conductivity of the substrate, and for a Gaussian laser beam:

$$\left\langle \frac{1}{r} \right\rangle = \frac{1}{w}(\pi)^{\frac{1}{2}}$$

where w is the diameter of the laser beam. For simplicity, this expression assumes the beam attenuation is so great that all the heat is generated in an infinitesimally thin substrate surface layer (i.e. perfect surface absorption).

Due to the linear relationship expressed by Equation 7.8, for a laser beam of fixed size, the ratio of laser power, P, for tungsten to that for boron nitride is effectively the ratio of

k for tungsten to that of boron nitride at the temperature of interest. Given its anisotropy, an average effective conductivity of BN lies somewhere between the values of 2.5 and 54 W/m-K. Thus, in order to achieve the same maximum temperature in the center of the laser spot, between 2.5 and 54 times more power is required when heating tungsten than when heating pyrolytic boron nitride. This suggests that a very large reduction in laser power should be necessary to maintain constant surface temperature as BN growth begins.

In addition to the material property changes associated with deposit growth, the geometry of the growing deposit also significantly affects the relationship between laser power and temperature. Specifically, the growth of a fiber restricts the heat conduction path back into the underlying substrate thus requiring a reduction in laser power to maintain constant temperature.

The reductions in substrate reflectivity, conductivity, and conduction paths all dictate a need for a significant reduction in laser power to maintain constant temperature as BN growth initiates, while the reduction in absorbtivity suggests a need for increased power. The finding of BN-4F that a high laser power was needed to initiate growth followed by a much reduced power to achieve sustained growth was consistent with these calculations. The coupling of these drastically different material properties in a dynamic and transient growth process highlights one of the challenges of depositing a ceramic on a metal substrate.

7.2.2 BN Fiber Refined Experiments

Experiment set BN-5F was designed to grow a series of fibers similar to Sample 6 of BN-4F. The goal of the experiment was to identify a repeatable process whereby fibers could be grown under relatively steady conditions. The general procedure was to initiate growth by applying a relatively high laser power of about 8–10 W until growth began (usually 1–5 min) and then quickly reduce the laser power to a level that maintained a constant

maximum temperature near 1100°C (usually 2–4 W). The process sensitivity found in experiments BN-3F and BN-4F prevented the automated control configuration used in carbon fiber deposition from working. A crude manual temperature control through the LabVIEW interface was only capable of keeping the temperature within ± 100 °C of the desired value. The pressure during BN-5F was held constant at 760 Torr. Specific conditions for the eight samples of BN-5F are provided in Table 7.8.

Table 7.8: BN-5F experiment conditions

No.	Borazine Temp (°C)	Carrier Flow (sccm)	Diluent Flow (sccm)	Borazine Flow (sccm)	Total Flow (sccm)	Borazine Conc (mol/m^3)	Max Temp (°C)	Time (min)
1	-9.8	25.0	0.0	1.40	26.40	2.45	1100	9.46
2	-11.9	25.0	0.0	1.24	26.24	2.20	1100	15.08
3	-12.0	25.0	0.0	1.23	26.23	2.19	1100	11.02
4	-10.5	25.0	0.0	1.34	26.34	2.36	1100	13.00
5	-9.8	25.0	0.0	1.40	26.40	2.45	1100	13.74
6	-8.8	25.0	0.0	1.48	26.48	2.57	1100	6.00
7	-7.9	25.0	0.0	1.55	26.55	2.69	1100	8.83
8	-6.3	25.0	0.0	1.70	26.70	2.91	1100	6.08

The results of BN-5F were very encouraging. All eight samples yielded significant deposit, and most of them were tall, cylindrical shapes with no volcano effect or black discoloration. Sample 5 is shown in Figure 7.14. The diameter and height of all fibers was measured and recorded as given in Table 7.9. A crude value of average growth velocity (μm/s) for each sample was computed by dividing the fiber height by the total time of laser engagement. Note that this time includes the delay time between laser engagement and growth initiation (1–5 min), and therefore represents an artificially low growth rate. The mean and standard deviation of these average growth velocities over all eight samples were 1.19 and 0.62 μm/s, respectively. Experiment BN-5F showed that a stepwise controlled boron nitride fiber deposition using high power to initiate growth followed by a quick transition to reduced power could yield deposits of desirable size and shape.

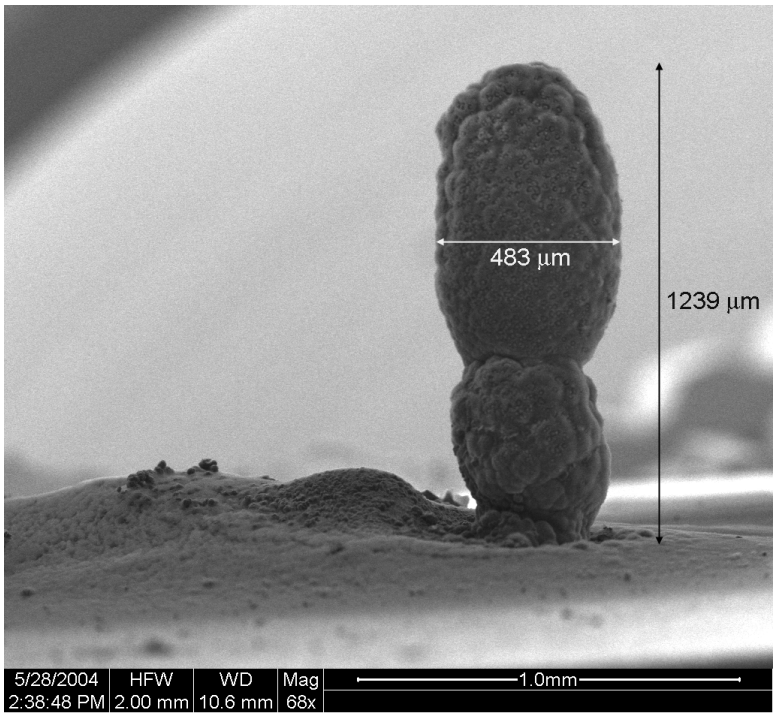

Figure 7.14: Sample 5 of BN-5F showing typical size and shape of BN fiber

Table 7.9: BN-5F experiment results

No.	Volcano (1-7)	Black (1-7)	Diameter (μm)	Height (μm)	Time (s)	Avg. Growth Velocity (μm/s)
1	1	1	530	631	568	1.11
2	1	1	621	717	905	0.79
3	2.2	1	799	885	661	1.34
4	1	1	658	890	780	1.14
5	1	1	483	768	824	0.93
6	1	1	597	935	360	2.60
7	1	1	465	546	530	1.03
8	2.2	2.2	359	207	365	0.57

Experiment BN-6F was similar in conditions and objective to BN-5F, but it incorporated two new aspects. First, a change in the experimental procedure was implemented. All previous BN deposition proceeded by opening the borazine vaporizer and allowing flow to stabilize for several minutes prior to engaging the laser. This experiment was setup to explore the effect of pre-heating the tungsten sheet substrate by engaging the laser for about ten minutes with no flow through the vaporizer. Thus, any transient heating of the substrate had time to stabilize providing a more constant surface temperature. When ready to commence deposition, the vaporizer flow was directed through the gas nozzle.

The second aspect of BN-6F that differed from BN-5F was the use of the thermal imaging camera to measure growth rates as described in Section 3.4.1. This required configuring the imager software to capture a continuous series of images throughout the deposition process. In addition to allowing growth rate measurements from the thermal images, the images inherently provided more precise temperature measurements throughout the deposition process.

The conditions for the BN-6F runs are shown in Table 7.10. The results of BN-6F were

Table 7.10: BN-6F experiment conditions

No.	Borazine Temp (°C)	Carrier Flow (sccm)	Diluent Flow (sccm)	Borazine Flow (sccm)	Total Flow (sccm)	Borazine Conc (mol/m^3)	Max Temp (°C)	Time (min)
1	-9.1	25.0	0.0	1.45	26.45	2.53	N/A	18.33
2	-10.8	25.0	0.0	1.32	26.32	2.33	1017	12.00
3	-9.0	25.0	0.0	1.46	26.46	2.55	1112	7.85
4	-4.6	25.0	0.0	1.87	26.87	3.15	1153	5.67
5	-2.3	25.0	0.0	2.12	27.12	3.51	1146	5.28
6	-0.3	25.0	0.0	2.36	27.36	3.86	N/A	4.28
7	-0.1	25.0	0.0	2.39	27.39	3.89	1121	6.00
8	0.1	25.0	0.0	2.41	27.41	3.93	1186	6.58
9	0.3	25.0	0.0	2.44	27.44	3.96	1080	4.95

fibers of desirable size and shape. Only minor evidence of volcano effects or discoloration

was observed. The fibers did show some asymmetry relative to the direction of the gas nozzle flow. The laser pre–heating of the substrate reduced the dwell time between experiment parameter setup and actual growth initiation. Measurements of deposit attributes along with average growth rate are given in Table 7.11.

Figure 7.15 is a side view of Sample 4 that illustrates the typical shape of BN fibers. The success of BN-6F was indicative that the process conditions used were likely near the optimum conditions for tall, slender fibers of uniform diameter exhibiting no volcano effect or black discoloration.

7.2.3 BN Fiber Designed Experiments

Experiment BN-17F was designed as a 2 factor 3 level full factorial experiment with 9 runs and no replicates. The objective of the experiment was to quantify the relationship among the process parameters and the deposit shape using conditions similar to those of BN-6F. The two factors studied were carrier flow rate and maximum deposition temperature and the levels were as presented in Table 7.12. Under the particular conditions shown in Table 7.12, changing the carrier flow rate was effectively equal to changing the borazine concentration. The total flow rate through the gas nozzle was kept essentially constant at 50 sccm by changing the diluent flow rate in conjunction with the carrier flow rate. This flow rate represented an increase in total flow rate over the previous BN fiber experiments necessitated by the need to explore reduced carrier flow rate (and borazine concentration) levels. The system pressure in all experiments was kept constant at 760 Torr.

This experiment was also designed to yield growth rate information; however, because of the exponential relationship between reaction rate and temperature, temperature must remain fairly constant during deposition to extract meaningful growth rate data. A new technique was used to stabilize the laser power during deposition. The analog voltage signal from the LabVIEW interface was disconnected from the laser control module. Laser power control was accomplished by using the manual knob on the control module. The

Table 7.11: BN-6F experiment results

No.	Volcano (1-7)	Black (1-7)	Diameter (μm)	Height (μm)	Time (s)	Avg. Growth Velocity (μm/s)
1	1	1	794	1266	1100	1.15
2	1	1	575	577	720	0.80
3	1	1	648	879	471	1.87
4	1	1	807	976	340	2.87
5	1	1	769	992	317	3.13
6	1	1	538	434	257	1.69
7	1	1	644	777	360	2.16
8	2.2	1	721	735	395	1.86
9	1	1	499	548	297	1.85

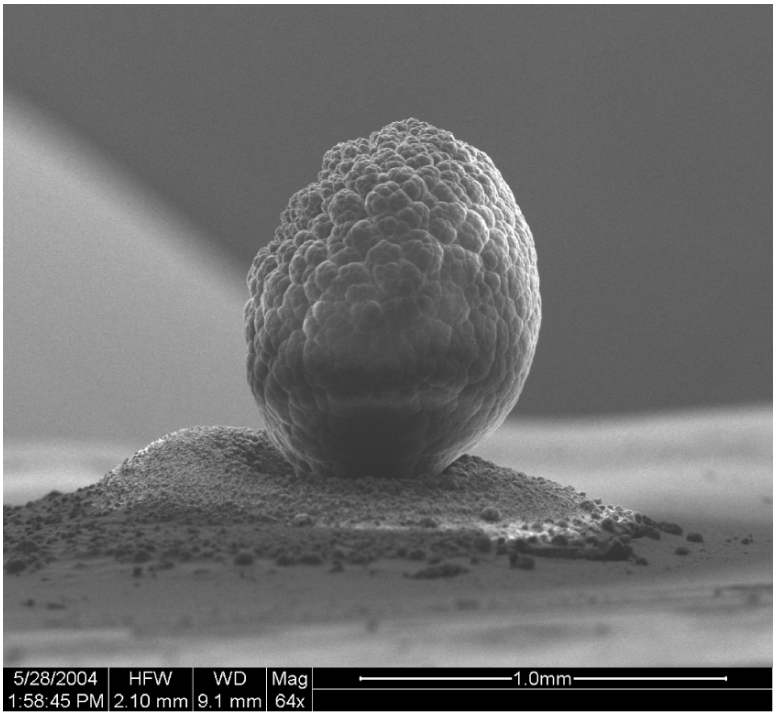

Figure 7.15: SEM micrograph side view of BN-6F Sample 4 fiber

Table 7.12: BN-17F experiment conditions

No.	Borazine Temp (°C)	Carrier Flow (sccm)	Diluent Flow (sccm)	Borazine Flow (sccm)	Total Flow (sccm)	Borazine Conc (mol/m^3)	Max Temp (°C)	Time (min)
1	-7.9	15.0	34.2	0.93	50.10	0.85	1012	10.00
2	-6.3	15.0	34.2	1.02	50.19	0.93	1194	8.00
3	-4.6	15.0	34.2	1.12	50.29	1.01	1097	8.00
4	-3.5	30.0	18.3	2.38	50.72	2.12	1006	5.00
5	-2.5	30.0	18.3	2.51	50.86	2.23	1100	3.50
6	-1.5	30.0	18.3	2.66	51.00	2.34	1172	3.75
7	-0.4	5.0	44.7	0.47	50.19	0.42	1207	9.00
8	-0.3	5.0	44.7	0.47	50.20	0.42	1024	13.00
9	-0.2	5.0	44.7	0.48	50.20	0.42	1120	13.37

overall procedure still used a high laser power to initiate growth, followed by a reduction in laser power until reaching the desired temperature. Preliminary tests showed this method to significantly reduce the random fluctuations previously observed in deposition temperature during boron nitride fiber growth. Due to the relative stability of the reaction temperatures using the new control method, the small adjustments necessary for maintaining a constant temperature could be made using the manual knob.

All nine runs in experiment BN-17F resulted in fiber deposits. These deposits were inspected using both a 40x optical microscope and an SEM. An array of attributes was recorded for each sample as given in Table 7.13.

Unlike the samples of BN-6F, the *Volcano* column in Table 7.13 indicates that most of the samples from BN-17F resulted in a moderate volcano effect. It was also observed that most of the BN-17F samples displayed a distinct asymmetry relative to the direction of gas nozzle flow. These characteristics must have arisen due to the reduced concentrations and increased total flow rates used in this experiment.

As far as the asymmetry, it was as if the nozzle flow directly increased the growth rate, but in doing so, the side nearest the nozzle shielded the side furthest from the nozzle and

Table 7.13: BN-17F experiment results

No.	Volcano (1-7)	Black (1-7)	Diameter (μm)	Height (μm)	Time (s)	Est. Growth Rate (μm/s)
1	1	1	718	839	600	1.40
2	3.4	1	1013	898	480	1.87
3	4.6	1	974	1098	480	2.29
4	2.2	1	807	745	300	2.48
5	2.2	1	920	912	210	4.34
6	4.6	1	1081	942	225	4.18
7	3.4	1	627	551	540	1.02
8	2.2	1	655	746	780	0.96
9	3.4	1	555	589	802	0.73

reduced the transport of borazine reagent to this area. The reduction of borazine transport to the short side of the fiber could be due to the consumption of reagent on the tall side or the convective flow pattern created by the emergence of the asymmetry. Figures 7.16 and 7.17 illustrate the asymmetry seen in most of the fibers.

The depression in the center of the deposit could also be explained by species transport phenomena. It is known that under transport–limited conditions, the growth rate in the center of an LCVD deposit is likely to lag that on the fiber perimeter. The concentration of reagent species directly over the laser spot varies with temperature per the ideal gas law; the center point of maximum temperature will also be the point of minimum species concentration. The high temperature in this region will assist species transport via diffusion; however, the diffusion path to the center of the deposit is directionally restricted in contrast to the diffusion paths for the perimeter of the fiber. Further discussion of the implications of a transport–limited process on deposit shape is given in Chapter 8.

A multiple regression analysis was done to develop the numerical relationship among the maximum fiber diameter and the two factors of interest: borazine concentration and maximum temperature. The regression equation included both the first and second order main effects as well as the first order interactions. The higher order effects were shown

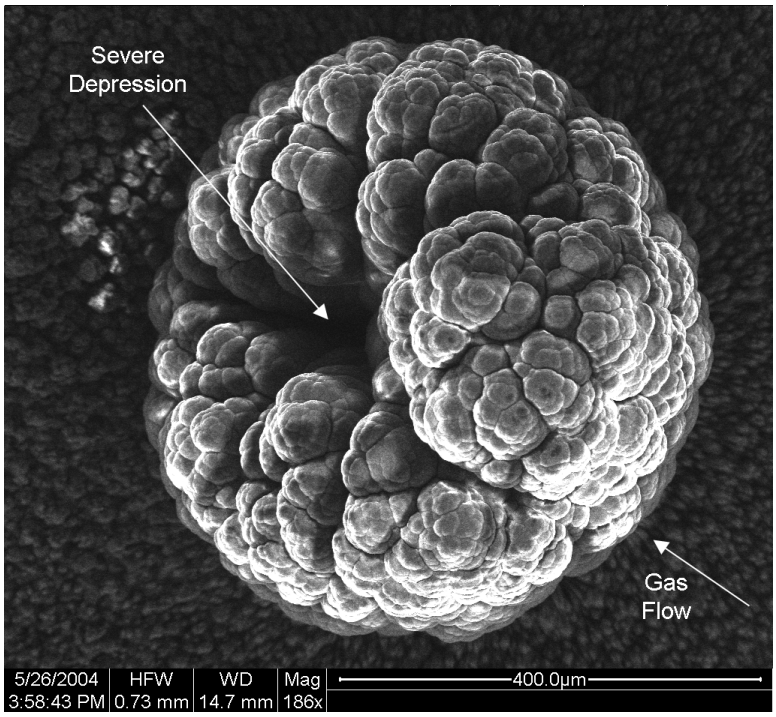

Figure 7.16: BN-17F Sample 9 SEM micrograph - top view

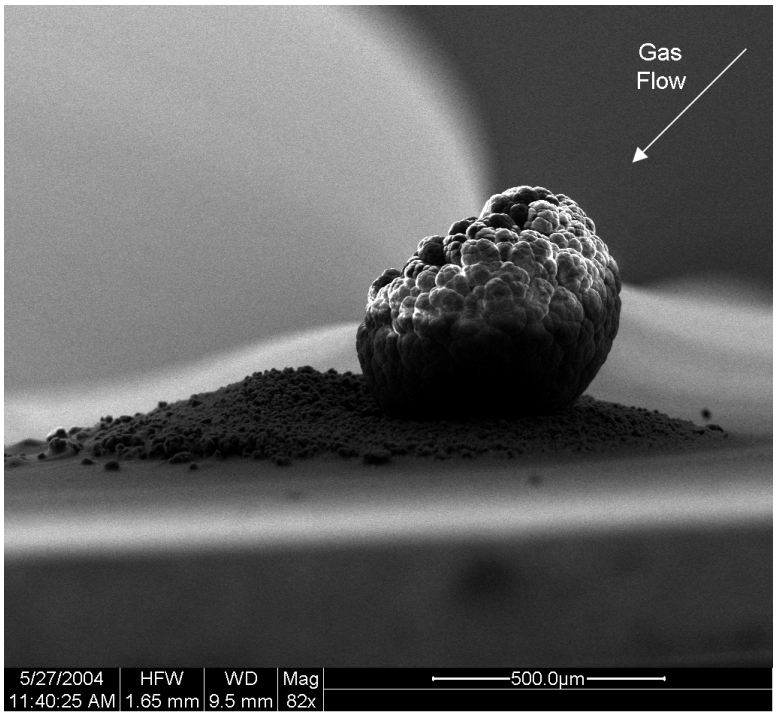

Figure 7.17: BN-17F Sample 9 SEM micrograph - side view

to be statistically insignificant and the model was reduced to first order. The regression output is given in Table 7.14. The fact that temperature was not shown to be statistically significant suggested this process might be transport–limited.

Table 7.14: Regression output for BN-17F fiber diameters

Dependent variable: Diameter

Parameter	Estimate	Standard Error	T Statistic	P-Value
CONSTANT	-290.514	728.003	-0.39906	0.7037
Concentration	163.431	62.1317	2.6304	0.039
Temperature	0.826545	0.64968	1.27223	0.2504

Analysis of Variance

Source	Sum of Squares	Df	Mean Square	F-Ratio	P-Value
Model	162901	2	81450.6	4.03	0.0776
Residual	121137	6	20189.5		
Total (Corr.)	284038	8			

R-squared = 57.4 percent
R-squared (adjusted for d.f.) = 43.1 percent
Standard Error of Est. = 142.09
Mean absolute error = 97.7838
Durbin-Watson statistic = 1.08615 (P=0.0136)
Lag 1 residual autocorrelation = 0.36375

The new laser power control method worked well and provided long periods of constant temperature growth which allowed a series of thermal images to be captured for use in measuring growth rates as described in Section 3.4.1. The results of the growth rate study are presented in Section 7.2.4. In sum, BN-17F provided useful data regarding the relation among fiber shape, total reagent flow rate through the nozzle, borazine concentration, and maximum deposition temperature. The experiment also provided anecdotal evidence that this reaction is transport limited under the given conditions. Further studies were needed to confirm this finding.

While the new method of controlling deposition temperature was very effective at reducing the random fluctuations in deposition temperature seen in all previous experiments, the observed deposition temperature remained extremely sensitive to the laser power level. A calculation of the heat of the boron nitride deposition reaction was executed to determine if it might be contributing to the apparent sensitivity of the reaction temperature to input laser power. The equation for the reaction was given in Equation 2.2:

$$B_3N_3H_6(g) + \text{xs } N_2(g) \rightarrow 3BN(s) + 3H_2(g) + \text{xs } N_2(g) \tag{2.2}$$

The overall heat of reaction was calculated from the standard enthalpy of formation values. At a temperature of 1200 K, which was well within the range of observed deposition temperatures, the standard enthalpy of formation values for reactant and product species are given in Table 7.15.[110] Note that values for the excess N_2 were not used in the calculation because they would simply cancel out.

Table 7.15: Enthalpy of formation values for constituents in boron nitride deposition reaction.

$B_3N_3H_6$	-525.9 kJ/mol
BN	-250.4 kJ/mol
H_2	0 kJ/mol

The heat of the reaction can be readily computed using Equation 7.9:

$$\Delta H_{rxn} = \sum A_i \Delta H_{f,i} - \sum B_j \Delta H_{f,j} \tag{7.9}$$

where A_i represents the stoichiometric coefficient of product i, $\Delta H_{f,i}$ represents the enthalpy of formation of product i, B_j is the stoichiometric coefficient of reactant j and $\Delta H_{f,j}$ is the enthalpy of formation of reactant j. For the reaction of interest, $(3 \times -250.4) - (1 \times -525.9) = -225.3$ kJ/mol.

In order to compare the magnitude of this exothermic heat of reaction value directly to the incident laser power, the heat of reaction must be multiplied by the growth rate of a typical deposit. Sample 6 of BN-5F was used as a typical fiber. The diameter of this

fiber was 597 μm with a height of 935 μm; the growth time was 6 minutes. The calculated volumetric growth rate was then computed to be 7.27×10^{-4} mm^3/s. Using standard values for the molecular weight of 24.82 g/mol and density of 1.9 g/cm^3 for boron nitride, the volumetric growth rate was converted to a molar growth rate of 5.565e-08 mol/s. Finally, multiplying the heat of reaction by the volumetric growth rate yielded a heat generation rate (power) of -1.25×10^{-5} W. This represents less than 0.0002% of the typical 5 W laser power level used during deposition. In conclusion, it seems unlikely that the heat of the reaction contributed significantly to the observed reaction sensitivity to laser power input.

BN-18F was used to further explore the characteristics found in BN-17F fibers. It was a two factor rotatable central composite response surface experiment. Specifically, it was designed with temperature levels expanded greatly and concentration levels reduced slightly compared to BN-17F. The expanded temperature levels would provide valuable data points to supplement a kinetic analysis. The reduced concentration values would hopefully minimize the white powder coatings surrounding the deposits seen previously. The system pressure was again held constant at 760 Torr. Table 7.16 highlights the experiment conditions used.

The results of BN-18F were varied. All but two of the samples, Sample 5 and Sample 9, yielded measurable fiber deposits. Sample 4 shown in Figure 7.18 was undoubtedly the best deposit of the group. Sample 12 shown in Figure 7.19 was a very small deposit with different morphology than previously observed. All other deposits exhibited volcano effects and severe asymmetry in relation to the direction of the gas nozzle. Table 7.17 summarizes the findings.

A statistical analysis was done to relate the volcano response to the two factors of interest. Figure 7.20 is a pareto chart of the first order factor effects. The vertical line indicates an $\alpha = 0.05$, and factor effects that have a P-Value of < 0.05 have a bar that extends beyond the line. The results show a weak statistical relation between both concentration and

Table 7.16: BN-18F experiment conditions

No.	Borazine Temp (°C)	Carrier Flow (sccm)	Diluent Flow (sccm)	Borazine Flow (sccm)	Total Flow (sccm)	Borazine Conc (mol/m^3)	Max Temp (°C)	Time (min)
1	0.0	5.0	44.5	0.48	50.00	0.43	1650	10.00
2	0.0	5.0	44.5	0.48	50.00	0.43	1650	10.00
3	0.0	5.0	44.5	0.48	50.00	0.43	1650	10.00
4	0.0	5.0	44.5	0.48	50.00	0.43	1014	12.00
5	0.0	0.8	49.1	0.08	50.00	0.07	1650	10.00
6	0.0	8.0	41.2	0.77	50.00	0.69	2100	10.00
7	0.0	8.0	41.2	0.77	50.00	0.69	1200	10.00
8	0.0	5.0	44.5	0.48	50.00	0.43	1650	13.00
9	0.0	2.0	47.8	0.19	50.00	0.17	2100	12.00
10	0.0	9.2	39.9	0.88	50.00	0.79	1650	10.00
11	0.0	5.0	44.5	0.48	50.00	0.43	2286	6.00
12	0.0	2.0	47.8	0.19	50.00	0.17	1200	10.00

Table 7.17: BN-18F experiment results

No.	Volcano (1-7)	Black (1-7)	Diameter (μm)	Height (μm)	Time (s)	Est. Growth Rate (μm/s)
1	N/A	N/A	837	780	600	1.30
2	5.8	1	863	729	600	1.21
3	4.6	1	847	646	600	1.08
4	1	1	275	440	720	0.61
6	5.8	1	1017	954	600	1.59
7	3.4	1	841	866	600	1.44
8	2.2	1	595	591	780	0.76
10	2.2	1	856	771	600	1.29
11	7	1	1264	538	360	1.49
12	1	1	132	118	600	0.20

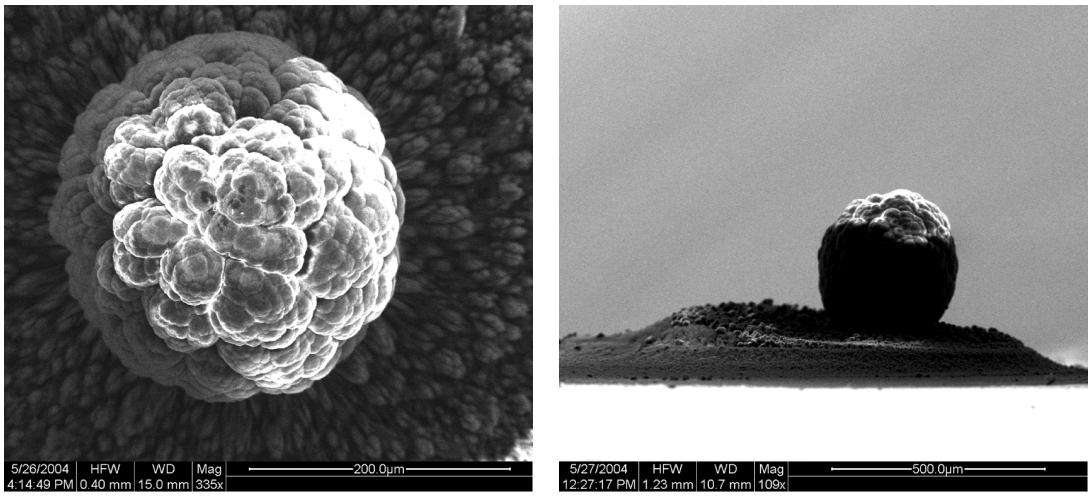

(a) Top View **(b) Side View**

Figure 7.18: BN-18F Sample 4 SEM micrographs

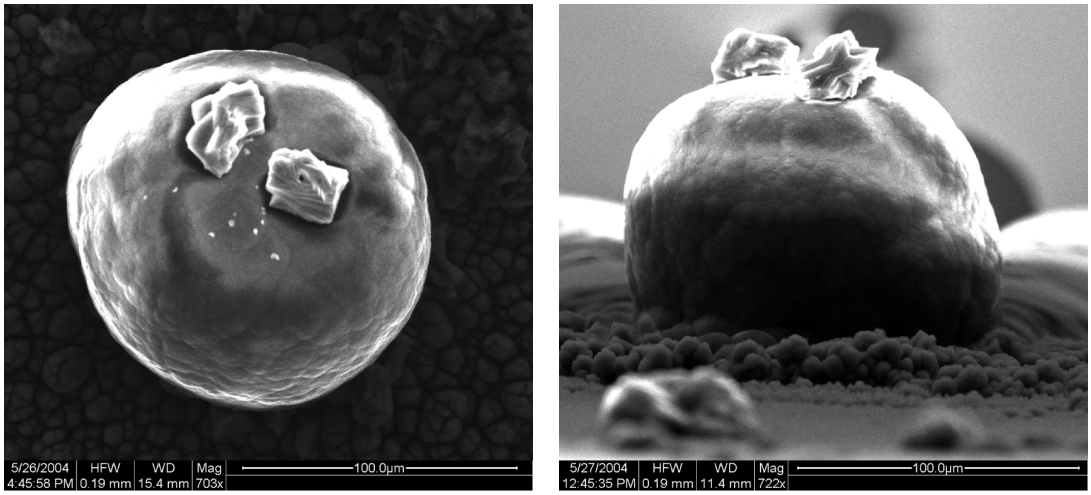

(a) Top View **(b) Side View**

Figure 7.19: BN-18F Sample 12 SEM micrographs

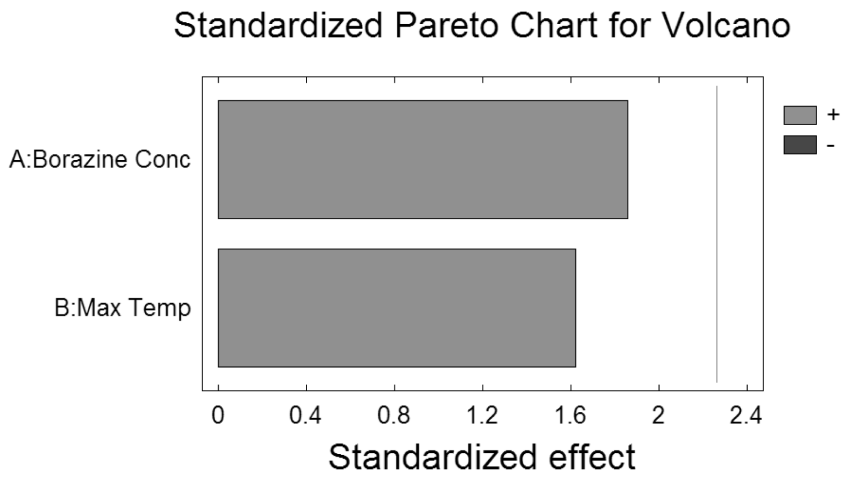

Figure 7.20: First order main effects on boron nitride volcano effect in BN-18F

temperature; however, these factors are known to be related to this volcano phenomenon. It may be that over the factor levels chosen for this experiment it is difficult to statistically resolve the relationship among the factors and the volcano response. Qualitatively, lower temperatures and higher concentration reduces the volcano effect which can be seen in BN-18F by observing the data.

A statistical analysis was also done to relate the estimated deposit growth rate to the temperature and borazine concentration factors. Figure 7.21 is the standardized pareto chart of the first and second order main effects and the first order interactions on the growth rate response variable. A very strong statistical relationship exists between the borazine concentration and the growth rate while no other factors are significant. The existence of a relationship between concentration and growth rate and little relationship between growth rate and temperature suggests that this process was in the transport–limited regime. However, the crude measurements of growth rates provided here could be significantly impacted by the presence of the volcano effect; therefore, a more rigorous analysis was required for determining the rate–limiting regime.

The results from all boron nitride fiber experiments were used to choose appropriate parameter levels for a final 4–factor rotatable central composite designed experiment. The

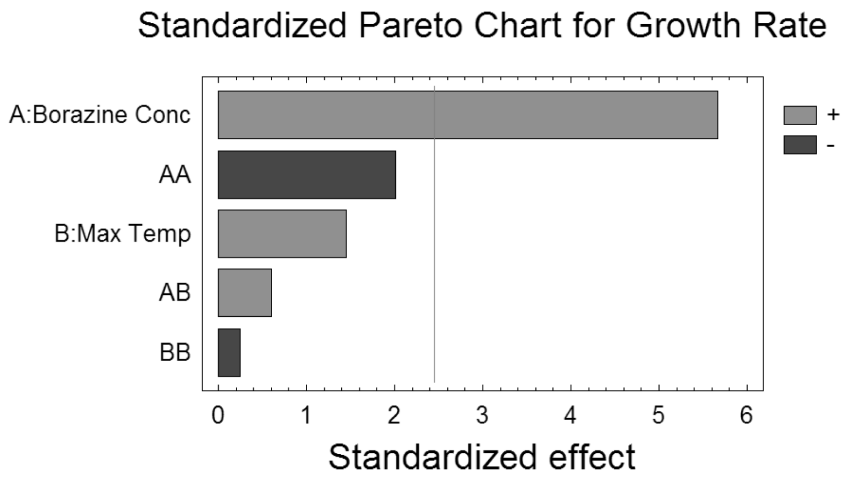

Figure 7.21: First and second order main effects on estimated boron nitride growth rate in BN-18F

factors studied were pressure, total nozzle flow rate, $B_3N_3H_6$ concentration, and temperature. All experiments were done on tungsten sheet substrates and used manual control via the knob on laser control module. The procedure was to initiate each experiment with a high power, approximately 80 W, until growth was seen to emerge from the substrate surface on the thermal imager screen. The power was then reduced to the appropriate level to maintain desired temperature. The sensitivity of BN deposition to laser power remained an issue and limited the controllability to about $\pm 50^{\circ}$C.

The factor levels used are given in Table 7.18. The carrier and diluent flow rates were computed for each run such that they yielded the desired factor levels. The borazine vaporizer was kept at $0 \pm 1^{\circ}$C throughout the experiment. The target time for each experiment was 5 minutes, but some runs produced slower or faster growth rates and the time was adjusted to allow all fibers to reach similar heights.

In general, the results of BN-19F were well–defined fibers over 1 mm tall with different shapes, morphologies, and color. Figure 7.22 contains thumbnail images of all samples that produced bulk deposit. Several distinct differences among the samples are obvious in the figure. First, the color of the fiber material varied from a white, opaque material as in

Table 7.18: BN-19F experiment conditions

No.	Total Press (Torr)	Carrier Flow (sccm)	Diluent Flow (sccm)	Borazine Flow (sccm)	Total Flow (sccm)	Borazine Conc (mol/m^3)	Avg Max Temp (°C)	Time (min)
1	540	2.52	19.62	0.35	22.5	0.50	1100	5
2	540	4.20	2.70	0.59	7.5	2.50	1100	6.25
3	540	12.61	8.11	1.77	22.5	2.50	1100	5
4	540	12.61	8.11	1.77	22.5	2.50	1100	5
5	540	12.61	8.11	1.77	22.5	2.50	900	5
6	540	21.02	13.52	2.96	37.5	2.50	1100	5
7	540	12.61	8.11	1.77	22.5	2.50	1300	5
8	100	4.81	8.11	9.58	22.5	2.50	1100	2
9	320	4.56	9.24	1.20	15.0	1.50	1000	5
10	320	4.56	9.24	1.20	15.0	1.50	1200	5
11	320	21.27	3.14	5.59	30.0	3.50	1000	4
12	320	9.11	18.49	2.40	30.0	1.50	1200	5
13	320	21.27	3.14	5.59	30.0	3.50	1200	3
14	320	9.11	18.49	2.40	30.0	1.50	1000	5
15	320	10.63	1.57	2.79	15.0	3.50	1000	5
16	320	10.63	1.57	2.79	15.0	3.50	1200	1.5
17	760	24.50	3.14	2.35	30.0	3.50	1000	6
18	760	12.25	1.57	1.18	15.0	3.50	1000	4
19	760	10.50	18.49	1.01	30.0	1.50	1000	5
20	760	12.25	1.57	1.18	15.0	3.50	1200	5
21	760	24.50	3.14	2.35	30.0	3.50	1200	4
22	760	5.25	9.24	0.50	15.0	1.50	1000	5
23	760	5.25	9.24	0.50	15.0	1.50	1200	5
24	760	10.50	18.49	1.01	30.0	1.50	1200	5
25	320	4.56	9.24	1.20	15.0	1.50	1000	7
26	540	2.52	19.62	0.35	22.5	0.50	1100	10
27	540	4.20	2.70	0.59	7.5	2.50	1100	13
28	540	12.61	8.11	1.77	22.5	2.50	1100	3.5
29	980	13.41	8.11	0.98	22.5	2.50	1100	10
30	540	14.83	4.38	3.29	22.5	4.50	1100	4

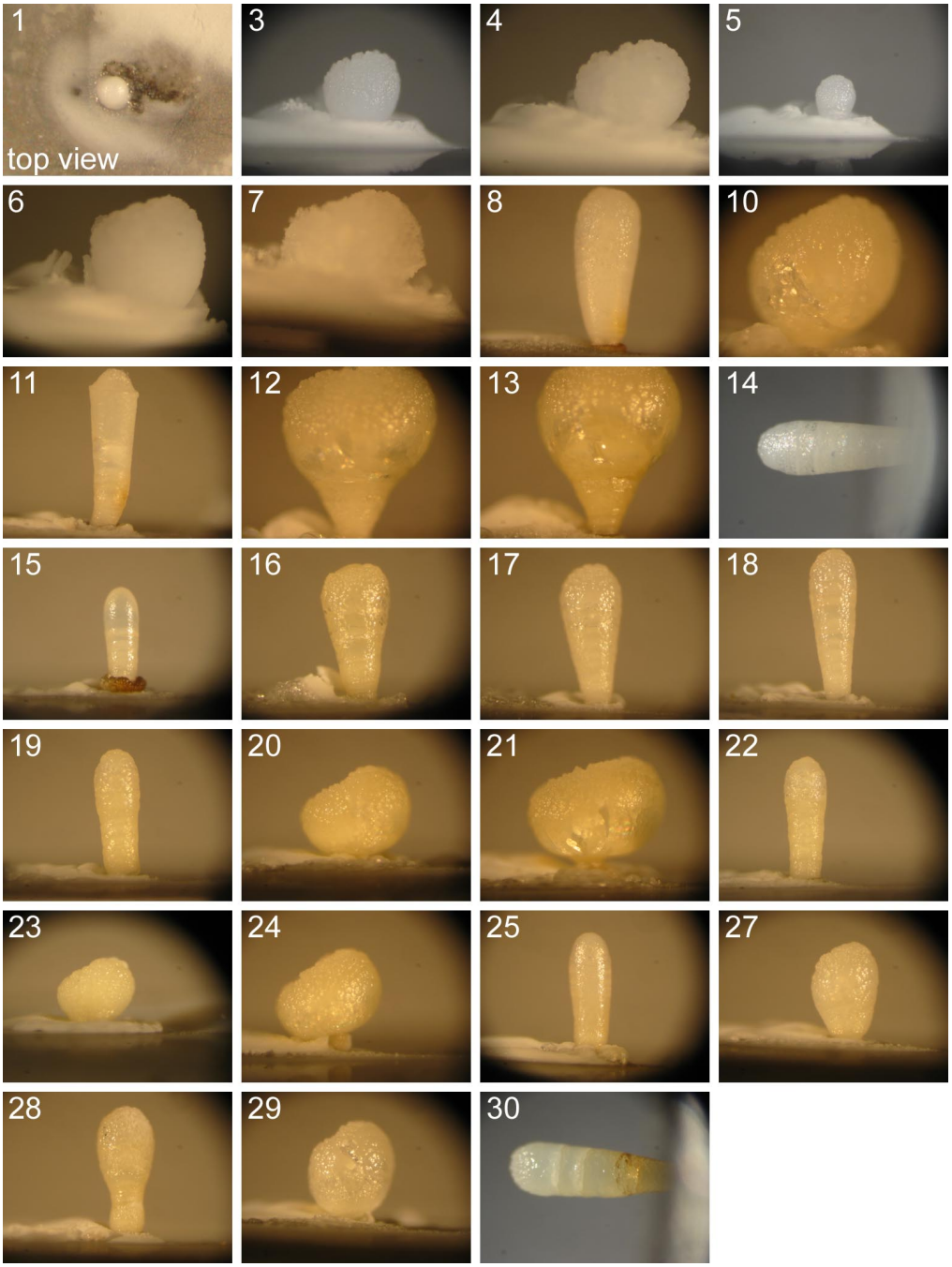

Figure 7.22: Optical images of BN-19F fibers

Sample 4 to a clear, translucent material as in Sample 15. The area surrounding the deposits was covered with varying degrees of white powder. The overall shape of the deposits varied from tall slender fibers such as Sample 22 to bulging balloon–shaped structures such as Samples 12 and 13. It is evident in the figure that some of the fibers had the common volcano shape. Some of the fibers also show an asymmetry in their overall shape relative to the direction of gas flow. Most of these attributes were quantified and the responses were used in regression analyses to study the significant factors and develop quantitative relationships between the factor levels and the responses. Equation 7.10 represents the full regression equation for any response, Y, in the four factor study:

$$\begin{aligned} Y &= \beta_0 + \beta_1 A + \beta_2 B + \beta_3 C + \beta_4 D + \beta_5 A^2 + \beta_6 B^2 + \beta_7 C^2 + \beta_8 D^2 \\ &\quad + \beta_9 AB + \beta_{10} AC + \beta_{11} AD + \beta_{12} BC + \beta_{13} BD + \beta_{14} CD \end{aligned} \tag{7.10}$$

where A is pressure, B is total flow, C is $B_3N_3H_6$ concentration, D is temperature, and the β's are the regression coefficients. The general procedure was to do a regression fit to this full model and then reduce the model by eliminating factors that were not statistically significant near a 95% confidence level. The reduced model results are most pertinent and are the ones presented below for the different attributes.

The first attribute studied was the powder formation surrounding the fiber deposit. In the fabrication of the dispenser cathode assembly, it was desirable to minimize the formation of this powder. A rating between 1 and 5 was assigned to each sample where 1 represented minimal powder formation and 5 represented heavy powder formation. The regression output is given in Table 7.19 along with a standardized pareto chart illustrating the relative significance of different factors.

The analysis revealed that all four factors were significant at a 95% confidence level. The second order concentration (CC) and pressure (AA) were both negatively correlated to powder formation while maximum temperature (D) and total flow (B) showed a positive relationship. Thus, a reduction in powder formation should accompany an increase in

Table 7.19: BN-19F powder formation multiple regression analysis

Estimated Effects for Powder Formation

average	= 3.81944	+/- 0.17664
B:Total Flow	= 0.458333	+/- 0.216339
D:Max Temp	= 0.708333	+/- 0.216339
AA	= -1.00521	+/- 0.20947
CC	= -1.38021	+/- 0.20947

Analysis of Variance

Source	Sum of Squares	Df	Mean Square	F-Ratio	P-Value
B:TotalFlow	1.26042	1	1.26042	4.49	0.0457
D:MaxTemp	3.01042	1	3.01042	10.72	0.0035
AA	6.46684	1	6.46684	23.03	0.0001
CC	12.1918	1	12.1918	43.42	0.0000
Total error	6.17795	22	0.280816		
Total (corr.)	26.1852	26			

R-squared = 76.4067 percent
R-squared (adjusted for d.f.) = 72.117 percent
Standard Error of Est. = 0.529921
Mean absolute error = 0.385545
Durbin-Watson statistic = 1.66708 (P=0.1728)
Lag 1 residual autocorrelation = 0.124866

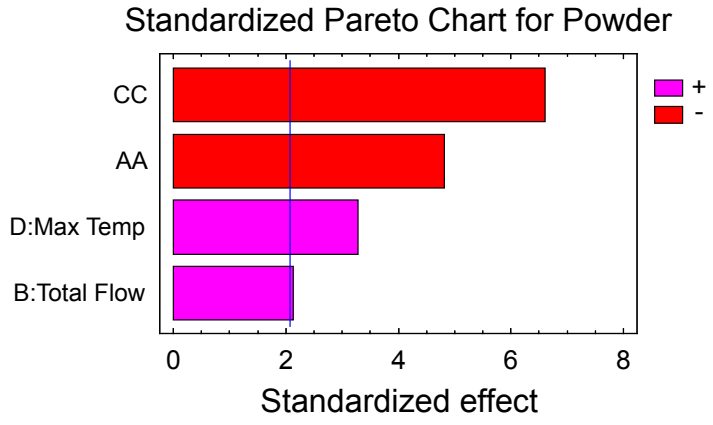

pressure or concentration or a reduction in temperature or total flow.

The next attribute studied was the volcano effect. Again, a scale of 1–5 was used to quantify the relative volcano shape where 1 represented no volcano and 5 represented a significant volcano. The output from the regression analysis given in Table 7.20 revealed that temperature (D) was the dominant factor with increasing temperature causing a more severe volcano. Other significant factors included the second order concentration (CC) which reduced the volcano effect and pressure (A) and and pressure–temperature interaction (AD) which both had a positive relationship with volcano severity.

Another attribute of the deposits that it was desirable to minimize was the asymmetrical shape such as can be seen in Sample 24 of Figure 7.22. A scale of 1 to 5 was used to relate the degree of asymmetry to the factor levels. The regression output is given in Table 7.21. Again, temperature is shown to be the most important factor with a strong positive relationship to asymmetry. Increasing pressure (A) and the pressure–temperature interaction (AD) are also shown to be correlated with a more asymmetrical shape. The second order concentration (CC) had a negative relationship with asymmetry.

Figure 7.22 shows that the BN fibers varied greatly in their shape profile. Two metrics were used to quantify the shape: maximum fiber diameter and the ratio of maximum diameter to minimum diameter. The results of the regression analyses are given in Tables 7.22 and 7.23.

The maximum diameter was shown to be strongly linked to the deposition temperature. This was consistent with observations made during the deposition process where increased temperatures correlated to increased diameters. Other factors shown to be important were the second order concentration (CC), total flow (B), and pressure–concentration (AC) interaction. The second order concentration showed a negative relation to maximum diameter while other factors exhibited a positive relationship.

The degree to which the maximum diameter differed from the minimum diameter of some deposits was remarkable. For example, Sample 21 was over 4.6 times wider at its

Table 7.20: BN-19F volcano effect multiple regression analysis

Estimated Effects for Volcano Effect

average	= 2.18333	+/- 0.180102
A:Pressure	= 0.541667	+/- 0.284767
D:MaxTemp	= 1.70833	+/- 0.284767
AD	= 0.5625	+/- 0.348767
CC	= -0.6625	+/- 0.270154

Analysis of Variance

Source	Sum of Squares	Df	Mean Square	F-Ratio	P-Value
A:Pressure	1.76042	1	1.76042	3.62	0.0703
D:MaxTemp	17.5104	1	17.5104	35.99	0.0000
AD	1.26563	1	1.26563	2.60	0.1210
CC	2.92604	1	2.92604	6.01	0.0226
Total error	10.7042	22	0.486553		
Total (corr.)	34.1667	26			

R-squared = 68.6707 percent
R-squared (adjusted for d.f.) = 62.9745 percent
Standard Error of Est. = 0.697534
Mean absolute error = 0.421296
Durbin-Watson statistic = 1.91696 (P=0.3905)
Lag 1 residual autocorrelation = -0.0022658

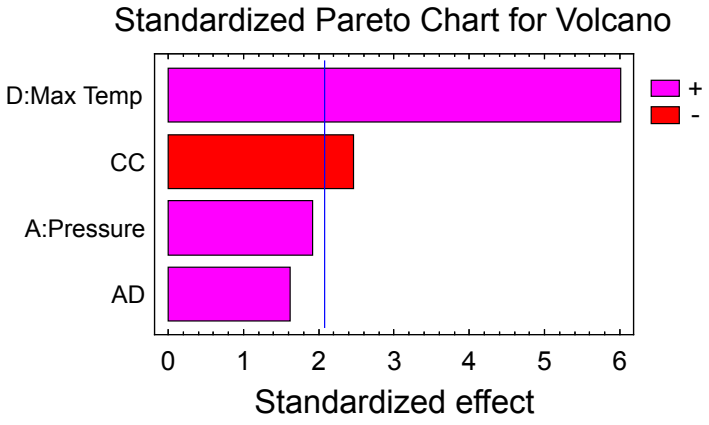

Table 7.21: BN-19F asymmetry multiple regression analysis

Estimated Effects for Asymmetry

average	= 2.66667	+/- 0.235702
A:Pressure	= 1.0	+/- 0.372678
D:MaxTemp	= 2.33333	+/- 0.372678
AD	= 1.0	+/- 0.456435
CC	= -0.833333	+/- 0.353553

Analysis of Variance

Source	Sum of Squares	Df	Mean Square	F-Ratio	P-Value
A:Pressure	6.0	1	6.0	7.20	0.0136
D:MaxTemp	32.6667	1	32.6667	39.20	0.0000
AD	4.0	1	4.0	4.80	0.0393
CC	4.62963	1	4.62963	5.56	0.0277
Total error	18.3333	22	0.833333		
Total (corr.)	65.6296	26			

R-squared = 72.0655 percent
R-squared (adjusted for d.f.) = 66.9865 percent
Standard Error of Est. = 0.912871
Mean absolute error = 0.549383
Durbin-Watson statistic = 2.29545 (P=0.2035)
Lag 1 residual autocorrelation = -0.17197

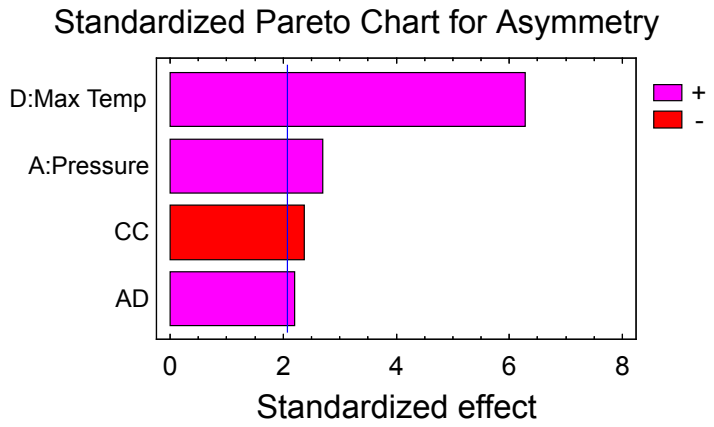

Table 7.22: BN-19F maximum diameter multiple regression analysis

Estimated Effects for Maximum Diameter

average	= 752.206	+/- 41.0784
B:TotalFlow	= 186.312	+/- 64.9506
D:MaxTemp	= 536.061	+/- 64.9506
AC	= 202.049	+/- 79.5479
CC	= -197.181	+/- 61.6175

Analysis of Variance

Source	Sum of Squares	Df	Mean Square	F-Ratio	P-Value
B:TotalFlow	208272.0	1	208272.0	8.23	0.0089
D:MaxTemp	1.72417E6	1	1.72417E6	68.12	0.0000
AC	163296.0	1	163296.0	6.45	0.0187
CC	259203.0	1	259203.0	10.24	0.0041
Total error	556852.0	22	25311.5		
Total (corr.)	2.91179E6	26			

R-squared = 80.8759 percent
R-squared (adjusted for d.f.) = 77.3988 percent
Standard Error of Est. = 159.096
Mean absolute error = 110.435
Durbin-Watson statistic = 2.52939 (P=0.1134)
Lag 1 residual autocorrelation = -0.302065

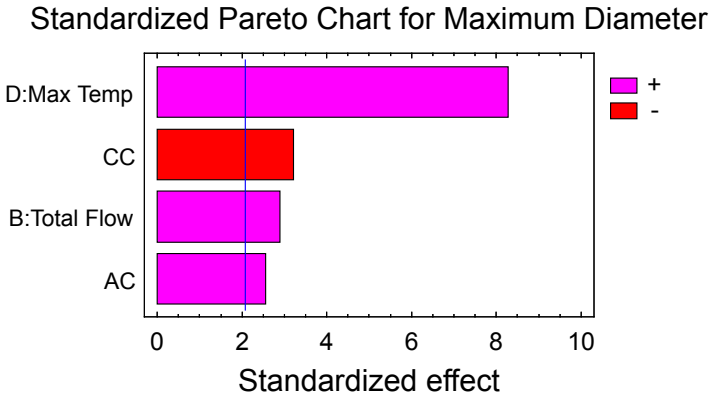

Table 7.23: BN-19F diameter ratio multiple regression analysis

Estimated Effects for Diameter Ratio

average	= 1.97632	+/- 0.218945
B:TotalFlow	= 0.688373	+/- 0.346182
C:B3N3H6Conc	= 0.569715	+/- 0.346182
D:MaxTemp	= 1.06498	+/- 0.346182
AA	= 0.442903	+/- 0.328417
AD	= -0.580998	+/- 0.423984
BD	= 0.839004	+/- 0.423984

Analysis of Variance

Source	Sum of Squares	Df	Mean Square	F-Ratio	P-Value
B:TotalFlow	2.84314	1	2.84314	3.95	0.0606
C:B3N3H6Conc	1.94745	1	1.94745	2.71	0.1154
D:MaxTemp	6.80504	1	6.80504	9.46	0.0060
AA	1.30775	1	1.30775	1.82	0.1925
AD	1.35024	1	1.35024	1.88	0.1858
BD	2.81571	1	2.81571	3.92	0.0618
Total error	14.381	20	0.719051		
Total (corr.)	31.4504	26			

R-squared = 54.2739 percent
R-squared (adjusted for d.f.) = 40.5561 percent
Standard Error of Est. = 0.847969
Mean absolute error = 0.597194
Durbin-Watson statistic = 1.41786 (P=0.0620)
Lag 1 residual autocorrelation = 0.266703

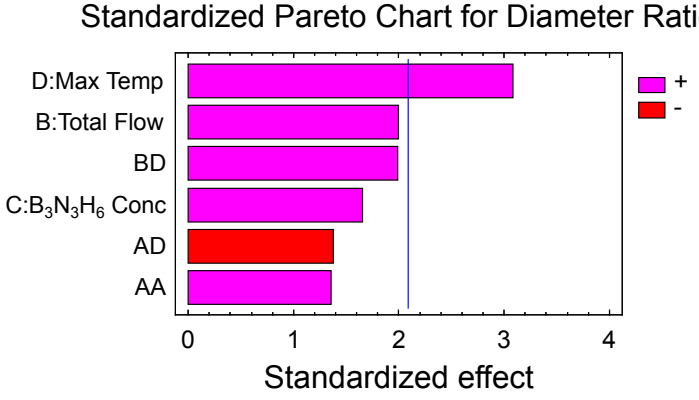

maximum diameter than its minimum diameter. Note that without exception, the minimum diameter of all samples occurred near the base and the substrate interface. This was believed to be related to the nodular growth preferred by the material. After a growth node was initiated, the BN preferred to deposit on itself rather than the tungsten substrate. This could be due to substrate material properties or something inherent in the process. In the line experiments to be discussed in Section 7.3, this issue becomes very significant.

At greater than a 95% confidence level, the diameter ratio is related to temperature (D) with an increase in temperature yielding an increased ratio. A number of other variables were more loosely correlated with the effect including total flow (B), $B_3N_3H_6$ concentration (C), second order pressure (AA), and the total flow–temperature (BD) and pressure–temperature (AD) interactions. All factors had a positive relation to the diameter ratio except the AD interaction.

The balloon shape exemplified by fibers with high diameter ratios could be seen to emerge on the thermal imager as the deposit grew. Interestingly, during the growth process, the vertical growth rate at the center of the deposit seemed to decelerate from its initial velocity and the diametral growth rate seemed to remain constant. This behavior could be related to several things. First, Section 5.3.5.4 discussed how the change in substrate conductivity and conduction paths leads to an increase in fiber diameter as the growth rises from the surface. Also, for increased stability, the substrate was not moved coaxially as the fibers grew which means that the laser spot diameter could have increased slightly over the height of a fiber.

Another cause for this shape could be an implication of a transport–limited process. Specifically, changes in $B_3N_3H_6$ concentration due to temperature, changes in concentration boundary layer thickness due to flow characteristics, and changes in the mass diffusion coefficients due to temperature and/or pressure could effect the surface deposition rate. Thermal diffusion of the reagent species also becomes a question. These phenomena are studied further in Chapter 8.

The fact that both kinetic and transport–limited variables appeared significant in the regression analysis of diameter ratio suggested that the shape might be an implication of all these factors.

The fiber growth velocity was another response of interest. For many samples, the growth velocity was measured from a series of thermal images. From those where thermal images were unavailable, measurements were made by dividing the fiber height by the growth time (this was the time when fiber growth was actually observed on the thermal imager, not the entire time the laser was engaged). In order to remain consistent with the assumption that the maximum fiber temperature occurred at the fiber tip, only samples with a volcano rating of ≤ 2 were included in the analysis. The results of the growth velocity regression analysis are included in Table 7.24.

Both first (A) and second order (AA) pressure effects were shown to significantly influence the growth rate with a decrease in pressure causing an increase in growth velocity. The AA effect on growth rate was positive. $B_3N_3H_6$ concentration (C) also showed a positive effect on growth rate. These findings are very consistent with a transport–limited process. Decreased pressure enhances ordinary diffusion through its effect on the diffusion coefficient while increasing concentration directly increases the diffusive flux to the surface.

Several of the fibers grown in BN-19F were mounted in epoxy and sectioned to allow better observation of the internal features of the deposits. Samples 13 and 15 were representative of two extremes of the experimental results. Optical images of these deposits are shown in Figures 7.23 and 7.24. Note that when mounted, both of these fibers developed a bubble in the epoxy near their base as shown by the large spherical anomaly in the figures. Sample 13 was a large deposit with a high diameter ratio. The cross section shows it to have a very large void in its center. The void is particularly obvious because the microscope's light source was shining down on the fiber. The deposit appears semi–translucent with a rough morphology.

Sample 15 was a smaller deposit that was very translucent throughout the fiber body.

Table 7.24: BN-19F growth velocity multiple regression analysis

Estimated Effects for Growth Velocity

average	= 4.5709	+/- 0.911254
A:Pressure	= -5.73746	+/- 1.45685
C:B3N3H6Conc	= 3.5708	+/- 1.32766
AA	= 3.39288	+/- 1.1743
AD	= -1.42052	+/- 1.93422

Analysis of Variance

Source	Sum of Squares	Df	Mean Square	F-Ratio	P-Value
A:Pressure	128.326	1	128.326	15.51	0.0015
C:B3N3H6Conc	59.8498	1	59.8498	7.23	0.0176
AA	69.0699	1	69.0699	8.35	0.0119
AD	4.46262	1	4.46262	0.54	0.4748
Total error	115.834	14	8.27386		
Total (corr.)	391.533	18			

R-squared = 70.4152 percent
R-squared (adjusted for d.f.) = 61.9624 percent
Standard Error of Est. = 2.87643
Mean absolute error = 1.93979
Durbin-Watson statistic = 1.02069 (P=0.0021)
Lag 1 residual autocorrelation = 0.475445

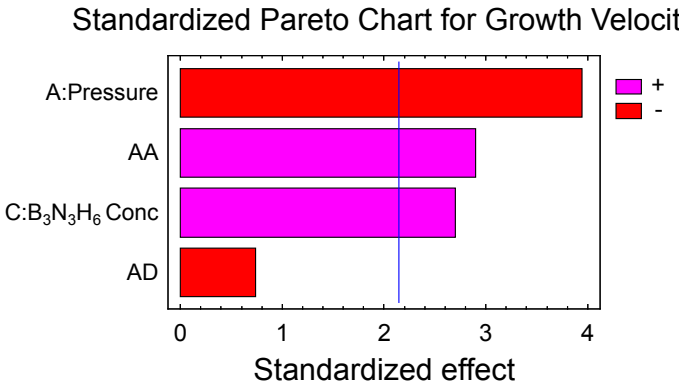

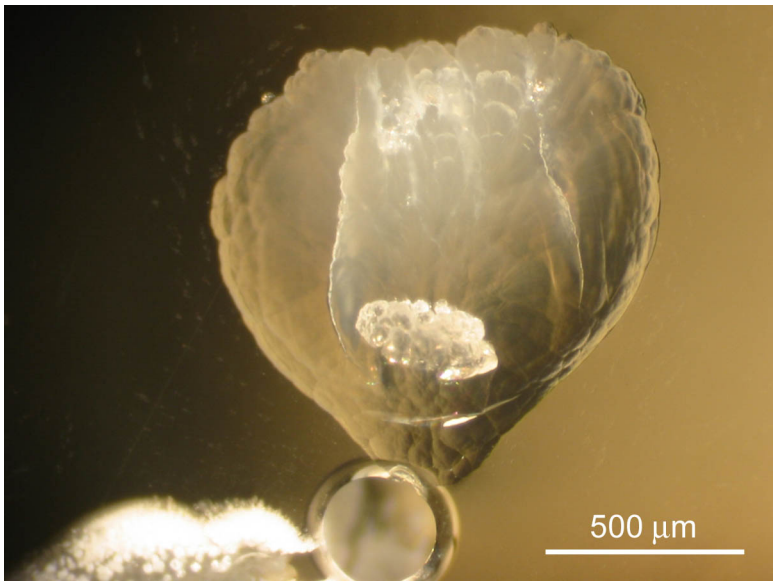

Figure 7.23: Cross section of Sample 13 from BN-19F

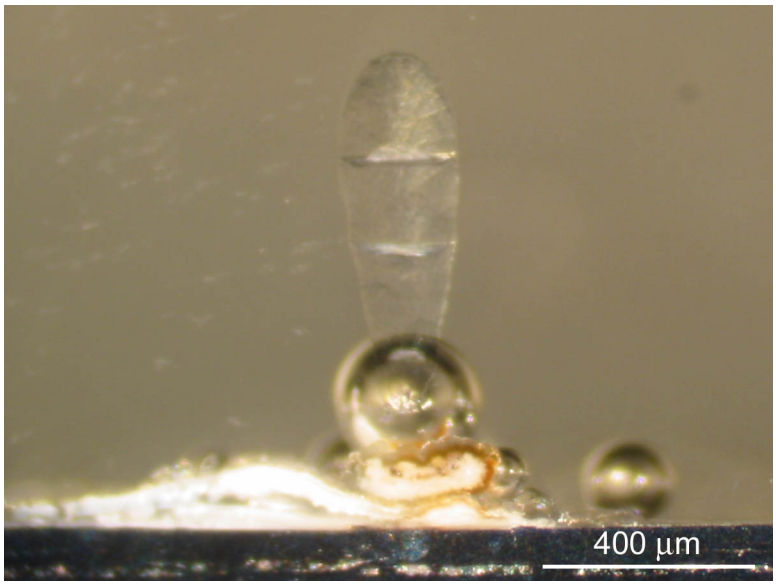

Figure 7.24: Cross section of Sample 15 from BN-19F

It is shown to have two distinct flaws oriented perpendicular to the growth direction that extend throughout the fiber diameter. These flaws are likely internal cracks. The degree of translucency of fibers was related to the number and size of internal cracks or voids. The base of Sample 15 consisted of several materials with very different appearances. Like many other BN deposits, there was a region of white powder near the substrate. Interestingly, some of this powder was contained in what looked like a shell of yellow–brown translucent material that had a glassy appearance. Unfortunately, during polishing, the region connecting the main fiber body to this glassy shell was removed. The complexity of materials near the substrate surface could be a result or a cause of the dynamic behavior seen during the initial BN growth period.

A fiber more representative of the typical result from BN-19F is shown in Figure 7.25. This material again has a translucent color that is interrupted by periodic cracks across the fiber diameter. The fiber has a very layered appearance. It is difficult to tell from this image whether the discoloration at the interface between each of these small "layers" is a crack or it represents a change in some material property. Growth appears to have originated from two distinct nodes at the surface. As growth continued, the two nodes merged into a single structure. In addition to the many small "layers" that appear in the structure, there are at least four large growth sections. These sections are defined by large, obvious cracks that extend across the fiber diameter. Internally, it appears that these growth sections represent a discontinuity in the growth process that could have resulted in growth re–initiation. However, the external shape of the deposit does not have such well–defined sections. Overall, the shape and internal features of LCVD boron nitride fibers shown here are very similar to those of LCVD carbon fibers.

Efforts were made to view the BN fibers in Figures 7.23, 7.24, and 7.25 using an SEM; however because neither BN nor mounting epoxy are good electrical conductors, the optical images shown here provided better information. An EDX analysis was done on all three of these fibers to ensure the material was indeed boron nitride. The EDX output was similar

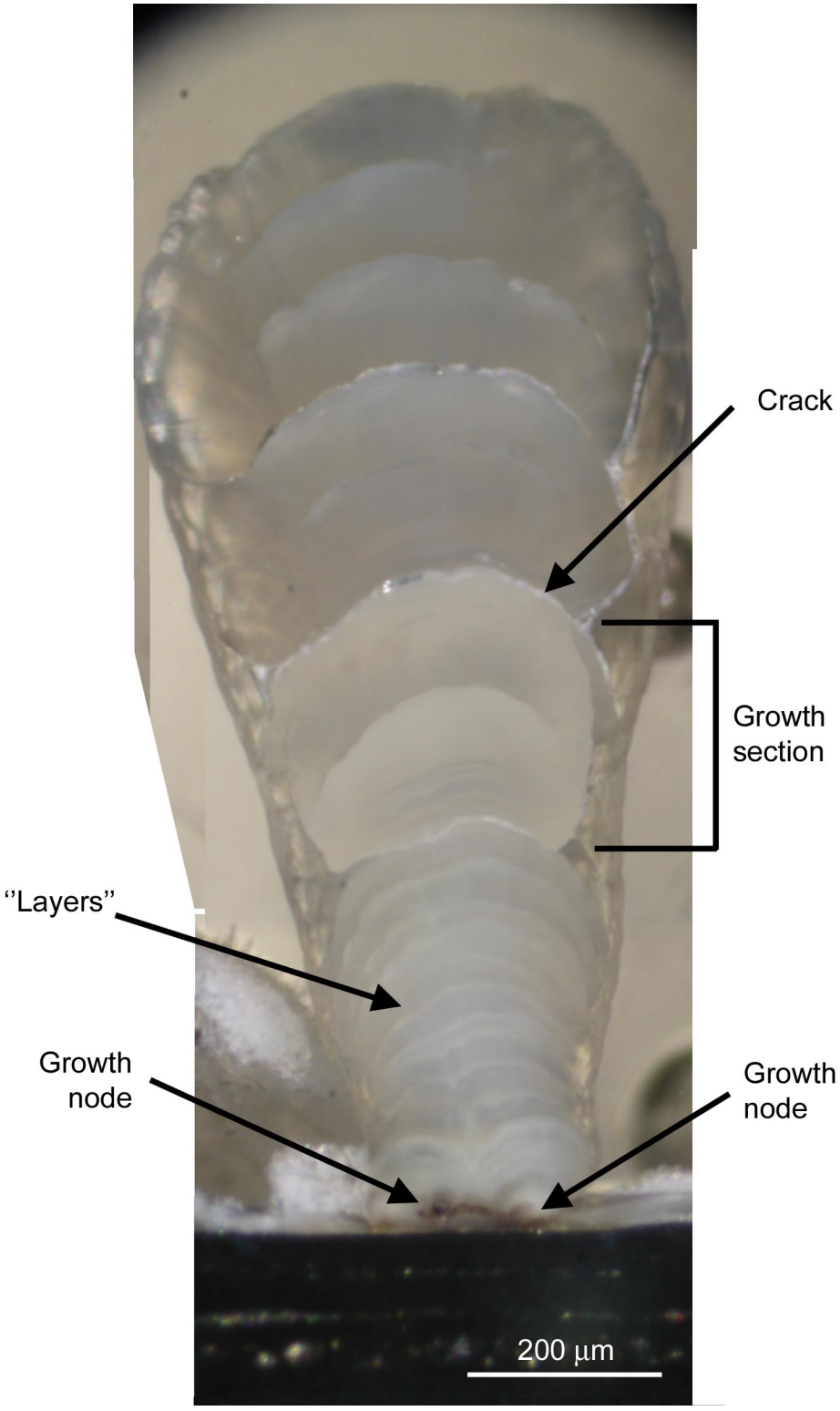

Figure 7.25: Cross section of Sample 16 from BN-19F

for all samples and an example is shown in Figure 7.26. It reveals that boron and nitrogen are the most dominant elements. The ratio of B:N was approximately 1:3, which is less than the 1:1 ratio of stoichiometric boron nitride. A commercially produced high purity boron nitride standard was analyzed for comparison.[111] Figure 7.27 is the response from the hot–pressed BN sample. The standard is shown to have a similar B:N ratio as was measured for the BN fibers of BN-19F. The trace amounts of Al and O in the response are most likely related to the polishing process that used aluminum oxide powder. The discrepancy from the B:N ratio of 1:1 could be related to the inherent ease of detecting nitrogen elements compared to boron elements due to their larger atomic mass.

7.2.4 Boron Nitride Fiber Growth Kinetics

In an effort to gain insight into the rate–limiting mechanism of boron nitride LCVD using the borazine reagent system, a kinetics analysis was performed using a combination of data from several of the BN fiber experiments. The set of fibers used were chosen based on several criteria. The sensitivity of the boron nitride deposition temperature to the laser power input prohibited extensive use of the real–time automatic temperature control subsystem. The use of manual control inevitably led to process temperature variations during fiber growth. In order to extract useful growth rate data over periods of relatively constant temperature growth, the growth rates were measured using the thermal imager as described in Section 3.4.1. For this technique to be viable, only fibers which were accompanied by a sufficient number of thermal images, and that exhibited no volcano effect were eligible for consideration in the analysis. A few fibers that did not have sufficient thermal images, but had extensive reliable experimental data were included by dividing the measured fiber height over the growth time (not the length of time the laser was engaged). The subset of boron nitride fibers meeting these criteria is given in Table 7.25 along with the pertinent experiment conditions.

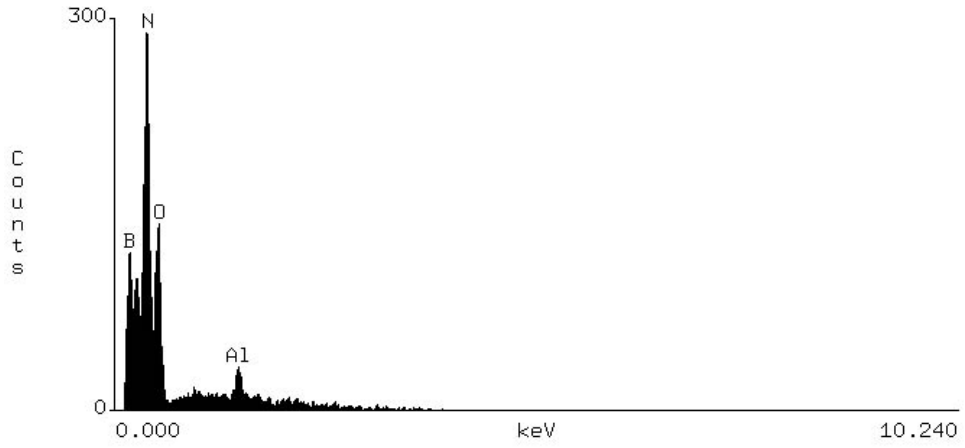

Figure 7.26: EDX output from analysis of BN-19F fibers

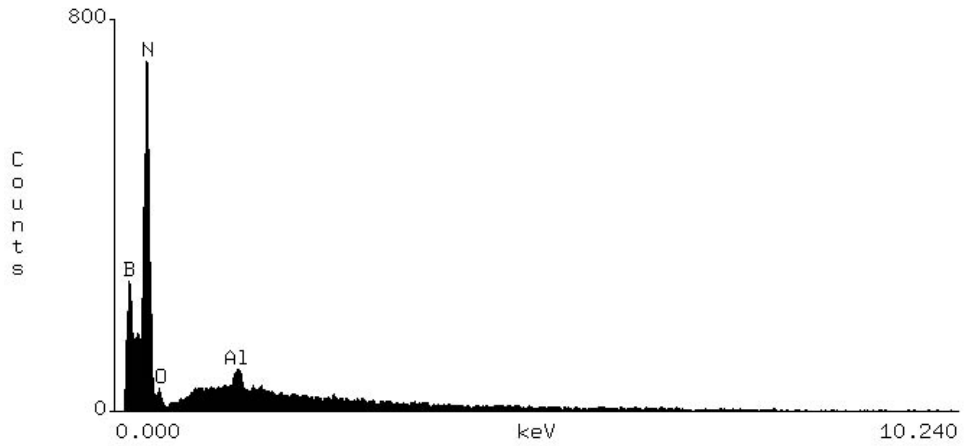

Figure 7.27: EDX output from reference boron nitride sample

Table 7.25: Data used in kinetic regression analysis for BN fibers

Experiment	Sample	Temp, T_{max} (°C)	Adj Conc, C_{CH_4} (mol/m^3)	Press (Torr)	Dep Vel (μm/s)
BN-6	2-1	1290	0.625	760	4.46
BN-6	3-1	1373	0.632	760	1.73
BN-6	3-2	1386	0.625	760	3.46
BN-6	4-1	1453	0.729	760	3.46
BN-6	4-2	1399	0.764	760	4.93
BN-6	5-1	1419	0.837	760	4.69
BN-6	7-1	1394	0.948	760	3.44
BN-6	8-1	1459	0.904	760	6.51
BN-6	8-2	1370	0.977	760	4.39
BN-6	9-1	1353	1.002	760	7.31
BN-17F	8	1297	0.112	760	0.70
BN-18F	4	1287	0.035	760	0.59
BN-18F	12	1473	0.010	760	0.16
BN-19F	1	1373	0.620	100	17.03
BN-19F	2	1273	0.956	320	14.43
BN-19F	3	1473	0.796	320	17.47
BN-19F	4	1273	0.409	320	8.74
BN-19F	6	1273	0.956	320	8.98
BN-19F	7	1273	0.409	320	5.30
BN-19F	8	1473	0.796	320	6.86
BN-19F	9	1473	0.341	320	5.25
BN-19F	10	1373	0.620	540	4.49
BN-19F	11	1373	0.620	540	3.28
BN-19F	12	1373	0.124	540	0.12
BN-19F	14	1373	0.620	540	5.19
BN-19F	15	1173	0.758	540	2.95
BN-19F	17	1373	1.117	540	5.77
BN-19F	19	1273	0.955	760	7.25
BN-19F	22	1273	0.410	760	4.70
BN-19F	23	1273	0.955	760	5.74
BN-19F	24	1273	0.409	760	4.25

Simple linear regression analyses were done on the data in Table 7.25 to characterize the relationship between growth rate and temperature (Table 7.26), growth rate and borazine concentration (Table 7.27), and growth rate and pressure (Table 7.28). The regression output from the analyses confirmed what was visibly apparent. There was not a statistically significant relationship between growth rate and temperature, but there was a strong relationship between growth rate and borazine concentration and growth rate and pressure. These findings strongly indicated that the deposition of BN fibers using $B_3N_3H_6$ under the conditions studied is a transport–limited process. Further support of this finding is presented in Chapter 8.

Table 7.26: Regression output for BN fiber growth velocity vs deposition temperature

Dependent variable: Deposition Velocity
Independent variable: Temp

Parameter	Estimate	Standard Error	T Statistic	P-Value
Intercept	2.34766	13.5102	0.173769	0.8633
Slope	0.00240314	0.00996335	0.241198	0.8111

Analysis of Variance

Source	Sum of Squares	Df	Mean Square	F-Ratio	P-Value
Model	1.07537	1	1.07537	0.06	0.8111
Residual	536.057	29	18.4847		
Total (Corr.)	537.132	30			

Correlation Coefficient = 0.0447444
R-squared = 0.200206 percent
R-squared (adjusted for d.f.) = -3.24117 percent
Standard Error of Est. = 4.29939
Mean absolute error = 2.87313
Durbin-Watson statistic = 0.985337 (P=0.0009)
Lag 1 residual autocorrelation = 0.505173

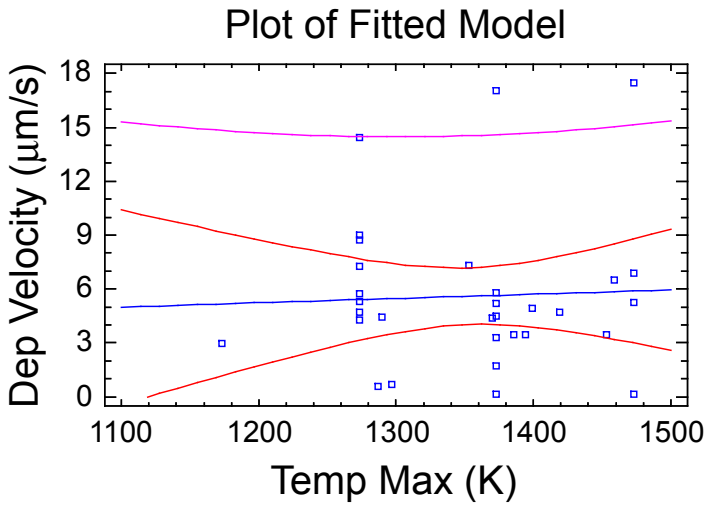

Table 7.27: Regression output for BN fiber growth velocity vs temperature adjusted $B_3N_3H_6$ concentration

Dependent variable: Deposition Velocity
Independent variable: Adj Conc

Parameter	Estimate	Standard Error	T Statistic	P-Value
Intercept	1.54818	1.64712	0.939932	0.3550
Slope	6.2596	2.3097	2.71014	0.0112

Analysis of Variance

Source	Sum of Squares	Df	Mean Square	F-Ratio	P-Value
Model	108.548	1	108.548	7.34	0.0112
Residual	428.584	29	14.7788		
Total (Corr.)	537.132	30			

Correlation Coefficient = 0.449541
R-squared = 20.2088 percent
R-squared (adjusted for d.f.) = 17.4573 percent
Standard Error of Est. = 3.84432
Mean absolute error = 2.53756
Durbin-Watson statistic = 0.799843 (P=0.0001)
Lag 1 residual autocorrelation = 0.598888

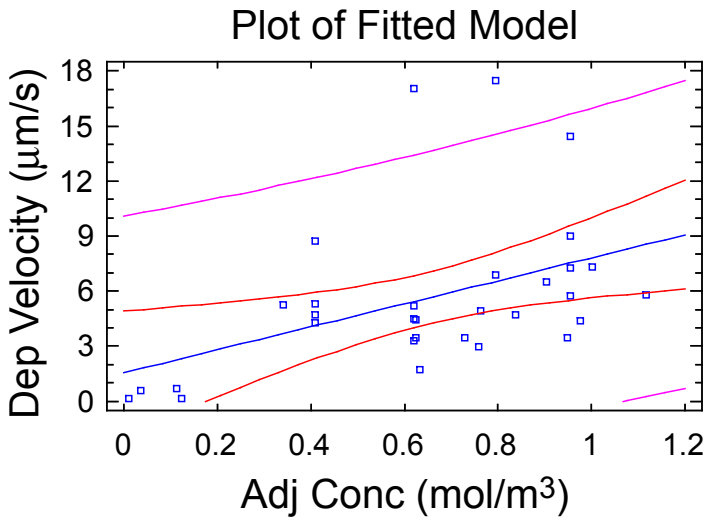

Table 7.28: Regression output for BN fiber growth velocity vs total pressure

Dependent variable: Deposition Velocity
Independent variable: Pressure

Parameter	Estimate	Standard Error	T Statistic	P-Value
Intercept	13.7724	1.81331	7.59519	0.0000
Slope	-0.0136927	0.00287923	-4.75566	0.0001

Analysis of Variance

Source	Sum of Squares	Df	Mean Square	F-Ratio	P-Value
Model	235.351	1	235.351	22.62	0.0001
Residual	301.781	29	10.4062		
Total (Corr.)	537.132	30			

Correlation Coefficient = -0.661938
R-squared = 43.8162 percent
R-squared (adjusted for d.f.) = 41.8789 percent
Standard Error of Est. = 3.22587
Mean absolute error = 2.48889
Durbin-Watson statistic = 1.09798 (P=0.0022)
Lag 1 residual autocorrelation = 0.447733

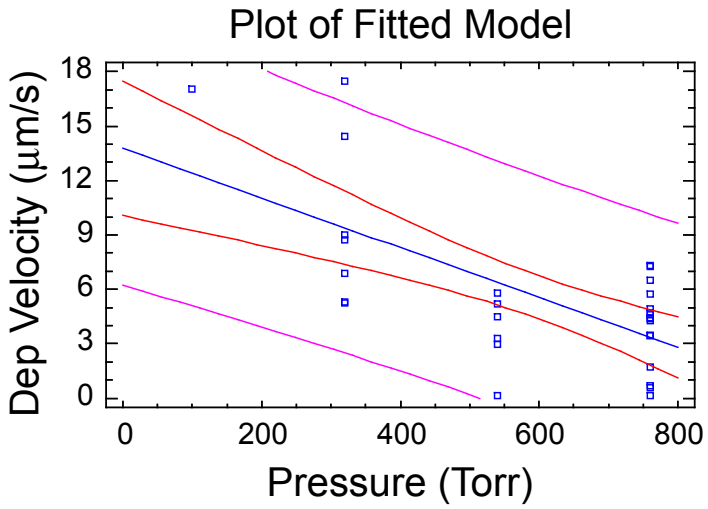

7.3 Boron Nitride Line Experiments

One of the primary goals of the boron nitride fiber experiments was to find suitable starting conditions for the investigation of BN line growth. Recall that a line typically refers to a structure with height $\ll$ width. LCVD line deposition involves the additional line scan speed variable and the complexity of a dynamic laser–substrate–deposit interaction. For BN , the complex interaction between the tungsten substrate material properties and the properties of the deposit exacerbate the complexity of the process. As with carbon, constant laser power was believed to be the best approach to the deposition of a single layer BN line. In fact, the sensitivity of the BN deposition process limited the use of feedback control and necessitated the use of constant intralayer laser power approach within multi–layered structures.

7.3.1 Exploratory Experiments

The first BN line experiment, BN-11L, was designed to study the appropriate power levels for the first and second layers of growth. In this case, conditions known to be favorable to BN deposition were used: pressure of 760 Torr, carrier N_2 flow of 25 sccm, and zero diluent N_2 flow. As with BN fibers, all BN line experiments utilized the reagent gas nozzle. A scan speed of 2.54 mm/min was chosen based on the successful deposition of carbon lines. All lines were 2.54 mm in length. Other values used are given in Table 7.29. The changes in borazine flow and concentration were due strictly to fluctuations in the vaporizer temperature.

In general, the resulting deposits had severe troughs in their center regions. The troughs seemed to be an extension of the volcano effect along the length of the line. Sample 1 however, showed no such occurrence. The single layer deposit of Sample 1 was a thin, faint coating of solid white powdery material, presumed to be boron nitride, in a wide line shape. The conditions for Sample 1 were used as the first layer conditions for many of the subsequent BN line experiments.

Table 7.29: BN-11L experiment conditions

No.	Borazine Flow (sccm)	Total Flow (sccm)	Borazine Conc (mol/m^3)	Scan Speed (mm/min)	No. Layers	Layer 1 Power (W)	Layer 2+ Power (W)
1	1.09	26.09	1.96	2.54	1	31.05	
2	1.16	26.16	2.07	2.54	2	31.05	31.05
3	1.23	26.23	2.19	2.54	2	15.91	15.91
4	1.64	26.64	2.82	2.54	2	31.05	15.91
5	1.72	26.72	2.93	2.54	2	31.05	7.73

7.3.2 Refined Experiments

After conditions that supported successful deposition of single layer BN lines were found in Sample 1 of BN-11L, experiments BN-12L and BN-13L were executed to find optimal conditions for the growth of additional layers. With the exception of Sample 13L-6, the laser power was kept constant during the growth of each layer. The results of BN-11L, and experience with BN fiber growth, indicated that the power level for layers 2+ should be significantly reduced from that of layer 1.

The conditions for BN-12/13L were again a total pressure of 760 Torr, carrier N_2 flow of 25 sccm, and zero diluent N_2 flow through the gas nozzle. The variations in borazine concentration were due strictly to fluctuations in the temperature of the vaporizer. Table 7.30 contains all of the other pertinent conditions.

Samples 12L-1 through 13L-1 represented a study of the second layer power level for two layered lines. Sample 12L-1 used a layer 2 power of 3.66 W and resulted in a thick line with a severe volcano effect in its center. Inside the crater of the volcano, additional fibrous structures grew. Figure 7.28 shows these features.

The line was tapered along its length with wide round growth on the end where scanning started, and no significant growth on the opposite end. The degree of taper was quantified through the taper ratio, computed by dividing the minimum width by the maximum width of a line. While not as exaggerated, similar asymmetry along the line length was observed

Table 7.30: BN-12/13L experiment conditions

No.	Borazine Flow (sccm)	Total Flow (sccm)	Borazine Conc (mol/m^3)	Scan Speed (mm/min)	No. Layers	Layer 1 Power (W)	Layer 2+ Power (W)
12L-1	2.24	27.24	3.69	2.54	2	31.05	3.66
12L-2	2.23	27.23	3.67	2.54	2	31.05	3.32
12L-3	2.19	27.19	3.62	2.54	2	31.05	2.98
12L-4	1.41	26.41	2.47	2.54	2	31.05	2.98
12L-5	1.40	26.40	2.45	2.54	2	31.05	2.98
12L-6	1.39	26.39	2.45	2.54	2	31.05	2.63
13L-1	1.61	26.61	2.78	2.54	2	31.05	2.29
13L-2	1.61	26.61	2.77	2.54	6	31.05	2.29
13L-3	1.59	26.59	2.74	2.54	6	31.05	2.63
13L-4	1.58	26.58	2.73	2.54	6	31.05	2.98
13L-5	1.58	26.58	2.72	2.54	6	31.05	3.32
13L-6	1.59	26.59	2.75	2.54	10	31.05	varies

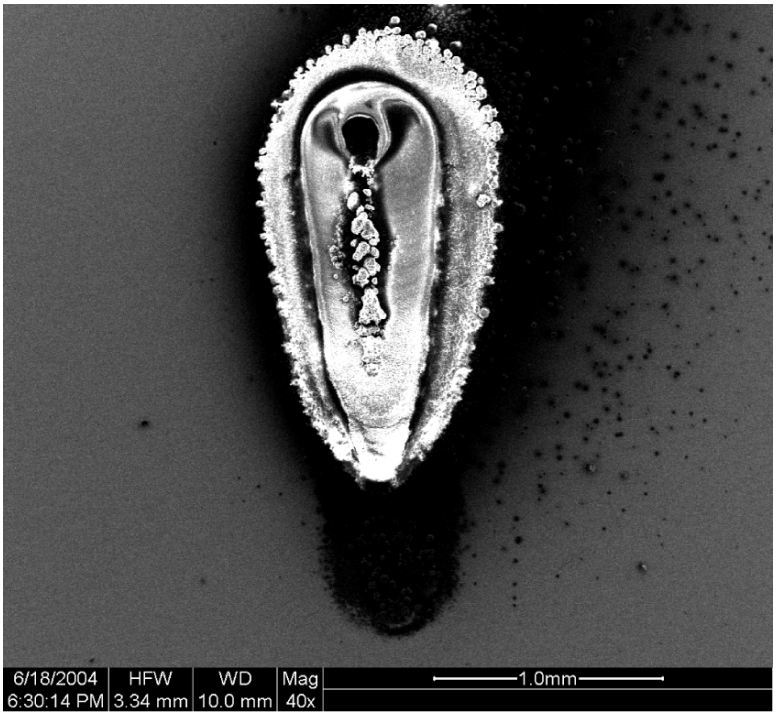

Figure 7.28: SEM micrograph of 2–layer BN line showing volcano effect

in carbon lies. However, with respect to the scan direction, the carbon lines exhibited opposite features: less significant growth at the initiation end and large rounded growth at the opposite transition end. The cause for the tapered BN line shape is likely related to the heat transfer through the deposit and the substrate.

The layer 2 power level was decreased incrementally over the next few experiments, and the severity of the volcano effect decreased accordingly. The tapered shape remained a constant feature, albeit the degree of tapering declined significantly. Line 12L-5 in Figure 7.29 is an example of improved line morphology with decreased laser power. As shown in the figure, lines were characterized by measuring the length, minimum width, and maximum width of the bulk growth region. Values for all 7 lines are given in Table 7.31.

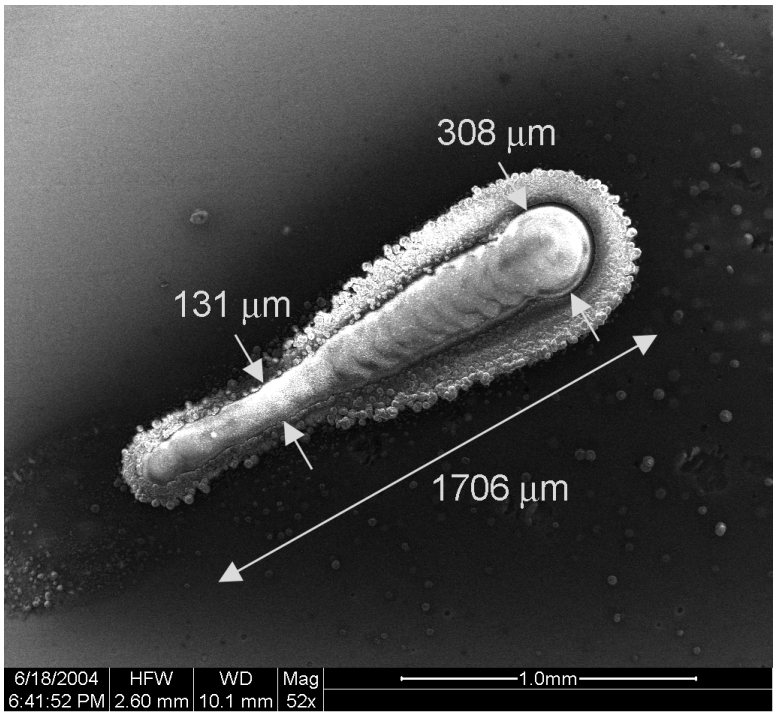

Figure 7.29: SEM micrograph of Sample 5 line indicating measurement locations

The presence of a well–defined starting point for bulk deposition along the line is further evidence of the binary nature of the process. The fraction of the total scan length covered by bulk line growth was termed the line length ratio. A simple linear regression related the length ratio to the layer 2 laser power. The regression output is given in Table 7.32.

Table 7.31: BN-12/13L 2 layer line results

No.	Length (μm)	Length Ratio	Min Width (μm)	Max Width (μm)	Mean Width (μm)	Taper Ratio
12L-1	1736	0.68	258	605	432	0.43
12L-2	1523	0.60	171	431	301	0.40
12L-3	1602	0.63	157	413	285	0.38
12L-4	1397	0.55	217	358	287	0.61
12L-5	1706	0.67	131	308	219	0.42
12L-6	80	0.03	100	100	100	1.00
13L-1	341	0.13	119	193	156	0.62

Table 7.32: Regression output for BN line length as a function of laser power

Dependent variable: LengthRatio
Independent variable: Layer 2 Power

Parameter	Estimate	Standard Error	T Statistic	P-Value
Intercept	-0.981885	0.495471	-1.98172	0.1043
Slope	0.488242	0.164869	2.96139	0.0315

Analysis of Variance

Source	Sum of Squares	Df	Mean Square	F-Ratio	P-Value
Model	0.280465	1	0.280465	8.77	0.0315
Residual	0.159903	5	0.0319806		
Total (Corr.)	0.440368	6			

Correlation Coefficient = 0.798052
R-squared = 63.6887 percent
R-squared (adjusted for d.f.) = 56.4265 percent
Standard Error of Est. = 0.178831
Mean absolute error = 0.123865
Durbin-Watson statistic = 2.24762 (P=0.1857)
Lag 1 residual autocorrelation = -0.170039

The coefficient for the layer 2 laser power term in the regression equation was 0.488 which indicated that a 1 W change in laser power would result in an increase in length ratio of about 0.5. This result highlights the sensitivity of line length to laser power.

Another simple linear regression was done to relate the mean line width to the layer 2 laser power. Results are given in Table 7.33 The regression output showed a strong correlation between these variables. The regression coefficient of 219 μm/W again indicated extreme sensitivity of deposit parameters to laser power. This predicted that a 1 W change in laser power would change the mean line width by over 200 μm.

Table 7.33: Regression output for BN line width as a function of laser power

Dependent variable: AvgWidth
Independent variable: Layer 2 Power

Parameter	Estimate	Standard Error	T Statistic	P-Value
Intercept	-398.805	144.832	-2.75358	0.0401
Slope	219.373	48.1931	4.55196	0.0061

Analysis of Variance

Source	Sum of Squares	Df	Mean Square	F-Ratio	P-Value
Model	56620.7	1	56620.7	20.72	0.0061
Residual	13663.1	5	2732.61		
Total (Corr.)	70283.7	6			

Correlation Coefficient = 0.897553
R-squared = 80.5601 percent
R-squared (adjusted for d.f.) = 76.6722 percent
Standard Error of Est. = 52.2744
Mean absolute error = 40.6819
Durbin-Watson statistic = 2.20417 (P=0.2039)
Lag 1 residual autocorrelation = -0.231167

Experiments 13L-2 through 13L-5 consisted of 6 layers of growth rather than two layers. The purpose of these experiments was to determine how the addition of more layers would effect the line deposits. The conditions used were identical to those used in the two layer experiments 12L-2 – 13L-1. The results of the 6 layer experiments were surprising.

With the exception of 13L-3, the 6 layer lines did not yield as much deposit as did the 2 layer lines. Figures 7.30 and 7.31 compare the 2 layer and 6 layer lines for corresponding layer 2+ laser power levels.

The explanation for the discrepancy between the 2 layer lines and the 6 layer lines could be related to several factors. First, the incidental variations in $B_3N_3H_6$ concentration due to changes in vaporizer temperature could effect the deposition rates. However, by observing the data, no correlation can be made between the concentration and deposit shape. The substrates used underwent identical preparation steps, but surface roughness or contact resistance between the tungsten sheet and the substrate holder could have been different between 12L and 13L. The variations in the CO_2 laser power level and the sensitivity of the process to incident laser power could combine to yield these different results. Whatever the cause, the sensitivity and lack of repeatability of the process was again highlighted.

Experiment 13L-6 was an effort to grow a BN wall; BN walls are discussed in Section 7.4 below.

7.3.3 Designed Experiments

Experiment BN-14L was an experiment designed to study two factors: carrier flow (which correlated to borazine concentration) and layer 2+ laser power. The setup was a two factor rotatable central composite design with factor levels given in Table 7.34. The pressure was held constant at 760 Torr, and the sum of the carrier and diluent flows was fixed at 25 sccm. The first layer laser power was 31.05 W for all experiments. The scan speed was a constant 2.54 mm/min with a scan length of 2.54 mm. All lines consisted of four layers.

The results of BN-14L varied. All deposits produced a faint white powder coating along the line length, but only some yielded bulk line growth on top of the powder coating. Those that gave significant deposits are listed in Table 7.35 along with the measured length and width values. Figure 7.32 illustrates one of the more successful deposits, Sample 8.

The results were analyzed using multiple linear regression that included second order

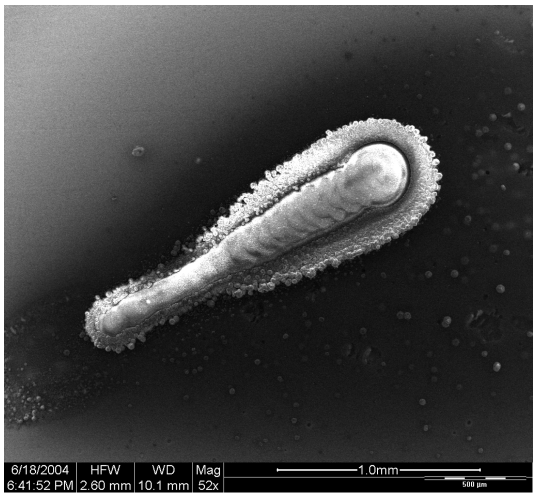

Sample 12L-5, 2 layers **Sample 13L-4, 6 layers**

Figure 7.30: BN-12/13L lines with layer 2+ laser power of 2.98 W

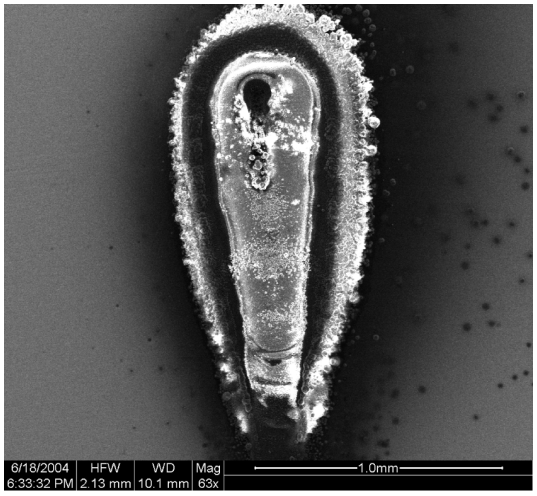

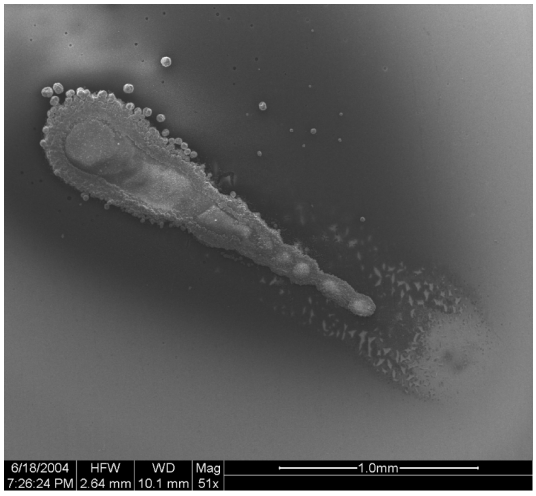

Sample 12L-2, 2 layers **Sample 13L-5, 6 layers**

Figure 7.31: BN-12/13L lines with layer 2+ laser power of 3.32 W

Table 7.34: BN-14L experiment conditions

No.	Borazine Temp (°C)	Carrier Flow (sccm)	Diluent Flow (sccm)	Borazine Flow (sccm)	Total Flow (sccm)	Borazine Conc (mol/m^3)	Layer 2+ Power (W)
1	-11.6	15.0	10.6	0.76	26.36	1.34	2.98
2	-11.1	8.0	17.9	0.42	26.32	0.73	3.48
3	-10.7	22.0	3.2	1.17	26.37	2.05	3.48
4	-10.2	25.0	0.0	1.37	26.37	2.41	2.98
5	-9.8	15.0	10.6	0.84	26.44	1.47	2.98
6	-9.4	8.0	17.9	0.46	26.36	0.80	2.48
7	-9.0	5.0	21.1	0.29	26.39	0.51	2.98
8	-8.5	22.0	3.2	1.32	26.52	2.30	2.48
9	-8.1	15.0	10.6	0.92	26.52	1.60	3.68
10	-7.7	15.0	10.6	0.94	26.54	1.63	2.98
11	-7.2	15.0	10.6	0.97	26.57	1.67	2.27
12	-6.9	15.0	10.6	0.99	26.59	1.70	2.98

Table 7.35: BN-14L 2 factor 3 level experiment results

No.	Length (μm)	Length Ratio	Min Width (μm)	Max Width (μm)	Mean Width (μm)	Taper Ratio
1	488	0.19	127	182	154	0.70
3	1666	0.66	86	308	197	0.28
4	1495	0.59	132	241	186	0.55
8	1287	0.51	68	102	85	0.67
9	1676	0.66	39	79	59	0.50
10	1229	0.48	45	124	84	0.36
12	900	0.35	46	63	55	0.72

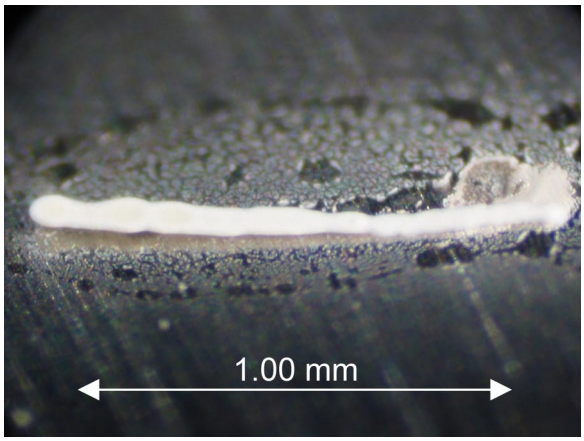

Figure 7.32: Sample 8 of BN-14L illustrating a typical BN line

main effects and first order interactions. The first response variable studied was the line length. The regression results are provided in Table 7.36 along with a pareto chart of the standardized effects. The analysis revealed that the only term that was statistically significant at the 95% level was the carrier flow rate.

All insignificant factors were removed from the analysis and a simple linear regression was executed to generate a regression equation. The resulting equation was:

$$Length = -644.526 + 90.4957 * CarrierFlow \tag{7.11}$$

which indicated that a 1 sccm change in carrier flow rate would result in an increase in line length of over 90 μm.

A similar analysis was done for the line width. The results of the regression analysis are given in Table 7.37. Again, the results showed that the only statistically significant variable at the 95% confidence level was the carrier flow rate. The fact that line length and width were only significantly affected by the carrier flow rate (or borazine concentration) was consistent with the finding that BN deposition from $B_3N_3H_6$ under these conditions is transport–limited.

A simple linear regression of line width versus the carrier flow rate resulted in the equation:

$$Width = -76.5333 + 9.74586 * CarrierFlow \tag{7.12}$$

Table 7.36: BN-14L line length multiple regression analysis

Estimated Effects for Line Length

average+block	= 572.567	+/- 300.678
A:Carrier Flow	= 1266.94	+/- 368.254
B:Laser Power	= 687.106	+/- 368.255
AA+block	= 147.845	+/- 438.31
AB	= 189.1	+/- 520.79
BB+block	= 238.097	+/- 438.313

Analysis of Variance

Source	Sum of Squares	Df	Mean Square	F-Ratio	P-Value
A:Carrier Flow	3.21027E6	1	3.21027E6	11.84	0.0184
B:Laser Power	944225.0	1	944225.0	3.48	0.1211
AA+block	30858.4	1	30858.4	0.11	0.7496
AB	35758.8	1	35758.8	0.13	0.7314
BB+block	80032.2	1	80032.2	0.30	0.6103
Total error	1.35611E6	5	271222.0		
Total (corr.)	5.63576E6	10			

R-squared = 75.9373 percent
R-squared (adjusted for d.f.) = 51.8747 percent
Standard Error of Est. = 520.79
Mean absolute error = 300.926
Durbin-Watson statistic = 1.38901 (P=0.0000)
Lag 1 residual autocorrelation = 0.263981

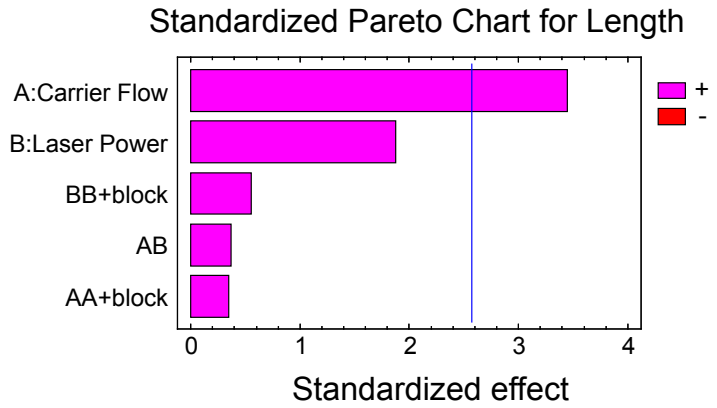

Table 7.37: BN-14L line width multiple regression analysis

Estimated Effects for Line Width

average+block	= 79.5333	+/- 28.5833
A:Carrier Flow	= 136.442	+/- 35.0072
B:Laser Power	= 48.8348	+/- 35.0073
AA+block	= 18.2418	+/- 41.6669
AB	= 55.95	+/- 49.5077
BB+block	= -45.4086	+/- 41.6672

Analysis of Variance

Source	Sum of Squares	Df	Mean Square	F-Ratio	P-Value
A:Carrier Flow	37232.8	1	37232.8	15.19	0.0114
B:Laser Power	4769.65	1	4769.65	1.95	0.2218
AA+block	469.782	1	469.782	0.19	0.6798
AB	3130.4	1	3130.4	1.28	0.3097
BB+block	2910.93	1	2910.93	1.19	0.3255
Total error	12255.0	5	2451.01		
Total (corr.)	61841.8	10			

R-squared = 80.1832 percent
R-squared (adjusted for d.f.) = 60.3665 percent
Standard Error of Est. = 49.5077
Mean absolute error = 18.1321
Durbin-Watson statistic = 1.36948 (P=0.0000)
Lag 1 residual autocorrelation = 0.0871837

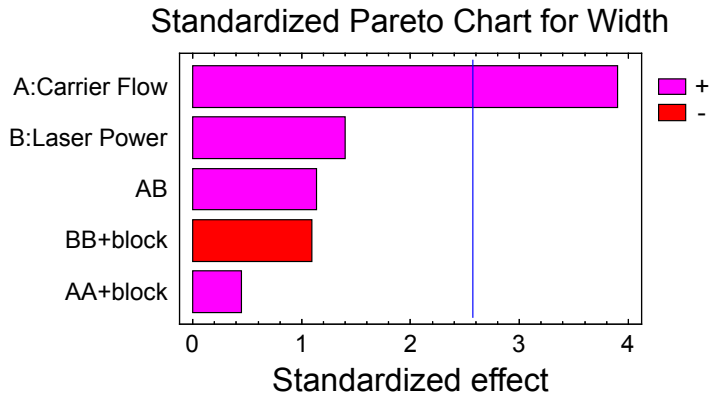

which states that an increase of 1 sccm in carrier flow will produce almost a 10 μm increase in line width.

Unfortunately, during the mounting and polishing process of some of the samples from BN-14L several of the samples were destroyed, thus prohibiting the measurement of line heights. Observations had indicated that most of the samples had similar heights on the order of 10–20 μm.

Experiment BN-15L was another two factor, three level rotatable central composite designed experiment that studied carrier flow rate and layer 2+ laser power. The system pressure was kept at 760 Torr. The sum of the carrier and diluent flow rates was kept constant at 50 sccm, a 25 sccm increase over previous experiments. The increased flow rates were intended to increase deposition rates for this transport–limited process. Due to the increase in total flow rate and the associated increase in convective cooling of the laser spot, laser power levels were increased to maintain similar substrate temperatures as previous experiments. The first layer laser power was increased to 56.7 W. The scan speed was 2.54 mm/min, and the lines were 2.54 mm long. All lines consisted of four layers of growth. Other conditions are given in Table 7.38

The results of BN-15L varied greatly. All samples produced some degree of bulk deposit. Sample 1 produced only a small amount of bulk growth, but yielded a coating of the white powder that consistently preceded bulk deposition. This powder was credited with changing the the properties of the substrate surface, namely decreasing the reflectivity and thermal conductivity, thus serving to facilitate nucleation and initiate the bulk reaction.

Samples 2, 3, 4, 6, and 7 produced wall structures with height $\geq$ width. For the most part, these walls exhibited extreme volcano effects with rough fibrous structures emerging from the craters of the volcanos similar to the first samples in Experiment BN-12L. It is believed that deposits showing these features experienced conditions too hot for optimal growth. For cases when the laser power was excessive, the use of constant laser power during layers 2 – 4 exacerbated the volcano problem. More wall experiments are presented

Table 7.38: BN-15L experiment conditions

No.	Borazine Temp (°C)	Carrier Flow (sccm)	Diluent Flow (sccm)	Borazine Flow (sccm)	Total Flow (sccm)	Borazine Conc (mol/m^3)	Layer 2+ Power (W)
1	-5.4	20.0	29.3	1.43	50.73	1.28	3.49
2	-6.1	44.1	3.4	3.03	50.53	2.74	5.20
3	-6.5	30.0	18.3	2.01	50.31	1.83	5.20
4	-6.9	40.0	7.8	2.63	50.43	2.39	3.49
5	-7.0	20.0	28.9	1.30	50.20	1.19	6.89
6	-7.2	40.0	7.8	2.59	50.39	2.35	6.89
7	-7.2	30.0	18.3	1.94	50.24	1.77	7.58
8	-7.0	30.0	18.3	1.96	50.26	1.78	5.20
9	-6.9	15.9	33.3	1.05	50.25	0.95	5.20
10	-6.7	30.0	18.3	2.00	50.30	1.82	2.79
11	-6.4	30.0	17.7	2.02	49.72	1.86	5.20

in Section 7.4 below.

Sample 5 exhibited a large amount of bulk growth at the initial end of the line and no significant growth at the other end. It also showed signs of a moderate volcano effect. Samples 8–10 yielded very good BN lines. These were lines of uniform width with a fairly smooth and consistent morphology. The lines had minimal extraneous white powder formation in the surrounding area. Dimensions of these lines are given in Table 7.39.

Table 7.39: BN-15L BN line dimensions - Samples 8–10

No.	Length (μm)	Length Ratio	Min Width (μm)	Max Width (μm)	Mean Width (μm)	Taper Ratio
8	1472	0.58	51	100	76	0.51
9	2113	0.83	73	212	142	0.35
10	1121	0.44	68	130	99	0.52

A review of the conditions used in Samples 8–10 indicated that the carrier flow rate was between 15 and 30 sccm and the laser power was between 2.75 and 5.25 W. This was the range of conditions studied in BN-14L, therefore, a suitable operating box for the

Table 7.40: Conditions from BN-19F multiple response optimization analysis used in BN-20L

Factor	Level
Pressure (Torr)	232
Carrier Flow (sccm)	12.25
Diluent Flow (sccm)	1.57
Total Flow (sccm)	15.7
$B_3N_3H_6$ Conc (mol/m^3)	3.58
Max Temp ($^\circ$C)	1009

deposition of BN lines at 760 Torr had been identified.

After the successful results of the fiber experiment BN-19F, a BN line experiment, BN-20L, was designed using the optimal fiber growth conditions. As stated previously, the growth of LCVD fibers is fundamentally different from that of lines which reduces the utility of most fiber attribute studies when designing line experiments. The optimal conditions were defined through a multiple response optimization analysis that sought to minimize powder formation, minimize the volcano effect, and minimize deposit asymmetry. The conditions found by the analysis and used in BN-20L are given in Table 7.40.

The factors studied in BN-20L were limited to those directly pertinent to line deposition: scan speed, layer 1 laser power, and layer 2+ laser power. Each line was 2.54 mm long and had 4 layers. The factor levels are listed in Table 7.41 in the order the experiments were executed.

The results of BN-20L varied greatly. Only 2 of the 16 runs, Samples 9 and 13, showed any sign of bulk growth, and these samples exhibited excessive growth and powder formation. These lines further represented the binary nature of BN deposition. The sporadic nature of BN growth on the substrate surface was the dominant factor complicating the deposition of BN lines. This process sensitivity combined with the limitations on using a constant laser power control scheme restricted the utility of more expansive BN line studies.

Table 7.41: BN-20L line conditions

No.	Scan Speed (mm/min)	Layer 1 Power (W)	Layer 2+ Power (W)
1	3.81	23.2	4.00
2	5.08	30.0	5.50
3	2.54	30.0	2.50
4	2.54	30.0	5.50
5	1.67	40.0	4.00
6	3.81	40.0	6.52
7	2.54	50.0	2.50
8	3.81	40.0	1.48
9	3.81	56.8	4.00
10	3.81	40.0	4.00
11	5.95	40.0	4.00
12	3.81	40.0	4.00
13	2.54	50.0	5.50
14	5.08	50.0	2.50
15	5.08	50.0	5.50
16	5.08	30.0	2.50

Sample 13 was used to test the BN line adherence to the tungsten substrate. A piece of transparent Scotch tape was applied to the line and gentle pressure was applied to ensure uniform adhesion. The tape was then pulled away from the substrate. The bulk BN line deposit separated from the substrate during this test. Upon close inspection, it appeared that the line sat atop a thin powder coating which was consistent with observations made during deposition experiments. The presence of this powder apparently enhances deposition, but negatively impacts the adhesion of the deposit to the substrate.

Experiment BN-21L was run to determine if use of a different substrate material would significantly enhance the BN line deposition process. The goal was to find a substrate that had similar properties to the deposit; thus hot–pressed boron nitride plates were used. Details of these substrates can be found in Section 9.1.2.

BN-21L used the same pressure and flow conditions used in BN-20L; however, no prior data on appropriate laser power or scan speed was available for BN substrates. A laser power of 15.9 W was found to yield an average maximum temperature of about 1000°C and was used in all trials. The scan speed and total number of layers varied with each run. The scan speed varied between 2.54 and 12.7 mm/min while the number of layers varied from 4 to 20. The basic procedure was to engage the laser and simultaneously initiate the horizontal stage motion. The scanning would continue until most of the line length showed evidence of deposition via the thermal imager.

Very sporadic growth similar to that on tungsten was still observed during BN-21L. Maintaining temperature control of the process was very difficult due to this behavior. The most important difference in depositing on BN versus tungsten was the ability to see the temperature on the thermal imager from the instant the laser was engaged. This allowed at least some degree of anticipation as to when a growth node might emerge. The temperature on tungsten did not reach a sufficient level for the imager to detect, therefore, only after enough growth had occurred to raise the temperature appreciably did the operator have a chance to respond.

Even with the ability to see the initial substrate temperature prior to growth, the process was still very binary and sporadic. For the case of BN deposition on tungsten, some of this behavior was attributed to material property differences between substrate and deposit as discussed in detail earlier. BN-21L showed that a significant amount of this behavior was also inherent in the process itself.

It summary, the deposition of BN lines was complicated by the sporadic nature of the process. This behavior prevented the control of deposition temperature and forced the use of a constant laser power approach. Unfortunately, a constant power approach was much less robust than a temperature control approach. The use of a high power during the first layers of growth and a much lower power during subsequent layers was a complexity associated with use of constant laser power. The stability and noise associated with the CO_2 laser was discussed in Section 7.2. In addition to these effects, a constant laser power approach was subject to variation in substrate surface preparation, laser optic alignment and cleanliness, gas nozzle alignment, convective cooling, and substrate material property changes. Active temperature control maintains a constant temperature regardless of all these effects and minimizes their importance. The negative impact on the robustness of BN line deposition due to these concerns made repeatability difficult. When successful line deposition was achieved, the adherence of the BN material to the substrate was not good. Thus, in terms of the dispenser cathode application, the LCVD of BN lines in general, and particularly on a tungsten substrate, became a concern.

7.4 Boron Nitride Wall Experiments

While not necessarily required for the dispenser cathode application, the fabrication of BN walls was investigated in order to characterize the sustainable robustness of BN line deposition. As with carbon deposition, the first layer of the walls was deposited under constant laser power. The first layer power was 31.1 W in all cases. In experiments BN-8W and BN-9W, for subsequent layers, the laser power was manually controlled through

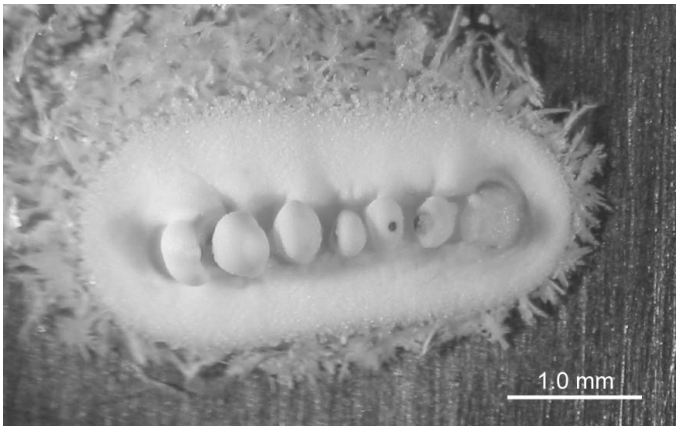

Figure 7.33: Optical microscope image of a fibrous BN wall

the LabVIEW interface in an effort to maintain the maximum temperature near 1000°C. All BN wall experiments were done at a pressure of 760 Torr. Carrier flow was held at 25 sccm with no diluent flow. Scan length was fixed at 2.54 mm. Other conditions were derived from successful BN fiber and line deposits and are given in Table 7.42.

Table 7.42: BN-8/9W BN wall experiment conditions

No.	Borazine Flow (sccm)	Total Flow (sccm)	Borazine Conc (mol/m^3)	Max Temp (°C)	Scan Speed (mm/min)	No. Layers
8W-1	2.40	27.40	3.91	1000	2.54	14
8W-2	2.40	27.40	3.91	1000	2.54	20
9W-1	2.40	27.40	3.91	1000	5.08	10
9W-2	2.40	27.40	3.91	1000	3.81	10
9W-3	2.40	27.40	3.91	1000	6.35	10
9W-4	2.40	27.40	3.91	1000	5.08	10

The experiments produced deposits of significant size. Observation revealed no distinct relationship between the scan speed and the resulting deposit morphology. The walls had a very bumpy appearance and were surrounded by large amounts of white powder, similar to many of the fibers. Figure 7.33 is an optical image of Sample 9-2. The walls appeared to be more of an array of individual fibers than a structure made of smooth continuous layers. This result was likely caused by the inadequate manual temperature control scheme that

was necessitated by the process sensitivity.

In order to combat the problem of inadequate manual temperature control, Experiment BN-10W was a set of 10 layer walls that used a constant power level throughout the growth of all layers. The first layer power was again 31.1 W, pressure was 760 Torr, carrier flow was 25 sccm, and diluent flow was 0. The only variation in borazine concentration was due to changes in the vaporizer temperature. The scan length of the walls was 2.54 mm. Table 7.43 contains additional conditions.

Table 7.43: BN-10W BN wall experiment conditions

No.	Borazine Temp (°C)	Borazine Flow (sccm)	Total Flow (sccm)	Borazine Conc (mol/m^3)	Layer 2+ Power (W)	Scan Speed (mm/min)	No. Layers
10W-1	-1.7	2.19	27.19	3.62	3.32	2.54	10
10W-2	-0.9	2.29	27.29	3.75	3.66	2.54	10
10W-3	-9.2	1.45	26.45	2.53	3.66	2.54	10
10W-4	-11.4	1.28	26.28	2.26	3.66	2.54	10
10W-5	-11.6	1.26	26.26	2.23	3.66	2.54	4

Even for the same experimental setup, the results of BN-10W varied greatly. Sample 1 was run at a lower laser power than samples 2 through 4, and samples 2, 3, and 4 were designed to be identical. For 2 through 4 there was an inadvertent change in $B_3N_3H_6$ concentration due to the changes in vaporizer temperature. SEM micrographs of these samples shown in Figure 7.34 revealed that samples 1 and 3 yielded very large deposits and samples 2 and 4 yielded very little.

These results did not correlate well with any of the changes in experimental conditions. The binary nature of this deposition process is again highlighted by the lack of repeatability shown in Samples 2–4. Due to this binary phenomenon and the observed sensitivity of the process to incident laser power, the deposition of boron nitride walls does not appear feasible without a more robust temperature control scheme. The deposition of walls is not required in the current target application, but future applications of LCVD may require

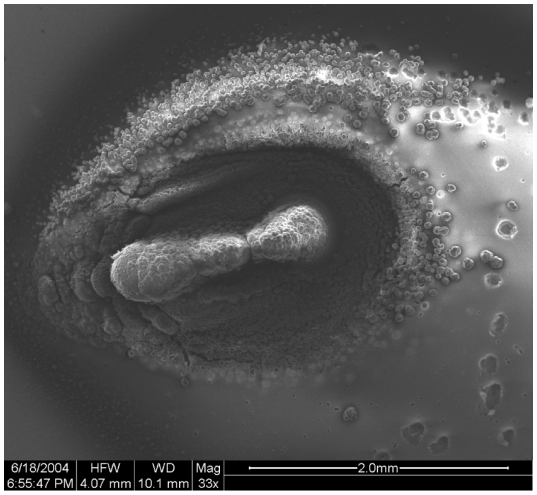

Sample 1

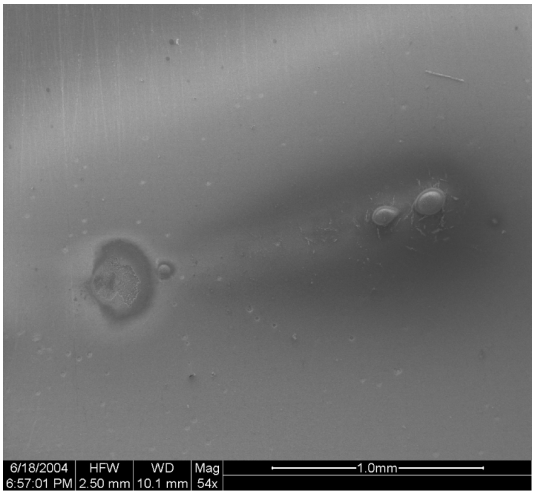

Sample 2

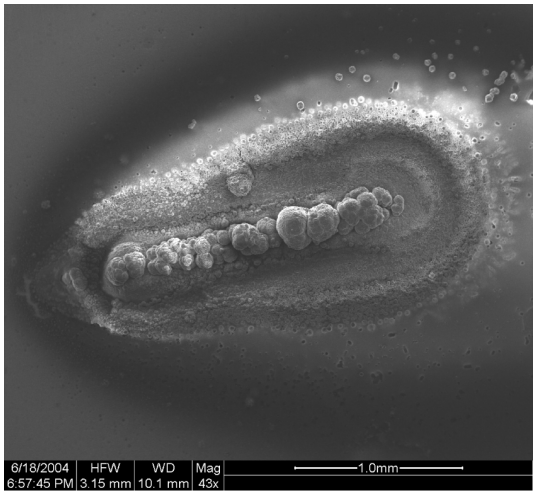

Sample 3

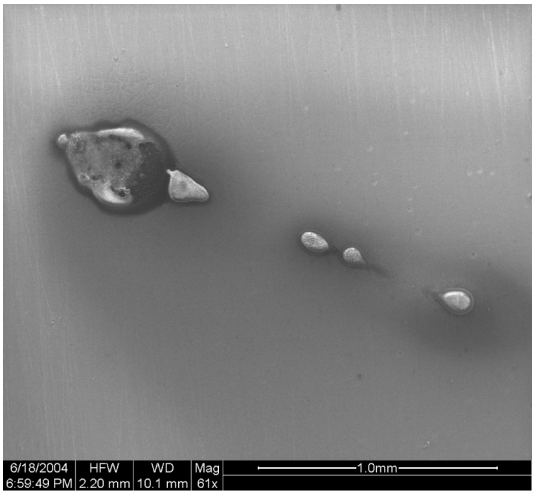

Sample 4

Figure 7.34: Variation in BN-10W walls under similar experimental conditions

such structures. In fact, it may be possible to generalize that the deposition of walls of ceramic material on metal substrates may not be feasible without significant improvements in LCVD process control technology.

7.5 Summary of Boron Nitride Deposition

The goal of the BN experiments was to identify conditions that enabled the deposition of BN lines suitable for use in fabricating the dispenser cathode assembly. Several of the BN lines produced in Experiments BN-14 and 15L met this criteria. The factor levels used in both experiments were at the lower limits of Georgia Tech's LCVD machine resolution. For example, the resolution of the 100 sccm mass flow controllers was about 1 sccm while the resolution of the laser power was about 0.1 W. Given the sensitivity of the process relative to the resolution of the machine, more refined experiments were not feasible. In order to determine recommended settings for the deposition of BN lines that closely conform to the requirements for the dispenser cathode, an optimization analysis was performed on the results of BN-14L.

The target results of the optimization analysis were to maximize length and achieve a line width of 100 μm. The analysis revealed that under similar experimental conditions, a pressure of 760 Torr, a carrier flow rate of 17.0 sccm, a diluent flow rate of 8.0 sccm, a layer 1 laser power of 31 W, and a layer 2+ laser power of 3.68 W should yield lines of suitable size and shape.

CHAPTER VIII

BORON NITRIDE DEPOSITION ANALYSIS

Boron nitride LCVD has not been studied significantly, particularly using the borazine reagent system; therefore, the advanced LCVD modeling environment developed in the FLUENT package described in Chapter 5 was used to gain insight into this process. The experimental results of Chapter 7 indicated the process was transport–limited. An analysis was devised to study the theoretical maximum deposition rate achievable under transport limitations.

When a process is transport–limited, by definition, the kinetics of the deposition process are much faster than the transport mechanisms. The governing equation for a kinetically–limited BN deposition process is the Arrhenius relationship:

$$J''_{BN} = k_r C^n_{B_3N_3H_6,0} \tag{8.1}$$

where J''_{BN} is the molar reaction rate of boron nitride (kmol/m^2-s), $C_{B_3N_3H_6}$ is the local concentration of borazine (mol/m^3), n is the order of the reaction, and the rate constant, k_r is given by:

$$k_r = k_0 e^{\frac{-Q}{RT}} \tag{8.2}$$

where k_0 is the pre–exponential factor (m/s), Q is the activation energy (kJ/mol), R is the universal gas constant (8314 J/kmol-K), and T is the local temperature (K). Usually, n, k_0, and Q are determined by fitting experimental data to the above equations when operating in a known kinetically–limited regime. Because the investigation of Chapter 7 primarily involved a transport–limited regime, data from the literature was used to find these kinetic parameters.

Conceptually, the governing equation for a transport–limited process in one dimension

is a simplified version of Fick's Law:

$$\vec{J}_{B_3N_3H_6} = k_t(C_{B_3N_3H_6,\infty} - C_{B_3N_3H_6,0}) \tag{8.3}$$

where $\vec{J}_{B_3N_3H_6}$ is the molar flux (mol/m^2-s) of borazine, $C_{B_3N_3H_6,\infty}$ and $C_{B_3N_3H_6,0}$ are the concentration of borazine in the bulk fluid and at the substrate surface (mol/m^3), respectively, and k_t is the mass transfer coefficient defined as:

$$k_t = -D_{B_3N_3H_6,m}/\delta \tag{8.4}$$

where $D_{B_3N_3H_6,m}$ is the binary diffusion coefficient (m^2/s) of borazine in the mixture, and δ is the thickness of the concentration boundary layer (m).

Under certain assumptions described in Chapter 1, the above equations can be rewritten as

$$\vec{J}_{B_3N_3H_6} = \frac{C_{B_3N_3H_6,\infty}}{\left(\frac{1}{k_t} + \frac{3}{k_r}\right)} \tag{8.5}$$

which elucidates the relationship between k_r and k_t in the different rate–limiting regimes. In a transport–limited case, $k_r \gg k_t$ and the equation reduces to Fick's Law. In a kinetically–limited case, $k_t \gg k_r$ and the equation reduces to the Arrhenius expression.

For the purposes of analysis, the reaction rate constant k_r can be artificially inflated to force the boron nitride LCVD process into the transport–limited regime. One implicit assumption of this technique is that the concentration of reagent species near the substrate surface approaches zero. Stated differently, there is 100% conversion of all $B_3N_3H_6$ reagent species that reach the substrate into solid BN . This assumption can be validated by a thermodynamic analysis of the deposition process. Once reasonable values for n, k_0, and Q have been obtained, and the thermodynamic analysis is complete, a FLUENT model similar to that described in Chapter 5 for carbon can be configured for boron nitride to calculate the maximum mass deposition rate obtainable given the transport limitations.

8.1 Extraction of Kinetic Parameters from Literature

Because boron nitride LCVD from borazine was transport–limited as presented in Chapter 7, the determination of the kinetic parameters n, k_0, and Q was not feasible. However, data from the CVD of boron nitride was available in the literature.[29,34] Gomez–Aleixandre studied the deposition of boron nitride in a CVD reactor from the diborane–ammonia mixture. Part of the study included an investigation of the reaction pathways from the diborane–ammonia reagents to the final deposition reaction. The conclusion was that at temperatures above 775°C, borazine, $B_3N_3H_6$, forms via an intermediate homogenous reaction, and that borazine was a likely precursor specie in the final deposition surface reaction. Gomez-Aleixandre reports an activation energy of the BN deposition from borazine of 35 kcal/mol or 147 kJ/mol, but does not report values of the reaction order n or the pre–exponential factor k_0.

A simple kinetic analysis was done using two data points provided by Gomez–Aleixandre similar to that done in Section 4.2. The two data points were the only ones available at temperatures above 775°C where the deposition reaction is believed to involve the borazine species. The conditions for the data points are given in Table 8.1.

The deposition rate in nm/min was converted to kmol/m^2-s by using values of 24.82 kg/kmol and 2000 kg/m^3 for the molecular weight and density of boron nitride, respectively. $C_{B_3N_3H_6}$ was computed by using the stoichiometric ratio of 3:2 for B_2H_6:$B_3N_3H_6$ through the intermediate homogenous reactions identified by Gomez-Aleixandre. An approximation of $n = 1$ was used as justified by the linear relationship of the deposition rate to the concentration.[29] In order to compute the needed parameters, the transformed equation

Table 8.1: Data points from literature used in boron nitride kinetics study

	j_{vel} (nm/min)	J''_{BN} (kmol/m^2-s)	$C_{B_2H_6}$ (kmol/m^3)	$C_{B_3N_3H_6}$ (kmol/m^3)	n	T (K)
Datum 1	30	4.03E-08	1.20E-05	8.00E-06	1	1048
Datum 2	90	1.21E-07	1.12E-05	7.47E-06	1	1123

for the Arrhenius rate constant, k_r

$$\ln k_r = \ln k_0 - \frac{Q}{R}\frac{1}{T} \tag{8.6}$$

was used in conjunction with a simple linear regression equation:

$$Y = \beta_0 + \beta_1 X \tag{8.7}$$

where

$$Y = \ln k_r = \ln \frac{J''_{BN}}{C^n_{\mathrm{B_3N_3H_6}}} \tag{8.8}$$

$$\beta_0 = \ln k_0 \tag{8.9}$$

$$\beta_1 = -\frac{Q}{R} \tag{8.10}$$

$$X = \frac{1}{T} \tag{8.11}$$

$$\tag{8.12}$$

The results of the regression analysis are summarized in Table 8.2.

The value of activation energy Q computed here is very close to the 1.47e08 J/kmol reported by Gomez–Aleixandre.[29] The combination of this activation energy along with the pre–exponential factor k_0 and the reaction order n provided a good starting point for the computational model developed below.

Table 8.2: Kinetic parameters extracted from literature for CVD of boron nitride from borazine

Parameter	Symbol	Value
Pre–exponential factor (m/s)	k_0	2.00e05
Reaction order	n	1.00
Activation energy (J/kmol)	Q	1.52e08

8.2 Thermodynamic Analysis of BN Deposition from Borazine

The equilibrium conversion efficiency of an LCVD reaction is defined as the number of moles of product divided by the number of moles of reactant put into the system. Specifically, for the borazine decomposition reaction, reaction efficiency is defined as the number of moles of solid boron nitride, BN (s) produced divided by number of moles of $B_3N_3H_6$ (g) put into the system. This ratio can be calculated from thermodynamics.

Others have presented thermodynamic analyses of the CVD of boron nitride from the borazine reagent.[68] The use of Kuznetsov's results in lieu of performing a new thermodynamic analysis was deemed inappropriate, because the pressures in his analysis were much lower than those used in Georgia Tech's LCVD system (0.01–1 versus 760 Torr).

Thermodynamic theory dictates that chemical reactions tend to occur within a system in a direction that minimizes the Gibbs free energy. A negative value for the free energy change of a reaction indicates that the reaction will proceed spontaneously. The equation for computing a change in Gibbs free energy, ΔG, for a reaction system is:

$$\Delta G = \Delta H - T\Delta S \tag{8.13}$$

where ΔH is the change in enthalpy ($H_{products} - H_{reactants}$), T is temperature, and ΔS is the change in entropy ($S_{products} - S_{reactants}$).

The concept of a formation reaction for a species refers to the chemical reaction occurring at standard state that forms the species from its pure elements in their standard states. The Gibbs free energy of formation, ΔG_f for a species can be computed from the enthalpy of formation, ΔH_f, the temperature T, and the change in entropy, ΔS, associated with the formation reaction.

$$\Delta G_f = \Delta H_f - T\Delta S \tag{8.14}$$

The ΔH_f of an element in its standard state is defined to be equal to 0.

A computer program, SOLGASMIX–PV, was available that computes the equilibrium

molar quantities of a set of species under defined conditions by minimizing the Gibbs free energy of all species within the system.[112,113] First, the system was defined by identifying all species containing the elements of interest that could exist. For each species, the enthalpy of formation ΔH_f and the entropy S were specified at all temperatures of interest. Next, the pressure and the temperature of the system were specified. Finally, the initial molar quantities of all elements in the system were defined. The code then iterated until finding the molar quantities of the defined species that minimize the overall Gibbs free energy of the system.

The species used in the analysis of boron nitride deposition from borazine are listed in the first column of Table 8.3. Values for ΔH_f and S were provided in the literature as a function of temperature.[110] Table 8.3 includes examples of these values at three representative temperatures: 1100, 1300, and 1500 K. Data from the full analysis is given in Appendix A.3

Initially, the system was specified to contain 6 moles of H_2, 28 moles of N_2, and 6 moles of solid boron, B(s). These values correspond to the ratios of elemental quantities contained in a setup using 25 sccm of N_2 carrier gas, and 2 sccm of $B_3N_3H_6$ reagent; values that were well within the experimental ranges used in Chapter 7. The pressure used in the analysis was 1 atm which also corresponded to experimental conditions. The Gibbs free energy minimization was done at temperatures between 800 and 2500 K in 100 K increments. The results of the analysis at 1100, 1300, and 1500 K are given in Table 8.4 in terms of molar quantities for each species. Figure 8.1 is a plot of the resulting mole quantities of each species for all species with quantities $\gg 10^{-3}$ moles.

The results of the thermodynamic analysis revealed that under the assumption of local equilibrium in the LCVD process, all of the $B_3N_3H_6$ reagent would eventually convert to BN (s). Thus, the implicit assumption that the concentration of reagent near the substrate surface in a transport–limited reaction approaches zero was validated for this material system.

Table 8.3: Enthalpy and entropy values of species used in boron nitride thermodynamic analysis

Species	Enthalpy, ΔH_f, (kJ/mol)			Entropy, S, (J/mol K)		
	1100 K	1300 K	1500 K	1100 K	1300 K	1500 K
H	222.943	224.006	224.986	-141.840	-145.315	-148.292
H_2	0.000	0.000	0.000	-169.121	-174.288	-178.843
NH	338.975	338.975	339.005	-220.154	-225.559	-230.324
NH_2	162.439	161.916	161.573	-243.303	-250.848	-257.626
NH_3	-55.563	-56.040	-56.099	-251.882	-262.043	-271.296
N_2H_2	206.535	206.836	207.439	-282.902	-293.951	-303.869
N_2H_4	87.931	89.384	91.381	-337.384	-354.559	-370.029
N	477.253	478.040	478.743	-180.451	-183.926	-186.903
N_2	0.000	0.000	0.000	-231.354	-236.989	-241.930
BH	439.224	437.742	436.122	-211.898	-217.621	-222.654
BH_2	195.687	194.753	193.803	-235.340	-244.103	-251.894
BH_3	93.395	91.519	89.907	-248.001	-258.560	-268.147
B_2H_6	22.764	23.094	23.965	-362.329	-386.856	-408.962
$B_3N_3H_6$	-527.532	-525.861	-523.580	-501.879	-540.356	-574.801
B	555.810	554.725	553.411	-180.602	-184.077	-187.053
B_2	810.425	807.319	803.819	-246.230	-252.397	-257.727
BN	474.448	473.003	471.358	-254.478	-260.469	-265.681
B-s	0.000	0.000	0.000	-31.409	-35.789	-39.703
BN-s	-251.124	-250.375	-249.646	-58.753	-66.578	-73.487

Table 8.4: Equilibrium mole quantities of species in boron nitride thermodynamic analysis

Species	1100 K	1300 K	1500 K
H	3.47E-07	1.49E-05	2.37E-04
H_2	6.00E+00	6.00E+00	6.00E+00
NH	1.08E-14	3.22E-12	2.11E-10
NH_2	7.08E-10	1.08E-08	7.97E-08
NH_3	7.53E-04	2.94E-04	1.47E-04
N_2H_2	5.44E-16	1.76E-14	2.26E-13
N_2H_4	4.64E-17	2.06E-16	6.27E-16
N	1.46E-18	4.51E-15	1.65E-12
N_2	2.50E+01	2.50E+01	2.50E+01
BH	1.06E-22	1.15E-17	5.50E-14
BH_2	1.10E-14	1.99E-11	4.77E-09
BH_3	6.10E-14	1.96E-11	1.31E-09
B_2H_6	7.68E-28	5.20E-24	3.31E-21
$B_3N_3H_6$	1.36E-21	6.04E-20	9.72E-19
B	4.24E-25	3.28E-19	6.67E-15
B_2	1.15E-42	4.30E-33	4.25E-26
BN	1.82E-23	3.58E-18	2.65E-14
B-s	0.00E+00	0.00E+00	0.00E+00
BN-s	6.00E+00	6.00E+00	6.00E+00

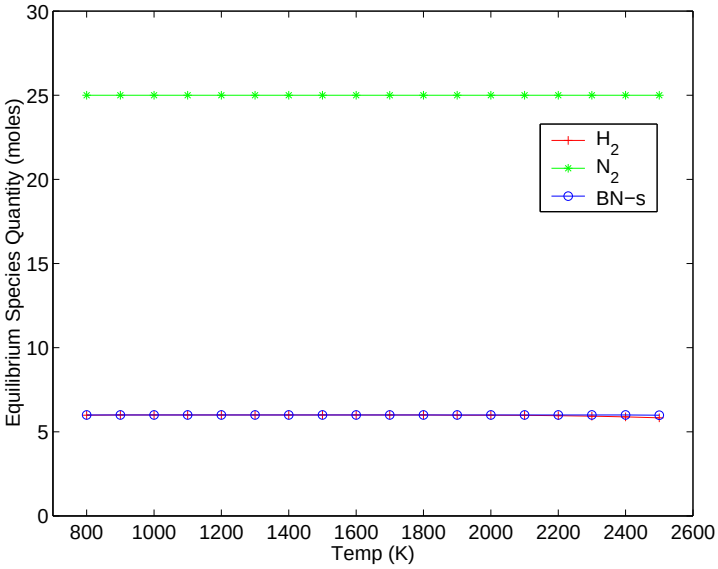

Figure 8.1: Change in boron nitride equilibrium species quantities with temperature

8.3 Computational Boron Nitride Deposition Rate Model

The three dimensional model geometry and mesh configuration used to study boron nitride deposition were identical to those used for carbon described in Section 5.1. Additionally, the universal boundary conditions described in Section 5.2 for each governing equation were applicable to the boron nitride case. The properties of the reagent mixture and its constituent species were specific to the borazine–nitrogen system, as were the results of the computational analysis.

8.3.1 Material Properties

The boron nitride deposition reaction described by Equation 2.2 used two reactant species, borazine, $B_3N_3H_6$, and nitrogen, N_2. The reaction yielded three product species: BN(s), H_2, and N_2. The definition of a gaseous mixture in the FLUENT software involved two steps. The first step was to identify and define the properties of individual species. Next, the fluid mixture was defined from the constituent species and the proper mixing rules for use in computing mixture properties were chosen. The mixture definition also involved specification of any chemical reactions that involved the mixture species. Finally, the properties of the substrate material were defined. The extreme temperatures involved in the LCVD process demanded that the material properties be defined as functions of temperature wherever possible.

8.3.1.1 Borazine, Nitrogen, and Hydrogen Species Properties

In general, all of the gaseous species used in the computational model were treated as ideal gases. The fact that all LCVD simulations were done at or below atmospheric pressure made the ideal gas assumption reasonable. For some of the material properties, it was not necessary or possible to define the properties as a function of temperature. Table 8.5 contains values for these properties. The properties that were defined as functions of temperature included:

- Specific heat capacity at constant pressure, C_p (J/kg-K)

Table 8.5: Constant properties of reagent gases used in boron nitride deposition simulation

Property	$B_3N_3H_6$	N_2	H_2
Molecular weight, M_w (kg/kmol)	80.50	28.01	2.016
Standard state enthalpy, H° (J/kmol)	-5.100E08	0	0
Standard state entropy, S° (J/kmol-K)	2.887E05	1.916E05	1.307E05
Reference temperature, T_{ref} (K)	298.15	298.15	298.15
Leonard–Jones characteristic length, σ (Å)	5.339	3.667	2.915
Leonard–Jones energy parameter, (ε/k_B) (K)	396.96	99.8	38.0

- Viscosity, μ (kg/m-s)
- Thermal conductivity, k (W/m-K)

The NIST Chemistry Webbook[98] provided a plethora of information for temperature dependent properties of gases. Values of C_p for borazine, nitrogen, and hydrogen were computed from the Shomate equation given in Equation 5.19. The coefficients in Equation 5.19 were provided by Chase[99] through NIST[98] as shown in Table 8.6.

The complex relationship between C_p and T given by the Shomate equation had to be simplified before inclusion in the model. The procedure was to use the Shomate equation to plot the temperature dependence of C_p, and then break the resulting curve into three pieces with a second order polynomial curve fit to each piece. Thus, for each species the data were described via a piecewise–polynomial. Figure 8.2 illustrates the relationship between C_p and T for all species.

Both viscosity, μ, and thermal conductivity, k, were computed for each species from kinetic theory using Equations 5.20 and 5.23, respectively. Details of these calculations were presented in Chapter 5. Figure 8.3 plots the viscosity of each species versus temperature while Figure 8.4 shows the relationship between thermal conductivity and temperature.

8.3.1.2 Reagent Mixture Properties

The mixture defined for use in the boron nitride deposition simulations consisted of $B_3N_3H_6$, N_2, H_2, and BN(s). The BN(s) species was required in the mixture definition to account

Table 8.6: Shomate equation coefficients used in boron nitride model

Borazine

Temp Range (K)	298 – 1200	1200 – 6000
A	-2.177701	243.4071
B	443.4831	20.29144
C	-307.0642	-3.87776
D	82.91977	0.257307
E	-0.720903	-46.84992

Nitrogen

Temp Range (K)	298 – 6000
A	26.092
B	8.218801
C	-1.976141
D	0.159274
E	0.044434

Hydrogen

Temp Range (K)	298 – 1000	1000 – 2500	2500 – 6000
A	33.066178	18.563083	43.413560
B	-11.363417	12.257357	-4.293079
C	11.432816	-2.859786	1.272428
D	-2.772874	0.268238	-0.096876
E	-0.158558	1.977990	-20.533862

for the removal of the elements from their gaseous source species. It played no role in the computations other than ensuring a mass balance.

The properties of the gas mixture that were derived from the properties of the individual species were computed using mixing laws. The specific mixing laws used are reported in Table 8.7.

Two different types of diffusion coefficients were needed in the boron nitride deposition model. For the ordinary diffusion calculation, the full multicomponent diffusion model was used as was presented in Equation 5.10. The diffusion coefficient for each specie pair was calculated using kinetic theory as in Equation 5.24. The second type of diffusion coefficient

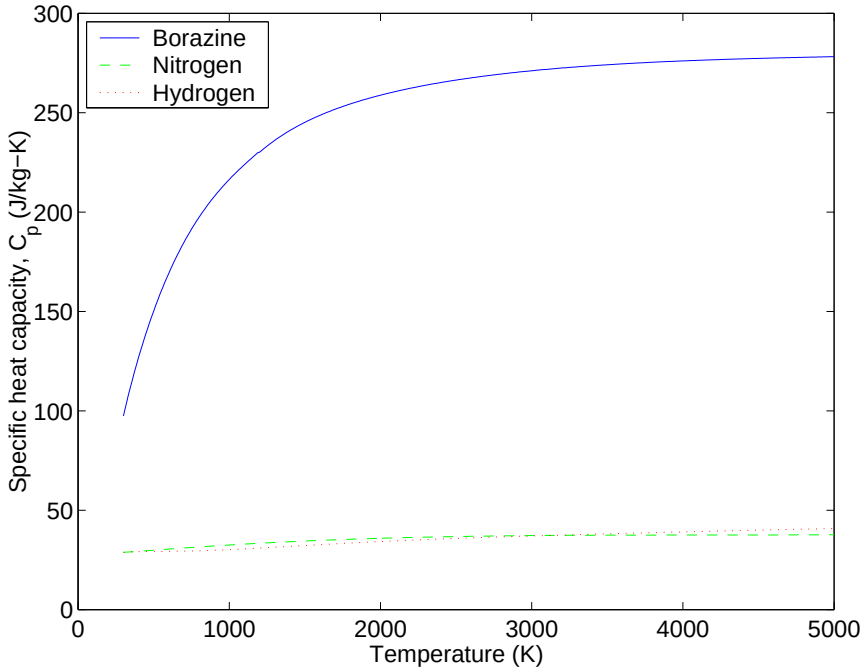

Figure 8.2: Heat capacity of boron nitride reagent gases

was the thermal diffusion coefficient which was computed for each specie using Equation 5.28.

The surface deposition reaction was also specified within the mixture definition module of FLUENT. Recall the equation that describes the overall boron nitride deposition reaction from borazine:

$$B_3N_3H_6(g) + \text{xs } N_2(g) \rightarrow 3BN(s) + 3H_2(g) + \text{xs } N_2(g) \tag{2.2}$$

This equation represents the only reaction included in the FLUENT analysis of the process. As part of the reaction definition, the code must be supplied with the kinetic parameters: k_0, n, and Q. The values in Table 8.2 were used as a starting point for these kinetic parameters.

Table 8.7: Mixing laws used in boron nitride reagent mixture definition

Density, ρ (kg/m^3)	ideal-gas
Specific heat capacity, C_p (J/kg-K)	mixing-law
Thermal conductivity, k (W/m-K)	ideal-gas-mixing-law
Viscosity, μ (kg/m-s)	ideal-gas-mixing-law

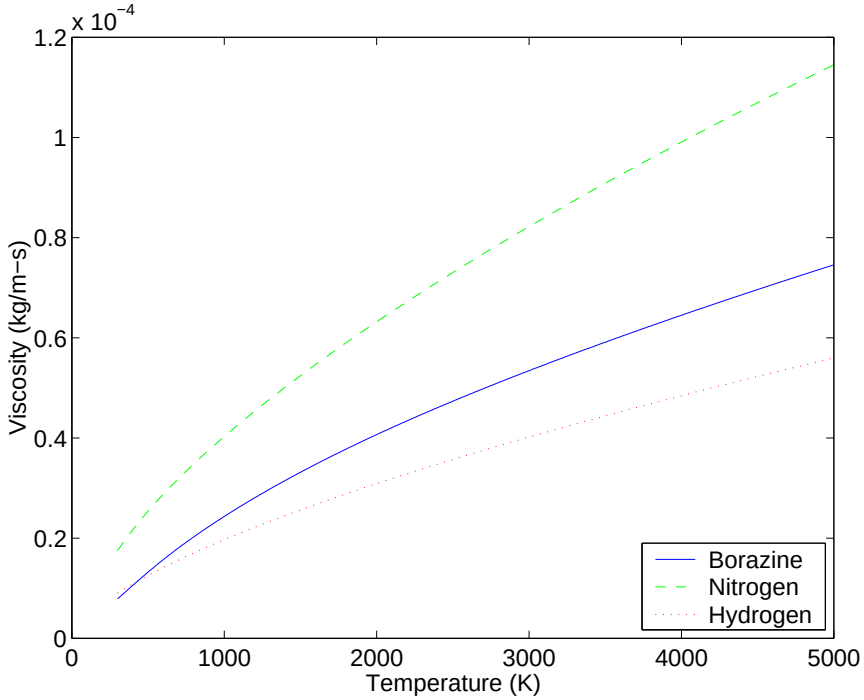

Figure 8.3: Viscosity of boron nitride reagent gases

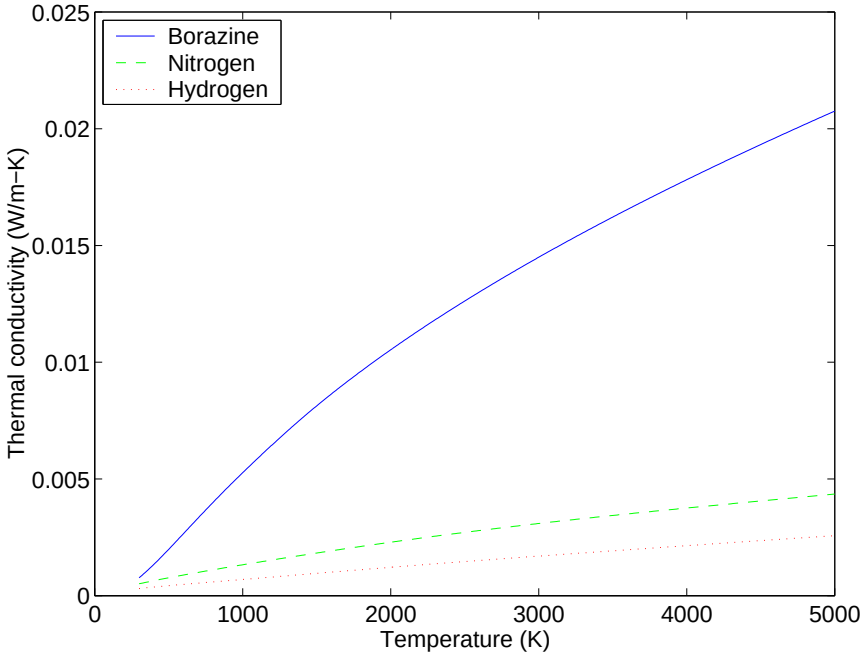

Figure 8.4: Thermal conductivity of boron nitride reagent gases

8.3.1.3 Substrate Properties

The substrates used in the boron nitride deposition experiments of Chapter 7 were tungsten sheets. However, for the purposes of the computational model being developed here to study the maximum theoretical rates of deposition, it was deemed unnecessary to develop an entirely new model mesh to represent the tungsten sheet on the graphite substrate holder. The implications of the tungsten substrate were on the temperature field, and Duty did extensive studies of the relationship between LCVD substrate materials and temperature fields in an angled–jet forced flow environment.[2,67] The same graphite substrate material used in the carbon deposition simulations of Chapter 5 was used in the boron nitride model. All boundary conditions and material properties of the substrate remained identical including the method of simulating laser heating through a volumetric heat generation function. Laser power levels were adjusted to levels that yielded temperatures within the range of successful boron nitride deposition. A value of 32 W corresponded to a maximum temperature of about 1300°C at a total flow of 27 sccm which is within the experimentally used range.

8.3.2 Boron Nitride Deposition Rate Model

The conditions used in the boron nitride model were chosen to be similar to those used in the experiments of Chapter 7. Table 8.8 gives an example of experimental conditions alongside model conditions.

Table 8.8: Comparison of boron nitride experimental and model conditions

ID	Total Press (Torr)	Carrier Flow (sccm)	Borazine Flow (sccm)	Total Flow (sccm)	Borazine Conc (mol/m^3)	Max Temp (°C)
BN-6F-5	760	25.0	2.12	27.12	3.51	1146
FLUENT-A	760	25.0	2.00	27.00	3.01	1307

The first investigation, with conditions shown in the table, involved artificially increasing the pre–exponential factor k_0 in order to force the BN deposition process well into

a transport–limited regime. Starting with k_0 = 2.0e05 m/s from the regression of Gomez–Aleixandre's data computed in Section 8.1, three additional values of k_0 were used: 2.0e07, 2.0e09, and 2.0e11 m/s.

The goal of these simulations was to quantify from fundamental principles the maximum deposition rate of boron nitride achievable in a transport–limited process. The large amount of numerical information provided by the CFD modeling environment not only enabled quantification of growth rates, but also allowed insight into the different phenomena that govern the detailed shape of the deposition rate profiles and deposit shapes.

In order to compare the cases of the different k_0 values, the variables of interest were extracted from the solution data and plotted. Two different types of plots were used: surface profile plots and boundary layer plots. Figure 8.5 illustrates where in the model domain these plots apply.

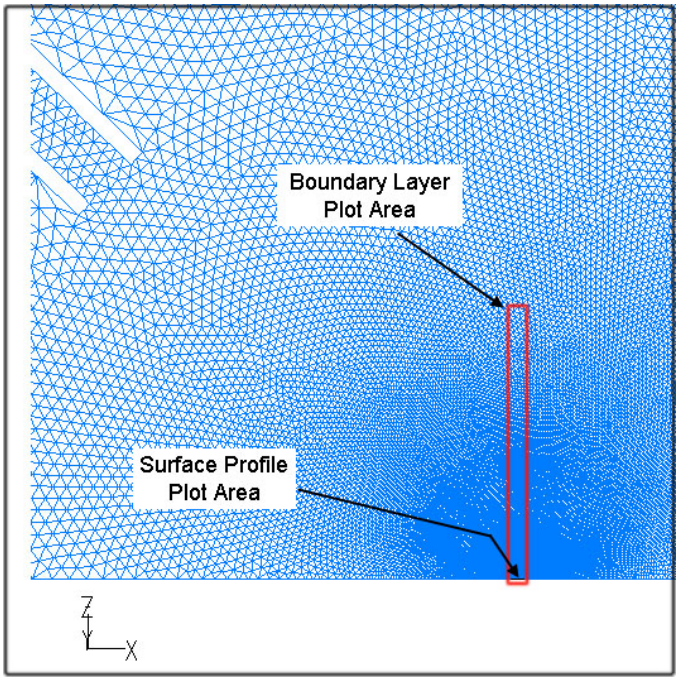

Figure 8.5: Illustration of regions used in generating surface profile and boundary layer plots

The first plot in Figure 8.6 compares the temperature profiles along the substrate surface within the symmetry plane. As expected, there was no significant difference in the

temperature profiles because the same laser power was used for all simulations. The second plot compares the mass fraction of borazine, $B_3N_3H_6$, while the third plot illustrates the deposition rate profiles along this surface for the four cases.

The plot of $B_3N_3H_6$ mass fraction profiles shows that the case of k_0 = 2.0e05 m/s did not consume all available reagent species even at the center of the laser spot. This indicated a kinetically–limited process. The $k_0 = 2.0e05$ m/s deposition rate profile in Figure 8.6 was very similar in size and shape to those of carbon deposition which has been shown to be kinetically–limited. The three cases of artificially inflated k_0 values indicated the presence of both a transport–limited and a kinetically–limited region across the surface of the laser spot. Figure 8.6 shows for each of these three cases a region where the borazine mass fraction was approximately equal to zero. For these cases, the deposition rate profiles showed a drastic transition in shape near the point where the mass fraction approached zero. The depletion of reagents in the center region was evidence that the rate–limiting mechanism had changed from kinetic to transport.

A second boron nitride deposition rate model was developed to study the effect of an increased gas nozzle flow rate. The nominal gas nozzle flow was increased to 50 sccm while the $B_3N_3H_6$ mole fraction was kept constant at 0.0741. Figure 8.7 contains plots of the temperature, $B_3N_3H_6$ mass fraction, and BN deposition rate across the surface of the laser spot. In general, these curves are very similar to those of Figure 8.6 for the 25 sccm carrier flow case.

For the case of $k_0 = 2.0e07$, a comparison of the temperature, mass fraction, and deposition rate profiles is shown in Figure 8.8 for the two different flow cases. The temperature profile plot indicates that the small change in flow rate had minimal effect on the laser spot temperatures. For the case of total flow equal to 50 sccm, the mass fraction of $B_3N_3H_6$ is shown to be significantly higher across the laser spot diameter, except where the transport–limited effects dominated. The increased flow rate is also shown to significantly effect the overall BN deposition rate which validated the use of the localized gas nozzle.

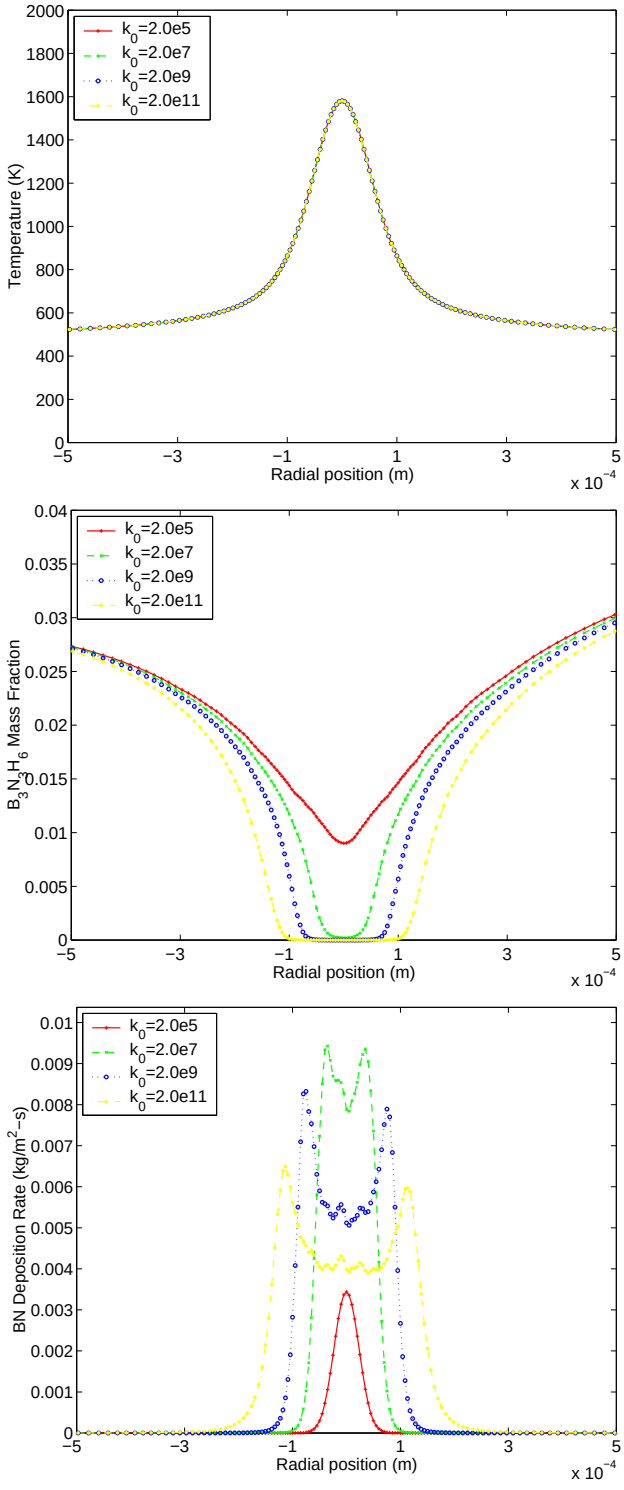

Figure 8.6: Effect of different k_0 values on temperature, $B_3N_3H_6$ concentration, and BN deposition rate profiles along the substrate surface within the fluid symmetry plane

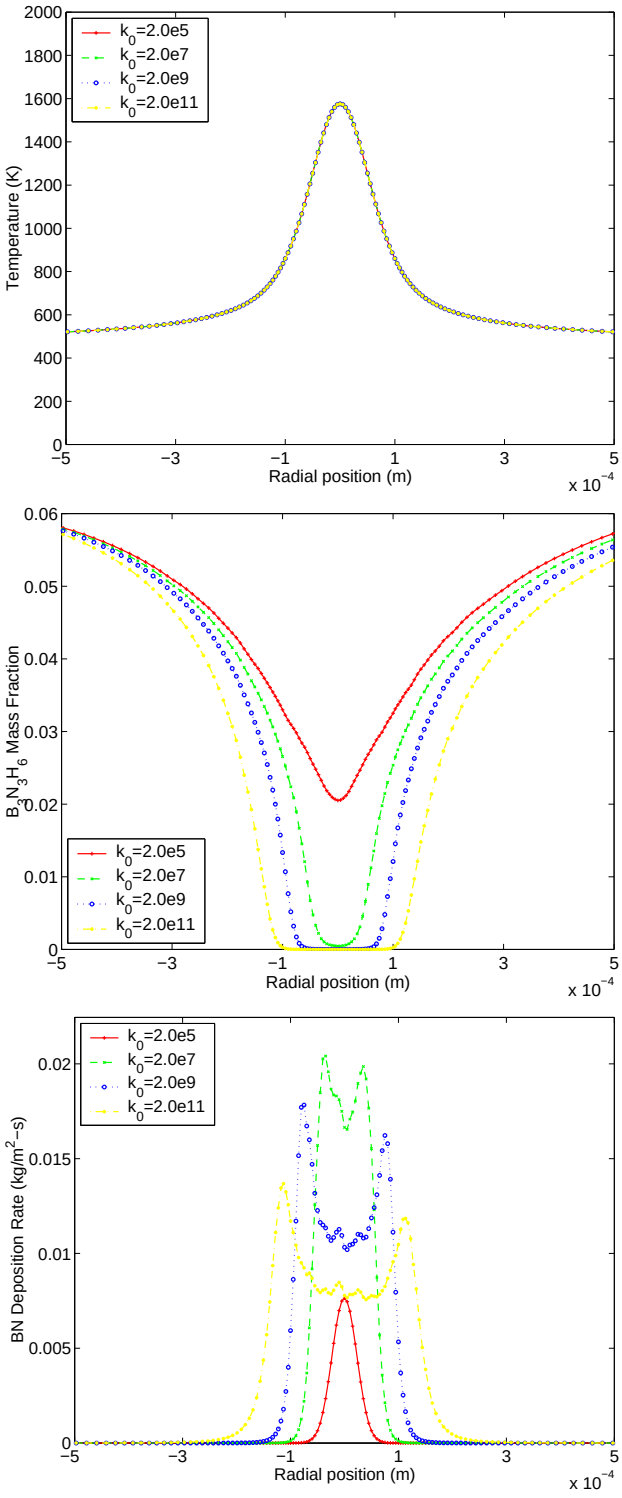

Figure 8.7: Effect of different k_0 values on temperature, $B_3N_3H_6$ concentration, and BN deposition rate profiles along the substrate surface within the fluid symmetry plane

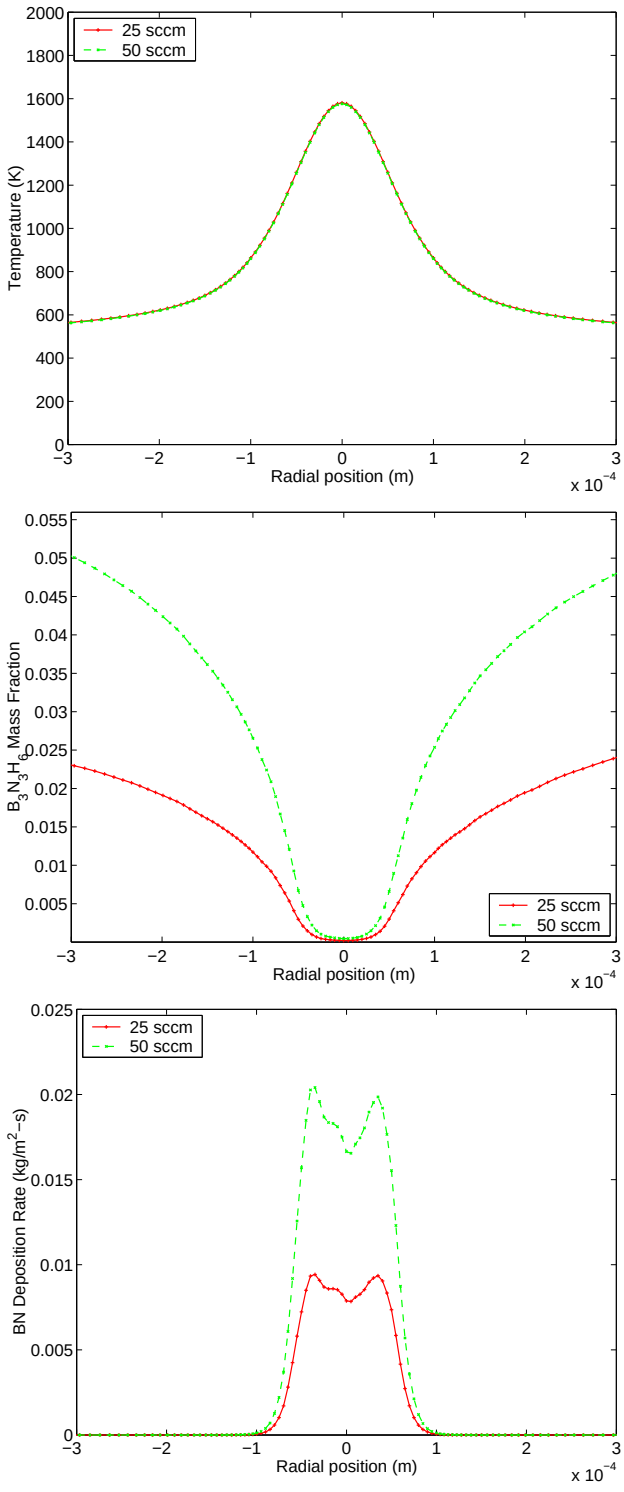

Figure 8.8: Effect of different carrier flow rates on temperature, $B_3N_3H_6$ concentration, and BN deposition rate profiles along the substrate surface within the fluid symmetry plane

More insight into the difference between the 25 and 50 sccm flow cases can be seen by investigating the boundary layers directly above the laser spot. Each transport equation has a boundary layer associated with it: thermal boundary layer, momentum boundary layer, and species (or concentration) boundary layer. Quantification of these boundary layer sizes and the resulting deposition rates at different gas nozzle flow rates was possible using the deposition rate model.

Data were taken from the vertical line extending into the fluid zone above the center of the laser spot. Figure 8.5 illustrates the relation of the boundary layer plot space to the overall model domain. Figure 8.9 contains plots of the temperature, momentum, and concentration boundary layers for $k_0 = 2.0\text{e}07$ for each of the two flow cases. The plots are arranged with the z axis position on the vertical axis and the variable of interest on the horizontal axis.

The temperature profiles for the two cases are very similar throughout the first 0.25 mm above the substrate surface. Above this point, the 25 sccm case is generally hotter than the 50 sccm case. The 25 sccm case has a thermal boundary layer thickness of approximately 2 mm while the 50 sccm case is closer to 1 mm.

The momentum boundary layer plot revealed two important things about the increased flow rates. First, doubling the flow rate from 25 sccm to 50 sccm resulted in an increase in bulk velocity near the surface of less than 25%. Second, the height of the boundary layer in the 25 sccm case was about 0.75 mm while the height of the 50 sccm boundary layer was about 1.2 mm.

The species boundary layer is extremely important in LCVD. The plot of species boundary layer profiles reveals that the increased flow rate through the gas nozzle increases both the bulk concentration near the substrate surface by about 25%, and reduces the boundary layer thickness in this same region from about 1.4 mm to 0.8 mm. It is this compression of the species concentration boundary layer that enabled the increase in deposition rate with increased flow rate as was shown in Figure 8.8.

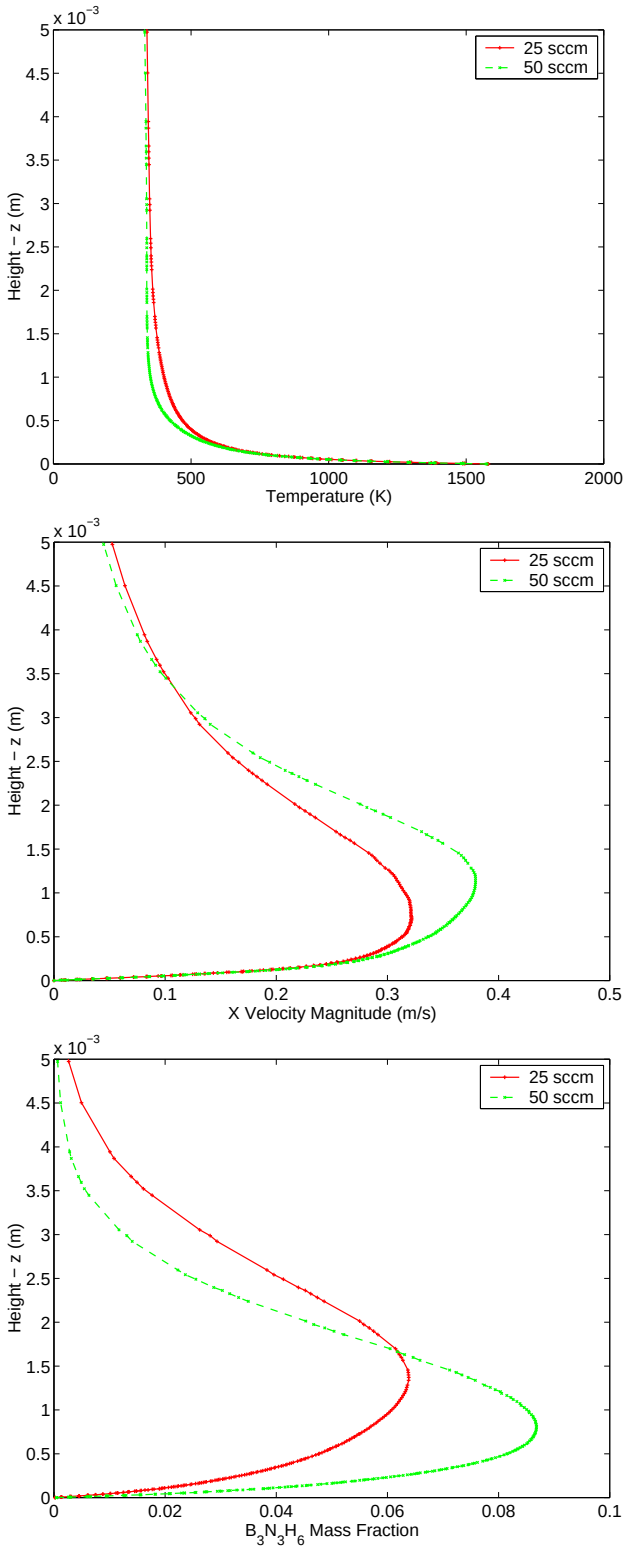

Figure 8.9: Effect of different carrier flow rates on thermal, momentum, and species boundary layer profiles in the fluid zone directly above the center of the laser spot

8.3.2.1 Deposition Rate Profile Shapes

The deposition rate profile plots in Figures 8.6, 8.7 and 8.8 for the cases of $k_0 \geq$2.0e07 exhibit an interesting shape. The shapes correlated well with the experimentally observed volcano effect in BN deposition. These shapes reflect one of the most complex attributes of the LCVD process. When one area of the deposition surface is operating in a transport–limited regime, there will be an adjacent region operating in a kinetically–limited regime. This fact is driven by the temperature gradients across the surface of the substrate.

Within the transport–limited region, the deposition rate is lowest near the center of the laser spot and increases gradually with increasing radial distance. The explanation for this difference in rates must lie in the variation of the local diffusive flux of $B_3N_3H_6$ toward the substrate surface. Recall the equation governing diffusion of a species within a dilute mixture from Chapter 5:

$$\vec{J_i} = -\rho D_{i,m} \nabla Y_i - D_{T,i} \frac{\nabla T}{T} \tag{5.9}$$

where $\vec{J_i}$ was the mass flux of species i, ρ was the density of the mixture, $D_{i,m}$ was the diffusion coefficient of species i in the mixture, Y_i was the local mass fraction of species i, $D_{T,i}$ was the thermal diffusion coefficient of species i, and T was the local temperature of the mixture.

The concentration gradient, ∇Y_i, represents the change in concentration relative to the different spatial directions. The issue of spatial directions and the dimensionality of the diffusion paths to the substrate surface during a transport–limited LCVD process could be one explanation for local variations in $B_3N_3H_6$ diffusive flux. The diffusion path above a transport limited LCVD surface reaction is effectively one dimensional. This is most true in the center of the laser spot. Moving out radially, as the kinetically–limited region is approached, the dimensionality of the diffusion paths increases accordingly. The "funneling down" of the diffusion paths toward the center of the deposit can restrict the diffusive transport to this region. Figure 8.10 depicts this situation.

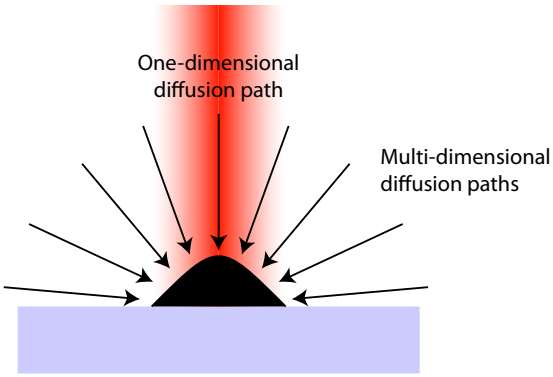

Figure 8.10: Spatial dependency of diffusion paths in LCVD

In one dimension (e.g. the x direction), the ∇Y_i term can be approximated by:

$$\nabla Y_i \approx \frac{\Delta Y_i}{\Delta x} \approx \frac{Y_{\infty,i} - Y_{0,i}}{\delta} \tag{8.15}$$

where $Y_{\infty,i}$ is the bulk mass fraction of species i, $Y_{0,i}$ is the surface mass fraction of species i, and δ is the species or concentration boundary layer thickness.

If we assume that the mass fraction of $B_3N_3H_6$ approaches zero at the substrate surface, variations in the local concentration gradient must be due to either variations in the bulk $B_3N_3H_6$ concentration or variations in the boundary layer thickness. Both of these possibilities can be investigated using data from the model results.

Boundary layer profiles at different points within the transport–limited region were plotted and are shown in Figure 8.11. The three radial points of 0, 25, and 50 μm represented points near the minimum, mean, and maximum within the transport–limited region of the deposition rate curves, respectively. The change in maximum $B_3N_3H_6$ mass fraction and boundary layer thickness at these three points is illustrated in Figure 8.12.

The decrease in mass fraction with increasing radial position would suggest a decline in the magnitude of diffusive flux due to the concentration gradient. This behavior is not consistent with observed deposition rate profiles. The decline in the concentration boundary layer thickness suggests an increase in diffusive flux which is consistent with the observed deposition rate profiles. Therefore, the relation between the variation in the local concentration gradient, ∇Y_i, and the radial position is inconclusive.

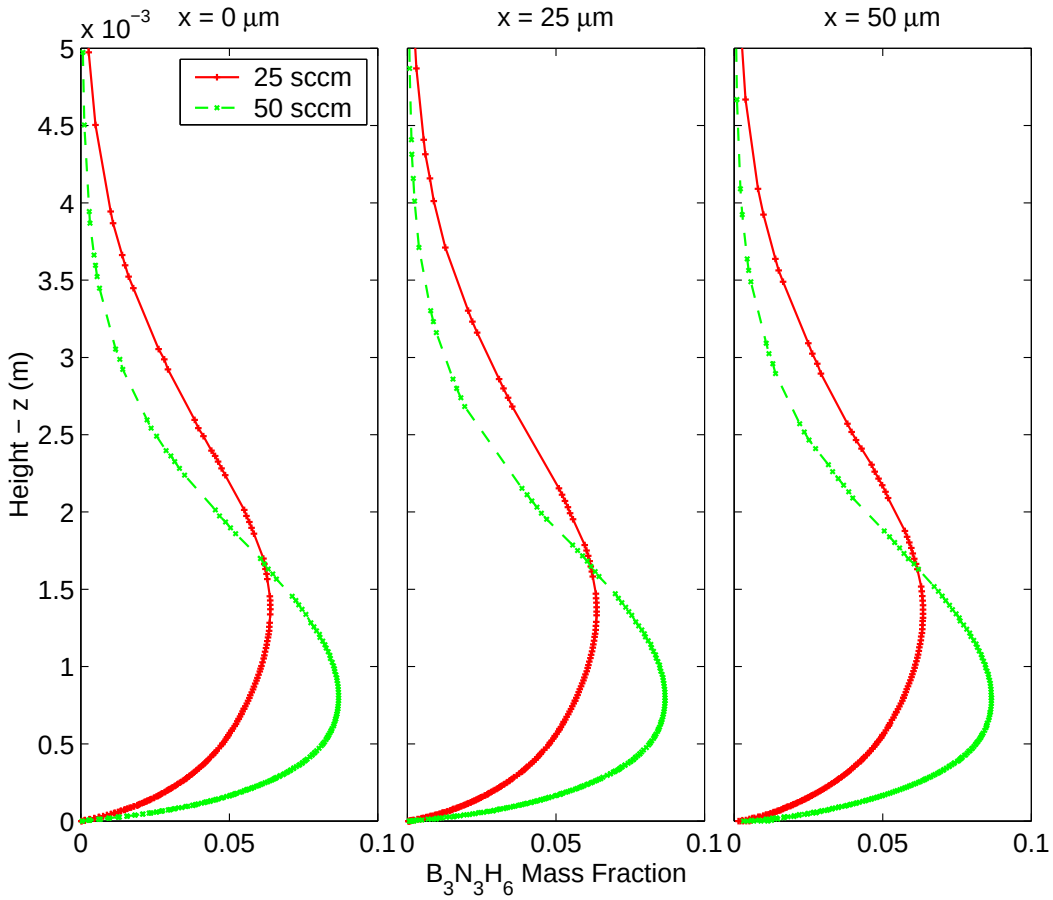

Figure 8.11: Concentration profiles at different radial positions above laser spot

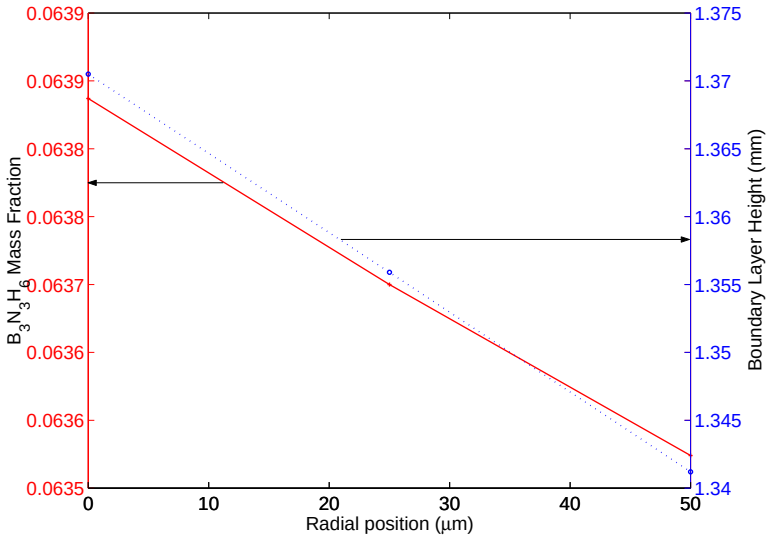

Figure 8.12: Change in $B_3N_3H_6$ mass fraction and concentration boundary layer thickness within transport limited region of deposition surface

Another explanation for variation in the local diffusive flux to the substrate surface is related to the thermal diffusion term of Equation 5.9. The general importance of thermal diffusion in LCVD was highlighted in Chapter 5 when analyzing carbon deposition. The contour plots in Figures 8.13 and 8.14 of the $B_3N_3H_6$ mass fraction and temperature fields in the fluid symmetry plane indicate conceptually the general directions of both ordinary and thermal diffusion. The magnitude and opposing directions of these diffusion mechanisms in the vicinity of the laser spot could cause variations in the local diffusive flux.

In order to quantify the significance of thermal diffusion in boron nitride LCVD, a simulation was run that disabled the computation of the thermal diffusion term in the species transport equation. The plots in Figure 8.15 show that when thermal diffusion was not considered, the concentration of $B_3N_3H_6$ above the substrate surface increased which caused the overall deposition rate to increase.

However, the overall shape of the deposition rate profile did not change appreciably from the case that did consider thermal diffusion. Therefore, these results again confirm the importance of thermal diffusion in determining overall growth rate, but they do not indicate that the variation in deposition rate within the transport–limited area of the deposition zone can be attributed to this phenomenon.

Also intriguing about the rate profiles, is the fact that both the maximum and the average deposition rate at a given point on the substrate surface decreased with increasing k_0 values. The profile did increase in overall width with increasing k_0 values. This behavior is somewhat difficult to interpret, because changing k_0 values is difficult to conceive experimentally. However, it is understood that the overall mass deposition rate should increase with increasing k_0 values. By looking at the area under the curves in Figures 8.6 and 8.7, we see that indeed the overall deposition rate does behave in this manner.

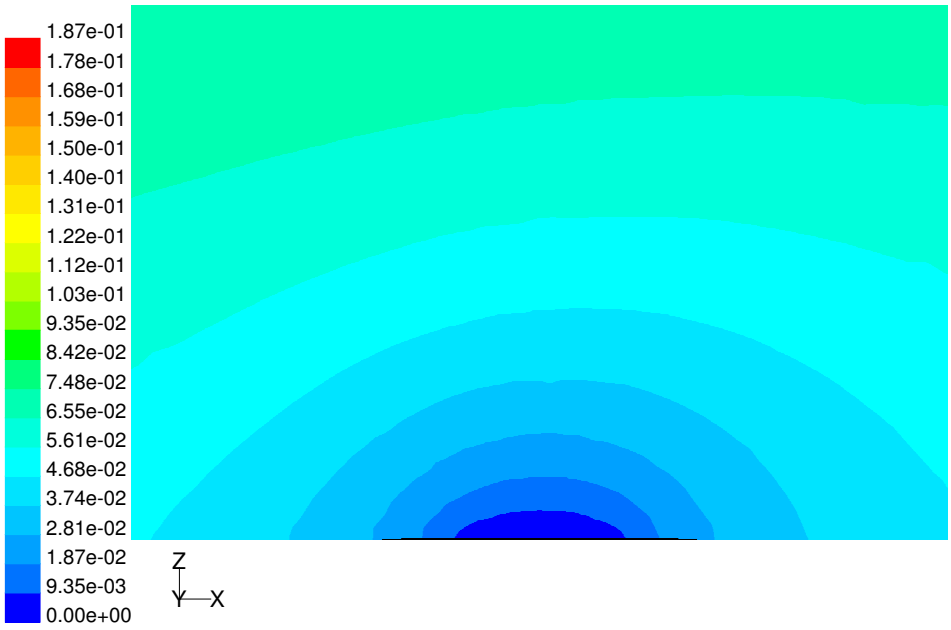

Figure 8.13: Concentration gradients that drive diffusive flux toward the deposition surface

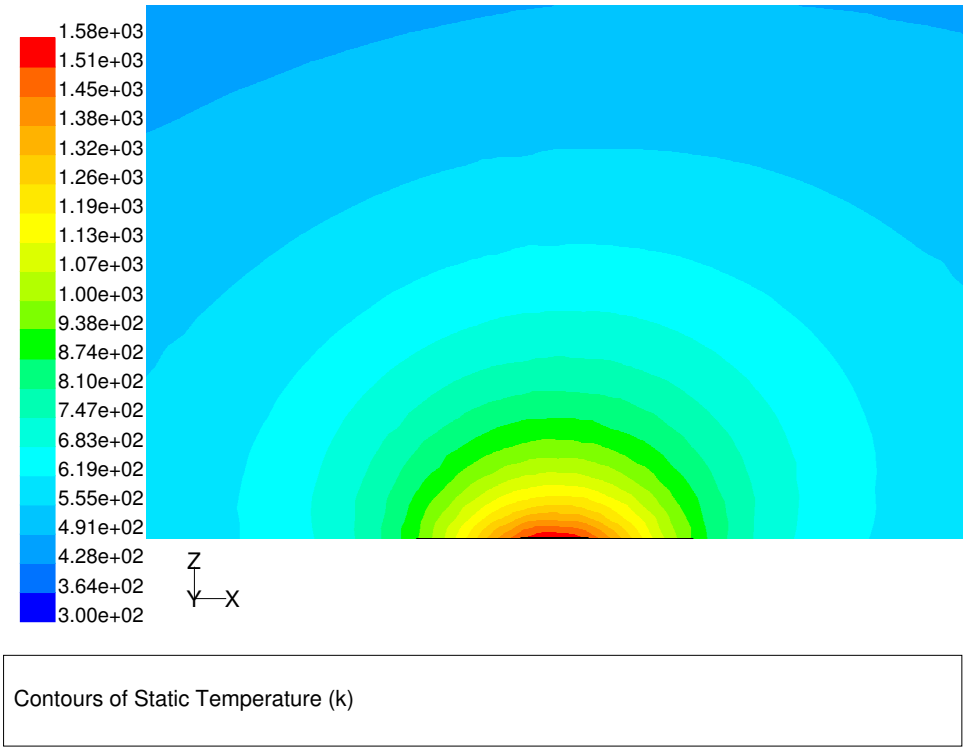

Figure 8.14: Temperature gradients that drive diffusive flux away from the deposition surface

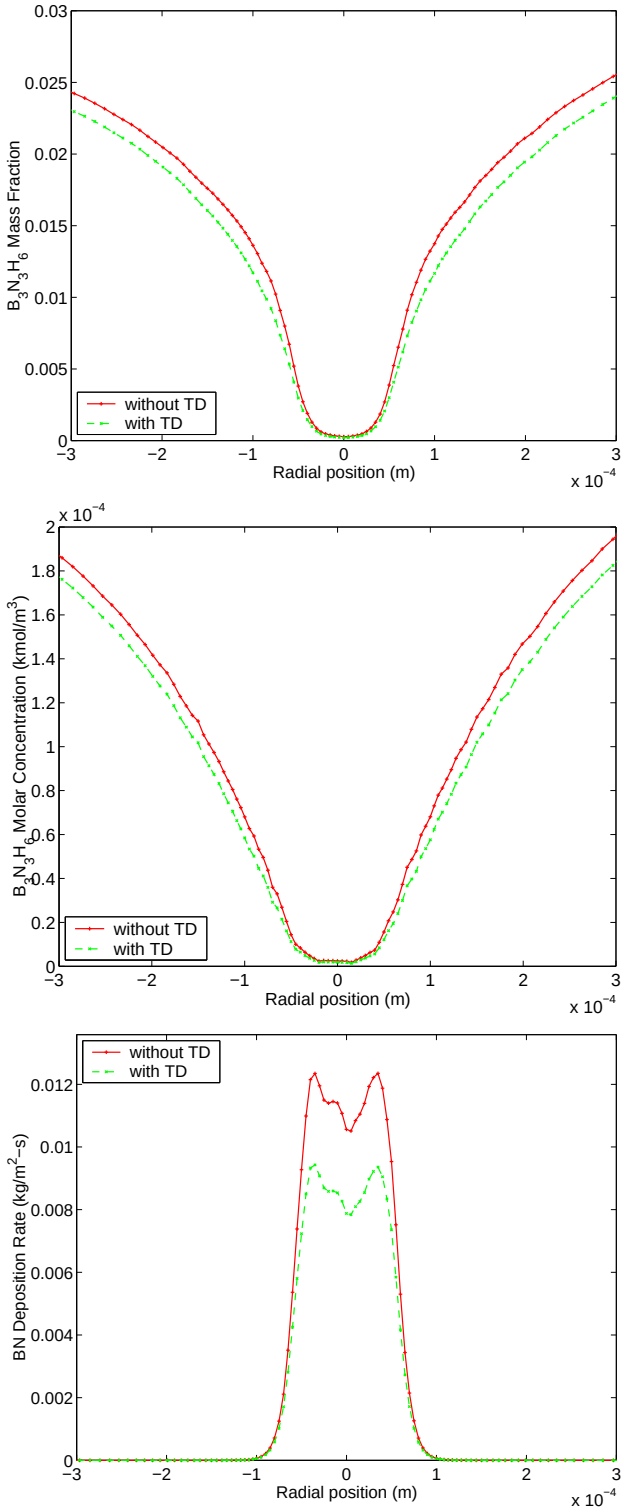

Figure 8.15: Effect of thermal diffusion on $B_3N_3H_6$ concentration and BN deposition rate profiles for 25 sccm flow case with $k_0 = 2.0e07$

8.3.3 Relation Between BN Deposit Shape and Deposition Rate Profiles

One limitation of the boron nitride deposition rate model that also applied to the carbon deposition rate model is that during the growth process, the shape and properties of the substrate itself change. The emergence of this new structure significantly effects the temperature profiles and flow characteristics. Therefore, the rigorous interpretation of the model results is that they are only valid during the first few instants of deposition; however, it is believed that much of the insight into the coupling of the thermal, momentum, and mass transport phenomena is applicable throughout the deposition process.

The deposition rate profiles in the transport–limited BN process were very different from those of the kinetically–limited carbon cases. An investigation into the shape of the transport–limited profiles was given in Section 8.3.2.1. An extensive discussion of the relation between the deposition rate profile and the deposit shape of the kinetically–limited carbon deposition process was given in Section 5.3.5.4. Some of the same considerations apply in a transport–limited process, but additional complexities also arise.

The additional complexities of a transport–limited case are related to the coupling between the underlying substrate surface shape and the deposition rate. As a deposit grows, and its shape becomes more pronounced from the underlying substrate surface, the boundary layer shapes are affected. Changes in species boundary layer thickness directly impact the magnitude of diffusive flux of reagent to the surface. Variations in diffusive flux along the substrate surface cause variations in deposition rates, thus, the surface shape becomes distorted. The detrimental aspect of this cycle is that regions where the deposition rate is increased cause protrusions from the surface which reduces the local boundary layer thickness, further increasing the deposition rate.[18]

It was mentioned in Chapter 7 that some of the BN deposits, particularly under the 50 sccm flow case, exhibited asymmetries with respect to the direction of the gas flow from the nozzle. The deposition rate profiles of Figures 8.7 and 8.8 indicate that some asymmetry can arise without considering the emerging deposit structure. This asymmetry in the rate

profiles can be attributed to enhanced reagent transport on the nozzle side of the deposition zone.

Additional asymmetries could arise due to changes in the convective flow patterns around the growing structure due to the structure itself. As the nozzle side of a deposit grows faster, it will change the flow streamlines and restrict convective transport to the center and opposite side of the deposit. Such a situation could explain the large asymmetries seen in BN-18F.

The deposit shapes in a transport–limited process are affected by the changes in deposition rate profiles and an increased sensitivity of deposition rates to the underlying surface shape. Moreover, the volcano shaped deposition rate profiles within this regime seem inherent in the process due to the spatial restrictions in the diffusive path to the center of the deposit zone. Using a gas nozzle to assist transport into the deposition zone helps increase overall deposition rates, but does not eliminate the volcano effect. In fact, the nozzle could be responsible for inducing asymmetries in the deposited structures. In summary, operating in a transport–limited regime poses many challenges for controlling LCVD deposit shapes.

8.3.4 Experimental Comparison

The primary impetus for developing the boron nitride deposition rate model was to identify the theoretical maximum deposition rate under transport–limited conditions. For each model case with $k_0 \geq$2.0e07, the deposition rate profiles contained a regime transition point. As the name implies, the regime transition point refers to the change from the kinetically–limited regime to the transport–limited regime. This regime transition point represented a local maximum deposition rate that corresponded to a particular radial position and surface temperature. The conceptual Arrhenius plot of $\ln J$ versus $1/T$ in Figure 8.16 illustrates the relationship between the different kinetic curves and the upper theoretical limit of mass transport.

The temperature, deposition rate, data pairs for cases with $k_0 \geq$2.0e07 and flow equal

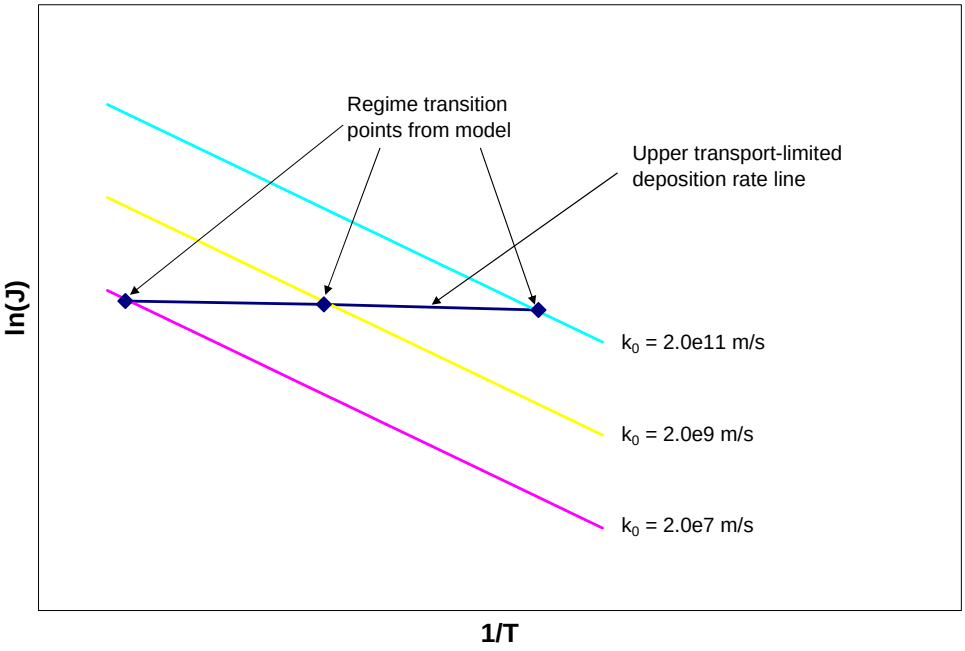

Figure 8.16: Arrhenius plot showing relation between kinetic lines and mass transport line

to 25 sccm were transformed and plotted on the Arrhenius plot shown in Figure 8.17. Experimental data from cases with a total flow of approximately 25 sccm were also plotted for comparison. The vertical axis represents the mass deposition rate of BN normalized by the temperature adjusted bulk $B_3N_3H_6$ concentration. Removing the concentration from the analysis allows a more direct comparison of the model and experimental results.

Overall, the plot shows good agreement between the predicted transport limit and the experimental data. The vertical scatter in the experimental data could be attributed to a variety of factors including variability in deposition temperature due to imperfect control schemes and error associated with the deposition rate measurement technique. The lack of horizontal range is due to physical limitations of the experimental setup. The lower temperature limit was dictated by the lower limit of the thermal imaging camera. The upper temperature was limited by the formation of undesirable deposit attributes such as the volcano effect or black coloration. Overall, these results further support the claim that under the conditions used in Chapter 7, BN deposition from $B_3N_3H_6$ is a transport–limited process.

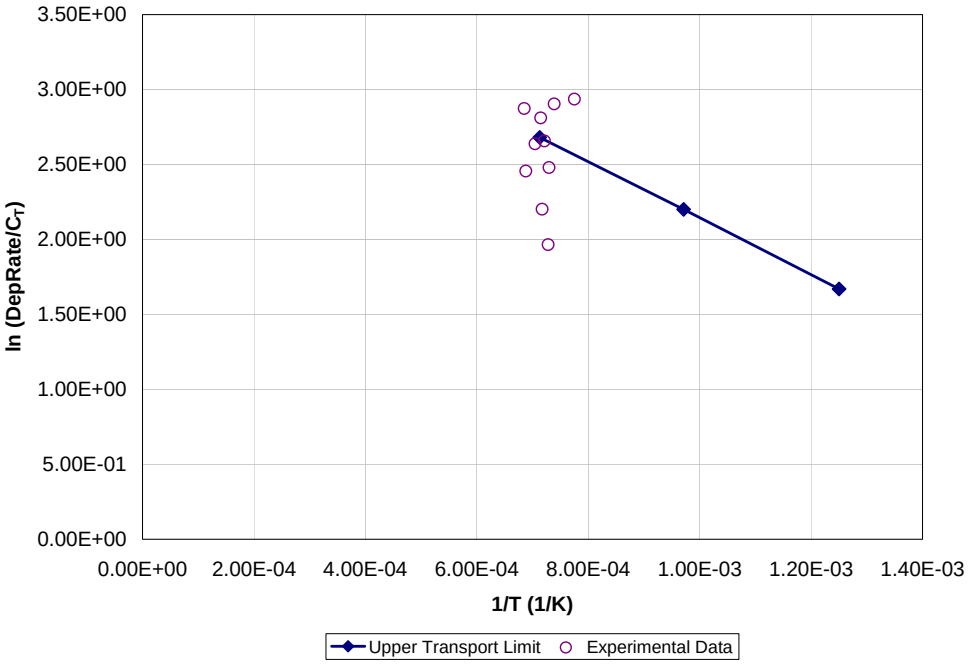

Figure 8.17: Arrhenius plot comparing theoretical upper limit of mass transport from model to experimentally measured growth rates

The slope of the transport–limit line in Figure 8.17 can be used to compute an apparent activation energy of this transport–limited process. This activation energy is a reflection of the influence of changing temperature on the diffusion process. A simple linear regression through the three data points gave a slope that was converted into an activation energy of 3.74 kcal/mol (15.6 kJ/mol). As expected, this value is significantly less than the 35 kcal/mol value for a kinetically–limited case reported by Gomez–Aleixandre.[29]

In summary, an advanced model of the LCVD process was used to verify that boron nitride deposition at the experimental conditions of interest was a transport–limited process. Both concentration and thermal diffusion were shown to be important molecular transport mechanisms in BN LCVD. The transport–limited environment posed significant challenges to controlling deposit shape, especially regarding avoiding the volcano effect. The theoretical upper mass transport limit of growth velocity under the conditions studied was identified to be between 3 and 5 μm/s.

CHAPTER IX

MOLYBDENUM EXPERIMENTS

The deposition of molybdenum in Georgia Tech's LCVD system is necessary for the fabrication of the integrated dispenser cathode device. Much like boron nitride, Duty has provided some "proof of concept" work that serves as the experimental foundation for molybdenum deposition.[2,44] Others have deposited Mo from $Mo(CO)_6$ as described in Chapter 2, but Duty's laser CVD of molybdenum from $MoCl_5$ serves as the only prior work in this particular area. As seen in Figure 9.1, the size and shape of Duty's deposits were significantly different than those required by the dispenser cathode application.

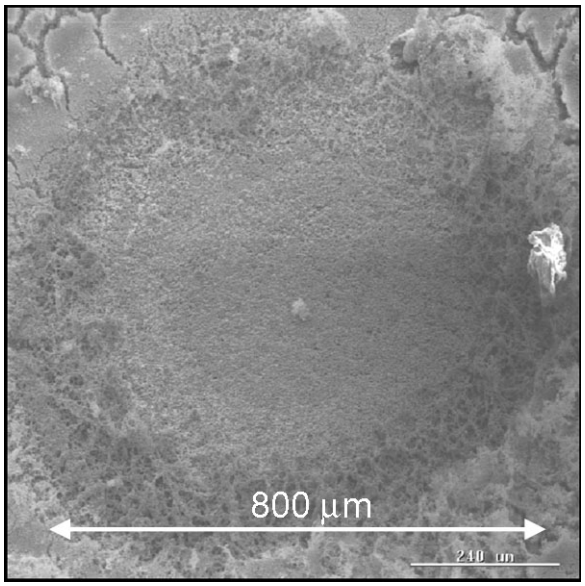

Figure 9.1: Example of Duty's molybdenum deposit on graphite

The focus of the molybdenum deposition experiments done here was to study the process-property relationships in an effort to find conditions that enabled the deposition of uniform molybdenum lines. The generic development path of Section 1.4.1 for the LCVD of new materials was used here to guide the progression of Mo deposition.

9.1 Experimental Setup for Mo Deposition

The overall reaction for deposition of the molybdenum from $MoCl_5$ was given by Equation 2.7:

$$MoCl_5(g) + \frac{5}{2}H_2(g) \rightarrow Mo(s) + 5HCl(g) \tag{2.7}$$

The experimental setup involved configuring a delivery system for the $MoCl_5$ reagent and acquiring and preparing the necessary substrates.

9.1.1 Molybdenum Pentachloride Setup and Delivery

Molybdenum pentachloride is a solid at room temperature. In order to generate the $MoCl_5$ vapor needed for the LCVD process, $MoCl_5$ powder was heated and vaporized in a sublimation chamber. The relationship between the temperature of the sublimation chamber and the vapor pressure of $MoCl_5$, P_{MoCl_5}, was approximated by Saeki's equation:[114]

$$\log P_{MoCl_5} = \frac{-3504}{T} + 9.465 \tag{9.1}$$

where P_{MoCl_5} was the vapor pressure (Torr), and T was the sublimation chamber temperature (K).

The sublimation chamber used in the setup was a stainless steel cylindrical vessel that contained a ceramic boat filled with $MoCl_5$ powder. The chamber itself was about 5.1 cm in diameter and 15.3 cm long. It was equipped with a thermocouple and a mechanical pressure gage. Prior to loading, all fittings were removed and the vessel was thoroughly cleaned with stainless steel brushes, paper towels, methanol, and compressed air. All fittings were similarly cleaned and the two high temperature valves on either side of the chamber were replaced with new valves. After reassembly, the vessel was checked for leaks by pressurizing with nitrogen gas and monitoring the pressure over a period of more than 24 hours. No detectable pressure change was recorded.

Two different batches of $MoCl_5$ powder were used during these experiments. The first batch was obtained from a sealed bottle of 250 g of 99.6% molybdenum (V) chloride powder packed under argon (Alfa Aesar Stock #11832) that was purchased in 1997. $MoCl_5$

powder is very sensitive to both oxygen and atmospheric moisture; therefore, it was transferred into the sublimation chamber in a nitrogen glove box. About 3 grams of powder were transferred into a ceramic boat that was placed in the sublimation chamber. This first batch of $MoCl_5$ powder was used for experiments Mo-1F through Mo-5F. The second batch used powder of the same specification from the same supplier; however, it was purchased new in August 2004. The new powder was loaded into two new ceramic boats that together held 13.7 grams of powder. These boats were secured inside the sublimation chamber and the chamber was sealed. This second batch of powder was used for all other Mo experiments.

In order to deliver $MoCl_5$ vapor to the upper reaction chamber of the system, the sublimation chamber was placed upstream of the gas nozzle. Figure 9.2 illustrates the configuration of the $MoCl_5$ reagent delivery system. MFC 5 was used to control the hydrogen carrier gas flow into the sublimation chamber while MFC 6 was used to regulate the flow of the hydrogen diluent gas. Both the carrier gas and diluent gas were delivered from the same industrial grade high purity hydrogen gas cylinder.

In order to prevent the condensation of $MoCl_5$ vapor downstream of the sublimation chamber, the reagent lines between the sublimation chamber and the reaction chamber were heated with heater tapes. These line temperatures were kept at about 150°C for most experiments. Heater tape was also used to pre-heat the diluent gas prior to mixing with the carrier and $MoCl_5$ vapor. Calculations showed that pre-heating 150 mm of tubing prior to the mixing zone would be sufficient to prevent condensation.

Preliminary experiments resulted in a clogged gas nozzle due to condensed $MoCl_5$ powder inside the nozzle tube. A nozzle heater was constructed by wrapping a 150 mm long ceramic tube with 24 AWG Nichrome heater wire. The heater wire was wrapped in high temperature electrical tape and the assembly was slid onto the nozzle tubing and secured. The power source for the heater was a 120 VAC variable transformer (variac). A pass-thru port was used in the upper reaction chamber to deliver the electric current to the heater element during operation. Calibration experiments showed that a variac setting of

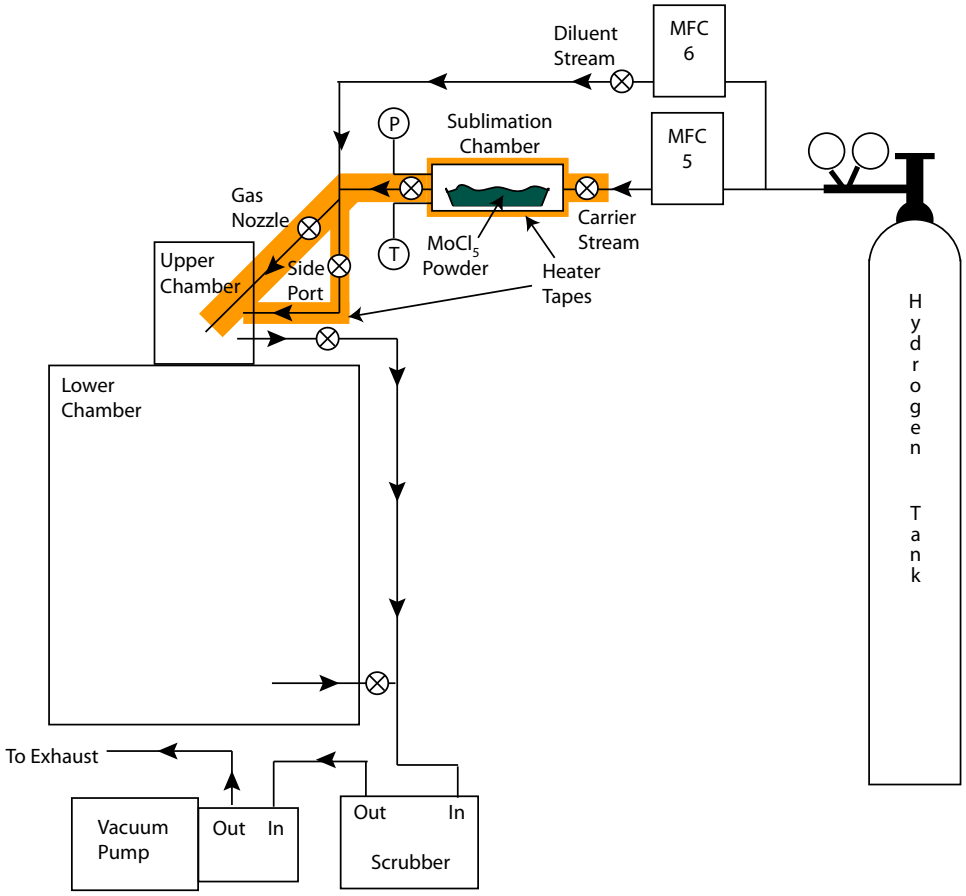

Figure 9.2: Piping configuration used to deliver $MoCl_5$ vapor to deposition zone

18% (21.6 V) yielded a nozzle tip temperature of over 150°C.

The partial pressure of the H_2 carrier gas can be computed from Equation 9.2:

$$P_{car} = P_{tot} - P_{Mo\,Cl_5} \tag{9.2}$$

where P_{tot} is the total pressure in the sublimation chamber which is assumed to be equal to the pressure in the upper reaction chamber.

The flow rate of $Mo\,Cl_5$ vapor from the sublimation chamber was computed using Equation 9.3:

$$Q_{Mo\,Cl_5} = Q_{car}\left(\frac{P_{Mo\,Cl_5}}{P_{car}}\right) \tag{9.3}$$

where $Q_{Mo\,Cl_5}$ and Q_{car} are the flow rates of $Mo\,Cl_5$ and carrier H_2, respectively.

The concentration of $Mo\,Cl_5$ vapor delivered through the gas nozzle was computed from the mole fraction of $Mo\,Cl_5$ and the ideal gas law. The mole fraction of the reagent flow can be computed using equation 9.4:

$$X_{Mo\,Cl_5} = \frac{Q_{Mo\,Cl_5}}{Q_{Mo\,Cl_5} + Q_{car} + Q_{dil}} \tag{9.4}$$

where Q_{dil} is the flow rate of diluent hydrogen. The concentration was then computed from equation 9.5

$$C_{Mo\,Cl_5} = X_{Mo\,Cl_5}\frac{P_{tot}}{RT} \tag{9.5}$$

where $C_{Mo\,Cl_5}$ is the concentration of molybdenum pentachloride (mol/m^3), R is the universal gas constant (0.062363891 Torr-m^3/mol-K), and T is the temperature of $Mo\,Cl_5$ (K).

9.1.2 Substrate Preparation

The dispenser cathode application requires the deposition of molybdenum on a boron nitride substrate. Hot pressed boron nitride shapes were acquired from GE Advanced Ceramics (Grade HBC). They came in 25.4 x 25.4 x 19.05 mm blocks which were dry cut on a diamond wafering saw into 25.4 x 19.05 x 2.54 mm plates. Because it was diffusion bonded and did not contain a binder, this material had a purity of $>$ 99%. It is widely used

in electronic applications because of its low dielectric constant, high thermal conductivity, and minimal moisture pickup. Specific material properties are given in Table A.2 in Appendix A.

After cutting, the BN substrates were sanded flat with 600 grit SiC grinding paper and blown off with compressed air. When not in use, the substrates were stored in an oven at 70°C to minimize moisture pickup.

9.1.3 General Procedure

The general procedure for Mo deposition was similar to other LCVD materials. It normally took the sublimation chamber, reagent lines, and gas nozzle about 2 hours to reach the operating temperature of between 100 and 150°C. Meanwhile, the substrates were loaded into the chamber and the chamber was evacuated. The system was refilled with high purity argon and subsequently evacuated. Next, the chamber was refilled with H_2 gas to the desired operating pressure. The desired flow rates were set and when ready to begin deposition, the laser was engaged, and the carrier H_2 flow was diverted through the sublimation chamber.

9.2 Molybdenum Fiber Experiments

Mo-1F was an exploratory experiment that was used to search for conditions conducive to molybdenum deposition. The strategy was to begin experiments with the sublimation chamber at a relatively low temperature so as to yield a low concentration of $MoCl_5$ through the nozzle and minimize the chance of condensation. The conditions used in the experiment are given in Table 9.1.

During the process, the deposition temperature measured using the thermal imager remained fairly stable at a fixed laser power. In contrast to carbon and boron nitride deposition, as the molybdenum grew on the substrate, the laser power had to be gradually increased over time to maintain a constant temperature. This behavior was likely related to changes in the optical and thermal properties of the substrate caused by the evolution

Table 9.1: Mo-1F experiment conditions

No.	Chamber Press (Torr)	Sub Temp (°C)	Carrier Flow (sccm)	Diluent Flow (sccm)	$MoCl_5$ Flow (sccm)	$MoCl_5$ Conc (mol/m^3)	Max Temp (°C)	Dep Time (min)
1	760	78.0	50.0	50.0	0.020	7.00E-03	1250	17.0
2	760	78.0	50.0	50.0	0.020	7.00E-03	1650	6.0
3	760	78.0	50.0	50.0	0.020	7.00E-03	1100	10.0
4	760	78.0	100.0	1.0	0.040	1.39E-02	1250	10.0
5	150	78.0	50.0	50.0	0.102	7.00E-03	1250	10.0
6	150	78.0	10.0	90.0	0.020	1.40E-03	1250	41.0

of the deposit. In a way, the interaction between the underlying ceramic (BN) substrate and the depositing metal (Mo) was directly opposite that discussed in Section 7.2 for the deposition of a ceramic on a metal.

Ceramics such as the hot–pressed boron nitride substrate usually have low reflectance and thus either absorb or transmit most impinging electromagnetic radiation. A study by Khelkhal and Herlemont determined the optical constants of hot–pressed boron nitride for a 10.59 μm CO_2 laser beam.[115] At a zero degree angle of incidence, the reflectance was measured to be about 0.10. The coefficient of refraction (complex refractive index $n^* = n - ik$) was found to be $1.94 - i0.20$ where the refractive index, n, is 1.94 and the absorption index, k, is 0.20. The absorbtion index can be used to compute an absorption coefficient from Equation 7.6:[107]

$$\beta = 4\pi k/\lambda \tag{7.6}$$

where λ is the wavelength of interest. For the case of CO_2 laser radiation on the BN substrate, β was found to be 0.237 μm^{-1}. Using Equation 7.7, the fraction of energy absorbed (I/I_0) as a function of depth, z, into the BN substrate can be plotted.

$$I/I_0 = e^{-\beta z} \tag{7.7}$$

Figure 9.3 contains this plot. The plot shows that 90% of the energy is absorbed in the top 10 μm of the substrate surface while virtually 100% is absorbed in the top 20 μm.

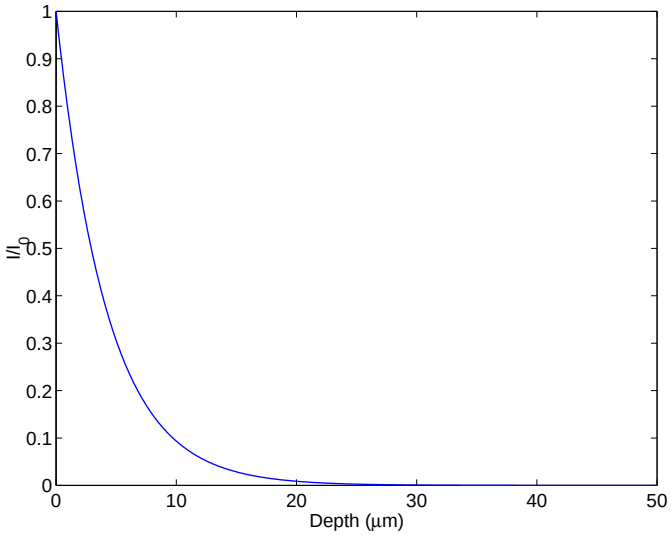

Figure 9.3: Fraction of incident laser energy remaining with increasing depth into hot–pressed BN substrate

Compared to ceramics, the optical properties of metals are characterized by high reflectance, high absorbtion, and low transmission. Thus, a large fraction of the energy from the CO_2 infrared laser beam will be reflected at a metal surface requiring increased laser power to maintain constant temperature. The fraction of energy that is not reflected will be quickly absorbed by the surface layer of material. Others have reported that the absorption coefficient of molybdenum is about 69.23 μm^{-1} which was used in conjunction with Equation 7.7 to show that 99% of the energy would be absorbed in the first 0.014 μm of the substrate surface.[2] This absorbed energy is converted into heat.

The thermal properties of the substrate dictate the nature of heat transport away from the substrate surface. The thermal conductivity of the hot pressed HBC boron nitride used here was given to be between 23 and 30 W/m-K with some anisotropy relative to the pressing direction. Relative to ceramics, metals are characterized by high thermal conductivities. Reported data shows the conductivity of molybdenum to decrease gradually and approximately linearly from 138 W/m-K at 300 K to 81.3 W/m-K at 2800 K. The high thermal conductivity will tend to flatten temperature gradients as the energy spreads through the deposit, thus in order to maintain a similar maximum temperature the laser power must be

increased over that required when heating a ceramic. As discussed in Section 7.2, Lax has shown that the maximum temperature in a laser spot for a given laser power is a linear function of the conductivity of the substrate;[55] therefore, the ratio of the thermal conductivity of BN to Mo gives insight into the magnitude of laser power change needed as the substrate material changes. Using the values above, at steady state, the laser power to maintain similar maximum temperature would be between 2 and 5 times higher on Mo than on BN.

The need to increase laser power slowly as Mo deposition proceeds is consistent with changes in the optical and thermal properties of the deposition surface as it transitions from a ceramic to a metal. The relatively slow growth of the molybdenum served to mitigate the rate of change in the substrate properties and appeared to enable sufficient process stability to utilize the automatic temperature control system.

Interestingly, during the process of decreasing the system pressure from 760 Torr to 150 Torr between Samples 4 and 5, the formation of a dark blue–green powdery coating and many sharp metallic fibers were observed on the substrate surface in the vicinity of the gas nozzle exit. During the setup of Sample 7, after raising the sublimation chamber temperature to 100°C and upon opening the exit valve, the formation of a white fibrous material was observed on the substrate below the nozzle exit. This material was similar to that observed in previous experiments.[2] The origin of the material was unknown but it was thought to be related to condensation of the $MoCl_5$ reagent on the substrate. Due to the formation of this material, the laser was not engaged during Sample 7. Upon completion of this experiment set, when the LCVD chamber was exposed to air, most of the white fibrous material on the sample quickly turned to a blue–green liquid.

A significant observation was made regarding the formation of the blue–green coating between Samples 4 and 5 and the white fibrous material of Sample 7. The elapsed time between the end of Sample 4 and the initiation of Sample 5 was about 15 minutes and that between the end of Sample 6 and the beginning of Sample 7 was in excess of 90 minutes. This was a very long time in comparison to the more typical 3 minutes between the other

samples. It has been shown that there is a significant residual heat effect associated with LCVD.[64] Residual heating in areas of the substrate far from the laser spot can account for a temperature rise in excess of 100°C. When the time between experiments was minimal, this residual heat could help prevent the condensation of the $MoCl_5$ vapor onto the substrate; however, when the time between experiments exceeded 5 or 10 minutes, the residual heat had time to dissipate, and the substrate could cool to a temperature that allowed condensation. In order to minimize the effect of different dwell times between experiments and discourage condensation of reagent on the substrate, a new procedure was adopted for Mo deposition. After Mo-1F, it was determined that all future experiments would utilize a period of laser preheating prior to diverting the $MoCl_5$ vapor flow through the nozzle.

Analysis of the resulting deposits was done through optical microscope observations. The color of most deposits was unfortunately obscured by the presence of the blue–green coating. All samples exhibited some deposited material with a very bumpy metallic surface. A severe hole in sample 2 suggested that a maximum deposition zone temperature in excess of 1650°C caused damage to the underlying BN substrate. The other samples showed a general trend of increasing deposit quantity with increasing temperature, increasing deposit quantity with decreasing pressure, and no readily apparent relationship between deposit quantity and concentration. Note however, that the range of concentrations used in Mo-1F was very limited.

Mo-2F was an exploratory experiment intended to further investigate the process parameters of $MoCl_5$ concentration and maximum deposition temperature. The experiment consisted of six runs whose conditions are given in Table 9.2.

All six samples of this experiment showed signs of deposit. The first three showed small quantities of deposit with Sample 3 having a large hole in the center as shown in Figure 9.4. Samples 4 and 5 were more substantial, also with holes in their center, although not as severe as that in Sample 3. The term “holes” was used to refer to substrate surface damage that extended into the bulk substrate material. This effect was fundamentally different from

Table 9.2: Mo-2F experiment conditions

No.	Chamber Press (Torr)	Sub Temp (°C)	Carrier Flow (sccm)	Diluent Flow (sccm)	$MoCl_5$ Flow (sccm)	$MoCl_5$ Conc (mol/m^3)	Max Temp (°C)	Dep Time (min)
1	760	90.0	50.0	50.0	0.043	1.45E-02	1170	15.0
2	760	90.0	75.0	25.0	0.065	2.17E-02	1200	8.0
3	760	90.0	25.0	75.0	0.022	7.23E-03	1600	5.5
4	760	112.0	50.0	50.0	0.154	4.86E-02	1408	6.3
5	760	112.0	100.0	1.0	0.307	9.60E-02	1409	10.0
6	760	130.0	100.0	1.0	0.787	2.34E-01	1250	15.0

the volcano effect which has been described previously and refers to the shape a deposit acquires as it grows. The formation of the holes was related to the maximum deposition temperature where increased severity occurred with increased temperature. Temperatures above 1200°C created holes. The cause of the holes in the BN substrate material was not fully clear. The hot–pressed BN was rated for use at temperatures up to 850°C in an oxidizing environment and 2000+°C in an inert environment.

Concentration and deposition time were increased incrementally for Samples 4, 5, and 6 resulting in increasingly larger quantities of deposit. Sample 6 yielded a large number of vertical fibers with fiber heights being proportional to the distance from the center of the deposit as shown in Figure 9.5. The reason for the rectangular footprint of Sample 6 as opposed to the more typical round footprint of other deposits is not fully understood. The new deposition procedure that utilized a period of laser preheating prior to reagent flow significantly reduced the formation of the blue–green powder.

Experiments 1 and 2 both resulted in deposits with similar features. With the exception of Sample 6, the deposits could be described as thin coatings with a small amount of bulk growth around the perimeter of the coating. The appearance of the thin coating varied from silver–metallic to a brown or bronze–metallic color depending upon processing conditions and distance from the center of the laser spot. The bulk growth around the perimeter was made up of many small fibers with a very bumpy surface appearance. Figure 9.6 illustrates

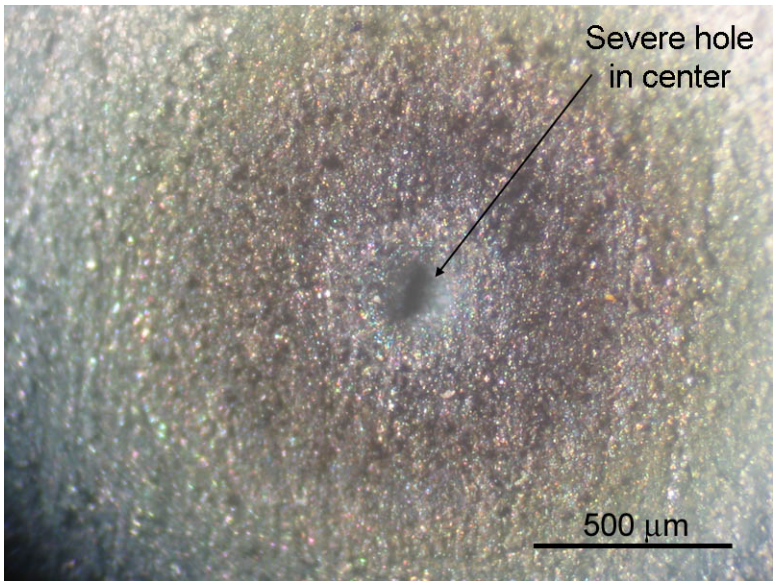

Figure 9.4: Sample 3 of Mo-2F showing severe hole in deposit center

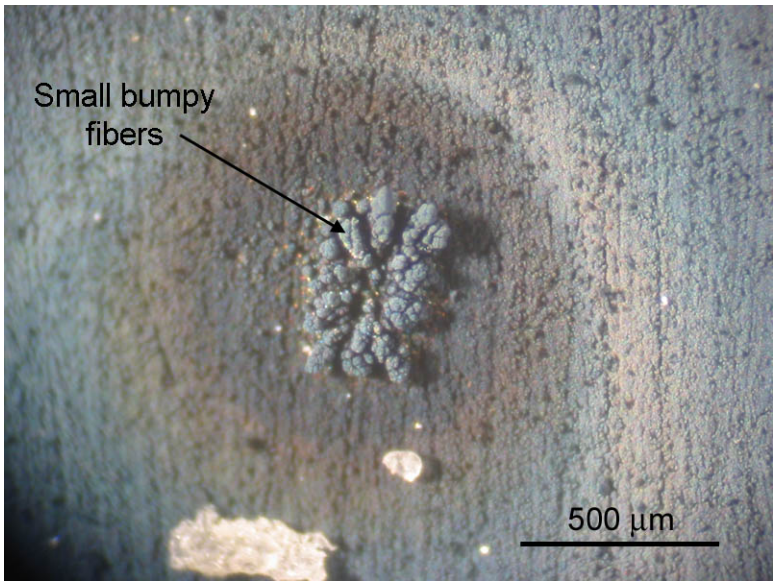

Figure 9.5: Sample 6 of Mo-2F showing array of small bumpy fibers

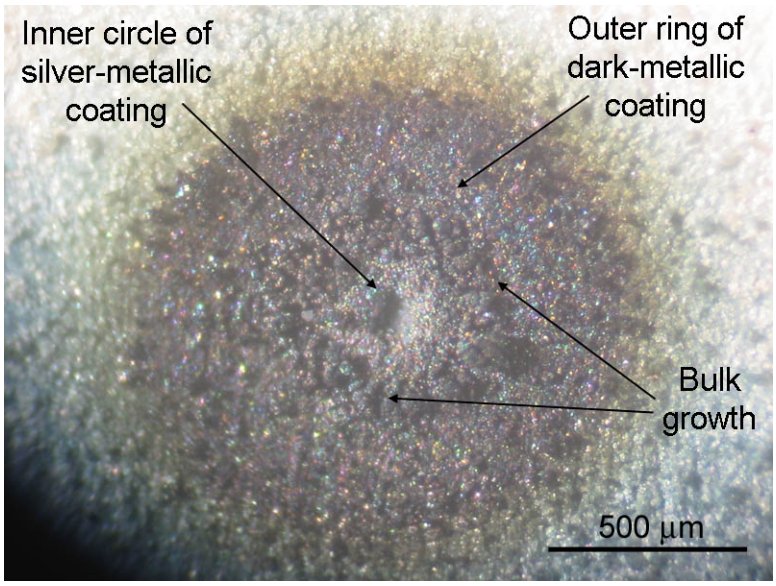

Figure 9.6: Sample 5 of Mo-2F showing typical features of Mo fiber deposits

these features. Note that the color of the deposits shown in the images is distorted because of the formation of blue–green powder on the substrate during later experiments.

The three experiment sets that followed were Mo-3F, Mo-4F, and Mo-5F. These experiments were designed to systematically refine and explore the variables of pressure, total flow rate, $MoCl_5$ concentration, and maximum deposition temperature. In hindsight, something appeared to happen during Mo-3F that changed the deposit attributes significantly from those observed in Mo-1F. Given the fact that the $MoCl_5$ concentration was increased sequentially for each of these experiment sets, the drastic reduction of substrate powder coating in Mo-3F–5F was suspicious.

The change in Mo-3F occurred during and after the four low pressure experiments that were run at 7.6 Torr. The $MoCl_5$ reagent delivery setup was configured such that the sublimation chamber was at approximately the same pressure as the reaction chamber. Operation of Georgia Tech's LCVD system at pressures this low raised concerns about air leaks into the system. If air leaked into the $MoCl_5$ sublimation chamber, the $MoCl_5$ powder could react with oxygen to form pentavalent and hexavalent oxy and hydroxy chlorides. In separate instances, it was observed to react quickly with moisture in the air to form a

colored liquid. The conversion of $MoCl_5$ powder to these undesirable compounds would significantly impact the vaporization rate, quality, and quantity of $MoCl_5$ vapor exiting the sublimation chamber.

After the completion of Mo-5F, calculations revealed that 2.7 of the 3 g of $MoCl_5$ that was originally loaded into the sublimation chamber should have been consumed. The sublimation chamber was opened and it was found that about 1.3 g of powder still remained. The blue–green color of some of the remaining powder suggested that the chamber had been contaminated with water vapor. The presence of water vapor also implied the presence of air and the conversion of the $MoCl_5$ to undesirable compounds. It was assumed that this contamination of the chamber occurred during the low pressure experiments. Unfortunately, the discrepancy in $MoCl_5$ consumption meant that the computed concentrations for experiments Mo-3F through Mo-5F were artificially high. The ambiguity of the experimental conditions during Mo-3F–5F precluded the use of their data in combination with other molybdenum deposition experiments. For completeness, Appendix C contains the nominal conditions used in these experiments along with some observations of the results.

After Mo-5F, a new batch of 13.7 g of $MoCl_5$ powder was loaded into the sublimation chamber. Mo-7F was designed as a 3 factor, 2 level full factorial experiment with 2 center points. The goal of the experiment was to identify the factor levels that reduced powder formation, eliminated substrate damage, and increased deposition rates. The factors studied included total flow rate, $MoCl_5$ concentration, and maximum deposition temperature. The levels chosen for Mo-7F were based on the most successful samples of Mo-2F. Table 9.3 contains the pertinent experimental conditions.

Several attributes of the resulting deposits were evaluated. Two of the undesirable features of previous Mo experiments, dark powder coatings on the substrate and substrate surface damage, were observed in some samples. The quantity of substrate powder coating was characterized by assigning each sample a rating between 1 and 7 with 1 representing no powder and 7 representing extremely heavy powder coating. A regression analysis did not

Table 9.3: Mo-7F experiment conditions

No.	Chamber Press (Torr)	Sub Temp (°C)	Carrier Flow (sccm)	Diluent Flow (sccm)	$MoCl_5$ Flow (sccm)	$MoCl_5$ Conc (mol/m^3)	Max Temp (°C)	Dep Time (min)
1	760	130.0	65.7	58.8	0.517	1.25E-01	1100	10.0
2	760	130.0	147.1	26.7	1.158	2.00E-01	1200	10.0
3	760	130.0	63.0	11.5	0.496	2.00E-01	1000	10.0
4	760	130.0	63.0	11.5	0.496	2.00E-01	1200	10.0
5	760	130.0	15.8	59.1	0.124	5.00E-02	1200	10.0
6	760	130.0	36.8	137.9	0.289	5.00E-02	1200	10.0
7	760	130.0	36.8	137.9	0.289	5.00E-02	1000	10.0
8	760	130.0	15.8	59.1	0.124	5.00E-02	1000	10.0
9	760	130.0	147.1	26.7	1.158	2.00E-01	1000	10.0
10	760	130.0	65.7	58.8	0.517	1.25E-01	1100	10.0

detect any statistically significant relationship among the factors studied and the substrate powder coating response.

During experiments, a propensity for the powder to form during later runs was observed. Thus, a linear regression analysis was done relating the run order to the powder response. Consistent with observation, this analysis detected a strong relationship between run order and powder formation. This relationship was likely related to the ambient $MoCl_5$ concentration within the deposition chamber. The procedure for Mo deposition delivered the $MoCl_5$ vapor exclusively through the gas nozzle. During preheating the Mo-7F substrate, $MoCl_5$ flow was not enabled. Thus, when Sample 1 of Mo-7F was begun, the ambient concentration within the deposition chamber was nominally zero. After several samples had been run, the ambient concentration at the initiation of a deposit was no longer zero, but was a function of previous flow conditions and dwell times.

Note that the total nozzle flow rate for these experiments ranged between 75 and 175 sccm. No window port or side port flow was used. The volume of the upper deposition chamber was estimated to be about 3000 cm^3; therefore, the residence time for the $MoCl_5$

reagent was between 15 and 40 minutes. During a 10 minute experiment, the ambient concentration gradually increased. After a sample was complete and reagent flow was halted, the combined setup and preheat time for the next sample was usually about 7 minutes which was insufficient time for the chamber to again approach an ambient concentration of zero. A simple best case approximation would be that when beginning a new sample, the ambient $MoCl_5$ concentration was approximately 50% of the previous sample's concentration. A worst case approximation would be that the ambient $MoCl_5$ concentration was over 80% of the previous sample setpoint.

Ideally, the ambient $MoCl_5$ concentration would have minimal impact on the local concentration in the deposition zone due to the use of the localized reagent gas nozzle. However, the analysis of Section 5.3.6 revealed that with a gas nozzle flow of 100% diluent flow in a chamber with a moderate global concentration of reagent, deposition could still occur. Reagent species diffused through the "pure stream" and to the deposition surface. Thus, the ambient reagent concentration definitely impacts the deposition process and could contribute to the formation of the powder on the substrate surface.

It had been observed in earlier exploratory experiments that substrate surface damage appeared to occur at higher deposition temperatures. The degree of substrate surface damage in Mo-7F samples was quantified by assigning values between 1 and 5 to each sample where 1 represented zero damage and 5 represented very significant damage. A multiple regression analysis showed there to be a strong statistical relationship among maximum deposition temperature and substrate damage. The analysis essentially showed that deposition temperature should be limited to a maximum near 1000°C. On the high zoom setting, the thermal imaging camera used to observe deposition temperature has a lower temperature limit of 955°C. Deposition below this limit could be possible by further reducing laser power, but only limited data could be acquired during the process. Thus, in order to avoid substrate surface damage and still monitor deposition temperature using the thermal imaging system, a target maximum deposition temperature of 1000°C for all subsequent Mo

fiber experiments was chosen.

The final molybdenum fiber experiment was designated Mo-13F. This was a 3 factor, rotatable central composite design that studied pressure, total gas flow rate, and $MoCl_5$ concentration. Per the results of Mo-7F, the temperature was manually controlled to a maximum value of 1000°C for all experiments. The run order was pseudo–random with the caveat that all runs with the same pressure were run in succession. This was a practical necessity due to the procedure required to change operating pressure that saved time and enhanced system stability. The conditions for each sample are given in Table 9.4 in the run order used.

The resulting deposits still showed little tendency to grow the large vertical structures typical of carbon or boron nitride. They were best described as thin coatings with some samples showing areas of bulk growth characterized by many small, nodular, fibers emerging from the substrate surface. A variety of metrics were used to quantify the results of Mo-13F.

One goal of Mo-13F was to find conditions that yielded minimum extraneous powder formation on the substrate surface near the laser zone. The powder coating was again quantified using the same 1–7 scale as in Mo-7F. A multiple regression analysis was performed and factors that were found not to be statistically significant at at least a 90% level were excluded. The ensuing analysis is summarized in Table 9.5. The analysis showed the second order effect of pressure (AA) to be the most significant factor. An interpretation of this result is that the effect of a change in pressure depends on the level of pressure. Other factors shown to be statistically significant at a 95% level were the pressure–total flow (AB) interaction and the total flow (B). The interaction between pressure and total flow is related to the exit velocity from the gas nozzle. For a fixed total flow, the nozzle exit velocity is higher at low pressures than at high pressures. The significance of this interaction suggested a positive relation between the nozzle exit velocity and the formation of powder on the substrate. The significance of the molar concentration of $MoCl_5$ was shown to be just

Table 9.4: Mo-13F experiment conditions

No.	Chamber Press (Torr)	Sub Temp (°C)	Carrier Flow (sccm)	Diluent Flow (sccm)	$MoCl_5$ Flow (sccm)	Total Flow (sccm)	$MoCl_5$ Conc (mol/m^3)	Dep Time (min)
1	760	130.0	4.2	20.8	0.033	25.0	4.00E-02	10.0
2	760	130.0	10.9	54.0	0.086	65.0	4.00E-02	10.0
3	760	130.0	5.5	59.5	0.043	65.0	2.00E-02	10.0
4	760	130.0	2.1	22.9	0.017	25.0	2.00E-02	10.0
5	304	130.0	4.2	20.8	0.083	25.0	4.00E-02	10.0
6	304	130.0	2.1	22.9	0.041	25.0	2.00E-02	10.0
7	304	130.0	5.4	59.5	0.108	65.0	2.00E-02	10.0
8	304	130.0	10.8	54.0	0.215	65.0	4.00E-02	10.0
9	915	130.0	5.7	39.3	0.037	45.0	3.00E-02	10.0
10	532	130.0	9.9	68.6	0.111	78.6	3.00E-02	10.0
11	532	130.0	5.7	39.3	0.064	45.0	3.00E-02	10.0
12	532	130.0	5.7	39.3	0.064	45.0	3.00E-02	10.0
13	532	130.0	2.5	42.5	0.028	45.0	1.32E-02	10.0
14	532	130.0	1.4	9.9	0.016	11.4	3.00E-02	10.0
15	532	130.0	8.8	36.1	0.100	45.0	4.68E-02	10.0
16	149	130.0	5.5	39.3	0.228	45.0	3.00E-02	10.0

Table 9.5: Mo-13F powder formation multiple regression analysis

Estimated Effects for Powder Formation

average	= 1.36577	+/- 0.157408
B:Total Flow	= 0.562486	+/- 0.244371
C:$MoCl_5$ Conc	= 0.515886	+/- 0.244371
AA	= 1.19321	+/- 0.257046
AB	= 0.75	+/- 0.319286

Analysis of Variance

Source	Sum of Squares	Df	Mean Square	F-Ratio	P-Value
B:Total Flow	1.08023	1	1.08023	5.30	0.0419
C:$MoCl_5$ Conc	0.908652	1	0.908652	4.46	0.0585
AA	4.39336	1	4.39336	21.55	0.0007
AB	1.125	1	1.125	5.52	0.0386
Total error	2.24276	11	0.203887		
Total (corr.)	9.75	15			

R-squared = 76.9973 percent
R-squared (adjusted for d.f.) = 68.6327 percent
Standard Error of Est. = 0.451539
Mean absolute error = 0.284526
Durbin-Watson statistic = 1.8579 (P=0.3171)
Lag 1 residual autocorrelation = -0.109256

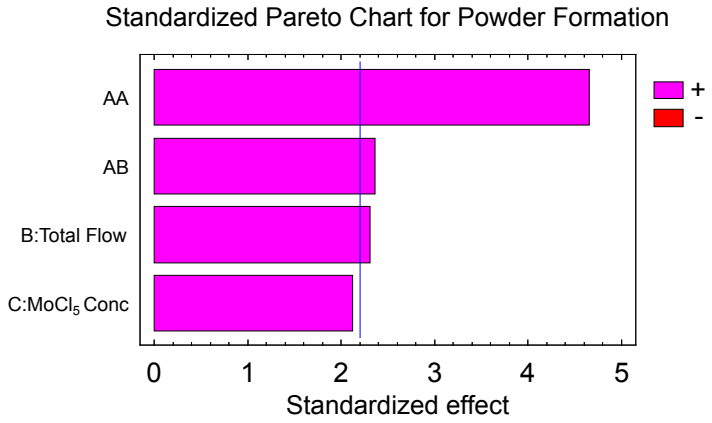

under the 95% confidence level.

A second attribute that was quantified was the maximum vertical height of the deposits. It was difficult to accurately measure the heights because they were not significantly larger than the surface roughness of the substrate. However, by viewing the deposits on a 30° angle at a magnification of 160X through an optical microscope, height differences could be seen. A scale of 1–5 was used to specify the relative height of each sample. A value of 1 was given to deposits that showed no deposit or were virtually flat while a value of 5 was given to the two tallest samples, Samples 8 and 16. Figures 9.7 and 9.8 illustrate these two prominent deposits. Table 9.6 contains the results of the regression analysis for the height response.

All three factors studied were shown to be significant at a 95% confidence level. Decreased pressures led to increased deposit height, while increased total flow and $MoCl_5$ concentration were shown to have the same effect. Pressure was shown to be most important, followed by concentration, and $MoCl_5$. The fact that these variables were strongly correlated with growth rate suggested perhaps this was a transport–limited process; however, the temperature was not varied for reasons previously discussed and without data at different temperature levels no final conclusion could be made about the rate–limiting regime.

Some of the molybdenum deposits that had sufficient height also showed a tendency for growth in the center of the deposit area to be shorter than that on the perimeter. This was consistent with the ubiquitous LCVD volcano effect. The degree to which each sample exhibited this shape was captured by rating each with a value between 1 and 5 where 1 was no volcano shape and 5 was significant volcano shape. Note that this effect refered only to the shape of the deposited material and did not incorporate any prevailing substrate surface damage. Samples 8 and 16 shown in Figures 9.7 and 9.8, respectively illustrate an example of a volcano rating of 5 and 1. Using the normal regression procedure, a full regression model was developed and those factors not statistically significant at a 95% level

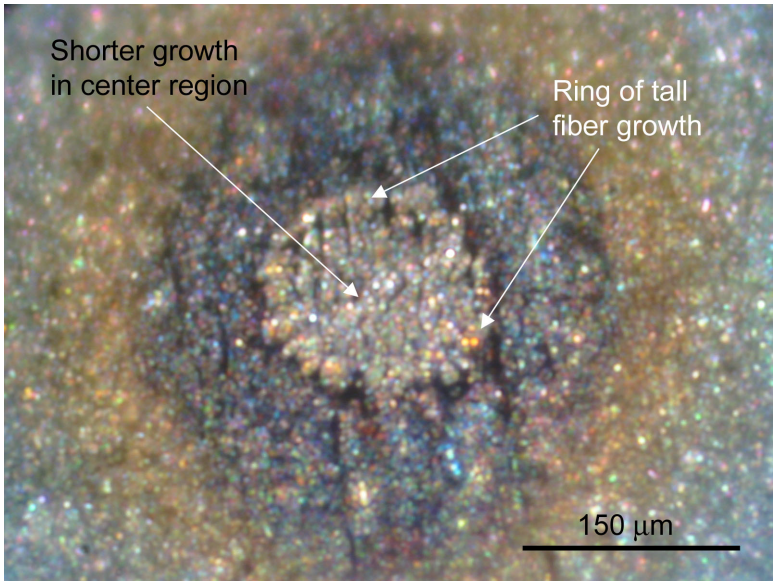

Figure 9.7: Sample 8 showing tall ring of fibers with volcano effect in center

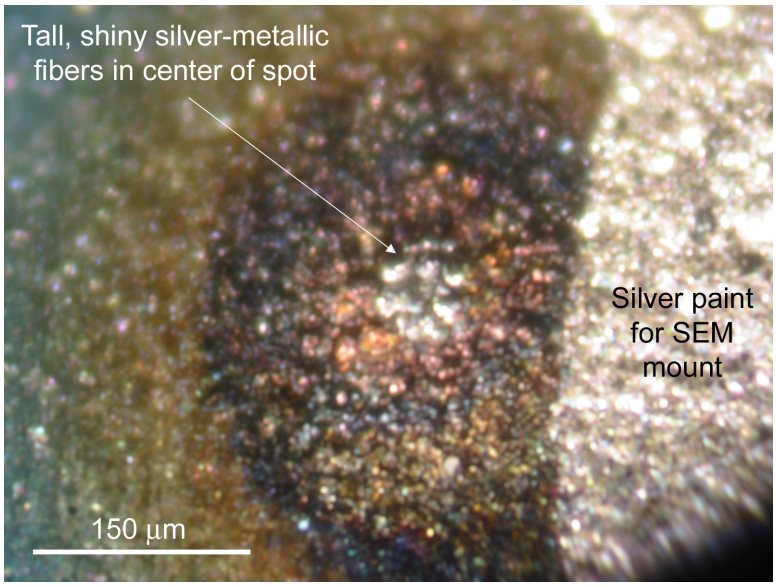

Figure 9.8: Sample 16 showing tall fibers in center of spot with no volcano effect

Table 9.6: Mo-13F maximum height regression analysis

Estimated Effects for Maximum Height

average	= 1.52636	+/- 0.2194
A:Pressure	= -1.47111	+/- 0.340611
B:Total Flow	= 1.39456	+/- 0.340611
C:$MoCl_5$ Conc	= 0.978527	+/- 0.340611
AA	= 1.32947	+/- 0.358279

Analysis of Variance

Source	Sum of Squares	Df	Mean Square	F-Ratio	P-Value
A:Pressure	7.38894	1	7.38894	18.65	0.0012
B:Total Flow	6.64	1	6.64	16.76	0.0018
C:$MoCl_5$ Conc	3.26916	1	3.26916	8.25	0.0152
AA	5.45414	1	5.45414	13.77	0.0034
Total error	4.35714	11	0.396103		
Total (corr.)	27.1094	15			

R-squared = 83.9276 percent
R-squared (adjusted for d.f.) = 78.083 percent
Standard Error of Est. = 0.629368
Mean absolute error = 0.468572
Durbin-Watson statistic = 2.65656 (P=0.0725)
Lag 1 residual autocorrelation = -0.349302

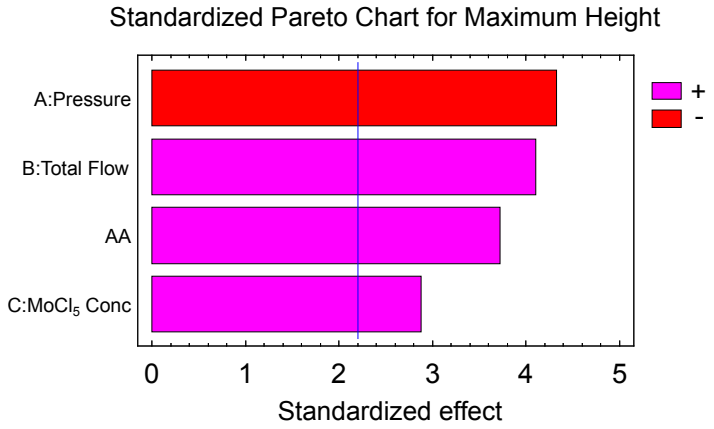

were eliminated. Table 9.7 contains the results of the reduced model.

$MoCl_5$ concentration was shown to be the most significant factor for the volcano response. This result suggests the origin of the volcano in Mo deposition could be related to mass–transport, and the process could perhaps be in the transport–limited regime. Further studies are needed to confirm this finding.

The contour plots shown in Figure 9.9 for the powder formation, maximum height, and volcano response were useful in visually interpreting the results of the regression analyses. Overall, the results of Mo-13F spanned a wide range of deposit attributes. The results of the different regression analyses were used in a multiple response optimization. Each response was weighted equally in formulating a desirability function, and the optimization constraints were to minimize powder formation, maximize the deposit height, and minimize the volcano effect.

The results of the optimization analysis are shown in the contour plots of Figure 9.10. The factor levels that yielded the maximum desirability function are given in Table 9.8.

The internal features of molybdenum deposits were also of interest. Unfortunately, the samples from Mo-13F with the largest bulk growth, Samples 8 and 16, were damaged during the mounting and polishing process. While the deposits from Mo-4F could not be used for process parameter studies, they remained an important asset for conducting an internal analysis of LCVD molybdenum growth. Sample 7 from Mo-4F was mounted and polished.

Figure 9.11 shows two SEM micrographs. The left side is the cross–section of the entire deposit area. The molybdenum formed a series of large bumps or nodes that did not always tend to coalesce. Overall, the growth nodes were about 20 μm in height. The right side of the figure shows a closer view of one of the growth nodes. This region appears to have formed from three independent growth initiation points. The growth from these three points eventually merged together, but even as the deposit grew, the different sections remained distinguishable at the growth surface. In fact, cracks can be seen between some

Table 9.7: Mo-13F volcano effect regression analysis

Estimated Effects for Volcano

average	= 1.26593	+/- 0.231405
B:Total Flow	= 0.732232	+/- 0.359248
C:$MoCl_5$ Conc	= 1.76401	+/- 0.359248
BC	= 1.25	+/- 0.46938
CC	= 0.98779	+/- 0.377884

Analysis of Variance

Source	Sum of Squares	Df	Mean Square	F-Ratio	P-Value
B:TotalF low	1.83058	1	1.83058	4.15	0.0663
C:$MoCl_5$ Conc	10.6241	1	10.6241	24.11	0.0005
BC	3.125	1	3.125	7.09	0.0221
CC	3.01087	1	3.01087	6.83	0.0241
Total error	4.847	11	0.440636		
Total (corr.)	23.4375	15			

R-squared = 79.3195 percent
R-squared (adjusted for d.f.) = 71.7993 percent
Standard Error of Est. = 0.663804
Mean absolute error = 0.445289
Durbin-Watson statistic = 2.06688 (P=0.4371)
Lag 1 residual autocorrelation = -0.0793257

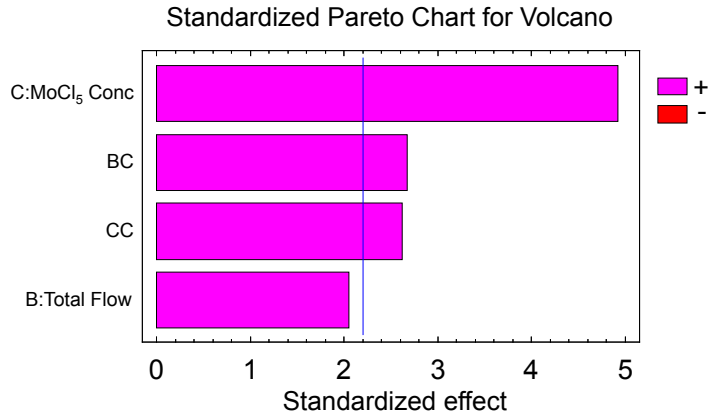

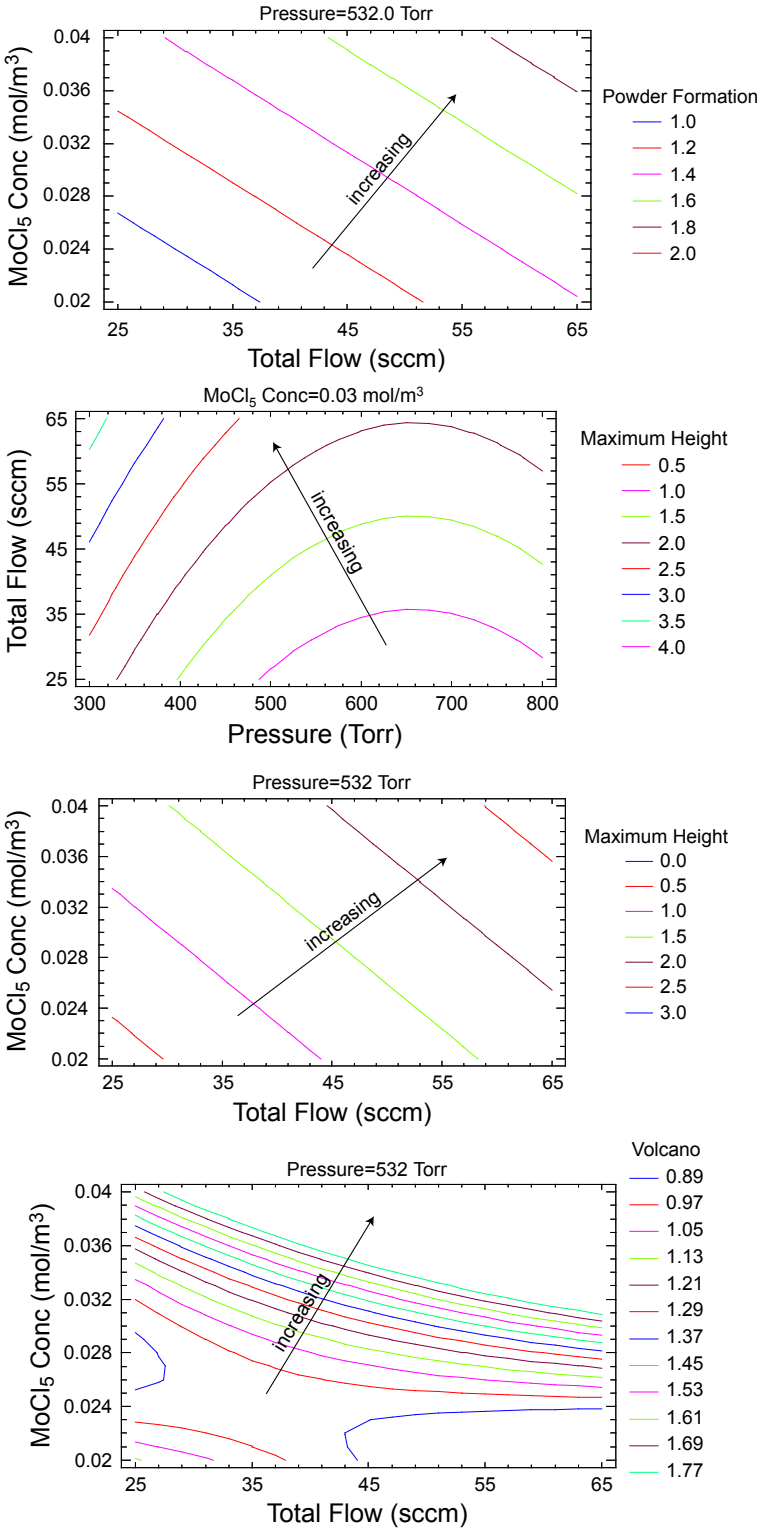

Figure 9.9: Contours of different response variables in parameter space defined by Mo-13F

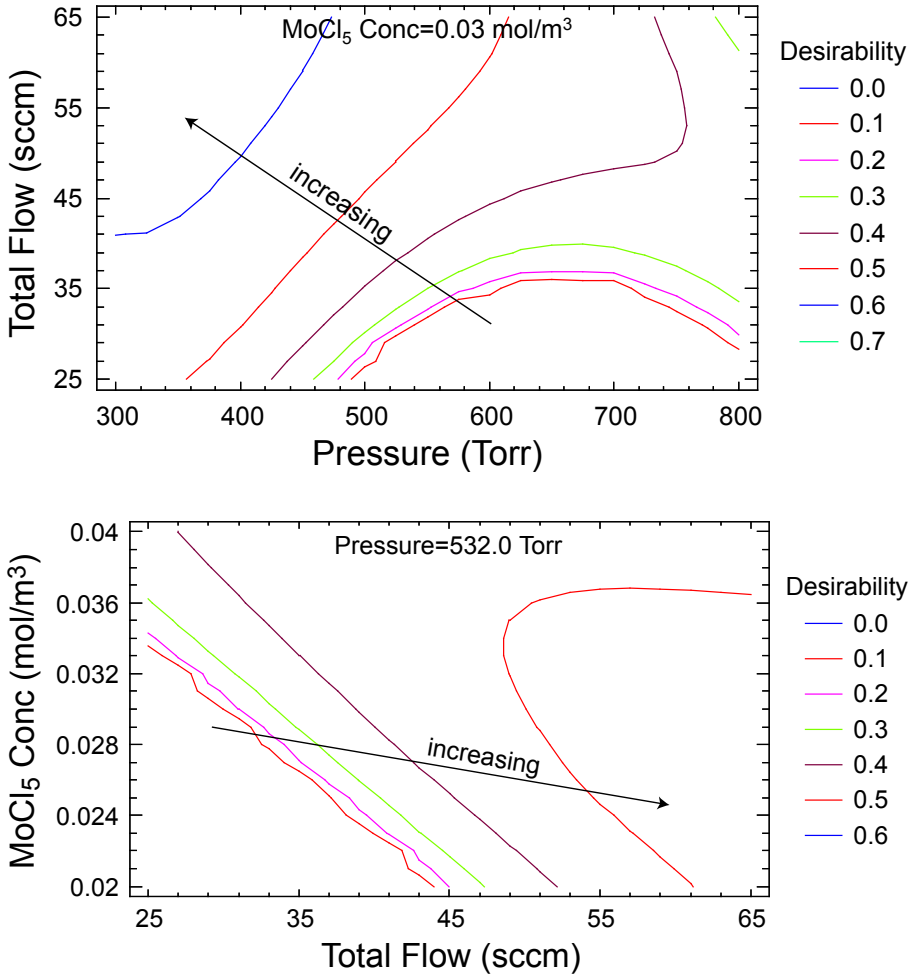

Figure 9.10: Contours of desirability function in space defined by Mo-13F factor levels

Table 9.8: Optimum factor levels for Mo fiber deposition as determined by Mo-13F

Factor	Level
Pressure (Torr)	209
Total Flow Rate (sccm)	78.6
$MoCl_5$ Conc (mol/m^3)	0.013

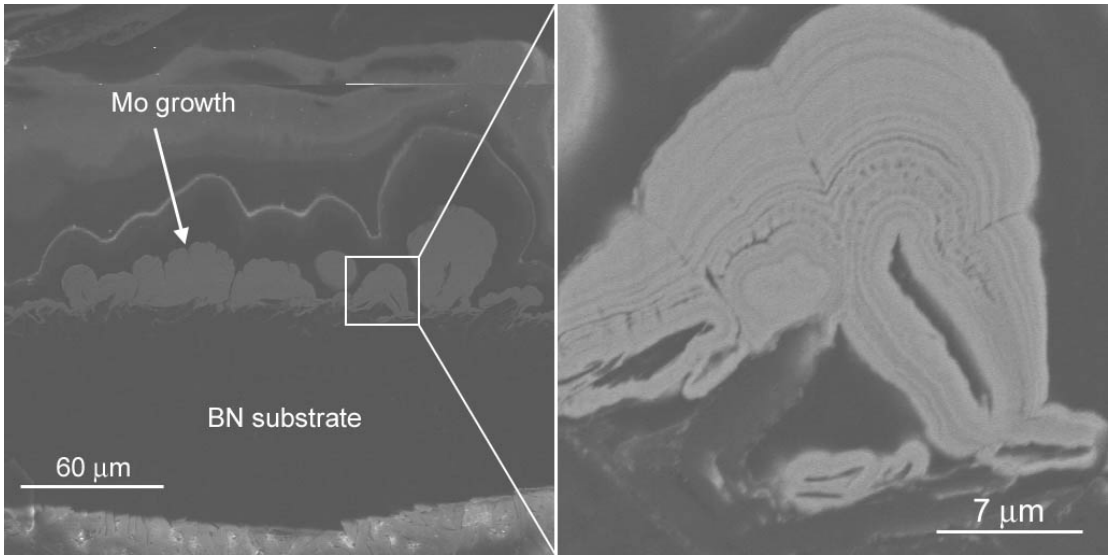

Figure 9.11: SEM micrographs of cross–section of Mo deposit

of the growth layers emerging from the different nodes. The molybdenum growth had a layered appearance. These layers are denoted by periodic striations that tend to appear parallel the growth surface.

An EDX analysis was done on the deposited material to ensure it was molybdenum. The results of the analysis are shown in Figure 9.12. The response was dominated by the presence of Mo, with no other elements present in significant amounts.

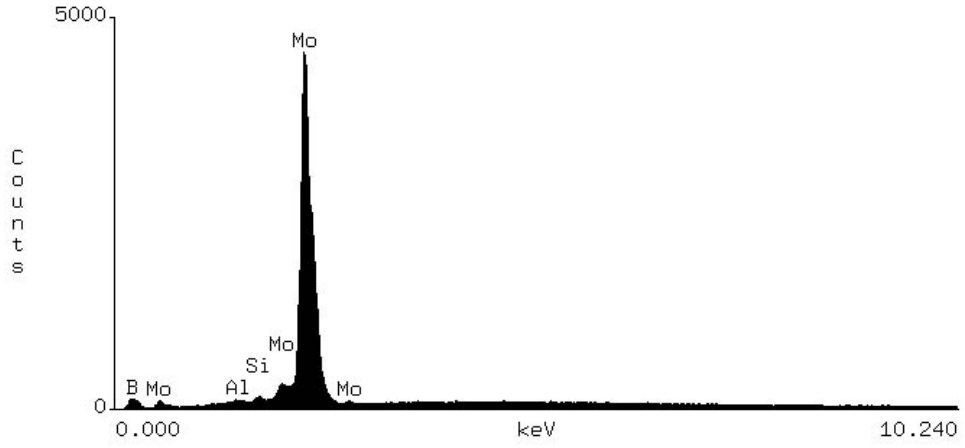

Figure 9.12: EDX results of Mo deposit

9.3 Molybdenum Line Experiments

Concurrent with the execution of molybdenum fiber experiments, molybdenum line deposition was also explored. Mo lines are required for the dispenser cathode application. Conditions from Mo fiber experiments were used to help identify suitable starting conditions for Mo lines. The slow deposition rates observed in the fiber experiments suggested that the deposition of Mo lines of any appreciable height would take much longer than for materials previously studied.

The same hot pressed boron nitride substrates were used for the Mo line experiments. The operational procedure for lines emulated that of the fiber experiments. Preheating involved scanning the laser over the length of the line 6 times prior to diverting the $MoCl_5$ flow through the gas nozzle. The maximum deposition temperature was kept just under 1000°C during the preheating process. After the final preheat scan, the $MoCl_5$ vapor was diverted through the nozzle and the surface temperature was manually increased to the desired setpoint by increasing the laser power. Upon reaching this temperature, the scan of the first layer was begun. Subsequent layers were created by scanning the laser back and forth over the same area.

The first molybdenum line experiment was based on Sample 2 of the fiber experiment Mo-7F which had produced good bulk growth, no substrate damage, and minimal powder formation on the substrate surface. The sublimation chamber temperature was kept fixed at 130°C during the experiment. The line length was 2.54 mm and 30 layers were run. Other conditions are summarized in Table 9.9.

Table 9.9: Mo-8L experiment conditions

No.	Chamber Press (Torr)	Carrier Flow (sccm)	Diluent Flow (sccm)	$MoCl_5$ Flow (sccm)	Total Flow (sccm)	$MoCl_5$ Conc (mol/m^3)	Max Temp (°C)	Scan Speed (mm/min)
2	760	147.1	26.7	1.158	175.0	2.00E-01	1200	2.54

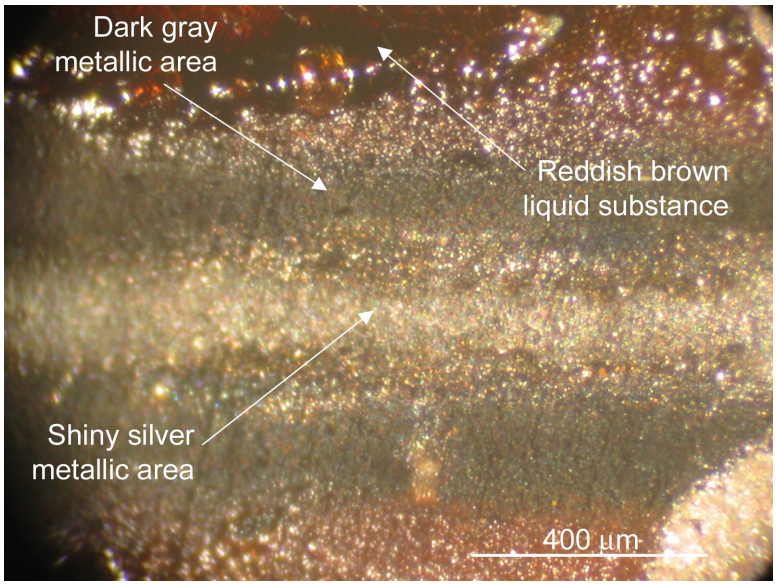

Figure 9.13: Mo line deposit from Mo-8L

Figure 9.13 is an optical microscope image of the line resulting from BN-8L. The deposit showed several distinct regions. In the center, was a shiny silver area that appeared metallic. This shiny area was recessed below the substrate surface indicating damage to the substrate occurred either during or prior to the deposition of the metallic material. The line was immediately surrounded by a region of dark gray metallic material that appeared to have deposited on the substrate surface without causing damage. A reddish brown liquid–looking substance surrounded the dark gray area. The reddish brown material did not emerge until after the substrate was removed from the deposition chamber. While still in the chamber in the absence of air, the area where the reddish–brown material emerged was covered in a heavy coating of the dark blue–green powder typical of other Mo experiments. Finally, surrounding the reddish brown substance was a very large area of the dark blue–green powder which covered the majority of the substrate.

Electrical conductivity is inherently required in the Mo to be used in the dispenser cathode application. A crude test was devised to determine whether the metallic material in the center of the line was electrically conductive. The continuity check function of a digital multimeter was used to confirm the conductivity, and using the same instrument, the

Table 9.10: Mo-9L experiment conditions

No.	Chamber Press (Torr)	Carrier Flow (sccm)	Diluent Flow (sccm)	$MoCl_5$ Flow (sccm)	Total Flow (sccm)	$MoCl_5$ Conc (mol/m^3)	Max Temp (°C)	Scan Speed (mm/min)
1	760	65.7	58.8	0.517	125.0	1.25E-01	1000	2.54
2	760	91.9	82.3	0.724	175.0	1.25E-01	1000	2.54
3	760	39.4	35.3	0.310	75.0	1.25E-01	1000	2.54
4	760	13.1	11.8	0.103	25.0	1.25E-01	1000	2.54
5	760	39.4	35.3	0.310	75.0	1.25E-01	1100	2.54

resistance of the line was measured to be 10–30 Ω. The substrate and the powdery coatings on its surface showed no evidence of electrical conductivity. This crude test strongly suggested the metallic material along the line was molybdenum, and although the coating appeared to be quite thin, it confirmed the continuity of the coating.

Experiment Mo-8L served to confirm the feasibility of depositing an electrically conductive Mo line on boron nitride. However, several attributes of the deposit were undesirable. First, the damage to the substrate surface was indicative that the deposition temperature was too high. Earlier fiber experiments showed that as long as the maximum deposition temperature did not exceed about 1000°C, no substrate damage would occur. In future experiments, the temperature would be kept closer to this limit. The large amount of dark powder surrounding the metal line was also undesirable. Subsequent experiments would focus on reducing the occurrence of this coating.

Experiment Mo-9L was designed to study the relationship between these line attributes and total gas flow rate. The sublimation chamber temperature was kept constant at 130°C and the reagent lines and gas nozzle were kept at the usual 150°C. All lines were 2.54 mm in length and 20 layers thick.

All samples of Mo-9L produced lines that showed evidence of metallic deposits. A strong relation between the surrounding powder coating and the gas flow rate was observed with increasing flow rate causing increased powder formation. From a powder formation

standpoint, Sample 4 was ideal in that it showed no evidence of the phenomenon.

While Sample 4 showed a minimum amount of powder formation, it also showed a minimal amount of metal deposition. Sample 3 showed the largest quantity of deposit as evidenced by observation under an optical microscope. The line was a bright, shiny–silver metallic color that was made up of a large number of very small fibers. The same crude electrical conductivity check used for Mo-8L was used to verify the conductivity of all samples in Mo-9L.

The conditions of Sample 5 were identical to those of Sample 3, except the maximum deposition temperature was increased by 100°C. A minimum temperature of 1100°C was required to effectively use the automatic temperature control system. This increase in temperature resulted in significant substrate surface damage along the entire length of the line. The run produced a large quantity of shiny metallic material that was measured to be conductive, but the substrate surface damage was disallowable given the requirements of the dispenser cathode assembly. This result provided further evidence that the upper temperature limit allowable in the study of Mo deposition on boron nitride was 1000°C. Temperatures below 955°C were not observable in the high zoom range of the thermal imager, thus it was preferred to keep the temperature above this limit. Given that under manual temperature control, the standard deviation of the temperature was estimated to be $\pm 25°$, the narrow range between 955 and 1000°C for maximum temperature did not allow further study of this variable. All subsequent Mo line experiments used a temperature setpoint of 1000°C.

Experiment set Mo-10L was setup to study the relationship among total gas flow rate and $MoCl_5$ concentration over the ranges shown in Table 9.11. The goal here was to minimize extraneous powder formation while increasing the quantity of bulk deposit. Again, the sublimation chamber temperature was kept constant at 130°C and the reagent supply lines were appropriately heated. All lines were 2.54 mm long and consisted of 20 layers.

Overall, the results of Mo-10L represented an improvement where all deposits showed

Table 9.11: Mo-10L experiment conditions

No.	Chamber Press (Torr)	Carrier Flow (sccm)	Diluent Flow (sccm)	$MoCl_5$ Flow (sccm)	Total Flow (sccm)	$MoCl_5$ Conc (mol/m^3)	Max Temp (°C)	Scan Speed (mm/min)
1	760	42.0	7.6	0.331	50.0	2.00E-01	1000	2.54
2	760	10.5	39.4	0.083	50.0	5.00E-02	1000	2.54
3	760	26.3	23.5	0.207	50.0	1.25E-01	1000	2.54
4	760	15.8	59.1	0.124	75.0	5.00E-02	1000	2.54
5	760	63.0	11.5	0.496	75.0	2.00E-01	1000	2.54

signs of metallic deposit with no accompanying substrate damage. Figure 9.14 contains figures of all five lines and their position on the substrate. As seen in the figures, Samples 1, 3, and especially 5 still resulted in significant powder formation.

The deposits of Mo-10L were affixed to SEM mounts using silver paste and carbon tape. The silver was painted right to the edge of each of the Mo lines. The conductivity of the deposits became apparent in the SEM when a low magnification view showed a drastic difference in the charging tendency of the deposit area versus the uncoated substrate. Figure 9.15 illustrates the surface morphology of the molybdenum line and compares it to the substrate surface.

The surface of the molybdenum deposit appears to be made of many large platelets with major dimensions of 10 and 20 μm. The platelets tend to be oriented vertically (standing on edge) perpendicular to the underlying substrate surface. The substrate micrograph shows the boron nitride to be composed of many small particles loosely bound together. The porosity of the BN corresponds to the value of 13% reported by the manufacturer.[111]

In summary, several important findings were made regarding the deposition of Mo lines on the hot pressed boron nitride substrates. Overall, the process was sensitive but stable. The sensitivity referred to the fact that a change in laser power of 0.1 W yielded a temperature change on the order of 50 – 100°C. The stability was related to the fact that under constant laser power, the temperature would only change gradually. Unfortunately,

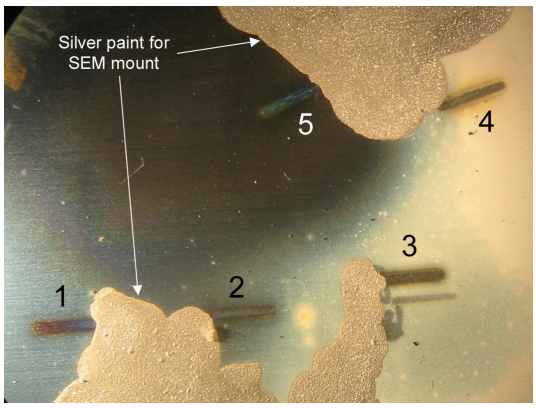

Layout

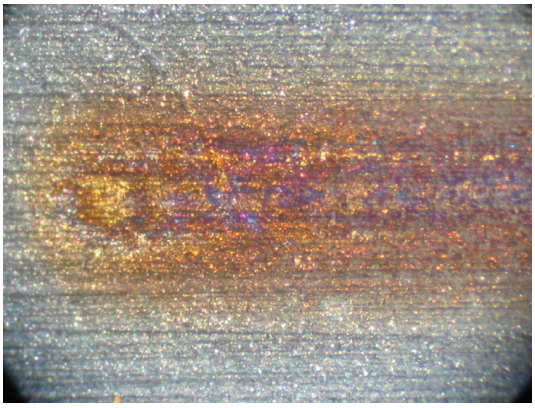

Sample 1

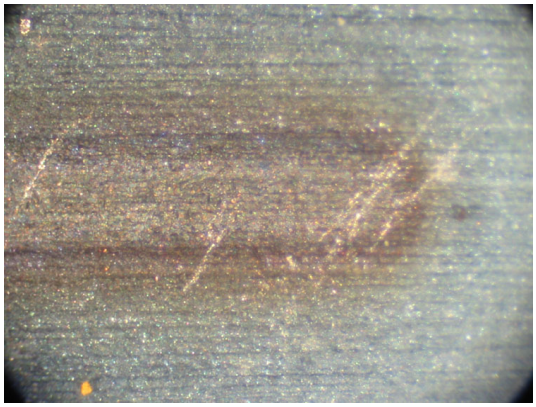

Sample 2

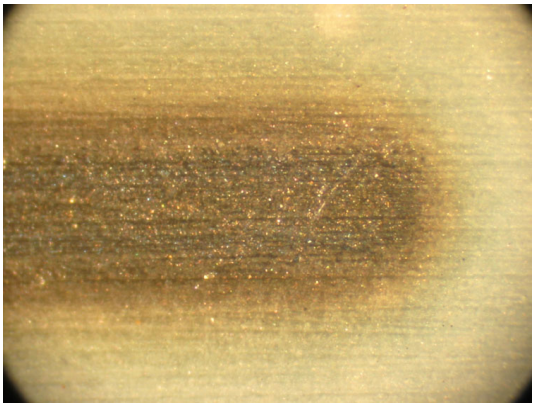

Sample 3

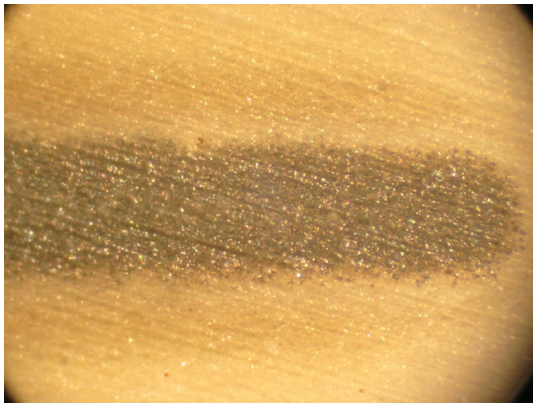

Sample 4

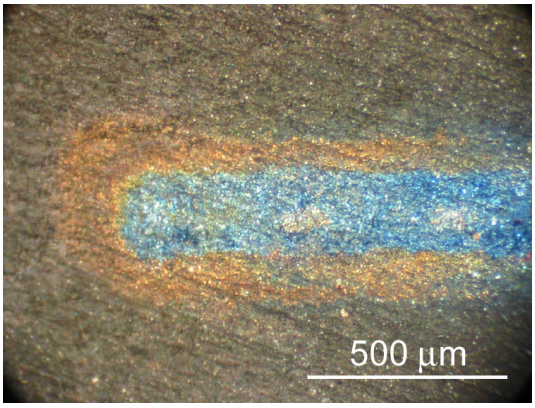

Sample 5

Figure 9.14: Optical images of lines from Mo-10L

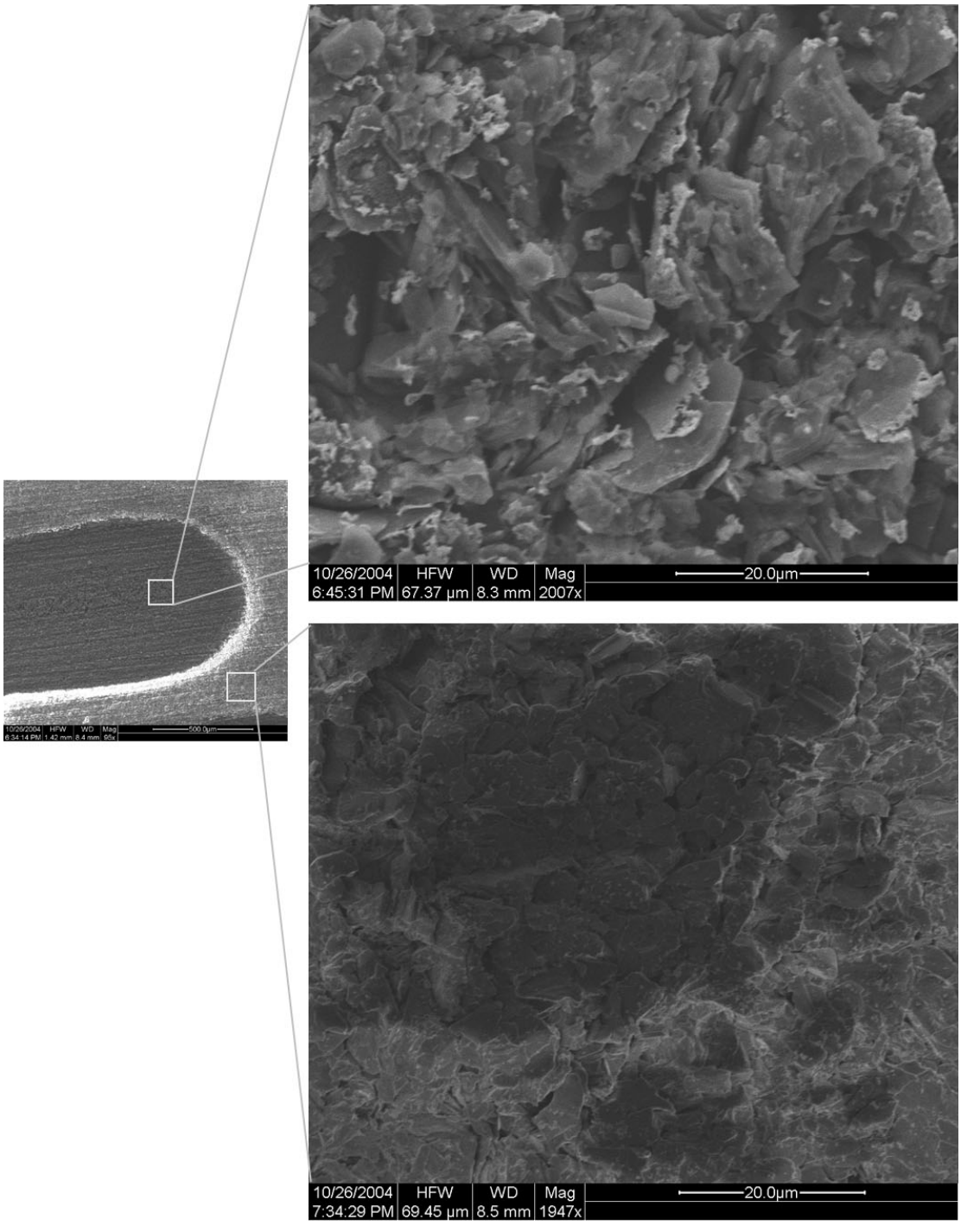

Figure 9.15: SEM images from Mo-10L showing the center of Sample 3 compared to the substrate surface

the maximum temperature value of 1000°C did not allow use of the automatic temperature control system. The slow deposition rate of Mo precluded the fabrication of 10 μm tall structures in a reasonable amount of time. Efforts to increase deposition rates usually caused the formation of excessive powder in the vicinity of the laser spot. Although the deposits were very thin, they did pass crude conductivity tests indicating that the material might be suitable in the dispenser cathode application.

CHAPTER X

DEPOSITION OF BN-MO COMPOSITES

Ultimately, the dispenser cathode application requires the deposition of alternating sections of boron nitride and molybdenum on a tungsten substrate. Figure 10.1 illustrates the conceived cross section of such a deposit. Experiments were done to study the feasibility of using LCVD to build this type of composite.

LCVD fabrication of the structure in Figure 10.1 involves three fundamentally different deposition processes:

1. BN deposition on W
2. Mo deposition on BN
3. BN deposition on Mo

Processes 1 and 2 were thoroughly investigated as described in Chapters 7 and 9. Process 3 was not investigated independently, but the general dynamics of ceramic deposition on metal as in the BN on W process provided reasonable guidance as to the nature of this process. The experimental procedure began with processes 1 and 2 in creating a two–material

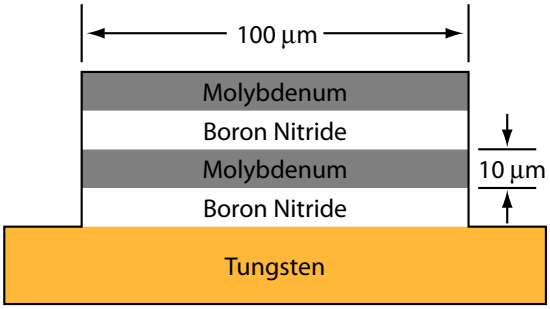

Figure 10.1: Required cross section of composite needed for dispenser cathode

BN-Mo composite. The final experiment involved all three processes in the deposition of a four–material BN-Mo-BN-Mo composite on a tungsten substrate.

10.1 Experiments

Conditions used in the experiments were derived from the most successful conditions found in the previous boron nitride and molybdenum experiments. The substrates used for all BN-Mo experiments were the same tungsten sheets used in the deposition of BN presented in Chapter 7. The tungsten was sanded with 400 grit sandpaper to decrease the reflectivity and provide a rough surface for the BN to adhere. The position repeatability of the z-axis rotation stage was inconsistent, therefore, the substrates were loaded into the chamber in such a configuration that the stages would not need to be rotated during the deposition process. All line scans were 2.54 mm in length and used a scan speed of 2.54 mm/min.

10.1.1 Two–layer experiments

Preliminary BN line deposition experiments used conditions from the multiple response optimization analysis of the results of BN-14L. Pressure was kept at 760 Torr, carrier flow at 17.0 sccm, diluent flow at 8.0 sccm, and the borazine temperature at 0°C. The first scan used a laser power of 31 W while additional layers used a power of 3.68 W.

After 10 line scans, these first experiments did not yield any appreciable deposit. This inability to reproduce similar results under the same experimental conditions was attributed to the sensitivity of BN deposition and the lack of robustness associated with a constant laser power approach.

The flow conditions were changed to a carrier and diluent N_2 flow of 25 sccm each in an effort to foster more growth. Two approaches were used to control the laser power. Some experiments used a manual approach whereby the BN deposition temperature was controlled using the knob on the laser control unit. Other experiments used a constant laser power approach in which the appropriate power levels were determined in situ by observing

the thermal behavior in the deposition zone. Both approaches fostered growth, and it was not readily apparent that one was significantly better than the other.

These preliminary BN line experiments reaffirmed the sporadic nature of BN deposition. Generally, the trials resulted in lines marked by large bumps of growth at random intervals along the length. The bumps developed so quickly that it was difficult to anticipate or prevent their growth. The bumps were surrounded by large areas of white powder, particularly on the downstream side of the lines.

After several lines of BN deposition were complete, the $B_3N_3H_6$:N_2 mixture in the chamber was evacuated and the chamber was refilled with H_2. The $MoCl_5$ sublimation chamber and reagent lines were heated to the normal operating temperature of 130 and 150°C, respectively. The heating process took approximately two hours which provided sufficient time for any residual N_2 gas to be purged from the chamber.

The experimental conditions for Mo were a pressure of 760 Torr, carrier and diluent flow of 25 sccm each, and the sublimation chamber temperature was kept at 130°C. When ready to begin deposition, the $MoCl_5$ flow was diverted from the bypass port through the gas nozzle. The laser power was slowly increased using the LabVIEW interface until the target temperature of 1000°C was reached at which point the line scan was initiated. The inherent stability of Mo deposition was advantageous as the laser beam encountered the rough BN line underneath. As with previous experiments, it was difficult to determine whether significant Mo growth was occurring due to the slow nature of the process. Most of the initial experiments consisted of 10 layers of Mo.

One of the most noticeable traits of these first composite deposits was that the substrate surface was covered with a large quantity of powder surrounding the lines. Figure 10.2 shows BN-Mo-2L Sample 2 covered with this powder. In Sample 3, the Mo deposition process created a deep trench through much of the BN powder coating. Also, the Mo line did not fall directly above the BN line. This result was attributed to a shift in substrate position that occurred with the change in chamber pressure when switching from the

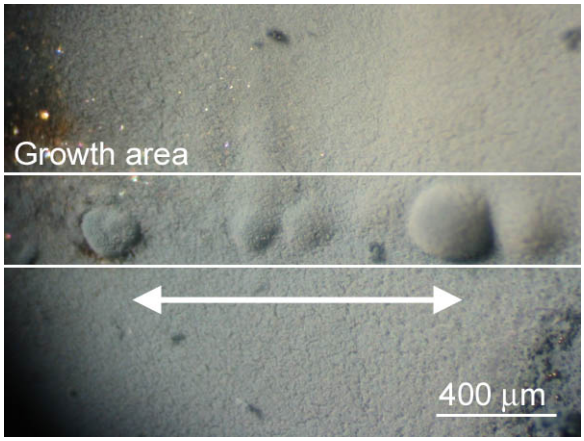

Figure 10.2: Optical image of results from BN-Mo-2L composite experiment

$B_3N_3H_6$:N_2 mixture to the $MoCl_5$:H_2 mixture.

BN-Mo-3L was designed to further explore the possibility of depositing the Mo on the underlying BN without causing damage. In order to remove the dynamic scanning effects from the process, two fiber deposits were included in this experiment. When depositing fibers, it was also possible to realign the laser after changing the system pressure because of their significant height. In addition to the two fibers, four lines were grown.

For the BN deposition, the flow conditions of BN-Mo-3L were carrier and diluent N_2 flows of 25 sccm each. System pressure was kept constant at 760 Torr, and the $B_3N_3H_6$ vaporizer was kept at 0°C. For the BN fibers, the normal laser control procedure using the manual knob on the control module was used to maintain a maximum temperature near 1000°C.

Due to the rapid deposit growth and powder formation during BN-Mo-3L BN line 3, the flow conditions for lines 4–6 were changed to reflect the conditions of the best results from BN-14L: 17 sccm carrier flow and 8 sccm diluent flow. Pressure was kept at 760 Torr and the vaporizer temperature at 0°C. The BN lines were again 2.54 mm long and used a scan speed of 2.54 mm/min. The laser power was controlled through the LabVIEW interface. The control procedure was to engage the laser using 30 W and simultaneously begin scanning the substrate. The laser power was kept at this level until the temperature

viewed on the thermal imager indicated that sustained growth had begun at which point the power was reduced and adjusted periodically using LabVIEW in an effort to maintain sustained growth. This more active temperature control approach was subsequently deemed no more effective than using a constant laser power approach.

The Mo deposition on both the fibers and lines of BN-Mo-3L was all done using identical flow conditions: 25 sccm carrier and diluent H_2 flow. Total pressure was kept at 760 Torr and the sublimation chamber temperature was kept at 130°C. The maximum temperature was kept near 1000°C by manual laser power adjustment through the LabVIEW interface. All Mo sections consisted of 10 growth layers.

When depositing on the BN fibers, the Mo deposition process was observed to be stable, but very sensitive. A change in laser power of 0.1 W would change the maximum deposition temperature by over 100°C. This represented more sensitivity than previous Mo experiments executed on the large BN plate substrates, and was attributed to the limited conduction paths through the underlying BN fiber to the tungsten substrate. Fibers 1 and 2 consisted of 12 and 10 minutes of Mo growth, respectively.

The resulting composite fibers showed significant bulk growth of both BN and Mo with minimal damage to the bulk BN at the interface. The surface of both materials was similar to that seen in previous fiber experiments with the BN having a cauliflower appearance and the Mo growth consisting of a multitude of small, nodular fibers growing from the underlying surface. Figure 10.3 is an optical microscope image of Sample 2.

In terms of the lines, it appeared that both materials deposited, but both produced significant amounts of powder and debris on the substrate surface. Misalignment between the BN and Mo layers due to stage shift was again apparent. As usual, the BN deposit was marked by large bumps of tall growth while the Mo deposit remained a very thin coating. The powdery coating produced by the Mo growth formed a brittle material that appeared to crack and peel away from the white powder underneath, upon exposure to atmospheric air.

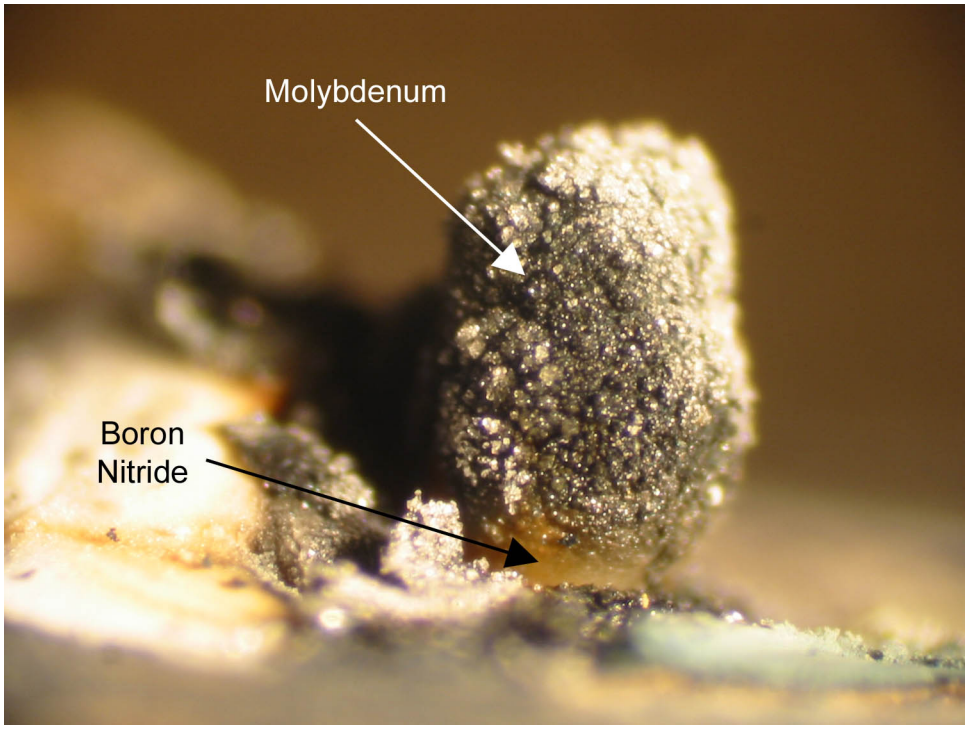

Figure 10.3: Optical image of BN-Mo composite fiber

The next series of BN-Mo experiments, BN-Mo-4L, were run with an increased emphasis on avoiding the large bumps in the BN line deposits. The goal for the BN lines was to proceed until one sustained layer of deposit was accomplished as judged through the thermal imager. The borazine flow rate was further reduced in an effort to reduce growth rates by changing the carrier and diluent flows to 12 sccm each. Pressure was kept at 760 Torr and the vaporizer was kept at 0°C. Laser power was kept constant until sustained growth began at which point the control method was changed to either a constant but significantly reduced power as in BN-14L and 15L or manual control through the LabVIEW interface with a target temperature of 1000°C. Laser power conditions specific to each run except number 1 are given in Table 10.1. Run 1 was a trial used to find approximate conditions that enabled acceptable growth.

Even with the changes in experimental conditions and procedure, the BN lines still tended to develop a large bumpy shape and growth was accompanied by significant powder formation. The results of run 6 produced a noticeably smoother line of uniform height and

Table 10.1: Various experimental parameters used in BN-Mo-4L

No.	BN Layer 1 Power (W)	BN Layer 2 Power (W)	BN Layer 3 Power (W)	BN Layer 4 Power (W)	No. of Mo Layers
2	31.1	31, var	-	-	10
3	15.9	15.9	15.9	15.9	10
4	23.7	23.7	var	var	-
5	38.0	var	var, -	-	10
6	31.1	5.4	-	-	16
7	31.1	5.2	5.2	5.2	1

well–defined width. This line was similar to the samples from the best results of BN-14L and 15L in that it did not extend the full length of the laser scan path.

In an effort to minimize the problems with stages shifting during pressure changes, a new procedure was employed. The chamber was not evacuated between the BN and Mo materials, but the reagent gas tank was simply switched from nitrogen to hydrogen under the same flow conditions. The sublimation chamber and reagent lines were heated while the flowing hydrogen displaced the remaining nitrogen in the system. It was apparent that even after using this new procedure to transition material systems, the laser spot had shifted slightly from its original spot on the substrate surface. The spot was realigned to the extent possible by visual observation through a top port in the upper chamber.

The conditions for the Mo line deposition were derived from the conditions of Sample 4 of Mo-10L because it exhibited a well–defined Mo line region with minimal blue–green powder on the substrate surface. Conditions included a pressure of 760 Torr, a sublimation chamber temperature of 130°C, a carrier H_2 flow of 15.8 sccm and a diluent H_2 flow of 59.1 sccm. Laser power was controlled manually through the LabVIEW interface to maintain a constant maximum temperature of 1000°C. The scan speed was the normal 2.54 mm/min and the number of layers varied depending on the perceived quality of the underlying BN line. Table 10.1 indicates the number of Mo layers associated with each sample.

Most of the samples still yielded large bumpy BN lines that were covered with a thin

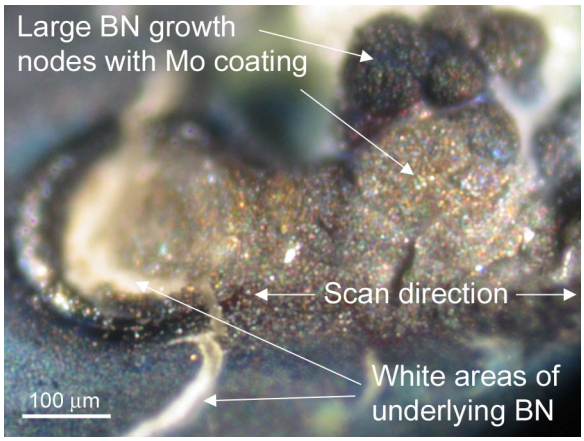

Figure 10.4: Top view of BN-Mo-4L Sample 7 showing bumpy surface

coating of Mo. Figure 10.4 highlights the shape and features of Sample 7.

The best result was that of Sample 6 as shown in Figure 10.5. The underlying BN line was fairly smooth and uniform and the Mo coating on the surface was apparent. The BN line was partially covered by the blue–gray brittle coating that accompanied Mo deposition. It was apparent here that the Mo layers were unfortunately offset significantly from the underlying BN material. This result suggested that even using a constant pressure material transition procedure did not alleviate the problem of stage drift. The excess powder surrounding the deposit was removed by cutting along the edges of the lines and scraping the powder away using a knife. A cross–sectional cut was made through the structure near the starting end of the line. Figure 10.6 is an optical microscope image taken on a 45° angle of the resulting cross section.

The cross–section of Sample 6 was inspected by mounting it in epoxy and cutting across the line. The orientation of this cross section is shown in Figure 10.5. Figure 10.7 contains an SEM micrograph of the cross section. The tendency of the BN to charge in the microscope made it difficult to get an ideal image. The figure also contains outputs for four EDX analyses of different regions within the cross section. The BN is the bright region as confirmed by the EDX analysis. The loosely packed powder region between the solid BN and the tungsten substrate was observed through an optical microscope to be polishing residue.

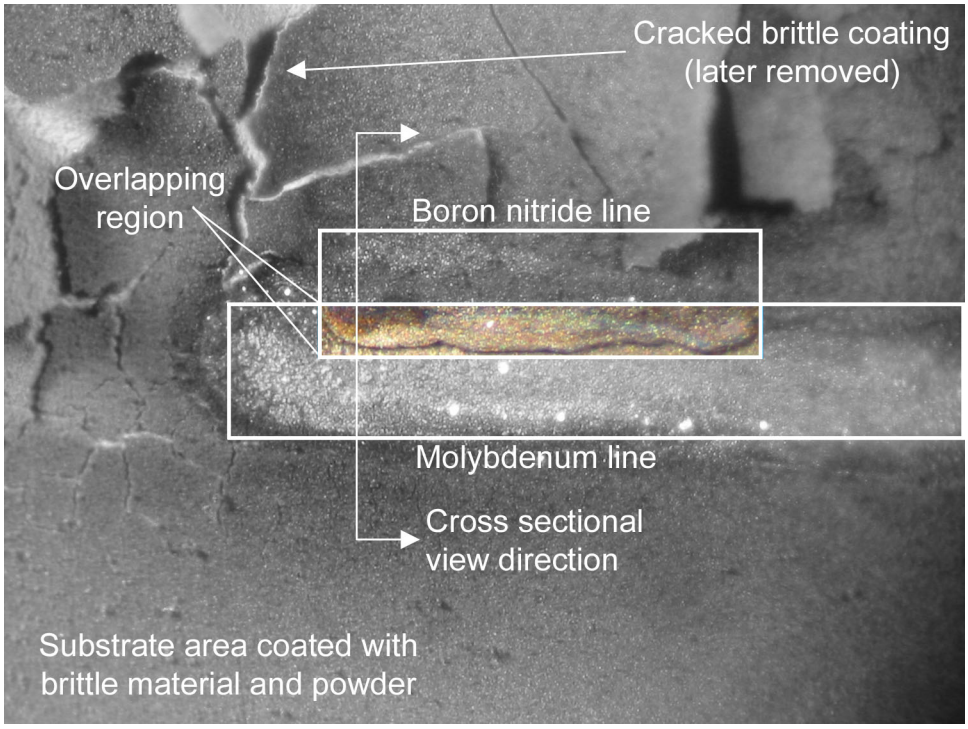

Figure 10.5: Top view of Sample 6 showing offset of different material layers

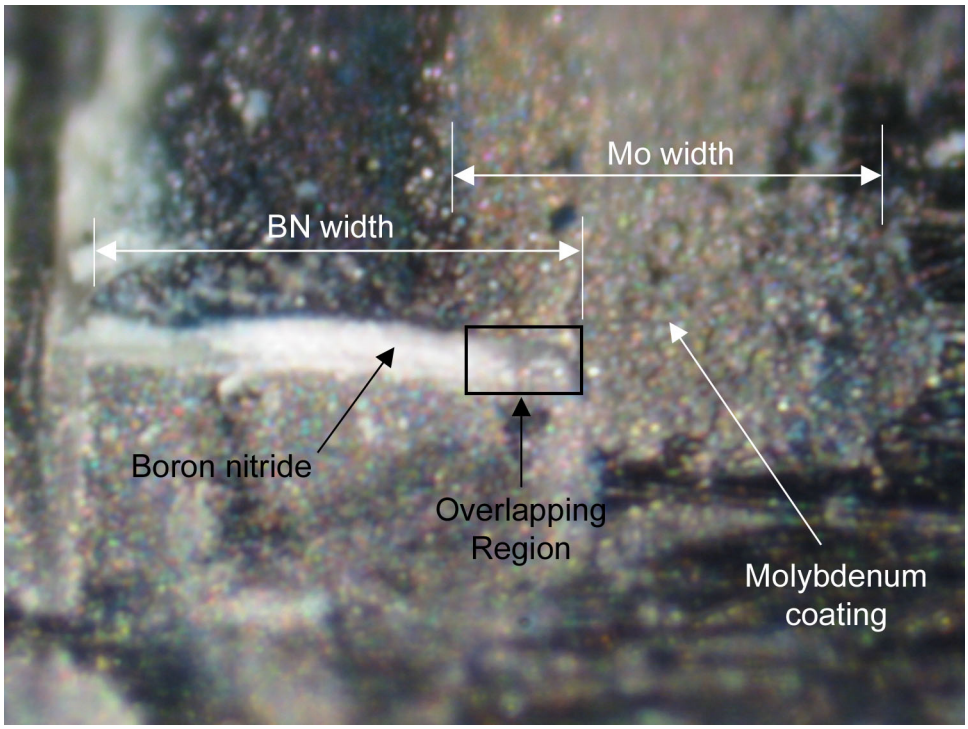

Figure 10.6: Cross section of Sample 6 showing offset of different material layers

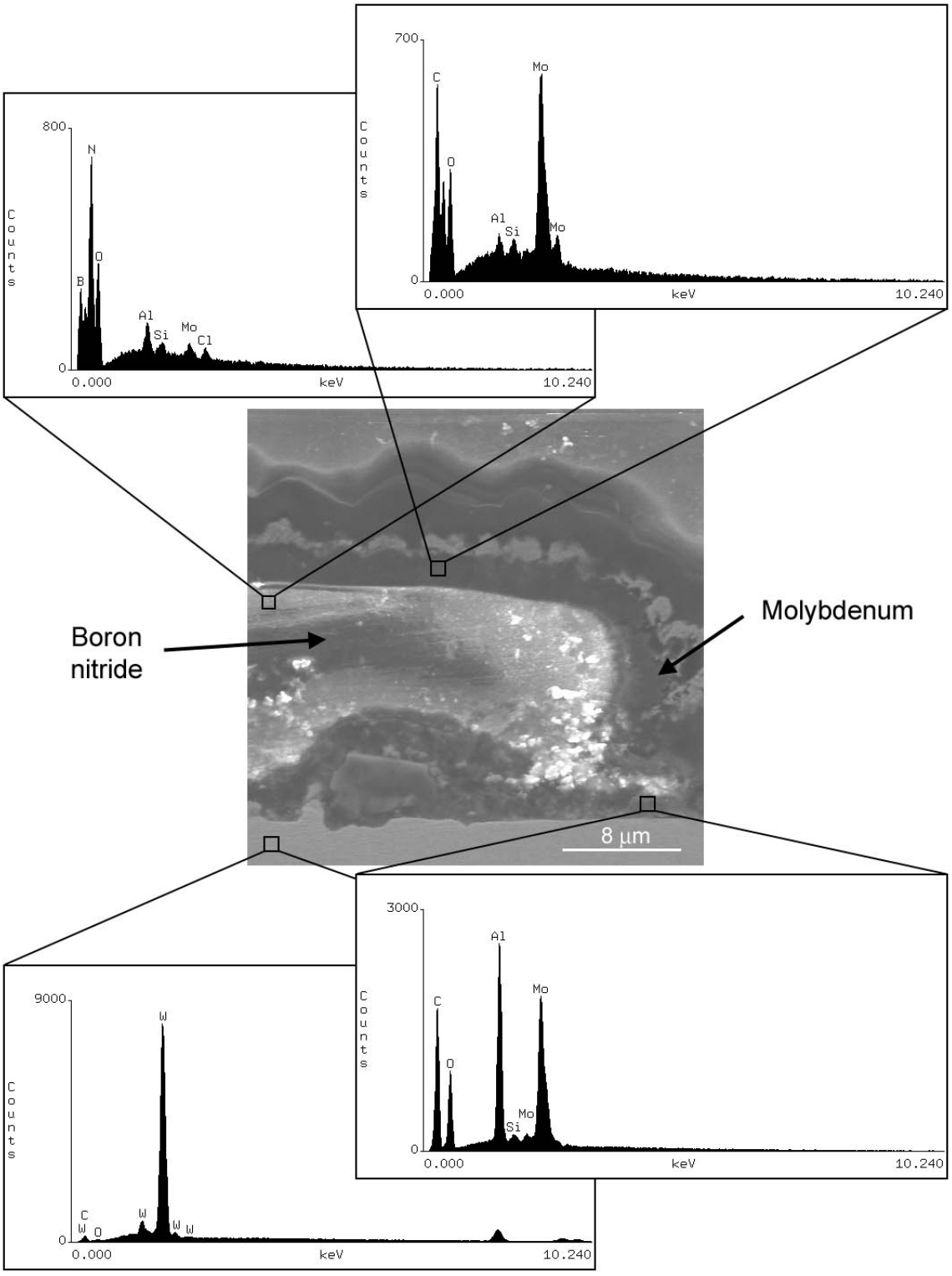

Figure 10.7: SEM micrograph of cross section of Sample 6 of BN-Mo-4L with multiple EDX analyses

This residue inhibits the ability to see the BN –W interface. The coating on the BN surface was shown by the analyses to contain significant molybdenum. Most of the other elements shown in the EDX responses could be related to the polishing process that used both SiC grinding paper and Al_2O_3 powder. The presence of chlorine was unsurprising given the use of the $MoCl_5$ reagent in the deposition process. In addition to the Al_2O_3 powder, the elemental O_2 could be due to air leaks into the chamber.

The total BN layer thickness within the composite was estimated to be ~ 20 μm, while the total thickness of all 16 Mo layers was $\sim$ 1–2 μm. These dimensions highlight the drastic difference in growth rates of the two materials. Some pores were observed in the BN region, but overall, the composite appeared to have good integrity. The results of this composite line illustrate that with sufficient process control, the fabrication of a ceramic–metal laminate is feasible using LCVD.

Experiment BN-Mo-5L was designed to improve upon the results of BN-Mo-4L by reducing the amount of excessive powder formation. The BN deposition conditions used were similar to those used in BN-20L which were computed from the multiple response optimization of BN-19F. These conditions included a pressure of 269 Torr, vaporizer temperature of 0°C, carrier N_2 flow rate of 4.33 sccm and diluent N_2 flow of 9.24 sccm which yielded a total flow of 15 sccm and a $B_3N_3H_6$ concentration of 1.5 mol/m^3. For all lines, the laser power was controlled manually using the external control module with a target temperature of 1000°C. The procedure was to use a high power ($\sim$ 80 W) until growth began, and then reduce the power until one complete layer of sustained BN growth was achieved. All lines were 2.54 mm long and the scan speed was kept at 2.54 mm/min.

Based on observations during the experiments, the BN lines appeared similar to those of previous experiments with sporadic growth that was difficult to control. Several experiments had large growth balls on the initial end of the lines while others showed very minimal deposit.

The Mo layers were deposited using conditions from Sample 3 of Mo-10L which had

shown good Mo growth with very little excess powder. The conditions included a pressure of 320 Torr, sublimation chamber temperature of 130°C, carrier H_2 flow of 26.3 sccm and diluent flow of 23.5 sccm. It was unclear a priori whether the slight change in pressure from the 269 Torr of BN deposition would cause a significant shift in substrate position. Laser power was controlled using the typical Mo procedure with manual control through the LabVIEW interface to maintain a target temperature of 1000°C. The Mo deposition process was again best described as being stable but sensitive.

The results of BN-Mo-5L-A were varied, but overall they were not significantly different from those of BN-Mo-4L. Significant powder formation still occurred, and the deposits were generally nonuniform. None of the deposits were as promising as Sample 6 of BN-Mo-4L.

10.1.2 Four–layer experiments

In accordance with the composite needed for the dispenser cathode assembly, a four material BN-Mo-BN-Mo trial was run. This experiment was denoted BN-Mo-6L. The substrate used was a tungsten sheet prepared as usual. In lieu of the problems with the mechanical stages shifting when chamber pressure changed, these experiments were run under a constant pressure of 760 Torr. Prior to beginning any deposition, the $B_3N_3H_6$ reagent was placed in its ice bath and allowed to stabilize to 0°C and the $MoCl_5$ sublimation chamber was preheated to operating temperature of 130°C. The lines were 2.54 mm long and a speed of 2.54 mm/min was used for all scans.

Flow conditions during the first layer of BN deposition were 12.25 sccm of N_2 carrier and 1.57 sccm of N_2 diluent. The laser power was controlled manually using the knob on the external control module to a target maximum temperature of 1000°C. The first layer of BN resulted in the normal nodular deposit with excessive powder formation.

The transition to Mo deposition was accomplished by changing the source of reagent gas from the N_2 tank to the H_2 tank. Flow through the side port of pure H_2 at 1000 sccm

was allowed for 5 minutes, and the $MoCl_5$ sublimation chamber was opened and the carrier flow was set to 26.3 sccm while the diluent flow was set to 23.5 sccm. After five additional minutes for the flow to stabilize, the laser was engaged using manual control with a target temperature of 1000°C. Ten layers of Mo were deposited.

The transition from Mo back to BN deposition used the same procedure as the change from BN to Mo. The H_2 tank was closed and the N_2 tank opened. After 5 minutes of 1000 sccm flow, the carrier and diluent flow were set to the same levels used in the first BN layer. Note that the final length of reagent lines and the gas nozzle remained at 150°C during this BN deposition. There was some concern that the hot lines could cause decomposition of the borazine or enable deposition within the lines and cause clogging, but such behavior was not immediately obvious. For the second BN layer, the laser power was again controlled using the manual knob.

This layer of BN deposit was even more unstable than the first layer. The pertubations in the first BN line amplified the tendency for the second BN line to grow faster at the high spots and slower in between. Not unlike other BN experiments, the deposition temperature was also observed to be very sensitive to the input laser power. This was expected because of the limited conduction paths through the underlying deposit to the substrate.

One more level of Mo was added by switching back to the H_2 gas source and allowing the normal 5 minutes for flow to stabilize and residual gases to be purged. The flow conditions and laser power control were all identical to the first Mo level experiments.

The deposit of BN-Mo-6L was a large bumpy line/wall structure that was surrounded by a plethora of white (from BN) and blue (from Mo) powder. It was difficult to determine the success of the layered deposition due to the rough morphology and the excessive quantity of debris surrounding the area. Figure 10.8 is an optical micrograph of the deposit showing these features. The majority of the powder was scraped away from the deposit, and the sample was mounted in epoxy and polished into the cross section. Figure 10.9 is an optical micrograph of this cross section.

Figure 10.8: Optical image showing rough surface of 4–layer composite

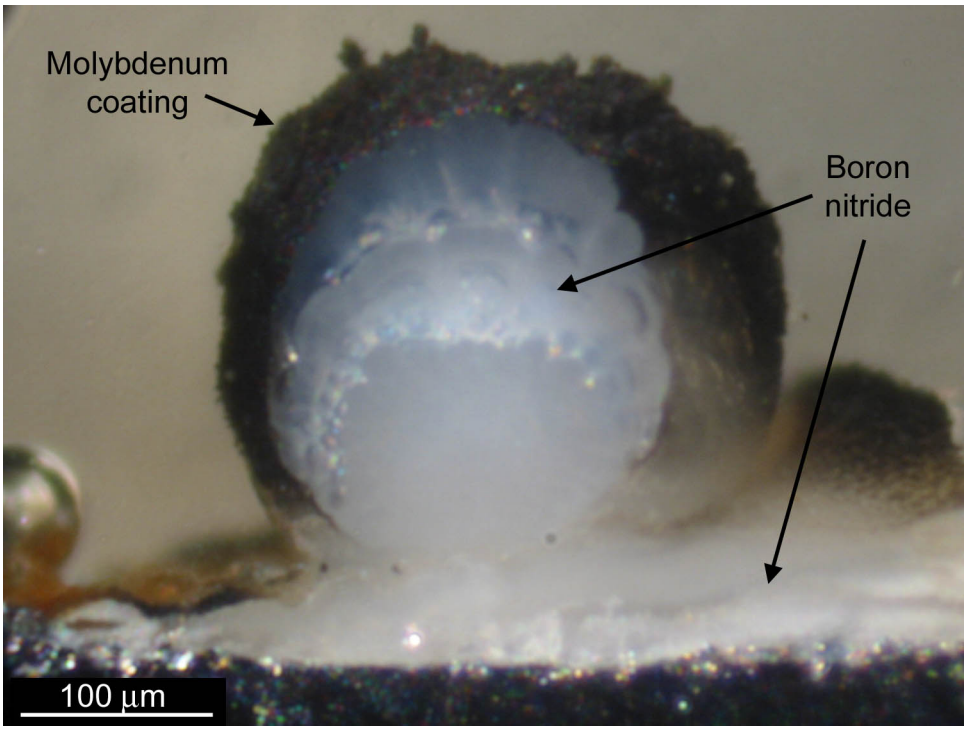

Figure 10.9: Optical image showing cross section of the 4–layer composite

The cross section looks very similar to the fiber shown in Figure 10.3. A significant layer of molybdenum can be seen on the deposit surface; however, no evidence of the inner Mo layer can be seen. This is perplexing given the fact that during the experiment, Mo deposition appeared to occur during the growth of this inner layer. Boron nitride growth remained very sporadic and difficult to control as evidenced by the fact that the deposit cross section resembles a BN fiber more than a line. The important finding from this experiment was that without better controlling the boron nitride line growth process, it will be even more difficult to deposit 4–layer deposits than 2–layer composites. In light of BN line deposition sensitivity, the limitations of Georgia Tech's LCVD system did not support a more refined further study of this process.

10.2 Summary and Discussion

The BN-Mo composite experiments were generally plagued by the same issues that were faced in the isolated material studies of Chapter 7 and 9. One issue that was studied was the tendency to form excessive powder on the surrounding substrate during the deposition of both BN and Mo. The powder could be removed easily using a scraper and was deemed a nuisance, but did not entirely prohibit the deposition of a composite structure.

For BN lines, the biggest challenge was the tendency towards erratic and unpredictable growth nodes. These nodes encouraged fast growth in their local regions and challenged the ability to achieve smooth, uniform lines. The Mo deposition process was very similar to previous experiments in that it was very slow, but generally stable and sensitive. Deposition on the underlying BN material was not significantly different from depositing on large BN plates. The high temperature of LCVD did not appear to affect the BN material. The deposition of overlapping lines was complicated by the tendency for the substrate to shift slightly when the system pressure was changed.

In summary, the deposition of a BN-Mo composite using LCVD was possible. The practicality of the process was limited by the LCVD machine configuration and hardware

limits. The controllability of BN line deposition complicated creation of the desired geometry. Overall, the investigation into deposition of BN-Mo composites has many broad implications for the creation of other ceramic–metal structures using LCVD.

CHAPTER XI

CONCLUSIONS AND RECOMMENDATIONS

Many conclusions drawn from this research were presented in the preceding chapters. Of those conclusions, some are of significant practical importance and represent major contributions in the field of LCVD. This work also provides a foundation for future studies of LCVD and its application. These conclusions and recommendations are given below.

11.1 Conclusions

The capability of the LCVD process has been further demonstrated through this work. Carbon deposition was used as a vehicle to develop a better understanding of the external shape of LCVD deposits through the execution of a large number of processing experiments, deposition of advanced structures, and development of an advanced computational model of the deposition process. Cross sections of carbon deposits were studied to permit determining their microstructure and to examine their structural integrity. A computational model of thermal stress within an LCVD fiber was developed to better understand the cause of internal cracks.

In terms of the external shape of LCVD deposits, several important findings came from the carbon deposition experiments. The best predictive models for carbon deposit shapes are based on theoretical deposition rate expressions. Fabrication of smooth, uniform, high aspect ratio, multi–layered wall structures is possible with a good understanding of the line deposition process and advanced real–time temperature control.

The computational deposition rate model that incorporated species transport allows the study of the complex local phenomena that govern the LCVD reaction. Also, the model allows prediction of overall deposition rates and deposition rate profiles under different

simulated conditions. The model can be used in lieu of experiments to study the relation among different process parameters and deposition rate, and the results of such analyzes can be fit using linear regression techniques to simple polynomial expressions that serve as a useful tool for predicting deposit shape.

There are a few limitations to using the computational model approach to studying LCVD. High quality experimental kinetic data must be supplied to the CFD code for accurate computation of deposition rates. In general, LCVD kinetic data are limited to a few material systems; therefore, experimental studies usually must occur before, or parallel to, modeling studies. Also, for a kinetically–limited process such as carbon deposition from methane, the predicted deposition rate profiles are extremely sensitive to numerical uncertainty due to the exponential relation between temperature and deposition rate.

Several important findings came from studying carbon deposition from methane using the computational model. As was shown by others,[2] because the process is kinetically–limited, the reagent gas nozzle has little effect on the carbon deposition rate. Even when different from the mixture exiting the gas nozzle, the mixture in the deposition chamber has a significant impact on deposition rate. Thermal diffusion also significantly impacts the deposition rate even for this kinetically–limited process.

Internal features of carbon deposits were also investigated. The crystal structure of the carbon was shown to be similar to that of hexagonal pyrolytic graphite. Cracks found in previously grown LCVD carbon fibers were related to thermal stress through development of a structural model. Creating the structural model highlighted the complexity of the material properties of an LCVD carbon deposit. There is directional orientation (anisotropy) in the material properties in addition to a spatial variation (inhomogeneity) due to the different deposition temperatures that exist within the region of the laser spot.

The results of the thermal model were very sensitive to the deposit properties because of the large amount of incident laser energy within the relatively small volume of the deposited fiber. The temperature results from the model did not agree well with experimental data

captured using the thermal imaging camera. This was attributed to the restricted conduction paths within the deposit due to likely cracks and contact resistance at the deposit–substrate interface. The thermal stresses computed from the structural model were extremely high and oriented consistent with observed crack sizes and shapes.

One of the unique features of the LCVD process is the ability to deposit directly from the gas phase useful engineering materials in small, complex geometries targeted for specific applications. The LCVD of boron nitride and molybdenum materials toward the fabrication of an integrated dispenser cathode assembly was the focus of much of this investigation. Specifically, the deposition of BN from borazine ($B_3N_3H_6$) on tungsten substrates was studied along with the deposition of Mo from molybdenum pentachloride ($MoCl_5$) on BN substrates. Finally, the fabrication of BN-Mo composites was addressed.

The BN LCVD process is very sensitive to input laser power. This sensitivity is most notable during growth initiation on the substrate surface. Deposits grow very rapidly after a growth node forms on the substrate surface, and laser power must be dropped significantly to maintain growth at a constant temperature. After passing through the transition period at the substrate surface, BN fiber growth is stable, but sensitive. The sensitivity is so high that in Georgia Tech's LCVD system, the most effective means of controlling reaction temperature is to make very slight adjustments using the control knob on the laser power module during growth. Experimental evidence suggests the process is transport–limited which makes it particularly sensitive to transport variables such as pressure, reagent concentration, and flow rates. BN fibers display a range of shapes depending on process conditions, and tend to develop internal cracks or voids similar to those of carbon fibers. BN deposits are often accompanied by excessive white powder formation on the substrate surface.

The computational deposition rate model was used to further explore the rate–limiting regime of BN fiber growth. The upper theoretical limit of deposition rate was computed and shown to agree very well with experimental data, thus confirming that this process is transport–limited. The shape of the deposition rate profiles for the transport–limited

process are very different from those of a kinetically–limited process and show that transport limitations will lead to the volcano effect. Consistent with original design intent, the reagent flow rate through the gas nozzle greatly impacts the deposition rate. Thermal diffusion, or the Soret effect, also has a significant impact on the deposition rate.

The findings of BN fiber growth do not lend much insight into BN line growth because of the importance of the surface effects. These surface effects are linked to both the differences in substrate and deposit material properties and the sporadic nature of the deposition process itself. Successful BN line growth can be accomplished using a constant intralayer laser power approach with an interlayer change in power level. The repeatability of this process is severely limited by the lack of robustness associated with a constant laser power approach. Adherence of BN lines to a tungsten substrate is marginal.

Mo deposition under the studied conditions is best characterized as a slow, sensitive, but stable process. Efforts to increase the deposition rate by increasing mass transport are plagued by the tendency for excessive powder to form on the substrate surface surrounding the deposit area. The ability to increase deposition rates by increasing temperature are limited by the tendency to damage the underlying BN material. The lower temperature limit is dictated by the range of the thermal imager and unfortunately is too close to the optimum temperature to allow use of the automatic temperature control system. The stability of Mo deposition, particularly near the substrate surface, lends tremendous insight into the Mo line growth process. In fact, identical conditions can be used for both processes, and line specific variables such as scan speed do not significantly change the results. In sum, Mo deposition from $MoCl_5$ on BN substrates is restricted to a small operating box that supports only slow growth rates.

BN-Mo composite growth is complicated by the sporadic nature of BN line growth and the slow rate of Mo line growth. During deposition, both materials also tend to deposit excess powder on the substrate surface that must later be removed. One synergy that exists in building the composite is that the stability of Mo deposition, likely due to its slow rate,

minimizes the importance of the bumpy nature of the BN lines. There are also a few problems with fabricating this structure in Georgia Tech's LCVD system. The mechanical stages tend to shift when the system pressure changes which makes it difficult to ensure alignment of the BN level with the Mo level. The system is not optimally configured for simultaneous use of a reagent that must be kept cool and delivered through unheated reagent lines (borazine) and a reagent that must be heated and delivered through heated reagent lines (molybdenum pentachloride). The deposition of a ceramic–metal composite using LCVD is certainly possible; however, for the material systems studied, it is not currently very practical.

Four layer BN-Mo-BN-Mo composite growth incorporates the challenges of growing the two–layer composite as well as one significant new challenge. Deposition of the second level of BN on the first Mo level is even more sensitive than BN deposition on a flat substrate surface. The inherent tendency for growth to occur at isolated nodes is exacerbated by the generally rough nature of the underlying BN deposit. The two biggest obstacles to using LCVD to fabricate an integrated dispenser cathode assembly were the difficulty in depositing smooth and consistent BN lines and the extremely slow deposition rate of Mo. Changes in the process, equipment, or experimental procedure will need to be made to enhance fabrication of this structure.

11.2 Significance and Contributions

The findings and conclusions presented in Section 11.1 above represent important contributions to the study of Laser Chemical Vapor Deposition, especially in regard to the integrated dispenser cathode application. The major contributions are presented below in bold along with an itemized description of the more specific accomplishments associated with each.

- **Characterized process–property relationships for carbon LCVD**
  - Established predictive models for deposit shape from experimental parameters

  - Using advanced temperature control, deposited first smooth, uniform multi-layered, high aspect ratio LCVD walls
  - Identified microstructure of carbon deposits to be graphitic

- **Developed first fully integrated forced flow CFD deposition rate model that incorporates species transport**
  - Provided detailed analysis of local phenomena in the deposition zone (e.g. showed importance of thermal diffusion)
  - Showed differences between kinetically–limited and transport–limited LCVD deposition rate profiles
  - Developed simple polynomial expressions from model results to express process–property relations for carbon deposition
  - Quantified upper theoretical deposition rate limit for BN deposition process

- **Developed first FEM thermal–structural model of an in situ LCVD deposit**
  - Provided a methodology for incorporating complex LCVD deposit material properties in a modeling environment
  - Quantified the thermal stresses that develop within an LCVD fiber during growth
  - Related the thermal stresses to failure criteria

- **First comprehensive processing studies of BN LCVD from borazine using continuous laser heating**
  - Achieved well–defined BN fiber and line shapes
  - Quantified the process–structure relations between deposit shape and experimental parameters
  - Addressed the implications of depositing a ceramic on a metal substrate

  - Identified the process to be transport–limited and discussed the implications of this on deposition rates and deposit shape
  - First investigation of internal features of LCVD boron nitride
  - First LCVD of BN lines

- **Most advanced study of Mo LCVD from $MoCl_5$ reported**
  - Identified an appropriate operating box for fabrication of Mo fibers and lines
  - Addressed the implications of depositing a metal on a ceramic substrate

- **First fabrication of a ceramic–metal composite using LCVD to grow both materials**
  - Demonstrated importance of process control in depositing composite laminates
  - Showed feasibility of producing BN-Mo structure needed for integrated dispenser cathode assembly
  - Identified needed changes to the LCVD machine for practical realization of the fabrication of an integrated dispenser cathode assembly

11.3 Recommendations and Future Work

While this body of work has advanced the current status of LCVD research, the complexity of the process dictates the need for continued work. Recommendations for future studies can be broken into three sections. The first section discusses future evolutions of the modeling and analysis of the general LCVD process. The second section is focused on the deposition of the materials of interest and ceramic–metal structures in general, and the third section involves deposit geometry and process control considerations.

11.3.1 Modeling and Analysis

One limitation of the computational deposition rate model developed herein was the simplified approach used to simulate chemical reactions. Future models could incorporate

additional species and consider homogenous chemical reactions that could enhance the accuracy and reliability of the model results. The FLUENT code has the ability to use species databases such as that provided via CHEMKIN in its calculations which would ease the implementation of these additional reactions.

CHEMKIN is software that is widely used for the study of complex chemical kinetics in reacting systems. One package in the CHEMKIN suite, TWAFER, is designed specifically for studying CVD reactions. While TWAFER is geared towards the semiconductor manufacturing industry, it offers many features that could be useful in studying the LCVD process. CHEMKIN would allow a more detailed study of the gas phase reactions taking place in the LCVD chamber and in particular would allow a detailed look at the types and concentrations of gas species near the substrate surface. The thorough database of materials and chemical reactions CHEMKIN utilizes in its calculations offers a detailed study of the reaction mechanisms not possible with FLUENT. As such, CHEMKIN would provide for thorough modeling of the chemical kinetics of LCVD and would contribute to the geometric modeling efforts.

Another limitation of the deposition rate model was the fact that it used a steady state approach that did not include the dynamic substrate effects associated with the LCVD growth process. Future models could include a changing substrate geometry that represents the evolution of deposit shape and could therefore consider changes in the substrate properties and the interaction among the deposit shape and process variables. For instance, fiber growth significantly changes the conduction of heat away from the laser–heated zone and changes the flow profiles in the deposit area. These changes undoubtedly have an impact on the resulting LCVD deposit shape.

If the transient analysis described above could be implemented using a solver that offers structural analysis in addition to the thermal–flow analysis, a transient structural analysis could provide further insight into the thermal stresses that evolve within a depositing structure. Such a comprehensive model would demand tremendous computing resources, but

would yield invaluable insight into manipulating the LCVD process toward achieving success in certain applications. Moreover, it could help understand how to change the process conditions and avoid the thermal cracks that are prevalent.

11.3.2 Materials

The deposition of boron nitride fibers and lines has been well–demonstrated. Future studies should focus on better characterizing the internal microstructure of the deposits and developing an understanding of how the microstructure changes with process conditions. Further investigations are also needed to seek ways to minimize the sporadic nodular growth of BN on the substrate surface. Perhaps a comprehensive study of substrates and growth initiation would yield valuable insight. If smooth uniform, BN lines are to be deposited, the growth initiation process must be understood and controlled. Control of the BN deposition process would be enhanced by use of a laser that had better resolution or perhaps fitting the current laser with a beam splitter to reduce the sensitivity of the process. Note however, that deposition on a highly reflective substrate such as tungsten requires very high laser power levels until the surface develops a coating that changes the surface properties.

Mo experiments should focus on finding conditions that enable faster growth rates. In order to identify the rate–limiting variables, the rate–limiting regime must be identified. Using a temperature measurement device that has a lower limit of 500°C would enable execution of kinetic studies and allow the use of a feedback temperature control system. Use of a substrate heater could help reduce the formation of the excess powder that plagued Mo deposition. Georgia Tech's LCVD system formerly included such a system, but leaks into the deposition chamber through the associated feedthru ports required that it be disabled. Modifications to the system that allow use of this device might be beneficial.

11.3.3 Deposit Geometry and Process Control

The deposition of the carbon walls presented herein illustrated the importance of a real–time LCVD control system and served to validate its role in producing well defined deposit

shapes and structures. Use of such a system is the only method of controlling the inherent positive feedback tendency of the layered deposition process.

Another issue that has not been sufficiently addressed and will affect the ability to produce the specified dispenser cathode geometry is that of depositing intersecting lines. Similar to layered deposition, without sufficient process control, the deposition of intersecting geometry poses the threat of causing excessive deposit growth at the intersection. The amplification of deposit volume and height at intersections has been observed in the past with carbon deposition.

Some weaknesses of Georgia Tech's LCVD system have been identified regarding the deposition of laminated structures. The pressure change required when changing reagent gases causes a shift in the substrate position and causes misalignment between the bottom and top materials. The configuration of the mechanical stages in the system should be modified to prevent such behavior.

APPENDIX A

MATERIAL PROPERTIES

A.1 Graphite Substrate Properties

Table A.1: Available properties of different graphite substrate materials

	Industrial Sales	
Supplier	Associates Inc.	POCO
Grade	**SK-85**	**AXF-5Q**
Manufacturing Mode	extruded	isostatically pressed
Bulk Density (g/cm^3)	1.76	1.78
Grain Size (mm)	0.2	0.005
Pore Size (μm)		0.8
Total Porosity (% Volume)		20
Specific Resistance ($\times 10^{-6}\Omega-$cm)	10.2	14.7
Flexure Strength (N/mm^2)	28.98	90
Compressive Strength (N/mm^2)	55.1	145
Tensile Strength (N/mm^2)		60
Modulus of Elasticity (N/mm^2)		11000
Tensile Strain (to Failure%)		0.95
Shore Hardness	50	74
Ash	0.10%	
CTE ($\times 10^{-6}/^{\circ}$C) (with grain)		7.9
Thermal Conductivity (W/m-K)		95
Oxidation Threshold ($^{\circ}$C)		450

A.2 Boron Nitride Substrate Properties

Table A.2: Properties of General Electric hot–pressed boron nitride shapes

Grade	**HBC**	
B+N (%)	>99	
Binder	None	
Max Rec Operating Temp (°C)		
- Oxidizing Atm	850	
- Inert/Vacuum Atm	2000–3000	
Density (g/cm^3)		
- Minimum	1.9	
- Typical	1.95	
Porosity (%)	13	
Hardness, Knoops (KHN, 100g)	16	
Specific Heat (J/kg-K)		
- @ 25°C	808	
- @ 700°C	1846	
Pressing Direction	$\parallel$	$\perp$
Thermal Conductivity (W/m-K)		
- @ 25°C	28	23
- @ 500°C	30	24
CTE (ppm/deg C)		
- 25 to 1500°C	0.4	0.8
Flexural Strength (Mpa)		
- @ 25°C	20.6	17.2
- @ 1500°C	48.2	27.5
Modulus of Elasticity (Gpa)	48.2	20.6
Compressive Strength (Mpa)	41.3	51.7
Electrical Properties		
Dielectric Strength (V/mm x 10^3)	54	
Dielectric Constant	4.1–4.3	
Volume Resistivity (Ohm-cm)		
- @ 25°C	$> 10^{15}$	
- @ 700°C	10^{10}	

A.3 Boron Nitride Thermodynamic Analysis

Table A.3: Species standard enthalpy of formation values (kJ/mol) used in BN thermodynamic analysis[110]

	800 K	900 K	1000 K	1100 K	1200 K	1300 K	1400 K	1500 K	1600 K	1700 K	1800 K	1900 K	2000 K	2100 K	2200 K	2300 K	2400 K	2500 K
H	221.213	221.804	222.382	222.943	223.487	224.006	224.509	224.986	225.438	225.869	226.280	226.673	227.050	227.402	227.741	228.063	228.373	228.662
H2	0.000	0.000	0.000	0.000	0.000	0.000	0.000	0.000	0.000	0.000	0.000	0.000	0.000	0.000	0.000	0.000	0.000	0.000
NH	339.042	339.013	338.992	338.975	338.971	338.975	338.988	339.005	339.022	339.047	339.072	339.105	339.135	339.168	339.197	339.235	339.269	339.302
NH2	163.758	163.235	162.799	162.439	162.150	161.916	161.728	161.573	161.439	161.334	161.246	161.179	161.116	161.062	161.012	160.966	160.924	160.869
NH3	-53.691	-54.495	-55.111	-55.563	-55.864	-56.040	-56.111	-56.099	-56.024	-55.881	-55.697	-55.475	-55.228	-54.952	-54.650	-54.315	-53.955	-53.578
N2H2	207.054	206.715	206.551	206.535	206.635	206.836	207.108	207.439	207.807	208.222	208.661	209.130	209.616	210.110	210.617	211.132	211.655	212.170
N2H4	87.383	87.290	87.491	87.931	88.576	89.384	90.334	91.381	92.503	93.709	94.969	96.288	97.640	99.022	100.420	101.848	103.284	104.716
N	475.871	476.365	476.822	477.253	477.659	478.040	478.400	478.743	479.074	479.392	479.694	479.991	480.276	480.552	480.824	481.088	481.347	481.599
N2	0.000	0.000	0.000	0.000	0.000	0.000	0.000	0.000	0.000	0.000	0.000	0.000	0.000	0.000	0.000	0.000	0.000	0.000
BH	441.234	440.589	439.923	439.224	438.500	437.742	436.955	436.122	435.247	434.334	433.388	432.412	431.416	430.398	429.364	428.309	427.233	403.582
BH2	197.324	196.725	196.189	195.687	195.213	194.753	194.288	193.803	193.288	192.752	192.186	191.600	190.997	190.369	189.716	189.046	188.351	165.073
BH3	97.205	95.765	94.509	93.395	92.411	91.519	90.699	89.907	89.141	88.392	87.651	86.918	86.194	85.461	84.728	83.995	83.242	59.921
B2H6	24.694	23.597	22.998	22.764	22.831	23.094	23.505	23.965	24.455	24.974	25.485	26.000	26.511	26.992	27.453	27.897	28.290	-16.475
B3N3H6	-527.406	-527.946	-527.934	-527.532	-526.808	-525.861	-524.752	-523.580	-522.365	-521.122	-519.874	-518.610	-517.333	-516.073	-514.821	-513.577	-512.363	-578.866
B	556.919	556.630	556.258	555.810	555.299	554.725	554.097	553.411	552.669	551.882	551.053	550.191	549.303	548.391	547.453	546.498	545.506	521.976
B2	814.244	813.096	811.824	810.425	808.922	807.319	805.619	803.819	801.930	799.954	797.903	795.797	793.645	791.455	789.228	786.967	784.672	737.240
BN	476.198	475.674	475.092	474.448	473.753	473.003	472.203	471.358	470.466	469.528	468.557	467.560	466.547	465.517	464.470	463.420	462.352	438.726
B-s	0.000	0.000	0.000	0.000	0.000	0.000	0.000	0.000	0.000	0.000	0.000	0.000	0.000	0.000	0.000	0.000	0.000	0.000
BN-s	-251.945	-251.744	-251.463	-251.124	-250.756	-250.375	-249.998	-249.646	-249.328	-249.068	-248.855	-248.687	-248.553	-248.453	-248.382	-248.336	-248.319	-270.877

Table A.4: Species standard entropy values (J/mol-K) used in BN thermodynamic analysis[110]

	800 K	900 K	1000 K	1100 K	1200 K	1300 K	1400 K	1500 K	1600 K	1700 K	1800 K	1900 K	2000 K	2100 K	2200 K	2300 K	2400 K	2500 K
H	-135.217	-137.666	-139.856	-141.840	-143.649	-145.315	-146.856	-148.292	-149.632	-150.896	-152.085	-153.207	-154.275	-155.288	-156.260	-157.181	-158.068	-158.918
H2	-159.546	-163.059	-166.224	-169.121	-171.797	-174.288	-176.628	-178.843	-180.941	-182.942	-184.847	-186.672	-188.423	-190.106	-191.726	-193.288	-194.799	-196.256
NH	-210.294	-213.882	-217.148	-220.154	-222.947	-225.559	-228.009	-230.324	-232.518	-234.599	-236.583	-238.476	-240.289	-242.026	-243.697	-245.300	-246.849	-248.340
NH2	-229.997	-234.762	-239.179	-243.303	-247.184	-250.848	-254.323	-257.626	-260.770	-263.772	-266.649	-269.399	-272.037	-274.574	-277.015	-279.364	-281.633	-283.819
NH3	-234.402	-240.590	-246.397	-251.882	-257.086	-262.043	-266.774	-271.296	-275.629	-279.783	-283.764	-287.587	-291.259	-294.796	-298.213	-301.512	-304.702	-307.796
N2H2	-263.617	-270.467	-276.877	-282.902	-288.579	-293.951	-299.038	-303.869	-308.470	-312.858	-317.049	-321.056	-324.899	-328.584	-332.126	-335.534	-338.821	-341.986
N2H4	-307.424	-318.071	-328.027	-337.384	-346.206	-354.559	-362.489	-370.029	-377.218	-384.084	-390.649	-396.942	-402.979	-408.778	-414.359	-419.730	-424.914	-429.917
N	-173.827	-176.277	-178.471	-180.451	-182.260	-183.926	-185.467	-186.903	-188.247	-189.507	-190.696	-191.818	-192.886	-193.903	-194.870	-195.795	-196.683	-197.533
N2	-221.054	-224.797	-228.210	-231.354	-234.272	-236.989	-239.535	-241.930	-244.191	-246.330	-248.361	-250.295	-252.137	-253.896	-255.583	-257.199	-258.752	-260.247
BH	-201.456	-205.245	-208.703	-211.898	-214.858	-217.621	-220.213	-222.654	-224.961	-227.146	-229.219	-231.199	-233.083	-234.892	-236.621	-238.283	-114.274	-241.419
BH2	-219.736	-225.329	-230.512	-235.340	-239.857	-244.103	-248.105	-251.894	-255.482	-258.890	-262.139	-265.238	-268.202	-271.036	-273.758	-276.370	-278.882	-281.307
BH3	-229.947	-236.303	-242.307	-248.001	-253.410	-258.560	-263.467	-268.147	-272.623	-276.906	-281.005	-284.937	-288.713	-292.343	-295.835	-299.197	-302.441	-305.577
B2H6	-320.206	-335.019	-349.045	-362.329	-374.915	-386.856	-398.189	-408.962	-419.224	-429.004	-438.345	-447.279	-455.837	-464.043	-471.923	-479.501	-486.799	-493.832
B3N3H6	-434.623	-458.492	-480.862	-501.879	-521.670	-540.356	-558.037	-574.801	-590.736	-605.905	-620.378	-634.203	-647.442	-660.128	-672.311	-684.022	-695.293	-706.162
B	-173.978	-176.427	-178.621	-180.602	-182.414	-184.077	-185.622	-187.053	-188.397	-189.658	-190.847	-191.973	-193.041	-194.054	-195.021	-195.946	-196.830	-197.680
B2	-234.691	-238.919	-242.742	-246.230	-249.432	-252.397	-255.152	-257.727	-260.146	-262.424	-264.580	-266.623	-268.566	-270.417	-272.188	-273.879	-275.504	-277.065
BN	-243.391	-247.435	-251.107	-254.478	-257.584	-260.469	-263.157	-265.681	-268.051	-270.291	-272.418	-274.436	-276.358	-278.196	-279.958	-281.646	-283.270	-284.836
B-s	-23.630	-26.419	-29.002	-31.409	-33.666	-35.789	-37.798	-39.703	-41.525	-43.262	-44.924	-46.515	-48.039	-49.500	-50.903	-52.251	-53.553	-64.012
BN-s	-44.975	-49.869	-54.453	-58.753	-62.789	-66.578	-70.137	-73.487	-76.639	-79.608	-82.409	-85.055	-87.567	-89.957	-92.239	-94.416	-96.501	-98.499

APPENDIX B

COMPUTER SOURCE CODE LISTINGS

B.1 MATLAB Code for Converting a Thermal Image to a Temperature Map

```
% temp_profile.m
% Used to compute temperature profiles of 24bit *.bmp files
% containing thermal images
% author:  Ryan W. Johnson

clear all;
close all;

% read in temp scale info
scale = dlmread('r1z4_5_data.txt', '\t');----------% read in scale file
Tmin = scale(length(scale),1);-->----------% extract Tmin↓
→      from end of file
Tmax = scale(length(scale),2);-->----------% extract Tmax↓
→      from end of file
scale = scale(1:length(scale)-1,:);----------% redefine ↓
→      scale w/o Tmin and Tmax

% import image file for temp calculation
[Imageint,map] = imread('8bit.bmp');
Imagenorm = ind2rgb(Imageint,map);----------% converts ↓
→      indexed 8 bit bmp to true color 24 bit
-------->----------↓
→      ---------->----------% with NORMALIZED ↓
→      values between 0 and 1 for each
-------->----------↓
→      ---------->----------% color channel

Image = Imagenorm*255;
[rows columns depth] = size(Image);

for i = 1:rows
   for j = 1:columns
      Redres = abs(Image(i,j,1)-scale(:,1));
%      Normredres = Redres/max(Redres);
      Greenres = abs(Image(i,j,2)-scale(:,2));
%      Normgreenres = Greenres/max(Greenres);
      Blueres = abs(Image(i,j,3)-scale(:,3));
%      Normblueres = Blueres/max(Blueres);
%      Score = 1/3*(Normredres + Normgreenres + Normblueres);
```

```
        Score = (Redres.^2 + Greenres.^2 + Blueres.^2);
        [Low_score Place] = min(Score);
        temp(i,j) = (length(Score)-Place)/length(Score)*(Tmax-Tmin)+↓
→           Tmin;
        if temp(i,j) > 2150
           temp(i,j) = Tmin;
        end
    end
end

%dlmwrite('L242_2crop_profile.txt', temp, ' ');

% get location and value of maximum temperature
% [rowvec rowpos] = max(temp);
% [maxT colpos] = max(rowvec);



% convert pixel number to microns
[pixelh pixelw] = size(temp);
rowpos = 400; % only set rowpos when Tmax is not unique
colpos = 300; % only set colpos when Tmax is not unique
r = 3.5*((1:pixelw)-colpos);


%%%%%%%%%%%%%%%%
% plot profile %
%%%%%%%%%%%%%%%%

% temp profile
%subplot(2,1,1)
figure(1)
plot(r,temp(rowpos,:));
title('Temp␣Profile␣for␣Line␣L231-11')
xlabel('Position␣(10^-6␣m)')
ylabel('Temp␣(deg␣C)')
axis([-200 200 Tmin-100 Tmax+100]);

figure(2)
mesh(temp);
colorbar;
```

B.2 Computation of Fiber Growth Rate from Series of Images

```
% temp_profile_plus_rate.m
% Used to convert thermal images (640x480 8 bit bmps) to temperatures
% and to compute the growth rate of the fiber between images
% author:  Ryan W. Johnson
% date:  08 March 2004

clear all;
close all;

% read in temp scale info
Tmin = 955;
Tmax = 1255;

% read in list of files in directory
numimages = 8;→→→→→→→→% total number of images to be used in calculation
numtoaverage = 10;→→→→→→→% number of temperatures on row of max temp to average
filenamelength = 14;
fid = fopen('filelisting.txt','r');
infilenames = fscanf(fid,'%s',numimages);

for image=1:numimages

    % import image file for temp calculation
    [Imageint,map] = imread(infilenames(((image-1)*filenamelength+1)↓
→       :image*filenamelength));
    Image = double(Imageint);

    % convert the 8 bit value in each pixel to a temp through linear interpolation
    temp = (Image/255)*(Tmax-Tmin)+Tmin;

    % make an pixel border around the image with temp = Tmin
    [pixelh pixelw] = size(temp);
    borderwidth = 10;
    temp(1:borderwidth,:) = Tmin;
    temp(pixelw-borderwidth:pixelw,:) = Tmin;
    temp(:,1:borderwidth,:) = Tmin;
    temp(:,pixelh-borderwidth:pixelh) = Tmin;

    % write out a file with the temperature data
    outfilename = sprintf('%s%s',infilenames(((image-1)*↓
→       filenamelength+1):image*filenamelength-4),'.txt');
    %dlmwrite(outfilename, temp, '\t');

    % seed the maxrow matrix with time values from the file names %
    maxrow(image,1) = str2num(infilenames(((image-1)*filenamelength↓
→       +1):image*filenamelength-4));

    % find the row in the image where the most number of maximum temperatures occur
    edges = [0 max(max(temp))];  →→→→→→→→% take values of only maxtemp
```

```
        % edges = [max(max(temp))-20 max(max(temp))];----------->% take values of anything↓
→           between maxtemp-20 and maxtemp
 48     colbins = histc(temp,edges);
        [maxcol(image,2) maxcol(image,1)] = max(colbins(2,:));
 50     rowbins = histc(temp',edges);
        [maxrow(image,3) maxrow(image,2)] = max(rowbins(2,:));

        % add the highest temperature value to the maxrow matrix
        maxrow(image,4) = max(max(temp));
 55
        % add the average of the top numtoaverage values to the maxrow matrix
        sorttempsinrow = sort(temp(maxrow(image,2),:));
        shorttemps = sorttempsinrow(length(sorttempsinrow)-numtoaverage:↓
→           length(sorttempsinrow));
        maxrow(image,5) = mean(shorttemps);
 60
        %%%%%%%%%%%%%%%%%
        % plot profiles %
        %%%%%%%%%%%%%%%%%

 65     % convert pixel number to microns
        rowpos = maxrow(image,2); % only set rowpos when Tmax is not unique
        colpos = maxcol(image,1); % only set colpos when Tmax is not unique
        r = 3.5*((1:pixelw)-colpos);

 70     % temp profile
        %subplot(2,1,1)
        figure(image)
        plot(r,temp(rowpos,:));
        title(outfilename)
 75     xlabel('Position␣(\mum)')
        ylabel('Temp␣(\circC)')
        axis([-300 300 Tmin-100 Tmax+100]);

    end
 80
    fclose(fid);

    maxrow;
    maxrowtrans = [maxrow(:,1)-maxrow(1,1) (3.5/cos(pi/4))*(maxrow(:,2)↓
→       -min(maxrow(:,2))) maxrow(:,3)];
 85 maxrowflip = [maxrowtrans(:,1) -(maxrowtrans(:,2)-maxrowtrans(1,2))↓
→         maxrowtrans(:,3)];

    %%%%%%%%
    % plot %
    %%%%%%%%
 90
    % plot height vs. time
    figure(image+1)
    plot(maxrowflip(:,1)/1000,maxrowflip(:,2),'x-');
    title('Fiber␣Height␣per␣Thermal␣Image')
 95 xlabel('Time␣(s)')
    ylabel('Fiber␣Height␣(\mum)')
```

```
% plot temp vs. time
figure(image+2)
plot(maxrowflip(:,1)/1000,maxrow(:,4));
title('Maximum Temp per Thermal Image')
xlabel('Time (s)')
ylabel('Temp (\circC)')
axis([min(maxrowflip(:,1)/1000) max(maxrowflip(:,1)/1000) Tmin-100 ↓
→    Tmax+100])
hold
%figure(image+3)
plot(maxrowflip(:,1)/1000,maxrow(:,5));
avetitle = sprintf('%s%i%s','Average of Top ',numtoaverage,' Temps ↓
→    in Row per Thermal Image');
title(avetitle)
xlabel('Time (s)')
ylabel('Temp (\circC)')
axis([min(maxrowflip(:,1)/1000) max(maxrowflip(:,1)/1000) Tmin-100 ↓
→    Tmax+100])


deltaheight = maxrowflip(image,2)-maxrowflip(1,2)
deltatime = maxrowflip(image,1)/1000 - maxrowflip(1,1)/1000
avgtemp = mean(maxrow(:,5))
stdtemp = std(maxrow(:,5))
```

B.3 C Source Code for FLUENT Laser Power Input UDF

```
/*************************************/*
/* udf for laser spot enery distribution /*
/*************************************/*

#include "udf.h"
#define PI 3.141592654
#define RO 0.0001
#define P_LASER 44
#define REFLECT 0.4
#define REFTEMP 300
#define SURF_DEPTH 0.000000911270983213429256594724220623 5
#define SIGMA 0.0000000567
#define EMIS 0.90

DEFINE_SOURCE(laserspot_profile, cell, thread, dS, eqn)
{
    real c[ND_ND], x, y, z, r, source, radiation, temp, laser;

    C_CENTROID(c, cell, thread);
    x = c[0];
    y = c[1];
    z = c[2];
    r = sqrt(x*x + y*y);

    if (r > 10*RO || z < (-1*SURF_DEPTH))
    {
        source = 0;
    }
    else
    {
        laser = (2*P_LASER*(1-REFLECT))/(SURF_DEPTH*(PI*RO*↓
→       RO))*exp((-2*r*r)/(RO*RO));
        temp = C_T(cell, thread);
        radiation = EMIS*SIGMA*(temp*temp*temp*temp - ↓
→       REFTEMP*REFTEMP*REFTEMP*REFTEMP)/SURF_DEPTH;
        /* divide by SURF_DEPTH to get W/m^3 */
        source = laser - radiation;
    }

    dS[eqn]=0;

    return source;
}
```

B.4 ANSYS APDL Listing for Thermal Model

```
FINISH
/CLEAR
/PREP7

! DEFINE GENERAL VARIABLES

SHORT = 1          ! 0=TALL,1=SHORT

! DEFINE ELEMENT
ET,1,PLANE77
KEYOPT,1,3,1    ! AXISYMMETRIC

! SET MESH DIMENSION PARAMETERS
FIBRAD = 0.0002
FIBHGHT = 0.0008
SUBTHCK = 0.00254
SUBRAD = 0.009525
MINMESH = 0.00001
ANGDIV = FIBRAD/MINMESH
SCALE1 = 5
SCALE2 = 10

! NEW MATERIAL PARAMETERS
NEWHGHT = 0.0002          ! ADD THIS MUCH MATERIAL

! DEFINE GEOMETRY
NUMDIV = 10
BLC4,0,0,FIBRAD,SUBTHCK
BLC4,FIBRAD,0,SUBRAD–FIBRAD,SUBTHCK

NUMSTR,AREA,50
*DO,DIVNO,0,NUMDIV–1,1
BLC4,DIVNO*FIBRAD/NUMDIV,SUBTHCK,FIBRAD/NUMDIV,FIBHGHT+FIBRAD+2*NEWHGHT
*ENDDO

K,99,0,SUBTHCK+FIBHGHT,0
CIRCLE,99,FIBRAD,,,90
CIRCLE,99,FIBRAD–2*MINMESH,,,90
L,49,51
L,51,99

ASEL,S,AREA,,50,50+NUMDIV–2,1    ! SELECT FIRST 9 MATERIAL STRIPS
ASBL,ALL,50                      ! BREAK MATERIAL STRIPS OVER INNER ↓
→ RADIUS R1
ASEL,S,AREA,,50+NUMDIV–1         ! SELECT LAST MATERIAL STRIP
ASBL,ALL,51                      ! BREAK LAST STRIP OVER INNER RADIUS R1
ASEL,S,LOC,Y,SUBTHCK+FIBHGHT+FIBRAD,SUBTHCK+FIBHGHT+2*FIBRAD
ASBL,ALL,49                      ! BREAK ALL UPPER STRIPS OVER OUTER ↓
→ RADIUS R2
ASEL,S,LOC,Y,SUBTHCK+.99*(FIBHGHT/2),SUBTHCK+1.01*(FIBHGHT+FIBRAD)/2
ASBL,ALL,52
```

```
ALLSEL
BTOL,0.10E-05
AADD,51,52,89
BTOL,0.10E-04

NUMCMP,ALL

! ADDITIONAL AREA REQUIRED BY NEW MATERIAL
K,1000,0,SUBTHCK+FIBHGHT+NEWHGHT,0
NUMSTR,LINE,999
CIRCLE,1000,FIBRAD,,,90
ASEL,S,LOC,Y,SUBTHCK+FIBHGHT+FIBRAD,SUBTHCK+FIBHGHT+2*FIBRAD
NUMSTR,AREA,500
ASBL,ALL,999      ! SUBTRACTS LINES FROM AREAS
AADD,519,502      ! ADDS TWO AREAS TO CREATE SINGLE AREA
ASEL,S,LOC,Y,SUBTHCK+FIBHGHT+FIBRAD+NEWHGHT,SUBTHCK+FIBHGHT+FIBRAD+2*↓
→ NEWHGHT
!ASEL,A,LOC,X,FIBRAD-2*MINMESH,FIBRAD
! NEXT LINE IS THE PROBLEM
!ASEL,R,LOC,Y,SUBTHCK+FIBHGHT+FIBRAD-0.5*NEWHGHT,SUBTHCK+FIBHGHT+2*↓
→ FIBRAD
ADELE,ALL,,,1

ALLSEL
BTOL,0.10E-06
AGLUE,ALL
BTOL,0.10E-04
NUMCMP,ALL

! DELETE EXTRA GROWTH
*IF,SHORT,EQ,1,THEN
ASEL,S,AREA,,9
ASEL,A,AREA,,30,37
ADELE,ALL,,,1
*ENDIF

! DEFINE MATERIAL PROPERTIES

! MATERIAL PROPERTIES FOR PYROLYTIC GRAPHITE
*DO,MATNUM,1,NUMDIV
THETA = ACOS((FIBRAD-MATNUM*(FIBRAD/NUMDIV)+(FIBRAD/NUMDIV)/2)/FIBRAD)
MAID = MATNUM

KXX1=0.2E+04
KXX2=0.169E+04
KXX3=0.1460E+04
KXX4=0.113E+04
KXX5=0.930E+03
KXX6=0.79E+03
KXX7=0.68E+03
KXX8=0.6E+03
KXX9=0.53E+03
```

```
KXX10=0.48E+03
KXX11=0.44E+03
KXX12=0.4E+03
KXX13=0.37E+03
KXX14=0.34E+03
KXX15=0.32E+03
KXX16=0.3E+03
KXX17=0.28E+03
KXX18=0.26E+03
KXX19=0.25E+03

KYY1=0.95E+01
KYY2=0.8E+01
KYY3=0.7E+01
KYY4=0.54E+01
KYY5=0.44E+01
KYY6=0.38E+01
KYY7=0.32E+01
KYY8=0.28E+01
KYY9=0.25E+01
KYY10=0.23E+01
KYY11=0.21E+01
KYY12=0.19E+01
KYY13=0.17E+01
KYY14=0.16E+01
KYY15=0.15E+01
KYY16=0.14E+01
KYY17=0.13E+01
KYY18=0.125E+01
KYY19=0.12E+01

KXX1PRIM=SQRT((KYY1*COS(THETA))**2+(KXX1*SIN(THETA))**2)
KXX2PRIM=SQRT((KYY2*COS(THETA))**2+(KXX2*SIN(THETA))**2)
KXX3PRIM=SQRT((KYY3*COS(THETA))**2+(KXX3*SIN(THETA))**2)
KXX4PRIM=SQRT((KYY4*COS(THETA))**2+(KXX4*SIN(THETA))**2)
KXX5PRIM=SQRT((KYY5*COS(THETA))**2+(KXX5*SIN(THETA))**2)
KXX6PRIM=SQRT((KYY6*COS(THETA))**2+(KXX6*SIN(THETA))**2)
KXX7PRIM=SQRT((KYY7*COS(THETA))**2+(KXX7*SIN(THETA))**2)
KXX8PRIM=SQRT((KYY8*COS(THETA))**2+(KXX8*SIN(THETA))**2)
KXX9PRIM=SQRT((KYY9*COS(THETA))**2+(KXX9*SIN(THETA))**2)
KXX10PRIM=SQRT((KYY10*COS(THETA))**2+(KXX10*SIN(THETA))**2)
KXX11PRIM=SQRT((KYY11*COS(THETA))**2+(KXX11*SIN(THETA))**2)
KXX12PRIM=SQRT((KYY12*COS(THETA))**2+(KXX12*SIN(THETA))**2)
KXX13PRIM=SQRT((KYY13*COS(THETA))**2+(KXX13*SIN(THETA))**2)
KXX14PRIM=SQRT((KYY14*COS(THETA))**2+(KXX14*SIN(THETA))**2)
KXX15PRIM=SQRT((KYY15*COS(THETA))**2+(KXX15*SIN(THETA))**2)
KXX16PRIM=SQRT((KYY16*COS(THETA))**2+(KXX16*SIN(THETA))**2)
KXX17PRIM=SQRT((KYY17*COS(THETA))**2+(KXX17*SIN(THETA))**2)
KXX18PRIM=SQRT((KYY18*COS(THETA))**2+(KXX18*SIN(THETA))**2)
KXX19PRIM=SQRT((KYY19*COS(THETA))**2+(KXX19*SIN(THETA))**2)

KYY1PRIM=SQRT((KYY1*SIN(THETA))**2+(KXX1*COS(THETA))**2)
KYY2PRIM=SQRT((KYY2*SIN(THETA))**2+(KXX2*COS(THETA))**2)
KYY3PRIM=SQRT((KYY3*SIN(THETA))**2+(KXX3*COS(THETA))**2)
```

```
KYY4PRIM=SQRT((KYY4*SIN(THETA))**2+(KXX4*COS(THETA))**2)
KYY5PRIM=SQRT((KYY5*SIN(THETA))**2+(KXX5*COS(THETA))**2)
KYY6PRIM=SQRT((KYY6*SIN(THETA))**2+(KXX6*COS(THETA))**2)
KYY7PRIM=SQRT((KYY7*SIN(THETA))**2+(KXX7*COS(THETA))**2)
KYY8PRIM=SQRT((KYY8*SIN(THETA))**2+(KXX8*COS(THETA))**2)
KYY9PRIM=SQRT((KYY9*SIN(THETA))**2+(KXX9*COS(THETA))**2)
KYY10PRIM=SQRT((KYY10*SIN(THETA))**2+(KXX10*COS(THETA))**2)
KYY11PRIM=SQRT((KYY11*SIN(THETA))**2+(KXX11*COS(THETA))**2)
KYY12PRIM=SQRT((KYY12*SIN(THETA))**2+(KXX12*COS(THETA))**2)
KYY13PRIM=SQRT((KYY13*SIN(THETA))**2+(KXX13*COS(THETA))**2)
KYY14PRIM=SQRT((KYY14*SIN(THETA))**2+(KXX14*COS(THETA))**2)
KYY15PRIM=SQRT((KYY15*SIN(THETA))**2+(KXX15*COS(THETA))**2)
KYY16PRIM=SQRT((KYY16*SIN(THETA))**2+(KXX16*COS(THETA))**2)
KYY17PRIM=SQRT((KYY17*SIN(THETA))**2+(KXX17*COS(THETA))**2)
KYY18PRIM=SQRT((KYY18*SIN(THETA))**2+(KXX18*COS(THETA))**2)
KYY19PRIM=SQRT((KYY19*SIN(THETA))**2+(KXX19*COS(THETA))**2)

MPTEMP
MPTEMP,      1, 0.0000000E+00,
MPDATA,DENS,       MAID,    1, 0.1760000E+04,
MPTEMP
MPTEMP,      1, 0.3E+03, 0.35E+03, 0.4E+03, 0.5E+03, 0.6E+03
MPTEMP,      6, 0.7E+03, 0.8E+03, 0.9E+03, 0.1E+04, 0.11E+04
MPTEMP,      11, 0.12E+04, 0.13E+04, 0.14E+04, 0.15E+04, 0.16E+04
MPTEMP,      16, 0.17E+04, 0.18E+04, 0.19E+04, 0.20E+04
MPDATA,KXX  ,       MAID,    1, KXX1PRIM,KXX2PRIM,KXX3PRIM,KXX4PRIM,↓
→ KXX5PRIM
MPDATA,KXX  ,       MAID,    6, KXX6PRIM,KXX7PRIM,KXX8PRIM,KXX9PRIM,↓
→ KXX10PRIM
MPDATA,KXX  ,       MAID,    11, KXX11PRIM,KXX12PRIM,KXX13PRIM,KXX14PRIM,↓
→ KXX15PRIM
MPDATA,KXX  ,       MAID,    16, KXX16PRIM,KXX17PRIM,KXX18PRIM,KXX19PRIM

MPDATA,KXX  ,       MAID,    1, KXX1PRIM,KXX2PRIM,KXX3PRIM,KXX4PRIM,↓
→ KXX5PRIM
MPDATA,KXX  ,       MAID,    6, KXX6PRIM,KXX7PRIM,KXX8PRIM,KXX9PRIM,↓
→ KXX10PRIM
MPDATA,KXX  ,       MAID,    11, KXX11PRIM,KXX12PRIM,KXX13PRIM,KXX14PRIM,↓
→ KXX15PRIM
MPDATA,KXX  ,       MAID,    16, KXX16PRIM,KXX17PRIM,KXX18PRIM,KXX19PRIM
MPTEMP
MPTEMP,      1, 0.3E+03, 0.35E+03, 0.4E+03, 0.5E+03, 0.6E+03
MPTEMP,      6, 0.7E+03, 0.8E+03, 0.9E+03, 0.1E+04, 0.11E+04
MPTEMP,      11, 0.12E+04, 0.13E+04, 0.14E+04, 0.15E+04, 0.16E+04
MPTEMP,      16, 0.17E+04, 0.18E+04, 0.19E+04, 0.20E+04
MPDATA,KYY  ,       MAID,    1, KYY1PRIM,KYY2PRIM,KYY3PRIM,KYY4PRIM,↓
→ KYY5PRIM
MPDATA,KYY  ,       MAID,    6, KYY6PRIM,KYY7PRIM,KYY8PRIM,KYY9PRIM,↓
→ KYY10PRIM
MPDATA,KYY  ,       MAID,    11, KYY11PRIM,KYY12PRIM,KYY13PRIM,KYY14PRIM,↓
→ KYY15PRIM
MPDATA,KYY  ,       MAID,    16, KYY16PRIM,KYY17PRIM,KYY18PRIM,KYY19PRIM
```

```
MPTEMP
MPTEMP,      1, 0.3E+03, 0.35E+03, 0.4E+03, 0.5E+03, 0.6E+03
MPTEMP,      6, 0.7E+03, 0.8E+03, 0.9E+03, 0.1E+04, 0.11E+04
MPTEMP,      11, 0.12E+04, 0.13E+04, 0.14E+04, 0.15E+04, 0.16E+04
MPTEMP,      16, 0.17E+04, 0.18E+04, 0.19E+04, 0.20E+04
MPDATA,KZZ  ,        MAID,    1, KXX1PRIM,KXX2PRIM,KXX3PRIM,KXX4PRIM,↓
→  KXX5PRIM
MPDATA,KZZ  ,        MAID,    6, KXX6PRIM,KXX7PRIM,KXX8PRIM,KXX9PRIM,↓
→  KXX10PRIM
MPDATA,KZZ  ,        MAID,    11, KXX11PRIM,KXX12PRIM,KXX13PRIM,KXX14PRIM,↓
→  KXX15PRIM
MPDATA,KZZ  ,        MAID,    16, KXX16PRIM,KXX17PRIM,KXX18PRIM,KXX19PRIM
MPTEMP
MPTEMP,      1, 0.1E+03, 0.2E+03, 0.4E+03, 0.6E+03, 0.8E+03
MPTEMP,      6, 0.1E+04, 0.12E+04, 0.15E+04, 0.2E+04,
MPDATA,C    ,        MAID,    1, 0.1360000E+03, 0.4110000E+03, 0.9920000E↓
→  +03, 0.1406000E+04, 0.1650000E+04
MPDATA,C    ,        MAID,    6, 0.1793000E+04, 0.1890000E+04, 0.1974000E↓
→  +04, 0.2043000E+04,
*ENDDO

! MATERIAL PROPERTIES FOR ATJ CARBON
MAID = 11
MPTEMP,      1, 0.0000000E+00,
MPDATA,EX   ,        MAID,    1, 0.1000000E+11,
MPTEMP
MPTEMP,      1, 0.0000000E+00,
MPDATA,NUXY,         MAID,    1, 0.1400000E−01,
MPTEMP
MPTEMP,      1, 0.373E+03, 0.773E+03, 0.1773E+04, 0.1973E+04, 0.2223E+04
MPTEMP,      6, 0.2523E+04, 0.2773E+04,
MPDATA,ALPX,         MAID,    1, 0.0000000E+00, 0.1200000E−02, 0.5000000E↓
→  −02, 0.5800000E−02, 0.7000000E−02
MPDATA,ALPX,         MAID,    6, 0.8600000E−02, 0.1020000E−01,
MPTEMP
MPTEMP,      1, 0.0000000E+00,
MPDATA,DENS,         MAID,    1, 0.2210000E+04,
MPTEMP
MPTEMP,      1, 0.1000000E+03, 0.2000000E+03, 0.3000000E+03, 0.4000000E↓
→  +03, 0.9000000E+03
MPTEMP,      6, 0.1000000E+04, 0.1300000E+04, 0.1500000E+04, 0.2000000E↓
→  +04,
MPDATA,KXX  ,        MAID,    1, 0.1140000E+03, 0.9500000E+02, 0.8750000E↓
→  +02, 0.8200000E+02, 0.6000000E+02
MPDATA,KXX  ,        MAID,    6, 0.5700000E+02, 0.5000000E+02, 0.4800000E↓
→  +02, 0.4600000E+02,
MPTEMP
MPTEMP,      1, 0.1E+03, 0.2E+03, 0.4E+03, 0.6E+03, 0.8E+03
MPTEMP,      6, 0.1E+04, 0.12E+04, 0.15E+04, 0.2E+04,
MPDATA,C    ,        MAID,    1, 0.1360000E+03, 0.4110000E+03, 0.9920000E↓
→  +03, 0.1406000E+04, 0.1650000E+04
```

```
MPDATA,C     ,          MAID,     6, 0.1793000E+04, 0.1890000E+04, 0.1974000E↓
→  +04, 0.2043000E+04,
MPTEMP
MPTEMP,       1, 0.0000000E+00,
MPDATA,PRXY,          MAID,     1, 0.1400000E-01,

!*****************SET MATERIAL PROPERTIES*********************
/PNUM,AREA,1
/PNUM,LINE,1
ASEL,S,AREA,,8
ASEL,A,AREA,,3
ASEL,A,AREA,,2
*IF,SHORT,EQ,0,THEN
ASEL,A,AREA,,9
*ENDIF
AATT,10
ASEL,S,AREA,,10
ASEL,A,AREA,,24
ASEL,A,AREA,,16
*IF,SHORT,EQ,0,THEN
ASEL,A,AREA,,30
*ENDIF
AATT,9
ASEL,S,AREA,,11
ASEL,A,AREA,,25
ASEL,A,AREA,,17
*IF,SHORT,EQ,0,THEN
ASEL,A,AREA,,31
*ENDIF
AATT,8
ASEL,S,AREA,,12
ASEL,A,AREA,,26
ASEL,A,AREA,,18
*IF,SHORT,EQ,0,THEN
ASEL,A,AREA,,32
*ENDIF
AATT,7
ASEL,S,AREA,,13
ASEL,A,AREA,,27
ASEL,A,AREA,,19
*IF,SHORT,EQ,0,THEN
ASEL,A,AREA,,33
*ENDIF
AATT,6
ASEL,S,AREA,,14
ASEL,A,AREA,,28
ASEL,A,AREA,,20
*IF,SHORT,EQ,0,THEN
ASEL,A,AREA,,34
*ENDIF
AATT,5
ASEL,S,AREA,,15
ASEL,A,AREA,,29
ASEL,A,AREA,,21
```

```
*IF,SHORT,EQ,0,THEN
ASEL,A,AREA,,35
*ENDIF
AATT,4
ASEL,S,AREA,,23
ASEL,A,AREA,,7
ASEL,A,AREA,,22
*IF,SHORT,EQ,0,THEN
ASEL,A,AREA,,36
*ENDIF
AATT,3
ASEL,S,AREA,,5
ASEL,A,AREA,,1
*IF,SHORT,EQ,0,THEN
ASEL,A,AREA,,37
*ENDIF
AATT,2
ASEL,S,AREA,,6
AATT,1

ASEL,S,AREA,,4    ! SET SUBSTRATE TO ATJ GRAPHITE
ASEL,A,AREA,,38
AATT,11
!********************END SET MATERIAL PROPERTIES**********************

! MESH LASER IMPINGING SURFACE AREAS
NUMSTR,NODE,1001
LSEL,S,LINE,,20
LSEL,A,LINE,,8
LSEL,A,LINE,,68,73,5
LSEL,A,LINE,,77,79,2
LSEL,A,LINE,,81,83,2
LSEL,A,LINE,,28,84,84-28
LSEL,A,LINE,,46,82,82-46
LSEL,A,LINE,,76,80,2
LSEL,A,LINE,,67,72,72-67
LSEL,A,LINE,,12
LESIZE,ALL,MINMESH,,,,,,,1
LPLOT
ASEL,S,AREA,,2
ASEL,A,AREA,,16,22
APLOT
MSHAPE,0,2D
MSHKEY,2
AMESH,ALL

! MESH OTHER AREA OF FIBER TIP
LSEL,S,LINE,,30
LSEL,A,LINE,,14
LSEL,A,LINE,,53
LSEL,A,LINE,,55
LSEL,A,LINE,,58,60,2
LSEL,A,LINE,,63,65,2
LSEL,A,LINE,,47
```

```
LESIZE,ALL,MINMESH,,,,,,1
LPLOT
ASEL,S,AREA,,3
ASEL,A,AREA,,24,29
ASEL,A,AREA,,7
APLOT
MSHAPE,0,2D
MSHKEY,2
AMESH,ALL

LSEL,S,LINE,,9,11
LSEL,A,LINE,,6,7
LESIZE,ALL,MINMESH,,,,,,1
LPLOT
ASEL,S,AREA,,1
APLOT
MSHAPE,0,2D
MSHKEY,2
AMESH,ALL

!STARTING HERE MUST FIX LINE NUMBERS

! MESH FIBER BODY
LSEL,S,LOC,Y,SUBTHCK+0.999*(FIBHGHT/2),SUBTHCK+1.001*(FIBHGHT/2)
LSEL,A,LINE,,48
LSEL,A,LINE,,50
LSEL,A,LINE,,54
LSEL,A,LINE,,56
LSEL,A,LINE,,59
LSEL,A,LINE,,61
LSEL,A,LINE,,64
LSEL,A,LINE,,85
LSEL,A,LINE,,42
LSEL,A,LINE,,44
LESIZE,ALL,MINMESH,,,,,,1
ASEL,S,LOC,Y,SUBTHCK+0.999*(FIBHGHT/2),SUBTHCK+1.001*(FIBHGHT/2)
MSHAPE,0,2D
MSHKEY,2
AMESH,ALL

! MESH SUBSTRATE UNDER FIBER
! MESH BOTTOM LINE
!LSEL,S,LINE,,1
!LESIZE,ALL,,,29,,1,,,1
!NUMSTR,LINE,300
!LDIV,1,,,10
!LSEL,S,LINE,,1
!LSEL,A,LINE,,300,305
!LESIZE,ALL,,,3,,1,,,1
!LSEL,S,LINE,,306
!LESIZE,ALL,,,4,,1,,,1
!LSEL,S,LINE,,307,308
!LESIZE,ALL,MINMESH,,,,1,,,1
```

```
! MESH SIDE LINES
LSEL,S,LINE,,3
LESIZE,ALL,(MINMESH+MINMESH*SCALE1)/2,,,SCALE1,,,,1
LSEL,S,LINE,,2
LESIZE,ALL,(MINMESH+MINMESH*SCALE1)/2,,,1/SCALE1,,,,1
MSHAPE,0,2D
MSHKEY,2
ASEL,S,AREA,,38
AMESH,ALL

! MESH OTHER SUBSTRATE
LSEL,S,LINE,,39
LESIZE,ALL,(MINMESH+MINMESH*SCALE2)/2,,,SCALE2,,,,1
LSEL,S,LINE,,40
LESIZE,ALL,(MINMESH+MINMESH*SCALE2)/2,,,SCALE2,,,,1
LSEL,S,LINE,,4
LESIZE,ALL,(MINMESH+MINMESH*SCALE1)/2,,,1/SCALE1,,,,1
MSHAPE,0,2D
MSHKEY,0
ASEL,S,AREA,,4
AMESH,ALL

*IF,SHORT,EQ,0,THEN
NUMSTR,NODE,100001
LSEL,S,LINE,,51
LSEL,A,LINE,,41
LSEL,A,LINE,,86,93
LSEL,A,LINE,,83,84
LSEL,A,LINE,,77,81,2
LSEL,A,LINE,,73
LSEL,A,LINE,,68
LSEL,A,LINE,,8
LESIZE,ALL,MINMESH,,,,,,,1
LPLOT
ASEL,S,AREA,,9
ASEL,A,AREA,,30,36
APLOT
MSHAPE,0,2D
MSHKEY,2
AMESH,ALL

LSEL,S,LINE,,94
LSEL,A,LINE,,74,75
LSEL,A,LINE,,11,38,28-11
LESIZE,ALL,MINMESH,,,,,,,1
LPLOT
ASEL,S,AREA,,37
APLOT
MSHAPE,0,2D
MSHKEY,2
AMESH,ALL
*ENDIF

! INPUT HEAT GENERATION ON FIBER TIP
```

```
*DIM,HEDGE,TABLE,25,1,1,TEMP
*TREAD,HEDGE,HEDGE,TXT,,

*DIM,HTOP,TABLE,25,1,1,TEMP
*TREAD,HTOP,HTOP,TXT,,

*IF,SHORT,EQ,0,THEN

! DEFINE LASER POWER INPUT TABLE
*DIM,LASERT,TABLE,192,1,1,X
*TREAD,LASERT,P219T10VAR,TXT,,

! APPLY LASER POWER TABLE BC
LSEL,S,LINE,,41
LSEL,A,LINE,,86,91
LSEL,A,LINE,,93
LPLOT
BFL,ALL,HGEN,%LASERT%
SFL,ALL,CONV,%HTOP%

! APPLY TOP SUBSTRATE SURFACE CONVECTION
LSEL,S,LINE,,40
SFL,ALL,CONV,%HTOP%

LSEL,S,LINE,,94
LSEL,A,LINE,,74
LSEL,A,LINE,,45
LSEL,A,LINE,,4
SFL,ALL,CONV,%HEDGE%,,,

LSEL,S,LINE,,1              ! APPLY CONVECTION ON BOTTOM EDGE
LSEL,A,LINE,,39
SFL,ALL,CONV,134
ALLSEL
LPLOT

*ELSEIF,SHORT,EQ,1,THEN

! DEFINE LASER POWER INPUT TABLE
*DIM,LASER,TABLE,197,1,1,X
*TREAD,LASER,P21T5VAR,TXT,,

! APPLY LASER POWER TABLE BC
LSEL,S,LINE,,8
LSEL,A,LINE,,68,73,73-68
LSEL,A,LINE,,77,83,2
LSEL,A,LINE,,84
LPLOT
BFL,ALL,HGEN,%LASER%
SFL,ALL,CONV,%HTOP%       ! APPLY FIBER TIP CONVECTION

! APPLY TOP SUBSTRATE SURFACE CONVECTION
LSEL,S,LINE,,40
```

```
SFL,ALL,CONV,%HTOP%

! APPLY EDGE CONVECTION
LSEL,S,LINE,,11
LSEL,A,LINE,,7
LSEL,A,LINE,,45
LSEL,A,LINE,,4
SFL,ALL,CONV,%HEDGE%,,,

LSEL,S,LINE,,1              ! APPLY CONVECTION ON BOTTOM EDGE
LSEL,A,LINE,,39
SFL,ALL,CONV,135                    ! 125 GIVES SUBSTRATE TEMP ~506 K
ALLSEL
LPLOT

*ENDIF

ALLSEL,ALL

/SOLU
ANTYPE,0
TIME,1
AUTOTS,-1
NSUBST,  ,  ,  ,1
KBC,0
TSRES,ERASE
/STATUS,SOLU
SOLVE
FINISH
/POST1
SET,LAST
/EFACE,1
PLNSOL,TEMP,  ,0,

FINISH
```

B.5 MATLAB Code for Converting Fiber Tip Temperature Image to Function of Radial Position

```
% image_to_fib_temp
% Used to convert thermal images (640x480 8 bit bmps) to temperatures
% on the surface of a fiber and plot vs "flat" horizontal direction
% author:  Ryan W. Johnson
% date:  14 October 2004

clear all;
close all;

% specify radius of fiber being considered
R_f = 200;

% read in temp scale info
Tmin = 1495;
Tmax = 2170;

% import image file for temp calculation
[Imageint,map] = imread('L228_3.BMP');
Image = double(Imageint);

% convert the 8 bit value in each pixel to a temp through linear interpolation
temp = (Image/255)*(Tmax-Tmin)+Tmin;
temp = temp+273.15;

% set the row and column to use for Tmax
%maxrow = 245;
maxcol = 255;
% generate column of temps
tempcol = temp(:,maxcol);

% find max temp in column of temps
[maxtemp maxrow] = max(tempcol);

% generate new position column with offset to Tmax x = 0
[numrows numcols] = size(temp);
rowpos = 1:numrows;
shiftrowpos = rowpos - rowpos(maxrow);
redrowpos = shiftrowpos(maxrow:maxrow+80);
redtempcol = tempcol(maxrow:maxrow+80);

% flatten the 45deg angled plane to 0deg plane
x_45 = 3.5*redrowpos*cos(pi/4);
% only valid for 0 <= x <= R_f
x_45 = x_45(1:81);

% adjust x45 vals to account for curvature of fiber tip
x_perp = (-(R_f - 2*x_45) + sqrt(2*R_f^2-(R_f - 2*x_45).^2))/2;

% write out position, temp file for other use
```

```
Tout = [x_perp' redtempcol];
dlmwrite('L228-3-temp-profile.txt',Tout,'\t');


%%%%%%%%%%%%%%%%%%%%%%%%%%%%%%%%%%%%%%%%%%%%%%%%%%%%%%%%%%%%%%%%%%%%%%%%%%%%%%%%%%%%%%%%%%%%%%%%%%%%
% read in fiber tip temp from ANSYS model
fibertempall = dlmread('P18-R0-pyro-theta.txt','\t',1,0);
fibertempsort = sortrows(fibertempall,3);
fibertempx = fibertempsort(:,3);
fibertemp = fibertempsort(:,6);
%%%%%%%%%%%%%%%%%%%%%%%%%%%%%%%%%%%%%%%%%%%%%%%%%%%%%%%%%%%%%%%%%%%%%%%%%%%%%%%%%%%%%%%%%%%%%%%%%%%%


%%%%%%%%%%%%%%%%%%%%%%%%%%%%%%%%%%%%%%%%%%%%%%%%%%%%%%%%%%%%%%%%%%%
% universal gas constant
R = 8.314;          % (Pa*m^3)/(mol*K)

% carbon molecular weight
MW = 12;            % kg/kmol

% laser beam parameters
R_0 = 0.0001;       %m

% conditions
press = 101325;
volfrac = 0.75;
flow = 250;
power = 44;
Ps_CH4 = volfrac*press;     % methane partial pressure in Pa

% kinetic parameters
k0 =  1.2856e08;        % m/s
n = 1.0185;
Q = 3.9911e08;  % J/kmol
%%%%%%%%%%%%%%%%%%%%%%%%%%%%%%%%%%%%%%%%%%%%%%%%%%%%%%%%%%%%%%%%%%%

% compute a deprate for the thermal image tip temp profile using temp-adj conc estimate
Cs_CH4_tip = (Ps_CH4./(R*redtempcol))/1000;     % conc in kmol/m^3
J_image = MW*k0*(Cs_CH4_tip.^n).*exp(-(Q/1000)./(R*redtempcol));
Jvel_image = 1000000*J_image/1760; % convert deprate to um/s
Jout = [x_perp'/R_f Jvel_image/max(Jvel_image)];
dlmwrite('L228-3-dep-profile.txt',Jout,'\t');

% compute a deprate for the ANSYS fiber tip temp profile using temp-adj concentration estimate
Cs_CH4_tip = (Ps_CH4./(R*fibertemp))/1000;      % conc in kmol/m^3
J_model = MW*k0*(Cs_CH4_tip.^n).*exp(-(Q/1000)./(R*fibertemp));
Jvel_model = 1000000*J_model/1760; % convert deprate to um/s
```

```
%%%%%%%%%%%%%%%%%%
% plot profiles %
%%%%%%%%%%%%%%%%%%
fignum = 1;
figure(fignum);
fignum = fignum + 1;
[h1] = plot(x_perp/1000000,redtempcol,'r+-');
set(h1,'Linewidth',1,'Markersize',3);
xlabel('Radial Position (m)','Fontsize',14);
ylabel('Temperature (K)','Fontsize',14);
hold on;
[h2] = plot(fibertempx,fibertemp,'bo:');
set(h2,'Linewidth',1,'Markersize',3);
legend('Measured','Computed')
set(gca,'Fontsize',14);
%axis([0 200 1900 2100])

figure(fignum);
fignum = fignum + 1;
[h1] = plot(x_perp/1000000,redtempcol/max(redtempcol),'r+-');
set(h1,'Linewidth',1,'Markersize',3);
xlabel('Radial Position (m)','Fontsize',14);
ylabel('T/T_{max}','Fontsize',14);
hold on;
[h2] = plot(fibertempx,fibertemp/max(fibertemp),'bo:');
set(h2,'Linewidth',1,'Markersize',3);
legend('Measured','Computed')
set(gca,'Fontsize',14);
%axis([0 200 1900 2100])

figure(fignum)
fignum = fignum + 1;
[h1] = plot(x_perp/1000000,Jvel_image,'r+-');
set(h1,'Linewidth',1,'Markersize',3);
xlabel('Radial Position (m)','Fontsize',14);
ylabel('Deposition Velocity, J_v (\mum/s)','Fontsize',14);
hold on;
[h2] = plot(fibertempx,Jvel_model,'bo:');
set(h2,'Linewidth',1,'Markersize',3);
legend('Measured','Computed')
set(gca,'Fontsize',14);
%axis([0 200 1900 2100])

figure(fignum)
fignum = fignum + 1;
[h1] = plot(x_perp/1000000,Jvel_image/max(Jvel_image),'r+-');
set(h1,'Linewidth',1,'Markersize',3);
xlabel('Radial Position (m)','Fontsize',14);
ylabel('J_v/J_{v,max}','Fontsize',14);
hold on;
[h2] = plot(fibertempx,Jvel_model/max(Jvel_model),'bo:');
set(h2,'Linewidth',1,'Markersize',3);
legend('Measured','Computed')
```

```
    set(gca,'Fontsize',14);
153 %axis([0 200 1900 2100])

155 figure(fignum)
    fignum = fignum + 1;
    [h1] = plot(x_45,x_perp,'r+-');
    set(h1,'Linewidth',1,'Markersize',3);
    %axis([0 200 1900 2100])
```

B.6 ANSYS APDL Listing for Structural Model

```
FINISH
/CLEAR
/PREP7

! DEFINE GENERAL VARIABLES

SHORT = 1          ! 0=TALL,1=SHORT

! DEFINE ELEMENT
ET,1,PLANE82
KEYOPT,1,3,1    ! AXISYMMETRIC

! SET MESH DIMENSION PARAMETERS
FIBRAD = 0.0002
FIBHGHT = 0.0008
SUBTHCK = 0.00254
SUBRAD = 0.009525
MINMESH = 0.00001
ANGDIV = FIBRAD/MINMESH
SCALE1 = 5
SCALE2 = 10

! NEW MATERIAL PARAMETERS
NEWHGHT = 0.0002          ! ADD THIS MUCH MATERIAL

! DEFINE GEOMETRY
NUMDIV = 10
BLC4,0,0,FIBRAD,SUBTHCK
BLC4,FIBRAD,0,SUBRAD–FIBRAD,SUBTHCK

NUMSTR,AREA,50
*DO,DIVNO,0,NUMDIV–1,1
BLC4,DIVNO*FIBRAD/NUMDIV,SUBTHCK,FIBRAD/NUMDIV,FIBHGHT+FIBRAD+2*NEWHGHT
*ENDDO

K,99,0,SUBTHCK+FIBHGHT,0
CIRCLE,99,FIBRAD,,,90
CIRCLE,99,FIBRAD–2*MINMESH,,,90
L,49,51
L,51,99

ASEL,S,AREA,,50,50+NUMDIV–2,1    ! SELECT FIRST 9 MATERIAL STRIPS
ASBL,ALL,50                      ! BREAK MATERIAL STRIPS OVER INNER ↓
→ RADIUS R1
ASEL,S,AREA,,50+NUMDIV–1         ! SELECT LAST MATERIAL STRIP
ASBL,ALL,51                      ! BREAK LAST STRIP OVER INNER RADIUS R1
ASEL,S,LOC,Y,SUBTHCK+FIBHGHT+FIBRAD,SUBTHCK+FIBHGHT+2*FIBRAD
ASBL,ALL,49                      ! BREAK ALL UPPER STRIPS OVER OUTER ↓
→ RADIUS R2
ASEL,S,LOC,Y,SUBTHCK+.99*(FIBHGHT/2),SUBTHCK+1.01*(FIBHGHT+FIBRAD)/2
ASBL,ALL,52
```

```
ALLSEL
BTOL,0.10E-05
AADD,51,52,89
BTOL,0.10E-04

NUMCMP,ALL

! ADDITIONAL AREA REQUIRED BY NEW MATERIAL
K,1000,0,SUBTHCK+FIBHGHT+NEWHGHT,0
NUMSTR,LINE,999
CIRCLE,1000,FIBRAD,,,90
ASEL,S,LOC,Y,SUBTHCK+FIBHGHT+FIBRAD,SUBTHCK+FIBHGHT+2*FIBRAD
NUMSTR,AREA,500
ASBL,ALL,999      ! SUBTRACTS LINES FROM AREAS
AADD,519,502      ! ADDS TWO AREAS TO CREATE SINGLE AREA
ASEL,S,LOC,Y,SUBTHCK+FIBHGHT+FIBRAD+NEWHGHT,SUBTHCK+FIBHGHT+FIBRAD+2*↓
→ NEWHGHT
!ASEL,A,LOC,X,FIBRAD-2*MINMESH,FIBRAD
! NEXT LINE IS THE PROBLEM
!ASEL,R,LOC,Y,SUBTHCK+FIBHGHT+FIBRAD-0.5*NEWHGHT,SUBTHCK+FIBHGHT+2*↓
→ FIBRAD
ADELE,ALL,,,1

ALLSEL
BTOL,0.10E-06
AGLUE,ALL
BTOL,0.10E-04
NUMCMP,ALL

! DELETE EXTRA GROWTH
*IF,SHORT,EQ,1,THEN
ASEL,S,AREA,,9
ASEL,A,AREA,,30,37
ADELE,ALL,,,1
*ENDIF

! DEFINE MATERIAL PROPERTIES

! MATERIAL PROPERTIES FOR PYROLYTIC GRAPHITE
*DO,MATNUM,1,NUMDIV
THETA = ACOS((FIBRAD-MATNUM*(FIBRAD/NUMDIV)+(FIBRAD/NUMDIV)/2)/FIBRAD)
MAID = MATNUM

ALPX1=-0.6E-06
ALPX2=-0.3E-06
ALPX3=0.3E-06
ALPX4=0.8E-06
ALPX5=1.4E-06
ALPX6=1.9E-06
ALPX7=2.3E-06
ALPX8=2.7E-06
ALPX9=3.1E-06
```

ALPX10=3.4E−06
ALPX11=3.7E−06
ALPX12=4.0E−06
ALPX13=4.2E−06
ALPX14=4.4E−06
ALPX15=4.6E−06
ALPX16=4.7E−06
ALPX17=4.7E−06

ALPY1=23.1E−06
ALPY2=23.8E−06
ALPY3=24.9E−06
ALPY4=25.9E−06
ALPY5=26.8E−06
ALPY6=27.6E−06
ALPY7=28.3E−06
ALPY8=28.9E−06
ALPY9=29.4E−06
ALPY10=29.8E−06
ALPY11=30.0E−06
ALPY12=30.2E−06
ALPY13=30.3E−06
ALPY14=30.3E−06
ALPY15=30.3E−06
ALPY16=30.3E−06
ALPY17=30.4E−06

KXX1=0.2E+04
KXX2=0.169E+04
KXX3=0.1460E+04
KXX4=0.113E+04
KXX5=0.930E+03
KXX6=0.79E+03
KXX7=0.68E+03
KXX8=0.6E+03
KXX9=0.53E+03
KXX10=0.48E+03
KXX11=0.44E+03
KXX12=0.4E+03
KXX13=0.37E+03
KXX14=0.34E+03
KXX15=0.32E+03
KXX16=0.3E+03
KXX17=0.28E+03
KXX18=0.26E+03
KXX19=0.25E+03

KYY1=0.95E+01
KYY2=0.8E+01
KYY3=0.7E+01
KYY4=0.54E+01
KYY5=0.44E+01
KYY6=0.38E+01
KYY7=0.32E+01

```
KYY8=0.28E+01
KYY9=0.25E+01
KYY10=0.23E+01
KYY11=0.21E+01
KYY12=0.19E+01
KYY13=0.17E+01
KYY14=0.16E+01
KYY15=0.15E+01
KYY16=0.14E+01
KYY17=0.13E+01
KYY18=0.125E+01
KYY19=0.12E+01

ALPX1PRIM=SQRT((ALPY1*COS(THETA))**2+(ALPX1*SIN(THETA))**2)
ALPX2PRIM=SQRT((ALPY2*COS(THETA))**2+(ALPX2*SIN(THETA))**2)
ALPX3PRIM=SQRT((ALPY3*COS(THETA))**2+(ALPX3*SIN(THETA))**2)
ALPX4PRIM=SQRT((ALPY4*COS(THETA))**2+(ALPX4*SIN(THETA))**2)
ALPX5PRIM=SQRT((ALPY5*COS(THETA))**2+(ALPX5*SIN(THETA))**2)
ALPX6PRIM=SQRT((ALPY6*COS(THETA))**2+(ALPX6*SIN(THETA))**2)
ALPX7PRIM=SQRT((ALPY7*COS(THETA))**2+(ALPX7*SIN(THETA))**2)
ALPX8PRIM=SQRT((ALPY8*COS(THETA))**2+(ALPX8*SIN(THETA))**2)
ALPX9PRIM=SQRT((ALPY9*COS(THETA))**2+(ALPX9*SIN(THETA))**2)
ALPX10PRIM=SQRT((ALPY10*COS(THETA))**2+(ALPX10*SIN(THETA))**2)
ALPX11PRIM=SQRT((ALPY11*COS(THETA))**2+(ALPX11*SIN(THETA))**2)
ALPX12PRIM=SQRT((ALPY12*COS(THETA))**2+(ALPX12*SIN(THETA))**2)
ALPX13PRIM=SQRT((ALPY13*COS(THETA))**2+(ALPX13*SIN(THETA))**2)
ALPX14PRIM=SQRT((ALPY14*COS(THETA))**2+(ALPX14*SIN(THETA))**2)
ALPX15PRIM=SQRT((ALPY15*COS(THETA))**2+(ALPX15*SIN(THETA))**2)
ALPX16PRIM=SQRT((ALPY16*COS(THETA))**2+(ALPX16*SIN(THETA))**2)
ALPX17PRIM=SQRT((ALPY17*COS(THETA))**2+(ALPX17*SIN(THETA))**2)

ALPY1PRIM=SQRT((ALPY1*SIN(THETA))**2+(ALPX1*COS(THETA))**2)
ALPY2PRIM=SQRT((ALPY2*SIN(THETA))**2+(ALPX2*COS(THETA))**2)
ALPY3PRIM=SQRT((ALPY3*SIN(THETA))**2+(ALPX3*COS(THETA))**2)
ALPY4PRIM=SQRT((ALPY4*SIN(THETA))**2+(ALPX4*COS(THETA))**2)
ALPY5PRIM=SQRT((ALPY5*SIN(THETA))**2+(ALPX5*COS(THETA))**2)
ALPY6PRIM=SQRT((ALPY6*SIN(THETA))**2+(ALPX6*COS(THETA))**2)
ALPY7PRIM=SQRT((ALPY7*SIN(THETA))**2+(ALPX7*COS(THETA))**2)
ALPY8PRIM=SQRT((ALPY8*SIN(THETA))**2+(ALPX8*COS(THETA))**2)
ALPY9PRIM=SQRT((ALPY9*SIN(THETA))**2+(ALPX9*COS(THETA))**2)
ALPY10PRIM=SQRT((ALPY10*SIN(THETA))**2+(ALPX10*COS(THETA))**2)
ALPY11PRIM=SQRT((ALPY11*SIN(THETA))**2+(ALPX11*COS(THETA))**2)
ALPY12PRIM=SQRT((ALPY12*SIN(THETA))**2+(ALPX12*COS(THETA))**2)
ALPY13PRIM=SQRT((ALPY13*SIN(THETA))**2+(ALPX13*COS(THETA))**2)
ALPY14PRIM=SQRT((ALPY14*SIN(THETA))**2+(ALPX14*COS(THETA))**2)
ALPY15PRIM=SQRT((ALPY15*SIN(THETA))**2+(ALPX15*COS(THETA))**2)
ALPY16PRIM=SQRT((ALPY16*SIN(THETA))**2+(ALPX16*COS(THETA))**2)
ALPY17PRIM=SQRT((ALPY17*SIN(THETA))**2+(ALPX17*COS(THETA))**2)

KXX1PRIM=SQRT((KYY1*COS(THETA))**2+(KXX1*SIN(THETA))**2)
KXX2PRIM=SQRT((KYY2*COS(THETA))**2+(KXX2*SIN(THETA))**2)
KXX3PRIM=SQRT((KYY3*COS(THETA))**2+(KXX3*SIN(THETA))**2)
KXX4PRIM=SQRT((KYY4*COS(THETA))**2+(KXX4*SIN(THETA))**2)
KXX5PRIM=SQRT((KYY5*COS(THETA))**2+(KXX5*SIN(THETA))**2)
```

```
KXX6PRIM=SQRT((KYY6*COS(THETA))**2+(KXX6*SIN(THETA))**2)
KXX7PRIM=SQRT((KYY7*COS(THETA))**2+(KXX7*SIN(THETA))**2)
KXX8PRIM=SQRT((KYY8*COS(THETA))**2+(KXX8*SIN(THETA))**2)
KXX9PRIM=SQRT((KYY9*COS(THETA))**2+(KXX9*SIN(THETA))**2)
KXX10PRIM=SQRT((KYY10*COS(THETA))**2+(KXX10*SIN(THETA))**2)
KXX11PRIM=SQRT((KYY11*COS(THETA))**2+(KXX11*SIN(THETA))**2)
KXX12PRIM=SQRT((KYY12*COS(THETA))**2+(KXX12*SIN(THETA))**2)
KXX13PRIM=SQRT((KYY13*COS(THETA))**2+(KXX13*SIN(THETA))**2)
KXX14PRIM=SQRT((KYY14*COS(THETA))**2+(KXX14*SIN(THETA))**2)
KXX15PRIM=SQRT((KYY15*COS(THETA))**2+(KXX15*SIN(THETA))**2)
KXX16PRIM=SQRT((KYY16*COS(THETA))**2+(KXX16*SIN(THETA))**2)
KXX17PRIM=SQRT((KYY17*COS(THETA))**2+(KXX17*SIN(THETA))**2)
KXX18PRIM=SQRT((KYY18*COS(THETA))**2+(KXX18*SIN(THETA))**2)
KXX19PRIM=SQRT((KYY19*COS(THETA))**2+(KXX19*SIN(THETA))**2)

KYY1PRIM=SQRT((KYY1*SIN(THETA))**2+(KXX1*COS(THETA))**2)
KYY2PRIM=SQRT((KYY2*SIN(THETA))**2+(KXX2*COS(THETA))**2)
KYY3PRIM=SQRT((KYY3*SIN(THETA))**2+(KXX3*COS(THETA))**2)
KYY4PRIM=SQRT((KYY4*SIN(THETA))**2+(KXX4*COS(THETA))**2)
KYY5PRIM=SQRT((KYY5*SIN(THETA))**2+(KXX5*COS(THETA))**2)
KYY6PRIM=SQRT((KYY6*SIN(THETA))**2+(KXX6*COS(THETA))**2)
KYY7PRIM=SQRT((KYY7*SIN(THETA))**2+(KXX7*COS(THETA))**2)
KYY8PRIM=SQRT((KYY8*SIN(THETA))**2+(KXX8*COS(THETA))**2)
KYY9PRIM=SQRT((KYY9*SIN(THETA))**2+(KXX9*COS(THETA))**2)
KYY10PRIM=SQRT((KYY10*SIN(THETA))**2+(KXX10*COS(THETA))**2)
KYY11PRIM=SQRT((KYY11*SIN(THETA))**2+(KXX11*COS(THETA))**2)
KYY12PRIM=SQRT((KYY12*SIN(THETA))**2+(KXX12*COS(THETA))**2)
KYY13PRIM=SQRT((KYY13*SIN(THETA))**2+(KXX13*COS(THETA))**2)
KYY14PRIM=SQRT((KYY14*SIN(THETA))**2+(KXX14*COS(THETA))**2)
KYY15PRIM=SQRT((KYY15*SIN(THETA))**2+(KXX15*COS(THETA))**2)
KYY16PRIM=SQRT((KYY16*SIN(THETA))**2+(KXX16*COS(THETA))**2)
KYY17PRIM=SQRT((KYY17*SIN(THETA))**2+(KXX17*COS(THETA))**2)
KYY18PRIM=SQRT((KYY18*SIN(THETA))**2+(KXX18*COS(THETA))**2)
KYY19PRIM=SQRT((KYY19*SIN(THETA))**2+(KXX19*COS(THETA))**2)

MPTEMP
MPTEMP,      1, 0.0000000E+00,
MPDATA,EX    ,        MAID,    1, 0.3000000E+11,
MPTEMP
MPTEMP,      1, 0.0000000E+00,
MPDATA,NUXY,          MAID,    1, 0.1400000E-01,
MPTEMP
MPTEMP,      1, 293, 400, 600, 800, 1000
MPTEMP,      6, 1200, 1400, 1600, 1800, 2000
MPTEMP,      11, 2200, 2400, 2600, 2800, 3000
MPTEMP,      16, 3200, 3300
MPDATA,ALPX,          MAID,    1, ALPX1PRIM,ALPX2PRIM,ALPX3PRIM,ALPX4PRIM,↓
→  ALPX5PRIM
MPDATA,ALPX  ,        MAID,    6, ALPX6PRIM,ALPX7PRIM,ALPX8PRIM,ALPX9PRIM,↓
→  ALPX10PRIM
MPDATA,ALPX  ,        MAID,    11, ALPX11PRIM,ALPX12PRIM,ALPX13PRIM,↓
→  ALPX14PRIM,ALPX15PRIM
MPDATA,ALPX  ,        MAID,    16, ALPX16PRIM,ALPX17PRIM
```

```
MPTEMP
MPTEMP,      1, 293, 400, 600, 800, 1000
MPTEMP,      6, 1200, 1400, 1600, 1800, 2000
MPTEMP,      11, 2200, 2400, 2600, 2800, 3000
MPTEMP,      16, 3200, 3300
MPDATA,ALPY,        MAID,    1, ALPY1PRIM,ALPY2PRIM,ALPY3PRIM,ALPY4PRIM,↓
→ ALPY5PRIM
MPDATA,ALPY ,       MAID,    6, ALPY6PRIM,ALPY7PRIM,ALPY8PRIM,ALPY9PRIM,↓
→ ALPY10PRIM
MPDATA,ALPY ,       MAID,    11, ALPY11PRIM,ALPY12PRIM,ALPY13PRIM,↓
→ ALPY14PRIM,ALPY15PRIM
MPDATA,ALPY ,       MAID,    16, ALPY16PRIM,ALPY17PRIM
MPTEMP
MPTEMP,      1, 293, 400, 600, 800, 1000
MPTEMP,      6, 1200, 1400, 1600, 1800, 2000
MPTEMP,      11, 2200, 2400, 2600, 2800, 3000
MPTEMP,      16, 3200, 3300
MPDATA,ALPZ,        MAID,    1, ALPX1PRIM,ALPX2PRIM,ALPX3PRIM,ALPX4PRIM,↓
→ ALPX5PRIM
MPDATA,ALPZ ,       MAID,    6, ALPX6PRIM,ALPX7PRIM,ALPX8PRIM,ALPX9PRIM,↓
→ ALPX10PRIM
MPDATA,ALPZ ,       MAID,    11, ALPX11PRIM,ALPX12PRIM,ALPX13PRIM,↓
→ ALPX14PRIM,ALPX15PRIM
MPDATA,ALPZ ,       MAID,    16, ALPX16PRIM,ALPX17PRIM
MPTEMP
MPTEMP,      1, 0.0000000E+00,
MPDATA,DENS,        MAID,    1, 0.1760000E+04,
MPTEMP
MPTEMP,      1, 0.3E+03, 0.35E+03, 0.4E+03, 0.5E+03, 0.6E+03
MPTEMP,      6, 0.7E+03, 0.8E+03, 0.9E+03, 0.1E+04, 0.11E+04
MPTEMP,      11, 0.12E+04, 0.13E+04, 0.14E+04, 0.15E+04, 0.16E+04
MPTEMP,      16, 0.17E+04, 0.18E+04, 0.19E+04, 0.20E+04
MPDATA,KXX ,        MAID,    1, KXX1PRIM,KXX2PRIM,KXX3PRIM,KXX4PRIM,↓
→ KXX5PRIM
MPDATA,KXX ,        MAID,    6, KXX6PRIM,KXX7PRIM,KXX8PRIM,KXX9PRIM,↓
→ KXX10PRIM
MPDATA,KXX ,        MAID,    11, KXX11PRIM,KXX12PRIM,KXX13PRIM,KXX14PRIM,↓
→ KXX15PRIM
MPDATA,KXX ,        MAID,    16, KXX16PRIM,KXX17PRIM,KXX18PRIM,KXX19PRIM
MPTEMP
MPTEMP,      1, 0.3E+03, 0.35E+03, 0.4E+03, 0.5E+03, 0.6E+03
MPTEMP,      6, 0.7E+03, 0.8E+03, 0.9E+03, 0.1E+04, 0.11E+04
MPTEMP,      11, 0.12E+04, 0.13E+04, 0.14E+04, 0.15E+04, 0.16E+04
MPTEMP,      16, 0.17E+04, 0.18E+04, 0.19E+04, 0.20E+04
MPDATA,KYY ,        MAID,    1, KYY1PRIM,KYY2PRIM,KYY3PRIM,KYY4PRIM,↓
→ KYY5PRIM
MPDATA,KYY ,        MAID,    6, KYY6PRIM,KYY7PRIM,KYY8PRIM,KYY9PRIM,↓
→ KYY10PRIM
MPDATA,KYY ,        MAID,    11, KYY11PRIM,KYY12PRIM,KYY13PRIM,KYY14PRIM,↓
→ KYY15PRIM
MPDATA,KYY ,        MAID,    16, KYY16PRIM,KYY17PRIM,KYY18PRIM,KYY19PRIM
MPTEMP
```

```
MPTEMP,      1, 0.3E+03, 0.35E+03, 0.4E+03, 0.5E+03, 0.6E+03
MPTEMP,      6, 0.7E+03, 0.8E+03, 0.9E+03, 0.1E+04, 0.11E+04
MPTEMP,      11, 0.12E+04, 0.13E+04, 0.14E+04, 0.15E+04, 0.16E+04
MPTEMP,      16, 0.17E+04, 0.18E+04, 0.19E+04, 0.20E+04
MPDATA,KZZ  ,        MAID,    1, KXX1PRIM,KXX2PRIM,KXX3PRIM,KXX4PRIM,↓
→  KXX5PRIM
MPDATA,KZZ  ,        MAID,    6, KXX6PRIM,KXX7PRIM,KXX8PRIM,KXX9PRIM,↓
→  KXX10PRIM
MPDATA,KZZ  ,        MAID,    11, KXX11PRIM,KXX12PRIM,KXX13PRIM,KXX14PRIM,↓
→  KXX15PRIM
MPDATA,KZZ  ,        MAID,    16, KXX16PRIM,KXX17PRIM,KXX18PRIM,KXX19PRIM
MPTEMP
MPTEMP,      1, 0.1E+03, 0.2E+03, 0.4E+03, 0.6E+03, 0.8E+03
MPTEMP,      6, 0.1E+04, 0.12E+04, 0.15E+04, 0.2E+04,
MPDATA,C    ,        MAID,    1, 0.1360000E+03, 0.4110000E+03, 0.9920000E↓
→  +03, 0.1406000E+04, 0.1650000E+04
MPDATA,C    ,        MAID,    6, 0.1793000E+04, 0.1890000E+04, 0.1974000E↓
→  +04, 0.2043000E+04,
MPTEMP
MPTEMP,      1, 0.0000000E+00,
MPDATA,PRXY,         MAID,    1, 0.1400000E−01,
*ENDDO

! SET REFERENCE TEMPS FOR THERMAL EXPANSION
MP,REFT,10,2290
MP,REFT,9,2077
MP,REFT,8,1887
MP,REFT,7,1733
MP,REFT,6,1620
MP,REFT,5,1540
MP,REFT,4,1480
MP,REFT,3,1435
MP,REFT,2,1395
MP,REFT,1,1355

!!!!!!!!!!!!!!!!!!!!!!!!!!!
! USE OF MPAMOD COMMAND??? !
!!!!!!!!!!!!!!!!!!!!!!!!!!!
MPAMOD,10,293
MPAMOD,9,293
MPAMOD,8,293
MPAMOD,7,293
MPAMOD,6,293
MPAMOD,5,293
MPAMOD,4,293
MPAMOD,3,293
MPAMOD,2,293
MPAMOD,1,293

! MATERIAL PROPERTIES FOR ATJ CARBON
MAID = 11
MPTEMP,      1, 0.0000000E+00,
MPDATA,EX   ,        MAID,    1, 0.1000000E+11,
```

```
MPTEMP
MPTEMP,      1, 0.0000000E+00,
MPDATA,NUXY,        MAID,    1, 0.1400000E-01,
MPTEMP
MPTEMP,      1, 0.373E+03
MPDATA,ALPX,        MAID,    1, 0.0000000E+00
MPTEMP
MPTEMP,      1, 0.0000000E+00,
MPDATA,DENS,        MAID,    1, 0.2210000E+04,
MPTEMP
MPTEMP,      1, 0.1000000E+03, 0.2000000E+03, 0.3000000E+03, 0.4000000E↓
→  +03, 0.9000000E+03
MPTEMP,      6, 0.1000000E+04, 0.1300000E+04, 0.1500000E+04, 0.2000000E↓
→  +04,
MPDATA,KXX ,        MAID,    1, 0.1140000E+03, 0.9500000E+02, 0.8750000E↓
→  +02, 0.8200000E+02, 0.6000000E+02
MPDATA,KXX ,        MAID,    6, 0.5700000E+02, 0.5000000E+02, 0.4800000E↓
→  +02, 0.4600000E+02,
MPTEMP
MPTEMP,      1, 0.1E+03, 0.2E+03, 0.4E+03, 0.6E+03, 0.8E+03
MPTEMP,      6, 0.1E+04, 0.12E+04, 0.15E+04, 0.2E+04,
MPDATA,C    ,        MAID,    1, 0.1360000E+03, 0.4110000E+03, 0.9920000E↓
→  +03, 0.1406000E+04, 0.1650000E+04
MPDATA,C    ,        MAID,    6, 0.1793000E+04, 0.1890000E+04, 0.1974000E↓
→  +04, 0.2043000E+04,
MPTEMP
MPTEMP,      1, 0.0000000E+00,
MPDATA,PRXY,        MAID,    1, 0.1400000E-01
MP,REFT,11,525

MPAMOD,11,293

/PNUM,AREA,1
/PNUM,LINE,1
ASEL,S,AREA,,8
ASEL,A,AREA,,3
ASEL,A,AREA,,2
*IF,SHORT,EQ,0,THEN
ASEL,A,AREA,,9
*ENDIF
AATT,10
ASEL,S,AREA,,10
ASEL,A,AREA,,24
ASEL,A,AREA,,16
*IF,SHORT,EQ,0,THEN
ASEL,A,AREA,,30
*ENDIF
AATT,9
ASEL,S,AREA,,11
ASEL,A,AREA,,25
ASEL,A,AREA,,17
*IF,SHORT,EQ,0,THEN
ASEL,A,AREA,,31
```

```
*ENDIF
AATT,8
ASEL,S,AREA,,12
ASEL,A,AREA,,26
ASEL,A,AREA,,18
*IF,SHORT,EQ,0,THEN
ASEL,A,AREA,,32
*ENDIF
AATT,7
ASEL,S,AREA,,13
ASEL,A,AREA,,27
ASEL,A,AREA,,19
*IF,SHORT,EQ,0,THEN
ASEL,A,AREA,,33
*ENDIF
AATT,6
ASEL,S,AREA,,14
ASEL,A,AREA,,28
ASEL,A,AREA,,20
*IF,SHORT,EQ,0,THEN
ASEL,A,AREA,,34
*ENDIF
AATT,5
ASEL,S,AREA,,15
ASEL,A,AREA,,29
ASEL,A,AREA,,21
*IF,SHORT,EQ,0,THEN
ASEL,A,AREA,,35
*ENDIF
AATT,4
ASEL,S,AREA,,23
ASEL,A,AREA,,7
ASEL,A,AREA,,22
*IF,SHORT,EQ,0,THEN
ASEL,A,AREA,,36
*ENDIF
AATT,3
ASEL,S,AREA,,5
ASEL,A,AREA,,1
*IF,SHORT,EQ,0,THEN
ASEL,A,AREA,,37
*ENDIF
AATT,2
ASEL,S,AREA,,6
AATT,1

ASEL,S,AREA,,4    ! SET SUBSTRATE TO ATJ GRAPHITE
ASEL,A,AREA,,38
AATT,11

! MESH LASER IMPINGING SURFACE AREAS
NUMSTR,NODE,1001
LSEL,S,LINE,,20
LSEL,A,LINE,,8
```

```
LSEL,A,LINE,,68,73,5
LSEL,A,LINE,,77,79,2
LSEL,A,LINE,,81,83,2
LSEL,A,LINE,,28,84,84-28
LSEL,A,LINE,,46,82,82-46
LSEL,A,LINE,,76,80,2
LSEL,A,LINE,,67,72,72-67
LSEL,A,LINE,,12
LESIZE,ALL,MINMESH,,,,,,,1
LPLOT
ASEL,S,AREA,,2
ASEL,A,AREA,,16,22
APLOT
MSHAPE,0,2D
MSHKEY,2
AMESH,ALL

! MESH OTHER AREA OF FIBER TIP
LSEL,S,LINE,,30
LSEL,A,LINE,,14
LSEL,A,LINE,,53
LSEL,A,LINE,,55
LSEL,A,LINE,,58,60,2
LSEL,A,LINE,,63,65,2
LSEL,A,LINE,,47
LESIZE,ALL,MINMESH,,,,,,,1
LPLOT
ASEL,S,AREA,,3
ASEL,A,AREA,,24,29
ASEL,A,AREA,,7
APLOT
MSHAPE,0,2D
MSHKEY,2
AMESH,ALL

LSEL,S,LINE,,9,11
LSEL,A,LINE,,6,7
LESIZE,ALL,MINMESH,,,,,,,1
LPLOT
ASEL,S,AREA,,1
APLOT
MSHAPE,0,2D
MSHKEY,2
AMESH,ALL

!STARTING HERE MUST FIX LINE NUMBERS

! MESH FIBER BODY
LSEL,S,LOC,Y,SUBTHCK+0.999*(FIBHGHT/2),SUBTHCK+1.001*(FIBHGHT/2)
LSEL,A,LINE,,48
LSEL,A,LINE,,50
LSEL,A,LINE,,54
LSEL,A,LINE,,56
LSEL,A,LINE,,59
```

```
LSEL,A,LINE,,61
LSEL,A,LINE,,64
LSEL,A,LINE,,85
LSEL,A,LINE,,42
LSEL,A,LINE,,44
LESIZE,ALL,MINMESH,,,,,,,1
ASEL,S,LOC,Y,SUBTHCK+0.999*(FIBHGHT/2),SUBTHCK+1.001*(FIBHGHT/2)
MSHAPE,0,2D
MSHKEY,2
AMESH,ALL

! MESH SUBSTRATE UNDER FIBER
! MESH BOTTOM LINE
!LSEL,S,LINE,,1
!LESIZE,ALL,,,29,,1,,,1
!NUMSTR,LINE,300
!LDIV,1,,,10
!LSEL,S,LINE,,1
!LSEL,A,LINE,,300,305
!LESIZE,ALL,,,3,,1,,,1
!LSEL,S,LINE,,306
!LESIZE,ALL,,,4,,1,,,1
!LSEL,S,LINE,,307,308
!LESIZE,ALL,MINMESH,,,,1,,,1

! MESH SIDE LINES
LSEL,S,LINE,,3
LESIZE,ALL,(MINMESH+MINMESH*SCALE1)/2,,,SCALE1,,,,1
LSEL,S,LINE,,2
LESIZE,ALL,(MINMESH+MINMESH*SCALE1)/2,,,1/SCALE1,,,,1
MSHAPE,0,2D
MSHKEY,2
ASEL,S,AREA,,38
AMESH,ALL

! MESH OTHER SUBSTRATE
LSEL,S,LINE,,39
LESIZE,ALL,(MINMESH+MINMESH*SCALE2)/2,,,SCALE2,,,,1
LSEL,S,LINE,,40
LESIZE,ALL,(MINMESH+MINMESH*SCALE2)/2,,,SCALE2,,,,1
LSEL,S,LINE,,4
LESIZE,ALL,(MINMESH+MINMESH*SCALE1)/2,,,1/SCALE1,,,,1
MSHAPE,0,2D
MSHKEY,0
ASEL,S,AREA,,4
AMESH,ALL

*IF,SHORT,EQ,0,THEN
NUMSTR,NODE,100001
LSEL,S,LINE,,51
LSEL,A,LINE,,41
LSEL,A,LINE,,86,93
LSEL,A,LINE,,83,84
LSEL,A,LINE,,77,81,2
```

```
LSEL,A,LINE,,73
LSEL,A,LINE,,68
LSEL,A,LINE,,8
LESIZE,ALL,MINMESH,,,,,,,1
LPLOT
ASEL,S,AREA,,9
ASEL,A,AREA,,30,36
APLOT
MSHAPE,0,2D
MSHKEY,2
AMESH,ALL

LSEL,S,LINE,,94
LSEL,A,LINE,,74,75
LSEL,A,LINE,,11,38,28-11
LESIZE,ALL,MINMESH,,,,,,,1
LPLOT
ASEL,S,AREA,,37
APLOT
MSHAPE,0,2D
MSHKEY,2
AMESH,ALL
*ENDIF


! SETUP TEMPERATURE LOADS AND SOLVE
ALLSEL,ALL

/SOLU
ANTYPE,0
KBC,0                ! LOADS ARE RAMPED BETWEEN LOAD STEPS

LSEL,S,LINE,,1
LSEL,A,LINE,,3
LSEL,A,LINE,,4
LSEL,A,LINE,,39
LSEL,A,LINE,,40
LSEL,A,LINE,,48
LSEL,A,LINE,,50
LSEL,A,LINE,,54
LSEL,A,LINE,,56
LSEL,A,LINE,,59
LSEL,A,LINE,,61
LSEL,A,LINE,,64
LSEL,A,LINE,,85
LSEL,A,LINE,,42
LSEL,A,LINE,,44

!!!!!!!!!!!!!!!!!!!!
! FIX BODY OF FIBER !
!!!!!!!!!!!!!!!!!!!!

!LSEL,A,LINE,,49
!LSEL,A,LINE,,13
```

```
!LSEL,A,LINE,,15
!LSEL,A,LINE,,16
!LSEL,A,LINE,,17
!LSEL,A,LINE,,18
!LSEL,A,LINE,,19
!LSEL,A,LINE,,29
!LSEL,A,LINE,,43
!LSEL,A,LINE,,5
!LSEL,A,LINE,,45
!LSEL,A,LINE,,14
!LSEL,A,LINE,,53
!LSEL,A,LINE,,55
!LSEL,A,LINE,,58
!LSEL,A,LINE,,60
!LSEL,A,LINE,,63
!LSEL,A,LINE,,65
!LSEL,A,LINE,,47
!LSEL,A,LINE,,6
!LSEL,A,LINE,,10

!!!!!!!!!!!!!!!!!!!
! TOP OF FIBER BCS !
!!!!!!!!!!!!!!!!!!!

!LSEL,A,LINE,,30,37
!LSEL,A,LINE,,9
!LSEL,A,LINE,,12
!LSEL,A,LINE,,67
!LSEL,A,LINE,,72
!LSEL,A,LINE,,76
!LSEL,A,LINE,,78
!LSEL,A,LINE,,80
!LSEL,A,LINE,,82
!LSEL,A,LINE,,46

DL,ALL,,ALL,0

! INPUT TEMPS FROM SHORT FIBER
LDREAD,TEMP,1,1,,,'fiber3t-short','rth',' '

!!!!!!!!!!!!!!!!!!!!!!!!!!!!!!!!!!!!
! SET INITIAL DISPLACEMENT TO ZERO !
!!!!!!!!!!!!!!!!!!!!!!!!!!!!!!!!!!!!
!D,ALL,ALL,0

OUTRES,ALL,LAST
ALLSEL
SOLVE

! INPUT TEMPS FROM TALL FIBER
LDREAD,TEMP,1,1,,,'fiber3t-tall','rth',' '

! SET DISPLACEMENT BCS
```

```
! RESTRICT MOVEMENT OF ALL EDGES INCLUDING FIBER

!DDELE,ALL,ALL,0

!!!!!!!!!!!!!!!!!!!!!!!!!!!!!!
! REMOVE ALL OTHER NODE DOFS !
!!!!!!!!!!!!!!!!!!!!!!!!!!!!!!

OUTRES,ALL,LAST
ALLSEL
SOLVE

/STATUS,SOLU      ! PROVIDES A SOLUTION STATUS SUMMARY
FINISH
```

APPENDIX C

ANOMALOUS MOLYBDENUM FIBER EXPERIMENTS

Molybdenum fiber experiment sets Mo-3F, Mo-4F, and Mo-5F were observed in hindsight to differ significantly from other molybdenum experiments. The change in results was linked to the low pressure experiments of Mo-3F, Samples 1 – 4. The $MoCl_5$ sublimation chamber appeared to become contaminated at the low pressures, and the conditions of the $MoCl_5$ powder in the chamber could no longer be validated. For this reason, the data from these experiments was not used in conjunction with the remaining molybdenum LCVD data. Nonetheless, for documentation purposes, the experimental conditions are given in Table C.1.

It was noteworthy that these experiments produced some very intriguing deposits. Specifically, the quantity of the dark blue–green powder that was ubiquitous in other Mo deposition experiments was significantly reduced. The shape and color of some of the deposits was also very interesting.

An experiment was designed around the best results of Mo-5F to be run after loading the new batch of $MoCl_5$ powder. After configuring the system for this experiment, preheating the substrate, and beginning $MoCl_5$ flow, a thick, dark, blue–green powder quickly covered the substrate surface. This result was inconsistent with the results of Mo-5F, and was more like the results of Experiments Mo-1F and Mo-2F.

Table C.1: Mo-3F, 4F, and 5F experiment conditions

No.	Chamber Press (Torr)	Sub Temp (°C)	Carrier Flow (sccm)	Diluent Flow (sccm)	$MoCl_5$ Flow (sccm)	$MoCl_5$ Conc (mol/m^3)	Max Temp (°C)	Dep Time (min)
1	7.6	85.0	5.0	95.0	0.337	1.14E-03	1200	12.0
2	7.6	85.0	80.0	20.0	5.395	1.74E-02	1200	12.0
3	7.6	85.0	5.0	95.0	0.337	1.14E-03	1000	12.0
4	7.6	85.0	80.0	20.0	5.395	1.74E-02	1000	12.0
5	760	125.0	100.0	0.0	0.611	1.86E-01	1200	12.0
6	760	125.0	6.3	93.7	0.039	1.18E-02	1000	12.0
7	760	125.0	6.3	93.7	0.039	1.18E-02	1200	12.0
8	760	125.0	100.0	0.0	0.611	1.86E-01	1000	12.0
1	760	150.0	100.0	400.0	2.052	1.18E-01	1000	10.0
2	760	150.0	50.0	450.0	1.026	5.90E-02	1000	10.0
3	760	150.0	50.0	450.0	1.026	5.90E-02	1000	10.0
4	760	150.0	100.0	400.0	2.052	1.18E-01	1000	10.0
5	760	150.0	100.0	400.0	2.052	1.18E-01	1200	10.0
6	760	150.0	50.0	450.0	1.026	5.90E-02	1200	10.0
7	760	150.0	100.0	0.0	2.052	5.79E-01	1200	10.0
1	760	150.0	10.0	100.0	0.205	5.36E-02	1000	10.0
2	760	150.0	110.0	0.0	2.258	5.79E-01	1200	10.0
3	760	150.0	110.0	0.0	2.258	5.79E-01	1400	10.0
4	760	150.0	10.0	100.0	0.205	5.36E-02	1400	10.0
5	760	150.0	60.0	50.0	1.231	3.19E-01	1000	10.0
6	760	150.0	60.0	50.0	1.231	3.19E-01	1400	0.0
7	760	150.0	60.0	50.0	1.231	3.19E-01	1200	10.0
8	760	150.0	110.0	0.0	2.258	5.79E-01	1000	10.0
9	760	150.0	10.0	100.0	0.205	5.36E-02	1200	10.0

REFERENCES

[1] Daniel Louis Jean. *Design and Operation of an Advanced Laser Chemical Vapor Deposition System with On–Line Control*. PhD dissertation, Georgia Institute of Technology, Mechanical Engineering, June 2001.

[2] Chad Edward Duty. *Design, Operation, and Heat and Mass Transfer Analysis of a Gas-Jet Laser Chemical Vapor Deposition*. PhD dissertation, Georgia Institute of Technology, Mechanical Engineering, December 2001.

[3] Chad E. Duty, Daniel L. Jean, and W. Jack Lackey. Laser Chemical Vapor Deposition: Materials, Models, and Process Control. *International Materials Review*, 46(6):271–87, 2001.

[4] Lloyd S. Nelson and Norman L. Richardson. Formation of thin rods of pyrolytic carbon by heating with a focused carbon dioxide laser. *Materials Research Bulletin*, 7:971–76, 1972.

[5] Thomas H. Baum and Paul B. Comita. Laser–induced chemical vapor deposition of metals for microelectronics technology. *Thin Solid Films*, 218:80–94, 1992.

[6] Y. Morishige and S. Kishida. Thick gold-film deposition by high-repetition visible pulsed-laser chemical vapor deposition. *Applied Physics A*, 59:395–99, 1994.

[7] W. M. Grossman and M. Karnezos. Localized laser chemical processing of tungsten films. *Journal of Vacuum Science Technology B*, 5(4):843–47, 1987.

[8] L. Economikos, D. E. Kotecki, and R. Surprenant. Controlling the dimensions of laser chemical vapor deposited metallurgy. *Journal of Electronic Packaging*, 118:7–10, March 1996.

[9] Michael C. Wanke, Olaf Lehmann, Kurt Muller, Qingzhe Wen, and Michael Stuke. Laser rapid prototyping of photonic band-gap microstructures. *Science*, 275:1284–86, 28 February 1997.

[10] Jr. Robert N. Dean, Paul C. Nordine, and Christos G. Christodoulou. 3-d helical thz antennas. *Microwave and Optical Technology Letters*, 24(2):106–111, 2000.

[11] Johnnie L. Hixson, Christopher S. Cassidy, Robert L. Stewart, Robert M. Taylor, Lowell R. Matthews, Kenneth H. Church, Robert Mamazza, and Christos S. Ferekides. Fabrication of solar-cell-quality cadmium sulfide layers via laser-assisted chemical vapor deposition (lcvd). In *Material Research Society Symposium Proceedings*, volume 668, pages H8.4.1–H8.4.6, 2001.

[12] J. Maxwell, M. Boman, K. Williams, K. Larson, N. Jaikumar, and G. Saiprasanna. High-speed laser chemical vapor deposition of amorphous carbon fibers, stacked conductive coils, and folded helical springs. In *SPIE Conference on Micromachining and Microfabrication Process Technology V*, volume 3874, pages 227–35, September 1999.

[13] K. Williams, N. Jaikumar, G. Saiprasanna, M. Hegler, and J. Maxwell. The laser microchemical lathe: Rapid freeform part fabrication from the vapor phase. In *Proc. Tenth Annual Solid Freeform Fabrication Symposium*, pages 543–51, August 1999.

[14] K. L. Bjorklund, C. Ribbing, H. Norde, and M. Boman. Containerless fabrication of tungsten single crystals using laser cvd for field emission applications. *Applied Physics A*, 75:493–6, 2002.

[15] Brian Thomas Fuhrman. *Fabrication of Advanced Thermionic Emitters Using Laser Chemical Vapor Deposition-Rapid Prototyping*. MS thesis, Georgia Institute of Technology, Mechanical Engineering, August 2001.

[16] Wayne Ohlinger. Conversation on the nature of dispenser cathodes, 1 March 2003.

[17] Frank P. Incropera and David P. DeWitt. *Fundamentals of Heat and Mass Transfer*. John Wiley & Sons, New York, fourth edition, 1996.

[18] C. H. J. van den Brekel. Characterization of chemical vapour–deposition processes. *Philips Research Reports*, 32:118–33, 1977.

[19] Donald C. O'shea. *Elements of Modern Optical Design*, chapter 7, pages 230–69. Wiley–Interscience, 1985.

[20] Z. Kang, R. W. Johnson, J. Mi, S. Bondi, M. Jiang, J. Gillespie, W. J. Lackey, S. Stock, and K. More. Microstructure of carbon fibers prepared laser lcvd. *Carbon*, 42:2721–27, 2004.

[21] Jyoti Mazumder and Aravinda Kar. *Theory and Application of Laser Chemical Vapor Deposition*. Plenum Press, New York, 1995.

[22] V. Hopfe, R. Jackel, and K. Schonfeld. Laser based coating and modification of carbon fibres: application of industrial lasers to manufacturing of composite materials. *Applied Surface Science*, 106:60–66, 1996.

[23] King Hong Kwok and Wilson K. S. Chiu. Open–air carbon coatings on fused quartz by laser–induced chemical vapor deposition. *Carbon*, 41:673–80, 2003.

[24] Joseph Pegna, David Messia, and Woo Ho Lee. Trussed structures: Freeform fabrication without the layers. In *Proc. Eigth Annual Solid Freeform Fabrication Symposium*, pages 49–58, 1997.

[25] Daniel L. Jean, Chad E. Duty, Ryan W. Johnson, Scott N. Bondi, and W. Jack Lackey. Carbon fiber growth kinetics and thermodynamics using temperature controlled lcvd. *Carbon*, 40(9):1435–45, 2002.

[26] Ryan W. Johnson, Scott N. Bondi, Daniel L. Jean, Chad E. Duty, M. Jiang, and W. Jack Lackey. Fabrication of multi-layered carbon structures using lcvd. In D. L. Bourell and et al., editors, *Proc. Twelfth Annual Solid Freeform Fabrication Symposium*, pages 61–68, University of Texas, Austin, Texas, August 2001.

[27] Ryan W. Johnson, Jae hyoung Park, David W. Rosen, and W. Jack Lackey. Deposition modeling in the laser chemical vapor deposition (lcvd) of metals and ceramics. In *Proc. First International Conference on Advanced Research in Virtual and Rapid Prototyping*, Leiria, Portugal, October 2003.

[28] Jae hyoung Park. *Process Planning for Laser Chemical Vapor Deposition*. MS thesis, Georgia Institute of Technology, Mechanical Engineering, 2003.

[29] Christina Gomez-Aleixandre, Domingo Diaz, Felipe Orgaz, and Jose M. Albella. Reaction of diborane and ammonia gas mixtures in a chemical vapor deposition hot-wall reactor. *Journal of Physical Chemistry*, 97:11043–46, 1993.

[30] V. N. Demin, I. P. Asanov, and Z. L. Akkerman. Chemical vapor deposition of pyrolytic boron nitride from borazine. *Journal of Vaccuum Science Technology A*, 18(1):94–98, 2000.

[31] M. V. Ugarov, V.P. Ageev, and V.I. Konov. Excimer laser induced chemical vapor deposition of boron nitride films from borazine. In *Proceedings of SPIE - The International Society for Optical Engineers*, volume 2547, 1995.

[32] P.A. Molian. Laser physico-chemical vapour deposition of cubic boron nitride thin films. *Journal of Materials Science*, 29(21):5646–56, Nov 1 1994.

[33] A. C. Adams. Characterization of films formed by pyrolysis of borazine. *Journal of the Electrochemical Society*, 128(6):1378–79, 1981.

[34] Christina Gomez-Aleixandre, Domingo Diaz, Felipe Orgaz, and Jose M. Albella. Influence of diborane flow rate on the structure and stability of cvd boron nitride films. *Journal of Physical Chemistry*, 100:2148–2153, 1996.

[35] Robert R. Rye. Hot filament activated chemical vapor deposition of boron nitride. *Journal of Vaccuum Science Technology A*, 9(3):1099–1103, 1991.

[36] J. Kouvetakis, V. V. Patel, C. W. Miller, and D. B. Beach. Composition and structure of boron nitride films deposited by chemical vapor deposition from borazine. *Journal of Vaccuum Science Technology*, 8(6):3929–33, Nov/Dec 1990.

[37] W. F. Kane, S. A. Cohen, J. P. Hummel, and B. Luther. Use of sibn and sibon films prepared by plasma enhanced chemical vapor deposition from borazine as interconnection dielectrics. *Journal of the Electrochemical Society*, 144(2):658–63, Feb 1997.

[38] M. L. Kosinova, Yu. M. Rumyantsev, N. I. Fainer, and F. A. Kuznetsov. Rpecvd boron nitride layers from borazine as single-source precursor. In M.D. Allendorf and C. Bernard, editors, *Electrochemical Society Proceedings*, volume 97, pages 441–46, 1997.

[39] Tamara P. Smirnova, Masami Terauchi, Futami Sato, Kichiro Shibata, and Michiyoshi Tanaka. Structure of the boron nitride films obtained by rpecvd from borazine. *Chemistry for Sustainable Development*, 8:63–67, 2000.

[40] Seon Hyo Kim, Ig Hyeon Kim, and Ki Sung Kim. Preparation of cubin boron nitride thin film by the helicon wave plasma enhanced chemical vapor deposition. *Applied Physics Letters*, 69(26):4023–25, December 23 1996.

[41] Seon Hyo Kim, Ig Hyeon Kim, and Ki Sung Kim. Characterization of helicon wave plasma for a thin film deposition process. *Journal of Vaccuum Science Technology A*, 15(2):307–12, Mar/Apr 1997.

[42] M. J. Paisley, L. P. Bourget, and R. F. Davis. Boron nitride thin films by microwave ecr plasma chemical vapor deposition. *Thin Solid Films*, 235:30–34, 1993.

[43] S. Shanfield and R. Wolfson. Ion beam synthesis of cubic boron nitride. *Journal of Vaccuum Science Technology A*, 1(2):323–25, Apr-Jun 1983.

[44] Chad E. Duty, Ryan W. Johnson, Scott N. Bondi, and W. Jack Lackey. Pyrolytic laser chemical vapor deposition of boron nitride and molybdenum. *Chemical Vapor Deposition*, 9(6):298–301, December 12 2003.

[45] S. M. Gates, C. M. Chiang, and D. B. Beach. Diffusion effects and nucleation of thin film boron nitride growth from borazine on the si(100) surface. *Journal of Applied Physics*, 72(1):246–52, July 1992.

[46] W. J. Childs, J. E. Cline, W. M. Kisner, and John Wulff. Molybdenum plating by reduction of the pentachloride vapor. In *Transactions of the ASM*, volume 43, pages 105–121, 1951.

[47] Takuo Sugano, Hsun-Kwei Chou, Minoru Yoshida, and Tateki Nishi. Chemical deposition of mo on si. *Japanese Journal of Applied Physics*, 7(9):1028–38, 1968.

[48] Kazumitsu Yasuda and Junichi Murota. Molybdenum film formation by low pressure chemical vapor deposition. *Japanese Journal of Applied Physics*, 22(10):L615–L617, October 1983.

[49] Noboru Yoshikawa and Atsushi Kikuchi. Growth rate and microstructure of mo film by chemical vapour deposition. *Materials Transactions, JIM*, 37(3):283–88, 1996.

[50] K. L. Bjorklund, P. Heszler, and M. Boman. Laser–assisted growth of molybdenum rods. *Applied Surface Science*, 186:179–83, 2002.

[51] F. A. Houle and K. A. Singmaster. Visible laser–induced nucleation and growth of cr, mo, and w films from the hexacarbonyls. reactivity of co on film surfaces. *Journal of Physical Chemistry*, 96:10425–39, 1992.

[52] W. Radloff and E. Below. Direct writing of metal thin film microstructures. In *Trends in Quantum Electronics*, volume 34, pages 931–33, Bucharest, 4 September 1989.

[53] G. Reisse, F. Gaensicke, R. Ebert, and U. Illmann. Laser–induced chemical vapour deposition of conductive and insulating thin films. *Applied Surface Science*, 54:84–88, 1992.

[54] S. A. Kokorowski, G. L. Olson, and L. D. Hess. Thermal analysis of cw laser annealing beyond the melt temperature. In *Proceedings of the Conference on "Laser and electron–beam solid interactions and material processing*, volume 1, pages 139–46, 1981.

[55] M. Lax. Temperature rise induced by a laser beam. *Journal of Applied Physics*, 48(9):3919–24, 1977.

[56] H. E. Cline and T. R. Anthony. Heat treating and melting material with a scanning laser or electron beam. *Journal of Applied Physics*, 48:3895–900, 1977.

[57] J. E. Moody and R. H. Hendel. Temperature profiles induced by a scanning cs laser beam. *Journal of Applied Physics*, 53(6):4364–71, 1982.

[58] A. Kar and J. Mazumder. Three–dimensional transient thermal analysis for laser chamical vapor deposition on uniformly moving finite slabs. *Journal of Applied Physics*, 65(8):2923–34, 15 April 1989.

[59] Tapio T. Rantala and Juhani Levoska. A numerical simulation method for the laser–induced temperature distribution. *Journal of Applied Physics*, 65(12):4475–79, 15 June 1989.

[60] Toivo T. Kodas, Thomas H. Baum, and Paul B. Comita. Surface temperature rise in multilayer solids induced by a focused laser beam. *Journal of Applied Physics*, 61(8):2749–53, 15 April 1987.

[61] The Thermal History of a Spot Heated by a Laser. W. m. steen. *Letters in Heat and Mass Transfer*, 4:167–78, 1977.

[62] D. Yu and A. B. Duncan. Investigation of induced thermal and fluid transport phenomena in laser assisted chemical vapor deposition. In *Proceedings of the ASME Heat Transfer Division*, volume 4, pages 183–91, 1998.

[63] Yuwen Zhang. Quasi–steady state natural convection in laser chemical vapor deposition with a moving laser beam. *Journal of Heat Transfer*, 125(3):429–37, June 2003.

[64] Scott Nicholas Bondi. *LCVD Synthesis of Carbon Nanotubes and their Characterization*. PhD dissertation, Georgia Institute of Technology, December 2004.

[65] Chad E. Duty, Brian Fuhrman, Daiel L. Jean, and W. J. Lackey. Heat transfer analysis of a gas-jet laser chemical vapor deposition process. In *Proceedings of the Solid Freeform Fabrication Symposium*, pages 461–68, Austin, TX, 2000.

[66] Chad E. Duty, Ryan W. Johnson, Daniel L. Jean, Scott N. Bondi, and W. J. Lackey. Thermal, fluid, and mass transport modeling of a gas–jet reagent delivery system for laser chemical vapor deposition. In *Proceedings of the Solid Freeform Fabrication Symposium*, pages 373–80, Austin, TX, 2001.

[67] Chad E. Duty, Ryan W. Johnson, Joshua Gillespie, Andrei Fedorov, and W. Jack Lackey. Heat and mass transfer modeling of an angled gas-jet lcvd system. *Journal of Applied Physics A*, 77(5):697–705, 2003.

[68] F. A. Kuznetsov, A. N. Golubenko, and M. L. Kosinova. A thermodynamic approach to chemical vapor deposition of boron nitride thin films from borazine. *Applied Surface Science*, 113/114:638–41, 1997.

[69] S. Park and S. Lee. Growth kinetics of microscopic silicon rods grown on silicon substrates by the pyrolytic laser–induced cvd process. *Japanese Journal of Applied Physics*, 29(1):L129–132, 1990.

[70] Jaesung Han and Klavs F. Jensen. Combined experimental and modeling studies of laser–assisted chemical vapor deposition of copper from copper(i)–hexafluoroacetylacetonate trimethylvinylsilane. *Journal of Applied Physics*, 75(4):2240–50, 15 February 1994.

[71] R. Nassar, C. Zhang, W. Dai, H. Lan, and J. Maxwell. Mathematical modeling of three–dimensional kinetically–limited laser chemical vapor deposition. *Microelectronic Engineering*, 60:395–408, 2002.

[72] A. Fischer, G. Reisse, and F. Gansicke. Theroretical and experimental studies of laser–induced chemical vapour deposition of silicon thin films. *Applied Surface Sciences*, 54:41–45, 1992.

[73] D. Bauerle, B. Luk'yanchuk, and K. Piglmayer. On the reaction kinetics in laser–induced pyrolytic chemical processing. *Applied Physics A*, 50:385–96, 1990.

[74] N. Arnold, E. Thor, N. Kirichenko, and D. Bauerle. Pyrolytic lcvd of fibers: A theoretical description. *Applied Physics A*, 62:503–08, 1996.

[75] G. N. Koutlas and N. S. Vlachos. Numerical modeling of pyrolytic laser–induced chemical vapor deposition. *Journal of Applied Physics*, 93(5):3049–56, 1 March 2003.

[76] C. R. Moylan, T. H. Baum, and C. R. Jones. Lcvd of copper: Deposition rates and deposit shapes. *Applied Physics A*, 40:1–5, 1986.

[77] V. N. Bagratashvili, A. F. Banishev, S. A. Gnedoy, V. I. Emelyanov, A. N. Jerikhin, K. S. Merzljakov, V. Ya. Panchenko, and V. N. Seminogov. Formation of periodic ring structures of relief and voids under laser vapor deposition of metallic films. *Applied Physics A*, 52:438–44, 1991.

[78] G. Leyendecker, D. Bauerle, P. Geittner, and H. Lydtin. Laser induced chemical vapor deposition of carbon. *Applied Physics Letters*, 39(11):921–23, 1 December 1981.

[79] Stefan Johansson, Jan-Ake Schweitz, Helena Westberg, and Mats Boman. Microfabrication of three–dimensional boron structures by laser chemical processing. *Journal of Applied Physics*, 72(12):5956–63, 15 December 1992.

[80] S. Boughaba and G. Auvert. Deposition of micron–size nickel lines by argon–ion laser–assisted decomposition of nickel tetracarbonyl. *Applied Surface Science*, 69:79–86, 1993.

[81] Helena Westberg, Mats Boman, and Jan-Otto Carlsson. Kinetics in thermal laser–assisted chemical vapour deposition of titanium carbide. *Thin Solid Films*, 218:8–14, 1992.

[82] D. Milne, J. Wilson, T. Rantala, and J. Lenkkeri. Morphological and structural changes in laser cvd of silicon: Comparison of theoretical temperature calculations with experimental results. *Applied Surface Science*, 43:81–86, 1989.

[83] Y. C. Du, U. Kempfer, K. Piglmayer, D. Bauerle, and U. M. Titulaer. New types of periodic structures in laser–induced chemical vapor deposition. *Applid Physics A*, pages 167–71, 1986.

[84] Joshua Gillespie. Fabrication of carbon/silicon carbide laminate composites by laser chemical vapor deposition and their microstructural characterization. Master's thesis, Georgia Institute of Technology, May 2004.

[85] G. Leyendecker, H. Noll, D. Bauerle, P. Geittner, and H. Lydtin. Rapid determination of apparent activation energies in chemical vapor deposition. *Journal of the Electrochemical Society: Solid–State Science and Technology*, 130(1):157–60, 1983.

[86] Mats Boman, Helena Westberg, Stefan Johansson, and Jan-Ake Schweitz. Helical microstructures grown by laser assisted chemical vapour deposition. In *Proceedings of the MicroElectroMechanical Systems Conference*, pages 162–167, Travemunde, Germany, 4–7 February 1992. IEEE.

[87] Frederick T. Wallenberger and Paul C. Nordine. Strong, small diameter, boron fibers by lcvd. *Materials Letters*, 14(4):198–202, 1992.

[88] Frederick T. Wallenberger and Paul C. Nordine. Strong, pure, and uniform carbon fibers obtained directly from the vapor phase. *Science*, 260:66–68, 2 April 1993.

[89] F. A. Houle, C. R. Jones, T. Baum, C. Pico, and C. A. Kovac. Laser chemical vapor deposition of copper. *Applied Physics Letters*, 46(2):204–06, 15 January 1985.

[90] M. Jubber, J. I. B. Wilson, J. L. Davidson, P. A. Fernie, and P. John. Laser writing of high–purity gold lines. *Applied Physics Letters*, 55(14):1477–79, 2 October 1989.

[91] Chad E. Duty, Daniel L. Jean, and W. Jack Lackey. Design of a laser CVD rapid prototyping system. In *Ceramic Engineering and Science Proceedings*, volume 20, pages 347–54, 1999.

[92] Daniel L. Jean, Chad E. Duty, Brian T. Fuhrman, and W. Jack Lackey. Precision lcvd system design with real time process control. In D. L. Bourell and et al., editors, *Proc. Tenth Annual Solid Freeform Fabrication Symposium*, pages 59–65, University of Texas, Austin, Texas, aug 1999.

[93] W. Jack Lackey, Chad E. Duty, Daniel L. Jean, Brian T. Fuhrman, and Wayne Ohlinger. Laser cvd rapid prototyping. In N.P. Bansal and J.P. Singh, editors, *Innovative Processing and Synthesis of Ceramics, Glasses, and Composites IV*, volume 115, pages 123–29, 2000.

[94] M. Bruggert, Z. Hu, and K. J. Huttinger. Chemistry and kinetics of chemical vapor deposition of pyrocarbon vi: Influence of temperature using methane as a carbon source. *Carbon*, 37(12):2021–30, 1999.

[95] K. Aoki, M. Y. Cheng, T. Hirai, and S. Yajima. Thermal expansion of siliconated pyrolytic carbon. *Journal of Materials Science*, 9:1159–64, 1974.

[96] R. Byron Bird, Warren E. Stewart, and Edwin N. Lightfoot. *Transport Phenomena*. John Wiley & Sons, Inc., New York, second edition, 2002.

[97] L. V. Gurvich, I. V. Veyts, and C. B. Alcock. *Thermodynamic Properties of Individual Substances*, volume 1 and 2. Hemishere, New York, 4th edition, 1989.

[98] P. J. Linstrom and W. G. Mallard. *NIST Chemistry WebBook, NIST Standard Reference Database Number 69*. National Institute of Standards and Technology, Gaithersburg, MD, 20899, March 2003. http://webbook.nist.gov.

[99] Jr. M. W. Chase. *NIST-JANAF Thermochemical Tables*. National Institute of Standards and Technology, fourth edition, 1998.

[100] Jr. Henry A. McGee. *Molecular Engineering*. McGraw-Hill, Inc., 1991.

[101] Y. S. Touloukian and E. H. Buyco. *Thermophysical Properties of Matter*, volume 5. IFI/Plenum, New York – Washington, 1970.

[102] Y. S. Touloukian, R. W. Powell, C. Y. Ho, and P. G. Klemens. *Thermophysical Properties of Matter*, volume 2. IFI/Plenum, New York – Washington, 1970.

[103] Y. S. Touloukian, R. W. Powell, C. Y. Ho, and P. G. Klemens. *Thermophysical Properties of Matter*, volume 13. IFI/Plenum, New York – Washington, 1970.

[104] Hugh O. Pierson. *Handbook of Carbon, Graphite, Diamond, and Fullerenes*. Noyes Publications, Park Ridge, New Jersey, USA, 1993.

[105] Cambridge. Cambridge material selector. In *CES*. Cambridge, 2000.

[106] Boron Technologies. Property data sheet. Technical report, Boron Technologies, 2001.

[107] James P. Schaffer, Ashok Saxena, Stephen D. Antolovich, Jr. Thomas H. Sanders, and Steven B. Warner. *The Science and Design of Engineering Materials*. Irwin, 1995.

[108] General Electric Advanced Ceramics. Pyrolytic boron nitride. Internet, last accessed 14 Nov 2004.

[109] Y. S. Touloukian, R. W. Powell, C. Y. Ho, and P. G. Klemens. *Thermophysical Properties of Matter*, volume 1. IFI/Plenum, New York – Washington, 1970.

[110] D. R. Stull and H. Prophet. *JANAF Thermochemical Tables*. Office of Standard Reference Data – National Bureau of Standards, Washington, D. C., second edition, 1971.

[111] General Electric Advanced Ceramics. Hot pressed boron nitride shapes. Internet, last accessed 27 Oct 2004.

[112] T. Besmann. SOLGASMIX-PV, a computer program to calculate equilibrium relationships in complex chemical systems. Technical Report ORNL/TM-5775, Oak Ridge National Laboratory, Oak Ridge, TN, April 1977.

[113] G. Eriksson. Thermodynamic studies of high temperature equilibria, xii. SOLGASMIX, a computer program for calculation of equilibrium compositions in multiphase systems. *Chem. Sce.*, 8:100–103, 1975.

[114] Yuzo Saeki and Ryoko Matsuzaki. Contributions to the chemistry of chlorides of molybdenum. ii. thermodynamic properties of molybdenum pentachloride. *Japanese Journal of the Electrochemical Society*, 33(1):59–60, 1965.

[115] M. Khelkhal and F. Herlemont. Infrared optical constants of polycrystalline boron nitride. *Applied Optics*, 32(1):57–59, 1 January 1993.

VITA

Ryan William Johnson, the son of Jim and Jean Johnson, is a native of Clinton, South Carolina where he attended Clinton High School and graduated at the top of his class in 1995. He entered Georgia Tech in the fall of 1995 and began pursuit of his bachelor's degree in mechanical engineering with a minor in economics. During his undergraduate years, between 1996 and 1998, he worked as a co-op mechanical engineer for the Kimberly–Clark Corporation in Lexington, North Carolina and Roswell, Georgia. In August 2000, after receiving his bachelor's degree in May, he entered graduate school at Georgia Tech to study mechanical engineering. In September 2002, he married another Georgia Tech alum, Ms. Alisha Mae Landers. In December 2003, he received his master's degree from Georgia Tech in mechanical engineering, and then continued working toward his Ph.D. under the direction of Dr. Jack Lackey.